NASA TECHNICAL MEMORANDUM

NASA TM X-2570

NASA TM X-2570

DISTRIBUTION STATEMENT A

Approved for public release; Distribution Unlimited

PLASTEC 17807

NASA SPACE SHUTTLE TECHNOLOGY CONFERENCE

Dynamics and Aeroelasticity; Structures and Materials

Held at
San Antonio, Texas
April 12-14, 1972

19960419 005

NATIONAL AERONAUTICS AND SPACE ADMINISTRATION • WASHINGTON, D. C. • JULY 1972

DTIC QUALITY INSPECTED 1

1. Report No. NASA TM X-2570	2. Government Accession No.	3. Recipient's Catalog No.
4. Title and Subtitle NASA SPACE SHUTTLE TECHNOLOGY CONFERENCE – Dynamics and Aeroelasticity; Structures and Materials		5. Report Date July 1972
		6. Performing Organization Code
7. Author(s)		8. Performing Organization Report No. L-8393
		10. Work Unit No.
9. Performing Organization Name and Address		11. Contract or Grant No.
		13. Type of Report and Period Covered Technical Memorandum
12. Sponsoring Agency Name and Address National Aeronautics and Space Administration Washington, D.C. 20546		14. Sponsoring Agency Code

15. Supplementary Notes

Held at San Antonio, Texas, April 12-14, 1972.

16. Abstract

A NASA Space Shuttle Technology Conference was held in San Antonio, Texas, April 12-14, 1972, in conjunction with the AIAA/ASME/SAE 13th Structures, Structural Dynamics and Materials Conference. The space shuttle conference reported the results to date by NASA and its contractors on the technology in the areas of (1) Aeroelasticity and Loads, (2) Structure/Liquid Interactions, (3) Vehicle Dynamic Test and Analysis, (4) Thermal Protection Systems, and (5) Structural Design. This publication is a compilation of the conference papers presented.

17. Key Words (Suggested by Author(s)) Space shuttle; Dynamics; Aeroelasticity; Structural design; Thermal protection	18. Distribution Statement Unclassified – Unlimited

19. Security Classif. (of this report)	20. Security Classif. (of this page)	21. No. of Pages	22. Price*
Unclassified	Unclassified	784	$9.00

*For sale by the National Technical Information Service, Springfield, Virginia 22151

DISCLAIMER NOTICE

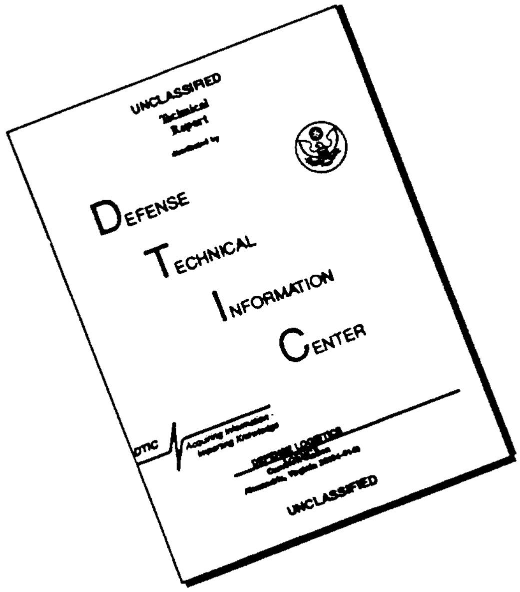

THIS DOCUMENT IS BEST QUALITY AVAILABLE. THE COPY FURNISHED TO DTIC CONTAINED A SIGNIFICANT NUMBER OF PAGES WHICH DO NOT REPRODUCE LEGIBLY.

PREFACE

This conference compilation is the third in a series of progress reports by the Dynamics and Aeroelasticity and the Structures and Materials Working Groups, which are two of the seven disciplinary teams organized within NASA to develop and enlarge the technology base for a space shuttle. The two previous major conferences were held in July 1970 at the Lewis Research Center in Cleveland, Ohio, and in March 1971 at the Langley Research Center in Hampton, Virginia. The 1972 technology conference was held in San Antonio, Texas, in conjunction with the AIAA/ASME/SAE 13th Structures, Structural Dynamics and Materials Conference.

We are now a little over 2 years into the planned shuttle technology development program and have made substantial progress. Because of the time required to achieve conclusive results in a program consisting of many long-lead-time experimental efforts, however, we are still on the uphill slope in achieving the data we set out to obtain. About 50 percent of the data are in hand, and progress reports on most of the critical program elements were presented at the conference. A major exception is the work on metallic materials; an extensive report was made at a SAMPE conference in Huntsville, Alabama, in October 1971.

Inasmuch as this conference fell in the midst of the time period in which industry was preparing proposals for design and construction of the space shuttle, most of the papers were prepared by NASA personnel. The data they are reporting have been obtained in-house at NASA centers and through contractual arrangements with many segments of American industry. Each author was asked simply to display all relevant data and state his views on its adequacy in meeting design objectives for the shuttle. These papers are supplemented by presentations of work carried out by The Aerospace Corporation, El Segundo, California, and Southwest Research Institute, San Antonio, Texas.

There has been a counterpart technology program carried out by various firms in Europe under the sponsorship of the European Space Vehicle Launcher Development Organization. Like the American program, the program in Europe has several tasks in different disciplines. They have been sharing their data with NASA and its shuttle contractors. Accordingly, this document also contains a paper summarizing work by several European firms on application of composite materials to a space shuttle.

CONTENTS

SESSION III - VEHICLE DYNAMIC TEST AND ANALYSIS

Co-Chairmen - Dennis J. Martin (LaRC) and R. S. Ryan (MSFC)

SESSION IV - THERMAL PROTECTION SYSTEMS

Co-Chairmen - Louis F. Vosteen (LaRC)
and David H. Greenshields (MSC)

SESSION V - STRUCTURAL DESIGN

Chairman - Robert W. Leonard (LaRC)

GLOSSARY

AFFDL	Air Force Flight Dynamics Laboratory
ARC	Ames Research Center
ASCEP	advanced structural concepts experimental program
ASSET	aerothermodynamic/elastic structural systems environmental tests
B/A	boron/aluminum
BBN	Bolt Beranek and Newman, Inc.
B/E	boron/epoxy
BGRV	boost-glide reentry vehicle
BOSOR	buckling of shells of revolution
CG c.g.	center of gravity
CONC	concentrated
CONDS	conditions
COMP. COMP	compression
COSMIC	Computer Software and Management Center
CP	central processing; center of pressure
CPI	closed pore insulation

CPU	central processing unit
CRT	cathode ray tube
CY	calendar year
CYL	cylindrical
DAWNS	design of aircraft wing structures
DDT&E	design, development, testing, and evaluation
DEG.	degrees
DF&T	design, fabrication, and test
DOF	degrees of freedom
D.S.	dispersion stabilized
EB	electron beam
EDM	electrical discharge machining
ELDO	European Space Vehicle Launcher Development Organization
ENVIRON	environmental
F	fuel
FAB	fabrication; fabricated
FAS	fixed airlock shroud
FORTRAN	FORMula TRANslation

FPL	fluctuating pressure level
FRACT	fracture
FS	full scale
FWD	forward
G/E	graphite/epoxy
GFR	glass fiber reinforced
GH_2	gaseous hydrogen
gox	gaseous oxygen
G/Pi	graphite/polyimide
HC	honeycomb
HCF	hard and compacted fiber
HI-PC	high chamber pressure
HO H-O H/O	hydrogen oxygen
HT	heat treatment
HTST	Langley 8-foot high-temperature structures tunnel
H.W.	hoopwrapped
HYDRO	hydrodynamic

HYPER	hypersonic
IRAD	internal research and development
IU	instrument unit
LaRC LRC	Langley Research Center
LeRC	Lewis Research Center
LH_2	liquid hydrogen
LMSC	Lockheed Missiles and Space Company
LN_2	liquid nitrogen
LOX lox	liquid oxygen
MAC	marker and cell
MAT MAT'LS	materials
MECHS	mechanics
mil spec	military specification
MPS	multipoint constraint
MS	modal survey test
MSC	Manned Spacecraft Center
MSFC	Marshall Space Flight Center

MTF	Mississippi Test Facility
NASTRAN	NASA STRuctural ANalysis
NDE	nondestructive evaluation; nondestructive engineering
NDI	nondestructive inspection
NDT	nondestructive testing
NO.	number
NOL	Naval Ordnance Laboratory
NSMO	NASTRAN System Management Office
NSRDC	Naval Ships Research and Development Center
O	oxidizer
OAFPL	overall fluctuating pressure level
OASPL OA SPL	overall sound pressure level
OP	optimum
OPP	opportunity
OWS	orbital workshop shroud
PS	payload shroud
Q.A.	quality analysis

Q.C. / QC	quality control
RB	rigid body
RCS	reaction control system
REF. / REF	reference
REF. MET.	refractory metal
REI	reusable external insulation
REQMTS	requirements
RFP	request for proposal
RSI	reusable surface insulation
RTD&E	research, tests, development, and engineering
SALORS	Structural Analysis of Layered Orthotropic Ring-Stiffened Shells
SAMSO	Space and Missile System Organization
SAS	stability augmentation system
SAVES	Sizing of Aerospace Vehicle Structures
SEM	scanning electron microscope
SNAP	structural network analysis program
SRA	Structures Research Associates

SRM	solid rocket motors
SST	supersonic transport
SSV	space shuttle vehicle
STAGS	Structural Analysis of General Shells
STARS II	Shell Theory Automated for Rotational Structures
SUB	subsonic
SUPER	supersonic
S-IVB	Saturn IVB
SV	Saturn V
SYM	symmetry
TECH	technology
TECHS	techniques
TEMP.	temperature
TPS	thermal protection system
TPSTF	Langley thermal protection system test facility
TRANS	transonic
TVC	thrust vector control
TWD	tail wags dog

ULT.	ultimate
UPWT	Langley Unitary Plan wind tunnel
UT	ultrasonic techniques (test)
VA	vibroacoustic test
WT	weight
XRD	X-ray diffraction
3-D	three-dimensional

FLUTTER TECHNOLOGY FOR SPACE SHUTTLE

By Robert C. Goetz

NASA Langley Research Center
Hampton, Virginia

SUMMARY

The space shuttle flutter technology program has been developed around three main objectives: (1) To identify unique new problems associated with proposed vehicle configurations and their related flight profiles, (2) to develop the analytical and experimental techniques needed to predict flutter boundaries and insure adequate flutter margins, and (3) to anticipate problems associated with aeroelastic-model and full-scale testing to validate flutter clearance. The emphasis of this paper is on the latter two phases of the program. Results illustrating the best available tools for subsonic and supersonic flutter prediction are presented. Programs currently underway which will help overcome the difficult problems envisioned for the transonic wind-tunnel and flight flutter test program are also discussed.

INTRODUCTION

Because the structural design of aerospace vehicles is often significantly influenced by flutter clearance requirements, the pertinent flutter boundaries must be accurately known early in the design process if sizable weight penalties and costly fixes are to be avoided. Generally, flutter requirements are established in several stages of combined analyses and tests. Preliminary flutter requirements are determined from subsonic flutter calculations and from an estimate of the transonic flutter characteristics based on experimental data since no reliable analytical method exists for the transonic range. From these preliminary estimates flutter problem areas are defined, and as the vehicle design evolves, further analyses and tests are made with more exactly scaled component models to explore these problem areas and to optimize the design from a flutter standpoint. Finally, as the vehicle design becomes fixed, detailed analyses and sophisticated large-scale complete-vehicle aeroelastic models are used to demonstrate flutter clearances and to provide guidance for flight flutter tests.

Since flutter is very much a function of a vehicle's configuration and the severity of its mission, the specific analytical programs and wind-tunnel and flight tests that comprise the general flutter program vary with each new class of vehicles. Often new flutter problem areas are uncovered which dictate refinements in flutter technology in order to understand, predict, and avoid them. It is the purpose of this paper to discuss several potential flutter problem areas that may be unique to emerging space shuttle configurations and to outline the approaches that have been, and are continuing to be, undertaken in the flutter technology program to insure minimum risk for the vehicle's development.

FLUTTER OF LIFTING AND CONTROL SURFACES

(Figure 1)

There appear at this time to be two potential flutter problem areas associated with the 040-A orbiter. The first is associated with the heavy reaction control system (RCS) modules that are mounted on the wing tips. These modules are positioned in an aft location on the tip chord to provide efficient control while avoiding induced aerodynamic heating effects. This RCS module arrangement lowers the modal frequencies of the wing - for example, the fundamental wing bending frequency would be reduced by about 50 percent. A flutter problem could exist if these lower wing frequencies coupled with other low frequencies of the vehicle system. The second potential problem area is associated with the large amount of fuselage flexibility which is inherent in the 040-A orbiter as a result of the large payload-bay cutout (presuming that the bay doors are not load-supporting structures). Preliminary analyses indicate that the lowest order flutter instability might be a coupling of fuselage and wing modes. Because of this possible occurrence, fuselage flexibility will have to be included in determining the lowest order flutter boundaries of the wing.

For the launch configuration, which is most critical for flutter since maximum dynamic pressures occur at transonic speeds during ascent, additional parameters appear to be important to the vehicle's flutter susceptibility. The aerodynamic interference between wing and first-stage tankage in the parallel arrangement is one such parameter. Flutter studies of wings in proximity (ref. 1) have shown that as the biplanar distance between them is reduced, flutter boundaries are lowered. A similar effect might be expected from the close proximity of the parallel tanks to the orbiter wing. Additionally, the flexible coupling of multibodies in proximity to the wing may influence the system's flutter susceptibility. Early testing is needed to determine the importance of these parameters.

FLUTTER OF LIFTING AND CONTROL SURFACES

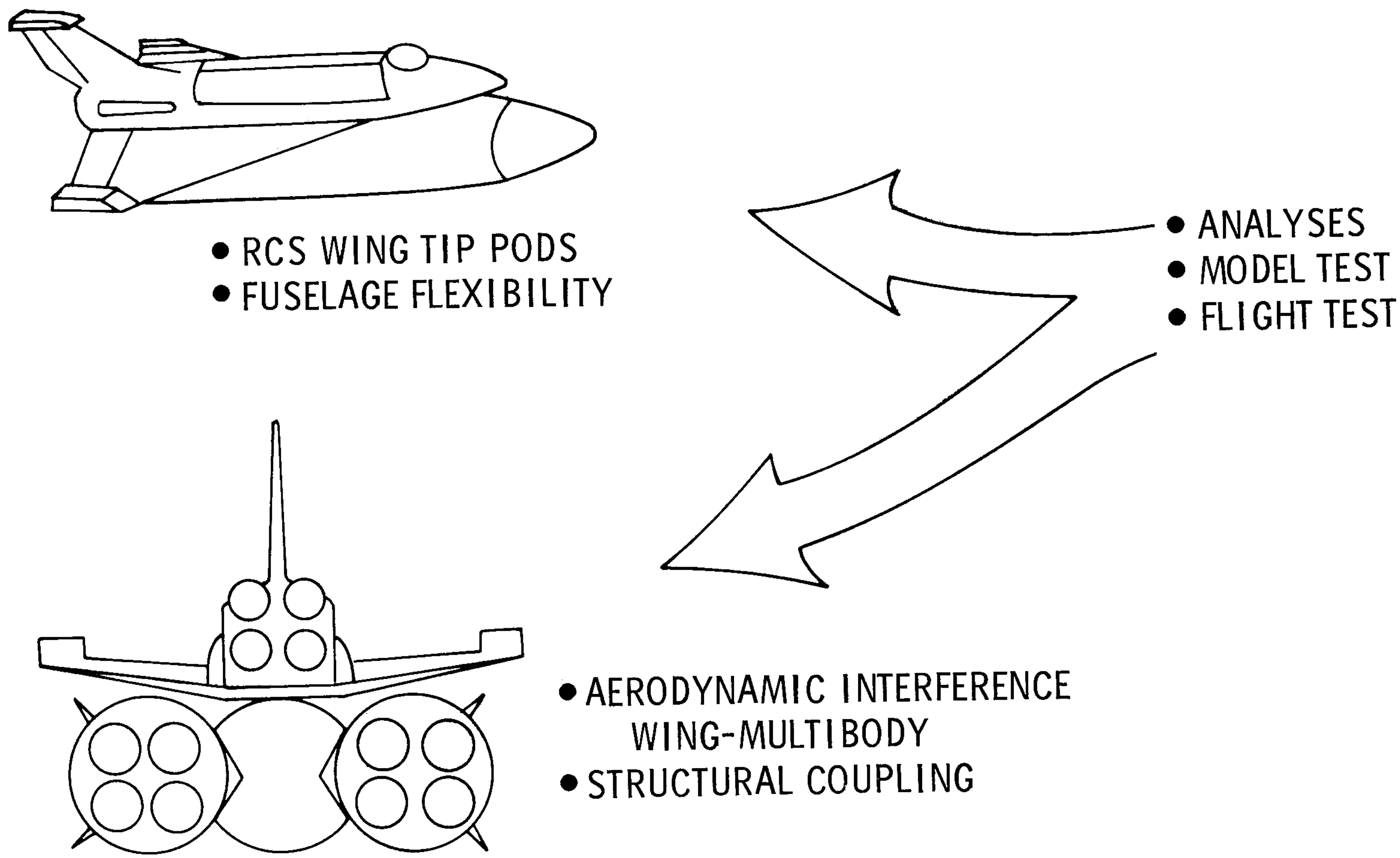

Figure 1

SPACE SHUTTLE FLUTTER TECHNOLOGY PROGRAM

(Figure 2)

The space shuttle flutter technology program of the Dynamics and Aeroelasticity Working Group was planned in three phases:

(1) Exploratory studies. These studies have been undertaken throughout phases A and B in an effort to uncover new flutter problem areas unique to shuttle configuration and operating concepts as they have evolved. These studies were designed to search for instabilities and unsteady detrimental loading conditions that normally are not the focus of the usual test program since they have not existed for previous new vehicles. If found, specific programs would have had to be designed to insure their avoidance.

(2) Develop experimental and analytical techniques. A continuing effort is made to have available reliable and the most up-to-date methods for conducting flutter evaluations of the shuttle vehicle, and to insure that these techniques for the shuttle are state-of-the-art in a timely manner.

(3) Preliminary evaluation. As configuration concepts evolve which incorporate features that are suspected of having flutter problems they are evaluated by analyses or tests. These results are obtained as early as possible since they might influence the vehicle design selection or necessitate design changes.

SPACE SHUTTLE FLUTTER TECHNOLOGY PROGRAM

- EXPLORATORY STUDIES
- DEVELOP EXPERIMENTAL AND ANALYTICAL TECHNIQUES
- PRELIMINARY EVALUATION

Figure 2

EXPLORATORY STUDIES

(Figure 3)

Examples of some of the exploratory flutter studies which have been conducted under the auspices of the technology program are indicated in figure 3. The stall flutter study included both straight and delta wings rotating through angle-of-attack ranges from 0° to 90° to simulate the reentry transition maneuver over the Mach number range from 0.2 to 1.2. Results from this study are given in reference 1. It might be noted that stall flutter of straight-wing designs dictated the torsional stiffness requirements for the wing.

The biplane flutter study depicted in figure 3 was another exploratory wind-tunnel program. This program was conducted because thick straight wings operating in close proximity at transonic speeds had never been investigated. It was found that as the wings were located closer to one another a severe flutter penalty resulted. Details of the study and the results can be found in reference 1.

Another exploratory program was conducted at Langley Research Center to determine the nature of an unsteady hypersonic flow phenomenon, often referred to as hypersonic buzz, on a model representative of a generalized orbiter configuration. The tests, conducted in helium at a nominal Mach number of 17.5, were specifically directed at obtaining a better understanding of the character of the hypersonic flow field in the vicinity of a deflected control surface. Power spectral densities and root-mean-square values of surface pressure fluctuations were measured along the center line of the vehicle ahead of and on the flap. Flap deflections of 0°, 20°, 30°, 35°, 40°, and 60° were tested at various angles of attack from 0° to 37°. Details of the tests and the complete results obtained are given in reference 2. It is quite clear from these tests that under certain conditions, extremely unstable hypersonic flow patterns resulted. Prominent spectral energy peaks ranging between 12 and 22 Hz, full scale, were observed and could be correlated directly with large unsteady flow fields. The presence of unstable flow conditions was found to be strongly dependent on the presence of multiple shock interactions and their positions relative to the shear-layer reattachment point. A high-speed schlieren movie provided a general perspective of the hypersonic buzz phenomena and the parametric boundaries within which large-scale oscillatory instabilities occurred.

EXPLORATORY STUDIES

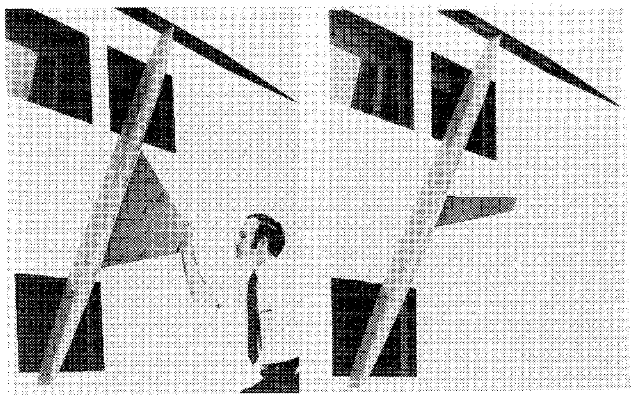

STALL FLUTTER

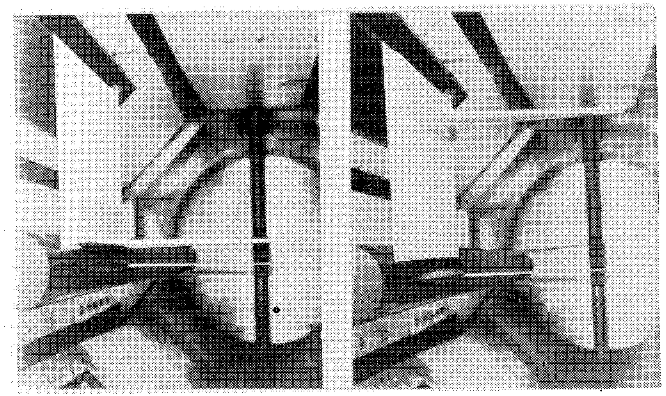

BIPLANE FLUTTER

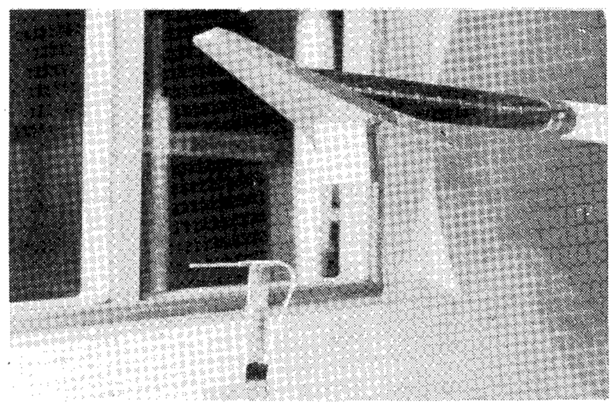

HYPERSONIC BUZZ

Figure 3

DEVELOPMENT OF EXPERIMENTAL AND ANALYTICAL TECHNIQUES

(Figure 4)

Assurance of flutter clearance is usually obtained in large wind tunnels, such as the Langley transonic dynamics tunnel, with aeroelastically scaled models. In these wind-tunnel tests representation of free-flight modes is an important aspect of flutter and aeroelastic studies which involve modeling the complete vehicle. A two-cable mount system that has been developed for flutter-model testing is illustrated in the photograph at the bottom of figure 4 flying the F-14 at high angles of attack. This mount system is being refined and adapted for shuttle configurations involving multibodies. In addition, the systems stability has to be evaluated, and testing techniques for buffet and flutter studies of shuttle configurations have to be developed.

An evaluation of the subcritical-response flutter techniques currently being used by industry has recently been initiated. Since the flight conditions will be rapidly changing with time for the shuttle during ascent and reentry, the emphasis is on transient methods. The existing candidate methods that appear applicable for flight flutter testing of shuttle vehicles will have their capabilities evaluated by means of mathematical models and wind-tunnel models.

Illustrated on the left of figure 4 are computer program cards symbolic of the computer programs that are essentially available and constitute the flutter prediction technology.

DEVELOP EXPERIMENTAL AND ANALYTICAL TECHNIQUES

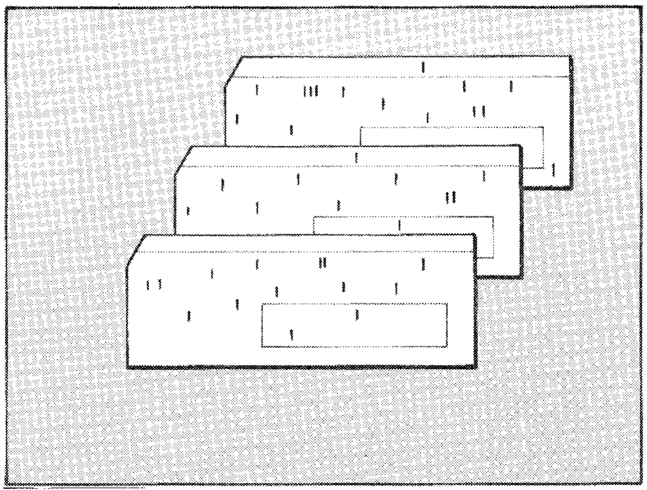

ANALYSES

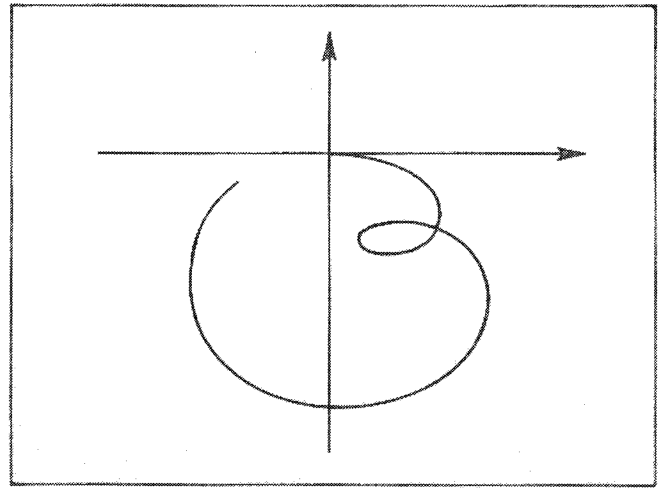

SUBCRITICAL RESPONSE

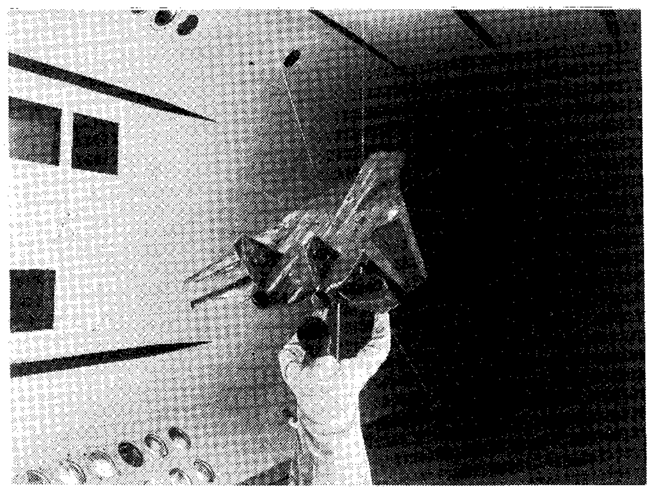

AEROELASTIC MODEL TEST

Figure 4

CURRENT STATE OF THE ART OF FLUTTER ANALYSES
(Figure 5)

Examination of the state of the art of flutter analyses indicates that transonic unsteady aerodynamics remains the unsolved problem. It is here that theoretical methods are most difficult and are not presently available. Some work has been done on the linearized theory for high-frequency oscillations, but nonlinear solutions seem to be unavoidable. Consequently, it does not appear that a viable transonic prediction method will be available for the shuttle development. The transonic regime will be the most critical for the space shuttle, not only because the minimum flutter speed will probably occur there, as it usually does, but also because that is where maximum dynamic pressures will be encountered. These facts place increased emphasis on the transonic test program, which will have to be relied upon heavily.

The prediction methods available in the subsonic and supersonic regimes are more highly developed. Linearized theory of unsteady aerodynamic flows has been developed to include intersecting and multiple surfaces. The shuttle technology program is supporting further development of these methods to make them applicable to a complete vehicle. Areas where the analyses still appear, to different degrees, to be marginal include wing thickness, bluntness, and angle of attack; control surfaces; and interference effects from large flexible fuselages.

Current efforts within the working group are concentrated on those methods which are developed to such a point that they will be useful tools for the shuttle program.

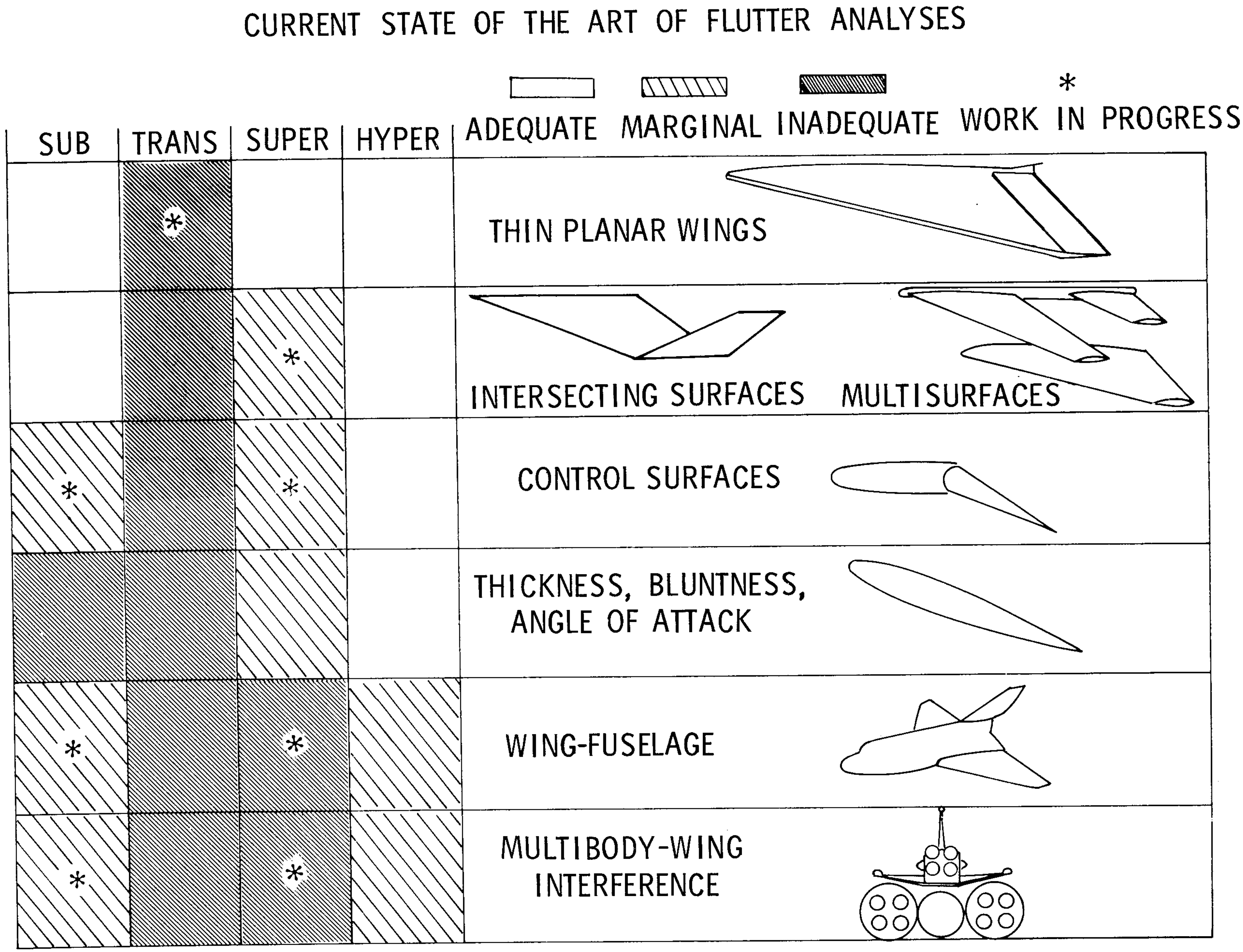
CURRENT STATE OF THE ART OF FLUTTER ANALYSES
ADEQUATE
MARGINAL
INADEQUATE
* WORK IN PROGRESS
SUB
TRANS
SUPER
HYPER
THIN PLANAR WINGS
INTERSECTING SURFACES
MULTISURFACES
CONTROL SURFACES
THICKNESS, BLUNTNESS, ANGLE OF ATTACK
WING-FUSELAGE
MULTIBODY-WING INTERFERENCE

Figure 5

ANALYTICAL TECHNIQUES

(Figure 6)

Computation of structural stiffness, inertia, and modal properties has reached a high degree of versatility and accuracy with the aid of finite-element techniques and high-speed digital computers. Evaluation of unsteady aerodynamic forces, with more involved fluid mechanics and boundary conditions, has progressed at a somewhat slower pace, but has over the past 10 years become more integrated with the structural aspects of the complete aeroelastic problem, also through the use of finite-element methods.

One such method is the doublet-lattice method, which is applicable to nonplanar configurations in subsonic flow. Reference 3 has shown the accuracy and versatility of the method for such nonplanar configurations as T-tails, wing-pylon combinations, annular wings, and, more importantly for shuttle application, multiple wings and wing-fuselage combinations. Through correlation (with results of other methods and with low-speed wind-tunnel data) excellent agreement has been obtained. High-subsonic and transonic data were not available on nonplanar configurations to complete the correlation throughout the subsonic regime. However, this is a deficiency that the shuttle technology program is currently attempting to overcome through wind-tunnel testing programs.

In the supersonic regime another nonplanar finite-element method which evaluates unsteady aerodynamic coefficients consistent with structural properties is the triangular-element method (ref. 4). This program has been evaluated for planar wings including controls, and the evaluation indicated that, with far less effort, better local as well as overall results could be obtained than with other methods such as the Mach box method. Recently the program has been extended to more complex problems, including nonplanar and interfering surfaces, and this extension is currently being evaluated. Conceptually, there is no barrier to the extension of the basis of the method to the complete wing-fuselage vehicle, and this will be the area of concentration for the shuttle technology support during the next year.

ANALYTICAL TECHNIQUES

SUBSONIC

DOUBLET-LATTICE

- MULTIPLE WINGS AND CONTROLS
- WING-BODY INTERFERENCE

SUPERSONIC

TRIANGULAR ELEMENT

- PLANAR WINGS
- NONPLANAR WINGS
- WING-BODY INTERFERENCE

Figure 6

ANALYTICAL RESULTS

(Figure 7)

Shown on the left of figure 7 is a subsonic (M = 0.4) analytical correlation with some biplane flutter-model test results. These test results were obtained from the biplane flutter study mentioned earlier, which was conducted in the Langley 26-inch transonic blowdown tunnel to determine the flutter characteristics of an unswept wing model with aspect ratio of 8 in proximity to a geometrically similar model. Both models had 12-percent-thick 64-series airfoil shapes. The tests were performed with the leading edges of the models alined and the distance between them varied from about $\frac{1}{4}$ to $2\frac{1}{4}$ mean-aerodynamic-chord lengths $\left(\frac{1}{4} \leqq \frac{h}{\bar{c}} \leqq 2\frac{1}{4}\right)$. The flutter speed V_f normalized by the flutter speed for a single wing $V_{f,o}$ is presented as a function of the inverse of the separation distance. It can be seen that the doublet-lattice results predict quite well the reduction in flutter speed as the distance between the wings is reduced. Additional correlations with experimental test results are underway to investigate interference effects on flutter for more realistic configurations over the entire subsonic regime.

Shown on the right of figure 7 are some flutter results obtained on a U.S. Army guided missile which had a newly added canard control surface. The missile experienced destructive flutter during its first flight, and the flutter speed is depicted by the solid circular symbol at a Mach number of 1.7. Two concurrent studies were undertaken, using two different aerodynamic theories to predict the flutter occurrence. Calculated flutter boundaries from these two studies are also shown in the figure. Of significance is the close agreement with the flight flutter point and the excellent agreement between the Mach box method and the newer triangular-element method. A "fix" was calculated by the triangular-element method and incorporated into the control-surface design, and the vehicle was then flown successfully (not shown in fig. 7).

ANALYTICAL RESULTS

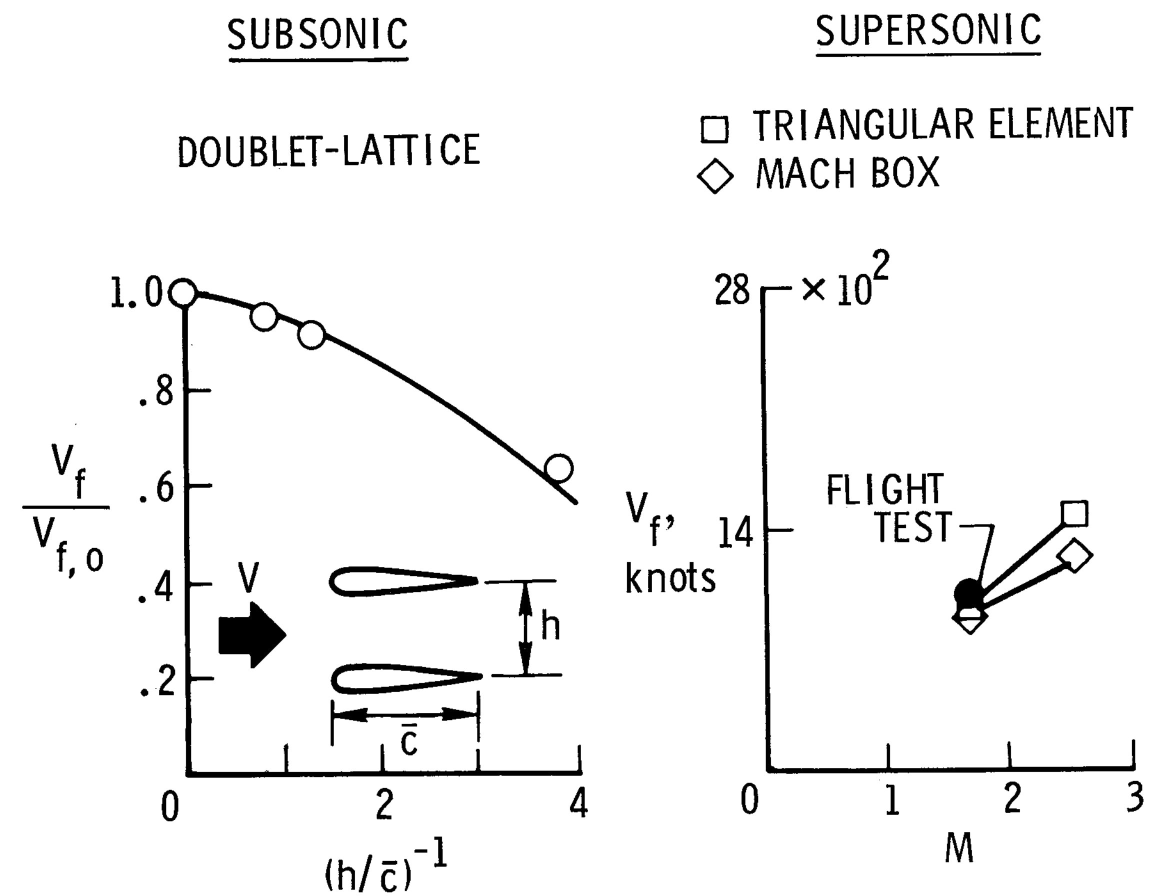

Figure 7

PRELIMINARY EVALUATION

(Figure 8)

The third phase of the flutter technology program, illustrated in figure 8, comprises some of the preliminary flutter evaluations that have been conducted as shuttle configuration concepts have evolved. One such study, shown on the left of the figure, was conducted to determine the effect of a large tip fin on the flutter characteristics of a scaled model of a proposed wing for a space shuttle launch vehicle. By comparing results for a model like the one shown with results for an identical model with the fin removed and replaced with ballast to simulate the mass and inertia of the fin, it was concluded that the tip fin had a detrimental effect on the flutter behavior of the proposed wing configuration. (See ref. 5.)

The photograph in the lower part of the figure illustrates aerodynamic interference effects of parallel first-stage tanks on the orbiter wing. These large, flexible, external tanks give rise to significant unsteady aerodynamic forces. It is postulated that shuttle wings in proximity with these bodies can experience substantial reductions in their flutter boundaries as a result of aerodynamic interference. To investigate this phenomenon a two-phase study has been initiated under the technology program, incorporating analysis and verification by model flutter testing of a typical complete shuttle configuration. In the first phase, characteristic flutter mechanisms of a representative configuration will be determined by the analytical study of such parameters as relative body geometries, body flexibilities, and coupling flexibilities. Analytical modeling techniques suitable for the solution of the problem will be developed. In the second phase, a model of the shuttle configuration will be wind-tunnel tested. Test results will be correlated with the analytically predicted trends. It is anticipated that this study will validate the applicability of the doublet-lattice method as a useful tool for the prediction of subsonic flutter of lifting surfaces in the presence of large flexible bodies.

In the photograph on the right of the figure is shown a 1/80-scale semispan model of the 040-A orbiter wing mounted on a reflection plane in the Langley 26-inch transonic blowdown tunnel. A flutter program was conducted to obtain a preliminary evaluation of the effect of the RCS pod on the flutter characteristics of the wing. Some preliminary flutter data have been obtained for the wing model with and without the RCS pod over the subsonic Mach number range from about 0.6 to 0.8.

PRELIMINARY EVALUATION

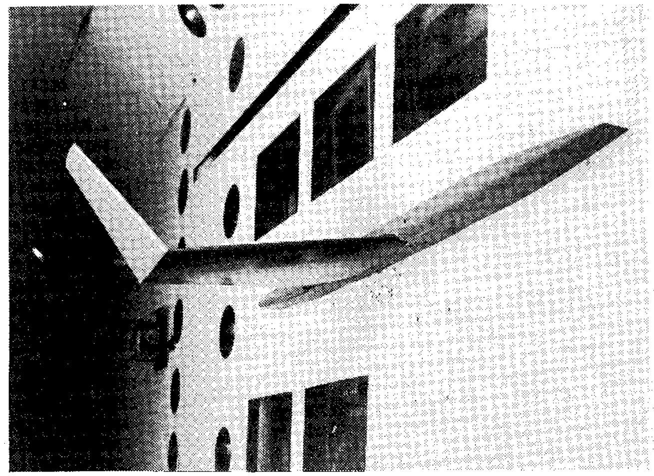

TIP FIN

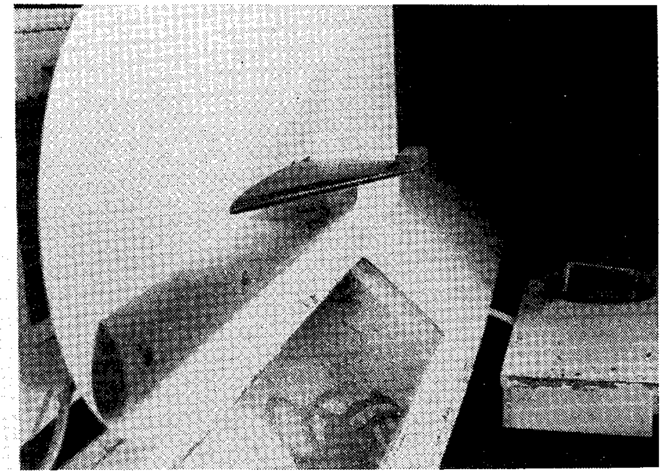

RCS POD

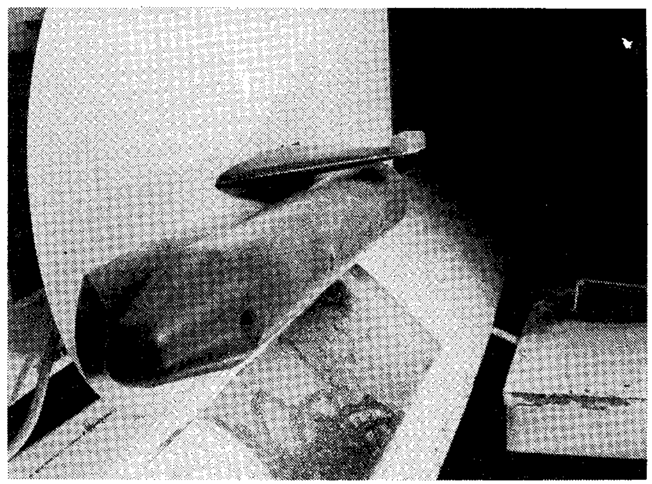

INTERFERENCE

Figure 8

EFFECT OF RCS POD ON THE SUBSONIC FLUTTER OF 040-A ORBITER WING

(Figure 9)

Some results of this program illustrating the effect of the RCS pod on the flutter behavior of the 040-A orbiter wing are shown in figure 9. These results are presented in terms of flutter velocity as a function of Mach number. The solid circular symbols define the flutter boundary for the wing with no RCS pod. The area under this boundary indicates no flutter, and the area above the boundary is the flutter region for the wing. The open circular symbols represent no-flutter points for the wing model with the RCS pod on its tip. Over the limited Mach number range of the test, the results indicate that the RCS pod had no detrimental effect on the flutter behavior of the wing, and in fact was slightly beneficial. A possible explanation for this unexpected result is that the frequency ratio of the two predominant modes associated with flutter has changed from about 0.45 to about 0.25. This is in spite of the fact that all the natural frequencies of the wing were lowered by the added mass of the RCS pod. New low-frequency modes introduced by adding the RCS pod do not appear to couple with existing wing modes because they are restricted to a local region on the wing in the vicinity of the RCS pod. It should be cautioned, however, that although the wing stiffness distribution was simulated by the model, no effort was made to take into account details of the attachment between the wing and RCS pod or changes in local stiffness of the wing tip due to addition of the pod. Larger scale models should be tested to confirm these preliminary findings and to extend the investigation into the transonic speed regime, which is more critical.

EFFECT OF RCS POD ON THE SUBSONIC FLUTTER SPEED OF A SPACE SHUTTLE ORBITER WING

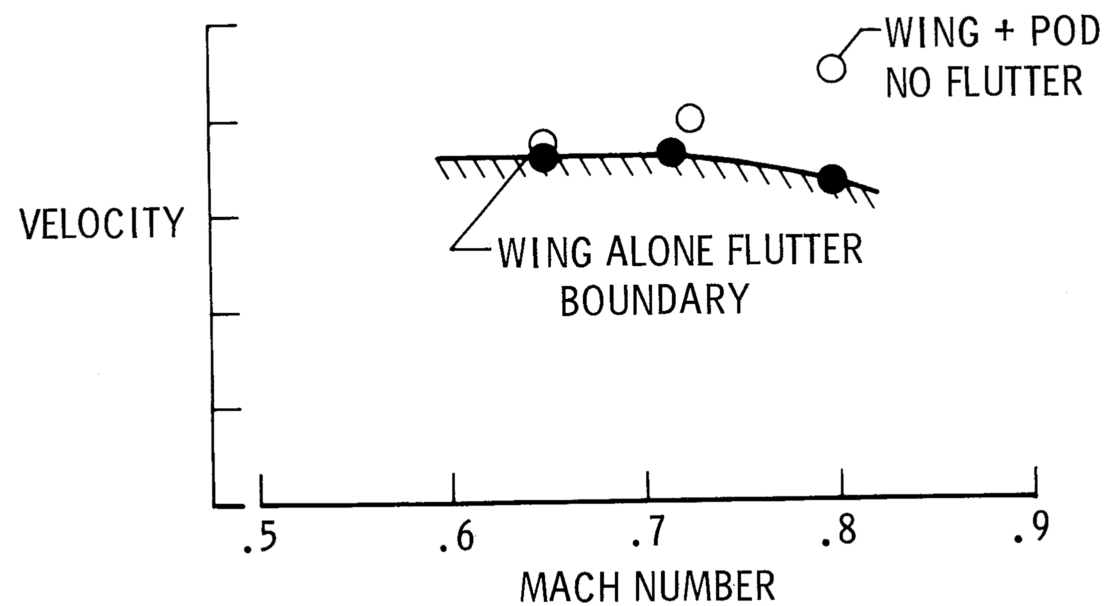

Figure 9

CONCLUDING REMARKS

(Figure 10)

The space shuttle flutter technology program being conducted by the Dynamics and Aeroelasticity Working Group has been developed around three main objectives: (1) To identify unique new problems associated with proposed vehicle configurations and their flight profiles through exploratory studies; (2) to develop the analytical and experimental techniques needed to predict flutter boundaries and insure adequate flutter margins, while anticipating problems associated with aeroelastic-model and full-scale testing to validate flutter clearance; and (3) to perform preliminary evaluations of configuration features that have suspected potential flutter problems so that flutter avoidance can be incorporated as early as possible into the configuration design.

An assessment of the results from these studies in light of the current configuration concept for the shuttle vehicle is summarized in figure 10. Among the theories applicable for flutter prediction of space shuttle designs there appear to be reliable nonplanar programs which will be adequate for the subsonic and supersonic speed regimes. However, transonic speeds during ascent will be the most critical for flutter, and since no analytical prediction programs are available for the transonic regime, a comprehensive model test program will have to be relied on.

Preliminary evaluations of some specific configuration features have indicated that flutter test results may influence the vehicle design and should therefore be obtained as early as possible during phase C/D. Features that have been identified that warrant testing to determine their effect on vehicle flutter include (1) orbiter wing-tip RCS modules, (2) fuselage flexibility, and (3) multibody-wing interference.

A unique problem concerning the flight flutter test program exists. For the orbiter horizontal flight with airbreathing engines the vehicle does not have the capability of reproducing the actual all-up vehicle ascent Mach number profile and maximum dynamic pressure profile simultaneously. To accomplish the flight flutter test program a rocket-augmented flight, suborbital flight, or other methods may have to be considered. Regardless of which test method is used, the problem of flutter testing at rapidly changing test conditions remains, since neither performance nor control capability is available to hold the test conditions constant. It appears that flight proof test of the actual launch configuration will not be accomplished until the first flight of the all-up vehicle.

CONCLUDING REMARKS

ASSESSMENT

- RELIABLE NONPLANAR ANALYSES (SUBSONIC AND SUPERSONIC)
- TRANSONIC RANGE MOST CRITICAL; THEREFORE HIGH RELIANCE ON MODEL TEST PROGRAM
- TEST RESULTS MAY IMPACT DESIGN AND SHOULD BE OBTAINED EARLY WITH EMPHASIS ON

    WING-TIP RCS MODULES
    FUSELAGE FLEXIBILITY
    MULTIBODY-WING INTERFERENCE

- FEASIBILITY OF FLIGHT FLUTTER-TEST PROGRAM UNKNOWN

Figure 10

REFERENCES

1. Goetz, Robert C.: Lifting and Control Surface Flutter. Space Transportation System Technology Symposium, NASA TM X-52876, Vol. II, 1970, pp. 177-198.

2. Goldman, Robert L.; and Obremski, Henry J.: Experimental Investigation of Hypersonic Buzz on a High Cross-Range Shuttle Configuration. RIAS Tech. Rep. 72-05c (Contract NAS1-10726), Research Institute for Advanced Studies, May 1972. (Available as NASA CR-112053.)

3. Kalman, T. P.; Rodden, W. P.; and Giesing, J. P.: Application of the Doublet-Lattice Method to Nonplanar Configurations in Subsonic Flow. J. Aircraft, vol. 8, no. 6, June 1971, pp. 406-413.

4. Kariappa; and Smith, G. C. C.: Further Developments in Consistent Unsteady Supersonic Aerodynamic Coefficients. J. Aircraft, vol. 9, no. 2, Feb. 1972, pp. 157-161.

5. Goetz, Robert C.: Effects of Space Shuttle Configuration on Wing Buffet and Flutter. Part I - Launch Vehicle Wing With Tip Fin. NASA Space Shuttle Technology Conference, Vol. III, NASA TM X-2274, 1971, pp. 181-199.

ASSESSMENT OF POTENTIAL BUFFET PROBLEMS ON THE SPACE SHUTTLE VEHICLE

By Lado Muhlstein, Jr.
NASA Ames Research Center, Moffett Field, Calif.

INTRODUCTION

Buffet of the space shuttle launch and reentry configuration is an area requiring continued evaluation to produce a safe reliable vehicle of minimum weight. Although in most cases, buffet does not present a serious structural problem, it is believed to be responsible for the failure of some early launch vehicles.

Buffet forces result from flow separation and therefore can not be predicted accurately. Buffet loads are highly sensitive to configuration, angle of attack, and Mach number and can be reliably determined only by wind tunnel tests of elastically scaled models.

POTENTIAL BUFFET SOURCES

(Figure 1)

Buffet of the space shuttle vehicle can be divided into three different types. They are (1) buffet due to periodic flow separation which is coupled to a vibration mode of the vehicle, (2) transonic shock and separated-flow induced buffet, and (3) buffet due to plume induced separation.

Buffet Due to Periodic Flow Separation

This type of buffet is generally associated with long slender, and hence flexible vehicles, which have regions of flow separation that produce forces which result in a dynamic aero-structural instability. This type of buffet couples with a vehicle vibration mode, often the first or second body bending mode and thus is actually a form of stall flutter.

Buffet Due to Transonic Shock Waves and Separated Flow

The same high intensity pressure fluctuations associated with the in-flight aero-acoustic environment cause a random buffet excitation of the overall vehicle. Separated flows and shock waves at transonic and supersonic speeds and interference flows are the primary sources of the excitation. The buffet intensity is dependent upon the intensity and spatial distribution of the pressure fluctuations. For conventional airplanes, the unsteady transonic flows on the wings are the primary sources of buffet excitation due to the large surface areas involved. Generally wing buffet occurs at high angles of attack, but the buffet boundary can also extend to $\alpha = 0°$ depending on geometry. This type of buffet also includes the wing stall case.

Buffet Due to Exhaust Plume Induced Separation

The expansion of rocket exhaust gases to a large plume at high altitude results in an effective obstruction of the flow field surrounding the vehicle causing separation of flow (like flare induced separation) ahead of the plume at supersonic speed. For a parallel-burn delta wing vehicle with the wing near the rocket exhaust, the separated flow region can cover a large portion of the wing and consequently the buffet loads can be large, even when the dynamic pressure is low.

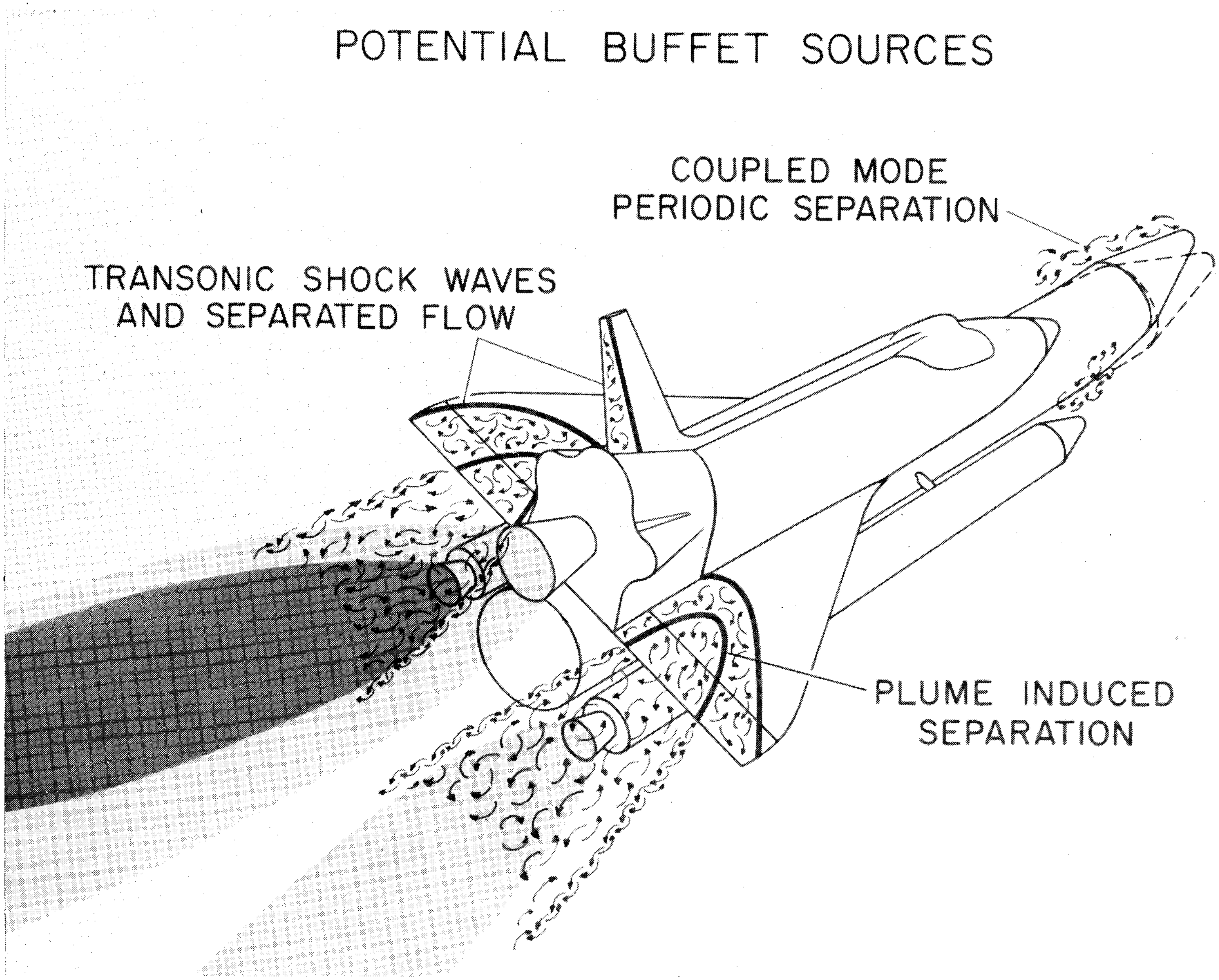
POTENTIAL BUFFET SOURCES
COUPLED MODE PERIODIC SEPARATION
TRANSONIC SHOCK WAVES AND SEPARATED FLOW
PLUME INDUCED SEPARATION

Figure 1

LAUNCH AND REENTRY TRAJECTORIES

(Figure 2)

At the present time, there are no buffet data available for the parallel-burn space shuttle configurations. Some speculation of excitation loads and buffet during ascent relative to reentry is possible by considering ascent and reentry dynamic pressure trajectories. For a given Mach number and flow condition, random buffet excitation (excluding buffet involving coupling with vehicle motion) is directly proportional to dynamic pressure q.

Typical launch and reentry trajectories for the space shuttle vehicle are shown in Figure 2. The launch trajectory shows the typical rapid increase in dynamic pressure q with increasing Mach number to a peak at low supersonic Mach numbers. Although this trajectory shows a maximum q of 22 000 N/m^2 (450 psf) some estimates for parallel-burn SRM configurations range as high as 31 000 N/m^2 (650 psf). Many of the buffet producing phenomena are associated with high subsonic and low supersonic flow phenomena. The high dynamic pressure at these Mach numbers, combined with the large amount of interference flows on the parallel-burn configuration, seriously aggravate the buffet problem. One sure way to minimize buffet loads is to minimize dynamic pressure.

The low dynamic pressure during reentry (10% to 20% of the peak launch dynamic pressure) significantly reduces the probability of serious buffet problems in this phase. Because of the low dynamic pressure, it is believed that buffet will not be a serious problem during the reentry portion of the flight, thus all further discussion will be concentrated on the launch phase.

EFFECT OF ANGLE OF ATTACK ON BUFFET RESPONSE OF A DELTA-WING ORBITER MODEL

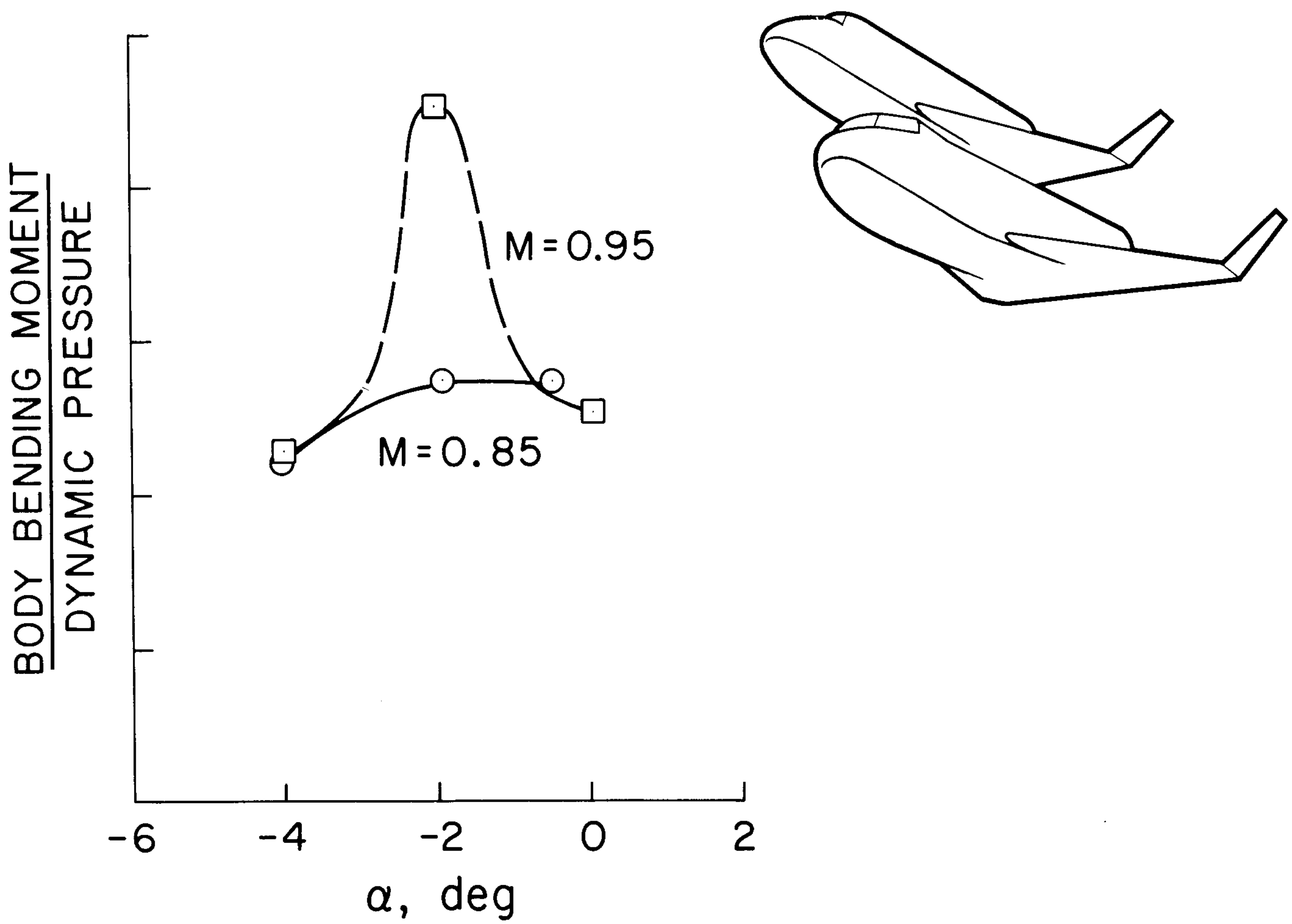

Figure 2

EFFECT OF ANGLE OF ATTACK ON BUFFET

(Figure 3)

Buffet information on the parallel-burn launch configuration is not available at this time, however, data previously obtained on elastically scaled models of a fully reusable configuration can be used to illustrate a type of buffet problem which can occur.

In Figure 3, body bending moments measured on a delta-wing orbiter mounted on a delta-wing booster, normalized by dynamic pressure, are shown as a function of angle of attack for Mach numbers of 0.85 and 0.95. Although the information presented is normalized body bending moment, the primary input force was from the wings and is believed to be a form of the coupled-mode type of buffet. This type of buffet generally produces the largest response at or near zero lift. The buffet response (normalized by dynamic pressure) shows a strong sensitivity to angle of attack at $M = 0.95$ with a peak in the response at $\alpha = -2°$. There was relatively little sensitivity to angle of attack at other Mach numbers as typified by the $M = 0.85$ data. It is significant that $\alpha = -2°$ corresponds to zero lift on the wings.

TYPICAL LAUNCH AND REENTRY TRAJECTORIES

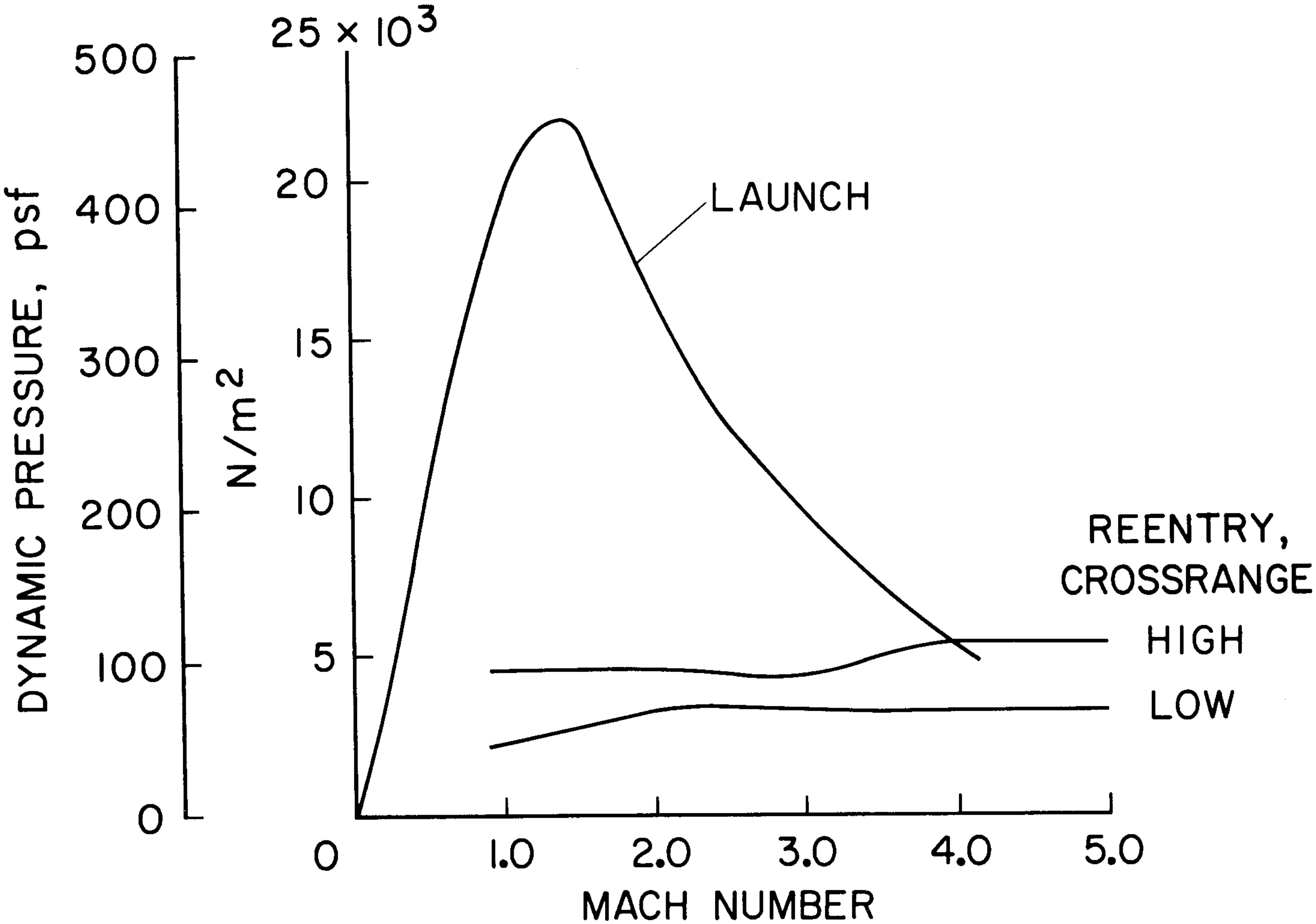

Figure 3

EFFECT OF MACH NUMBER ON BUFFET

(Figure 4)

The effect of Mach number on the same buffet data discussed in Figure 3 is shown in Figure 4 for two angles of attack. These data show that the previously observed large response that occurred at $\alpha = -2°$ is not only angle of attack sensitive but is also highly dependent on Mach number. High buffet response of this type would therefore only occur momentarily during the ascent of a space shuttle vehicle.

The fact that the coupled-mode type of buffet is highly Mach number and angle-of-attack dependent dictates that when buffet tests are conducted, care must be exercised to assure that the maximum buffet condition is detected. Buffet tests are frequently conducted at arbitrary constant increments of Mach number and angle of attack, and it is therefore possible that the critical test condition may be overlooked.

EFFECT OF MACH NUMBER ON BUFFET RESPONSE OF A DELTA-WING ORBITER MODEL

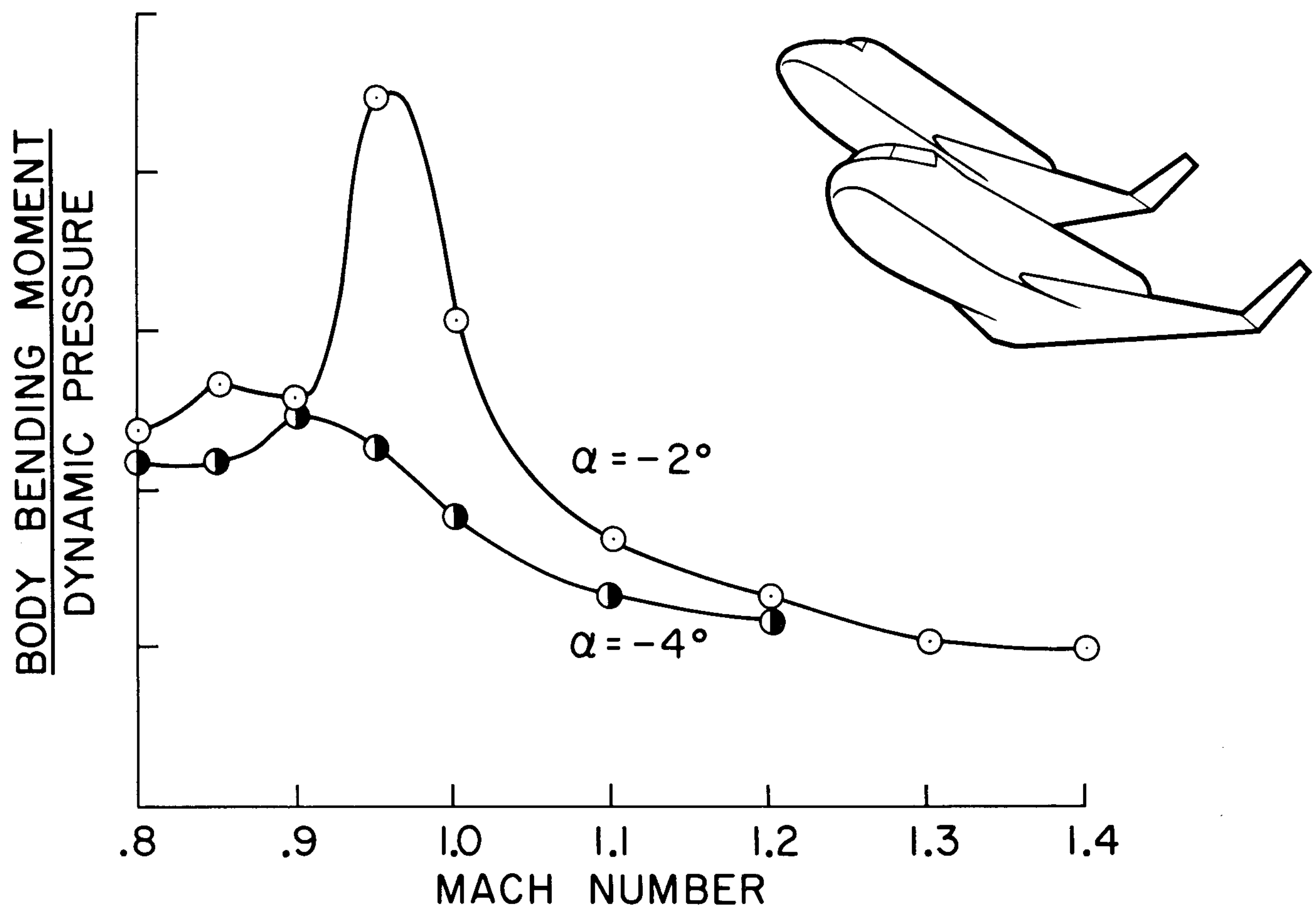

Figure 4

BUFFET OF VERTICAL FINS

(Figure 5)

Buffeting of vertical fins should not be overlooked as a potential problem. Although the random buffet due to separated flow is expected to be low at the angles of sideslip encountered, shock induced separation which couples with some vibration mode of the fin can be encountered at zero flow angle. This is actually a type of limited amplitude transonic flutter. Figure 5 shows the normalized rms root bending moment as a function of Mach number for three angles of attack for a model which resembles a vertical fin. The model has an aspect ratio of 4 and a thickness-to-chord ratio of 0.08. The airfoil section is NACA 0008-64.

For the $\alpha = 0°$ case the response was generally low except for a very narrow Mach number range near $M = 0.9$. At this Mach number, a coupled mode type of instability (a limited amplitude transonic flutter) produced a very large response.

For the $\alpha = 2°$ case the response was the same as for the $\alpha = 0°$ case except in the vicinity of $M = 0.9$ where the high response occurred. Note that $\alpha = 2°$ completely suppressed the instability and resulted in buffet as low or lower than for $\alpha = 0°$ at other Mach numbers.

The buffet response for $\alpha = 12°$ is also presented. These data correspond approximately to the maximum buffet condition and indicate that the response due to the transonic flutter at $\alpha = 0°$ was greater than the buffet at $\alpha = 12°$. Since the vehicle generally flies at or near $\beta = 0°$ (the equivalent of $\alpha = 0°$ for a vertical fin), the greatest dynamic load problem for the vertical fins could arise from transonic flutter. It should be noted that the above discussion on buffet of vertical fins does not include the problem of plume induced separation. Such a problem can occur even though the vertical fin is otherwise buffet free.

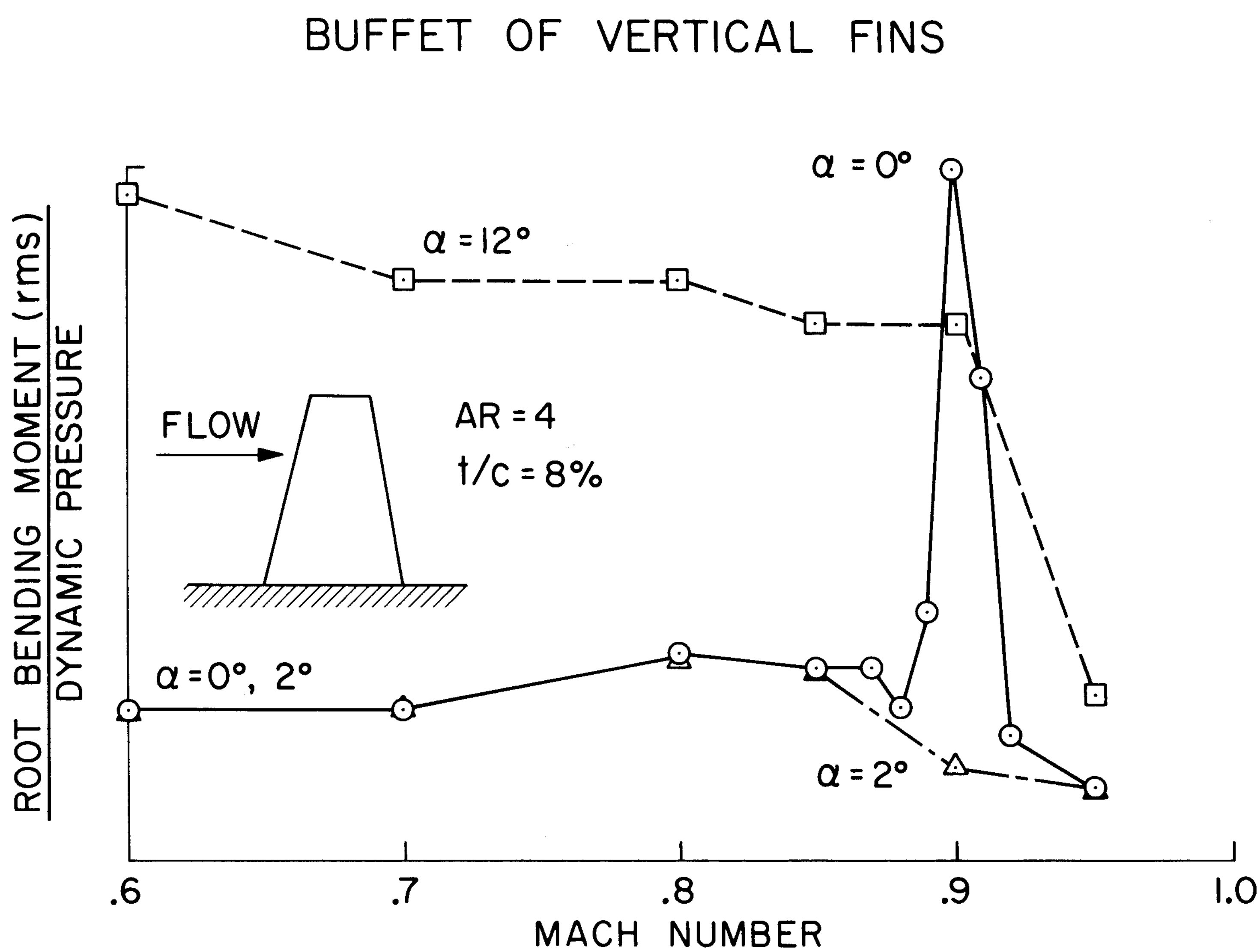
BUFFET OF VERTICAL FINS
ROOT BENDING MOMENT (rms) / DYNAMIC PRESSURE
α = 0°
α = 12°
FLOW
AR = 4
t/c = 8%
α = 0°, 2°
α = 2°
.6
.7
.8
.9
1.0
MACH NUMBER

Figure 5

INVESTIGATION OF PLUME INDUCED SEPARATION ON PARALLEL-BURN LAUNCH CONFIGURATION

(Figure 6)

The expansion of the rocket exhaust at high altitudes can act as a flow obstruction resulting in a separated region ahead of the plume similar to a flare induced separation. On prior launch vehicles, plume induced separation has occured only at high altitude and hence high Mach number.

There is some concern that the parallel-burn launch configuration will encounter plume induced separation at lower altitudes (hence higher dynamic pressures). Along with the large surface area provided by the delta wings this could result in signficant buffet. To quickly evaluate the effect of the rocket exhaust plumes at low altitudes, a test using solid simulation of plumes was conducted in the Ames 9- by 7-foot supersonic wind tunnel. Two photographs of the model installed in the wind tunnel are shown in Figure 6. This is a model of a parallel-burn configuration with simulated 3.96-meter (156-inch) SRM's. The solid simulated plumes were properly sized for each of the test Mach numbers of 1.60 and 2.20. The rapid change in plume size with increasing Mach number (increasing altitude) is clearly evident from these photographs. Both fluorescent oil flow visualization and surface pressure fluctuation tests were conducted.

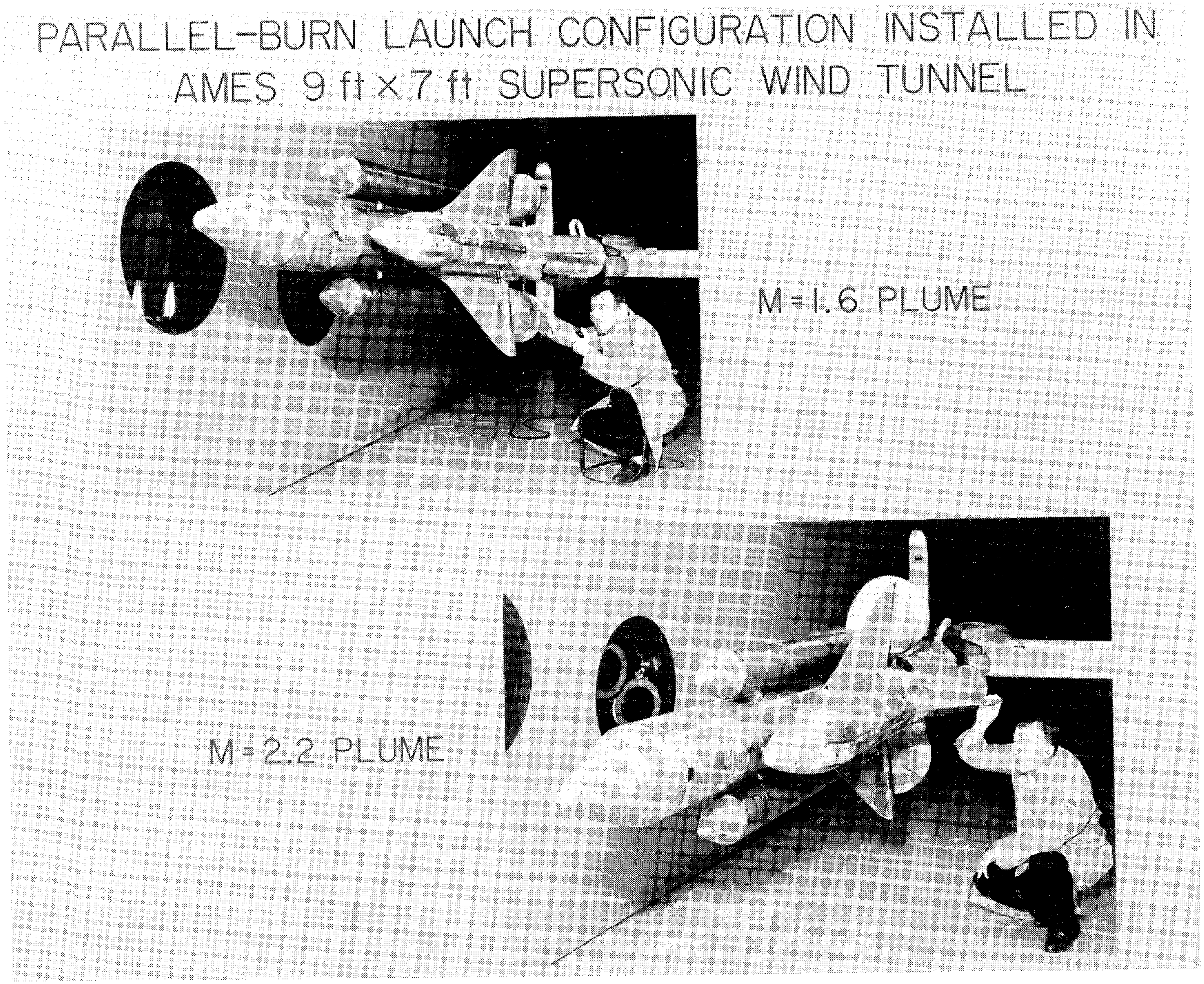
PARALLEL-BURN LAUNCH CONFIGURATION INSTALLED IN
AMES 9 ft × 7 ft SUPERSONIC WIND TUNNEL
M = 1.6 PLUME
M = 2.2 PLUME

Figure 6

RESULTS OF TEST TO DETERMINE PLUME INDUCED SEPARATION

(Figure 7)

A fluorescent oil flow visualization technique was used to determine the size and location of regions of separated flow. A photograph showing typical results is shown in Figure 7. The model is at $\alpha = -8°$, $\beta = -5°$ (view is from leeward side), and $M = 2.20$. No flow separation due to the plumes is observed. Plume induced flow separation was not observed at any test conditions at either $M = 1.60$ or 2.20. Test angles of attack ranged from $-8°$ to $+8°$ for angles of sideslip of $0°$ and $-5°$. Based on these results, it is expected that plume induced separation will not occur until the vehicle reaches significantly higher altitudes and Mach numbers than those represented by these tests. Although the dynamic pressures will be lower under these conditions, it is still possible that the area experiencing separated flow will be large enough to cause a buffet problem.

ROCKET PLUME SIMULATION

$M = 2.20 \qquad \alpha = -8° \qquad \beta = -5°$

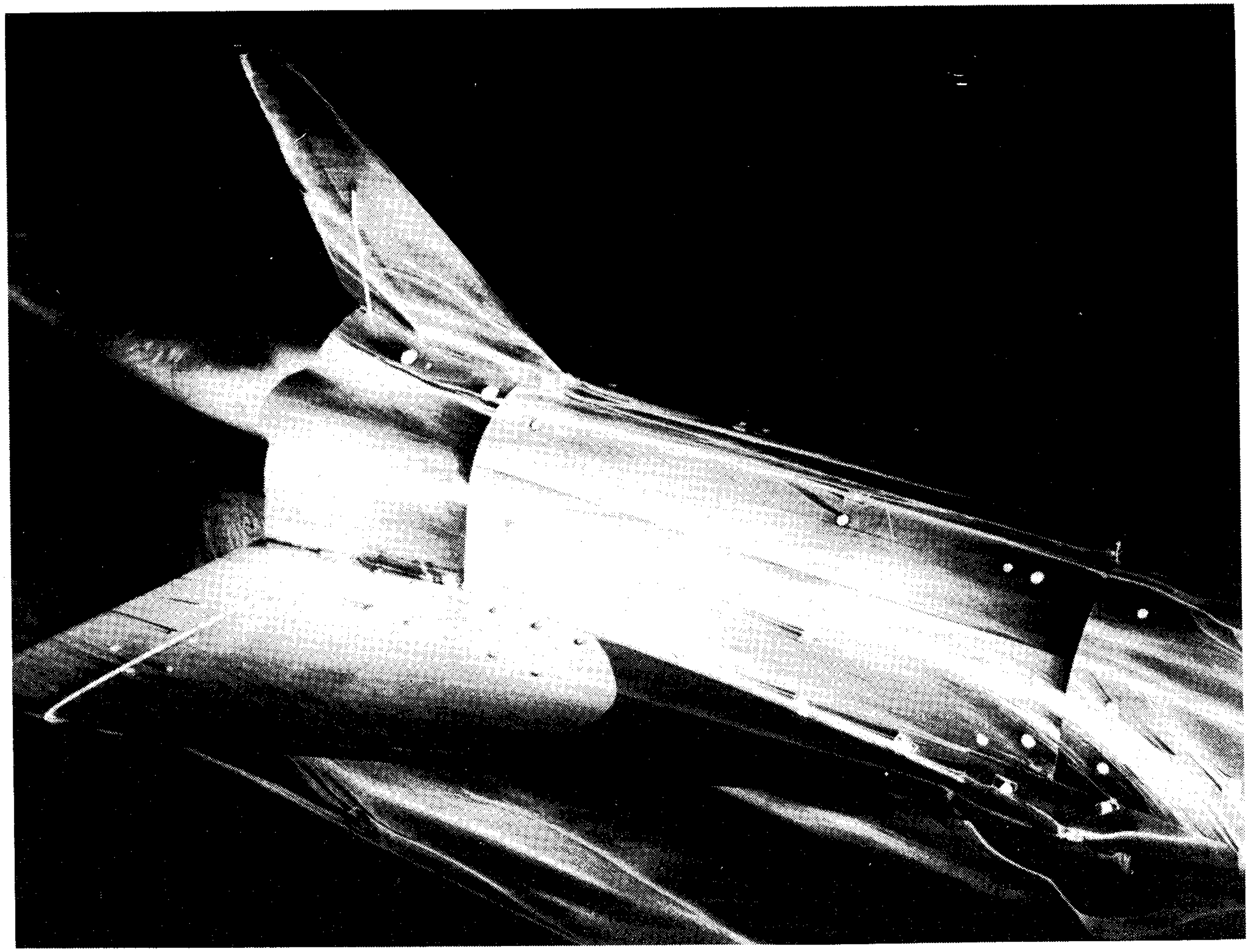

Figure 7

ANTICIPATED WING BUFFET OF A PARALLEL-BURN LAUNCH CONFIGURATION

(Figure 8)

Although buffet data for a parallel-burn launch configuration is not available it is possible to get an indication of the relative buffet intensity for the parallel- and series-burn configurations by comparing the fluctuating surface pressures. This has been done in Figure 8 which shows the relative wing buffet loads normalized by dynamic pressure as a function of Mach number. The configurations are a series-burn model and a parallel-burn model with 3.96-meter (156-inch) SRM's.

These data indicate that the wing buffet forces for the parallel-burn configuration will be significantly higher than for the series-burn configuration. This is believed to be due to the increased amount of flow interference produced by the SRM's.

RELATIVE WING BUFFET OF SERIES AND PARALLEL-BURN LAUNCH CONFIGURATIONS

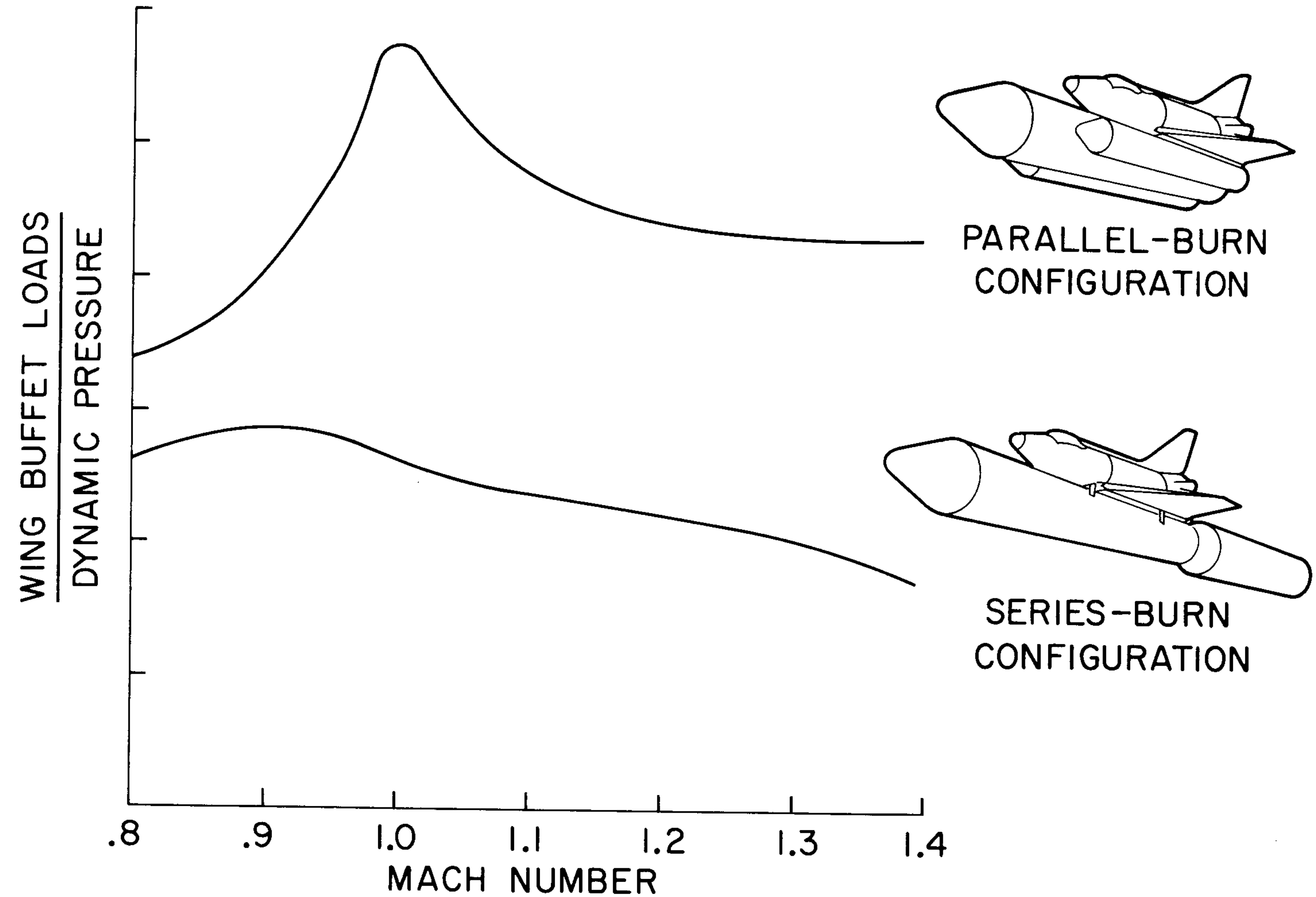

Figure 8

CONCLUDING REMARKS

(Figure 9)

Coupling of flow separation with vehicle vibration modes is generally considered to be the most serious form of buffeting. The probability of this type of buffet occurring on the body of the relatively stiff parallel-burn configuration is believed to be small. The probability that this type of buffet will occur on the wings and vertical tail is somewhat greater because of their lower stiffness. Although the probability of occurrence of buffet involving coupling is relatively low, the mission risk if it does occur is high.

Buffet can be very sensitive to configuration, angle of attack, and Mach number, thus when tests are conducted care must be taken to search out test conditions where maximum response occurs.

- BUFFET LOADS CAN NOT BE PREDICTED ANALYTICALLY.
- BUFFET IS VERY SENSITIVE TO CONFIGURATION, ANGLE OF ATTACK, AND MACH NUMBER.
- CAREFUL AND DETAILED WIND TUNNEL TESTS ARE NECESSARY TO ASSURE THAT A POTENTIALLY SERIOUS BUFFET PROBLEM HAS NOT BEEN OVERLOOKED.

Figure 9

STRUCTURAL DAMAGE CLAIMS RESULTING FROM ACOUSTIC ENVIRONMENTS DEVELOPED DURING STATIC TEST FIRING OF ROCKET ENGINES

By Stanley H. Guest and Robert M. Slone, Jr.

NASA Marshall Space Flight Center

SUMMARY

During static testing of multi-million pound thrust rocket engines at Marshall Space Flight Center's Mississippi Test Facility, areas adjacent to the test site have been subjected to the noise generated by rocket engines.

Structural damage claims and subjective complaints were filed by those who alleged that the noise levels were excessive. The statistical analysis of these claims and complaints which were filed during these rocket engine development programs led to the determination of a relationship between claims and overall sound pressure level. Community exposure criteria can then be assessed based on what can be considered allowable acoustic environments from large rocket engines.

INTRODUCTION

A NASA facility was developed in Southern Mississippi for static testing of the booster stage (S-IC) and the second stage (S-II) of the Saturn V rocket system. The S-IC and S-II stages produce 1.26×10^8 and 5.13×10^6 acoustic watts, respectively, during static firing. From surrounding communities arose complaints and claims of damage from the resulting acoustic environments. These community responses are treated herein with respect to the sound pressure levels involved and the number of people or households exposed.

POLITICAL FEATURES

The Mississippi Test Facility is located on the western boundary of the Mississippi panhandle. It extends into Pearl River County, Mississippi, in the northwest; Hancock County in the east; Saint Tammany Parish, Louisiana, in the west. The buffer zone and the test facilities area contain 525 km^2 ($\simeq$ 196 $miles^2$ or 125,500 acres) with the northern boundary approximately 14 km (9 miles) from the test site.

When NASA established the facility, five existing communities were completely removed and relocated to nearby areas. Involved were: 786 residences, 16 churches, 3 schools, 10 commercial buildings, and some 7600 subdivision lots, affecting approximately 300 landowners. Major towns in the vicinity of the test site are Picayune, Mississippi, 32 km to the north of the buffer zone boundary, Slidell to the west (6.5 km) and Bay St. Louis to the east (11 km). Other towns, 32 to 48 km away are: Covington, New Orleans and Bogalusa, Louisiana; Poplarville and Gulfport, Mississippi.

Test Description

There were 15 static test firings of the S-IC booster at MTF between February 1967 and August 1970, with a total test duration of 1519 seconds (11 of the tests were 125 seconds duration). There were 30 S-II stage static firings from October 1965 to October 1970 (18 of the tests were more than 345 seconds duration).

Acoustic Description

The S-IC static test firings directed the engine exhaust flow downward into a 105° bucket deflector with exit pointing northward. Water injection was used for deflector cooling. The acoustic power level was reported at 201.0 dB, Re: 10^{-12} watts.

Terrain in the buffer zone sloped less than 2% with swamp areas along the west and north portions and also in the southeast corner. The main ground cover is medium-tall grasses, scrub, and pine trees over the generally flat regions surrounding the test site.

Constraints

The meteorological inhomogeneities of a layered atmosphere with varying wind components and temperature gradients induce refraction into the acoustic wave propagation. The refraction and the acoustic energy are dependent on these wind and temperature gradients, the scale of the gradients, spatial position of the gradient region, and wavelength of the propagating wave. In the areas around the test site these meteorological variables are measured and provided as an input to a conventional ray-tracing prediction program to compute the effects of refraction on the ground plane environments in the farfield community areas. This provides an estimate of the environment prior to actual testing in an attempt to avoid severe focal conditions and unacceptable levels. In regard to the meteorological factors, the

short-time-varying conditions, lack of data resolution and shortage of measurements in many directions, all detract from the accuracy of any farfield environmental prediction. These predictions for MTF, however, have been in very close agreement on the average with the measured acoustic environments, even though they lack some exactness and detail with respect to the directional properties of the pressure field.

At MTF, in addition to predictions of the effects of the refractive medium, a test sound from a high-powered horn source was utilized prior to the rocket test to compare predicted ray paths with actual ray paths. The horn is energized just prior to testing and measurements are made via mobile units and selected permanent stations to ascertain the environments relative to predictions. Then the decision is made to conduct the test or to postpone, based on the measured impact of the meteorological conditions at that time and their predicted rate of change; thus meteorological selectivity is exercised for each test firing.

Claims and Complaints

The claim and complaint data utilized herein were acquired from NASA Legal Offices.

Claims against the U. S. Government for alleged property damages from rocket acoustic environments were for remuneration. Complaints were generally of damage but were not seeking payment; some were obviously only complaints of annoyance or disturbance.

With regard to the claims and any resulting litigation, the damages alleged and the acoustic environmental exposure were of specific concern. Every effort was made to verify the acoustic environment; many measurements were made during the actual test and in close proximity to areas where claims resulted. Also, for each claim, inspectors were sent to each site of alleged damage where statements and photographs concerning the claims were acquired.

DETERMINATION OF COMMUNITY RESPONSE

The fact that a given number of complaints or claims were recorded from a specific test does not directly establish the response criteria or determine the response rate for the observed exposure levels. Not until the total exposures and complaints per exposure band are considered can an average response be properly defined. To reach this objective the overall sound pressure level contours from each test were acquired in 5 dB bands. (NOTE: The OA SPL was herein used as a quantitative unit of exposure since the farfield spectrum shape, as measured, did not change significantly from test to test or area to area). The number of people or households exposed within the various OA SPL bands was then determined. The number of claims for each band then was utilized , specifically providing the responses per exposure for each OA SPL band of concern.

In attempting to provide maximum resolution and reasonable accuracy in handling the OA SPL values associated with each damage claim, 5 dB bands are thought to be more compatible with current problem application. In some cases 10 dB bands were utilized in order to minimize errors possibly induced by grouping into the smaller bands, i.e., the larger the band the higher the probability of inclusion of a given OA SPL with its inherent variations. In general, the trends indicated from use of both the 5 and 10 dB bands imply that there are no gross discrepancies introduced into smaller bands; thus the 5 dB bands with the greater

resolution can be utilized.

The statistics of the community responses and exposure are categorized into specific exposure bands for MTF and an attempt is made to specify the claim rate, defined herein as claims per 1000 households exposed. The results from this study do not imply that similar responses would necessarily be observed from all other rocket tests or launch sites, but no significant difference would be anticipated under similar environmental conditions and with similar community characteristics, such as physical and socio-economic features.

TYPICAL ACOUSTIC SPECTRUM

Presented here is a measured sound pressure level spectrum typical of those which prompted claims of acoustic damage. This spectrum was measured during static testing of S-IC-508 at MTF at a point 20 km from the S-IC static test stand along an azimuth of 330° from the stand. Measurements indicated that the spectrum shape is typical for the farfield community areas. Note that the peak octave band is at approximately 4 Hz, which is infrasonic. While sound energy in this frequency range is inaudible, it, nevertheless, is potentially damaging to structures.

TYPICAL MEASURED ACOUSTIC SPECTRUM
20 km FROM THE S-IC TEST STAND
AND 330° (NW) - MTF
S-IC - 508

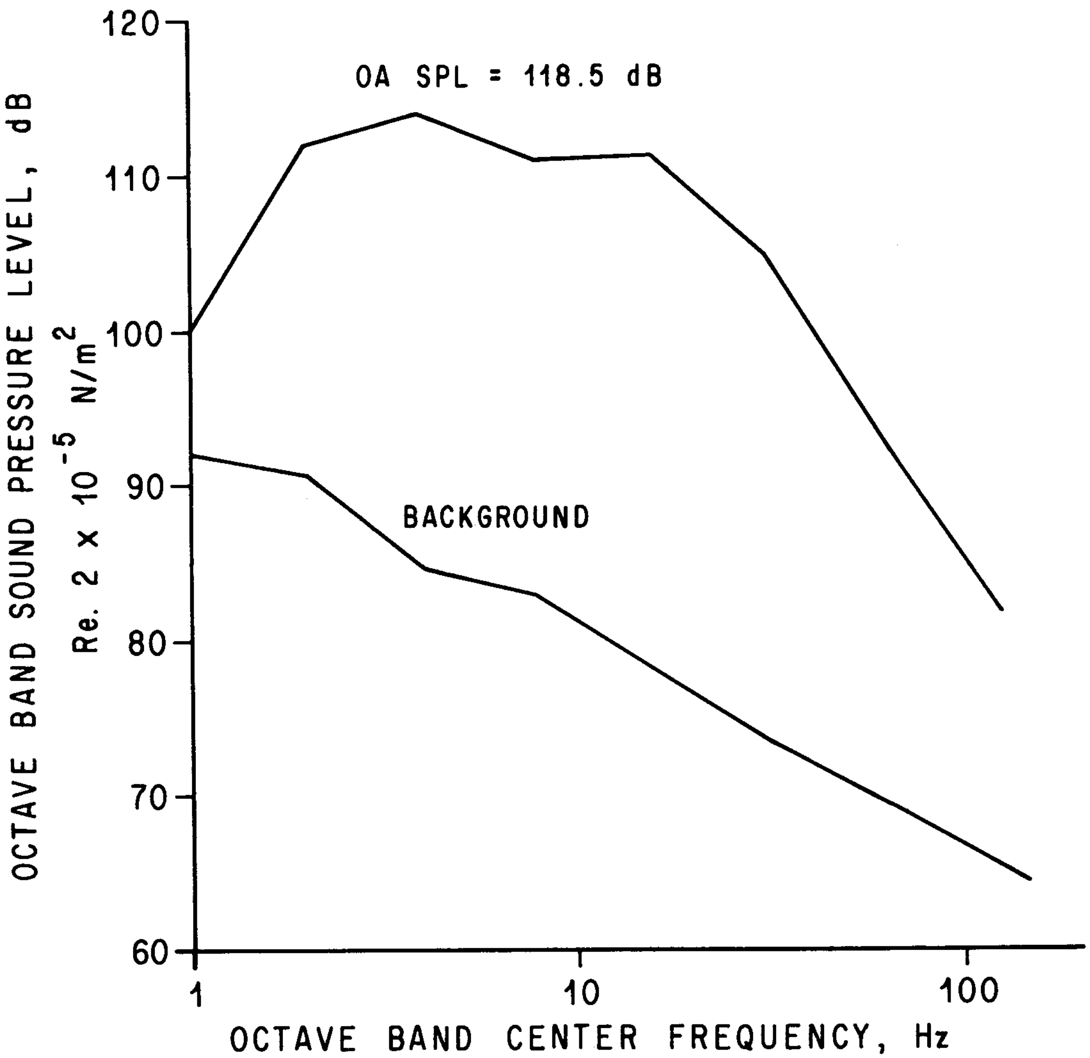

S-IC-508 OA SPL CONTOUR MAP

The MTF map locates the test site near the center of the buffer zone and the OA SPL contour lines (lines of equal OA SPL) as acquired from a ray-tracing program and impacted by the measured data at the 21 various farfield stations. Most of Picayune was between 115 and 120 dB. Just south of the Kiln Community an OA SPL of 121 dB was measured. Just east of Kiln was a localized focal region induced by the meteorological conditions at the time of firing. Relative to the OA SPL contours indicated for test S-IC-509, the S-IC-508 contours cover vastly greater areas, e.g., the 100 dB contour from S-IC-509 is shown as not exceeding the buffer zone limits ($\simeq$14 km or $\simeq$9 miles) whereas for S-IC-508 the 100 dB line is out as much as 71 km or 44 miles. The total area inside the 100 dB contour line on S-IC-508 is 5200 square km; for S-IC-509 $\simeq$363 square km (2000 and 140 square miles, respectively).

There were 48 community reactions from this test, 17 claims for damages and 31 complaints.

OVERALL SOUND PRESSURE LEVEL CONTOURS AT MISSISSIPPI TEST FACILITY
S-IC-508

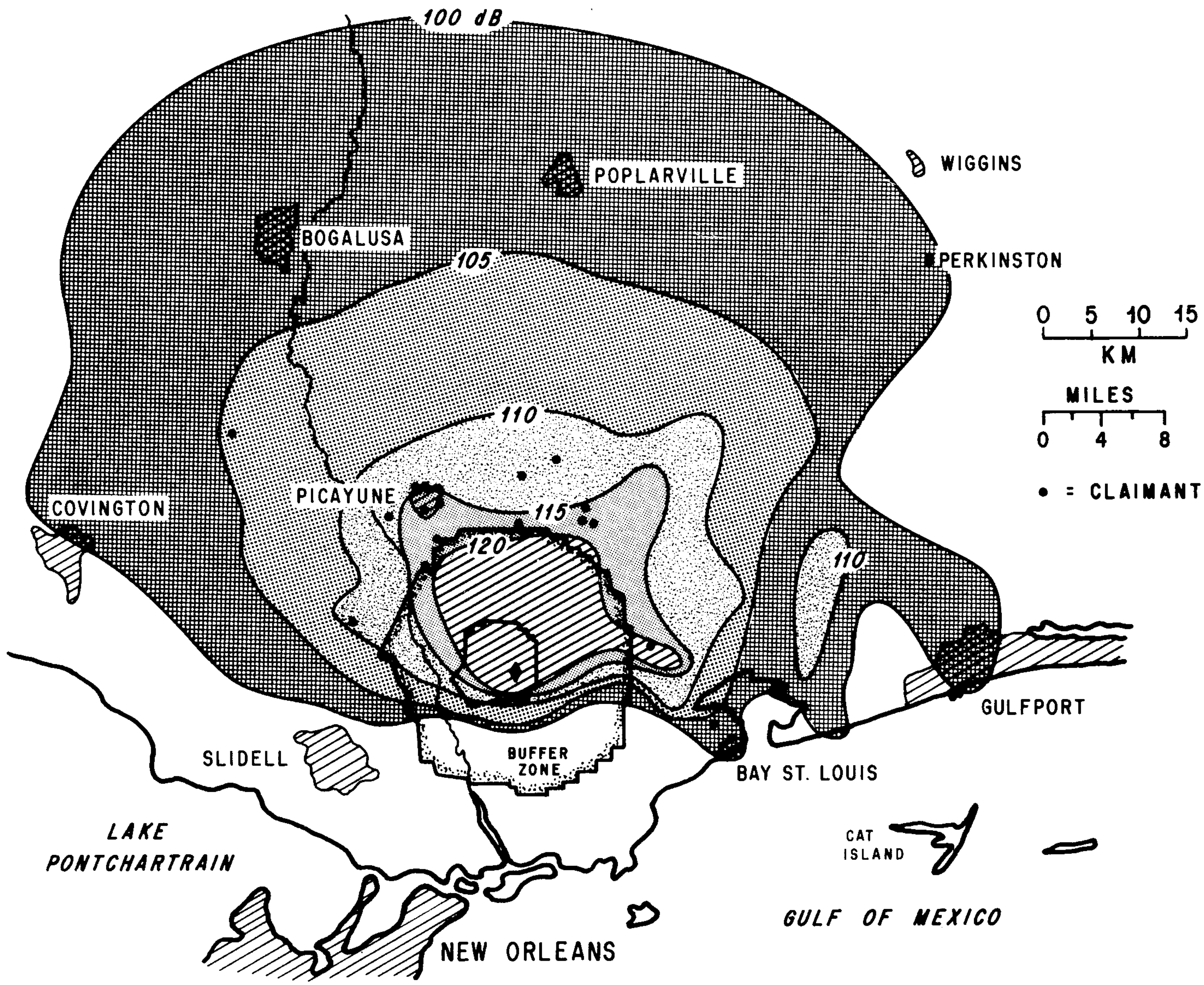

S-IC-509 OA SPL CONTOUR MAP

The OA SPL contour lines indicated on the map were derived from a ray-tracing program and from measured data from 20 farfield locations. The meteorological conditions at the time of firing were such that much of the energy was turned upward into the atmosphere and not returned to the ground. Obviously, there were no complaints or claims from this test.

SOUND PRESSURE LEVELS
MISSISSIPPI TEST FACILITY
S-IC - 509

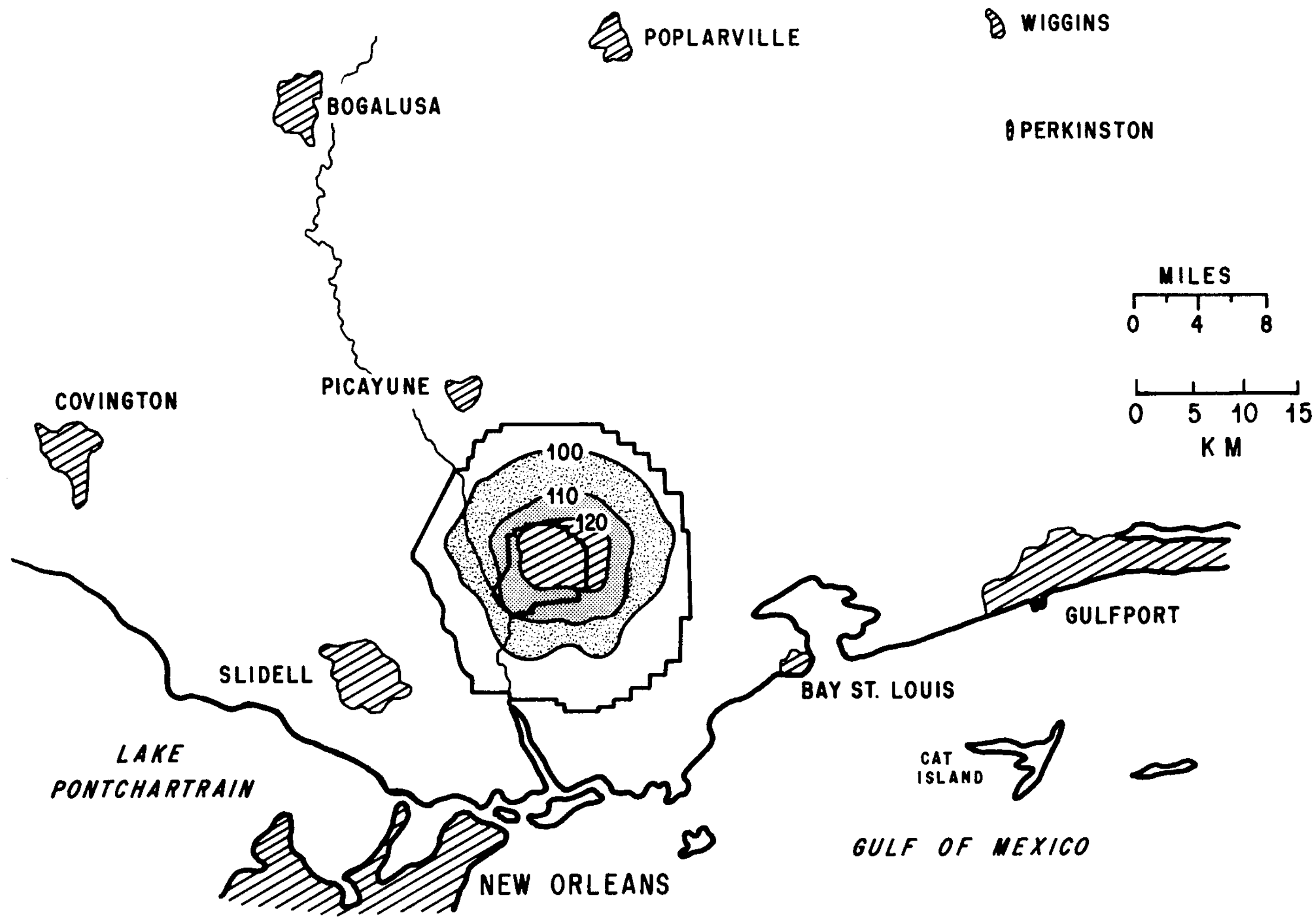

TOTAL LAND AREA EXPOSED DURING S-IC STATIC TESTS

Presented here are curves showing total land area contained within given constant overall sound pressure level contours for S-IC static tests at MTF.

The total land area contained within any constant overall sound pressure level contour for the S-IC booster in a theoretically homogeneous medium was computed and is shown here. However, in reality, the medium is never homogeneous and the sound field is therefore distorted, e.g., acoustic energy may be returned to the ground or may be turned away from the ground plane. Variation in the refraction is evidenced from the two other curves. The higher of these curves was obtained as an average from six "less-favorable" days on which S-IC static testing took place at MTF; the lower curve is an average for four "more-favorable" days on which the S-IC's acoustic energy was obviously directed away from the ground plane.

It was found that tests on the "less favorable" days, when grouped together, produced an average of more than 16 total claims and complaints per test. When the tests on the "more favorable" days were grouped together, they prompted an average response of less than one total claim and complaint per test.

TOTAL LAND AREA CONTAINED WITHIN OA SPL CONTOURS FOR S-IC STATIC TESTS - MTF

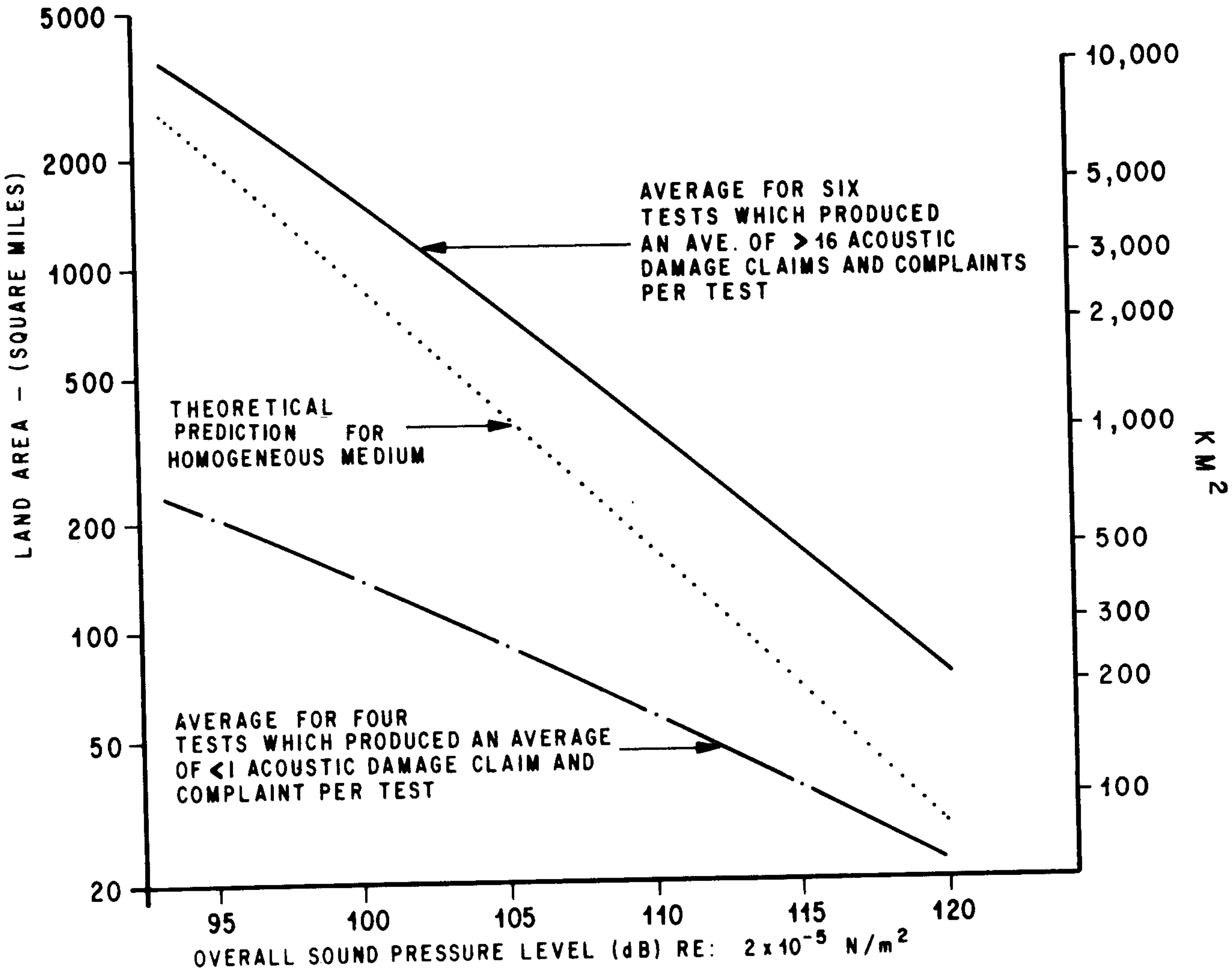

COMMUNITY RESPONSE TO S-IC STATIC TESTS AT MTF

The number of community responses (both claims and complaints) due to acoustic environments from the S-IC rocket tests are indicated in a time history format with a cumulative duration of the firing times. It is seen that some tests provoked very few claims or complaints, i.e., six tests with a total of seven responses, and four tests with zero responses. Yet there were five other tests from which a total of 94 responses were received. Since all tests utilized the same acoustic source, the propagational characteristics thus determined the environmental exposure conditions to a large degree.

There has been no attempt to separate the effects of exposure duration or frequency of testing on the number of claims and complaints received because of the lack of sufficient data. However, no obvious effects have been noted from the study, possibly because exposure to higher OA SPL levels would appear to override any secondary influences.

NUMBER OF CLAIMS AND COMPLAINTS OF ALLEGED ACOUSTIC DAMAGES FROM MTF S-IC STATIC TESTS WITH TEST DURATION

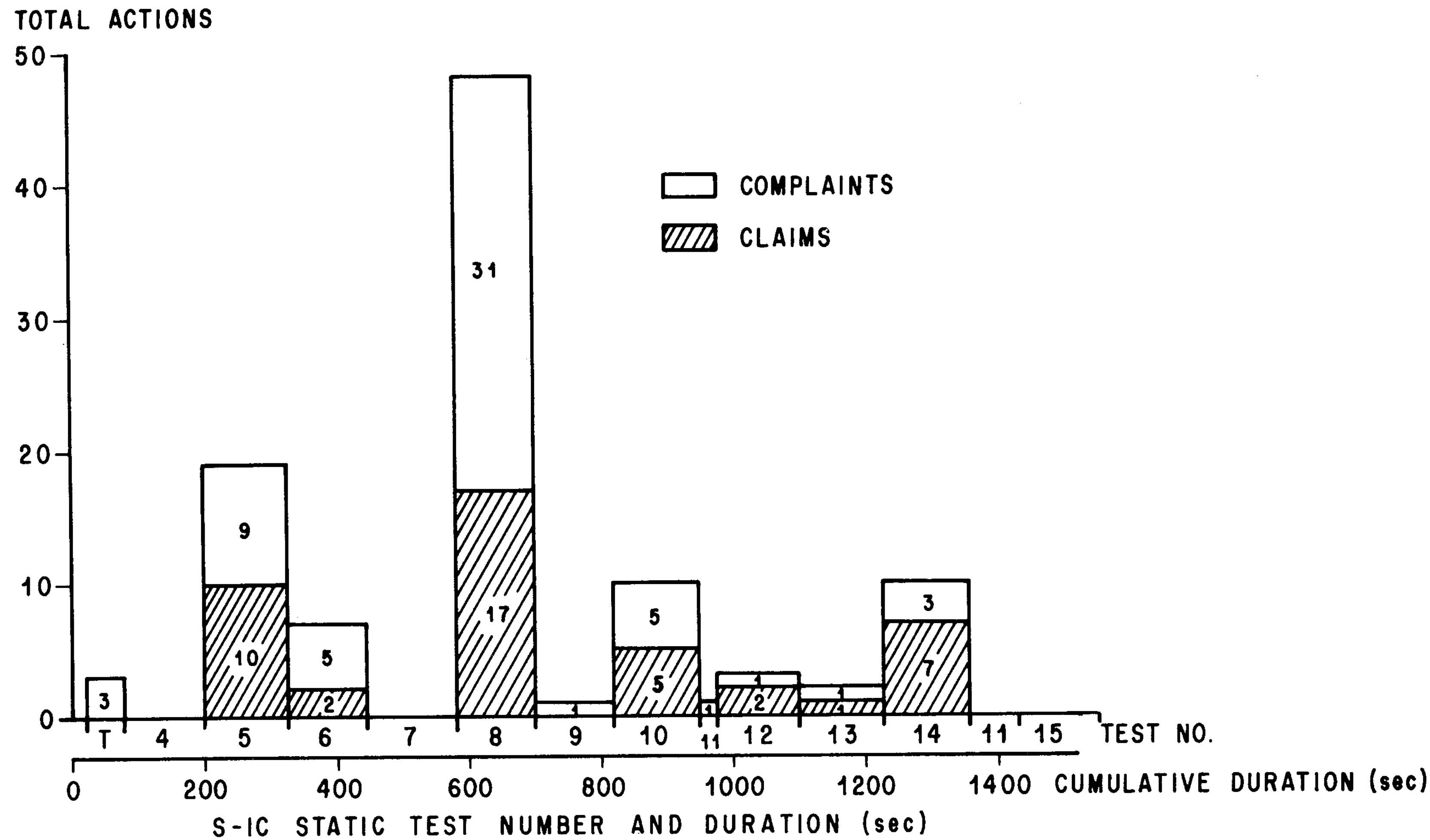

PERCENTAGE OF ACOUSTIC DAMAGE CLAIMS FOR S-IC STATIC TESTS AT MTF

The number of acoustic-induced damage claims from S-IC static tests at MTF is provided with the exposure levels, the OA SPL in 5 and 10 dB bands. The number of claims increase with exposure level as is observed from the data. Less than 10% of the claims resulted between 90 and 100 dB; 16% from 100 to 110 and 65% from 110 to 120 dB, indicating the increase with OA SPL. The percentage of claims resulting above 120 dB as indicated here, however, is misleading though clearly explained. The number of households exposed to levels above 120 dB was very small relative to the number exposed to less than 120 dB. The number of claims thereby are few since few were exposed. This representation here implies nothing in regard to the claim rate, only the number of claims observed per OA SPL band. If many were exposed to levels over 120 dB then more claims would probably result. Also a larger percentage of those exposed to the higher levels would expectedly respond.

The probability of a given exposure level being bounded by a specified dB band is improved by increasing the width of the band, i.e., from 5 dB to 10 dB band. In comparing the claim percentages from both bands no gross discrepancies were observed; thus use of the claim information in the 5 dB bands provides more resolution in the acoustic exposure levels and yet is a practical bandwidth for current applications.

PERCENTAGE OF ACOUSTIC DAMAGE CLAIMS FROM S-IC STATIC TESTS AT MTF

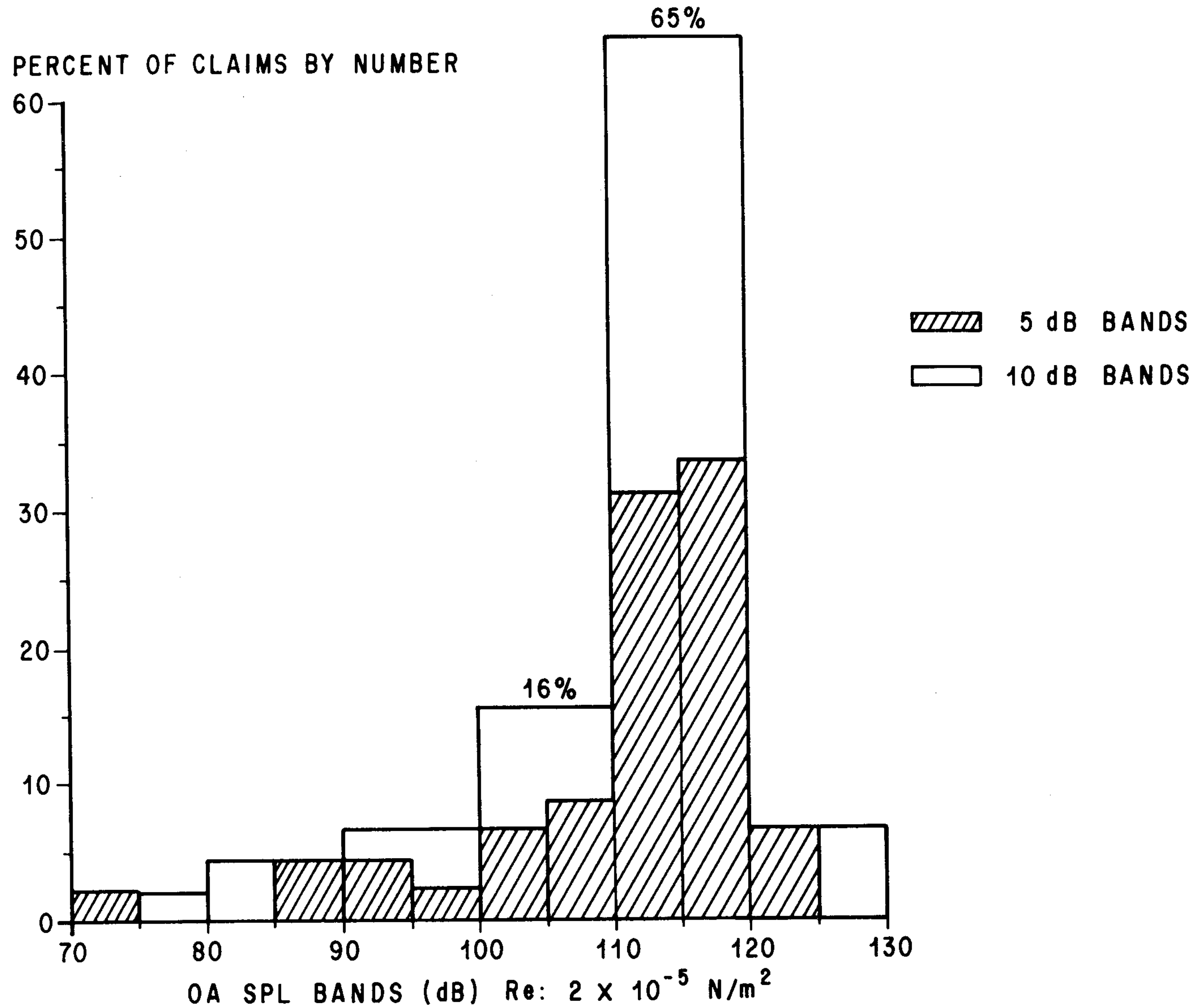

CLAIMS OF ACOUSTIC DAMAGE IN 5 dB OA SPL BANDS

Shown here are monetary statistics for the acoustic damage claims at MTF. The split ordinates indicate both actual dollar amounts and that percent of the total dollar claims which fell within a particular OA SPL band. Claims were grouped in five dB OA SPL bands for presentation, except for very low level claims. All claims at levels less than 90 dB were grouped together. Although damages amounting to more than $37,000 were claimed as a result of levels below 110 dB OA SPL, less than $500 (1.35%) was paid to the claimants in this category.

As can be seen from the graph, a majority of the claims (dollarwise) were at levels between 110 dB and 120 dB OA SPL. Claims in this region amounted to more than $189,000, of which claims for $37,500 (20%) were judged valid and consequently paid.

The number of claims of the acoustic damage from levels above 120 dB is small from this test history because few households received such levels. Admittedly, the statistics concerning this region are lacking; however, it is believed that the claim rate will increase with exposure to greater energy levels. It can be speculated that significantly greater energy levels will induce more and larger damage claims and a higher "paid to claimed" fraction.

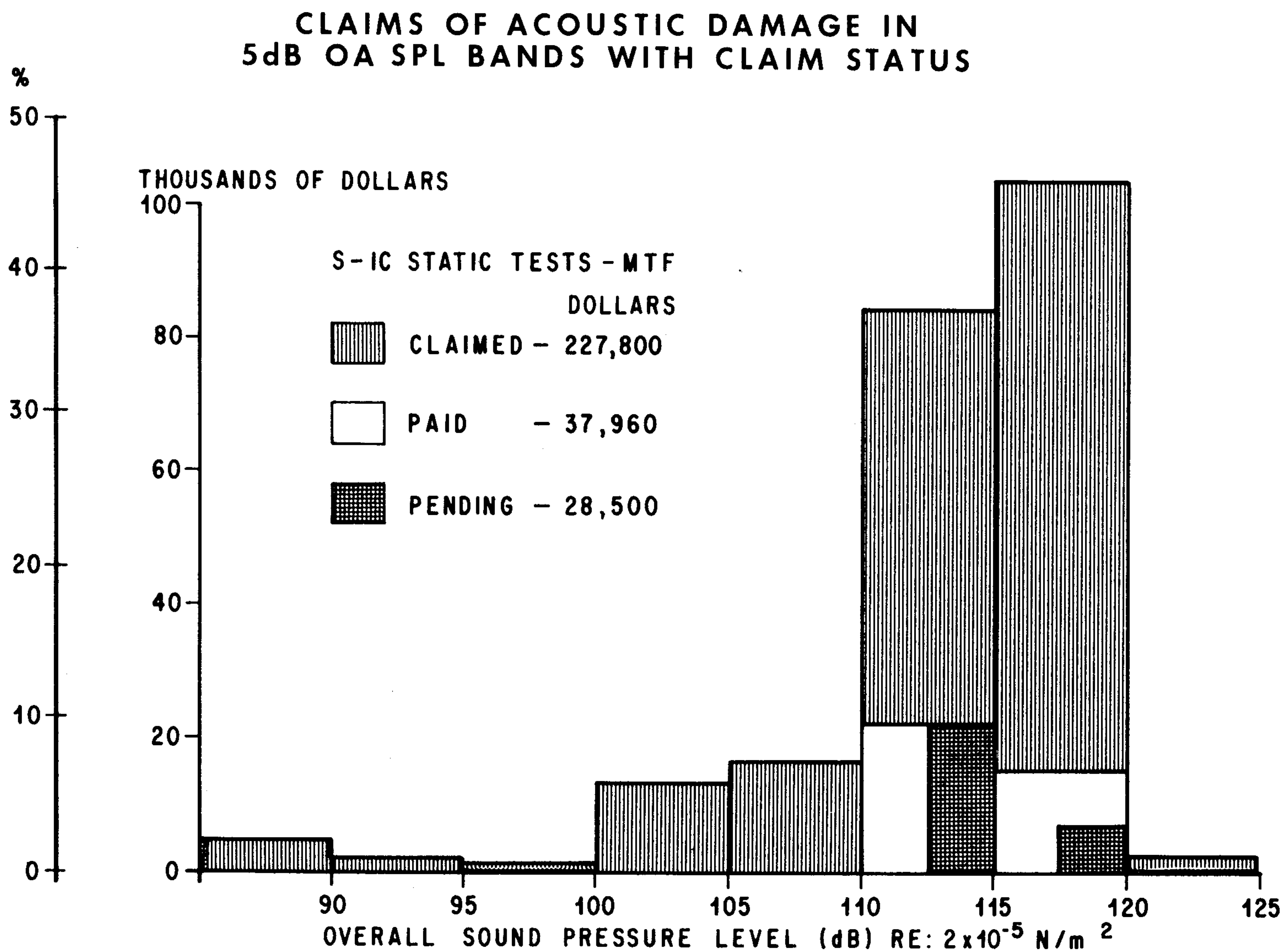
CLAIMS OF ACOUSTIC DAMAGE IN
5dB OA SPL BANDS WITH CLAIM STATUS
%
THOUSANDS OF DOLLARS
S-IC STATIC TESTS - MTF
DOLLARS
CLAIMED - 227,800
PAID - 37,960
PENDING - 28,500
OVERALL SOUND PRESSURE LEVEL (dB) RE: 2x10^-5 N/m 2

ACOUSTIC DAMAGE CLAIMS PER 1000 HOUSEHOLDS EXPOSED vs OA SPL IN 5 dB BANDS

S-IC STATIC TESTS - MTF

Delineated here is the relationship between acoustic claims per exposure and OA SPL as found from the S-IC data at MTF. The average is a best fit through the data (44 claims reported) and is thought to fit well within the upper bound, where practically the whole community would respond vigorously, and the lower bounds where responses are rare.

It was found that with an increase in OA SPL there is a corresponding nonlinear increase in the claim rate. The MTF claims per thousand households (C/T), exposed to farfield rocket noise is expressed by

$$C/T = 10^{-12.95 + .1162\,(OA\ SPL)} \qquad \text{NOTE: OA SPL Re: } 2 \times 10^{-5}\ N/m^2$$

Verification from this data is available only from the 100 to 125 dB range.

For application to other sources it must be remembered that the acoustic spectrum at the point of environmental concern must be similar to the spectra observed in this study. Community differences may likewise significantly affect the application of these claim rates.

ACOUSTIC DAMAGE CLAIMS PER 1000 HOUSEHOLD EXPOSURE vs. OVERALL SOUND PRESSURE LEVEL IN FIVE dB BANDS

S-IC STATIC TEST - MTF DATA

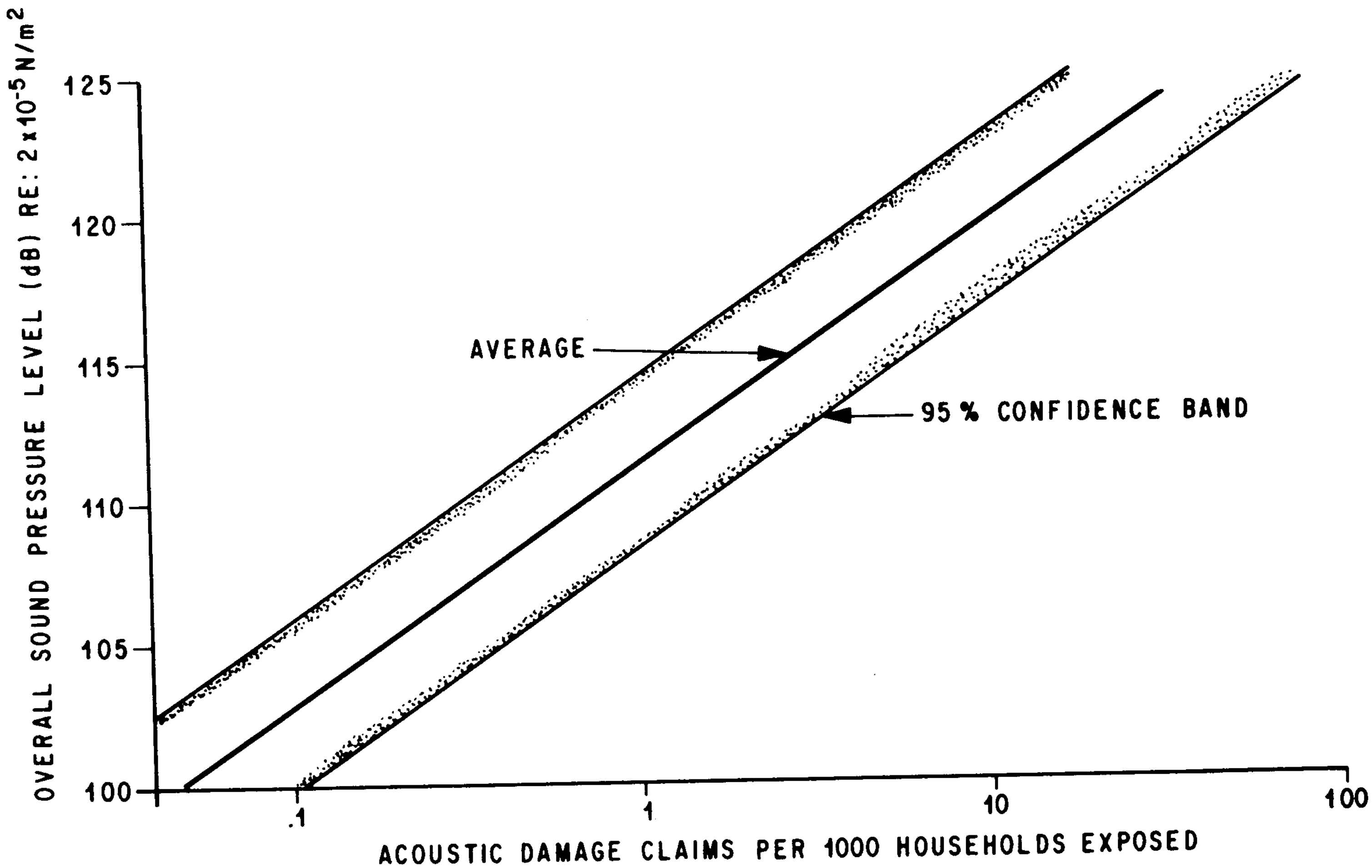

IN-FLIGHT AEROACOUSTIC ENVIRONMENTS ON PROSPECTIVE SPACE SHUTTLE VEHICLES

By Jules B. Dods, Jr. and Richard D. Hanly
NASA Ames Research Center, Moffett Field, Calif.

INTRODUCTION

The problem of in-flight aerodynamic noise has been studied extensively and it is known that reliable estimates of full-scale surface-pressure fluctuations can be made from scale-model tests in wind tunnels. Scaling relationships have been verified, and many details of the fluctuating pressure characteristics such as spatial correlation and convection velocities are understood. The effects of the wind-tunnel environmental turbulence and noise have also been investigated sufficiently so that threshold levels of usable data are known.

Although the background of general research information and previous scale model data can generally be used for preliminary estimates of aerodynamic noise, the locations and intensities of the pressure fluctuations are very dependent upon the configuration and attitude of the vehicle. In particular, because of the complexities of space shuttle configurations and expectations of much flow interference, tests have been necessary in order to make an acceptable assessment of the aerodynamic noise problem on shuttle configurations. Such tests of 4-percent-scale models of series-burn and parallel-burn launch configurations have recently been completed at Ames Research Center. The tests were conducted in the 11- by 11-foot TWT at Mach numbers from 0.8 to 1.4 The Reynolds number varied between 2.2 to 4.2 million per foot. Tests were also conducted in the 9- by 7-foot supersonic wind tunnel at M = 1.6 and 2.2. The Reynolds number in the 9- by 7-foot tunnel varied between 2.4 and 3.0 million per foot.

Although several configurations were investigated, the main emphasis in this paper will be on the parallel-burn launch configuration. Samples of flow visualization and some preliminary estimates of full-scale overall sound pressure levels and 1/3-octave spectra are presented. Additional data analysis is still in progress and will be reported at a later date.

VIBRO-ACOUSTICS INFLIGHT AERODYNAMIC NOISE

(Figure 1)

This figure illustrates the problem of high intensity pressure fluctuations due to transonic and supersonic shock waves and to areas of separated flow for the parallel-burn configuration of the space shuttle vehicle. The solid-rocket-motors add to the many existing regions of flow interference. The possibility of large areas of separated flow caused by the expansion of rocket exhaust gases at high altitude, or plumes, must be investigated at supersonic Mach numbers. The locations and intensities of the pressure flucutations are thus seen to be dependent not only upon the configuration but also upon Mach number and attitude and, therefore, can only be reliably estimated by wind tunnel tests. Once the unsteady pressure field is described, empirical methods based on similarity are currently employed to evaluate the structural response and noise transmission into cockpit areas and instrument bays. Because of uncertainty of response and particularly fatigue prediction techniques, heavy reliance is placed on environmental proof tests in acoustic test facilities.

VIBRO-ACOUSTICS
IN-FLIGHT AERODYNAMIC NOISE

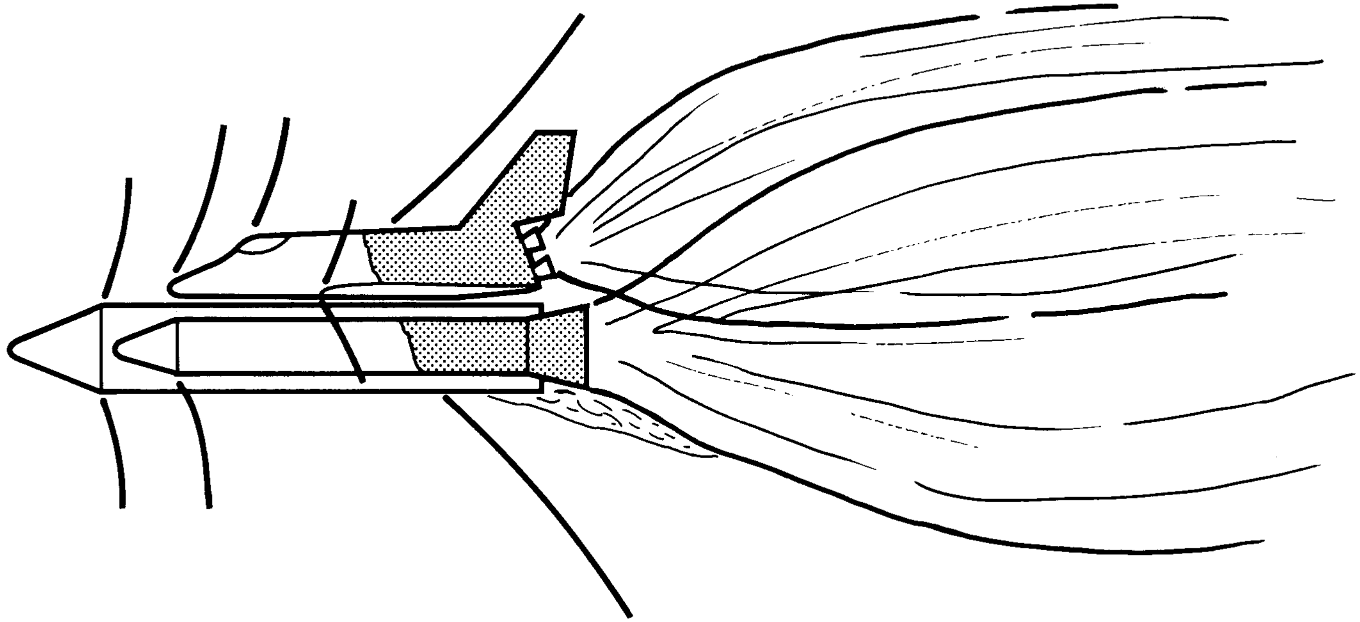

PARALLEL BURN

- HIGH PRESSURE FLUCTUATIONS DUE TO TRANSONIC SHOCK WAVES AND FLOW SEPARATION
- MANY REGIONS OF FLOW INTERFERENCE
- PLUME INDUCED SEPARATION AT SUPERSONIC MACH NUMBERS

Figure 1

FLOW VISUALIZATION - PARALLEL BURN CONFIGURATION

(Figure 2)

Flow visualization studies are necessary to detect regions of severe turbulence on a vehicle. Although some regions can be anticipated by visual inspection of the geometry, final definition of the environmental fluctuating pressures should be preceded by flow visualization studies. Presented here are shadowgraph photographs at $M = 0.9$ and 1.4 to illustrate the type of flow existing in the region between the orbiter and the HO tank, in the region of the canopy, and also the typical shock patterns. Although the SRM's are obscured by the HO tank, the shock pattern from the nose of these tanks can be seen. Although not illustrated here, studies of other shadowgraphs in which the HO tank had a 15° nose angle instead of the 20° nose on this configuration would indicate that the 15° nose would result in less flow turbulence along the HO tank at transonic Mach numbers. The fluorescent oil flow visualization technique is perhaps more useful than the shadowgraph technique in defining areas of flow turbulence and is actually used more extensively at Ames for this purpose. Examples of the fluorescent oil technique are presented later (figure 11) and also have been previously presented[1,2].

FLOW VISUALIZATION PARALLEL-BURN CONFIGURATION

$\alpha = \beta = 0°$

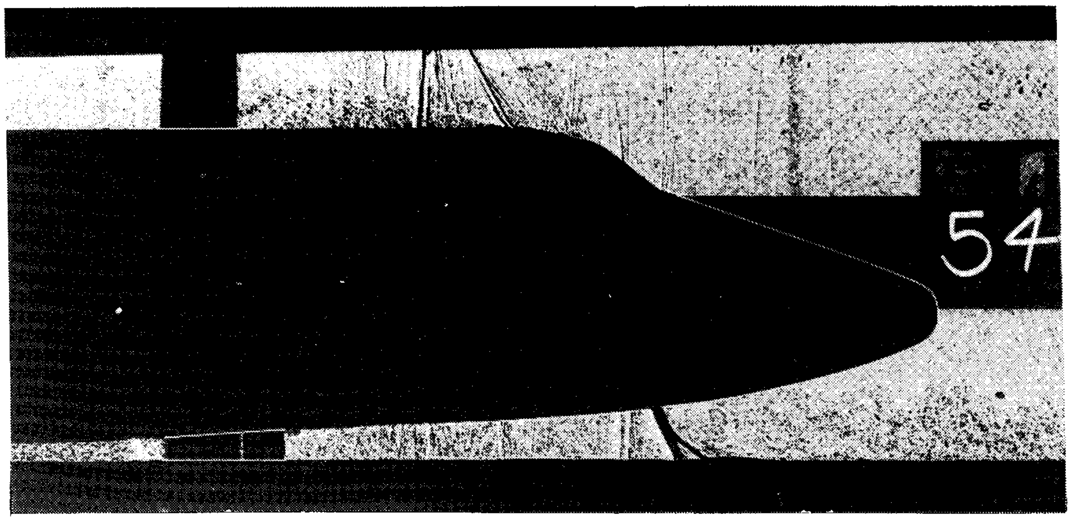

M = 0.9

M = 1.4

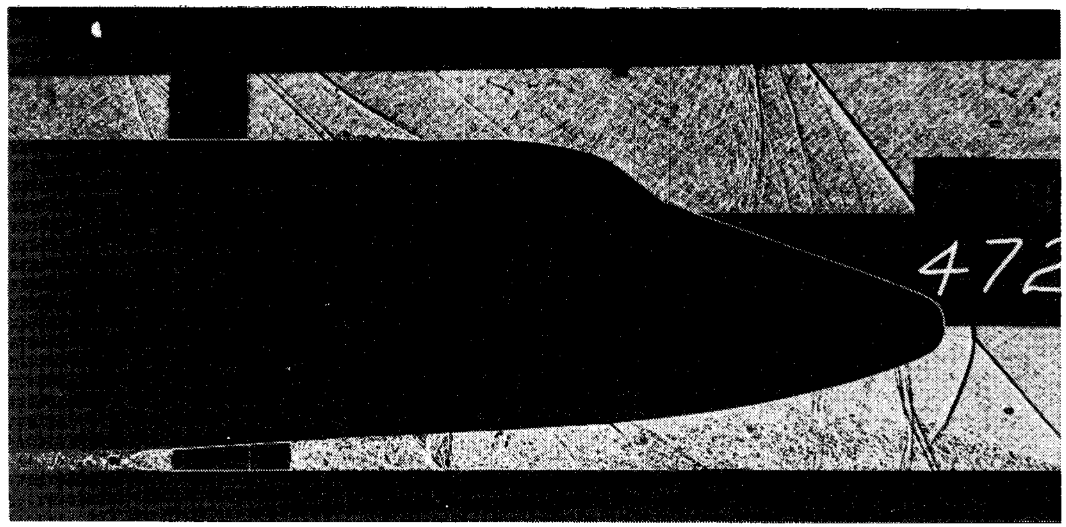

Figure 2

0.04-SCALE AERODYNAMIC NOISE MODELS IN TRANSONIC TUNNEL

(Figure 3)

The 0.04-scale aerodynamic noise models are shown in Figure 3 installed in the Ames Research Center 11- by 11-foot transonic wind tunnel. In addition to the series-burn and parallel-burn configurations, two canopy configurations, two positions of the orbiter nose relative to the HO tank nose, and two HO tank nose-cone angles (15° and 20°) have been tested. The HO tank represented a 6.60-meter (260-inch) full-scale tank. The series-burn configurations included a constant diameter 6.60-meter (260-inch) section of booster and also a 15° interstage flare followed by a cylindrical section representing a 10.06-meter (396-inch) booster. The parallel-burn configuration included a combination of orbiter, HO tank, and two scaled 3.96-meter (156-inch) solid rocket motors. The models were instrumented with approximately 65 static pressure orifices and with approximately 50 dynamic transducers. The dynamic transducers had an effective diaphragm diameter of 0.12 cm (0.048 inch) and were mounted flush with the model surfaces. Transition was artificially fixed on the nose of the orbiter, the nose of the HO tank, on the noses of the SRM tanks, and on the wings and vertical tail of the orbiter.

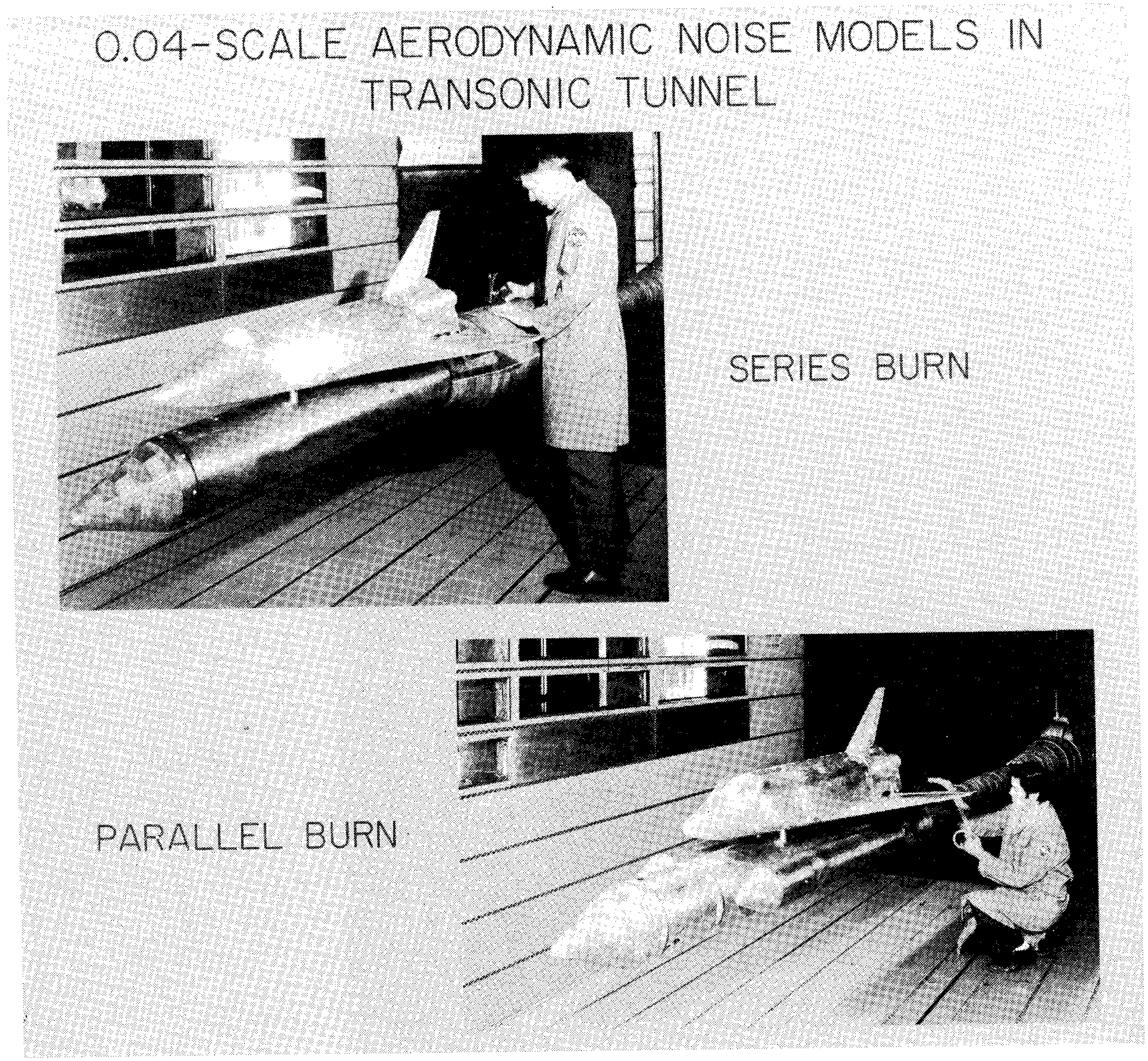
0.04-SCALE AERODYNAMIC NOISE MODELS IN TRANSONIC TUNNEL
SERIES BURN
PARALLEL BURN

Figure 3

LIFT-OFF AND TRANSONIC OASPL

(Figure 4)

Estimated lift-off noise levels are shown for comparison with estimated transonic in-flight levels obtained from the 4-percent-scale model tests. The results indicate that a large amount of surface area on the orbiter could be exposed to noise levels in excess of 160 dB. The noise levels shown represent the maximum measurements for the range of Mach numbers, angles of attack, and angles of sideslip tested and generally are slightly higher than would be obtained for a nominal $\alpha = 0°/\beta = 0°$ trajectory. The most significant effects of the parallel-burn configuration were to increase the noise levels on the underside of the orbiter nose and, although not shown, to increase the Mach number duration of high noise levels at some locations. The results show that the transonic noise exceeds the lift-off noise at many locations on the orbiter for either launch configuration. The higher lift-off noise on the parallel-burn vehicle combined with possible extended duration of aero-noise into supersonic Mach numbers from the exhaust plumes can adversely affect the fatigue of the orbiter TPS.

LIFT-OFF AND TRANSONIC OASPL

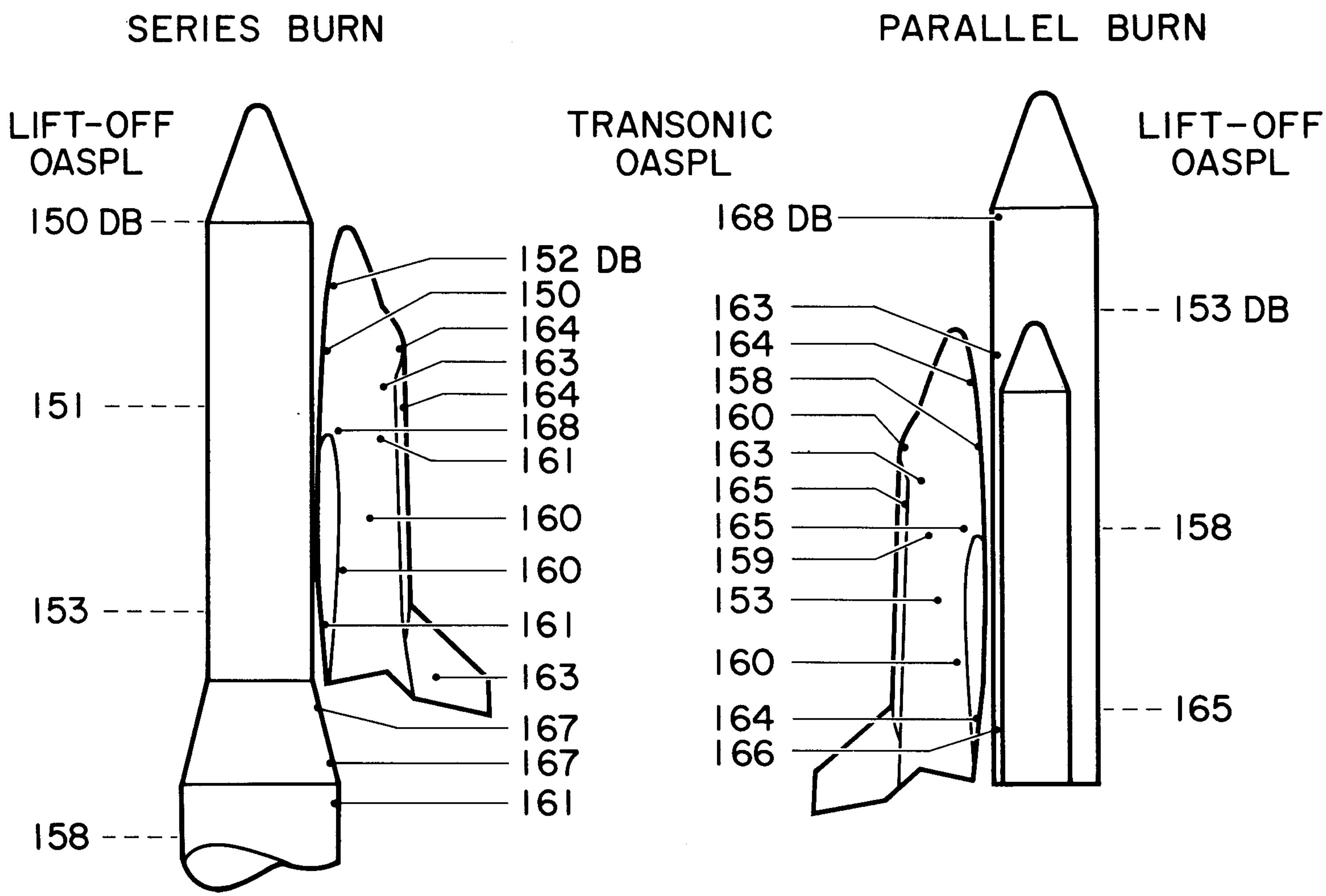

Figure 4

ESTIMATED PRESSURE FLUCTUATIONS DURING ASCENT - ORBITER NOSE REGION

(Figure 5)

The estimated pressure fluctuations in the region of the orbiter nose during ascent are shown in Figure 5 through the Mach number range of 0.8 to 2.2. The data in this figure and in the following Figures 6, 7, and 8 were scaled to full-scale conditions using standard scaling relationships. The full-scale dynamic pressures and velocities used for the launch trajectory are tabulated below. The data in Figures 5 and 6 represent maximum measurements obtained through the full range of angles of attack and sideslip tested.

The maximum overall fluctuating pressure levels (OAFPL) in the region of the orbiter nose HO tank reached peak levels of approximately 163 dB for the first two transducers (No. 1 and 2) at transonic and low supersonic Mach numbers. The OAFPL for transducer 3 appears to be increasing up to M=1.4 (the maximum Mach number for which data were available), and the level for transducer 4 is still increasing at M=2.2 which was the highest Mach number tested. Representative maximum one-third octave spectra peak at levels from 154 to 158 dB and at full-scale frequencies from 25 to 90 Hz. The lower frequency peaks of 25 to 30 Hz are for the two transducers (No. 1 and 2) that had maximum levels in the transonic Mach number range and thus are believed to be associated with shock oscillations. The higher frequency peaks for the other two transducers are associated with separated flows.

M	0.8	0.9	1.0	1.4	1.6	2.2
q_{FS}, N/m^2 (lb/ft^2)	21,929. (458.)	24,036. (502.)	26,095. (545.)	30,021. (627.)	30,021. (627.)	25,281. (528.)
U_{FS}, m/sec (ft/sec)	262.1 (860.)	292.6 (960.)	320.0 (1050.)	417.6 (1370.)	466.3 (1530.)	640.1 (2100.)

ESTIMATED PRESSURE FLUCTUATIONS DURING ASCENT

ORBITER NOSE REGION

$\alpha = 4°$ $\beta = 0°$

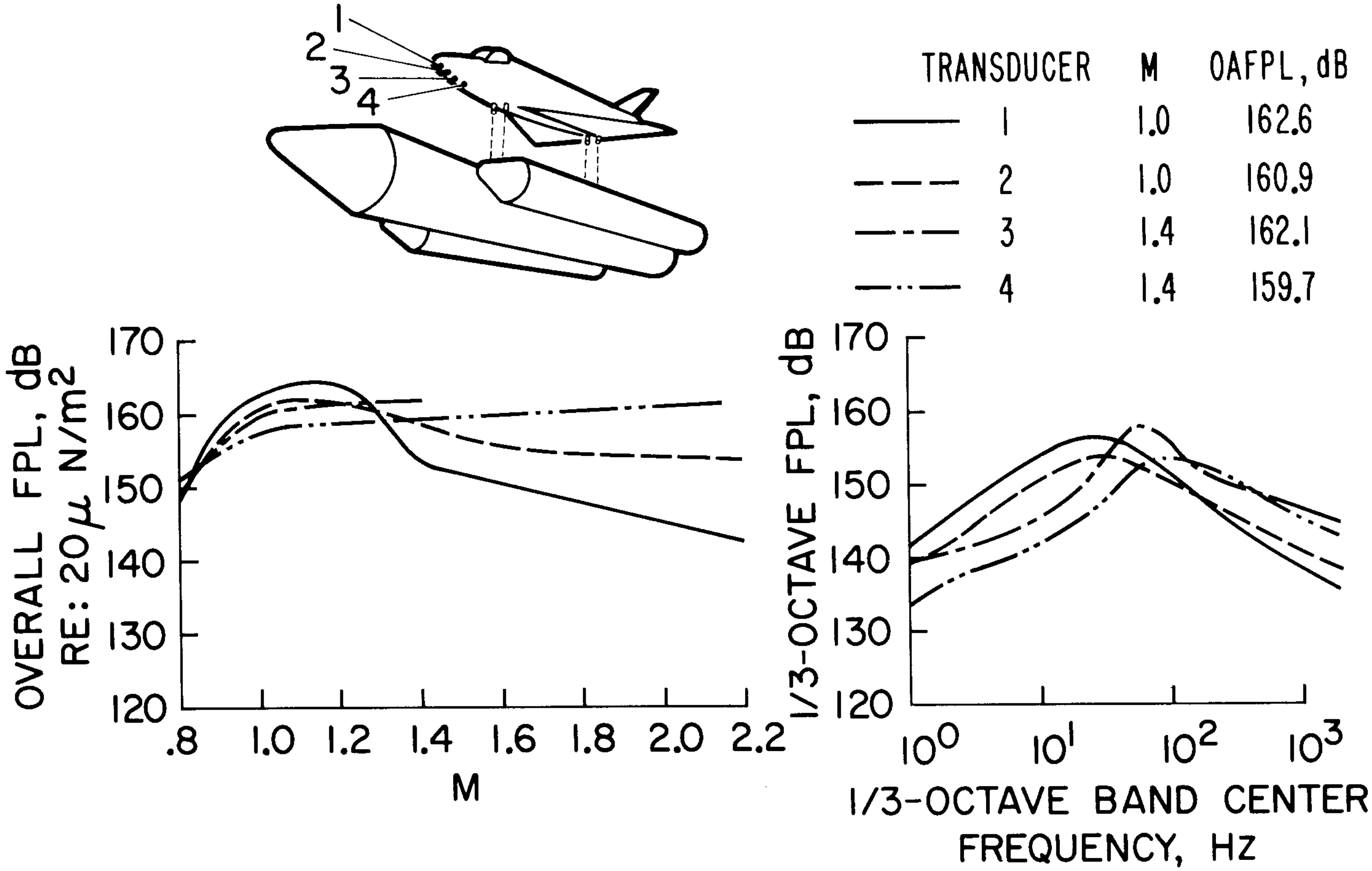

Figure 5

ESTIMATED PRESSURE FLUCTUATIONS DURING ASCENT - HO TANK REGION

(Figure 6)

Estimated full-scale pressure fluctuations on the HO tank due to flow interference from the orbiter nose are shown in Figure 6. The maximum overall fluctuating pressure level of 161 dB occurred at a Mach number of 1.0 for the forward transducer (No. 21), and the corresponding one-third-octave band pressure level peaked at about 154 dB. The frequency at which the peak occurred was 25 Hz, which corresponds closely with the frequencies measured for the forward transducers on the orbiter nose. Cross spectral analysis between transducers 2 and 21 (not shown here) indicates that the two transducers are being influenced by the same shock oscillation.

ESTIMATED PRESSURE FLUCTUATIONS DURING ASCENT

HO TANK REGION

$\alpha = 4°$ $\beta = 0°$

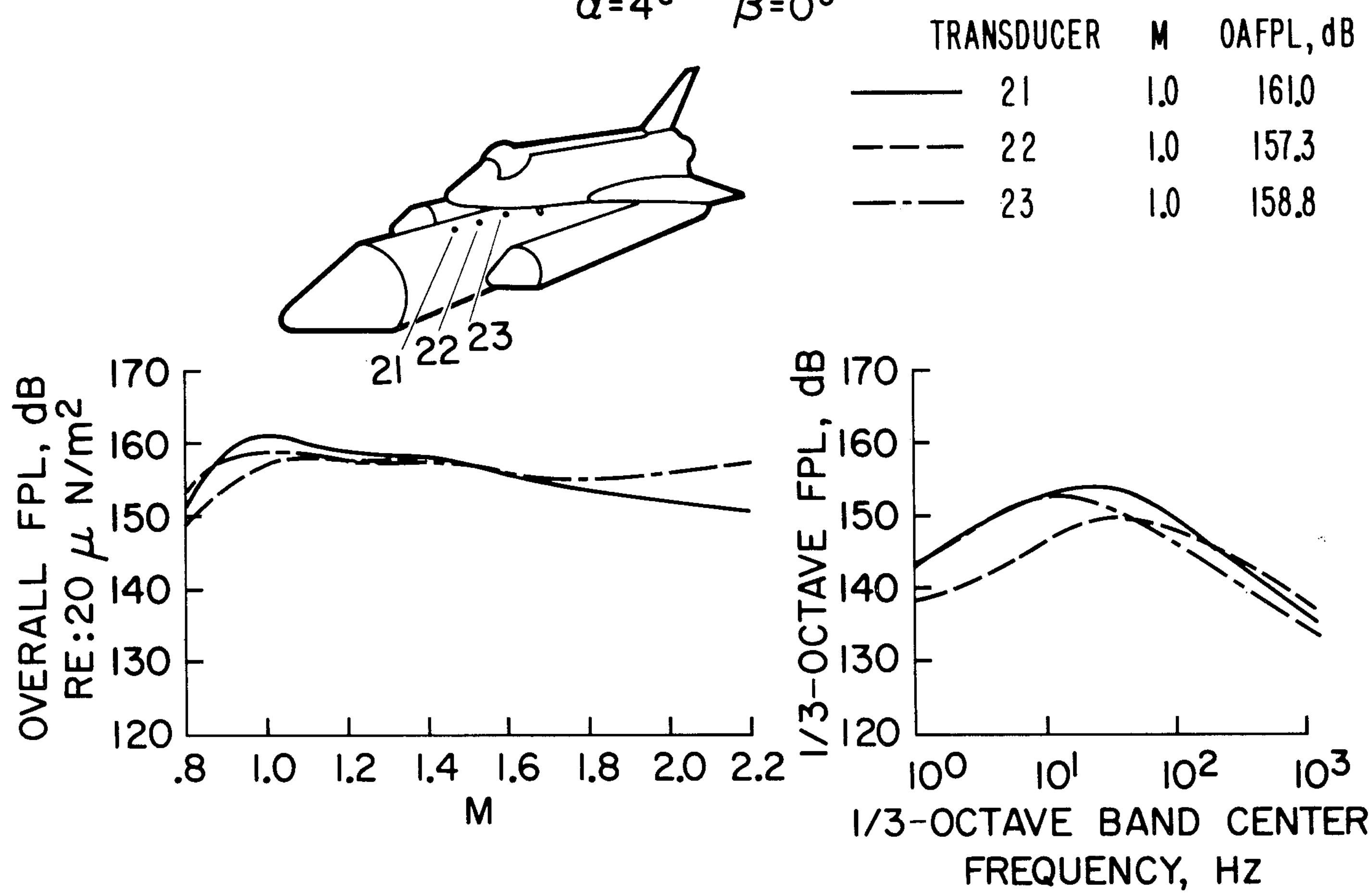

Figure 6

ESTIMATED PRESSURE FLUCTUATIONS DURING ASCENT - CANOPY REGION

(Figure 7)

Figure 7 shows the estimated pressure fluctuations on the canopy region of the orbiter throughout the Mach number range tested. The various cross-hatch codings indicate the excursions in intensity over the range of angles of attack from -8° to 8° and angles of sideslip from -5° to 5°, and the curves within the cross-hatchings are for $\alpha = \beta = 0°$. Peak fluctuating pressure levels occur in the transonic Mach number range for all transducers. As might be expected, as the Mach number is increased the overall fluctuating pressure level for the transducer on the canopy decreases considerably more than the two transducers located in the flow interference region downstream of the canopy. An examination of the one-third octave spectra shows that the three transducers all peak at about the same level (157 dB), but the frequency for the peaks vary considerably. As previously discussed, the lower peak frequency for the forward transducer is associated with shock oscillations whereas the higher peak frequencies for the downstream transducers are more characteristic of separated flow regions.

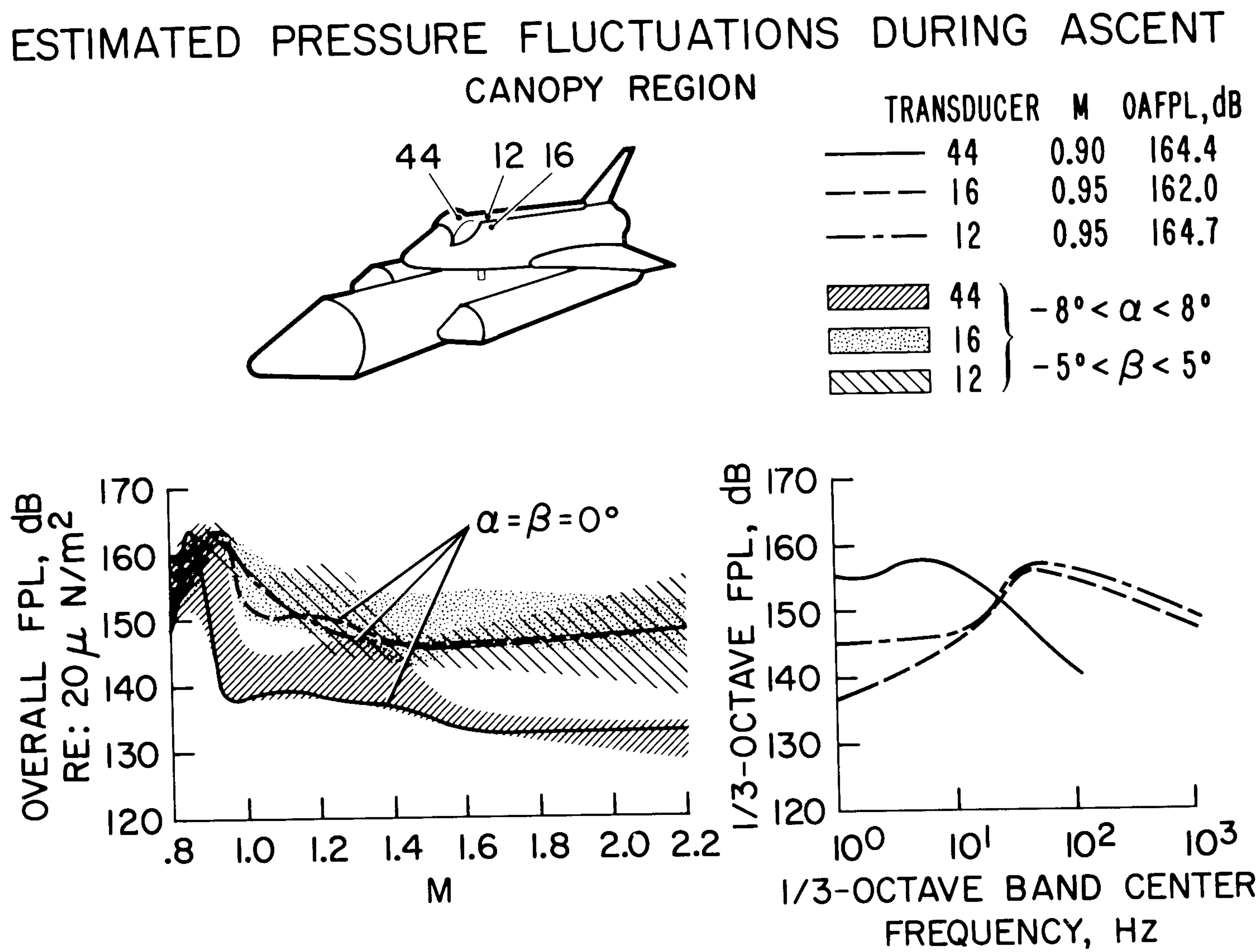

ESTIMATED PRESSURE FLUCTUATIONS DURING ASCENT
CANOPY REGION
44
12 16
TRANSDUCER M OAFPL, dB
44 0.90 164.4
16 0.95 162.0
12 0.95 164.7
44
16
12
$-8° < \alpha < 8°$
$-5° < \beta < 5°$
OVERALL FPL, dB
RE: 20 μ N/m²
170
160
150
140
130
120
.8 1.0 1.2 1.4 1.6 1.8 2.0 2.2
M
$\alpha = \beta = 0°$
1/3-OCTAVE FPL, dB
170
160
150
140
130
120
10^0 10^1 10^2 10^3
1/3-OCTAVE BAND CENTER FREQUENCY, HZ

Figure 7

ESTIMATED PRESSURE FLUCTUATIONS DURING ASCENT - WING, WING-BODY, AND TAIL REGIONS

(Figure 8)

This figure shows the estimated pressure fluctuations in several additional areas of interest for the parallel-burn configuration. For example, transducers 45 and 46 were located on the undersurface of the wing at a spanwise location corresponding to the edges of the SRM's.

The overall fluctuating pressure level of the inboard transducer is considerably larger, by about 10 dB, than the outboard transducer through most of the Mach number range. The large overall levels of the transducer located just ahead of the wing-body intersection (transducer 33) tend to be greater with the SRM tanks than without them particularly at positive angles of attack. The surprisingly large level measured on the tail at $M = 1.6$ would indicate that the flow over the tail is probably separated at this Mach number. The relatively high frequency (about 100 Hz) at which the spectral intensity peaks also would indicate that the flow is separated. This flow separation on the tail may be due to the diamond-shaped airfoil section.

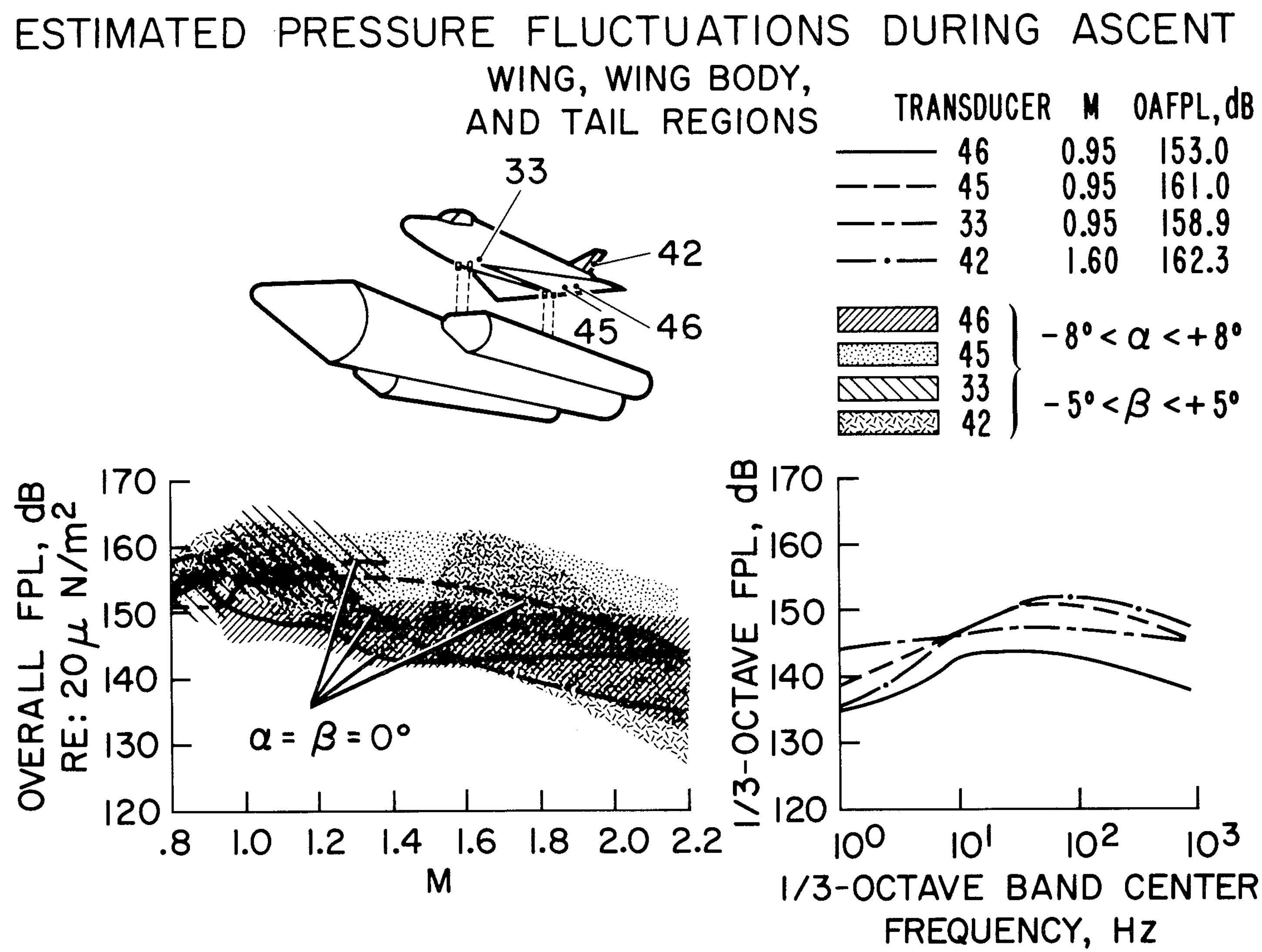
ESTIMATED PRESSURE FLUCTUATIONS DURING ASCENT
WING, WING BODY, AND TAIL REGIONS
33
42
45
46
TRANSDUCER M OAFPL, dB
46 0.95 153.0
45 0.95 161.0
33 0.95 158.9
42 1.60 162.3
46
45
33
42
$-8° < \alpha < +8°$
$-5° < \beta < +5°$
$\alpha = \beta = 0°$
OVERALL FPL, dB RE: 20μ N/m²
170
160
150
140
130
120
.8 1.0 1.2 1.4 1.6 1.8 2.0 2.2
M
1/3-OCTAVE FPL, dB
170
160
150
140
130
120
10^0 10^1 10^2 10^3
1/3-OCTAVE BAND CENTER FREQUENCY, Hz

Figure 8

HIGH ALTITUDE PLUME INDUCED FLOW SEPARATION - PRIOR INVESTIGATIONS

(Figure 9)

The phenomena of the high altitude plume induced flow separation has been reported by Jones[3] wherein photographic records of a Saturn V flight indicated that as much as one-third of the vehicle could be affected. An investigation[1,2] was reported on this effect on a 0.008-scale model of a space shuttle vehicle at a Mach number of 2. As shown in Figure 9 the simulated plume caused a large area of flow separation to occur on the booster delta wing. Although the plume simulation was not correct for the Mach number of the test, the results served to illustrate that the plume separation effects at higher Mach numbers could be severe. The proximity of the rocket nozzles to the orbiter wing, the vertical tail, and the control surfaces for the parallel-burn configuration will no doubt result in separation of the flow on these surfaces at some as yet undefined higher supersonic Mach number. A systematic investigation of jet-plume induced flow separation on axisymmetric bodies at Mach numbers of 3.00, 4.50, and 6.00 has been reported by McGhee[4]. The results of this investigation showed that increasing the jet-pressure ratio resulted in boundary layer separation over large regions of the test models at free-stream Mach numbers of 4.50 and 6.00. Only small amounts of flow separation occurred at a free-stream Mach number of 3.00 for which the test jet pressure ratios were considerably smaller than those for the higher Mach numbers. The problem of correctly simulating plume induced separation effects is thus seen to be important in defining the proper environmental conditions for space shuttle vehicles.

HIGH ALTITUDE PLUME INDUCED FLOW SEPARATION
PRIOR INVESTIGATIONS

REFERENCE 3

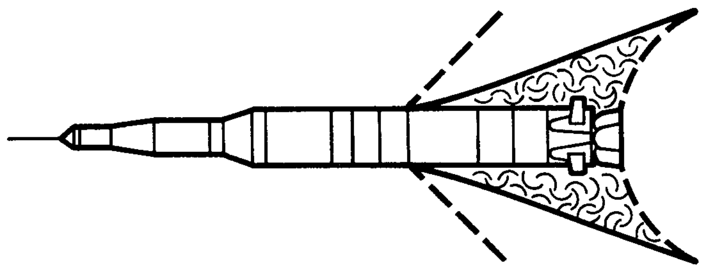

SATURN V FLIGHT
MACH No. 5.44
ALTITUDE 150 000 ft (45 700 m)
$\alpha = 2°$

REFERENCE 1

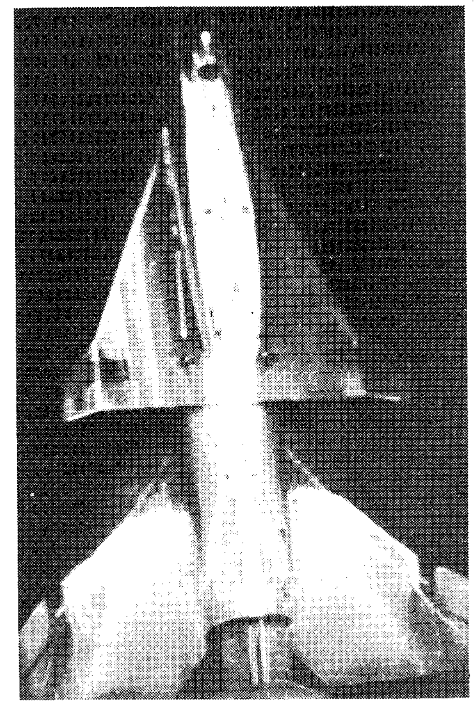

0.008-SCALE MODEL WITH
DELTA WINGS AND TIP FINS
MACH No. 2.0
$\alpha = 0°$ $\beta = 5°$

Figure 9

0.04-SCALE AERODYNAMIC NOISE MODELS IN SUPERSONIC WIND TUNNEL

(Figure 10)

During the course of the 4-percent-scale model tests it was learned that some earlier smaller scale tests of a parallel-burn configuration with simulated exhaust plumes showed separation of flow on the orbiter wings and tail. Similar plumes were then made for the 4-percent-scale model from solid bodies of revolution and the tests were extended to Mach numbers of 1.6 and 2.2. Photographs of the model with plumes as installed in the Ames 9- by 7-foot supersonic wind tunnel are shown in Figure 10. The model is shown in the parallel-burn configuration with plumes simulating the underexpanded exhaust gases from the SRM's and from the orbiter engines. Separate plumes were used to simulate conditions at Mach numbers of 1.6 and 2.2.

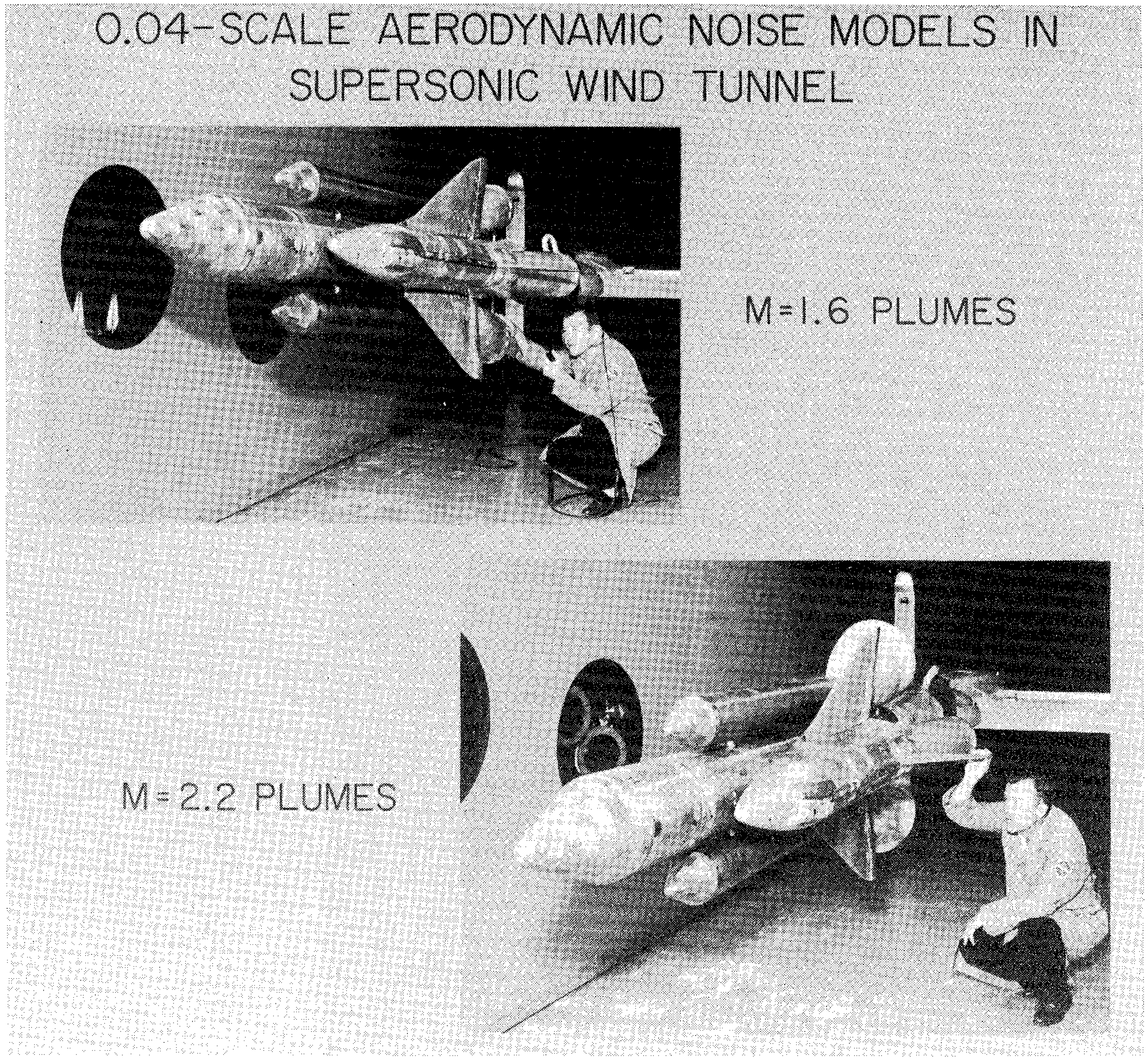
0.04-SCALE AERODYNAMIC NOISE MODELS IN
SUPERSONIC WIND TUNNEL
M=1.6 PLUMES
M=2.2 PLUMES

Figure 10

HIGH ALTITUDE PLUME INDUCED FLOW SEPARATION - PRESENT INVESTIGATION

(Figure 11)

In addition to the fluctuating pressure measurements, fluorescent oil flow studies were conducted with the parallel-burn configuration at $M = 2.2$ through an angle-of-attack range of $-8°$ to $8°$ and angles of sideslip of $0°$ and $-5°$. The photographs presented in Figure 11 are for angles of attack of -8, 0, and 8° at $-5°$ angle of sideslip. These three views, then, are for the leeward side of the model. A photograph for $\alpha = \beta = 0°$ is included for reference.

The pictures for $\alpha = \pm 8°$ indicate that there is a considerable amount of unsteady flow on the SRM's and on the HO tank. However, there appears to be no flow separation on the wings at these extreme angles. The view at $\alpha = -8°$ is apparent in the picture. Although the view at $\alpha = 8°$ does not show the wing, notes in the shadowgraph test log specifically indicated that there was no wing flow separation. The small amount of flow separation on the vertical tail is not caused by plume effects since the flow at $\beta = 0°$ appears to be attached.

HIGH ALTITUDE PLUME INDUCED FLOW SEPARATION

PRESENT INVESTIGATION

$M = 2.2$ PLUME SIMULATION; $q = 477$ lb/ft^2 (22 839 N/m^2)

$\alpha = -8°$ $\beta = -5°$ | $\alpha = 8°$ $\beta = -5°$

$\alpha = 0°$ $\beta = -5°$ | $\alpha = 0°$ $\beta = 0°$

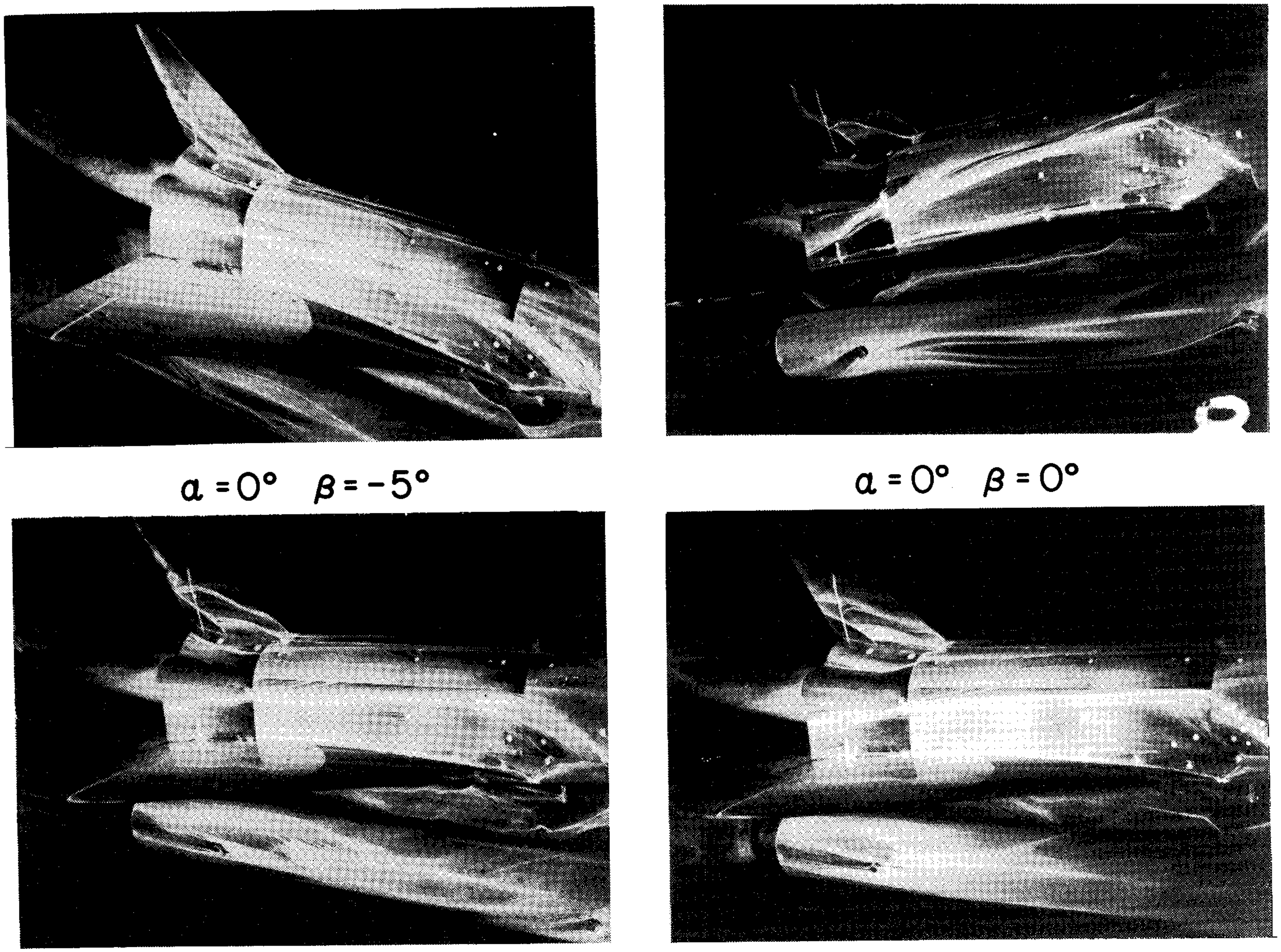

Figure 11

ESTIMATED PRESSURE FLUCTUATIONS DURING RE-ENTRY AT $\alpha = 60°$

(Figure 12)

Figure 12 presents some estimations of full-scale pressure fluctuations on a low-cross-range re-entry configuration at $\alpha = 60°$. The estimates have been made by Bolt, Beranek and Newman, Inc., as a part of a Langley Research Center sponsored contract to investigate boundary-layer noise and base pressure fluctuations at supersonic Mach numbers. Although this figure has been previously presented in Reference 1 (see Figure 9), it is repeated herein to illustrate that the re-entry configuration will probably have lower fluctuating pressures than the launch configuration and as a result will not determine the design aeroacoustic environment. The re-entry levels will be even less than shown here because the angle of attack for re-entry will be reduced from $\alpha \doteq 60°$ to $\alpha \approx 20°$, and a very small amount of separated flow, if any, will occur.

ESTIMATED PRESSURE FLUCTUATIONS DURING RE-ENTRY AT $\alpha = 60°$

0.004- AND 0.0077-SCALE BBN MODELS

$M = 4$; $q_{FS} = 4788\ N/m^2$ ($100\ lb/ft^2$)

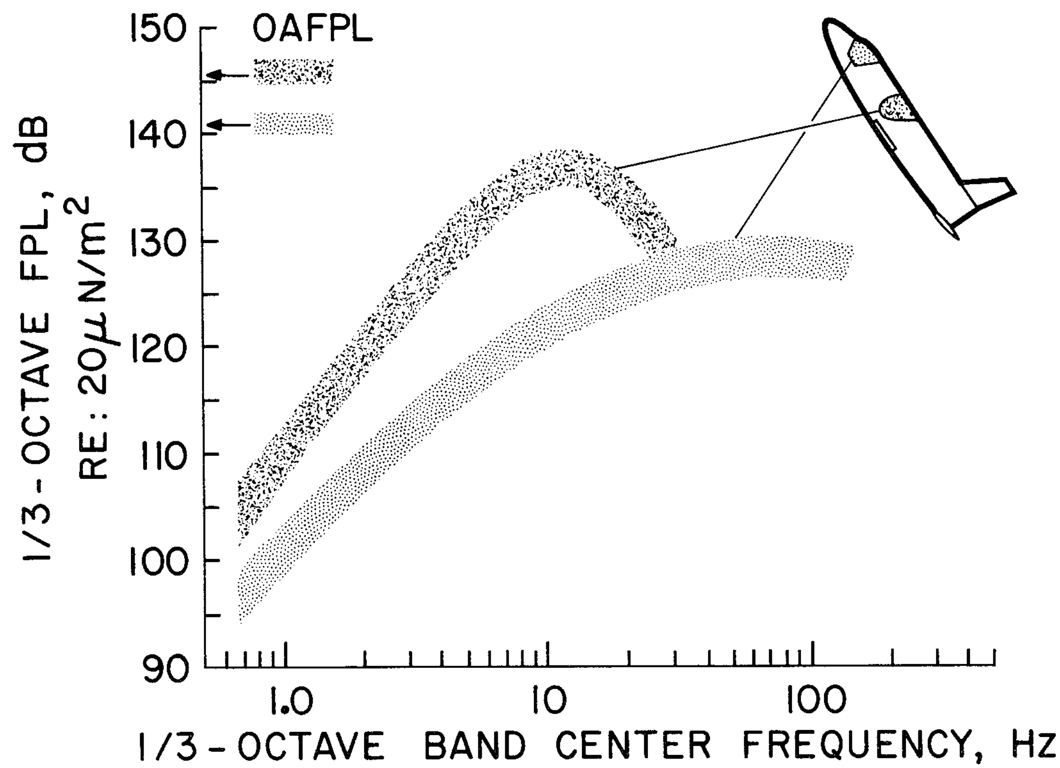

Figure 12

REFERENCES

1. Coe, Charles F.; Dods, Jules B., Jr.; Robinson, Robert C.; and Mayes, William H.: Preliminary Measurements and Flow Visualization Studies of Pressure Fluctuations on Space Shuttle Configurations. NASA TM X-2274, Vol. III, April 1971.
2. Dods, Jules B., Jr.; and Cangie, Carl D.: Flow Visualization Studies of Three Space Shuttle Launch Configurations at Mach Numbers from 0.8 to 2.0. NASA TM X-62074, Sept. 1971.
3. Jones, Jess H.: Acoustic Environment Characteristics of the Space Shuttle. NASA TM X-52876 Vol. II, July 1970.
4. McGhee, Robert J.: Jet-Plume-Induced Flow Separation on Axisymmetric Bodies at Mach Numbers of 3.00, 4.50, and 6.00. NASA TM X-2059, August 1970.

NEW CONSIDERATIONS FOR POGO PREVENTION ON SPACE SHUTTLE

By S. Rubin
The Aerospace Corporation
El Segundo, California

5

Complexity and variability are the basic factors which will complicate the effort to achieve pogo stability on the Space Shuttle vehicle system. Complexities of the liquid propulsion system result from (1) the multiple organ-pipe modes of the long oxidizer feedline in the frequency range of the active structural modes and (2) the complex flow circuits of the engine, particularly the presence of two turbopumps for each propellant. The structural complexities result from (1) the multibody configuration giving rise to strong coupling of longitudinal to other motions and (2) the nonaxisymmetric stiffness of the main liquid tanks leading to complications in the mathematical modeling of their hydroelastic behavior.

From the standpoint of variability, the wide range of payloads have a substantial influence on the structural modes. In addition, thrust control of the engine introduces variability into the propulsion dynamics. Pogo suppression, therefore, will be complicated by the fact that stability will have to be established over a much wider range of system variables than has heretofore been required. As a consequence additional burdens will be placed on the mathematical modeling, on the experimental programs, and on the analysis techniques to assure that stability can be achieved for this complex and variable system.

This presentation is not an overview of technology considerations for pogo; that is the subject of the following presentation. Here we offer certain recommendations for improving the methodology of pogo suppression for the Space Shuttle. These recommendations draw from investigations carried out for NASA at The Aerospace Corporation.

INTRODUCTION

- COMPLICATING ASPECTS FOR ACHIEVING POGO STABILITY
  - * SYSTEM COMPLEXITY
    - PROPULSION SYSTEM: LONG LOX LINE, COMPLEX ENGINE
    - STRUCTURAL CONFIGURATION: MULTIBODY, NONAXISYMMETRY
  - * SYSTEM VARIABILITY
    - PAYLOAD
    - ENGINE OPERATION
- CONSEQUENCES
  - * MORE STRINGENT REQUIREMENTS ON MATH MODELING AND ON SUPPORTING EXPERIMENTATION
  - * MAY NEED MORE POWERFUL APPROACHES TO SYSTEM MODIFICATION FOR STABILITY
  - * GREAT NEED FOR SIMPLIFIED ANALYTICAL TOOLS TO GUIDE STUDIES
- INVESTIGATIONS AT AEROSPACE ARE OUTLINED

The objective of one study was to investigate the relative effectiveness of booster lox accumulators at (1) the engine inlet (ahead of the boost pump), (2) between the boost pump and the main pump (inter-pump), and (3) at the discharge of the first-stage of the main pump. The engine-inlet location has been employed on all past vehicles. The main-pump-discharge location was recommended for study by an engine contractor as a means of reducing peaks in propulsion frequency response and to permit use of available gox within a heat exchanger for the accumulator pressurant. The boost-discharge location was conceived at Aerospace as a means of increasing the damping in feedline modes by forcing upstream oscillatory flow to pass through the relatively large resistance of the boost pump.

Note the indicated pressures at the three locations (appropriate during the latter portion of the burn period). For a given volume of pressurant gas in the accumulator, the compliance is inversely proportional to the steady pressure. Thus for equal volumes we see that the inter-pump accumulator has about 0.4 of the compliance of the engine-inlet accumulator, and for the main-discharge accumulator the factor is 0.04. The question is whether the lower compliances at the downstream locations for the accumulator, in combination with the associated higher upstream resistances, result in greater effectiveness.

ALTERNATIVE PLACEMENTS OF LOX ACCUMULATORS FOR HI-PC ENGINE

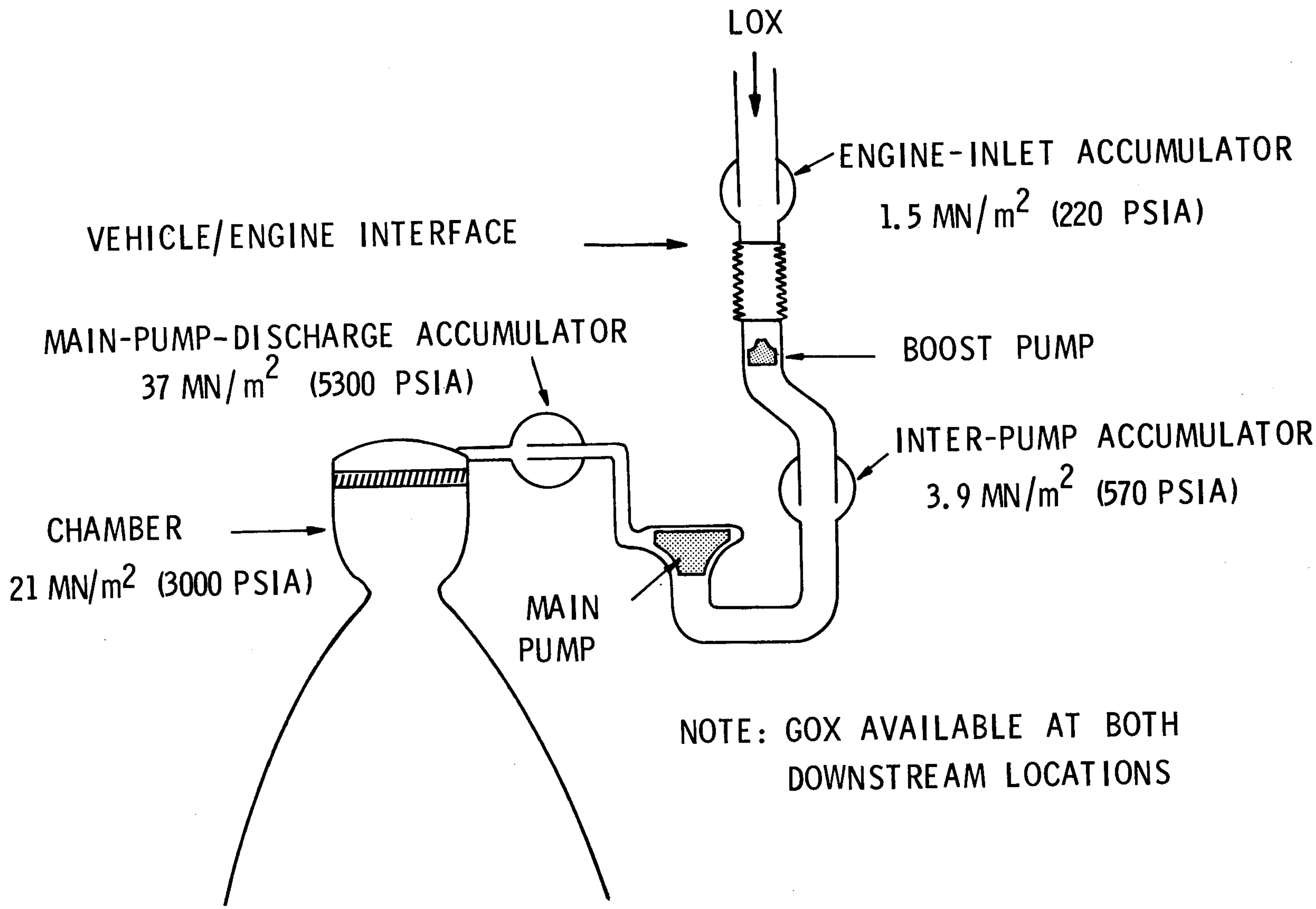

NOTE: GOX AVAILABLE AT BOTH DOWNSTREAM LOCATIONS

Certain coincidences of a structural mode and an open-open mode of the long lox feedline led to indication of potentially severe stability problems on the Phase B booster. For these cases tank-bottom pressure tended to dominate over engine motion as the exciter of the propulsion system (feedlines plus engines). Strong coupling could be achieved when the modal tank-bottom pressure per unit engine acceleration and the open-open organ-pipe modes combined to yield a positive propulsion feedback. The relationship of the structural and organ-pipe mode frequencies was extremely critical. The critical tuning was obtained by setting the nearby structural mode at the frequency for which the negative imaginary part of the propulsion feedback (H_I) is a maximum (Ref. 1). This frequency is slightly above the open-open organ-pipe frequency by an amount which depends upon the termination impedance at the engine end of the feedline. So cavitation and an accumulator, for example, are influencing factors.

With an accumulator at the engine inlet, even the small distributed feedline resistance was shown to have a large effect on the maximum value of H_I at high-frequency peaks (of the order of 20 dB or more). Moreover, it was shown that damping in the feedline modes due to distributed flow resistance is inversely proportional to the modal frequency, in contrast to the usual assumptions of constant or increasing damping with modal frequency. A consequence of the lesser damping of the higher feedline modes was a substantially greater susceptibility to instability involving those modes.

The study of the three accumulator locations on one of the Phase B vehicle configurations showed the inter-pump one required the smallest volume. It was also insensitive to feedline damping, in contrast to the great sensitivity for the engine-inlet location. The study on another configuration produced a condition of instability when the system was behaving in essentially a passive manner (that is, with negligible chamber pressure). An investigation revealed that the probable cause of this unreasonable result was neglect of the effect of oscillatory outflow from the vehicle tank on the internal pressures within the tank.

A new study of accumulator location should be conducted with appropriate account for tank outflow. The inter-pump accumulator location may or may not prove to be advantageous. In any case, the unexpected identification of a deficiency in mathematical modeling for tank outflow has been a most worthwhile consequence. The resulting study is discussed next.

CONCLUSIONS FROM PHASE B STUDY OF ACCUMULATOR LOCATION FOR BOOSTER

- MAJOR STABILITY DIFFICULTIES CAN ARISE FROM COINCIDENCE OF LOX ORGAN PIPE AND STRUCTURAL MODES
  - * TANK-BOTTOM PRESSURE EFFECTS DOMINATE
  - * TUNING CRITICAL, FREQUENCY ALIGNMENT INADEQUATE
- DISTRIBUTED FEEDLINE RESISTANCE SIGNIFICANT FOR ENGINE-INLET LOCATION
  - * FLOW RESISTANCE LEADS TO LINE MODAL DAMPING $\propto 1/\omega_n$
- INTER-PUMP LOCATION IS SUPERIOR
  - * SMALLER VOLUME REQUIRED
  - * INSENSITIVE TO FEEDLINE DAMPING
- A CERTAIN PHYSICALLY UNREASONABLE RESULT OBTAINED BECAUSE TANK OUTFLOW EFFECTS NOT CONSIDERED
- SHOULD RESTUDY WITH TANK OUTFLOW CONSIDERED

Two approaches have been employed for coupling a hydroelastic tank to the feedline it supplies. The most common one is to determine the modes of the structural system with the tank closed and the feedline absent. The coupling of the feedline to the tank then assumes that pressures in the tank interior are unaffected by flow into the feedline. Reference 2 correctly concluded that this assumption was invalid based on an elementary model of the tank (even though the derivation is somewhat erroneous). It was shown that the integrated effect of the small change in tank-interior pressures can easily produce a generalized force on the structural mode which is of the same order of significance as the engine-inlet force. This result has been ignored until recently.

Another approach is to include a lumped-parameter model of the feedline in the structural system. An account for flow continuity into the tank was derived based upon a tank model consisting of a fluid mass acting on a tank-bottom spring. This method of accounting for flow continuity was then assumed to be applicable to a single-mass representation of the hydroelastic tank. For the Space Shuttle a multimode representation of hydroelastic tanks is required and this approach is inapplicable.

By a method involving an application of Hamilton's principle and the superposition of one potential function for a closed flexible tank and another function for an outflowing rigid tank, R. G. Wagner at Aerospace developed the feedline coupling equations for a structural system containing an incompressible liquid in a general elastic tank. These coupling equations in combination with transmission equations across the feedline show that the principal effect of tank outflow can be viewed as a modification of the engine-inlet force excitation of the structural system. It is anticipated that tank outflow will have great importance for the Shuttle because the high-chamber-pressure engines tend to produce a large engine-inlet force relative to thrust. As a corollary, the usefulness of "engine gain" (thrust divided by engine-inlet force) as a simple indicator for the stability of one vehicle relative to another is now seen to be even more questionable than it was previously.

Several assessments of the importance of the structural excitation due to tank outflow have been made. One result was a change of 3 dB at the time of minimum stability for a Titan Centaur vehicle. Other cases led to a stabilizing propulsion feedback because of outflow, when without outflow there were strong instabilities involving coincidence of open-open organ-pipe modes with a structural mode (including the Phase B case which originally prompted the investigation of tank outflow).

ANALYTICAL COUPLING OF HYDROELASTIC TANKS AND FEEDLINE

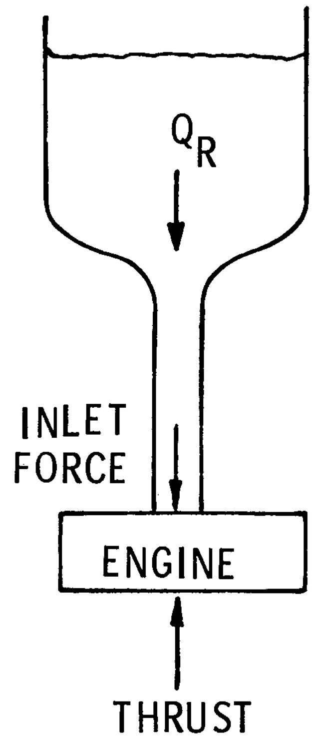

- TWO APPROACHES USED IN PAST

  1. STRUCTURAL MODES FOR CLOSED TANKS ($Q_R = 0$); WRONGLY NEGLECT EFFECTS ON PRESSURE TANKS DUE TO OUTFLOW INTO FEEDLINES
  2. INCLUDE FEEDLINES IN STRUCTURAL SYSTEM, ACCOUNT FOR TANK/FEEDLINE COUPLING LIMITED TO ELEMENTARY TANK MODEL

- APPROPRIATE COUPLING EQUATIONS NOW AVAILABLE FOR INCOMPRESSIBLE LIQUID IN GENERAL ELASTIC TANK

- EFFECT ON STRUCTURAL EXCITATION PRIMARILY A MODIFICATION OF ENGINE-INLET FORCE

- STUDIES CONFIRM IMPORTANCE FOR STABILITY

Reference 1 presents a derivation of a propulsion-feedback transfer function for a simplified single-propellant circuit. This function expresses the effective thrust per unit engine acceleration, accounting for tank-bottom pressure as prescribed by the structural mode shape. The effective thrust accounts for the net effect of the actual thrust and the engine-inlet force (sometimes called the suction-pressure feedback force).

For the purpose of our Shuttle pogo studies, additional items are included in the propellant circuit, tank outflow effects are added, and a new transfer function is derived. The additional items in the propellant circuit are uniformly distributed resistance in the feedline, two pumps with branch devices (cavitation and/or accumulators) at the inlet of each, and a combustion impedance which accounts for both a transport time delay and a chamber residence time.

As shown in Ref. 1, the closed-loop system damping is approximately proportional to the imaginary part of the propulsion-feedback transfer function evaluated at the structural natural frequency. This is valid when the feedback function is slowly varying relative to the structural transfer function in the neighborhood of a structural mode. On this basis, a good deal of estimating of effects on system stability can be made using the feedback function. The significance of uncertainties in propulsion parameters can be assessed, critical conditions of the coupled system for stability can be identified, and preliminary studies can be made of system corrections for stability.

PROPULSION-FEEDBACK TRANSFER FUNCTION

- EXPRESSION DERIVED FOR EFFECTIVE THRUST PER UNIT ENGINE ACCELERATION
  - * SIMPLIFIED SINGLE PROPELLANT CIRCUIT: TWO PUMPS, TWO BRANCH DEVICES, ORGAN PIPE
  - * EXPRESSION DERIVED FOR CHANGE DUE TO TANK OUTFLOW
- UTILITY BASED ON APPROXIMATE RELATION OF CLOSED-LOOP DAMPING WITH IMAGINARY PART
- APPLICATIONS
  - * ASSESSMENT OF PARAMETER SIGNIFICANCE
  - * IDENTIFICATION OF CRITICAL CONDITIONS
  - * PRELIMINARY STUDIES OF CORRECTIONS

Experience has shown that turbopump dynamic tests are difficult to perform and even more difficult to interpret. Because of the Shuttle engine's complexity and variability, past procedures for dynamic testing of the turbopumps will be most inadequate and indeed wasteful of resources. The difficulties are associated with the questionable inference of dynamic flow from pressure data, test setups which produce an inordinate sensitivity of the results to data inaccuracies, inattention to the linearity of turbopump behavior, and insufficient test conditions for independent determination of the turbopump parameters.

From the standpoint of what it is we should be trying to measure, consider a turbopump to be endowed with the input-output state variables of inlet pressure and flow, discharge pressure and flow, and turbine speed and flow. A full description of the turbopump dynamics involves a dynamical matrix relationship among these variables of order 3 by 3 containing nine functions of frequency as its elements. Our goal should be to determine these nine functions, for perturbation behavior of the turbopump, from test data and to correlate these functions with a linearized physical model of the turbopump. In addition the variation of these linear dynamics with changes in turbopump operating point must be established. This must be done with acceptable accuracy as efficiently as possible.

Needed is thorough test planning regarding such things as the completeness of the determination of turbopump dynamics, dynamic flow instruments, linearity evaluations, and a host of other matters. A three-step program is recommended, involving tests of the subscale pumps which are built for water flow testing in connection with turbopump development for operational performance.

EXPERIMENTAL DETERMINATION OF TURBOPUMP PERTURBATION DYNAMICS

- IMPROVED PROCEDURES NEEDED
- SCHEMATIC REPRESENTATION OF TURBOPUMP DYNAMICS

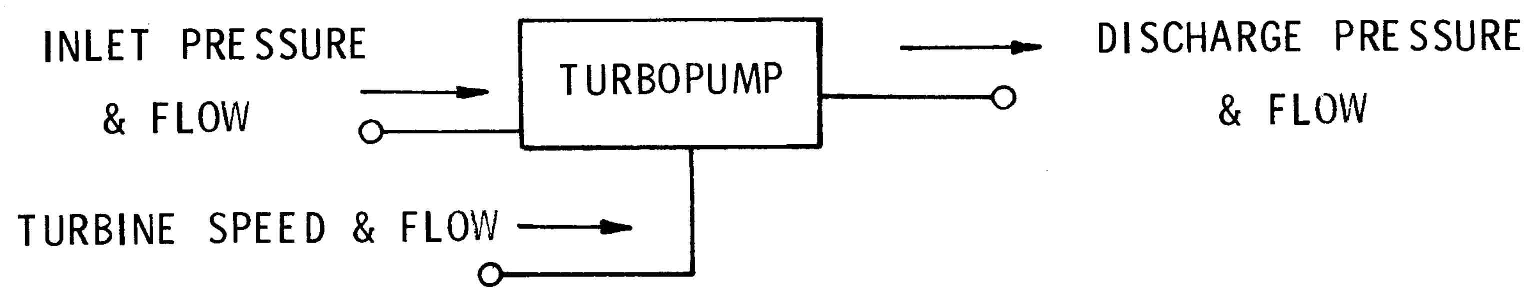

- IDEAL GOAL: OBTAIN NINE TRANSFER FUNCTIONS IN LINEAR RANGE AND CORRELATE WITH A PHYSICAL MODEL (OVER RANGE OF OPERATION)
- NEW PRACTICES RECOMMENDED
  * TEST CONDITIONS FOR INDEPENDENT DETERMINATIONS
  * DYNAMIC FLOW INSTRUMENTATION
  * LINEARITY EVALUATIONS
  * THREE-STEP PROGRAM FOR GREATEST EFFECTIVENESS

Up to recently the usefulness of any cavitation compliance data on a subscale pump with water would have been regarded as highly questionable. However, results obtained during recent studies at Aerospace on the empirical correlation of cavitation compliance data for Saturn turbopumps should alter this attitude. Test-derived compliance data were available for H-1, F-1 and J-2 fuel and oxidizer turbopumps (designated by (F) and (O), respectively). One result of our study is the plot shown giving nondimensional compliance versus a normalized ratio of suction specific speed, a standard nondimensional pump performance parameter.

Consider the following range of parameters among these pumps: inducer diameters from 0.15 m. (6 in.) for the H-1 (F) to 0.41 m (16 in.) for the F-1 (O); propellants from RP-1 to liquid oxygen to liquid hydrogen for the J-2 (F); and from single-stage centrifugal pumps to an axial pump for the J-2 (F). Since the indicated degree of correlation exists over all these differences, isn't it reasonable to expect a good correlation between say a half-scale replica pump tested with water and the full-scale pump with the actual propellant? We feel that it is and that use be made of tests on subscale pumps for obtaining dynamic as well as the usual performance data.

BASIS FOR USEFULNESS OF SUBSCALE PUMP TESTING

- EMPIRICAL EVALUATION OF CAVITATION COMPLIANCE OF SATURN PUMPS SUGGESTS SCALE AND FLUID EFFECTS CAN BE ACCOUNTED FOR

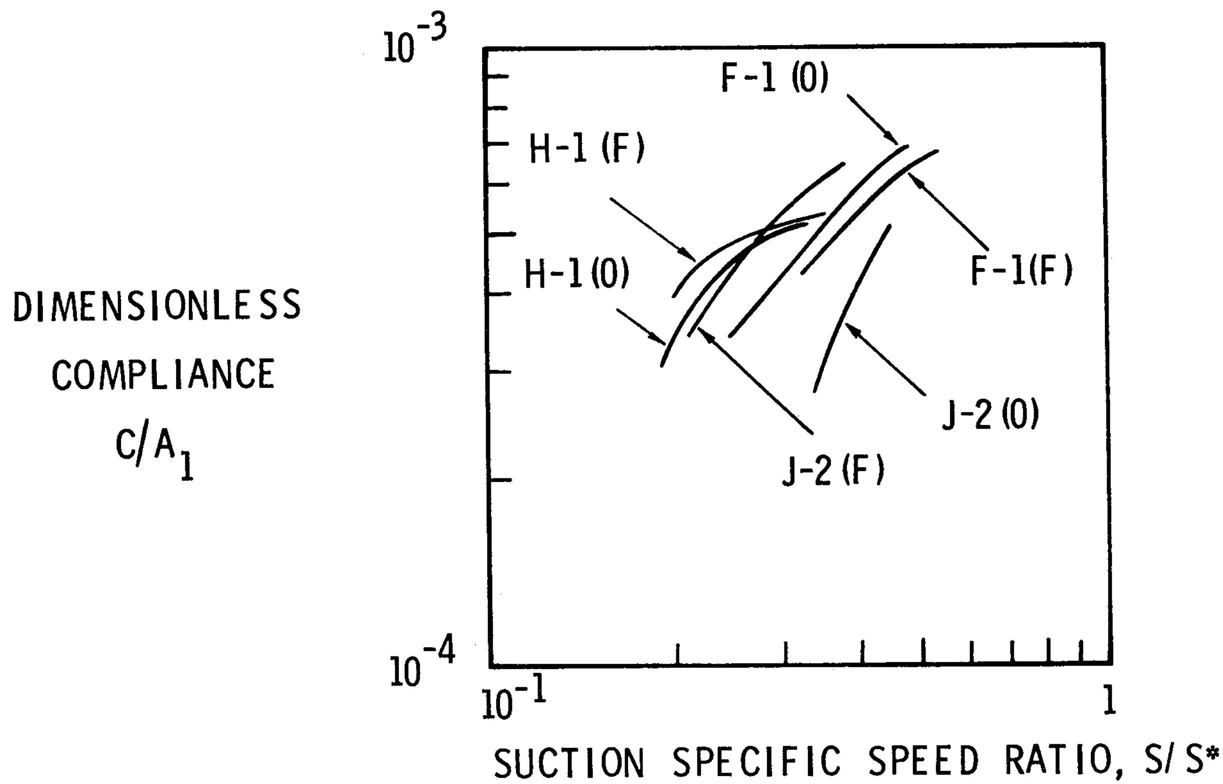

C ~ COMPLIANCE, A_1 ~ INLET AREA

S ~ SUCTION SPECIFIC SPEED (S* AT 5 PERCENT DROP IN HEAD)

The first step in a program for determination of turbopump dynamics should be studies on a computerized test simulator. A best-estimate nonlinear representation of turbopump would be employed and alternative test procedures would be evaluated. Excitation techniques for collection of the most useful data in a minimum of test time is a most important area for study. One of the major limitations for turbopump testing is the run time per test and the number of tests that the budget will allow. Sinusoidal excitation techniques to be studied are (a) step changes of frequency, (b) a predetermined frequency sweep, (c) a closed-loop controlled frequency sweep (ref. 3), and (d) a multisinusoidal frequency sweep involving several simultaneous sinusoids. Also to be studied is random testing using the self-noise of the system or externally applied random excitation. Perhaps some combination of excitation techniques is best; for example, an initial approximate determination of major resonant characteristics from self-noise, followed by harmonic testing tailored on the basis of the initial results.

Additonal studies would be addressed to the matter of independent determination of turbopump dynamics by performing tests with several boundary conditions on the turbopump and/or by exciting the system at several different positions (that is, inlet, discharge, turbine). Exciter requirements could be established, plans for linearity evaluation could be checked, accuracy of the results could be estimated based on presumed instrumentation accuracies, and so on.

The next step is to test the subscale pumps with water to get information on the pump dynamics over its operating range. This testing should be much less expensive than full-scale tests with propellant and may be able to be started as much as a year or more before the full-scale dynamic tests could begin. The subscale testing would also be used to evaluate test procedures, instrumentation, data reduction methods, and the degree of correlation with a physical model of the pump.

The final phase is testing of the full-scale turbopump with propellant on a highly selective basis. This phase should be aimed at verification of the available dynamic model based on the subscale testing augmented to account for the turbine dynamics (since the model probably will have been driven by an electric motor).

The benefits of such a three-step program are indicated.

THREE-STEP PROGRAM FOR TURBOPUMP DYNAMICS

1. COMPUTERIZED TEST SIMULATOR STUDIES TO EXPLORE ALTERNATIVE TEST APPROACHES

2. TESTS OF SUBSCALE DEVELOPMENT BOOST PUMPS WITH WATER
   * DATA LIKELY TO BE VALID
   * CHECK OUT PROCEDURES

3. TESTS OF FULL-SCALE TURBOPUMPS WITH PROPELLANT
   * SELECTIVE EVALUATION FOR PROPELLANT, SCALE, TURBINE EFFECTS

- BENEFITS RE FULL-SCALE TESTS ONLY
  * BETTER UTILIZATION OF MANPOWER AND FACILITIES
  * MINIMIZES POSSIBILITY OF PANICS LATE IN DEVELOPMENT PROGRAM
  * MORE THOROUGH AND ACCURATE RESULTS FOR SAME TOTAL COST

The first four recommendations have been covered by previous discussion.

The last recommendation has to do with the manner in which the engine dynamics are expressed. We have had a practice for the Saturn vehicle of representing an engine by transfer functions expressed in functional form without relation to physical parameters. This must be augmented for the Space Shuttle by a physical mathematical model consisting of a system of equations expressing the linearized dynamics of the significant elements of the engine. This is needed for a number of reasons: (a) for parametric studies of the engine components (b) for correlation of test data (including data for internal engine variables) with the mathematical model, (c) to maintain visibility over the consequences of varying thrust, off nominal conditions, or malfunctions, and finally (d) to maintain full cognizance over the assumptions made in deriving the transfer functions.

RECOMMENDATIONS

- INTER-PUMP LOCATION SHOULD BE CONSIDERED FOR ACCUMULATOR OR ACTIVE DEVICE
- TANK OUTFLOW EFFECTS MUST BE INCLUDED IN ANALYSES
- SIMPLIFIED TRANSFER FUNCTIONS SHOULD BE USED AS AN AID FOR SYSTEM STUDIES
- PLAN NEW APPROACH FOR TURBOPUMP DYNAMIC TESTING
  - THREE PHASE PROGRAM RECOMMENDED
  - DYNAMIC FLOWMETERS SHOULD BE DEVELOPED
- LINEARIZED MATH MODEL OF ENGINE PHYSICS SHOULD BE AVAILABLE FOR STUDIES

REFERENCES

1. Rubin, S.: Longitudinal Instability of Liquid Rockets Due to Propulsion Feedback (POGO), J. Spacecraft and Rockets, vol. 3, no. 8, pp. 1188-1195, Aug. 1966.

2. Lewis, W.: Simplified Analytical Model for Use in Design of Pump-Inlet Accumulators for the Prevention of Liquid-Rocket Longitudinal Oscillation (POGO), NASA TN D-5394, Aug. 1969.

3. Lorenzo, C. F.: Variable-Sweep-Rate Testing: A Technique to Improve the Quality and Acquisition of Frequency Response and Vibration Data, NASA TN D-7022, Dec. 1970.

OVERVIEW OF TECHNOLOGY RELATIVE TO THE POGO INSTABILITY ON SPACE SHUTTLE

By Larry D. Pinson
NASA Langley Research Center

and

John E. Harbison
NASA Marshall Space Flight Center

INTRODUCTION

The prediction of pogo, which is an instability, has frustrated analysts for many years. Much progress has been made but deficiencies still exist. There are two major sources of uncertainty with regard to pogo. One source is the sensitivity of the system to small random variations from nominal conditions. This sensitivity is illustrated by a recent analysis of a launch vehicle in which nominally the zero-phase gain margin was 4.7 dB, but this value was reduced to 0.5 dB when the parameters of the system were varied within their estimated tolerances. Some parameters which combine to cause large changes in the stability margin are structural gain, structural damping, and engine gain. The other source of uncertainty is the difficulty in defining the dynamic characteristics of certain components. This last source of uncertainty will be discussed herein. Emphasis is placed upon the areas in which work is most needed. In this paper, an overview of the technology with respect to each of the elements of the pogo problem is presented. For purposes of discussion, the problem is divided into the following areas: structure, tank-liquid interaction, feedline, engine (pump), pogo-loop/control-loop interaction, and stability analysis.

SYMBOLS

A, B, C, D	elements of transfer matrix
C	damping matrix
K	stiffness matrix
M	mass matrix
p	pressure
q	flow rate
s	Laplace variable
ΔT	thrust variation
α, β	constants of proportionality
ω	circular frequency

Subscripts:

d	discharge
j	component number
s	suction

STRUCTURE

(Figure 1)

The dynamic characteristics of a linear structure are fully described by expressions for three properties: mass, stiffness, and damping. Each of these expressions is related to an appropriate and convenient set of coordinates.

There are two methods in use for describing mass properties. These are lumping and the consistent-mass approach (ref. 1). Lumping leads to a diagonal mass matrix, whereas the consistent-mass approach in general leads to a nondiagonal mass matrix. The advantage of the consistent-mass approach over lumping is that the consistent-mass approach is based upon energy considerations. When the same assumed functions are employed to obtain the mass matrix as are employed for the stiffness matrix, statements concerning bounds on the natural frequencies can be made. These statements are well known and will not be discussed herein.

With regard to stiffness, the finite-element method is now widely used throughout industry for detailed loads and stress analyses. In this method, stiffness matrices for elements of certain shapes are derived and programed, or they may be generated on the computer by numerical methods. These element matrices are then assembled to form an overall stiffness matrix based upon input data. The detail and accuracy which may be obtained by this approach seem to be limited only by computer size and the perseverance of the analyst.

Damping is the least known of the three elements which comprise the dynamic characteristics of a linear structure. Normally, in the development of a structural system, analyses for mass and stiffness properties are performed very comprehensively, and the vibration modes and frequencies are determined through the solution of an eigenvalue problem in which the eigenvectors (modes) and eigenvalues (squares of natural circular frequencies) are known to be real. When these quantities are used in response analyses, a damping value is assumed to exist which is associated with each mode of vibration. This process has been acceptable in the past primarily for two reasons. One reason is that a very large computational convenience results in that only the real eigenvalue problem needs to be solved. The other reason is that experimental information on damping was not sufficiently accurate to warrant a more complex approach. The development of the space shuttle, however, requires a more sophisticated treatment in the event that the component-synthesis approach is employed.

STRUCTURE

FULLY DESCRIBED BY MASS, STIFFNESS, AND DAMPING MATRICES WHICH ARE RELATED TO AN APPROPRIATE SET OF COORDINATES

- TECHNIQUES FOR DESCRIBING MASS PROPERTIES ARE LUMPING OR CONSISTENT MASS
- THE FINITE-ELEMENT METHOD IS NOW WIDELY USED TO OBTAIN THE STIFFNESS REPRESENTATION
- DAMPING IS THE LEAST KNOWN OF THE THREE ELEMENTS

Figure 1

DAMPING SYNTHESIS

(Figure 2)

In figure 2, one scheme for determining the dynamic properties of the space shuttle is depicted. The figure illustrates several problems which must be treated in order to achieve confidence in the component-synthesis approach. Damping synthesis is viewed as the major problem area in this procedure (hence the title given to the figure). In this approach, the dynamic characteristics of each component are determined analytically and verified by tests. This verification probably would be performed by comparisons of calculated natural frequencies and mode shapes with those determined experimentally. Damping factors for each mode would be determined by observation of the free decay of vibration. When the verification is considered to be satisfactory for all components, the dynamic model of the free-free system is assembled analytically. Tests of the completely assembled structure thus are unnecessary.

Although problem areas exist, the technology for accomplishing this synthesis is probably available except in the area of damping. Several questions arise. Does proportional damping (defined by the equation on the left in the figure) exist at the component level? If the structure is not very complex, the assumption may be realistic; however, in a structure such as the orbiter, the occurrence of proportional damping is highly unlikely. Even postulating that proportional damping exists for each component, the proportionality is very unlikely to be the same from one component to another. In addition, suspension-system effects must be determined and the interface damping, which must be estimated since the structure is never tested in the mated condition, must be estimated and accounted for in the synthesis.

Although much work has been performed in this area (ref. 2, for example), a combined analytical and experimental program is needed to answer some of the following questions: What combination of viscous and structural damping best represents the physical behavior of a structure and its contained propellants? Over what range of amplitudes can damping be considered linear? How can the damping distribution within a structure be determined experimentally? Can damping be reliably estimated from drawings? If so, can these properties be enhanced in order to increase stability margins and limit dynamic response? What analytical techniques and approximations can be evolved to simplify the treatment of the complex arithmetic involved when realistic damping distributions are treated? How can suspension-system damping be determined? How can interface damping be estimated?

Many of the above questions can be answered, at least partially, with model studies. In-house and contractual efforts are in progress both at the Langley Research Center and Marshall Space Flight Center. Much information concerning damping of past vehicles is assembled in reference 3.

DAMPING SYNTHESIS

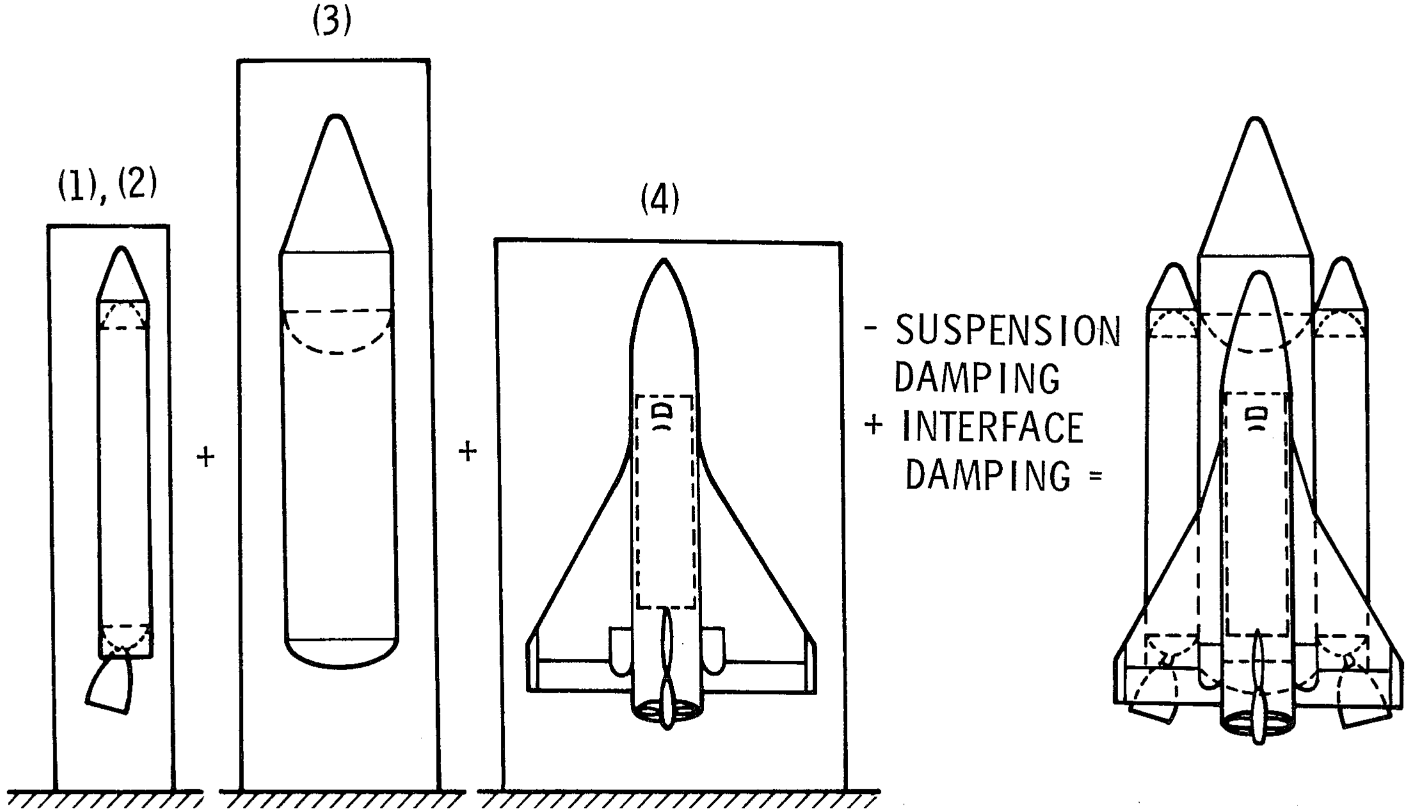

$$[C]_j \stackrel{?}{=} \alpha_j[M]_j + \beta_j[K]_j \qquad [C] \neq \alpha[M] + \beta[K]$$

Figure 2

TANK-LIQUID INTERACTION

(Figure 3)

In the area of tank-liquid interaction, the technology is being developed to a level which will enable a timely solution to the problem. Analytically, the primary feature of the hydrogen-oxygen (HO) tank is the nonaxisymmetric stiffness distribution. The SNAP (structural network analysis program) and NASTRAN (NASA STRUCTURAL ANALYSIS) analyses have the capability to treat this problem. In paper no. 7 by Stephens and Kiefling this problem is discussed further.

TANK-LIQUID INTERACTION

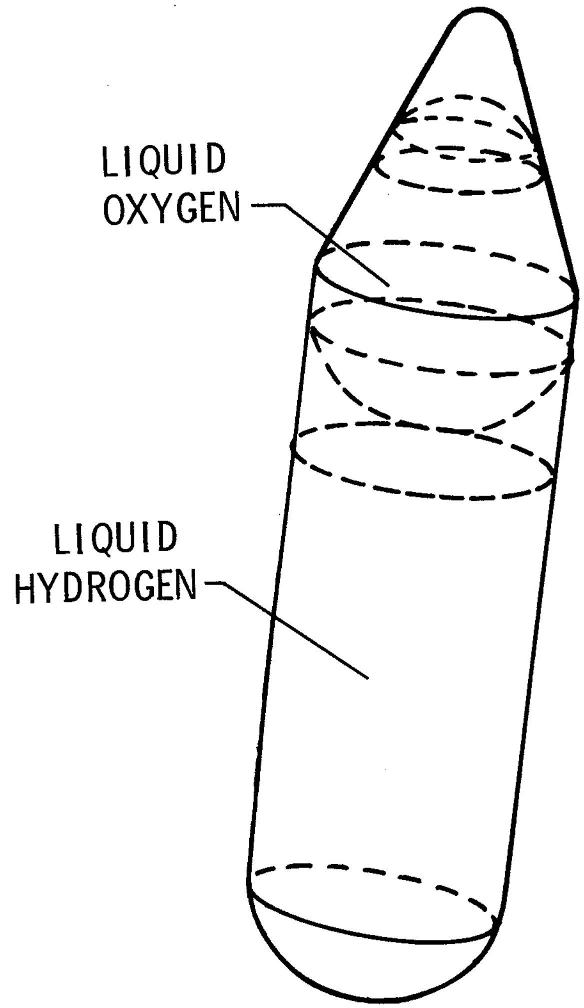

CHARACTERISTICS OF HO TANK

- CIRCULAR CROSS SECTION
- CONE-CYLINDER-BULKHEAD COMBINATION
- NONAXISYMMETRIC STIFFNESS DISTRIBUTION

APPLICABLE ANALYSES

- SNAP
- NASTRAN (LEVEL 15)

Figure 3

FEEDLINE DYNAMICS

(Figure 4)

In the area of feedline dynamics, work is underway contractually both at the Langley Research Center and Marshall Space Flight Center. Work has been performed in the past at the Lewis Research Center (ref. 4), and work there is underway presently in connection with the Centaur vehicle. Much analytical work in this area has been done by Oldenburger. (See ref. 5, for example.)

Usual methods of representing the dynamics of feedlines are given in figure 4 with some of the characteristics of each. The principal problem area is that of line losses or damping in the feedline. Experiments are needed to determine the true variation of damping with frequency when such effects as structural damping in the line and support damping are included. This area is discussed further in paper no. 5 by Rubin.

FEEDLINE DYNAMICS

MODAL APPROACH

- REQUIRES A PARTICULAR DISTRIBUTION OF DISTRIBUTED AND CONCENTRATED LOSSES
- REQUIRES FEW DEGREES OF FREEDOM
- CAN BE SYNTHESIZED FROM FINITE-ELEMENT APPROACH

PRODUCT SERIES

- RESONANT FREQUENCIES ARE RETAINED PRECISELY
- FOR COMPLEX CONFIGURATIONS COMPLEX ROOTS MUST BE FOUND BY NUMERICAL METHODS BEFORE WRITING TRANSFER FUNCTION

POWER SERIES

- DOES NOT RETAIN ROOTS PRECISELY
- TRANSFER FUNCTION CAN BE SYNTHESIZED FROM ANALYSES OF SEGMENTS; THIS APPROACH ALLOWS TREATMENT OF COMPLEX CONFIGURATIONS

PROBLEM AREA: THEORETICALLY, DAMPING $\sim 1/\omega$; EXPERIMENTS ARE NEEDED TO DETERMINE TRUE VARIATION

Figure 4

ENGINE (PUMP)

(Figure 5)

One of the largest areas of uncertainty in pogo analyses is that of pump dynamics. To experimentally determine pump dynamics, two tests are required at independent states for each steady operating condition. Each test furnishes two equations for the four unknowns in the transfer matrix, designated A(s), B(s), C(s), and D(s) in figure 5. In each test, complete determination of the two equations requires measurement of the dynamic flow as well as the unsteady component of the pressure. (It is assumed for this illustration that the pump speed is constant.) The flow measurement has not been possible in the past because of the lack of a dynamic flowmeter.

ENGINE (PUMP)

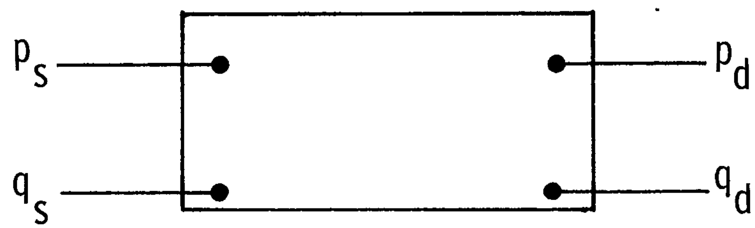

$$\begin{Bmatrix} p_d \\ q_d \end{Bmatrix} = \begin{bmatrix} A(s) & B(s) \\ C(s) & D(s) \end{bmatrix} \begin{Bmatrix} p_s \\ q_s \end{Bmatrix}$$

- TESTS AT TWO INDEPENDENT STATES ARE REQUIRED
- BOTH PRESSURE AND FLOW MEASUREMENTS ARE REQUIRED FOR EACH TEST
- TRANSFER QUANTITIES VARY WITH STEADY OPERATING CONDITION SO THAT SEVERAL TESTS ARE NEEDED

Figure 5

FLOWMETER

(Figure 6)

The requirements for a dynamic flowmeter are principally that it should not disturb the flow pattern in the stream that is being measured and that it should be able to sense the low-amplitude oscillatory flows which vary about a large steady flow value. The Langley Research Center is supporting a program for the design and development of a dynamic flowmeter. Some approaches which have been suggested are listed in figure 6.

FLOWMETER

REQUIREMENTS

- NO SIGNIFICANT PERTURBATION OF FLOW PATTERNS
- CAPABILITY FOR RESPONSE TO LOW-AMPLITUDE OSCILLATORY FLOWS WHICH VARY ABOUT A LARGE STEADY FLOW

SOME APPROACHES

- ULTRASONIC
- MICROWAVE
- ELECTROMAGNETIC
- HEAT TRANSFER
- LASER
- TIME CORRELATION

Figure 6

POGO-LOOP/CONTROL-LOOP INTERACTION
(Figure 7)

A new problem area has arisen because of directional coupling in the vibration modes of the space shuttle. Although this coupling has been present to some degree on past vehicles, its magnitude has not been sufficient to consider the effects of lateral disturbances on the pogo loop.

Figure 7 shows schematically a space shuttle and the directions of the thrust vectors. Also shown is a greatly simplified block diagram which indicates the manner in which the pogo loop can interact with the control loop. A disturbance in thrust will cause response in one or more vibration modes and lateral, as well as longitudinal, motion results. The lateral component of the motion is detected by the control sensors with the result that the engines gimbal. The change in gimbal angle produces a new force on the structure. The longitudinal component of the motion is fed back through the propulsion system and results in a new perturbation in thrust which also produces a force on the structure.

The Langley Research Center is supporting work to study this interaction. A configuration which was current in June 1971 is being utilized for the study. One preliminary result is that the motion of propellant in lateral runs of feedlines can have a destabilizing effect on the control system. The effect occurs because the lateral runs occur in an area of high structural gain.

POGO-LOOP/CONTROL-LOOP INTERACTION

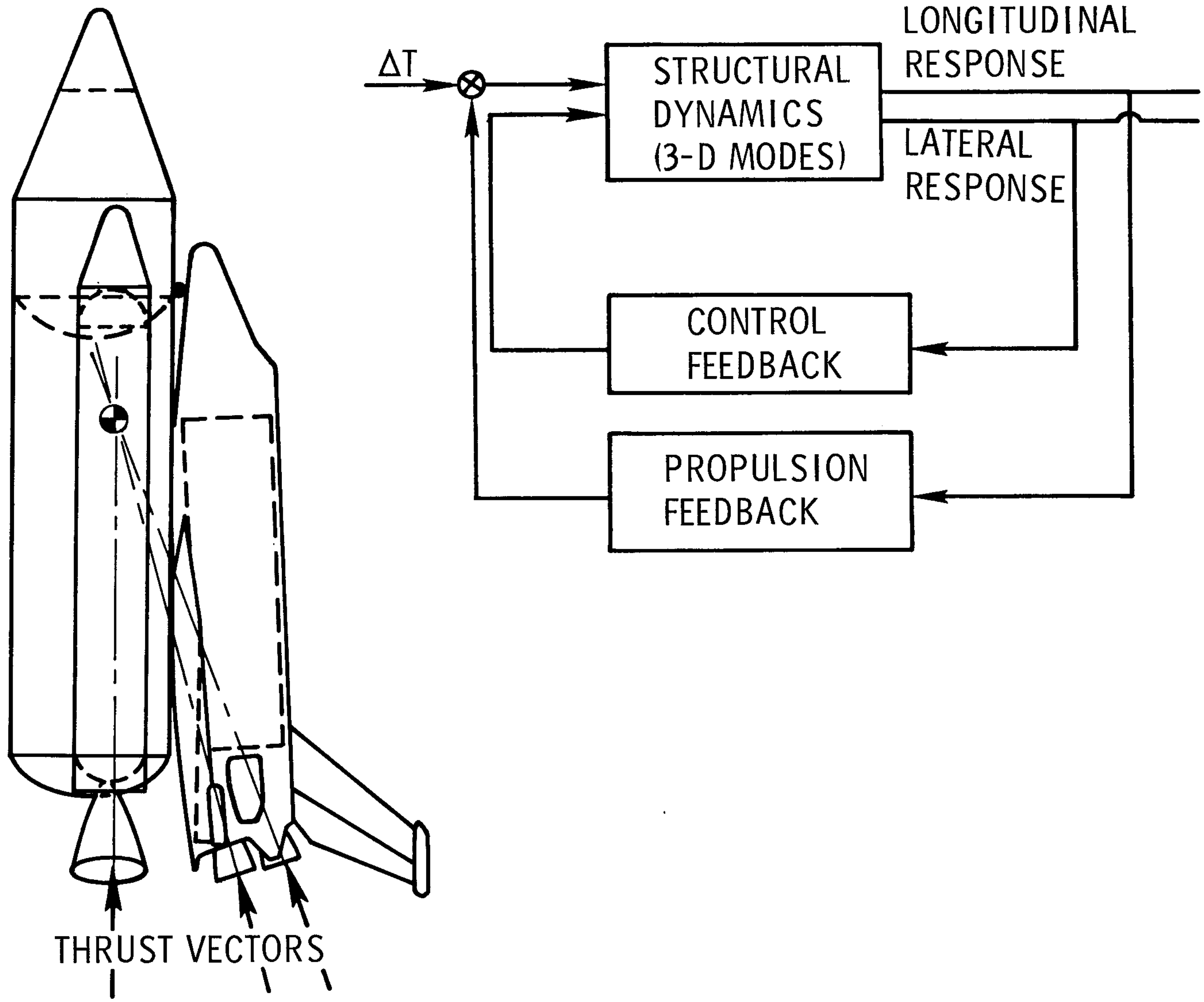

Figure 7

POGO STABILITY ANALYSIS

(Figure 8)

In order to meet requirements imposed by the space shuttle on pogo analyses, it is necessary that additional analytical capability be obtained. Proposals have been received at Marshall Space Flight Center in response to a request for proposals for a new pogo-stability-analysis computer program. Figure 8 indicates the major characteristics of the program. Most of the problems discussed in this paper are being treated in this program development. The single exception is treatment of the structure with nonproportional damping. However, since realistic damping distributions cannot presently be obtained experimentally, this treatment is commensurate with the state of the art. Included in the program development are treatment of active or passive suppression devices and treatment of feedlines by a spring-mass approach or an approximation to the transmission-line equations.

POGO STABILITY ANALYSIS

- FIFTY OR MORE STRUCTURAL MODES
- SELECTION ROUTINE FOR POGO-IMPORTANT MODES
- FOUR OR MORE ENGINE SETS
- POGO-LOOP/ CONTROL-LOOP INTERACTION
- CLOSED-LOOP OR OPEN-LOOP ANALYSIS
- TANK OUTFLOW EFFECT

Figure 8

POGO TECHNOLOGY

(Figure 9)

A greatly simplified time-line summary of the status of pogo technology with respect to the phases of the shuttle procurement is shown in figure 9. When shuttle studies began, experience was restricted to vehicles which were nearly axisymmetric. Therefore, there was no need to calculate pogo-loop/control-loop interactions. However, during the second phase problems, such as pogo-loop/control-loop interactions, associated with the space shuttle were identified and study contracts and in-house studies have developed technology in these areas. Development of capability to deal with these new problems will continue and will be utilized in the shuttle development. This work will consist mainly, as indicated, in development of the much-needed dynamic flowmeter, development of an improved pogo-analysis capability, and work in structural and feedline damping.

POGO TECHNOLOGY

EXPERIENCE

- AXISYMMETRIC VEHICLES
- NO TANK OUTFLOW
- NO FLOWMETER
- NO POGO/ CONTROL ANALYSIS

IDENTIFIED PROBLEMS

- FLOWMETER
- TANK OUTFLOW
- DAMPING: STRUCTURAL AND FEEDLINE
- POGO/ CONTROL INTERACTION

FUTURE WORK

- FLOWMETER DEVELOPMENT
- POGO ANALYSIS
- DAMPING: STRUCTURAL AND FEEDLINE

——— PHASE A ——— ▼ ——— PHASE B ——— ▼ ——— PHASE C/ D ———→

Figure 9

REFERENCES

1. Archer, J. S.: Consistent Mass Matrix for Distributed Mass Systems. J. Struct. Div., Amer. Soc. Civil Eng., vol. 89 (ST 4), no. 3591, Aug. 1963, pp. 161-178.
2. Lazan, Benjamin J.: Damping of Materials and Members in Structural Mechanics. Pergamon Press, 1968.
3. Kiefling, Larry; and Pack, Homer: Structural Damping in Saturn Vehicles and Scale Models. NASA TM X-64607, 1971.
4. Regetz, John D., Jr.: An Experimental Determination of the Dynamic Response of a Long Hydraulic Line. NASA TN D-576, 1960.
5. Oldenburger, Rufus; and Goodson, R. E.: Simplification of Hydraulic Line Dynamics by Use of Infinite Products. Trans. ASME, Ser. D: J. Basic Eng., vol. 86, no. 1, Mar. 1964, pp. 1-8.

LIQUID-PROPELLANT DYNAMICS AND SUPPRESSION

By David G. Stephens

NASA Langley Research Center

and

Larry A. Kiefling

NASA Marshall Space Flight Center

SUMMARY

Technology related to liquid-propellant interactions with space shuttle vehicles is reviewed. Potential problems unique to the shuttle include liquid-structure interactions resulting from coupled lateral and longitudinal deformations, traveling-wave phenomena at shallow propellant levels, and liquid impact during abort, staging, or docking. Technology efforts to define the slosh dynamics under shuttle operating conditions are described with emphasis on analytical representations of the liquid by finite-element and marker-and-cell methods. In addition, slosh suppression is discussed and includes baffle damping and pressure loads for tanks fitted with multiple baffles both above and below the undisturbed liquid surface.

7

INTRODUCTION

SHUTTLE LIQUID-STRUCTURE INTERACTIONS

(Figure 1)

A broad technology base for liquid dynamics and liquid-structure interactions has developed during the design and operation of liquid-propellant launch vehicles and spacecraft. (See refs. 1 to 3, for example.) Typical areas of interest are represented schematically in figure 1 and include vibration frequencies and mode shapes of liquids as well as coupled liquid-tank systems; loads associated with sloshing liquids and/or propellant motions (often referred to as dome impact) which may occur during separation, abort, or docking; suppression of the liquid motion by means of baffles, bladders, or other damping devices; management of liquids during low-g operation to insure satisfactory engine restart and to avoid adverse control conditions; and stability and control which involve the interaction of the propulsion system, structure, and liquid. In addition to these areas, the development of the space shuttle will introduce new liquid-structure interactions due to vehicle asymmetries, relatively large angles between the tank center line and the effective acceleration vector, large center-of-gravity offsets, and liquid payloads. This paper describes some recent technology studies which address space shuttle liquid-structure interactions.

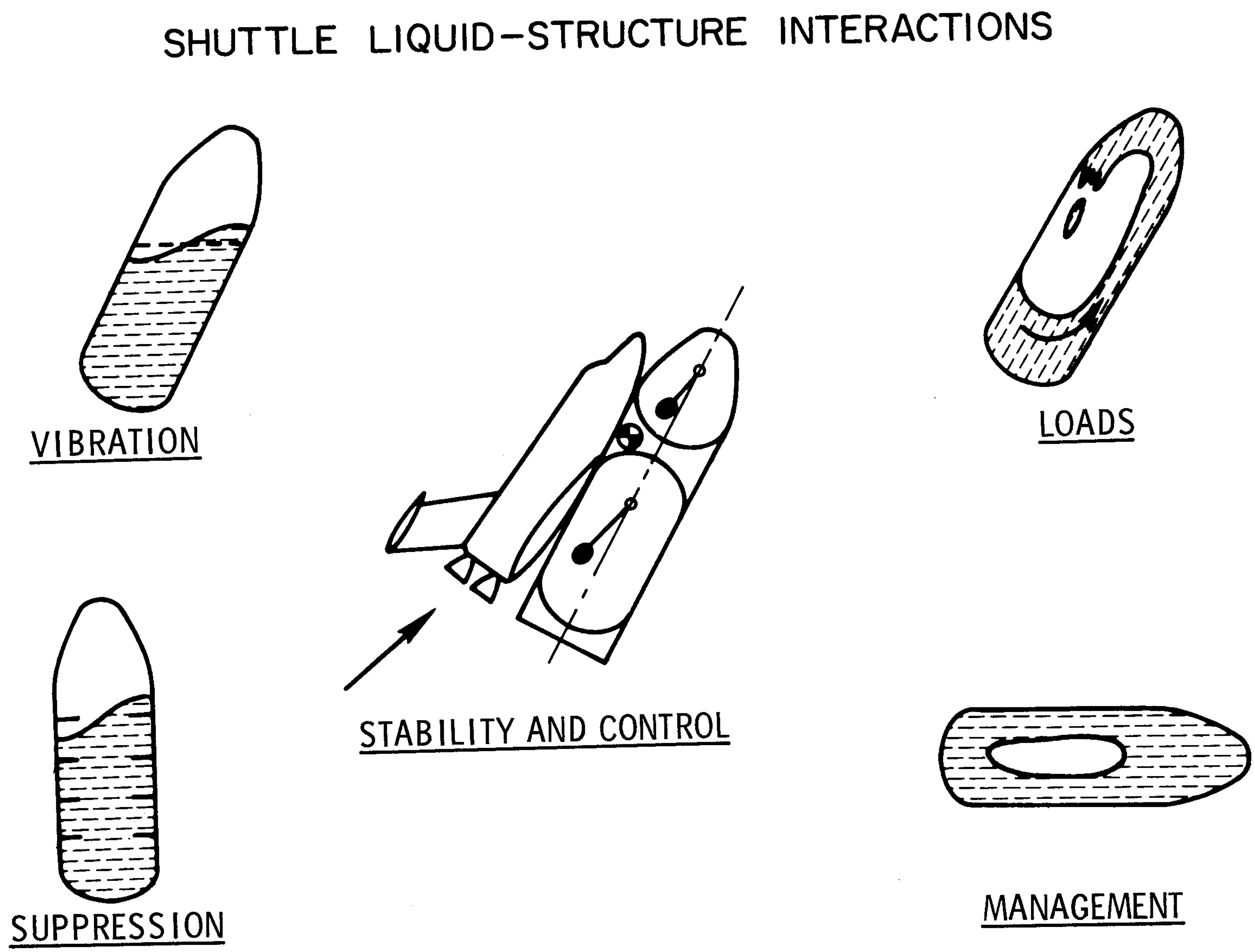
SHUTTLE LIQUID-STRUCTURE INTERACTIONS
VIBRATION
STABILITY AND CONTROL
LOADS
SUPPRESSION
MANAGEMENT

Figure 1

LIQUID MODES AND FREQUENCIES IN INCLINED TANKS

(Figure 2)

The axis of the propellant tank does not generally coincide with the effective acceleration vector because of the center-of-gravity offset. The free surface is elliptical and may slosh in a "long mode" or "short mode," as shown in figure 2. For a given depth to diameter ratio h/d, both the analytical and experimental frequencies are shown in reference 4 to decrease with increasing tilt angle. The frequency is specified by the nondimensional parameter $\omega^2 R/g$, where ω is the circular slosh frequency, R is the tank radius, and g is the tank acceleration.

A mathematically equivalent mechanical model has also been derived in reference 4 to simulate the forces and moments associated with the long and short modes. The model gives an oscillating force parallel to the thrust which could be important in pogo applications.

LIQUID MODES AND FREQUENCIES IN INCLINED TANKS

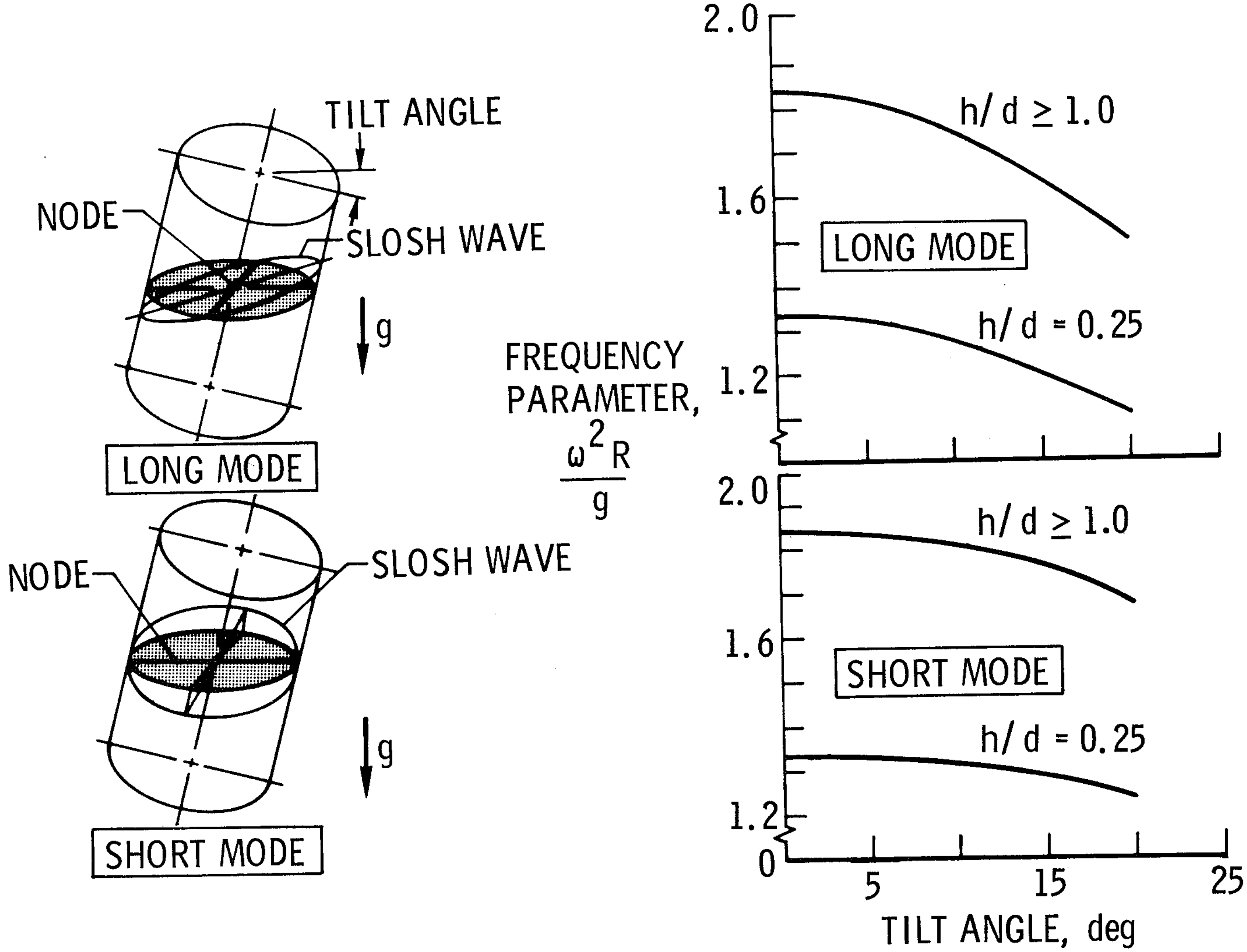

Figure 2

THE NASTRAN HYDROELASTIC ANALYZER

(Figure 3)

The NASTRAN (NASA STRUCTURAL ANALYSIS) hydroelastic analyzer is a recent addition to NASTRAN, which is a general-purpose finite-element program developed for the analysis of large and/or complex structures. The addition of the hydroelastic capability will allow the treatment of axisymmetric fluid volumes held in elastic containers. Several sample fluid topologies which can be treated by the program are shown in figure 3. Although the fluid volume must be axisymmetric, the program will handle nonaxisymmetric liquid motions (antisymmetric slosh modes, for example) and tank properties.

Some of the more important characteristics and capabilities of the hydroelastic analyzer include the ability to analyze liquid free-surface effects, variable fluid density and compressibility, rigid and/or elastic structural boundaries, and motion of both coupled and uncoupled fluid-structure systems. The NASTRAN capability for control-system modeling can be utilized along with the hydroelastic analyzer to study coupled fluid-structure-control systems.

THE NASTRAN HYDROELASTIC ANALYZER

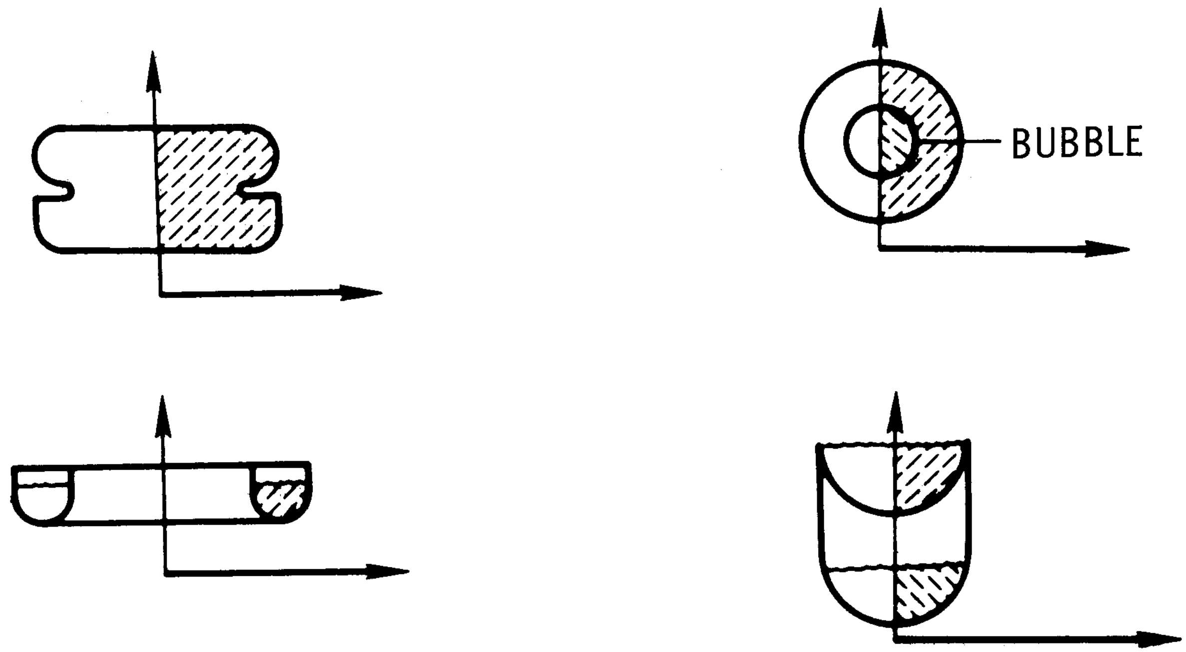

- FINITE-ELEMENT PROGRAM
- AXISYMMETRIC FLUID VOLUMES
- NONAXISYMMETRIC FLUID MOTION
- NONAXISYMMETRIC TANK ELASTIC PROPERTIES
- COMPATIBLE WITH NASTRAN SYSTEM CAPABILITY

Figure 3

FINITE-ELEMENT ANALYSIS OF GENERAL LIQUID-STRUCTURE SYSTEM

(Figure 4)

Whereas the NASTRAN hydroelastic analyzer (fig. 3) is restricted to axisymmetric fluid volumes, a study is underway to develop a method for calculating the normal modes of an arbitrary liquid or liquid-structure system. The general approach is to make the liquid element completely compatible with the very efficient structural-dynamics programs which now exist. This compatibility is being insured by making the basic element a tetrahedron with displacements at the corners as degrees of freedom. A linear-displacement field within the element was selected for simplicity. It is also necessary that the stiffness matrix be sparse for efficient computation. A compressible element formulation is needed to accomplish this. For a typical tank with a flexible wall, the large sparse matrix will result in many times less numerical operations than the smaller full matrix.

Numerical problems were expected and have arisen to a moderate extent. Roundoff is troublesome since the elastic potential energy is five or six orders of magnitude higher than gravitational potential energy for typical cases. Routines are being written in double precision. Many zero-frequency degrees of freedom may exist, and these in general would be skipped over. Results of some simple two- and three-dimensional cases are shown in figures 5, 6, and 7 as examples of the application of the general finite-element approach.

FINITE-ELEMENT ANALYSIS
GENERAL LIQUID-STRUCTURE SYSTEMS

OBJECTIVE

- CALCULATE THE NORMAL MODES OF AN ARBITRARY LIQUID OR LIQUID-STRUCTURE SYSTEM

APPROACH

- LIQUID ELEMENT MUST BE COMPATIBLE WITH EXISTING STRUCTURAL-ANALYSIS SYSTEMS
  - A TETRAHEDRON WITH DISPLACEMENTS AT THE CORNERS AS DEGREES OF FREEDOM IS THE BASIC ELEMENT
  - THE ELEMENT SHOULD BE COMPRESSIBLE TO PERMIT CONVENTIONAL STRUCTURAL-ENERGY METHODS

PROBLEMS EXPECTED

- ROUNDOFF IS TROUBLESOME; ELASTIC POTENTIAL ENERGY IS 5 OR 6 ORDERS OF MAGNITUDE HIGHER THAN GRAVITATIONAL POTENTIAL ENERGY FOR TYPICAL CASE
- MANY ZERO-FREQUENCY CIRCULATION ROOTS

Figure 4

RESULTS FROM SIMPLEST TWO-DIMENSIONAL MODEL

(Figure 5)

The simplest possible model was set up by dividing a 2-meter by 1-meter two-dimensional tank of water into four elements. This model has five degrees of freedom, one slosh mode and four compressible modes. Systems of this type are used for checking out the element formulation, investigating convergence, and evaluating numerical errors. For more complex tank configurations, a network synthesis routine is being developed to calculate the propellant level in the tank and divide the liquid into a suitable set of elements. The solution will be accomplished by the SNAP (Structural Network Analysis Program) computer program, which has a capability for several thousand degrees of freedom and good solution speed.

RESULTS FROM SIMPLEST TWO-DIMENSIONAL MODEL

2-METER BY 1-METER TANK

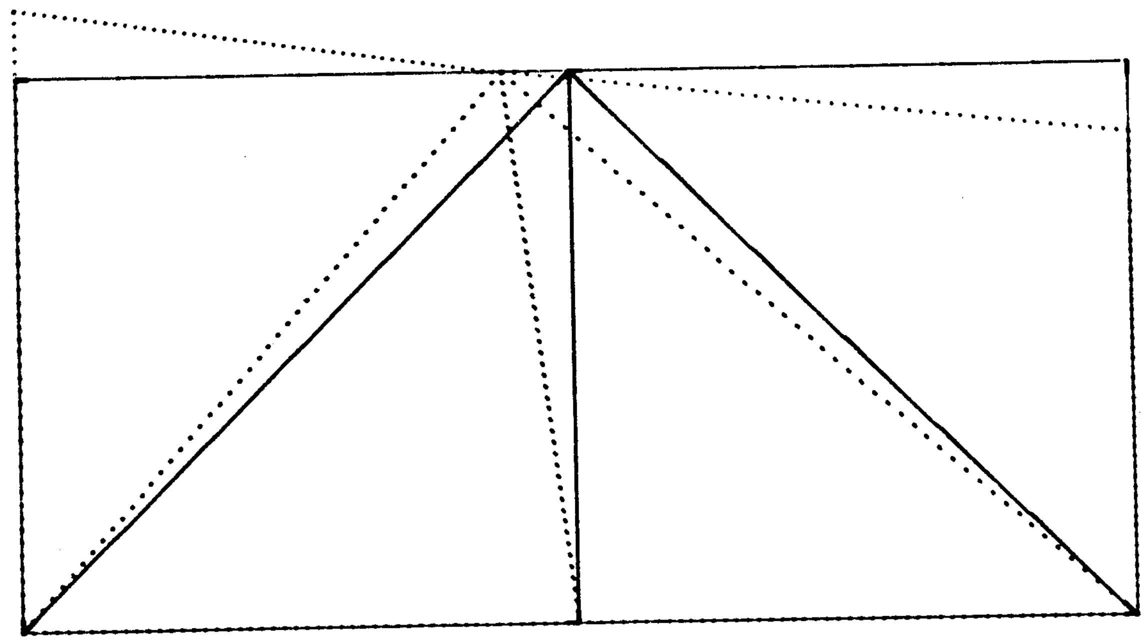

MODE 1; FREQUENCY = 0.57547 Hz

Figure 5

RESULTS FROM SIMPLE MODEL WITH CIRCULATION

(Figure 6)

The nine-degree-of-freedom model shown has one zero-frequency circulation mode. The two slosh modes for this model are also shown. The mode shapes are very nearly those for the incompressible model, and very simple relationships exist between the various displacements. The mass flow is slightly less constrained than in the model shown in figure 5, and the frequency therefore increases slightly. Results have been limited to these simple configurations because of the difficulty in visualizing modes for three-dimensional elements.

RESULTS FROM SIMPLE MODEL WITH CIRCULATION

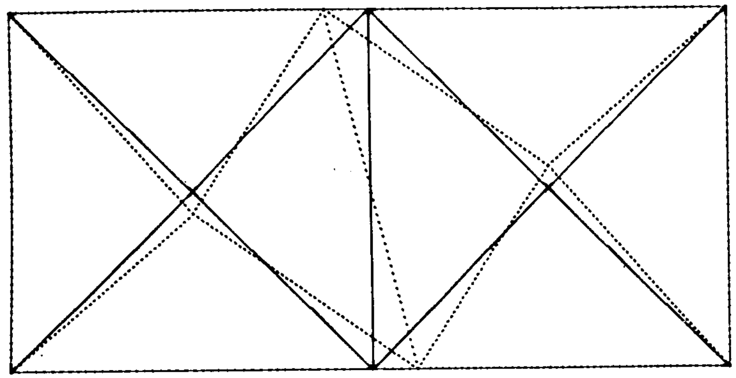

MODE 1; FREQUENCY = 0 Hz

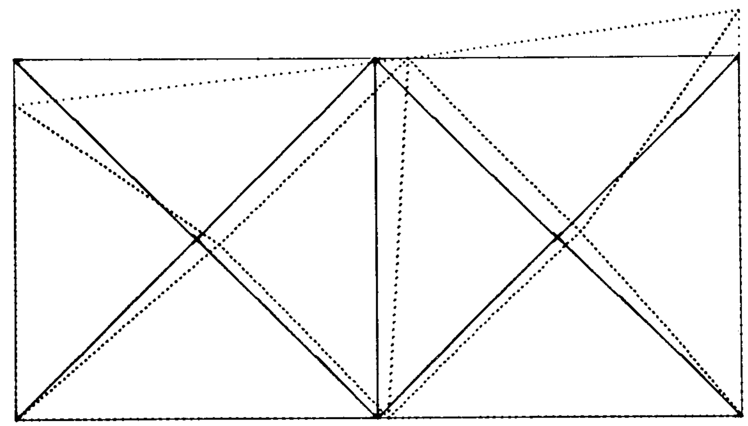

MODE 2; FREQUENCY = 0.58787 Hz

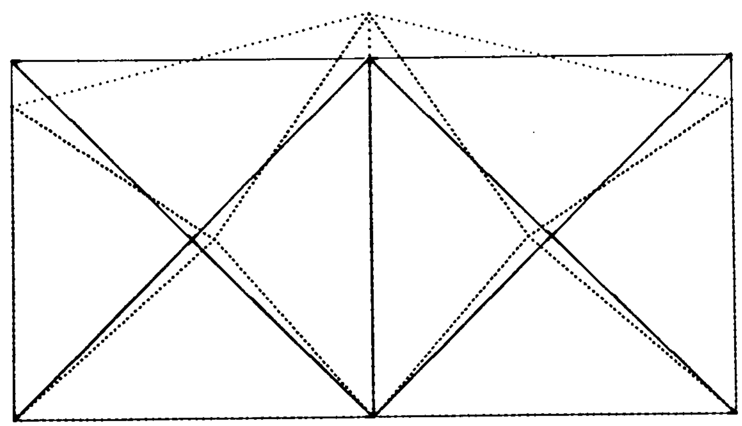

MODE 3; FREQUENCY = 0.70481 Hz

Figure 6

SUMMARY OF FINITE-ELEMENT ANALYSIS OF SIMPLE MODELS

(Figure 7)

The influence of the mesh size is shown in figure 7. For the series of models shown, the modal frequencies f_1, f_2, f_3, and f_4 are seen to converge to the closed-form solution as the mesh is made finer. The lower slosh modes for each configuration appear to agree well with the closed-form solutions. All calculations were made in single precision. The three-dimensional slosh formulation appears to be good also since it provides the same accuracy as that of the two-dimensional model with the corresponding element configuration.

One significant advantage of the compatible liquid-structure analysis is that dynamic loads on the structure are directly determined.

SUMMARY OF FINITE-ELEMENT ANALYSIS OF SIMPLE MODELS

MODELS	FREQUENCIES, Hz			
	f_1	f_2	f_3	f_4
CLOSED FORM	0.59823	0.88124	1.082	1.249
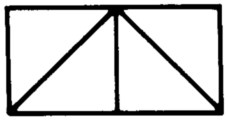	0.57547			
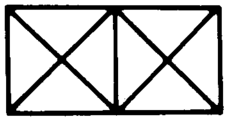	0.58787	0.70481		
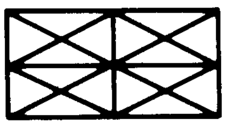	0.59531	0.79052		
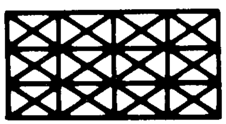	0.59893	0.88927	1.059	1.081
3-D 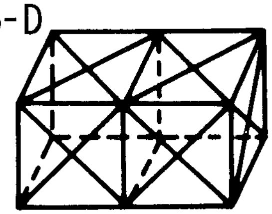	0.58868	0.70912		

Figure 7

FREQUENCIES OF AN ELLIPSOIDAL BULKHEAD CONTAINING LIQUID

(Figure 8)

A special-purpose computer program has been written for a three-dimensional determination of the natural modes and frequencies of a flexible bulkhead partially filled with liquid. (See ref. 5.) A finite-surface-element representation of the tank and of the liquid free surface was used. As a sample problem, the first three axisymmetric natural frequencies were calculated for a spherical tank half filled with liquid and supported by a ring 1/2 tank radius above the tank bottom. The results from the three-dimensional hydrodynamic program (3-DHYDRO) are compared with results from a previously developed axisymmetric program (HYDRO). The effect on frequency of changes in the number of elements used to represent the tank and liquid is shown by cases 1 to 3 for HYDRO and 4 and 5 for 3-DHYDRO. Case 3 was considered adequate for good agreement with an exact solution and is therefore used as the comparison standard. NUMBLO is the number of meridional divisions of the sphere below the liquid free surface, NUMABV is the number above the surface, NUMCIR is the number of circumferential divisions, NUMRAD is the number of radial divisions on the free surface, DOF is degrees of freedom, and CPU is the central processing unit. From the results for cases 4 and 5, it appears that several more grid divisions are required before convergence to the desired solution is obtained by 3-DHYDRO.

FREQUENCIES OF AN ELLIPSOIDAL BULKHEAD CONTAINING LIQUID

FREQUENCY COMPARISON OF HYDRO AND 3-DHYDRO

PARAMETERS	HYDRO			3-DHYDRO	
	CASE NUMBER				
	1	2	3	4	5
NUMBLO	4	7	21	4	6
NUMABV	2	2	9	2	3
NUMCIR				8	12
NUMRAD	2	4	10	2	4
ORIGINAL DOF	14	25	103	316	708
REDUCED DOF	4	9	29	32	96
f_1, Hz (% ERROR)	69.2 (17.1)	52.7 (-10.8)	59.1 (0)	78.8 (33.3)	67.7 (14.5)
f_2, Hz (% ERROR)	98.4 (9.0)	85.9 (-4.9)	90.3(0)	124.0 (37.3)	106.5 (17.9)
f_3, Hz (% ERROR)	123.3 (9.1)	104.2 (-7.8)	113.0 (0)	130.6 (15.6)	116.9 (3.5)
CPU TIME, min	0.18	0.20	0.66	5.48	28.46

Figure 8

MARKER-AND-CELL FLOW RESULTING FROM TANK DECELERATION

(Figure 9)

In an effort to develop technology for studying large liquid motions and loads resulting from tank disturbances, a two-dimensional version and a preliminary three-dimensional version of a marker-and-cell (MAC) computer program for solving transient fluid-dynamics flow problems were recently developed and reported in reference 6. These programs are applicable for analysis of liquid dynamics at cut-off, separation, docking, and engine restart.

The two-dimensional program was used in analyzing the motion of propellant residuals during a recent detailed study of the Saturn V S-IC/S-II stage separation dynamics. Results are shown as a function of time t for an axisymmetric simulation of liquid-oxygen motion in the bottom of an S-IC tank during the separation. The simulation assumes a 1 g deceleration of the S-IC stage applied for 0.7 second. The initially flat free surface is neutrally stable, so it was necessary to assume a small starting radial acceleration. The forces resulting from this simulation are shown in figure 10.

MARKER-AND-CELL FLOW RESULTING FROM TANK DECELERATION

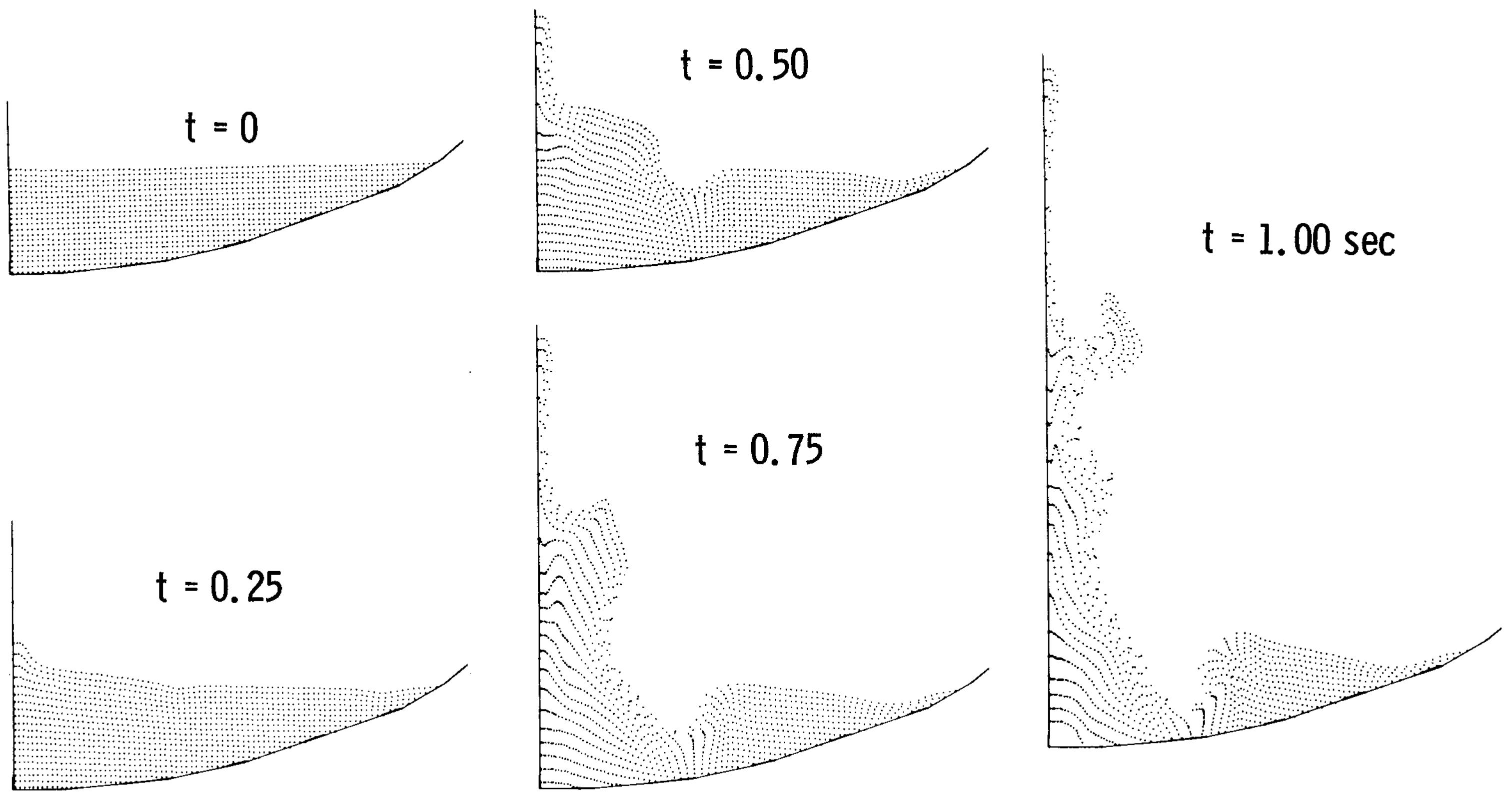

Figure 9

FORCE EXERTED ON TANK BOTTOM BY PROPELLANT

(Figure 10)

The force results for the two-dimensional marker-and-cell simulation are shown in figure 10. The force of 100 kN represents the force the fluid would exert upward on the tank bottom during retroacceleration if the fluid remained fixed to the tank. These results indicate that for the S-IC/S-II separation analysis, it would be correct to assume that most of the residual propellant is attached to and decelerated with the tank.

Several cases have been successfully run using the three-dimensional program to analyze liquid transient motion in a rectangular tank. Feasibility studies indicate that the three-dimensional program can be extended to axisymmetric tanks, and problems of liquid motion during docking or separation can be analyzed.

FORCE EXERTED ON TANK BOTTOM BY PROPELLANT

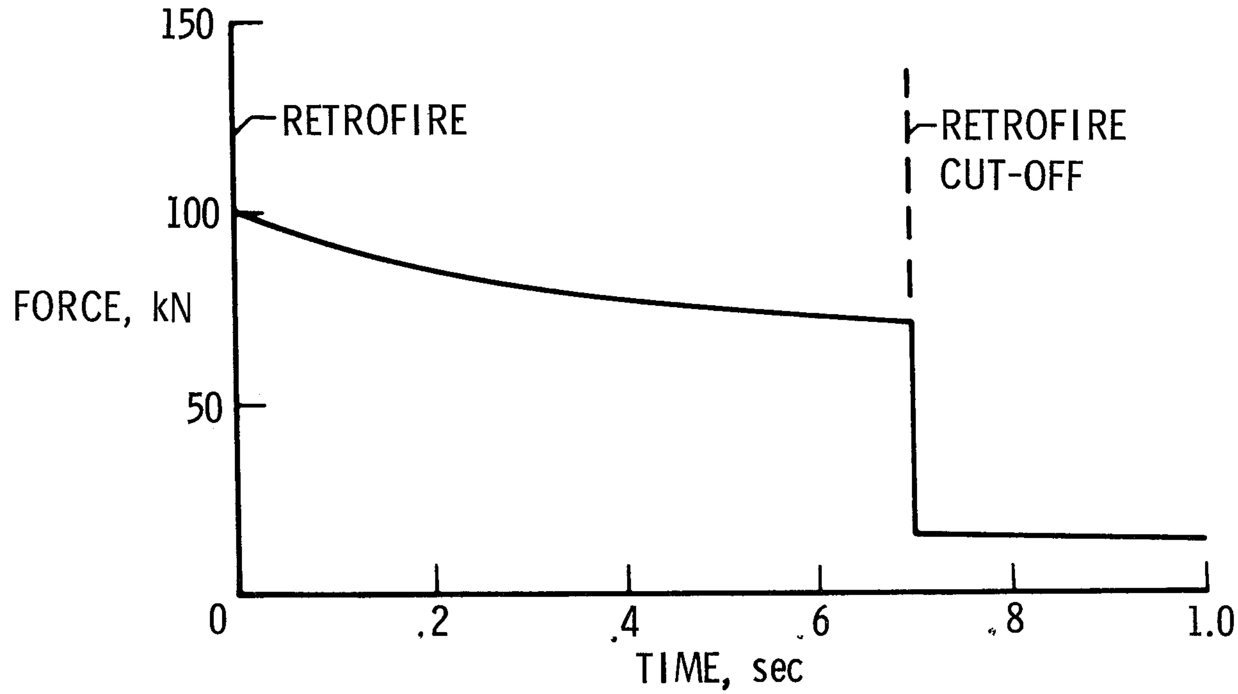

Figure 10

ANTISLOSH BAFFLE TECHNOLOGY
(Figure 11)

Antislosh baffles are usually required in liquid-propellant space vehicles in order to minimize propellant oscillations. The most common configuration consists of a number of annular rings fitted around the internal periphery of the tank. Although such baffles are effective in attenuating slosh, they often comprise a high percentage of the tank weight. It is important, therefore, that the baffle design be efficient in terms of the damping per unit of baffle weight. To obtain the desired efficiency, a detailed understanding of the slosh loads as well as the damping associated with the baffle configuration is required.

An investigation was recently conducted at the Langley Research Center to determine the pressure loads and damping associated with rigid ring baffles in relatively large cylindrical tanks. The radial and circumferential pressure distribution as well as the damping was measured on an annular ring baffle subjected to fundamental antisymmetric slosh in a 3-meter-diameter rigid tank, as depicted in figure 11. Experimental data were determined as a function of slosh velocity, baffle location both above and below the quiescent liquid surface, and baffle spacing and were compared with available theories. The tank system used in this study is shown in figure 12.

ANTISLOSH BAFFLE TECHNOLOGY

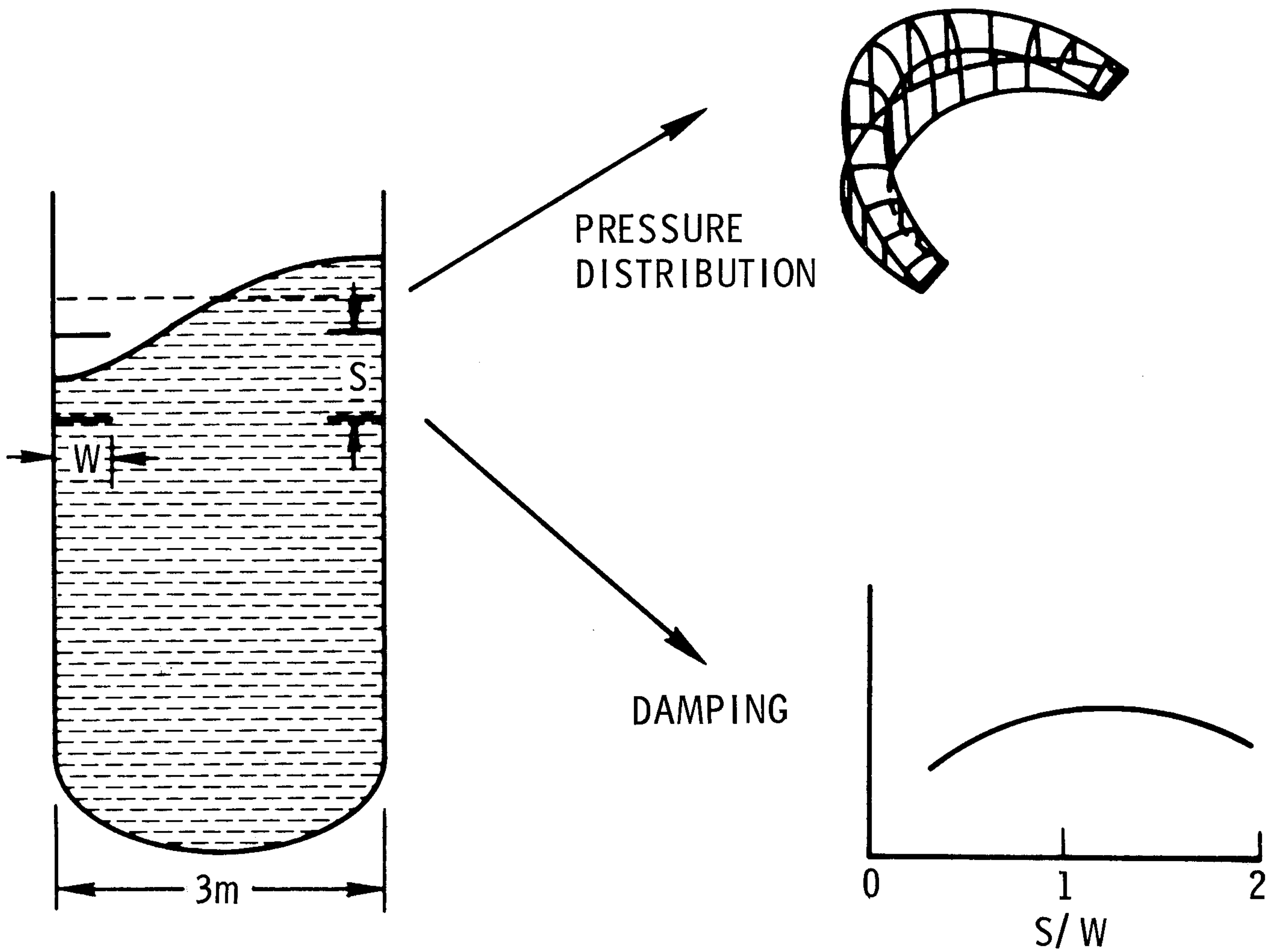

Figure 11

ANTISLOSH BAFFLE AND TANK SYSTEM

(Figure 12)

The tank used in this study was a stationary cylinder having a diameter of 3 meters. The tank could be fitted with one or more annular-ring baffles having a width-to-radius ratio W/R of 0.1. The baffle spacing S/W ranged from 0 for the single baffle to a value of 2. (See fig. 11.) The liquid was manually excited in the fundamental antisymmetric mode, and the pressures across the baffle as well as the liquid amplitude were sensed by calibrated differential pressure transducers. In addition, the damping of the mode was determined by measuring of free decay of the oscillation.

ANTISLOSH BAFFLE AND TANK SYSTEM

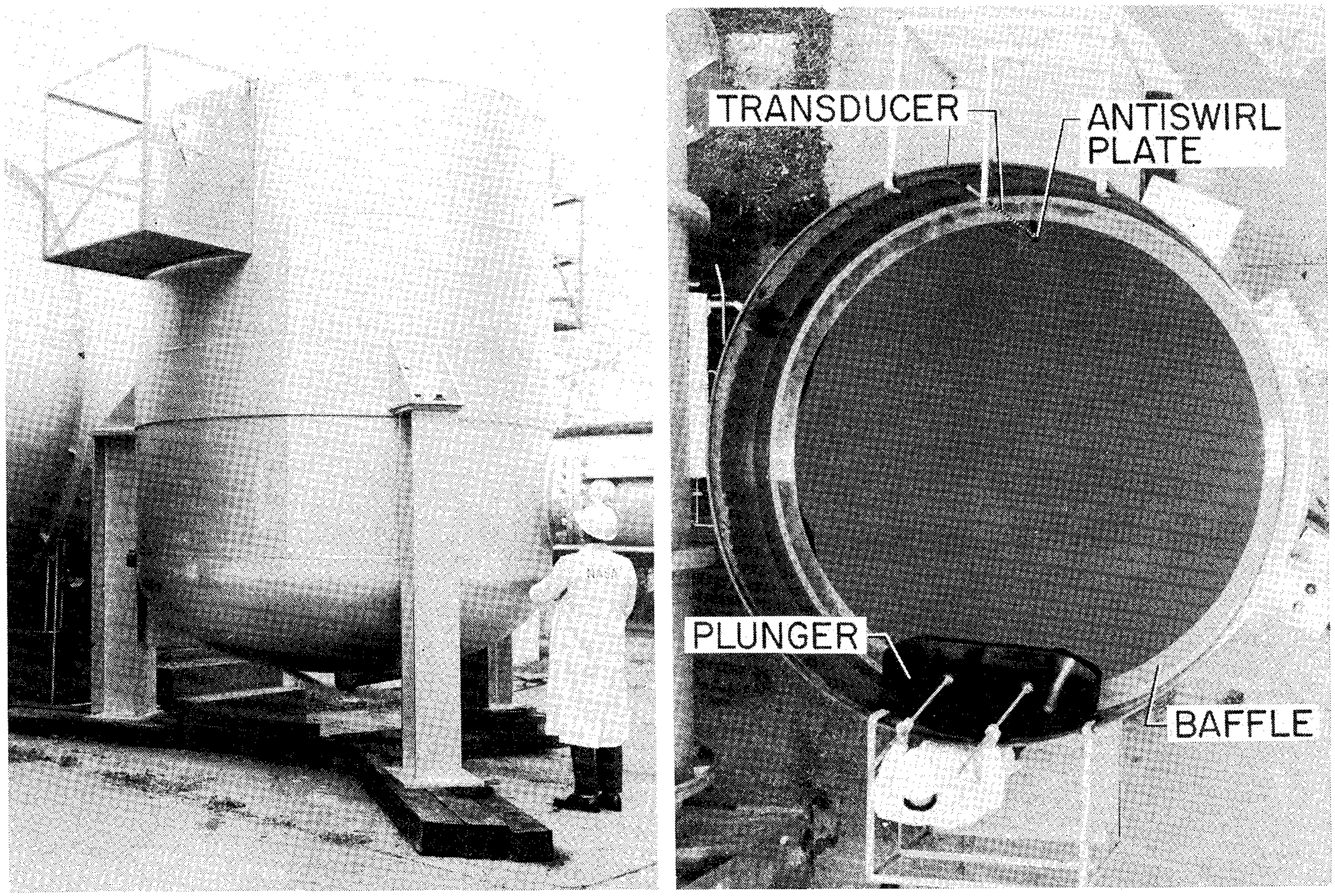

Figure 12

BAFFLE PRESSURE THEORIES

(Figure 13)

In considering baffle pressure loads p, two conditions are of interest: the condition where the baffle is below the oscillating surface and the condition where the baffle is exposed and subjected to a periodic slapping action. Theories have been proposed for both conditions although previous experimental verification has been very limited. For the submerged baffle, the theory contains terms involving the oscillating liquid velocity and the liquid acceleration, as shown in the figure. The theory involves a coefficient of drag C_D (ref. 7), liquid density ρ, liquid velocity at the baffle V, oscillatory frequency ω, and radial and circumferential positions r and β, respectively. The theory for the exposed baffle is based upon an impulse-momentum formulation and assumes that the velocity of the liquid is completely reversed when it strikes the baffle.

BAFFLE PRESSURE THEORIES

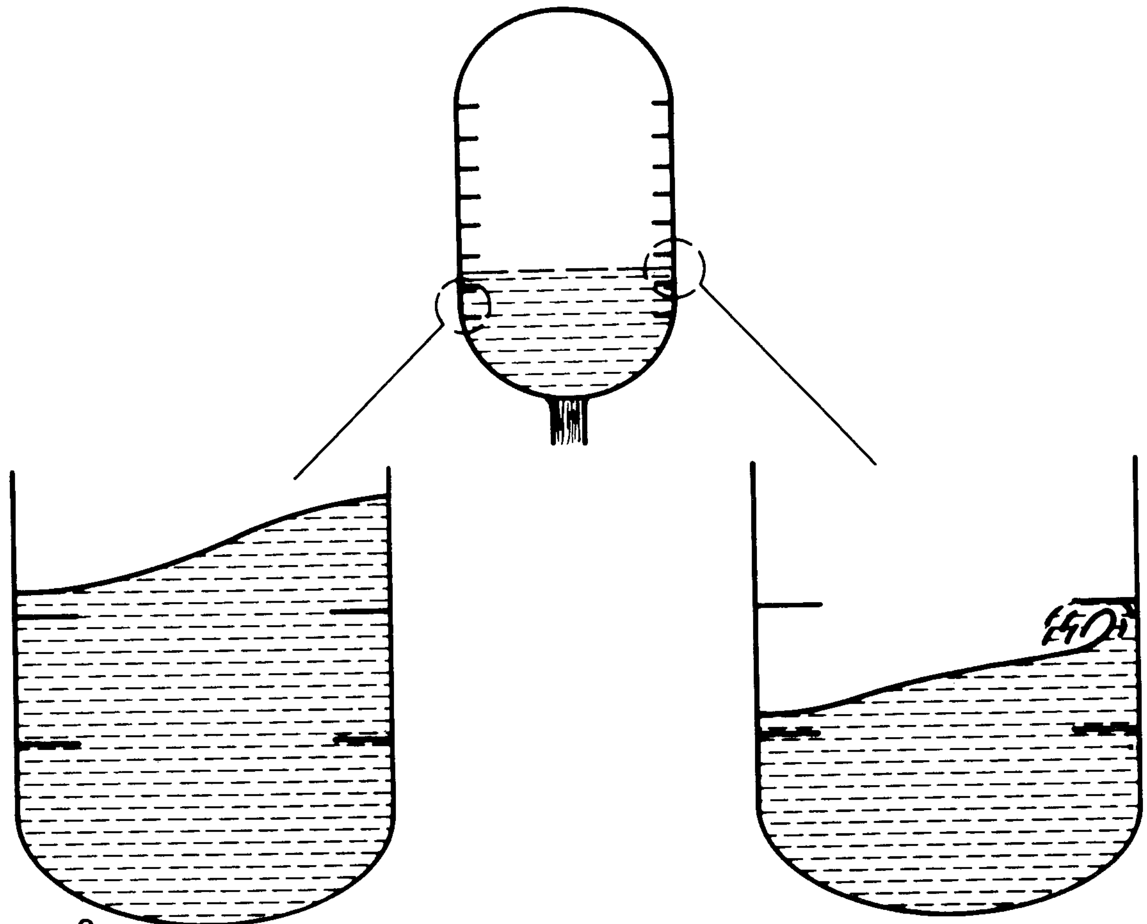

$$p = \underbrace{f(C_D \rho V^2,\ r,\ \beta)}_{\text{VELOCITY}} + \underbrace{f(\rho \omega V,\ r,\ \beta)}_{\text{ACCELERATION}}$$

$$p = f(2\rho V^2)$$

Figure 13

BAFFLE-PRESSURE-TEST RESULTS

(Figure 14)

Theoretical and experimental results are shown for the condition where the baffle is one width W below the surface and one width W above the surface. The pressure across the baffle is presented as a function of a nondimensional velocity parameter, referred to as the period parameter (ref. 7). This parameter involves the liquid velocity at the baffle location V, the period of the oscillation T, and the baffle width W and may be written as $VT/2W$. In general the theoretical and experimental agreement has been good for both the baffle pressures and damping. The effects of baffle spacing are summarized in figure 15.

BAFFLE-PRESSURE-TEST RESULTS

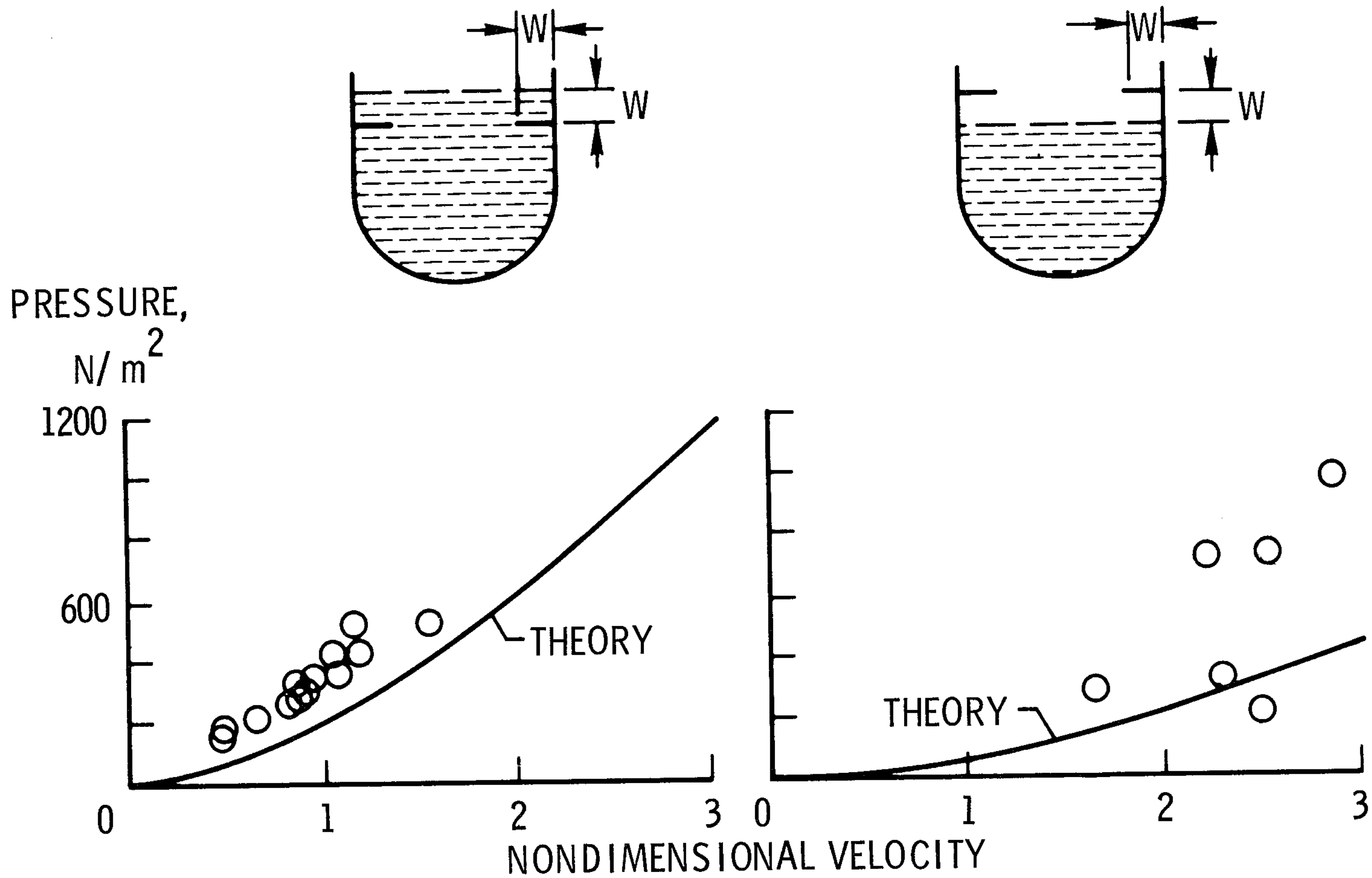

Figure 14

BAFFLE SPACING EFFECTS

(Figure 15)

Pressure and damping data are summarized for the tank fitted with two baffles of width W and spacing S. Pressures measured across the upper baffle p_m are divided by pressures measured across a single baffle p_s at the same location, and the ratio is presented as a function of baffle spacing S/W. The band width represents the effect of baffle position with respect to the free surface. Damping coefficients δ_m and δ_s are presented in a similar format. For the range of variables considered, the pressure data are not highly dependent upon baffle spacing. In general, the pressures are somewhat higher for the multiple baffles because of the added turbulence. The damping data suggest that closely spaced baffles are less effective than widely spaced baffles. This result is undoubtedly due to the interference or shielding provided by the closely spaced baffles.

Improvements in damping and baffle weight can be achieved by using lightweight flexible materials in the baffle design as shown in figure 16.

BAFFLE SPACING EFFECTS

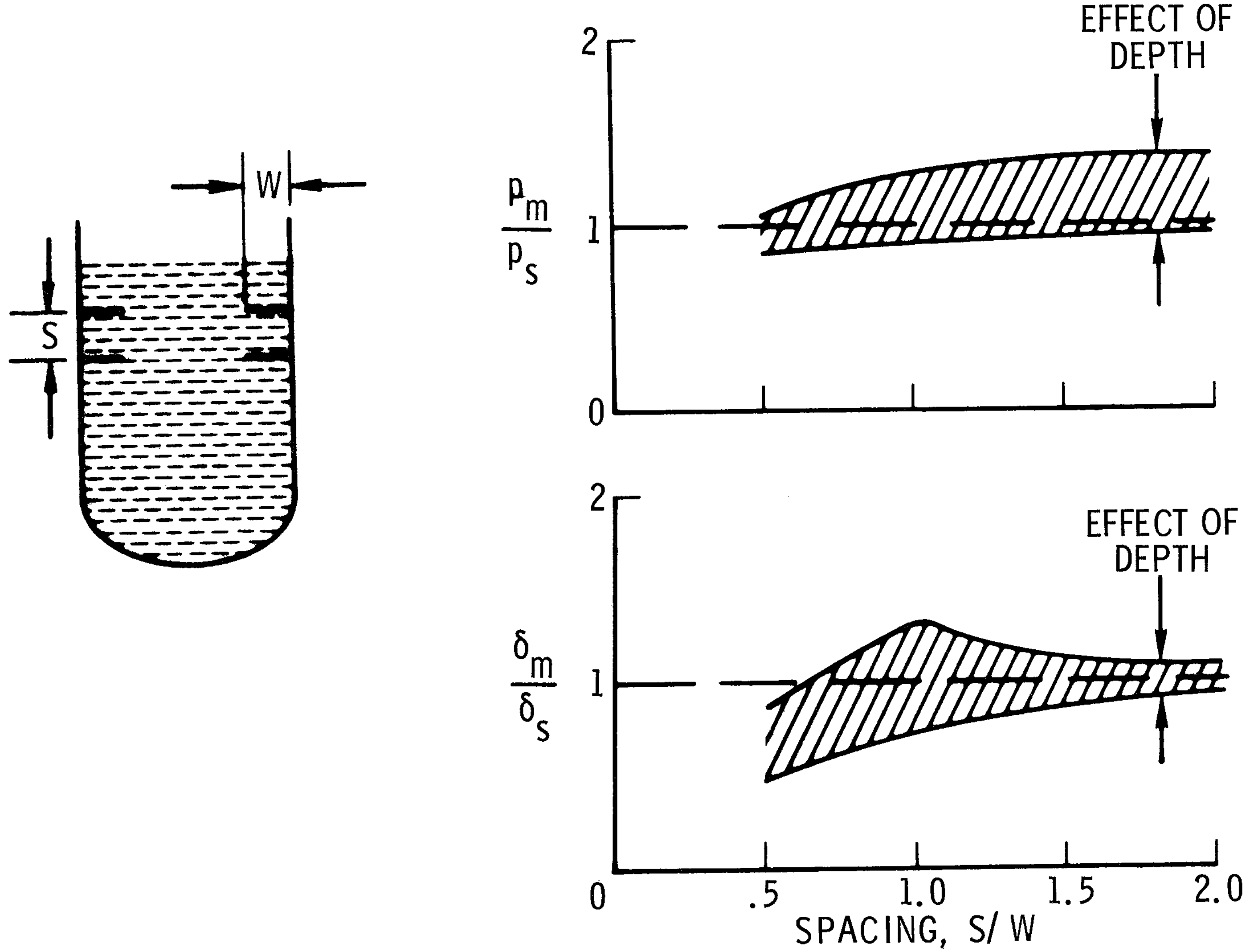

Figure 15

FLEXIBLE-BAFFLE-STUDY RESULTS

(Figure 16)

In studies of baffle efficiency, flexible ring baffles have been found (ref. 8) to offer substantial improvements in damping as well as weight savings as shown in figure 16. Several candidate materials (ref. 9) have been found to be compatible with LOX (liquid oxygen). Proof-of-concept tests utilizing these materials will be conducted in a 4-meter-diameter cylindrical tank at Marshall Space Flight Center (MSFC) using nitrogen as the test liquid.

In summarizing liquid suppression technology, it is believed that available pressure and damping theories are directly applicable to space shuttle stability and control analyses as well as baffle designs for the hydrogen-oxygen tank. Additional suppression studies may be required if slosh at large tank angles is anticipated or liquid payloads present loads or stability problems.

FLEXIBLE-BAFFLE STUDY RESULTS

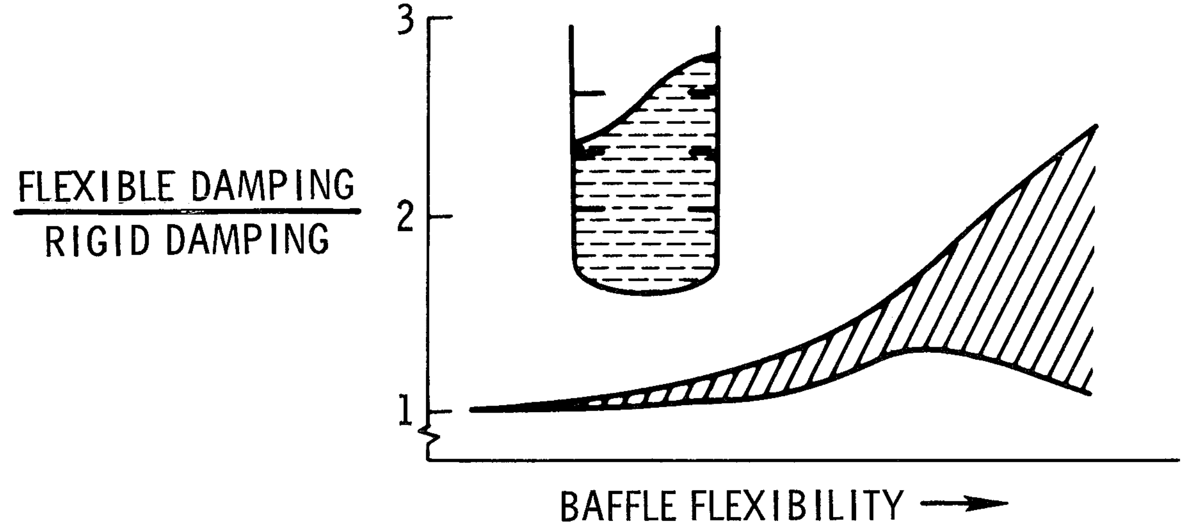

- WEIGHT 4 TO 12 PERCENT OF RIGID BAFFLE
- BAFFLE MATERIAL COMPATIBLE WITH LOX
- NO OBSERVED FATIGUE
- PROOF-OF-CONCEPT TESTS BEING CONDUCTED AT MSFC

Figure 16

SUMMARY OF SHUTTLE LIQUID-DYNAMICS TECHNOLOGY

(Figure 17)

An approximate time-line chart is presented in figure 17 which summarizes the status of liquid-dynamics technology for shuttle application. Studies prior to and including phase A concentrated on defining unique slosh problems associated with shuttle operations. Numerous studies were conducted to examine the dynamic behavior of liquids in rigid tanks and more recently efforts have been concentrated on coupled liquid-tank interactions using sophisticated computer programs. During phase C/D, it is anticipated that efforts will continue toward the development of more general and efficient computer programs as well as instrumentation such as flow meters and quantity gages. In addition, stability and control studies will be conducted which will result in baffle requirements. Pogo and liquid payloads must be considered in these analyses.

Based on past experience, a number of new and unique liquid-dynamics problems will undoubtedly be uncovered during shuttle development because of the relatively high maneuverability, high density of structural modes, liquid payloads, orbital maneuver system, and so forth. However, it is believed that the basic technology for solving these problems is available and directly applicable to the development of the space shuttle.

SHUTTLE-LIQUID DYNAMICS TECHNOLOGY

<u>LIQUID BEHAVIOR</u>

- FREQUENCY AND DAMPING
- SIMULATION
- LOW-g MANAGEMENT

<u>LIQUID/TANK INTERACTION</u>

- MODES (FINITE ELEMENT)
- LOADS (MAC)
- MORE EFFICIENT PROGRAMS

<u>INSTRUMENTATION</u>

- QUANTITY GAGE
- FLOW METERS

<u>VEHICLE STABILITY AND CONTROL</u>

- BAFFLE DESIGN
- POGO ANALYSIS
- LIQUID-PAYLOAD ANALYSIS

— PHASE A —▼——— PHASE B ———▼——— PHASE C/D ———→

Figure 17

REFERENCES

1. Abramson, H. Norman, ed.: The Dynamic Behavior of Liquids in Moving Containers. NASA SP-106, 1966.
2. Anon.: Propellant Slosh Loads. NASA Space Vehicle Design Criteria (Structures). NASA SP-8009, 1968.
3. Anon.: Slosh Suppression. NASA Space Vehicle Design Criteria (Structures). NASA SP-8031, 1969.
4. Dodge, Franklin T.; and Garza, Luis R.: Propellant Dynamics in an Aircraft-Type Launch Vehicle. Project 02-2879 (Contract NAS 8-25920), Southwest Res. Inst., July 1971. (Available as NASA CR-119891.)
5. Guyan, R. J.: Study on Dynamics of an Ellipsoidal Bulkhead Containing Fluid. SD71-184 (Contract NAS 8-25895), North American Rockwell, Sept. 20, 1971.
6. Feng, G. C.; and Robertson, S. J.: Study on Propellant Dynamics During Docking. LMSC-HREC D225632 (Contract NAS 8-25712), Lockheed Missiles & Space Co., Mar. 1972.
7. Keulegan, Garbis H.; and Carpenter, Floyd H.: Forces on Cylinders and Plates in an Oscillating Fluid. J. of Res. of the Nat. Bur. of Stand., vol. 60, no. 5, May 1958, pp. 423-440.
8. Stephens, David G.; and Scholl, Harland F.: Effectiveness of Flexible and Rigid Ring Baffles for Damping Liquid Oscillations in Large-Scale Cylindrical Tanks. NASA TN D-3878, 1967.
9. Dodge, Franklin T.: Engineering Study of Flexible Baffles for Slosh Suppression. NASA CR-1880, 1971.

FLIGHT LOADS AND CONTROL

By David K. Mowery and Stephen W. Winder
NASA Marshall Space Flight Center

ABSTRACT

The prediction of flight loads and their potential reduction, using various control logics for the Space Shuttle vehicles, is very complex. Some factors, not found on previous launch vehicles, that increase the complexity are large lifting surfaces, unsymmetrical structure, unsymmetrical aerodynamics, trajectory control system coupling, and large aeroelastic effects. This paper will discuss these load producing factors and load reducing techniques. Identification of potential technology areas will be included.

INTRODUCTION

This presentation is divided into two distinct parts. The first section identifies the basic guidance and control concepts that lead to structural and structural dynamic loads. A general discussion of Space vehicle ascent flight loads, as well as load relieving mechanisms, is given. In the second section the characteristics and special problems are given for the Space Shuttle launch vehicle. A summary is given of the special dynamics and control analyses and test problems that are apparent at this time.

ASCENT LOAD SOURCES

Structural loads on a space vehicle have their source in longitudinal acceleration (thrust) and the lateral loads resulting from following the desired path in the presence of disturbances. These lateral loads are a function of the vehicle aerodynamic and mass configuration, and the control system force source and logic. The following figure illustrates the three types of loadings: aerodynamics, lateral acceleration, and control. In flying a given trajectory, the disturbances (winds) create an angle of attack that loads the vehicle aerodynamically. This is illustrated by individual force vectors distributed over the vehicle length. The dynamic response of the vehicle to this aerodynamic force and the commanded control force creates an inertial force which is illustrated as the mass element (cross hatched) times its local acceleration $\ddot{Z}(x,t)$. This local acceleration includes rigid body lateral acceleration, lateral acceleration due to rigid body rotation about the c.g., and lateral acceleration from the vehicle bending. An additional trim load occurs due to vehicle asymmetries as the vehicle trims itself about the desired trajectory. A convenient means of expressing all these vehicle loads except the longitudinal load is through the bending moment. Since rigid body accelerations (rotational and lateral) can be expressed in terms of their sources, aerodynamic moment and control force, the expression for the bending moment is a function of angle of attack, control force deflection, and bending mode accelerations. There are some other terms, but in general they are negligible. Maneuver loads have not been discussed; however, they can be treated in the same manner. In summary, as the guidance and control systems exercise their functions of achieving a desired vehicle performance in the presence of disturbances, interaction between structure and control occurs which creates loads on the vehicle.

ASCENT STRUCTURAL LOADS

ASCENT LOAD SOURCES

1. **AERODYNAMICS**
2. **THRUST**
3. **TRIM (TRAJECTORY)**
4. **DYNAMICS**
   - o **RIGID BODY**
   - o **ELASTIC BODY**

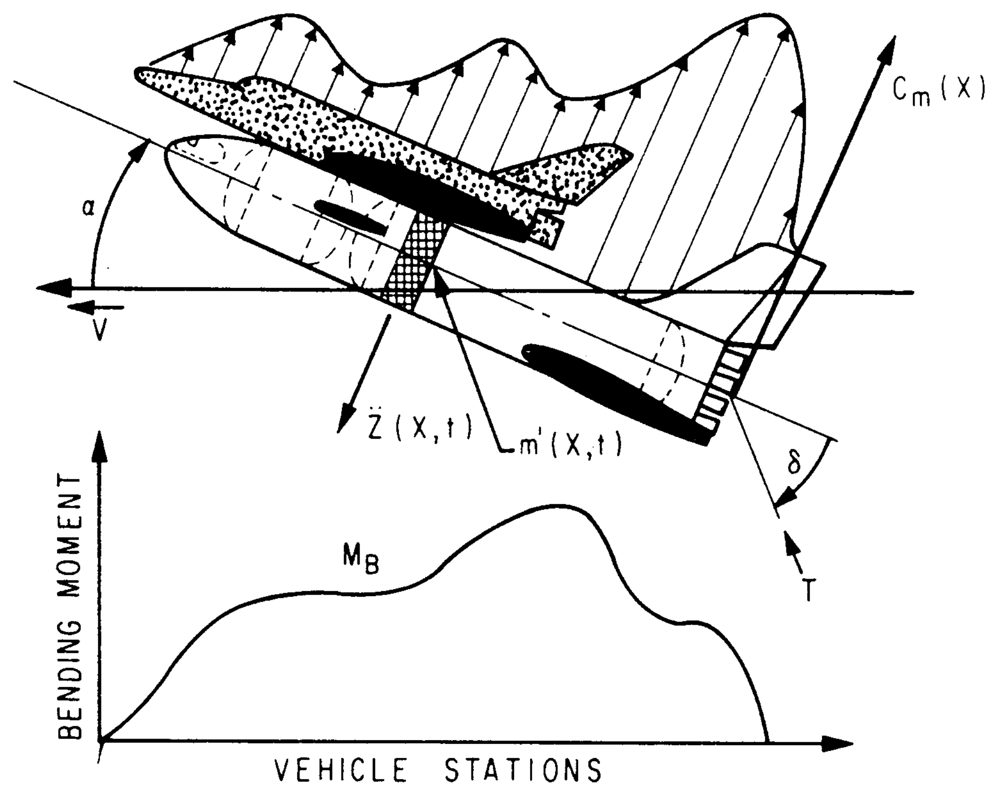

BENDING MOMENT

$$M_B = M'_\alpha \alpha + M'_\delta \delta + M_T + \sum M'_\eta \ddot{\eta}$$

$$\ddot{Z} = \ddot{Z}_{cg} + \sum \ddot{\eta}_\mu Y_\mu (X)^* + \bar{X} \ddot{\varphi}$$

* $\sum \ddot{\eta}_\mu Y_\mu (X)$ = LATERAL ACCELERATION DUE TO BENDING DYNAMICS

TRAJECTORY TRIM LOADS

Shuttle configurations have exhibited significant coupling between trajectory, guidance, and control so that trim loading could not be neglected in tradeoff studies. The problem has been to find the type of trajectory to fly which best meets the stated objectives of maximum payload with minimum disturbances.

The reason for the coupling is illustrated at the left of the chart. Rigid body geometries are such that different local angles of attack are present on the major structural elements, such that a vehicle orientation cannot be found which decreases the aerodynamic normal force to zero on each element simultaneously and thus unloads the vehicle. Although the summation of the aerodynamic normal forces can be brought to zero by proper orientation (such as angle of attack, wing incidence, etc.), an aerodynamic moment still exists because of the difference in distance of the individual forces from the center of gravity. This says, then, that a particular aerodynamic normal force and moment are inherent with the particular angle of attack for which the trajectory is designed.

Other geometric considerations have occurred because of the placement of the engines and mass properties offset and its movement with fuel depletion. Because of the nonsymmetric placement of the engines and thrust levels about the center of gravity, cant angles have been needed to trim the vehicle throughout flight with a minimum of actuation angle requirements. These cant angles and other thrust deflection angles required to trim the moments also produce normal forces that load the vehicle.

A choice on how to balance the moments between aerodynamics and engines, with the resulting normal forces and their loading, has existed for given wind conditions (usually no wind). Zero aerodynamic lift trajectories, or zero aerodynamic moment trajectories, are two such possible choices and have a large influence on the amount of gimbal angle required. The results of a special angle of attack history is shown on the right side of the chart. The angle of attack and the resulting thrust deflection required to fly total (engine and aerodynamic force) moment and force balance is shown. By flying different angle of attack histories, the blend between aerodynamic and control force loads could be changed. The blending between aerodynamic and control loads has been influenced also by the control system logic and force application positions. If, then, a given location became structurally critical, control and trajectory shaping could be used to change to the proper blend that best reduces the criticality. On the other hand, these different blends produce different normal force combinations which in turn influence the trajectories.

TRAJECTORY TRIM LOADS

$\Sigma M = 0$

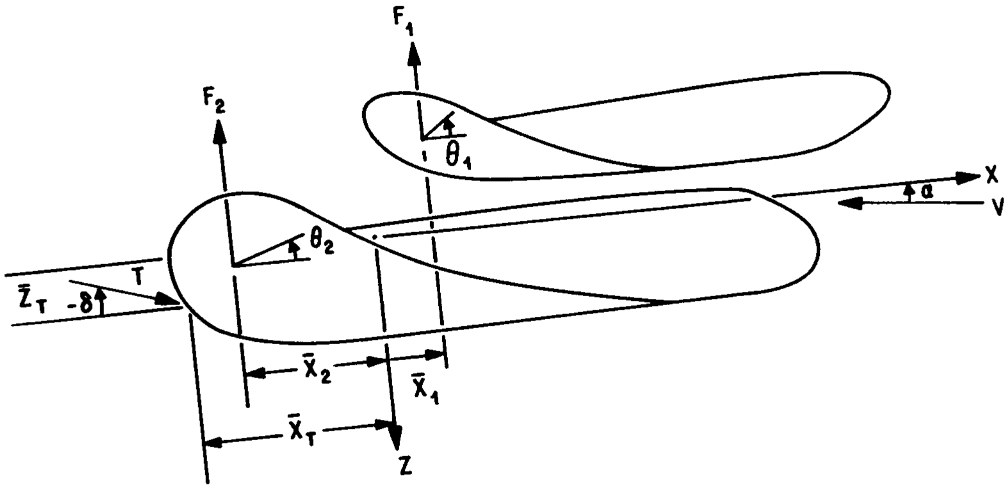

$$+\Sigma M = -F_1(\theta_1+\alpha)\bar{X}_1 + F_2(\theta_2+\alpha)\bar{X}_2 - T\delta\bar{X}_T - T\bar{Z}_T = 0$$

$$+\ \Sigma L = F_1(\theta_1+\alpha) + F_2(\theta_2+\alpha) - T\delta$$

$$C_{M_o} = F_1\bar{X}_1\theta_1 - F_2\bar{X}_2\theta_2$$

$$C_{M_\alpha} = F_1\bar{X}_1 - F_2\bar{X}_2$$

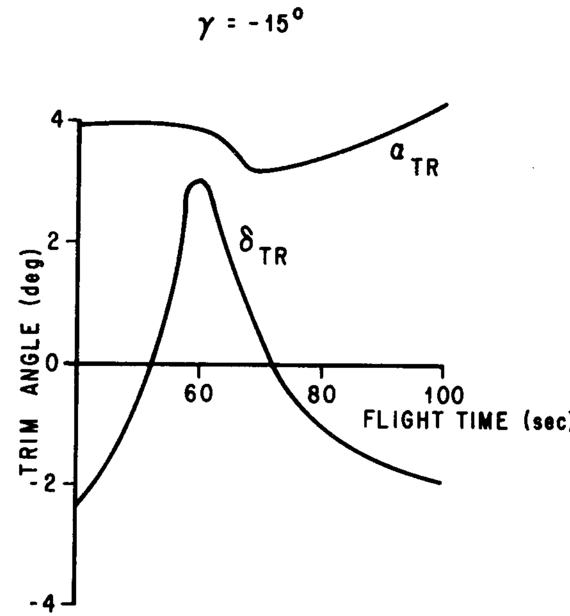

RIGID BODY LOADS

The most favorable flight conditions are those that cause the vehicle to fly at such an orientation with respect to its velocity vector and at such thrust deflection angles as to minimize the total loading at the structurally most critical location in the presence of disturbing winds, while still meeting constraints on performance and control deflections. For a given configuration and aerodynamics, this optimizing process involves: (1) the basic trajectory shaping to give the most favorable velocity vector orientation for performance, dynamic pressure-angle of attack product, and longitudinal acceleration constraints by flying a given angle of attack history either in a no-wind condition or for an expected wind (trajectory biasing), (2) the control and dynamics philosophies and logic employed for the system which determine the extent to which the reference attitude will be enforced in the presence of disturbances (within the control force constraints) and the blend of control forces between the available sources to minimize the loads at the critical stations and to stabilize the vehicle modes, and (3) the structural design which determines the more critical load stations and the basic mass properties and mass unbalances. Additionally, loads due to the expected headwinds and tailwinds will want to be balanced (or the no-wind loads biased) such that an approximately equal percentage of the vehicle capability is taken by equal probability head and tail wind levels. Control system philosophies have historically been looked to for initial relief from rigid body loads without excessive cost. From a knowledge of the most critically loaded vehicle station, and the ratio of the bending moment partial with respect to angle of attack to the bending moment partial with respect to control deflection, a decision can be reached as to whether reducing thrust deflection or reducing angle of attack (when one must choose) will give greater load relief. Other vehicle characteristics may influence the particular type of control that is chosen. Control logics, such as an attitude control, will require large control deflections and pull high angles of attack but will give good trajectory following. Maximum load-relief type of control will reduce angle of attack and control deflections but will experience large gust responses. This control will build up large drifts and trajectory shaping is thereby lost. By relaxing a tight hold on the attitude and causing the vehicle to nose into the wind by lateral acceleration or angle of attack feedback, the angle of attack (or sideslip) can be decreased. For many vehicles, such a reduction in angle of attack is sufficient to decrease the loads. There are other control logics and state feedbacks available which can reduce loads and performance losses; for example, lateral velocity or position feedback or integral of attitude position feedback. These are not discussed since they do not add significantly to the concepts shown. For some shuttle configurations, however, turning into a pitch wind produces enough loss of altitude that the dynamic pressure builds up faster than the angle decreases and excessive dynamic pressure-angle of attack products are reached. Therefore, other means of load relief must be obtained or the basic structure will have to be strengthened to take the load. The lower altitude is not necessarily detrimental from a performance standpoint. Still a third control, rotational minimum, effectively minimizes vehicle rotational response to disturbances so that little gust response is experienced, but control deflections are large. Substantial drift is also encountered. Responses such as those just described also have effects upon the flexible body excitation of the vehicle so that selection of the basic type of control will of itself involve several tradeoffs.

RIGID BODY ACTIVE LOAD RELIEF CONCEPTS

ATTITUDE CONTROL

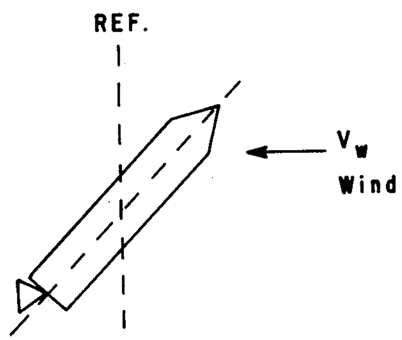

$$\delta = a_0\phi + a_1\dot{\phi} + b_0\alpha$$

1. TRAJECTORY SHAPING
2. MINIMUM PERFORMANCE LOSS
3. MEDIUM TRIM LOADS
4. AVERAGE GUST RESPONSE
5. LARGE CONTROL FORCES
6. POTENTIAL LARGE LOCAL LOADS

LOAD MINIMUM

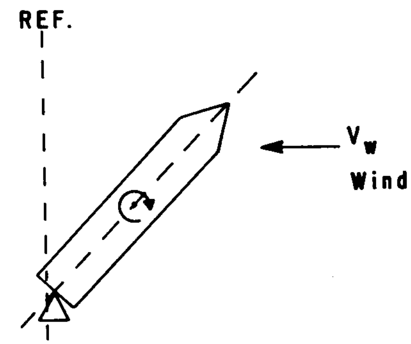

$$\delta = a_1\dot{\phi} + b_0\alpha$$

1. LARGE GUST RESPONSE
2. LARGE DRIFT
3. SMALL CONTROL FORCES
4. LOSS OF TRAJECTORY SHAPING
5. POTENTIAL LARGE LOCAL LOADS

ROTATIONAL MINIMUM

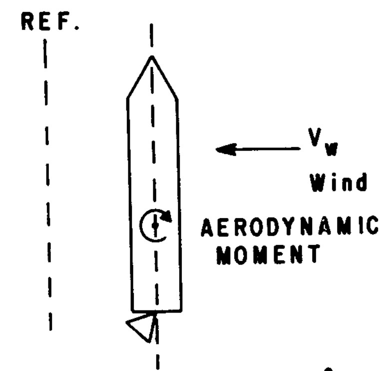

$$\delta = a_0\phi + a_1\dot{\phi} - \frac{c_1}{c_2}\alpha$$

1. MINIMUM GUST RESPONSE
2. LARGE TRIM LOADS
3. LARGE CONTROL FORCES
4. SUBSTANTIAL DRIFT

WIND BIASING

Wind biasing techniques can be employed to reduce loading when the wind can reasonably be assumed to have known directional characteristics for the period of time over which the biasing is being considered. In the extreme, this can be carried to onboard sensing and computation of the wind mean. More practically, this can be carried to a period of about 8 hours prior to launch using dependence on wind persistence statistics, where computer read in can be accomplished and verified just prior to launch. Previous Saturn vehicles have made use of a seasonal bias, but the loading gains are not as great when such a long time period for wind change must be accommodated.

Wind biasing essentially programs the vehicle to fly at its most load favorable angle of attack (as discussed on the rigid body loads chart) in the high dynamic pressure region in the presence of the expected (or predicted) wind. Before and after the dynamic pressure region, various corrections can be given to compensate for the expected off-trajectory drift build up while maintaining the load relieving angle of attack.

Angle of attack is composed of the relative velocity angular change due to wind, the vehicle drift, and the vehicle attitude. The angle of attack experienced by the vehicle can then be manipulated by creating the correct relationship between the three listed variables. Since the wind is predicted (or the expected value is known), adjustments of the relative drift and vehicle attitude can be made to cancel the effects of the known wind to any desired degree. Still a fruitful area of study is the most favorable relationship between the amount of drift and the amount of attitude error to be used in counteracting the angular change in relative velocity due to winds. Two such choices are illustrated on the next chart for a typical yaw plane bias. Work on Skylab indicated that either too much drift or too much attitude angle was not optimum for that vehicle.

Although, to this point, wind biasing has been considered to reduce the loading, it may also be employed to minimize the sideslip angle and the resulting roll-yaw coupling so inherent in many of the Space Shuttle proposed configurations. This coupling and, if not well controlled, its shift of loads from the yaw plane to the pitch plane is also an area that needs to be studied. In this case, it is possible to wind bias in another way. Roll the vehicle around the wind vector to maintain a minimum load or minimum control system requirements.

WIND BIASING CONCEPTS

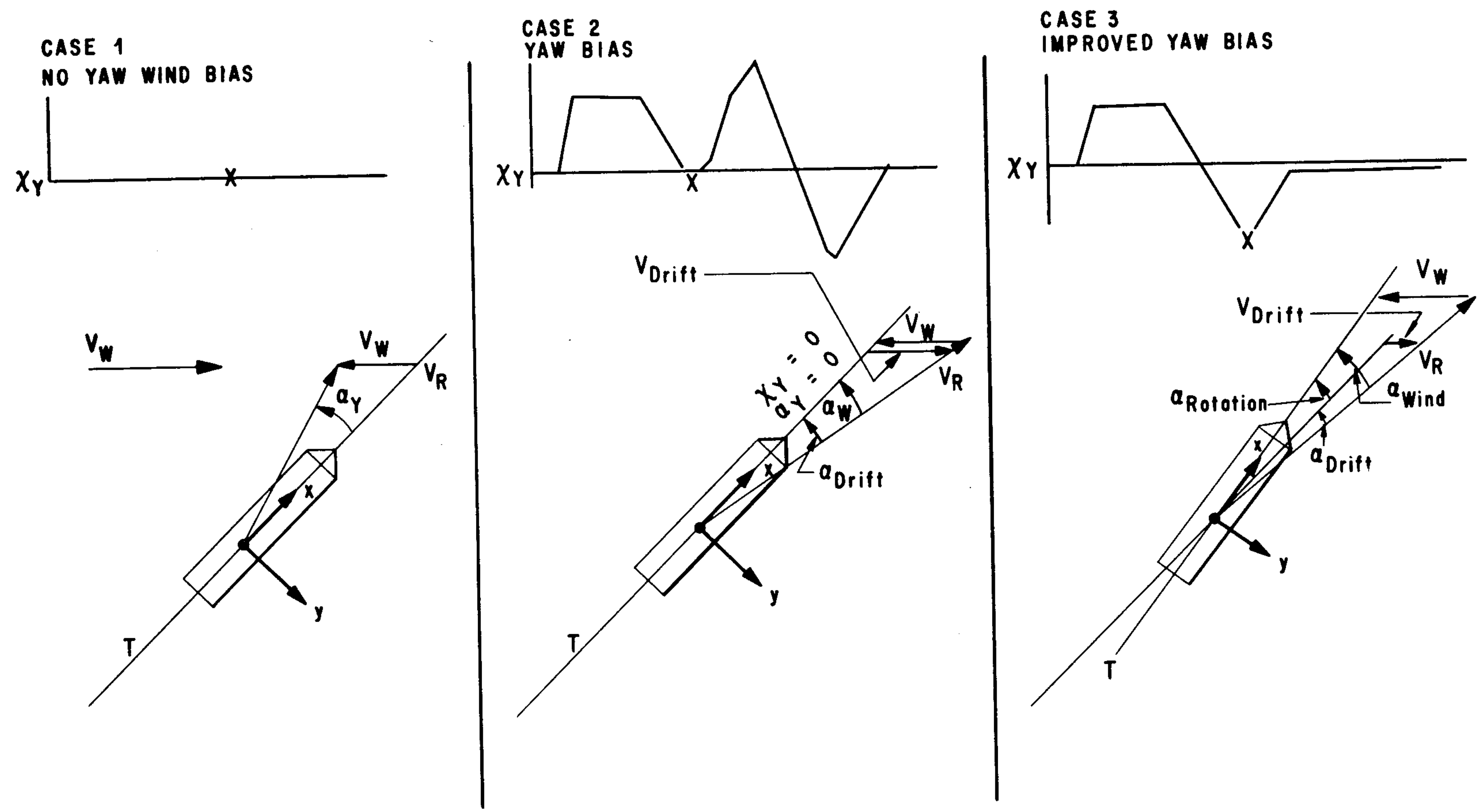

MODAL SUPPRESSION

The loads induced from elastic body accelerations were discussed under load sources. These elastic body motions are usually driven by the atmospheric turbulence. Through the use of various control sensors, located at appropriate vehicle stations, the bending state of the vehicle can be determined and appropriate signals sent to the control forces to decrease the response. This can be done by adding damping to the mode, increasing or decreasing the effective modal mass, or detuning the mode from the gust frequency. Rate gyros can be used for damping, position gyros for frequency shift, and accelerometers to change the effective modal mass. This figure shows the bending mode response to a sinusoidal gust for various amounts of acceleration feedback using one accelerometer. In this case, the response is reduced substantially by increasing the accelerometer feedback. Obviously, a wrong choice on sensor location, etc., could have the opposite effect. The same trend can be seen by increasing the effective modal damping through use of rate feedback using rate gyros. Since the vehicle response is determined by the zeros and poles, another way of looking at closed loop control effect on modal suppression is by the freedom that the sensor complement gives in locating the closed loop poles. The question of how pole-placement quality measures for a sensor complement relate to measures of quality with respect to controller performance is too lengthy to be discussed here.

MODAL SUPPRESSION

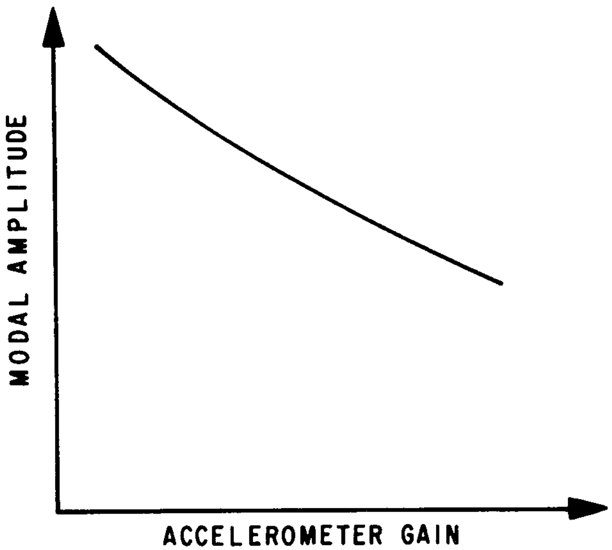

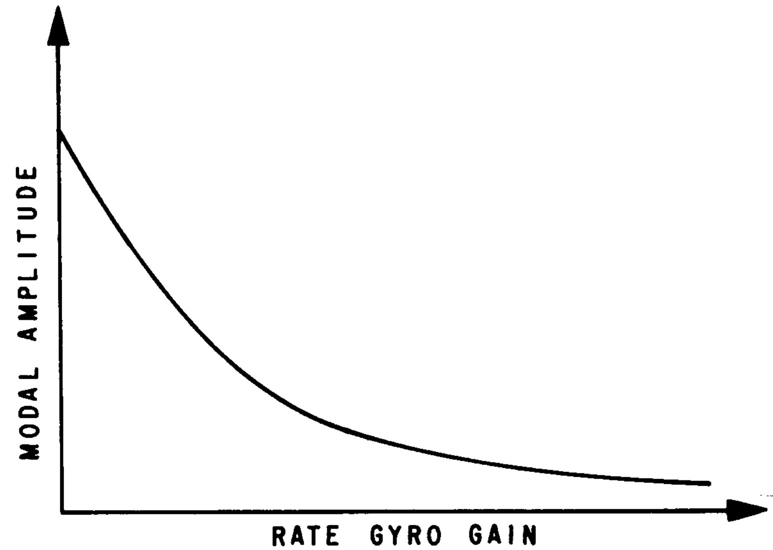

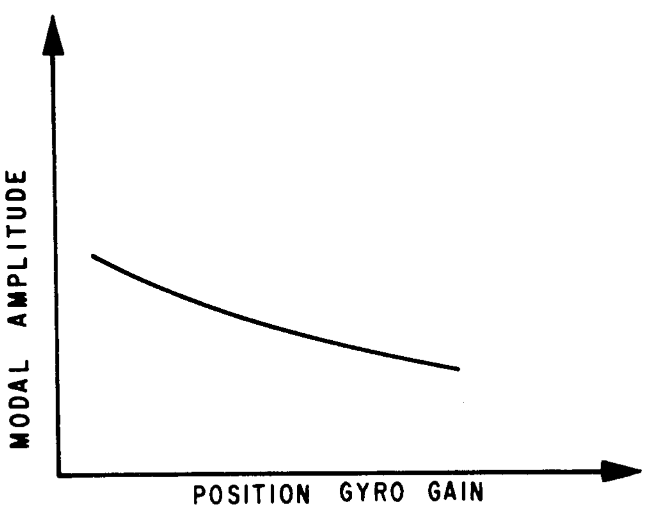

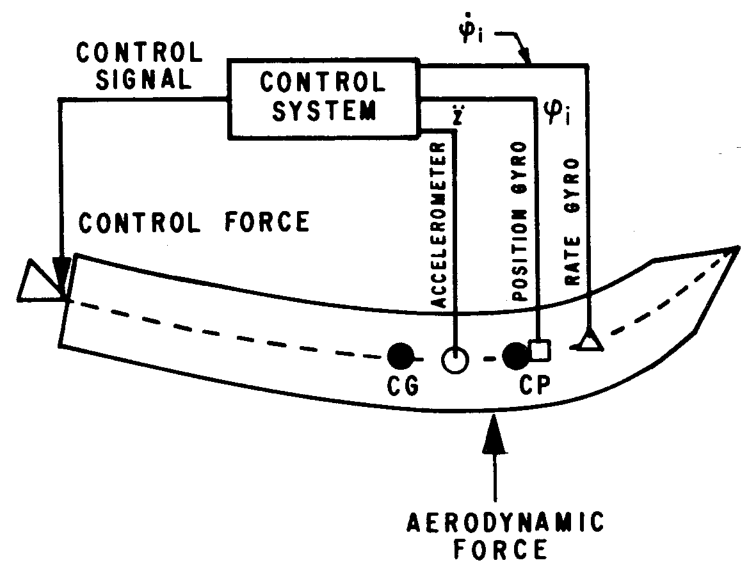

AN ADAPTIVE SYSTEM

In many cases, predictions of modal characteristics are so poor that one cannot resort to the simple approach shown for accelerometers and rate gyros using proportional feedback. This forces one to take these same signal sources and use some form of modal identification (spectral identification for example) to build an adaptive system which adjusts the vehicle modal response to an acceptable level. This is illustrated on the next figure showing the various steps: (1) Sense the vehicle state, (2) identification of the state, (3) a proper decision based on the state, and (4) adjust the control logic to control the response. This process results in an acceptable bending dynamics response level without accurate pre-prediction modal characteristics. It does, however, require a much more complicated control system and logic.

AN ADAPTIVE SYSTEM

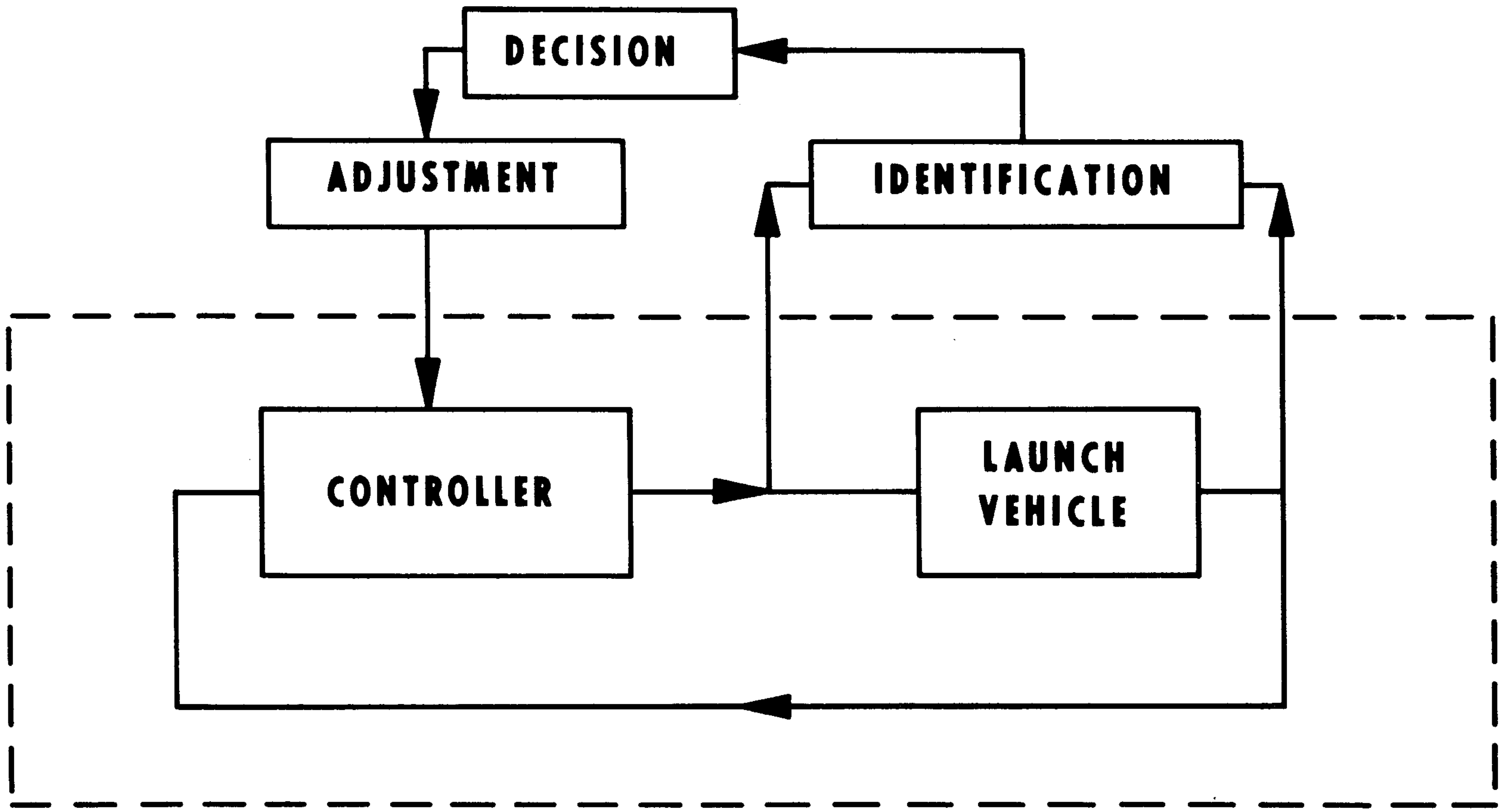

SHUTTLE CHARACTERISTICS

The Space Shuttle is a vehicle designed to be reused, with a lifetime of approximately one hundred missions. This means that it must have the ability to perform as a booster, as an orbital vehicle which reenters the earth's atmosphere at a high angle of attack, and finally as an aircraft which cruises and lands. Incorporating the aerodynamic, propulsion, structure, and control system characteristics necessary to meet these performance criteria leads to several unusual characteristics. These characteristics are not compatible with present symmetrical boosters or conventional aircraft since the Shuttle must be a cross (blend) between both, as well as a high velocity reentry vehicle. The chart lists the resulting characteristics that lead to key design issues and problems associated with the Shuttle vehicle. Several of these will be discussed in detail on later charts.

SHUTTLE CHARACTERISTICS

The Shuttle is a space vehicle designed for reuse: This dictates ability to perform:

(a) as a booster
(b) as an orbiter vehicle
(c) during high angle of attack atmospheric reentry
(d) in cruise and landing

Meeting these varied performance criteria leads to:

1. large control, trajectory, aerodynamic, structural coupling
   - o bias aerodynamic forces
   - o static mass trim forces
2. yaw-roll coupling
   - o aerodynamics
   - o structure
   - o control
3. highly coupled lateral-longitudinal structure
   - o asymmetric liftoff
   - o several elastic bodies elastically coupled
   - o high modal density
   - o lateral c.g. offset
   - o large ascent aeroelastic effects
   - o complex modal prediction
4. multi-aerodynamic loading points, control force application points not necessarily on principal axis of inertia
5. poor pilot handling qualities (reentry design predominates)
6. thermal stresses
7. hundred mission lifetime design
8. hula-pogo potential

KEY SHUTTLE ISSUES

The major goal associated with the shuttle concept of reusability is to have a maximum payload placed in orbit with minimum vehicle impacts resulting from disturbances. This is to be accomplished for a variety of missions and payload profiles, possibly from more than one launch site. In order to accomplish this goal, tradeoffs must be made on many key issues in terms of cost, reliability, complexity, and maintainability. The chart shows in schematic form the key issues associated with control concepts, guidance concepts, trajectory shaping, aerodynamic configuration, control system complexity, structural weight, and modal characteristics. If each of these were an entity in itself, the problem would be fairly simple; however, this is not the case. In general, there is a very large correlation between the choice in one area dictating the choice of the other. The Space Shuttle vehicle, therefore, requires a highly sophisticated integrated flight analysis approach that requires the combined joint efforts of all facets of the engineering disciplines and a highly talented system engineer to insure the proper trades. Several of these effects are shown on the next charts.

KEY SHUTTLE ISSUES

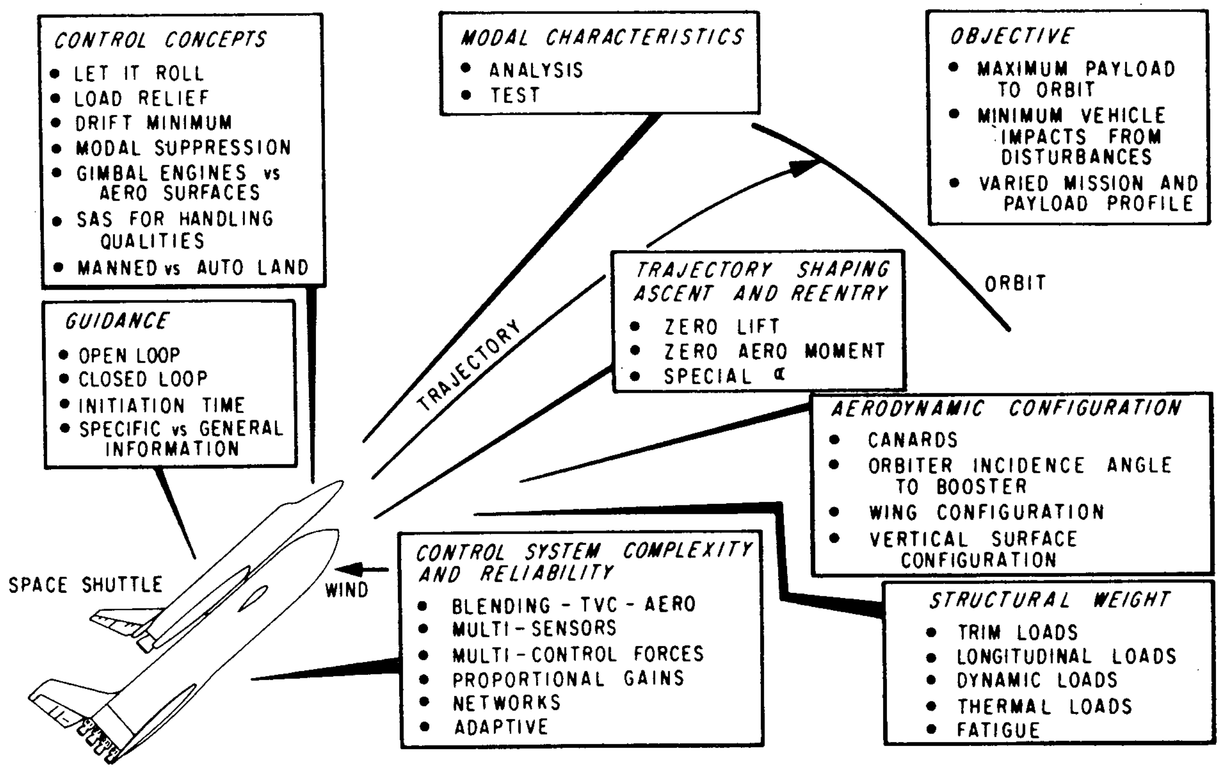

TRAJECTORY AND CONTROL CONCEPTS

The trajectory control coupling effects are illustrated further on the following chart. The four basic types of trajectory shaping discussed previously affect control requirements (δ), structural loads (dynamic pressure), and performance (altitude). Using a trajectory shaped for zero aerodynamic moment gave the lowest control requirements for the configuration considered. The engines were gimbaled a maximum of 10° for only a few seconds, while the payload optimum trajectory required large control forces (engines at 10° for 80 seconds). The same is true for the dynamic pressure, which was higher for the payload optimum trajectory. The lower altitude and higher q combine with a higher velocity (flatter trajectory) to achieve the increased payload. No impact was made on structural weight to fly these trajectories. Obviously this would have to be done to make a final trajectory shaping decision.

There is a very interesting trade, from the control standpoint, between using gimbal engine and aero surfaces for control. This is illustrated under blending on the chart. In this case, the payload losses include performance loss from gimbaled thrust, aero surface drag, aero surface hinge moments, and hydraulic system. The lowest payload loss occurred using only TVC, while large uses of aero surfaces had the largest payload loss. Using the gimbal engines to their maximum (10°) and supplementing with minimum use of aero surfaces gave the best overall solution.

TRAJECTORY AND CONTROL CONCEPTS

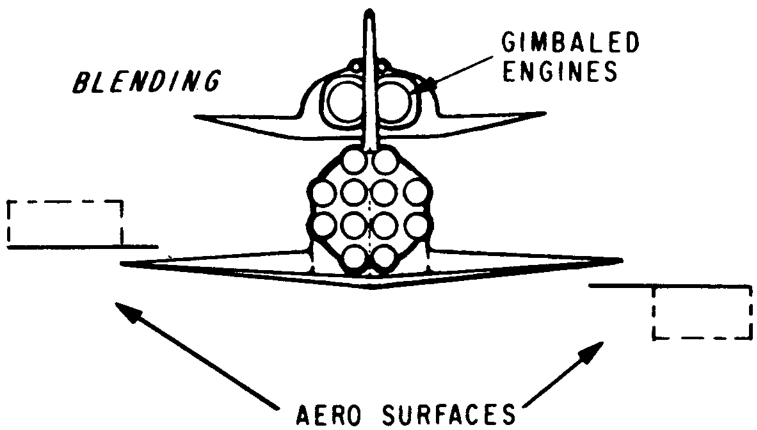

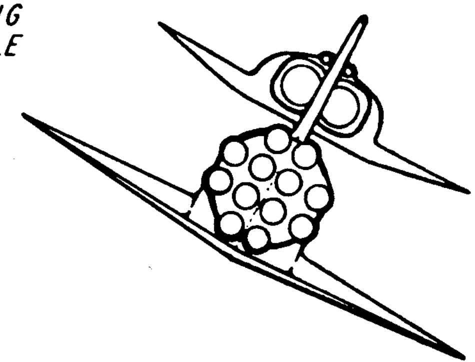

	δ ENGINE	δ AERO	Δ PAYLOAD N(lb)
TVC ONLY	± 13.2°	0	-5533 (-1,244)
TVC + AERO	± 8.2°	± 8.4°	-11565 (-2,600)
TVC (10° + AERO	± 10°	± 3.4°	-7562 (-1,700)

	Δ PAYLOAD N(lb)
ROLL CONTROLLED	-890 (-200)
FREE ROLL (DAMPED)	-8900 (-2000)

TRAJECTORY SHAPING
EFFECT OF HEADWIND

Z.A. - ZERO AERODYNAMIC MOMENT
Z.L. - ZERO AERODYNAMIC LIFT
q α - SPECIAL α FOR LOADS
OP - OPTIMUM (TRAJECTORY ONLY)

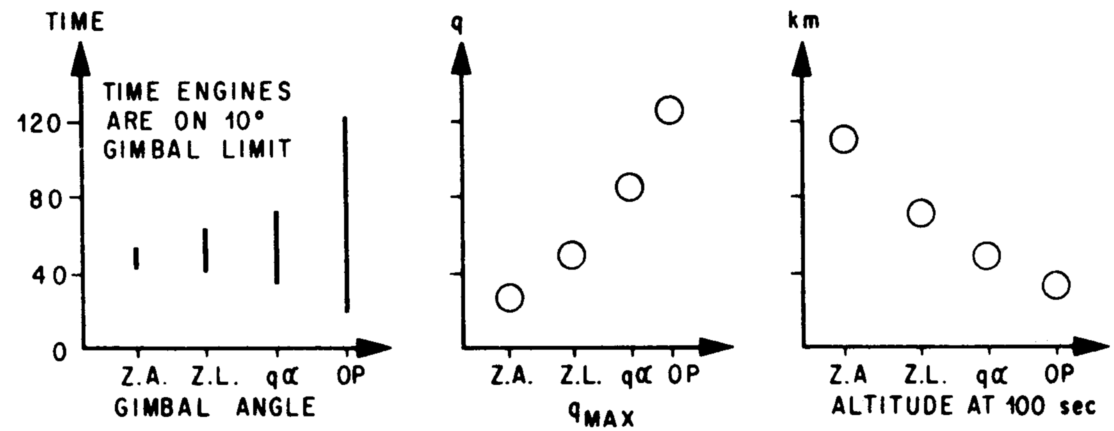

ELASTIC BODY DYNAMIC AND CONTROL TRADES

One of the high risk areas on the shuttle vehicle is aeroelastic effects, including modal stability and loads. This is obvious since the multi-body vehicle is also not symmetrical in the pitch plane. This leads to elastic body modes that are coupled laterally, longitudinally and in yaw-roll. Analysis, then, must depict 3-D characteristics which result in symmetric and antisymmetric modes. In general, the many bodies are connected by a two point attachment, which creates unsymmetric loads and complicates the analysis. All the structural characteristics lead to high modal density and complex modes. There are two points to be made relative to modal density (chart at the bottom of figure). First, the large number of elastic modes (symmetric and antisymmetric) that exist in a low frequency band are many more than the present symmetrical vehicles have. Second, the closeness of the symmetric and antisymmetric modes indicates a strong tendency for coupling. This leads to the various trades between control system complexity, trajectory shaping, and dynamic testing, as shown on the figure, which raises the general question as to what is the solution to the dynamics and control aeroelastic problem.

SOLUTIONS TO AEROELASTIC PROBLEMS

STRUCTURAL BEEFUP: One way to solve the loads problem encountered via aeroelastic effects is through structural stiffening to carry the additional loads. This increased stiffening also changes the modal frequencies, usually raising them, which helps to remove them from the zone of critical concern. However, sometimes the structural additions may create new vibration problems rather than solve the ones they were intended to solve. Probably the most serious penalty of structural beefup is the additional weight. Thus, the main trade we will have to make is the structural weight increase (payload loss) versus cost and complexity of control development.

CONTROL SYSTEM DEVELOPMENT: The other general means of reducing aeroelastic effects on loads and stability is to use active control. Earlier studies on the interaction of aeroelastic vehicle and control system tended to try to remove vibration influence from the control system by filtering the elastic body signals from the sensors. Two of the most popular techniques employed were gain and phase stabilization and notch filtering. Gain and phase stabilization attenuates the signal's high frequencies, while phase stabilization shifts the phase of the signals to insure they will not add sufficient lag to the system to cause instability. The notch filter concept selectively filters a specific frequency while letting all other frequencies through the filters. This passive type of controller was used mainly as a device to insure system stability. The use of control actuators to actively stabilize modes is a relatively new concept and is particularly suited to vehicles with multicontrol actuators. The main

concepts are concerned with providing increased damping to remove the energy impacted by the wind or to detune the system to remove resonances.

To make these active flexure control systems attractive, a method must be found which finds the minimum number of actuators and sensors that adequately control the modes but at the same time have a simple structure that is easy to implement. Also, in the shuttle vehicle, the mode shapes and frequencies change rapidly during ascent, and the precise knowledge of the plant that is required will not be available unless extensive vehicle testing is done. Thus, a system that tracks the vehicle modes (i.e., adaptive in nature) could be developed. The alternative is to be absolutely sure of the vibrational characteristics of each configuration prior to launch (detailed analysis and testing). The chart illustrates these different trades and also compares a typical set of modal frequencies to the Saturn V Apollo, illustrating the frequency grouping and high density.

DYNAMIC AND CONTROL TRADES

DYNAMIC CHARACTERISTICS
- SEVERAL BODIES, SPRING COUPLED
- MULTI-PROPULSION SYSTEMS
- HIGH MODAL DENSITY-3 DIMENSIONAL - UNCERTAIN PREDICTION
- COMPLEX DYNAMICS ANALYSIS AND TEST

AERODYNAMICS
- GENERALLY VERY STABLE
- GUSTS CAUSE LARGE DYNAMIC RESPONSES
- YAW - ROLL COUPLING

CONTROL PROBLEMS
- TRAJECTORY, STRUCTURAL, CONTROL COUPLING REQUIRES COMPLEX CONTROL FORCE SOURCES
- ADAPTIVE MODE SUPPRESSION
- BLENDING MULTIPLE SENSORS, CONTROL FORCES, DYNAMIC COMPONENTS
- YAW - ROLL COUPLING

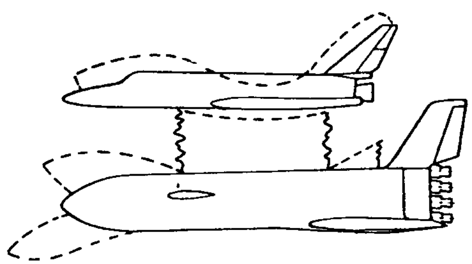

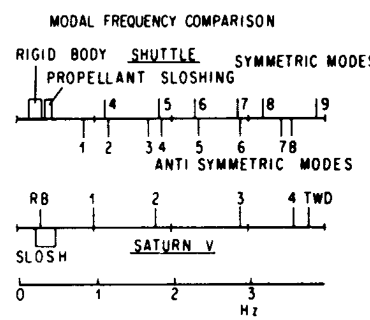

REENTRY

The Space Shuttle during reentry has unique dynamic, control, and structures problems. The vehicle must enter at a high angle of attack in order to obtain the drag necessary to kill off the large velocity from orbit. During this time, high temperatures are present, necessitating some angle of attack modulation to maintain temperature control. Due to the high angle of attack, center vertical rudders are not effective; however, wing tip fins can be used for directional control. The tradeoff here becomes RCS versus fin location. Around Mach 2 the vehicle must make a transition from high to low angle of attack. The chart shows the corridors it must stay within to maintain stability and make a safe transition. Obviously, elevon size and hinge moments are a very critical design parameter for this phase of flight. Due to the overall stability problems, some form of stability augmentation will probably be needed to supplement the handling qualities of the vehicle. Also, the present mil spec handling qualities criteria are not applicable which necessitates new criteria. Preliminary cuts have been made in this area but further work is probably still needed.

RE-ENTRY

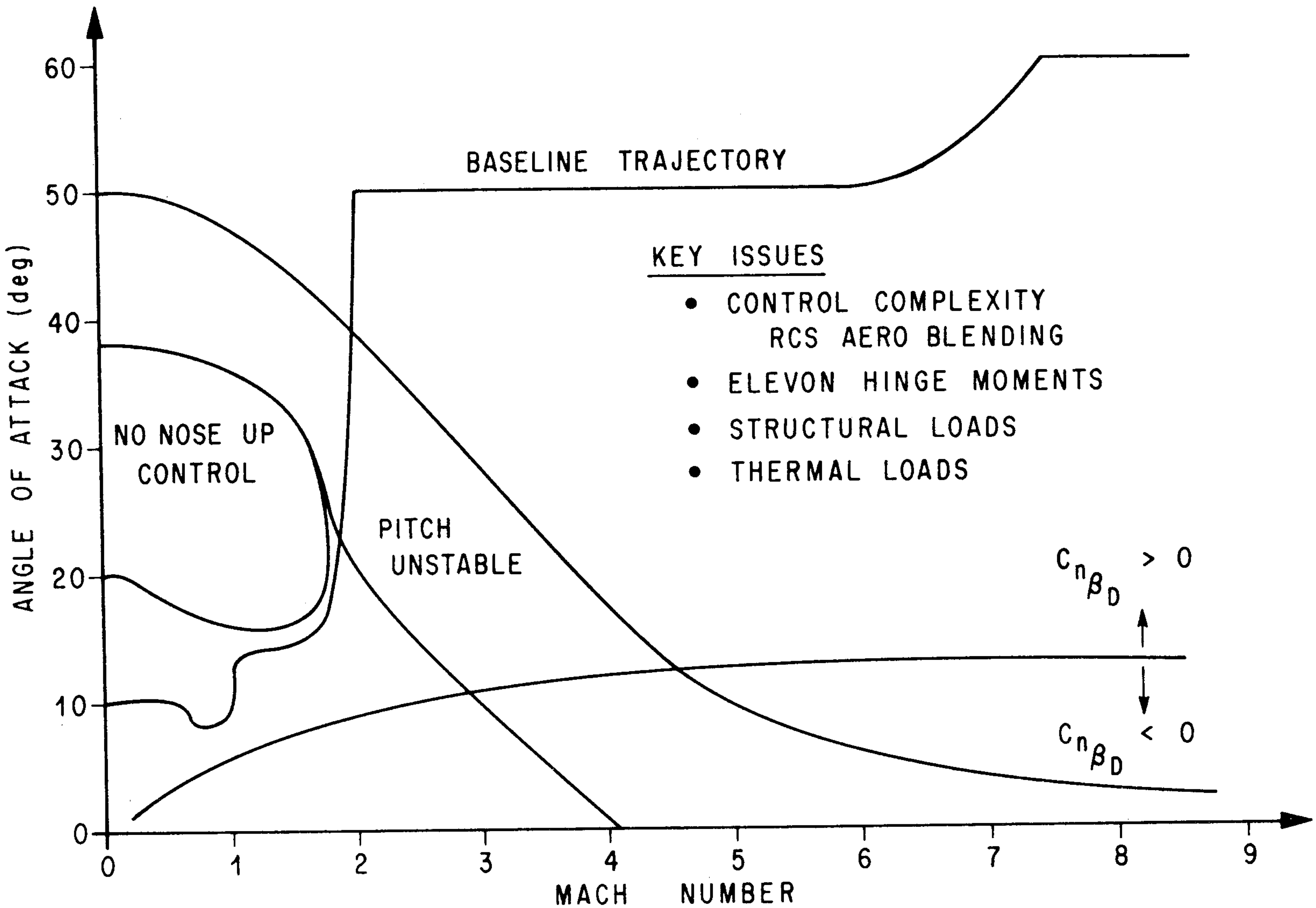
BASELINE TRAJECTORY
KEY ISSUES
• CONTROL COMPLEXITY
RCS AERO BLENDING
• ELEVON HINGE MOMENTS
• STRUCTURAL LOADS
• THERMAL LOADS
NO NOSE UP CONTROL
PITCH UNSTABLE
$C_{n_{\beta_D}} > 0$
$C_{n_{\beta_D}} < 0$
ANGLE OF ATTACK (deg)
MACH NUMBER
0
10
20
30
40
50
60
1
2
3
4
5
6
7
8
9

MAJOR TASK AREAS REQUIRING TECHNOLOGY

All of the future space vehicles require certain common areas of technology. However, the details or characteristics may be grossly different. For example, the prediction of the dynamic characteristics is common to all vehicles, but a highly flexible spinning spacecraft has quite different modeling problems than a SV Apollo launch vehicle. The overall goal for space vehicle design and, in particular, the considerations of this discipline, is to develop a vehicle that is optimum in design and performance. In general, this optimality is minimum structural weight and minimum dynamic response. The common requirements of technology are: (1) models, (2) performance criteria, (3) analysis techniques, and (4) environment. The following charts show some of these criteria.

MAJOR TASK AREAS REQUIRING TECHNOLOGY

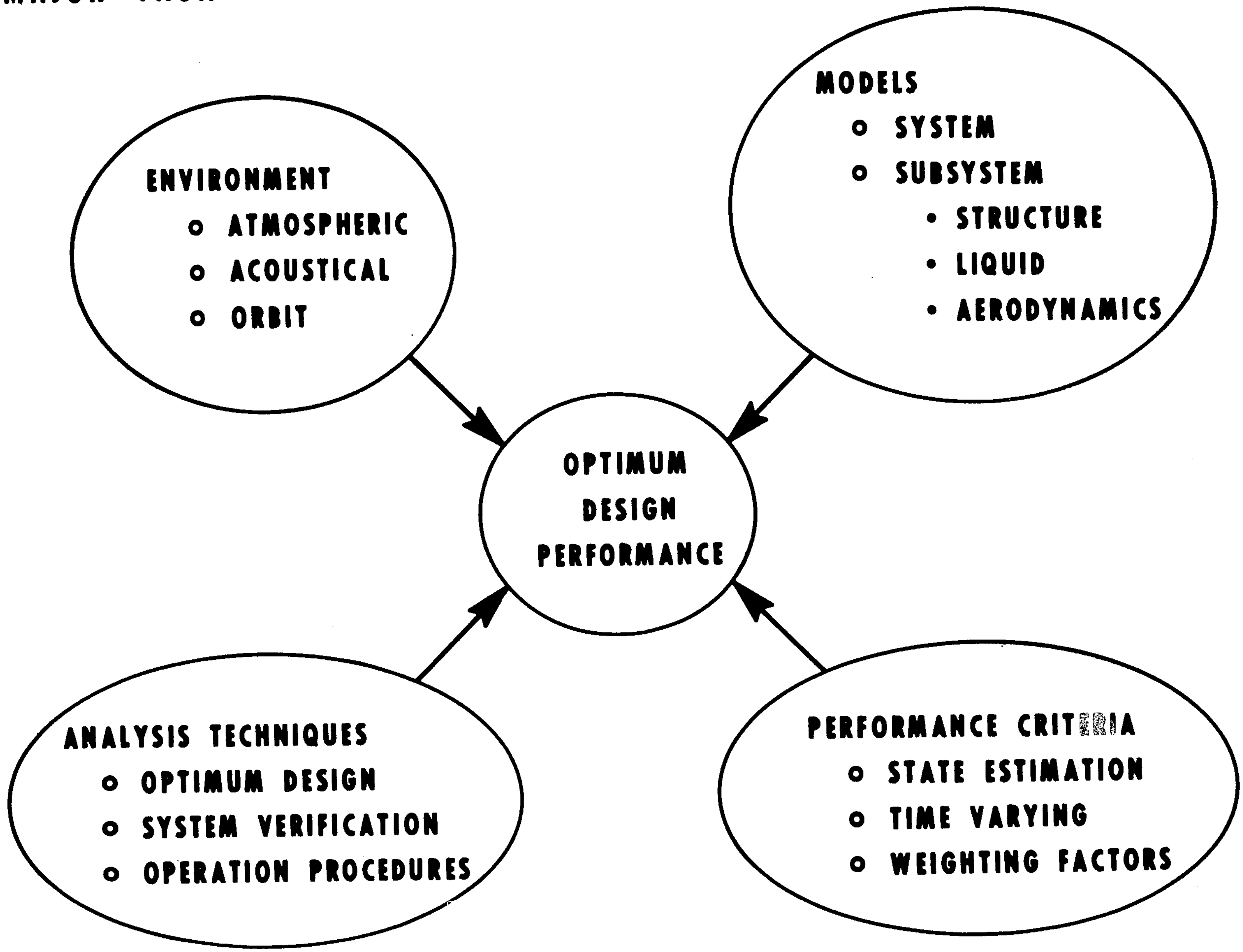

VEHICLE OPTIMUM DESIGN APPROACH

The basic need from structures, dynamics, and control aspects is an integrated optimization program that considers all aspects of the mission and vehicle characteristics. This is illustrated in flow diagram form for the Space Shuttle vehicle. Obviously it might not be possible to consider all mission phases simultaneously; however, the constraints or a band on certain characteristics, for example, for the orbiter flight alone, can be input and the ascent phase optimized within these constraints. Through a proper definition of structural characteristics, trajectory and performance, aerodynamics, etc., an iteration procedure or optimal procedure can be generated that looks at these trades and comes up with a best design. The same approach would apply to other space vehicles. The development of this type of program is greatly needed, since at the present time all these various elements are treated separately with the trades made in a more or less hit or miss fashion. A procedure of this type should save time and money and result in a higher performance vehicle.

The need for this approach was emphasized during the Shuttle Phase B activities, when it became obvious that the reentry aerodynamic design was penalizing both ascent and cruise flight regimes. Many brute force methods were used that compromised each flight regime but resulted in a compatible system.

VEHICLE OPTIMUM DESIGN APPROACH

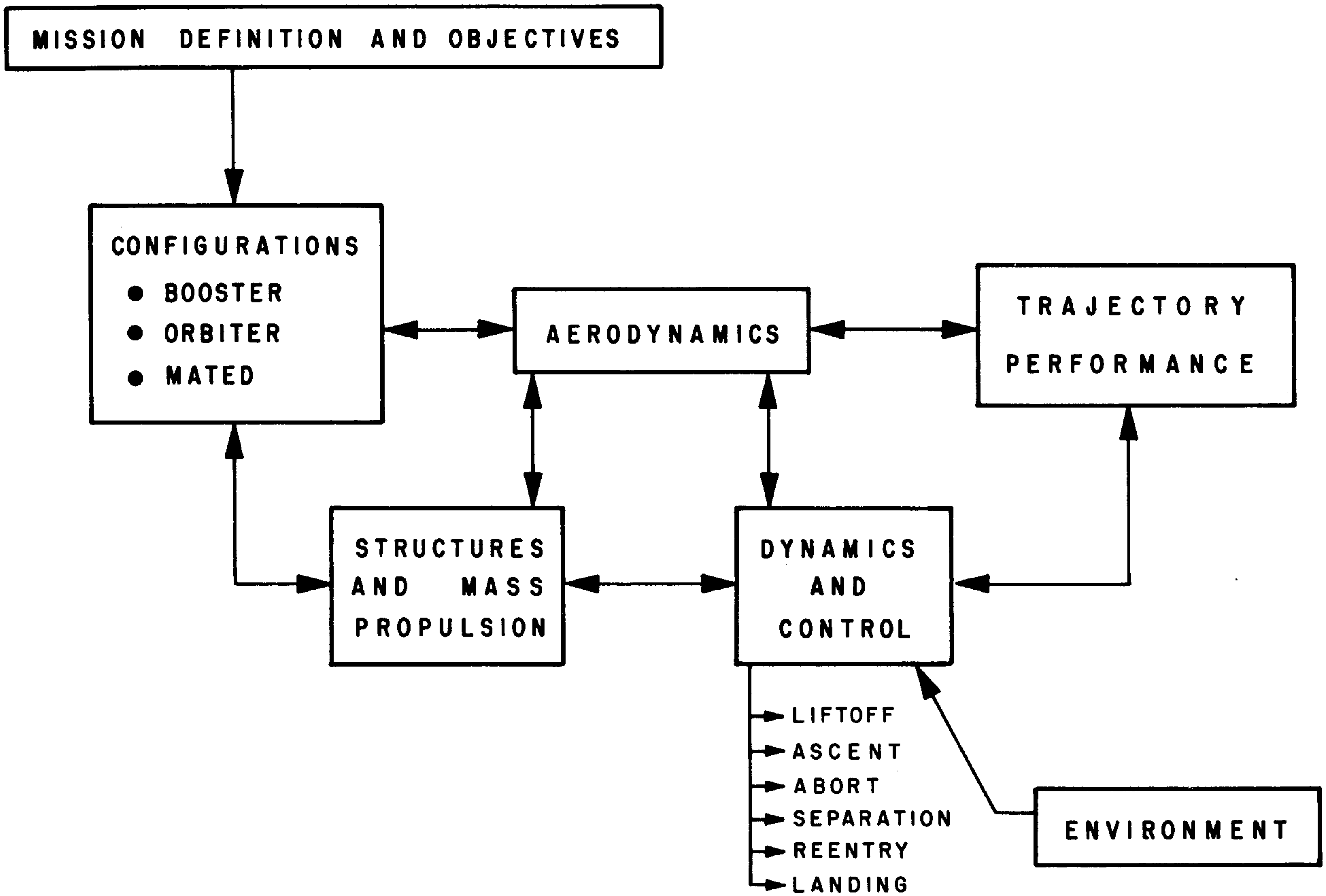

LOAD RELIEF AND MODAL SUPPRESSION

Much effort has been and is being expended by industry, NASA, and the military on load relief and modal suppression analysis. At the present, these approaches only result in a fairly good benchmark for brute force design responses comparison. The objectives of this development have been stated previously and include reduced loads, increased fatigue lifetime, improved pointing accuracy, etc. State of the art characteristics of optimal approaches are listed on the chart. The major shortcomings are high computer time and simplicity of the model. The need for an optimal design approach is great. The chart lists several areas where improved technology is needed. The list includes both sensors (hardware) and analysis approaches. Adaptive gain schemes are a real need since vehicle dynamic characteristics are becoming very complex and more difficult to predict. Adaptive approaches would allow for less accurate modal data and insure a more reliable design. Wind biasing procedures, based on either very near launch time winds or in-flight wind sensing, wind predictions and a wind biasing scheme, could greatly reduce structural loads and control system requirements. Present schemes deal only with the total system. There is a dire need for procedures that optimize a subsystem in terms of system optimal performance. Present schemes, in general, sense a mixed state of the system. Techniques for separating the signals from the various modes (states) would simplify control system logic and design. Present control approaches couple the system, for example; a yaw rudder command induces roll that must be compensated for with ailerons. Techniques for designing control systems with minimum coupling are needed. Choice of sensors and sensor location continually plagues control and structure engineers. Criteria and procedures are needed for achieving a reasonable and adequate number of sensors, appropriately located in terms of structural and environmental constraints.

Computer costs associated with optimum procedures are so high that indepth analysis usually can not be performed. More efficient procedures would add greatly to optimum design, especially in light of structural and performance constraints.

One other important problem is lack of procedure for including vehicle parameter variation in the optimum approaches. Present approaches only include ideal vehicle characteristics. It is a well known fact that parameter variations, in most cases, dictate the design. This shortcoming of present approaches greatly limits the usefulness and insight available.

LOAD RELIEF AND MODAL SUPPRESSION

STATE OF ART:

- COMPUTATIONAL COSTS HIGH
- PROGRAMMED GAINS
- SENSOR CHOICE: ACCELEROMETERS, RATE GYROS, POSITION GYROS
- MONTHLY MEAN WIND TRAJECTORY BIASING (ALL PLANES)
- MIXED STATE ESTIMATION
- YIELDS LINEAR CONTROL LAW
- MULTI-LOOP DESIGN
- CONTROL LAW REQUIRES FULL STATE FEEDBACK

TECHNOLOGY NEEDED:

- ADAPTIVE GAIN SCHEMES
- PREFLIGHT WIND BIASING SCHEMES
- INFLIGHT WIND SENSING AND WIND BIASING
- TECHNIQUES FOR DESIGNING PRACTICAL OPTIMAL SUBSYSTEM CONTROLLER USING OPTIMAL PERFORMANCE CRITERIA AS GOAL
- SEPARATE (MODES) STATE ESTIMATION
- TECHNIQUE FOR MINIMUM INTERFERENCE (COUPLING) THROUGH CONTROL SYSTEM
- SENSOR CHOICE AND LOCATION CRITERIA
- MORE EFFICIENT ITERATION PROCEDURES
- SIMPLIFICATION OF OPTIMUM CONTROLLER TO PRACTICAL SENSOR COMPLEMENT
- INCLUSION OF PARAMETER VARIATIONS IN DESIGN

DYNAMIC ANALYSIS FOR SHUTTLE DESIGN VERIFICATION

By Robert W. Fralich, NASA Langley Research Center, Hampton, Virginia

and

Claude E. Green and Mario H. Rheinfurth, NASA Marshall Space Flight Center

INTRODUCTION

A review is made of dynamic analysis techniques that are currently being studied for design verification of space shuttle structures. The current parallel-burn shuttle configuration is a relatively complex structure that gives rise to large asymmetric masses. These asymmetries make it necessary to reassess many of the dynamic problems that have been associated with earlier stacked axisymmetric launch vehicles. Examples of these problems are classical flutter, pogo vibration, control interaction, and dynamic responses to gusts, lift-off, and staging. Before these problems can be attacked, a thorough understanding of the modal characteristics of the structure must be in hand.

This paper discusses two approaches that are used for determining the modes and frequencies of space shuttle structures.

9

METHODS OF ANALYSIS FOR OBTAINING MODES AND FREQUENCIES

(Figure 1)

The type of structure that is to be analyzed is shown in figure 1. This structure, consisting of an orbiter, a tank, and two boosters, is typical and embodies the dynamics problems of any of the multi-bodied shuttle configurations being considered. Two types of approaches are used for determining the modes and frequencies of structures of this type. The first approach, direct numerical analysis, usually involves a finite-element mathematical modeling of the structure in order to make use of computer programs that have been developed for dynamic analysis. Typical programs available for such large-scale analyses are (1) the NASA Structural Analysis Program (NASTRAN), (2) the Structural Network Analysis Program (SNAP), and (3) many company-owned computer programs.

The need for the second approach, which uses modal-coupling techniques, is brought about by consideration of a proposed method that may be used for experimental verification. There is some reluctance to performing full-scale vibration tests on the complete vehicle because of anticipated difficulties in testing a structure of this size and complexity. In the proposed method experimental verification would be made only by vibrating its components. In order to make such a procedure feasible, methods must be available for obtaining the modes and frequencies of the complete vehicle from the results obtained in the component tests. These methods are known as modal-synthesis or modal-coupling techniques.

The first part of the paper discusses a direct analysis approach and gives its application to an early space shuttle configuration. The last part of the paper discusses some of the techniques and potential problem areas of using modal-coupling analyses.

METHODS OF ANALYSIS FOR OBTAINING MODES AND FREQUENCIES

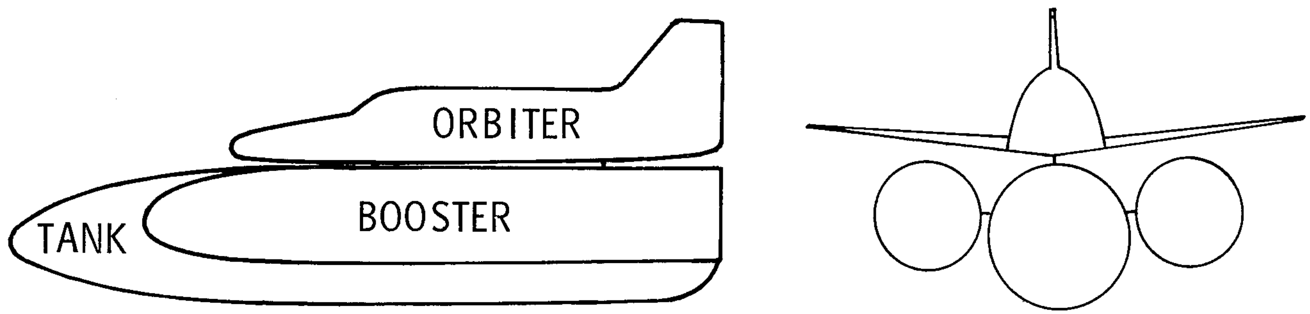

- DIRECT NUMERICAL ANALYSIS
- MODAL COUPLING TECHNIQUES

Figure 1

STRUCTURAL NETWORK ANALYSIS PROGRAM (SNAP) — BASIC VERSIONS

(Figure 2)

The series of SNAP programs developed in recent years represent one of the most important analytical techniques in structural engineering and are suitable for accurately determining the structural characteristics of complex structures. These programs have been used extensively in a wide variety of built-up structures including about a dozen proposed space shuttle configurations.

The basic version of the SNAP series is the static analysis program, a finite-element program based on the displacement method. Stresses and strains in the structure caused by applied forces are computed by inverting the stiffness matrix for the complete structure via a direct reduction sequence. This method, unlike band-matrix, active-column or partitioning solution methods, avoids virtually all unnecessary arithmetic operations by recognizing in essentially complete detail the sparsity characteristics of system stiffness matrices.

Loadings of the structure include point forces and moments at joints, nonzero specified joint motions, and thermal loading. Numerical accuracy checks are automatically executed. There are three checks: (1) A comparison between strain energy and external work, (2) a comparison between total applied force and reaction, and (3) an equilibrium check at all joints. An option is included for automatically executing an iterative accuracy-improvement procedure.

The dynamic analysis program uses the same class of large finite-element networks as the basic static analysis program. Undamped vibrational modes and frequencies of free or constrained systems are computed by using an iterative technique which is essentially a generalization of the well-known Stodola method. As a preliminary step, the program executes a Rayleigh-Ritz analysis to obtain initial approximations for the natural frequencies and mode shapes of the structure. The generalized functions used in this preliminary analysis are static displacement functions of the total structure obtained from a sequence of static loading conditions as specified by the user. Beginning with the initial approximation of a system mode, an equivalent inertial loading acting on the total system is computed. The corresponding static deflection provides an improved approximation for the second iteration step. Higher modes are obtained by sweeping out lower modes through the use of the orthogonality relationship for normal modes. Routines from the basic static analysis program are used to compute the deflection of the system due to the inertial loading, with full advantage taken of the sparsity characteristics of the system stiffness matrix. Advantage is also taken of the sparsity of the system mass matrix in computing equivalent inertial loadings and in the sweeping process.

In the substructure analysis program, the system is mathematically modeled as a set of substructures, with the deformations of each substructure represented by generalized functions. Two associated computer programs were developed: (1) the substructure function-generator program, which is a modification of the SNAP dynamic analysis program, and (2) the substructure synthesis program, which forms mass, stiffness, and damping matrices.

The function-generator program has three optional procedures for calculating terms of the substructure mass matrix. The generalized-function repertoire created by this program includes rigid-body functions, boundary-mode motion functions, and uniform acceleration modes. The substructure synthesis program contains provisions for determining the undamped modes and frequencies of the assembled system by the Cholesky/Householder technique, for constructing a system damping matrix based on the energy dissipation characteristics of individual substructures, and for performing a damped transient-response analysis of the system.

STRUCTURAL NETWORK ANALYSIS PROGRAM (SNAP)
GENERAL PROGRAM INFORMATION

1. INPUT
2. OPERATION
3. OUTPUT

Figure 2

STRUCTURAL NETWORK ANALYSIS PROGRAM (SNAP) – GENERAL PROGRAM INFORMATION

(Figure 3)

Input.- The data input procedure is designed to minimize the amount of manual effort required to prepare data decks for large-scale applications. Extensive use is made of libraries of beam and shell section properties, material constants, and so forth in generating problem definitions. This method usually reduces greatly the amount of manual effort (and probability of error) in preparing data decks for large structures. For example, the section properties of a beam are defined by referring to the applicable set of data in one of the libraries. Accordingly, the detailed definition of each unique section appears in the input data only once, regardless of how many elements have that particular section.

Multidimensional "network generators" of input data for element definitions, position coordinates, constraints, applied loading, and so forth are provided.

Input data for element definitions, joint position coordinates, and beam and shell section properties are read in "block" formats; thus, local reference frames and local joint numbering arrangements can be used in various parts of the structure. Then, through the block input formats and the associated block input control cards, the program translates from local to global reference frames in synthesizing the definition of the complete structure.

Operation.- The computer execution costs achieved by the basic static solution routines are very close to the minimum that can be attained for direct solution techniques. SNAP's size capacity, that is, the allowable number of degrees of freedom, is extremely large. Structures having over 15 000 elements and 12 000 degrees of freedom have been solved, and much larger systems can be handled. Maximum capacity is now approximately 30 000 degrees of freedom on UNIVAC 1108.

Output.- Detailed checks of numerical accuracy of the output data are automatically executed. In performing these checks, the program returns to the basic problem definition; that is, the checks reflect not only the errors accumulated in the reduction and displacement evaluation techniques, but also the effects of roundoff in assembling the system stiffness matrix.

An option is included for using double-precision arithmetic.

The complete results of each analysis may be stored on magnetic tape and the execution resumed at a later time. These tapes provide a convenient means of permanently storing the massive amount of solution data accumulated in analyses of large systems. A highly flexible SC-4020 plot package is included.

STRUCTURAL NETWORK ANALYSIS PROGRAM (SNAP)
BASIC VERSIONS

1. SNAP/STATIC ANALYSIS
2. SNAP/DYNAMIC ANALYSIS
3. SNAP/SUBSTRUCTURE ANALYSIS

Figure 3

EARLY TWO-STAGE LAUNCH CONFIGURATION

(Figure 4)

As an example of a typical vibration analysis using the SNAP dynamics program, a low-cross range space shuttle configuration was analyzed. This configuration consists of a straight-wing orbiter and a delta-wing booster. The vehicle was mathematically modeled as an assemblage of beam elements and three- and four-node plate/shell membrane elements. Since the vehicle is symmetric with respect to the pitch plane, only one-half of the vehicle was modeled. Symmetric and antisymmetric constraint conditions were imposed on all joints in the symmetry plane. The size characteristics of the finite-element model were as follows:

Degrees of freedom	4206
Number of joints	701
Number of beam elements	40
Number of three-node elements	1392
Number of four-node elements	301
Total number of elements	1733

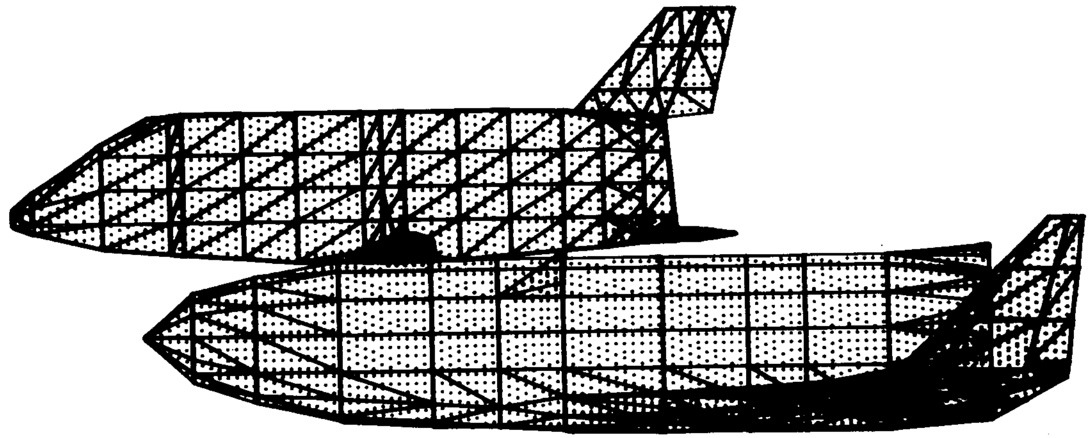

EARLY TWO–STAGE LAUNCH CONFIGURATION

SYMMETRIC HALF-MODEL HAS APPROXIMATELY:

700 STRUCTURAL JOINTS

1700 STRUCTURAL ELEMENTS

4200 DEGREES-OF-FREEDOM

ABOUT 1/3 OF STRUCTURAL ELEMENTS ARE SHOWN

Figure 4

SUMMARY OF FREE-FLIGHT MODES AND FREQUENCIES – LIFT-OFF CONDITION

(Figure 5)

The free-flight modes and frequencies were computed for lift-off conditions. In order to improve the visualization of the characteristic features of these modes, the computer plots were converted into an animated film supplement, which is available on loan.* It should be pointed out that the absolute amplitudes of the mode shapes – being arbitrary – were selected to provide a good visualization and are not representative of the actual amplitudes to be expected during powered flight through the atmosphere. However, the relative motion between the various structural elements of the vehicle is typical and can serve as a guide in assessing the severity of the motion at stations of particular interest from a dynamics and control viewpoint. Also, for reasons of visibility, the motion of all mode shapes is shown at the same frequency, about $\frac{1}{2}$ Hz.

The motion picture shows the first four symmetric modes in a side view of the configuration and the first five antisymmetric modes in a front view as well as in an isometric view. Frequencies and a descriptive code characterizing each mode are shown in the table. For instance, the second symmetric mode exhibits predominantly a first bending mode of the orbiter and booster as well as sizable excursions of the booster fin and orbiter main wing at a frequency of 4.0038 Hz. Other modes can be described similarly.

---

*This film supplement (16 mm, $3\frac{1}{2}$ min, B & W, silent) may be obtained on loan by requesting film serial number L-1116 from NASA Langley Research Center, Att.: Photographic Branch, Mail Stop 171, Hampton, Virginia 23365.

SUMMARY OF FREE-FLIGHT MODES AND FREQUENCIES
(LIFT-OFF CONDITION)

MODE	DESCRIPTION		FREQUENCY (Hz)
	BOOSTER	ORBITER	
S-1	W	–	2.7832
S-2	FB1,F	FB1,W	4.0038
S-3	–	W	4.5071
S-4	F	–	5.0378
A-1	W	–	2.4232
A-2	W,F	YAW	3.2514
A-3	–	W	4.2887
A-4	FB1,W,F	W	4.7338
A-5	F	–	5.2242

S = SYMMETRIC
A = ANTISYMMETRIC
F = FIN
W = WING
FB1 = FIRST FUSELAGE BENDING

Figure 5

INGREDIENTS OF MODAL COUPLING

(Figure 6)

The process of applying modal-coupling techniques to the space shuttle is illustrated in figure 6. The coupling analysis takes the experimentally obtained modes and frequencies of the component parts and the appropriate rigid-body modes and combines them to find the modes and frequencies of the complete vehicle.

At the bottom of the figure are listed some of the important ingredients of modal coupling. First, a selection of component parts or substructures must be made. A possible method of substructuring would use the orbiter, tanks, and boosters as separate substructures. Another method illustrated in the sketch would use the orbiter as one substructure and the tank-booster combination as another substructure.

Next, the interfaces that join together the component parts of the complete vehicle must be modeled. As will be shown later in the paper, an accurate modeling of the interfaces is vital to obtaining accurate modes for the complete vehicle.

A choice of component-support conditions must be made before the components can be tested. One possibility is to fix the components at the interfaces as shown in the figure. Another possibility is to softly support the components with cables to represent free-free boundary conditions. The choice of component-support conditions is guided by a combination of considerations. These relate to the ease of attaining the support conditions experimentally and to the accuracy that can be obtained by the coupling of the component modes. The question of which boundary conditions are most practical is still under investigation.

Finally, the number of component modes needed for accurate determination of the modal characteristics of the total vehicle must be determined.

INGREDIENTS OF MODAL COUPLING

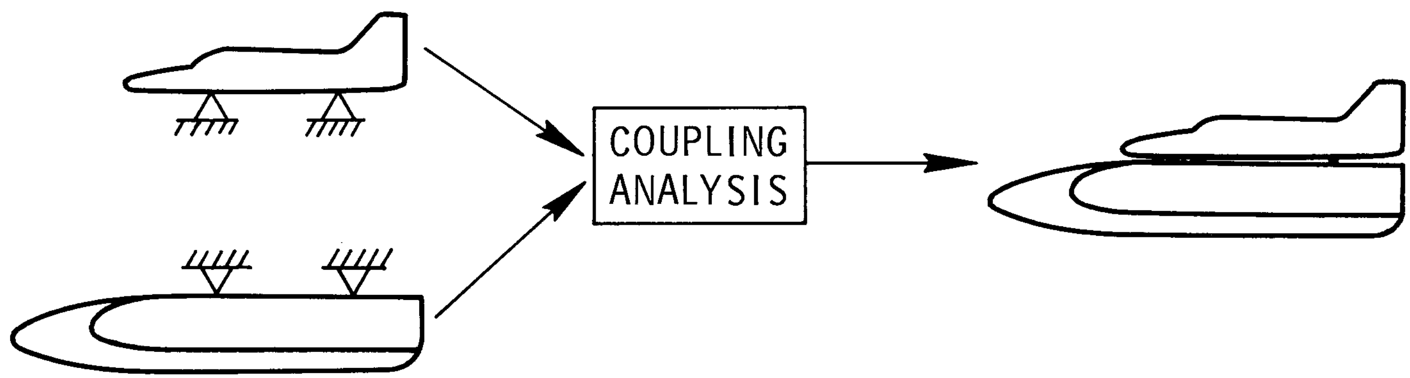

- SELECTION OF SUBSTRUCTURES
- MODELING OF INTERFACES
- CHOICE OF COMPONENT SUPPORT CONDITIONS
- NUMBER AND TYPE OF MODES NEEDED

Figure 6

MODEL FOR CONVERGENCE STUDY OF CLOSED-LOOP STRUCTURE

(Figure 7)

Note in figure 6 that the two substructures and the two interfaces form a closed loop. Closed-loop structures such as this present potential problem areas for convergence of modal-coupling procedures.

In order to make an assessment of convergence of modal-coupling methods for closed-loop structures, a study is made of the simple model shown in figure 7. This study considers the in-plane vibrations of an unsupported rectangular frame. The modal-coupling methods use calculated modes and frequencies for each of the four uniform-cross-section beams. Both free-free and cantilever component modes are used. Static deflection shapes are used as a supplement to the component modes as a means of improving convergence.

MODEL FOR CONVERGENCE STUDY OF CLOSED-LOOP STRUCTURE

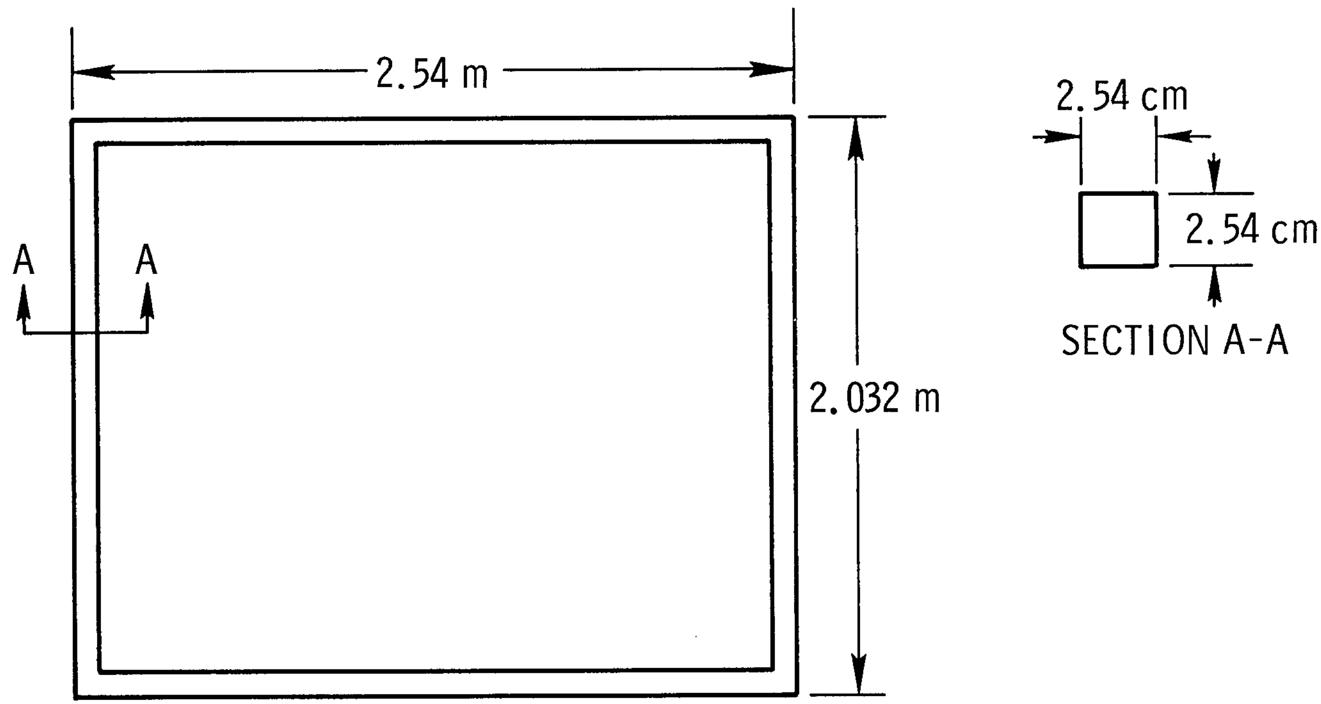

IN-PLANE VIBRATIONS OF RECTANGULAR FRAME

- FREE-FREE COMPONENT MODES
- CANTILEVER COMPONENT MODES
- STATIC DEFLECTION SHAPES

Figure 7

CONVERGENCE OF MODAL-COUPLING METHODS FOR RECTANGULAR FRAME

(Figure 8)

Figure 8 shows convergence of modal-coupling methods for the rectangular frame by a plot of frequency against the number of component beam modes used from each member. The solid lines give the results for cantilever component modes. As the number of component modes is increased, the calculated frequencies approach the exact values shown on the right side of the broken lines. Results are shown for the first four frequencies, whose mode shapes are sketched at the right-hand side. Convergence is not attained for all four frequencies unless an unwieldly number of modes is chosen. For example, with four cantilever modes chosen from each substructure, errors of over 10 percent are obtained for the first and third frequencies.

In order to obtain a better representation of the stress conditions near the corners of the rectangular frame, the selected modes from each component are supplemented with two static deflection shapes with quadratic and cubic variations. With this modification, the choice of only two cantilever modes from each component yields errors of less than 1 percent for all four calculated modes, as shown by the X symbols on the figure.

Similar results are obtained by use of free-free component modes but convergence is even slower than for cantilever modes. However, the addition of static-deflection shapes again yields errors of less than 1 percent when only two flexible free-free modes are chosen from each component.

CONVERGENCE OF MODAL COUPLING METHODS FOR RECTANGULAR FRAME

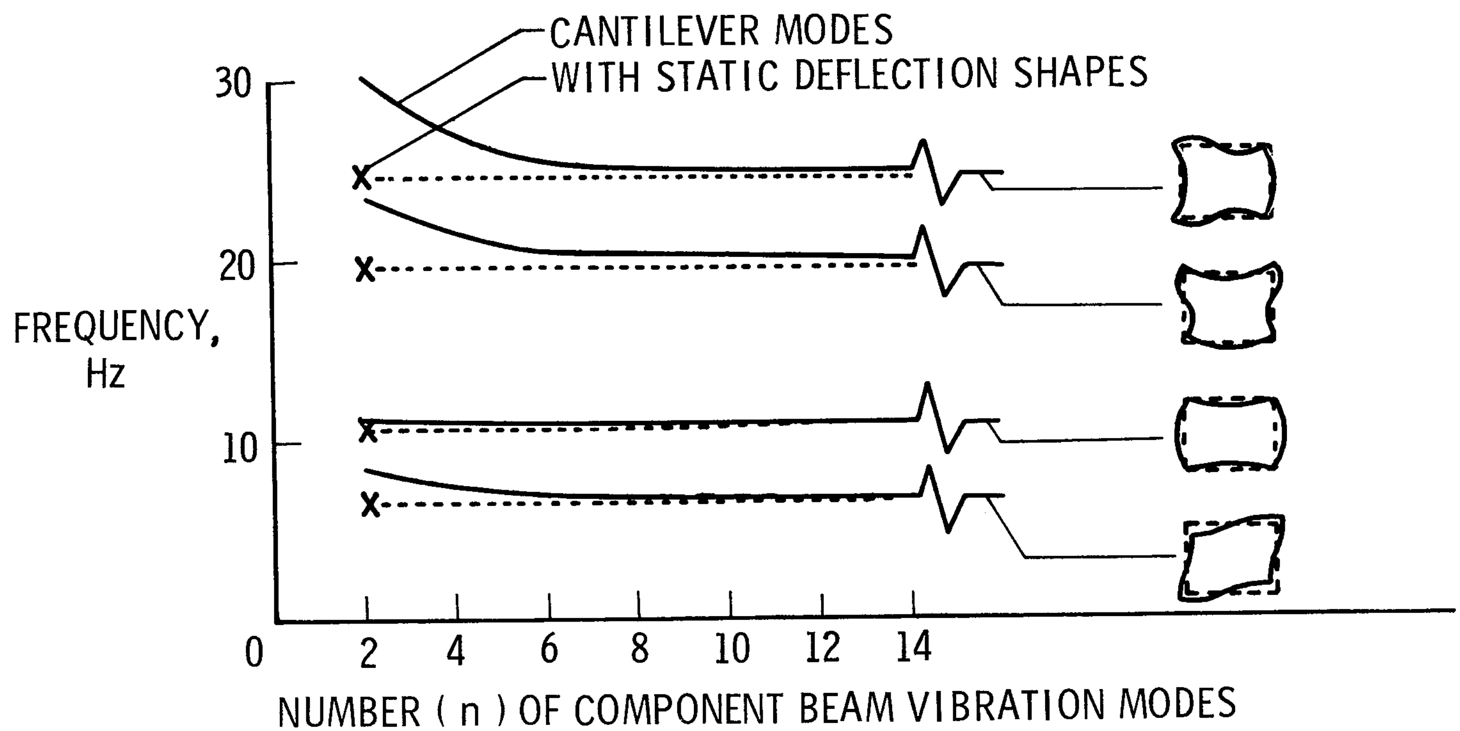

Figure 8

DYNAMIC MODEL

(Figure 9)

In order to evaluate analytical procedures for modal coupling, companion experimental and analytical studies are being conducted on the dynamic model of an early shuttle concept shown in figure 9. Pitch-plane vibration is determined for this parallel-beam type of structure that dynamically represents the mass and stiffness properties of an early version of the space shuttle. The tubular-type beams are joined together by two interconnecting spring assemblies. The model considered for the studies presented in this paper did not include the wing structures that are shown in the photograph. A more detailed description of the dynamic model is given in reference 1.

DYNAMIC MODEL

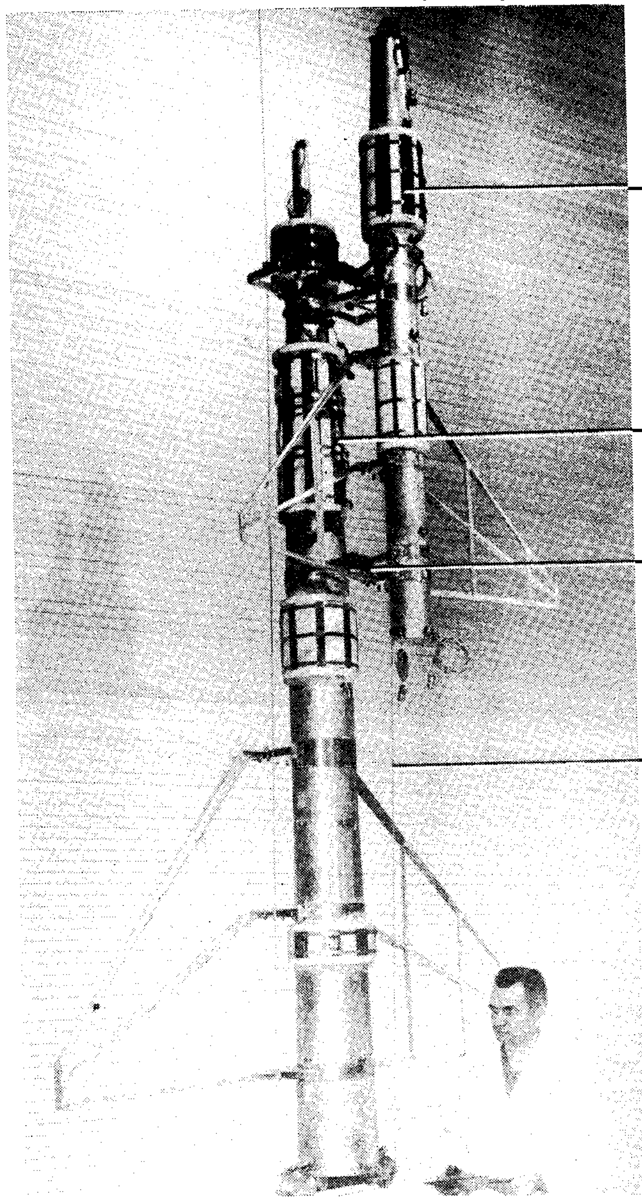

Figure 9

ANALYTICAL MODELS FOR STUDY OF DYNAMIC MODEL

(Figure 10)

For the analytical part of the study the three analytical models shown in figure 10 were investigated. The models differ in the way the interfaces are attached to the booster and orbiter. These three models have the interface connections pinned, fixed, and flexible.

The first model with the pinned interface connections was considered by a contractor in order to evaluate a specific modal-coupling procedure. The spring interface assemblies are assumed to be simple massless deflectional springs. Three experimental free-free modes were used for the booster and two for the orbiter. Modes obtained from this modal-coupling procedure are pure beam-bending modes.

The model with the fixed interface connections was analyzed by a direct approach with the use of NASTRAN (ref. 2). Here the interface spring assemblies were analyzed to obtain influence coefficients for the restraints given against rotation and axial and lateral deflections. In determining these influence coefficients the assumption was made that the interfaces are attached to rigid bodies rather than to the flexible tubular bodies of the experimental vehicle. The influence coefficients were also verified experimentally under clamped conditions obtained in the laboratory. The fixed-interface model allows a coupling between beam-bending and axial motions.

The third model with the flexible interface connections was analyzed when it was found that neither the pinned-interface model nor the fixed-interface model could accurately yield the vibration mode with a predominance of axial motion. Indications are that the rotational restraints supplied by the interfaces are too large when rigid connection points are used. Attachment of the interfaces to the orbiter and booster may not be in a fully clamped condition. Local deformations of the orbiter and booster at the attachment points could reduce rotational restraint. In order to allow for this unknown interface-joint flexibility, the interfaces are attached to the orbiter and booster by means of rotational springs with the as yet undetermined stiffness c. A parametric study will be made in order to find effects of local rotation at the attachment points. The interfaces themselves are modeled by the same influence coefficients developed for the model with the rigid connections. A modal coupling is made that uses the improved convergence method with three calculated free-free booster modes and two calculated free-free orbiter modes.

ANALYTICAL MODELS FOR STUDY OF DYNAMIC MODEL

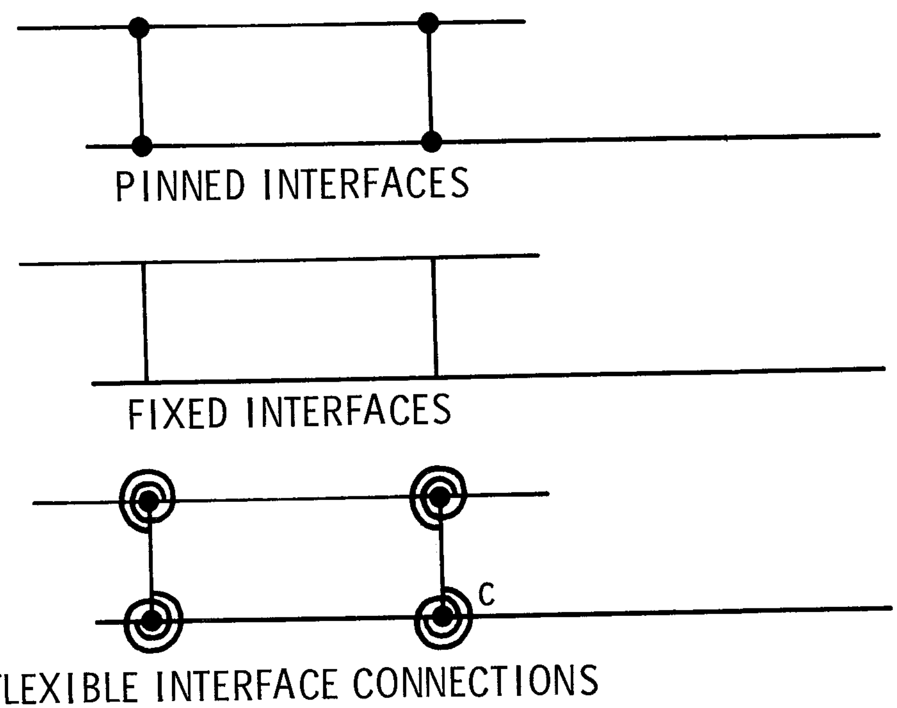

Figure 10

EXPERIMENTAL AND CALCULATED FREQUENCIES

(Figure 11)

The results for the three analytical models are compared with the experimental results in figure 11. Here the frequencies are listed for the first six experimental modes. For each mode values are given first for the experimental frequency and then for the calculated frequencies with the pinned, fixed, and flexible interface connections. In general, the agreement between the calculated and experimental frequencies is good, except for the fourth mode. It should be noted that the calculated values were obtained from three different investigations, which used different mathematical idealizations for the booster and orbiter structures. Therefore, these calculated values cannot be expected to give the proper trends on changing from one support condition to another.

The fourth experimental mode was observed to be a mode with a large amount of axial motion. Since the model with the pinned interface connections did not allow for axial motions, the fourth frequency is missing from this column. The model with the rigid interface connections did permit a coupling of beam-bending and axial motion; however, the frequency of the fourth mode at 75.2 Hz is more than $1\frac{1}{2}$ times too high. Although this mode is basically an axial mode, its bending content was of the wrong form. The results for the model with the flexible joint connections were obtained by adjusting the value of the spring stiffness c to make the fourth frequency agree with the experimental value. The corresponding mode shape is compared with the experimental one in the lower part of the figure, and the agreement was found to be good.

EXPERIMENTAL AND CALCULATED FREQUENCIES

MODE	FREQUENCIES, Hz			
	EXPERIMENTAL	INTERFACE		
		PINNED	FIXED	FLEXIBLE
1	11.1	10.4	11.2	11.0
2	26.5	29.4	24.9	26.6
3	38.1	40.0	37.4	37.8
4	48.3	----	75.2	48.3
5	98.3	103.5	104.9	100.0
6	101.9	101.5	118.7	113.2

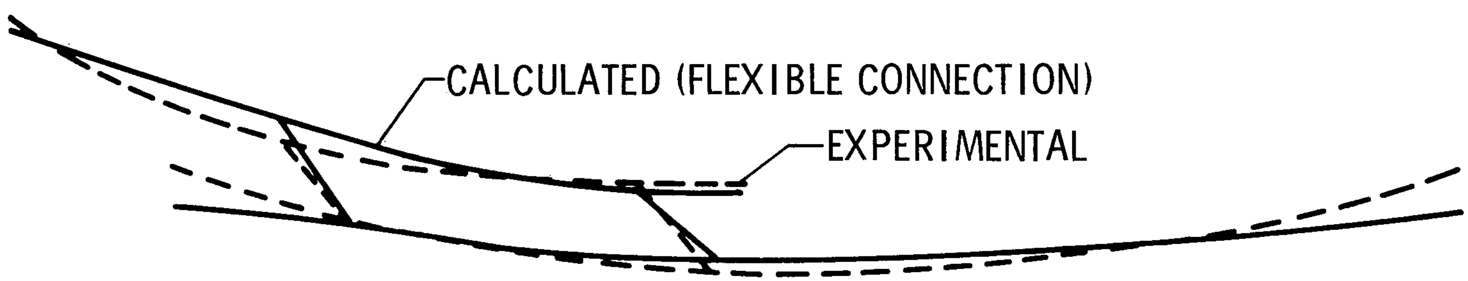

FOURTH MODE SHAPE

Figure 11

EFFECT OF INTERFACE FLEXIBILITY

(Figure 12)

The effect of varying the joint flexibility is shown in figure 12. The curves show the variation of the first six frequencies with the spring stiffness c. The frequencies calculated for $c = 0$ give the case where the interface joints are considered pinned. At the other end of the figure, the frequencies calculated for $c = \infty$ are results obtained for the rigid interface joints. These end values are slightly different from those presented in figure 11 because of the previously mentioned differences in the three analyses.

The nearly horizontal portions of the curves denote modes with predominantly bending content. The portions of the curves that rise as c is increased represent modes with significant amounts of axial motion. It can be seen that a small change in joint flexibility c can make a large change in the frequency of the mode with the predominance of axial motion.

The experimental values are given by the circles at the value of c that makes the calculated frequency of the fourth mode agree with experiment. The agreement between theory and experiment is good except for the sixth mode. The main factor contributing to this discrepancy is the neglecting of the masses of the interfaces in the calculation.

It can be seen from these results that accurate modeling of the interfaces is one of the most important parts of the analysis of multibody vehicles. This is true both for direct analysis of the whole vehicle or for modal-coupling techniques. Accurate modeling of the interfaces must include effects of local deformation of the orbiter and booster bodies at the attachment points. The mode that is most sensitive to modeling of the interfaces is the one that is predominantly axial motion. An accurate determination of this mode is necessary to predict pogo-type instability.

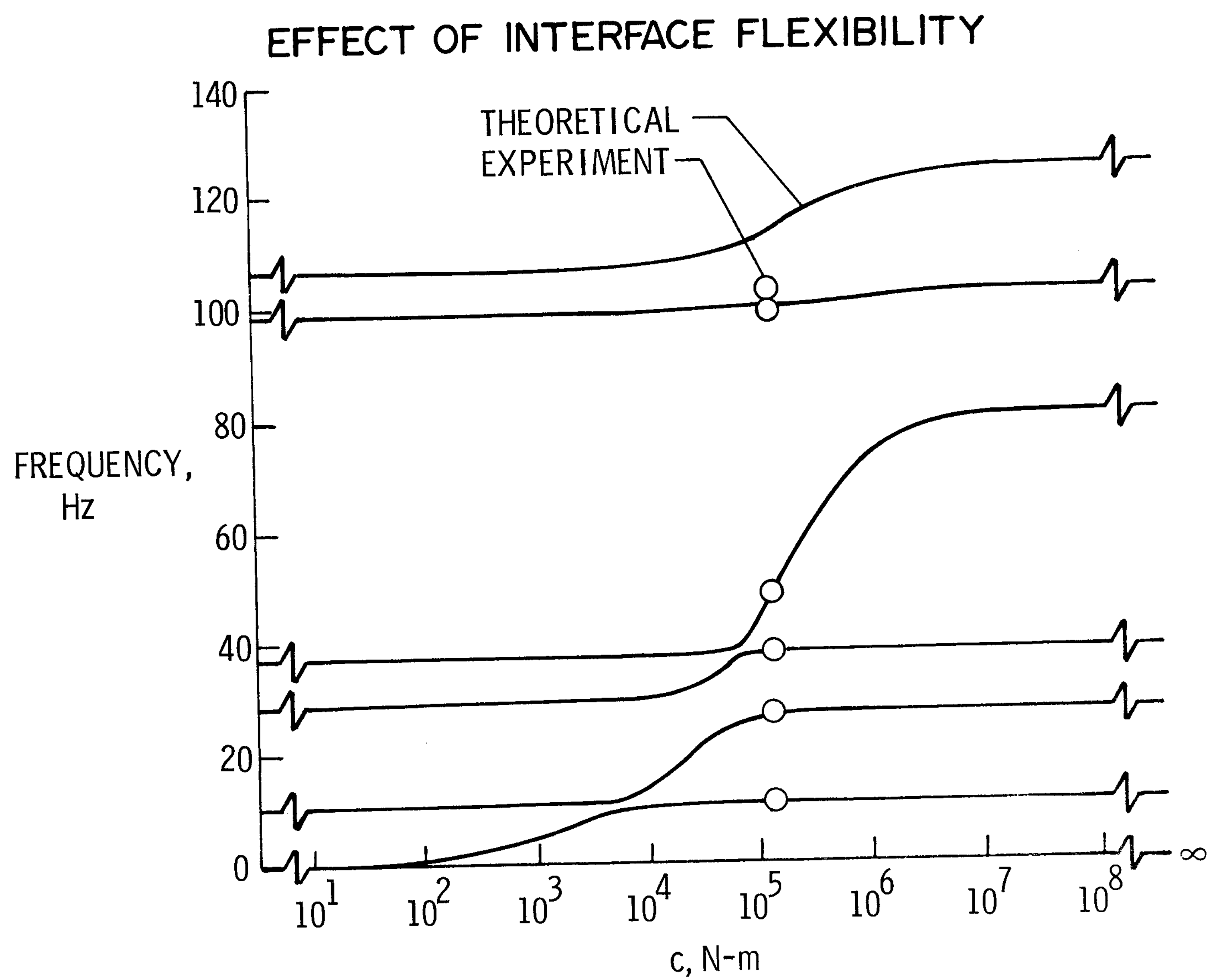
EFFECT OF INTERFACE FLEXIBILITY
THEORETICAL
EXPERIMENT
FREQUENCY, Hz
140
120
100
80
60
40
20
0
10^1
10^2
10^3
10^4
10^5
10^6
10^7
10^8
∞
c, N-m

Figure 12

CONCLUSIONS

The following conclusions are made concerning dynamic analysis for shuttle design verification:

Methods are available for direct analysis of the total vehicle. With the use of the general-purpose computer programs NASTRAN and SNAP, modes and frequencies of very complicated structures with many degrees of freedom can be obtained.

A convergence study of modal-coupling methods shows that convergence can be improved significantly by inclusion of static deflection shapes that permit a better representation of the stress conditions at the component interfaces.

Analysis also shows that improper modeling of the interfaces between joined vehicles can result in missing a critical lower mode of the total structure that contains predominantly axial motion. Accurate representation of such modes is vital for prediction of pogo-type instability.

REFERENCES

1. Leadbetter, Sumner A.; and Kiefling, Larry A.: Recent Studies of Space Shuttle Multibody Dynamics. NASA Space Shuttle Technology Conference, Vol. III, NASA TM X-2274, 1971, pp. 1-25.
2. Thornton, E. A.: Vibration Analysis of a 1/15 Scale Dynamic Model of a Space Shuttle Configuration. Grant No. NAS1-9434-20, Old Dominion Univ., [1972]. (Available as NASA CR-111984.)

DYNAMIC TESTING FOR SHUTTLE DESIGN VERIFICATION

Claude E. Green
NASA Marshall Space Flight Center

Sumner A. Leadbetter
NASA Langley Research Center, Hampton, Virginia

Mario H. Rheinfurth
NASA Marshall Space Flight Center

DYNAMIC TESTING TECHNOLOGY DEFICIENCIES

- **SYNTHESIS OF SHUTTLE DYNAMICS UTILIZING SUBSTRUCTURE TESTING**

  EVALUATE THE ABILITY OF MODAL SYNTHESIS TECHNIQUES TO DESCRIBE DYNAMIC CHARACTERISTICS OF COUPLED SYSTEMS LIKE THE SHUTTLE AND TO PROVIDE A METHOD TO SYNTHESIZE THE DAMPING OF THE COMPLETE SYSTEM FROM SYNTHESIS OF THE INDIVIDUAL ELEMENTS.

- **OPTIMIZATION OF MODAL SURVEY TESTS**

  DEVELOP CRITERIA TO PROVIDE ACCURATE, USABLE, DATA CONSISTENT WITH PRACTICAL TEST TECHNIQUES INCLUDING SUCH PARAMETERS AS TEST SETUP, MULTI-SHAKER PLACEMENT, DATA VALIDATION AND MATH MODEL REFINEMENT TO MATCH TEST DATA.

- **TRADE STUDY OF SCALED MODEL AND ALL-UP DYNAMIC TESTING**

  DETERMINE THE LIMITATIONS AND CONSTRAINTS OF SCALED MODEL DYNAMIC TESTS IN PROVIDING THE SAME INFORMATION OBTAINED FROM FULL SCALE TESTS AND THE RELATIONSHIP OF BOTH TESTS TO THE REQUIREMENTS AND NEEDS OF THE ANALYTICAL MODEL.

PURPOSES FOR DYNAMIC TESTING OF SHUTTLE

- VERIFICATION OF DESIGN
- QUALIFICATION OF HARDWARE
- ACCEPTANCE OF HARDWARE

Dynamics Data Needed for Design Verification

During the early design and development of the space shuttle, certain dynamic test data must be available for design verification. Some areas where this need exists are shown on the figure.

A large area of concern involves the early verification of control and stability analyses where the adequacy of the math models and analytical methods used to predict flight characteristics must be proven. To insure adequate margins of safety from pogo instabilities, vehicle modal data, propellant tank data, transfer line responses and engine characteristics are required for the analytical math model of both powered flight configurations. Loads resulting from the lift-off, rebound, and staging transients must be analyzed for the overall vehicle and for subsystem effects. Test data are required to verify the flight loads analysis for the vehicle and the attach points between the orbiter, the HO tank and the solid rocket motors. Historically, wind tunnel tests with scaled models have been used to study aerodynamic loads caused by pressure distributions, flutter, buzz, and buffet. The same technique has been used to provide the data for verification of the ground wind loads math model used to analyze structural responses at various fill conditions. The verification of predicted vibration and acoustic environments and responses has always been a costly problem requiring extensive test data.

Many of these dynamics data requirements needed for design verification can be obtained only from full scale structural components and assembly tests. However, in some areas it is impossible or impractical to test full scale hardware, so wind tunnel and other scaled model tests are required early in the program to support the analytical models used in design verification.

This paper presents a philosophy of design verification based on math modeling of the structural system strongly supported by a comprehensive test program and concludes by showing some of the types of tests that may be required.

DYNAMIC DATA NEEDED FOR DESIGN VERIFICATION

- FLIGHT CONTROL & STABILITY ANALYSIS
- POGO STABILITY ANALYSIS
  - PARALLEL BURN
  - ORBITER BURN
- TRANSIENT LOADS ANALYSIS
  - VEHICLE
  - SUB-ASSEMBLIES FLIGHT
- FLIGHT LOADS ANALYSIS
  - VEHICLE
  - ATTACH POINTS
- AERODYNAMIC LOADS ANALYSIS
  - VEHICLE
  - SURFACES
- GROUND WIND LOADS ANALYSIS
  - EMPTY
  - VARIOUS FILL CONDITIONS
- VIBRATION & ACOUSTIC ENVIRONMENTS

Shuttle Dynamic Verification Flow

A mutually supportive test and analysis approach for structural dynamics design verification is shown. This approach is based on a building block concept that would closely integrate analytical math modeling and testing techniques. Scaled model tests, full scale tests, and flight tests would serve to provide data for constantly refining the analytical models of the vehicle. The time sequence is roughly indicated from left to right in this illustration.

Early tests and analysis of scaled models would lead to test verified analytical models prior to the availability of full scale test hardware. Therefore, this concept begins with the utilization of simple beam math models and scaled model testing to verify design concepts early in the program. The simple models, modified with test data, would be used to develop finite element math models and establish full scale testing requirements. Full scale testing would be supported by finite element models of the specific test configuration and may include all major vehicle system elements. The types of tests would include major assembly vibroacoustic testing, modal survey testing, influence coefficient testing, and component testing.

The refined models of each of the vehicle system elements would be assembled into a finite element vehicle math model. This model would be used to establish requirements for orbiter horizontal modal survey tests, horizontal and vertical flight tests, and full-up vehicle dynamic tests. Data from these fully assembled vehicle tests would be used to insure that the math model correctly treats pogo, cross coupling, control parameters, and other characteristics that can only be obtained from all-up tests.

After the completion of the ground test program, the finite element vehicle math model would be continually updated with data obtained from flight operations. Updating the model with flight data would provide an invaluable tool in case of flight anomalies or to assess effects of vehicle design or payload changes.

SHUTTLE DYNAMIC VERIFICATION FLOW

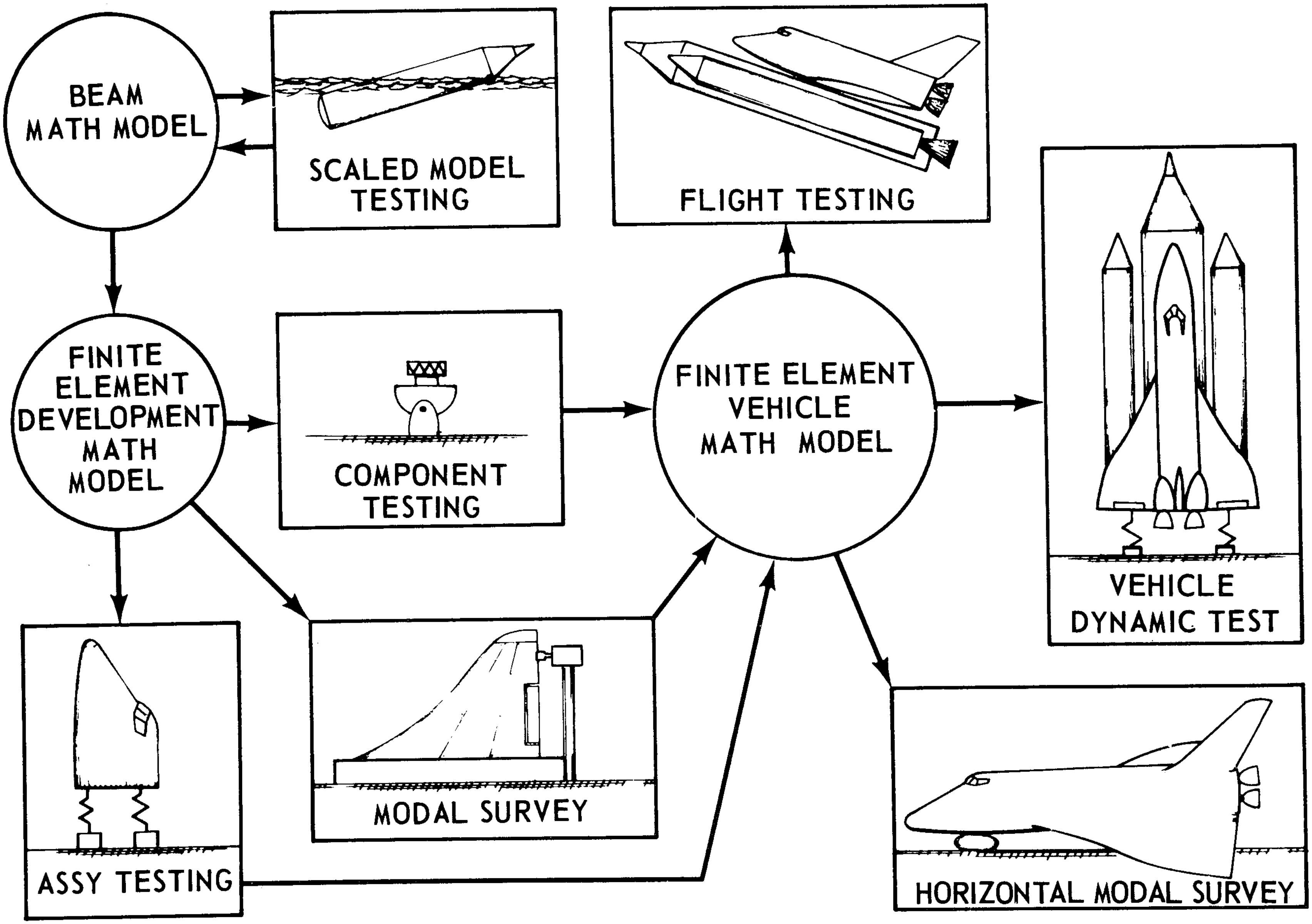

Typical Math Model Evolution

This slide, from a Boeing Company report, shows the evolution of typical math models; in this case, models of the Saturn V space vehicle. The original math models were simple beam types used to establish full scale testing requirements. These models were used to determine the effect of replacing flight hardware with dynamic simulators, the force required to excite the dynamic test vehicle, the sensor locations needed to define the mode shape, and the sensitivity to parameter changes to guide development of more refined models.

The next step in the evolution was a quarter shell model which took advantage of the vehicle symmetry and considered computer size limitations. Because this model was used to predict the modal response at flight sensor locations to gimbaling, local detail was provided for both the thrust structure and sensor locations.

The third step in the evolution was a quarter shell representation of the total Saturn V vehicle based on a process of modal stacking. Cantilever modes of the spacecraft and S-IVB stage were obtained and used in the analyses, stage by stage, of the total vehicle. This model was used to predict the response of the dynamic test vehicle and proved to be highly accurate. However, the model proved inadequate in predicting local flight sensor slopes and cross coupling between pitch, yaw, and longitudinal planes. The model was revised with test data to establish correlation in the flight sensor area.

The fourth and final model was a three dimensional model of the total vehicle which represented the cross coupling in sensitive areas and simplified insensitive areas. This test verified model was used to analyze pogo and loads and was used for flight control predictions to support Saturn V flights.

TYPICAL MATH MODEL EVOLUTION

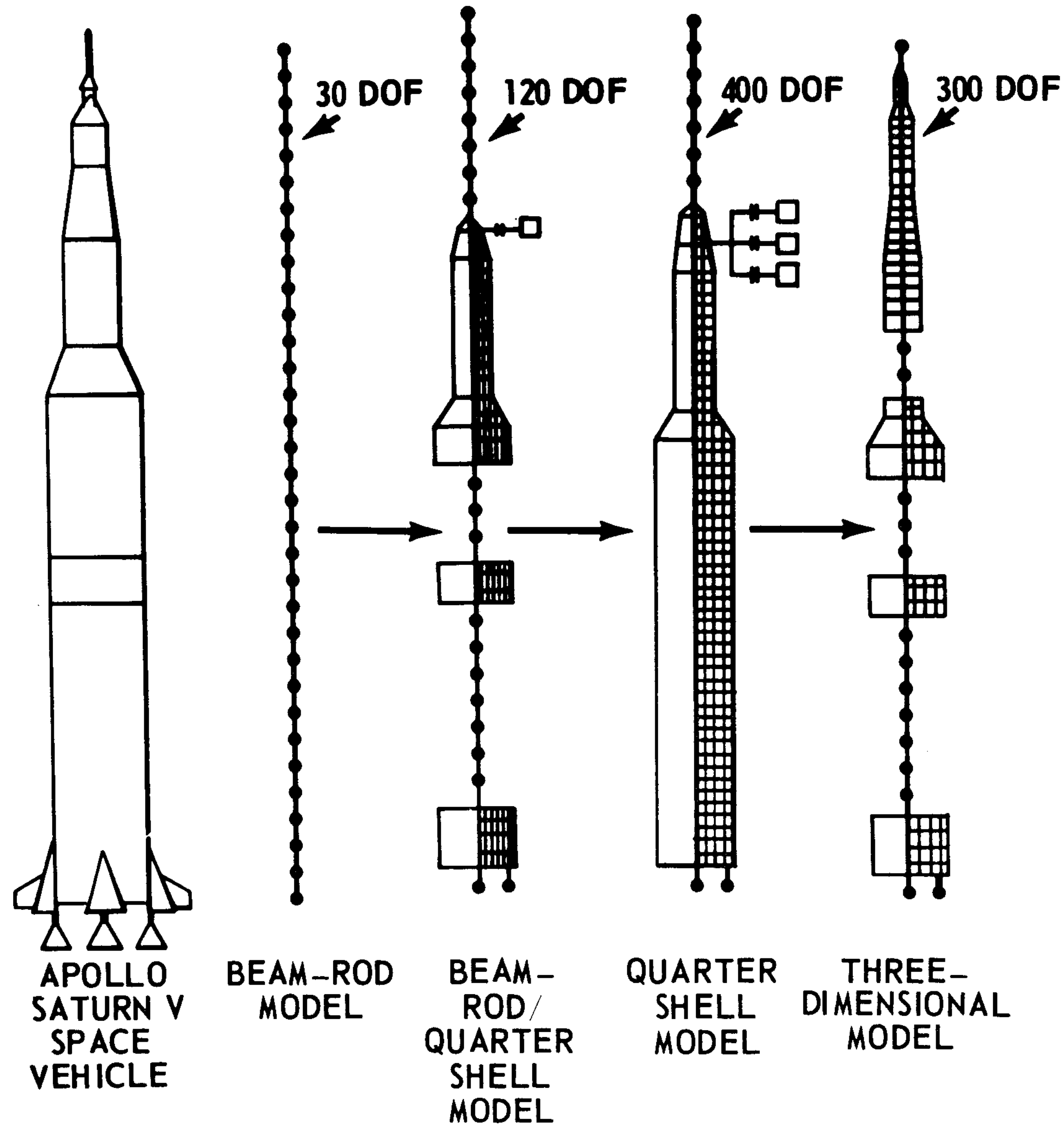

Math Model Related to Test

Before any space shuttle structural test, a pretest analytical math model will be required. This math model will be used to develop a test configuration math model and will be revised to become the basis for the final finite element model.

This chart shows the relationships between the math models and the test program. The pretest and test math models support the test program in the order shown. Data from the test program feed back to update the test configuration model and the final finite element model. Also, some improvement will be obtained for this final model from the pretest analytical and test configuration models as shown.

MATH MODEL RELATED TO TEST

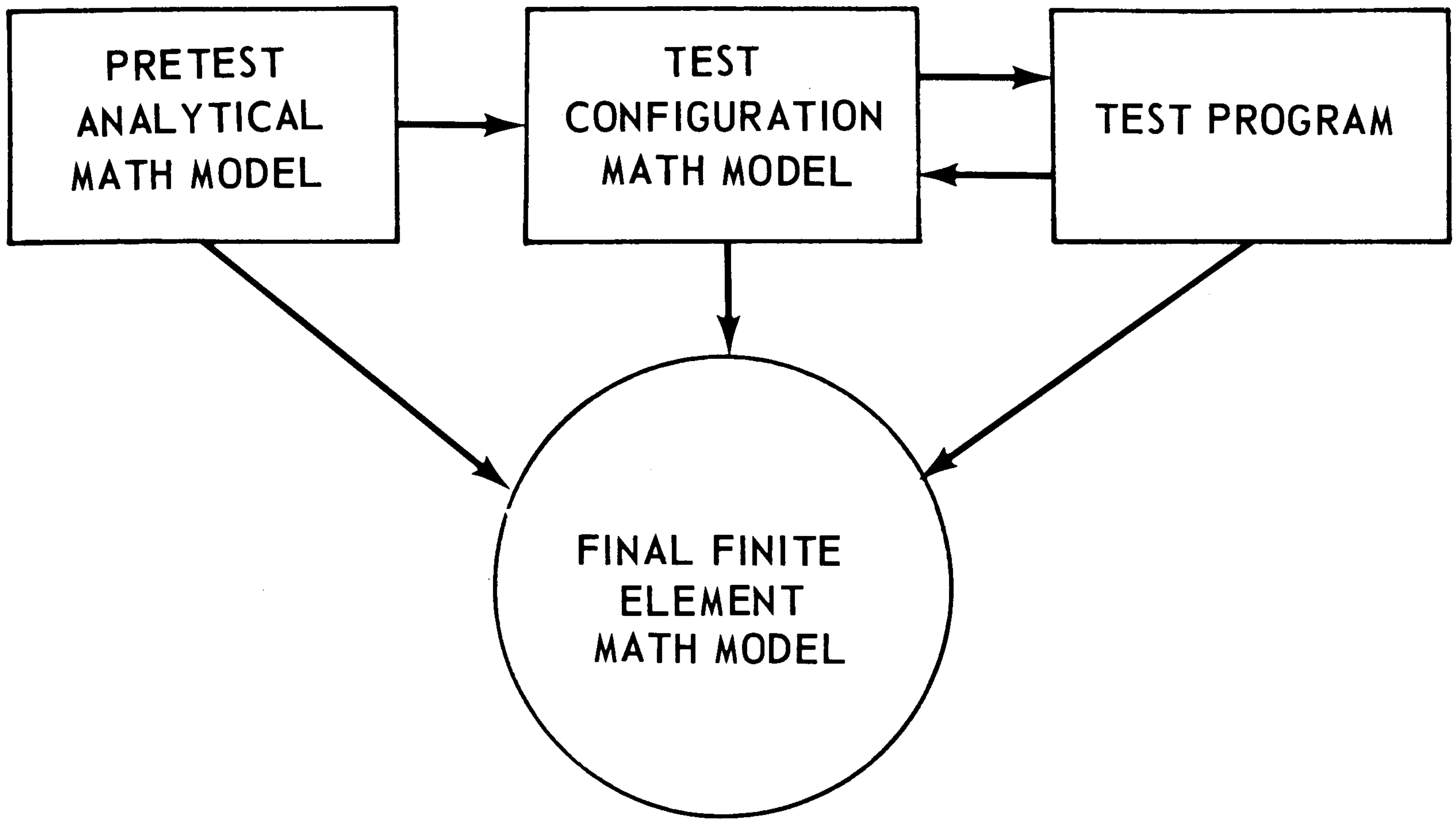

A Critique on Scaled Dynamic Model Testing

Although limited by the involved scaling laws, scaled models have been used extensively in the aerospace field. A critique on some advantages and disadvantages of dynamic model testing is given on this figure. Properly designed and fabricated models can provide timely data early during the development cycle of the prototype vehicle.

Primarily because of their simpler construction and smaller size, models can be modified and retested in a relatively short time at less cost in manpower and money. For solving specific problems, a model can be relatively easily designed and tested. Generally the model test program will be less complex than the program required for full scale testing. From a schedule viewpoint, data can be obtained earlier in the program and tests can be recycled or new tests introduced in less time.

Some of the more significant disadvantages are shown. Such factors as local response effects and damping, are extremely difficult if not impossible, to represent at a scaled reduced size. Model joints may not be representative of full scale hardware. It should be noted that accurate damping data is essential for control and stability analysis. There also exists significant scaling law incompatibilities such as the slosh frequency scaling varying as the square root of the scale factor instead of directly with scale factor as does the body bending frequency.

A CRITIQUE ON SCALED DYNAMIC MODEL TESTING

- ADVANTAGES
  - TIMELINESS
  - ECONOMIC
  - TEST SIMPLICITY
  - SCHEDULE
- DISADVANTAGES
  - LOCAL STRUCTURE NOT REPRESENTATIVE
  - INCORRECT DAMPING VALUES
  - SCALING LAW INCOMPATIBILITIES

Scaled Model/Math Model Relationship

The relationship between a simple beam math model and the scaled model it represents is shown in this illustration of the shuttle in the lift-off configuration. Lumped masses are corrected by simple beams to model the orbiter, the HO tank, the two solid rocket motors, and the orbiter wings. The propellant and oxidizer are simulated by a single mass. Pinned connections are shown between the orbiter and the HO tank and between the tank and the SRM's because these connections are not yet defined but will be different than shown.

This math model would be updated with test data by adding more complexity and then would be used to calculate higher vehicle modes. Results from this typical test/math model would be used to define the first few vehicle modes and to verify the math modeling techniques.

SCALED MODEL/MATH MODEL RELATIONSHIP SIMPLE BEAM MODEL

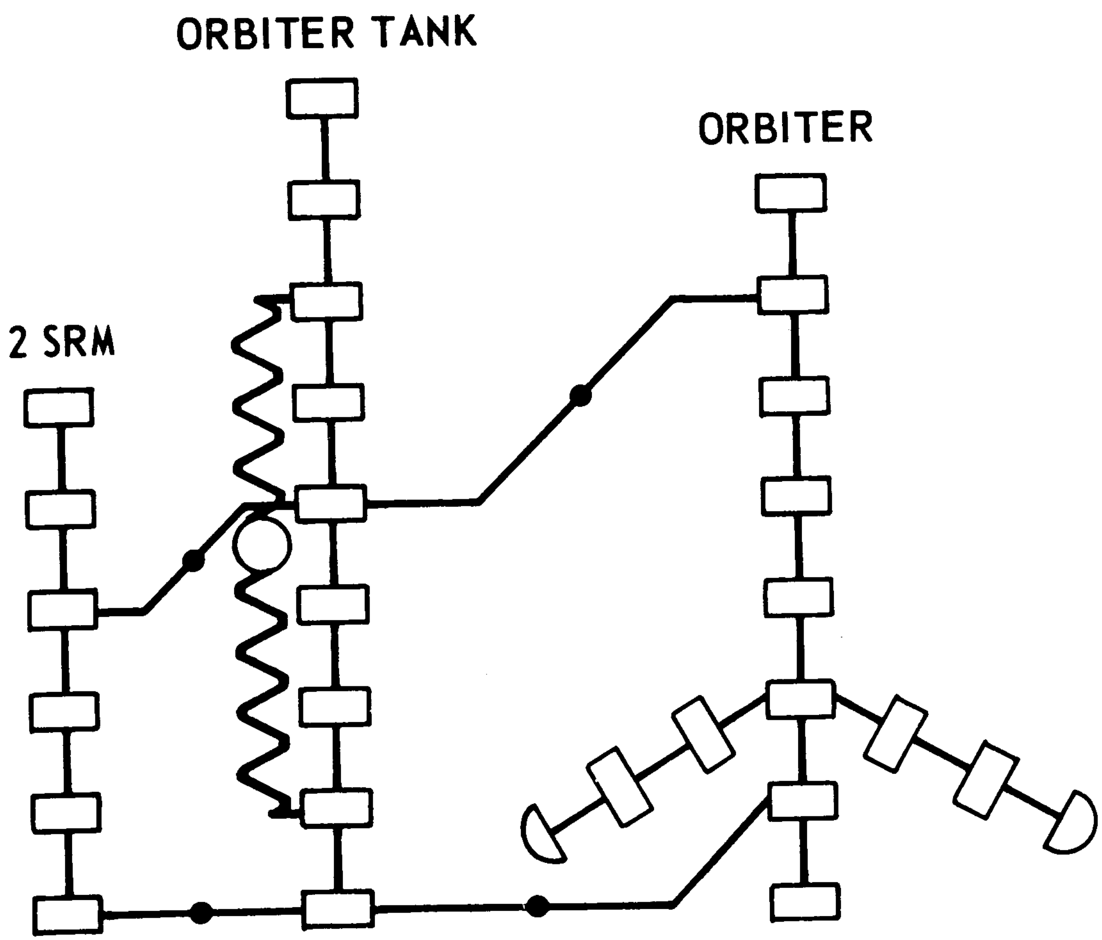

BEAM MODEL

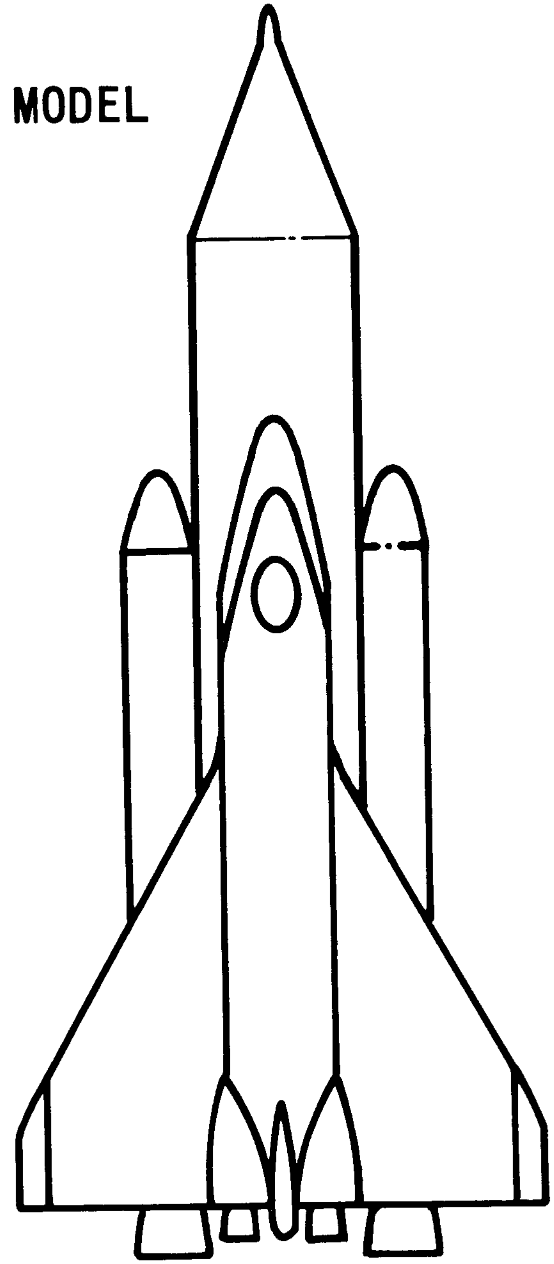

SCALED MODEL

Water Recovery Test Program

This balloon chart shows how a specific scaled model test program will be used to provide data for SRM design verification. Each scaled model test will be supported by a math model of the configuration to be tested. The objectives of the program are:

1. To verify scaling parameters and theory
2. To determine SRM loads from water entry and towback
3. To determine SRM pressure distributions for water entry and towback
4. To establish effects of model elasticity on loads
5. To evaluate effects of various SRM configurations on loads and pressure distributions
6. To evaluate effects of atmospheric pressure versus scaled pressure on scaled model test results

The proposed program uses 4, 8, and 12 percent models of a constant configuration with later testing of the booster final configuration. The program will culminate in a series of water recovery tests of a 75 to 100 percent model of the final configuration.

WATER IMPACT–CAVITY–REBOUND–TOWBACK

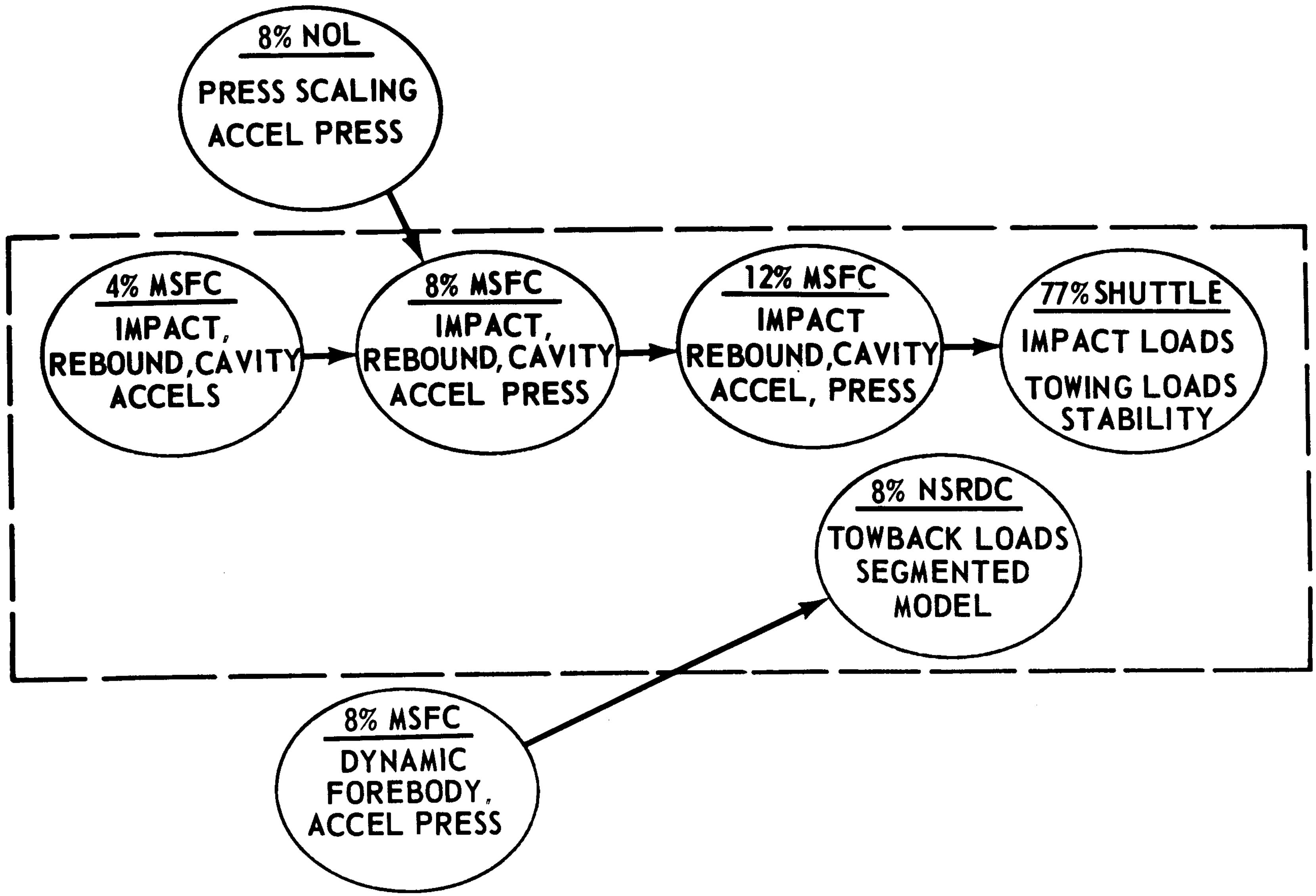

Orbiter Forward Body Vibroacoustic Test

The following full scale hardware tests are shown to illustrate some of the kinds of tests that may be required to verify the shuttle design. These figures should not be considered as recommending specific structural tests but are shown to illustrate the continuation of the building block concept of integrating analytical math modeling and testing.

This first full scale test would require a complete forward body assembly with all significant masses installed or simulated on flight bracketry. Although titled a vibroacoustic test, the test program would include a comprehensive modal survey test to determine the modal characteristics of the assembly.

ORBITER FORWARD BODY VIBROACOUSTIC TEST

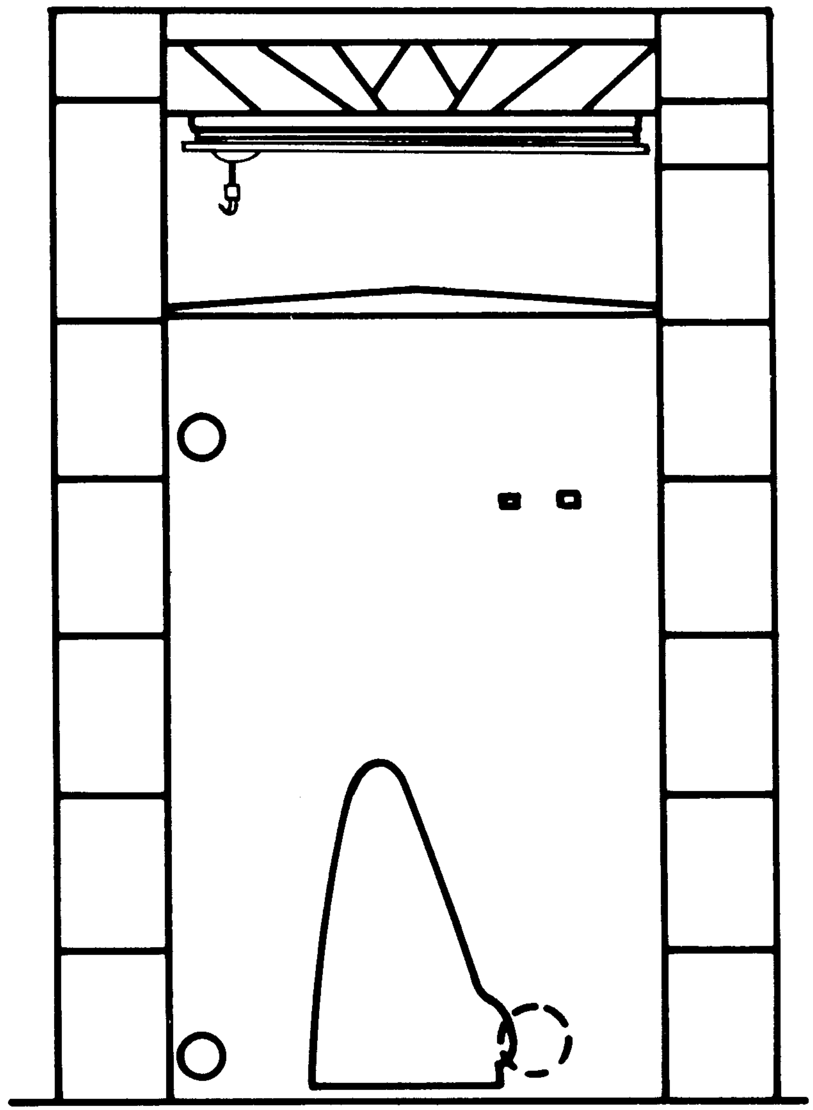

Orbiter Aft Body Vibroacoustic Test

The aft body test would require an aft body up to the payload bay without the vertical stabilizer or wings but with the thrust structure and all significant masses installed or simulated on flight bracketry. In addition to acoustic testing, a modal survey test would be conducted to determine the modal characteristics of the assembly and to determine structural interaction for pogo assessment.

ORBITER AFT BODY VIBROACOUSTIC TEST

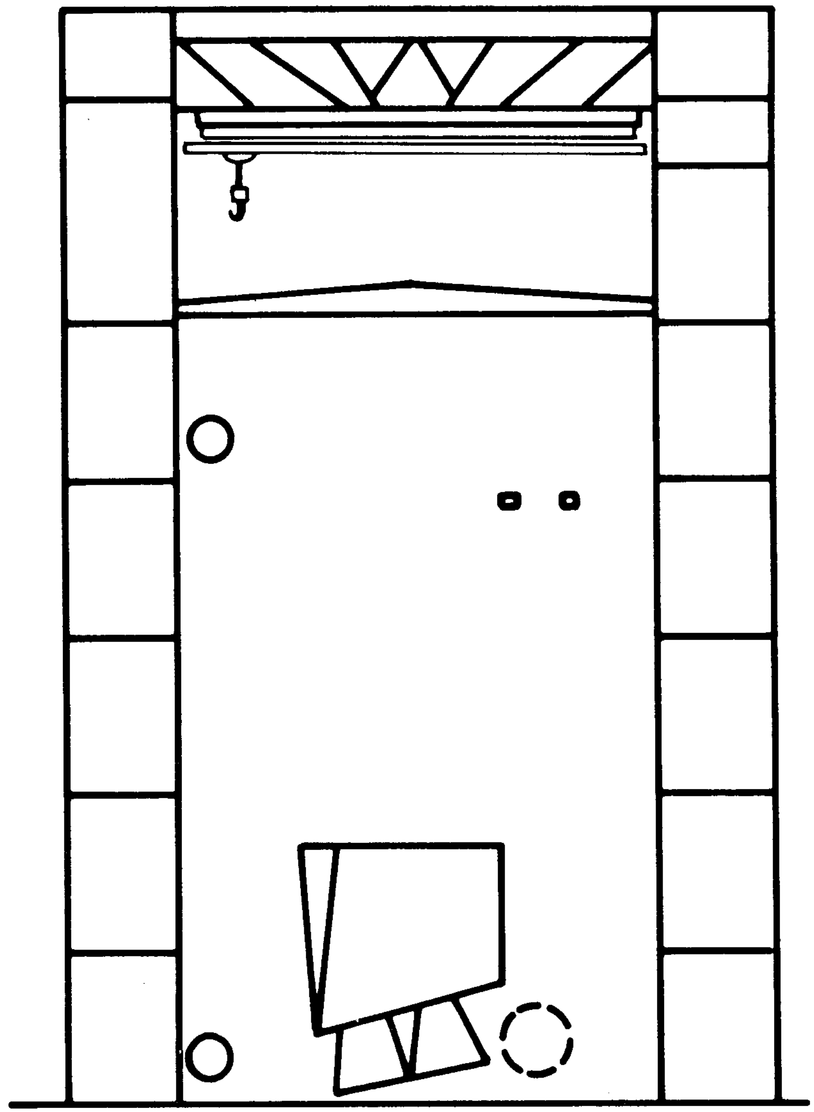

Orbiter Payload Bay Modal Survey Test

The modal survey of the payload bay would require that the hardware be complete with forward and aft compartment bulkheads and all significant masses installed or simulated on flight bracketry. Data from this test would be particularly useful in revising the analytical model's capability to assess effects of payload changes.

ORBITER PAYLOAD BAY MODAL SURVEY TEST

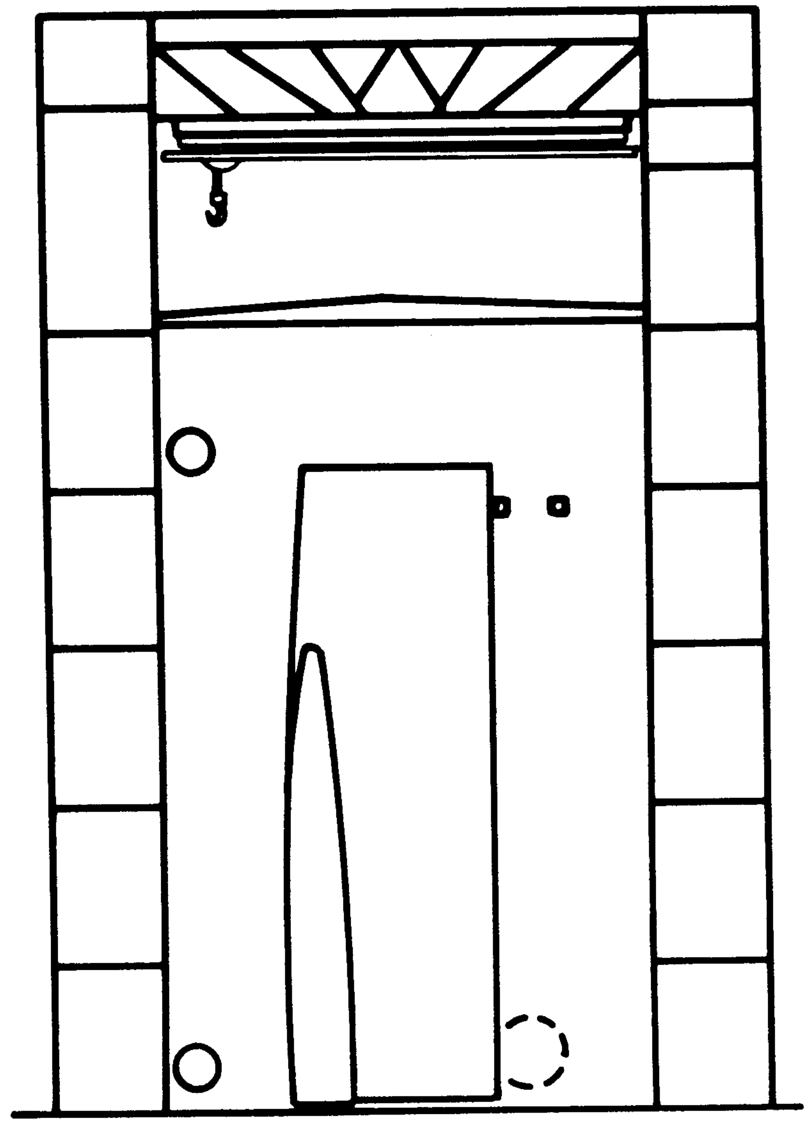

Orbiter Wing Assembly Modal Survey

This test would require a complete wing assembly including elevons and all significant masses installed or simulated on flight bracketry. Also required would be a partial or complete wing box to provide proper boundary layer conditions for the test.

ORBITER WING ASSEMBLY MODAL SURVEY

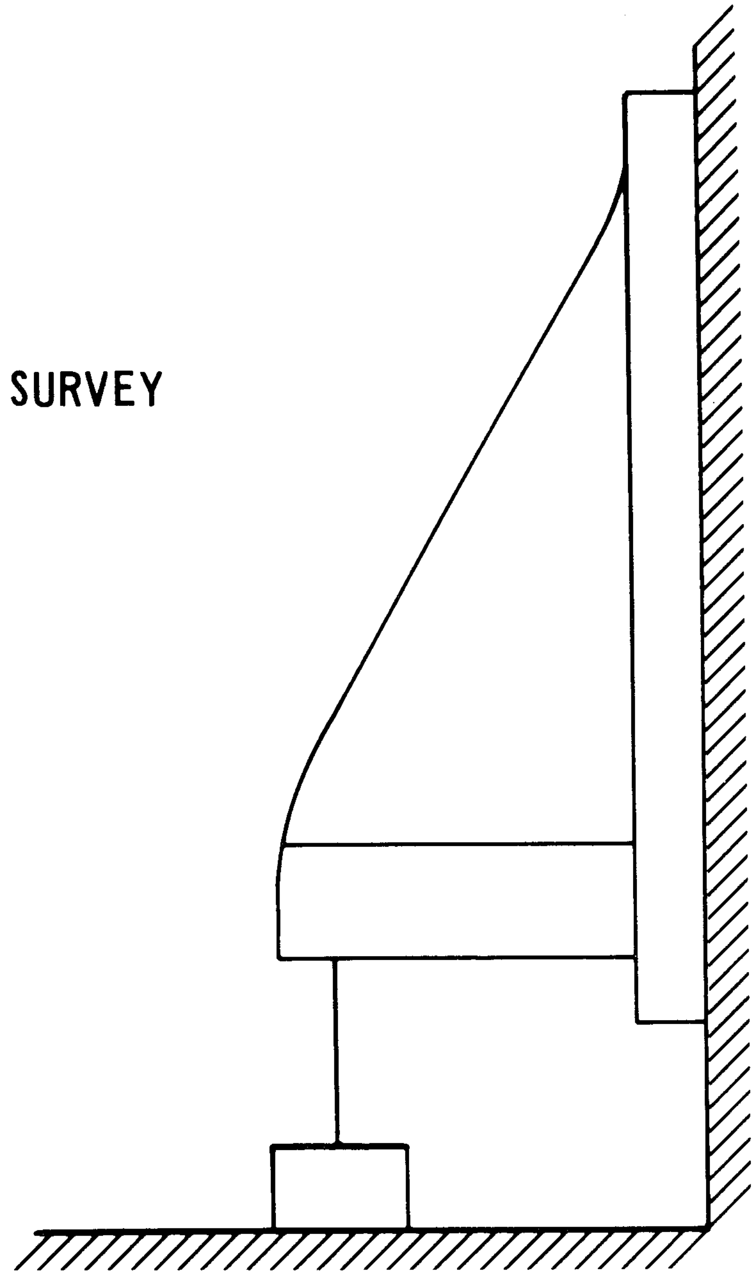

Orbiter Horizontal Vehicle Modal Survey

The test hardware required would be the first horizontal flight orbiter. Data from the test would be used to determine the modes and frequencies of the vehicle in the horizontal configuration.

ORBITER HORIZONTAL FLIGHT VEHICLE MODAL SURVEY

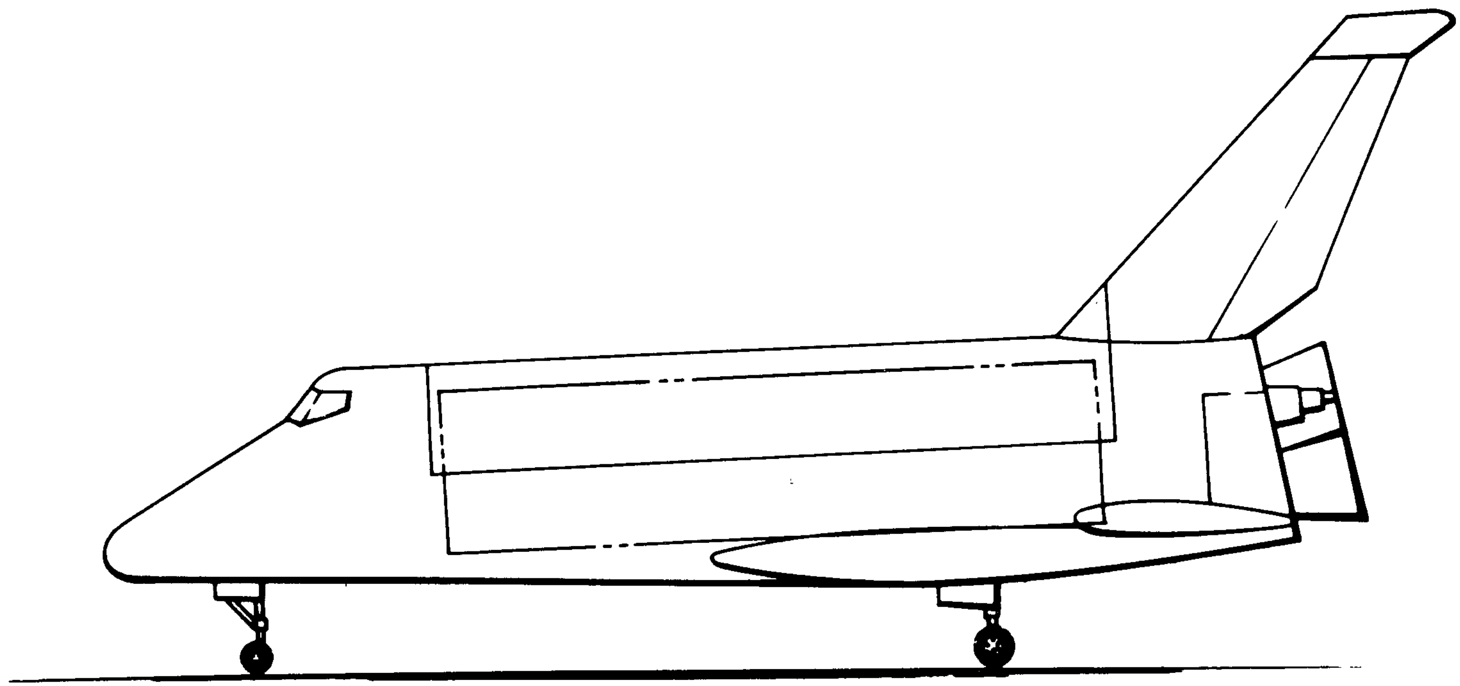

HO Tank Forward Structure Modal Survey

This test would utilize a forward tank of the HO tank assembly complete with bulkheads and nose fairing. The test would determine the modal characteristics of the assembly and the fluid/structure interactions. Data from this test will be used in pogo stability analysis.

HO TANK FORWARD STRUCTURE MODAL SURVEY

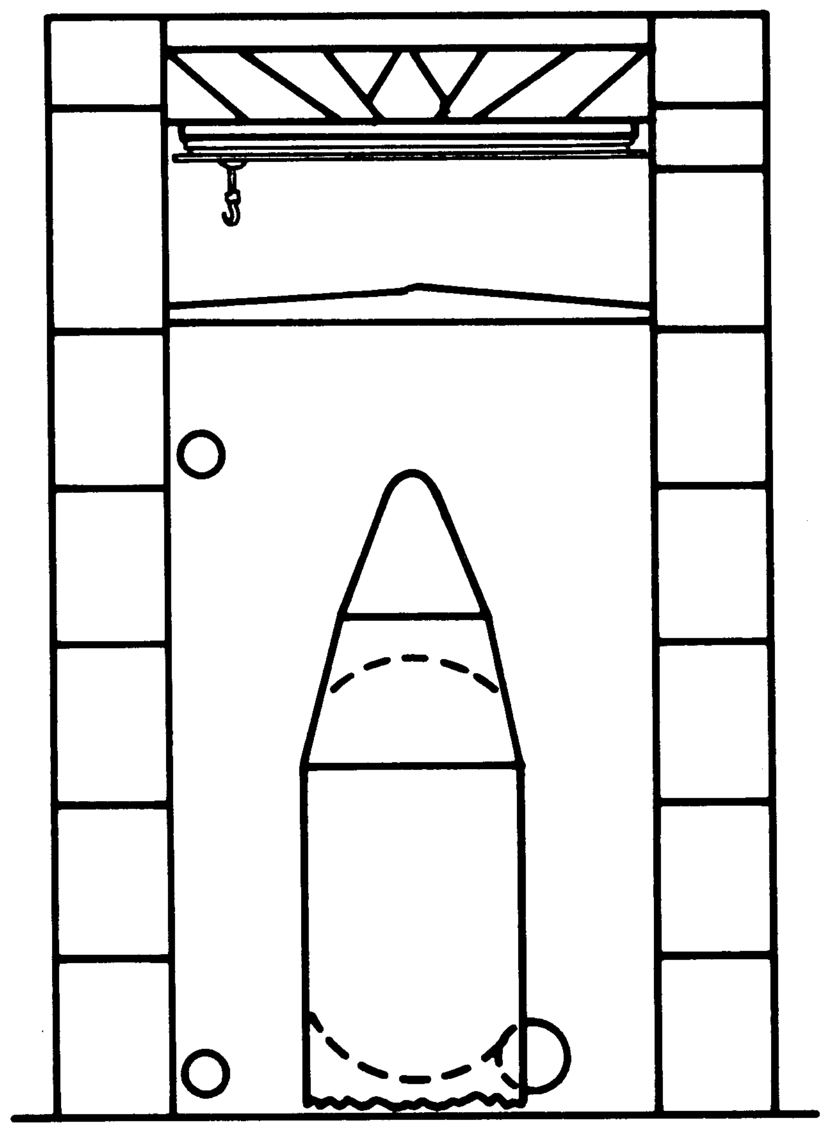

Orbiter Assembly Dynamic Test

The hardware for this test would be a complete orbiter with all major masses installed, including a payload and the HO tank. The objectives of the test would be to obtain vehicle joint and fluid damping for updating the vehicle math model. The test would also provide an orbiter system pogo assessment and a verification of flight control parameters.

ORBITER ASSEMBLY DYNAMIC TEST

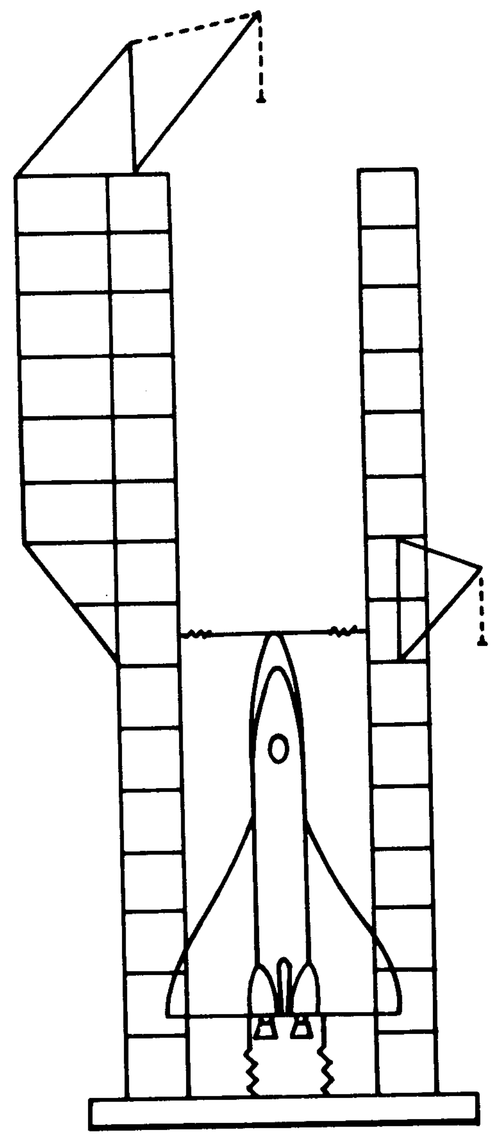

Summary of Shuttle Dynamic Tests

This chart summarizes the full scale hardware tests that may be required to provide the data for the analytical models planned for design verification. The time sequence of these tests is from left to right in this figure.

The first item in this figure is an inert SRM modal survey test. This test item may not be required if SRM analytical techniques can, with a high degree of confidence, model the motor and its critical attach points. The next six items are the orbiter and HO tank tests shown in the previous illustrations. The orbiter and the HO tank may be integrated into an orbiter assembly for dynamic and modal survey testing from which verification would be obtained for the analytical treatment of local response, fluid and structural damping, cross coupling, and joint damping. The orbiter assembly and the SRM fully mated dynamic and modal survey test are shown to illustrate the logical next step in the building block concept of integrating analytical math modeling and testing. Lastly, the first horizontal flight orbiter modal survey test and horizontal flight test are shown as sources of data for shuttle design verification.

SUMMARY OF SHUTTLE DYNAMIC TESTS

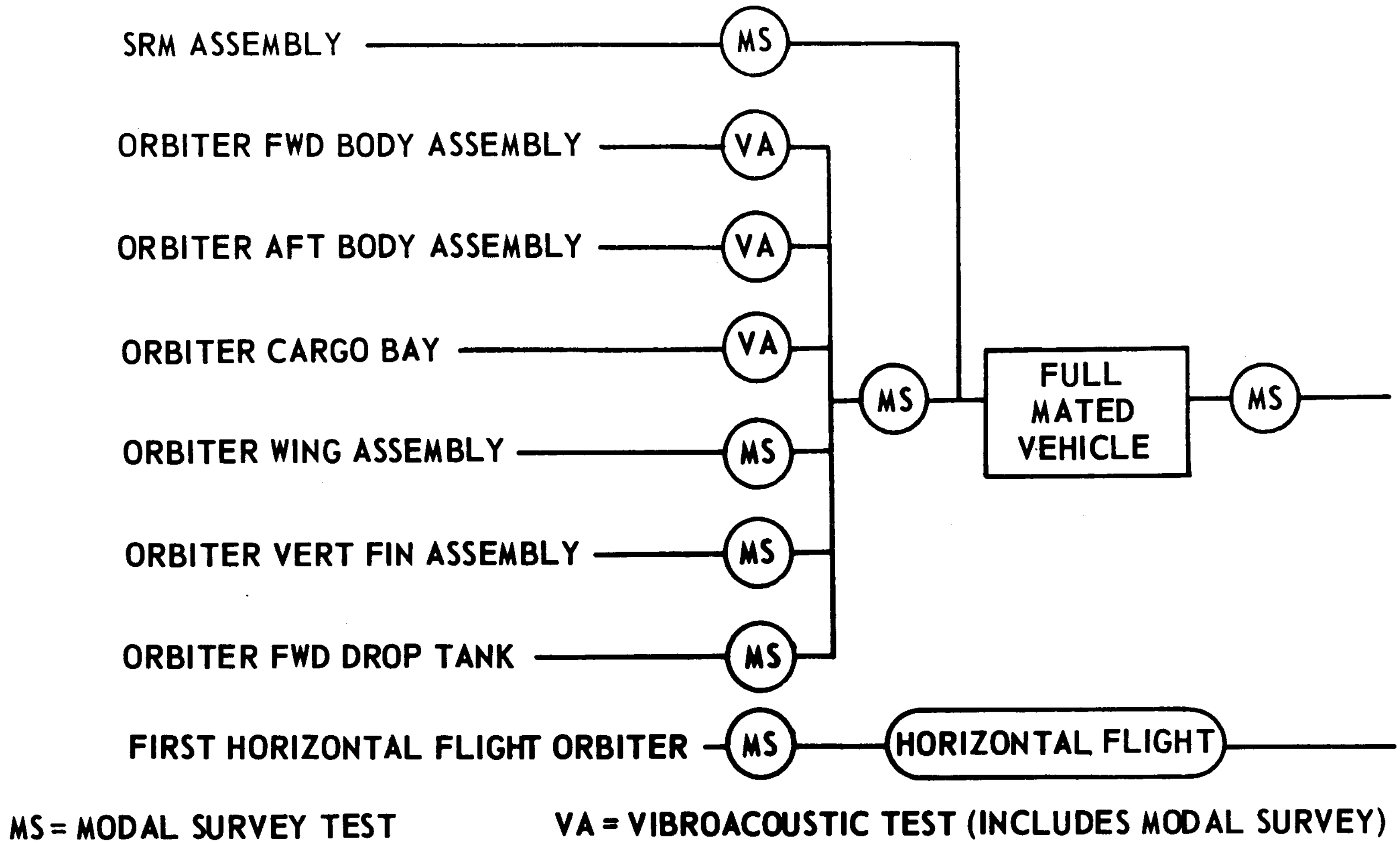

Summary

This paper has presented a rational approach to the dynamic testing needed for space shuttle design verification. The approach was shown to be based on a building block concept that would integrate analytical math modeling and testing techniques. Starting with simple beam math models and both rigid and dynamically scaled models, tests would provide the data to constantly refine and improve the vehicle math models. Scaled models provided early test data that was timely and economical but did not eliminate the subsequent requirement for data from full scale and flight tests to provide the final verification of the analytical models.

Finally, three dynamic testing technology deficiencies were discussed. These three technology areas are directly related to this approach to the dynamic testing needed for shuttle design verification. They are synthesis of shuttle dynamics, optimization of modal survey testing, and scaled model/full scale dynamic testing trade studies.

SUMMARY

- BUILDING BLOCK APPROACH

SIMPLE BEAM MATH MODELS

↓

SCALED MODEL TESTING

↓

FINITE ELEMENT DEVELOPMENT MATH MODEL

↓

FULL SCALE ASSEMBLY TESTING

↓

FINITE ELEMENT VEHICLE MATH MODEL

↓

VEHICLE FLIGHT TESTING

- DYNAMIC TESTING TECHNOLOGY DEFICIENCIES

AN ASSESSMENT OF RADIATIVE METALLIC THERMAL PROTECTION SYSTEMS FOR SPACE SHUTTLE

By Bland A. Stein, Herman L. Bohon, and Donald R. Rummler

NASA Langley Research Center

SUMMARY

When the NASA space shuttle technology program began, the uncertainties in the existing technology base for radiative metallic thermal protection systems (TPS) were considered significant enough to possibly preclude flight-weight designs for the multiple flight mission capability required for shuttle. During the past 2 years, the TPS technology program and other current metallic-heat-shield programs have reduced these uncertainties to the level where only optimization of flight-weight designs depends on further research. This report reviews the metallic TPS technology program in the areas of environmental uncertainties, materials data base, TPS design concepts and heat-shield panel configurations, and testing and evaluation of materials, panels, and complete systems. Recent results are noted and current programs are described. Areas of future research to reduce remaining uncertainties are indicated. It is concluded that continuation of current programs and implementation of currently planned programs will generate enough information through concept evaluation and testing studies to permit designers to make rational decisions on materials and the structural integrity of radiative metallic thermal protection systems for shuttle.

INTRODUCTION

When the NASA space shuttle technology program began 2 years ago, a technology base for radiative metallic thermal protection systems (TPS) existed, based largely on previous U.S. Air Force and NASA programs such as X-15, X-20, ASSET, ASCEP, BGRV, Mercury, and Gemini. It was recognized, however, that the complex projected shuttle operating environment required considerable advancement in the state of the art for existing metallic TPS concepts. The need to develop a reliable, lightweight, reusable metallic thermal protection system was the prime driver for the NASA-TPS technology program in this area. This report is an assessment of the program's progress and of the areas which still remain to be completed. Portions of this paper were drawn from a recent NASA/industry assessment of radiative metallic TPS, and the authors wish to acknowledge the NASA ad hoc committee members and the industry consultants who participated in that assessment.

SYMBOLS

a,b	panel dimensions
H_t	total enthalpy
k_D	deflectional spring constant
M	Mach number

P	load
P_{max}	maximum load
p	pressure
p_{O_2}	partial pressure of oxygen
p_s	surface pressure
p_t	stagnation pressure
q	dynamic pressure
T	temperature
T_{max}	maximum temperature
Δt	tunnel run time

KEY AREAS OF RADIATIVE METALLIC TPS ASSESSMENT

(Figure 1)

Figure 1 shows a typical radiative metallic thermal protection system. The important components of the system are the metallic heat shield and supports, the joints and seals, and the fibrous thermal insulation, packaged in metallic foil.

The key areas of metallic TPS technology development needs, as recognized at the start of the program, are listed at the bottom of figure 1. At one time, it was thought that uncertainties in these areas might preclude flight-weight design, but the current assessment is that the technology program and other current studies have reduced the uncertainties to the levels where only optimization of flight-weight designs depends on further research in certain of these areas. The key remaining environmental uncertainties for metallic TPS include joint and protuberance heating, gas intrusion at joints, crossflow effects, surface roughness and distortion effects, and leeward surface heating of the orbiter vehicle. Application of wind-tunnel data to flight conditions is a continuing uncertainty. These and other environmental factors affect all thermal protection systems. They are being studied and appear to be increasingly resolvable; however, they will not be discussed further in this paper.

The second item in the list at the bottom of figure 1 - the materials data base - was most uncertain in the areas of maximum use temperature of a given heat-shield material, materials mix, cyclic creep, oxidation behavior, emittance stability, and residual properties.

In the design concept area, the necessity to withstand multiple acoustical, thermal, and aerodynamic loading cycles in the shuttle application required verification or development of TPS in the areas of panel configurations, insulations, joints and seals, fasteners, and inspection methods.

In testing and evaluation of materials, panels, and complete systems, shuttle requirements dictated new testing environments for materials and panel tests. The accomplishment of cyclic testing of large systems in realistically simulated shuttle environments was a significant concern both for system development and verification at the start of the program.

KEY AREAS OF RADIATIVE METALLIC TPS ASSESSMENT

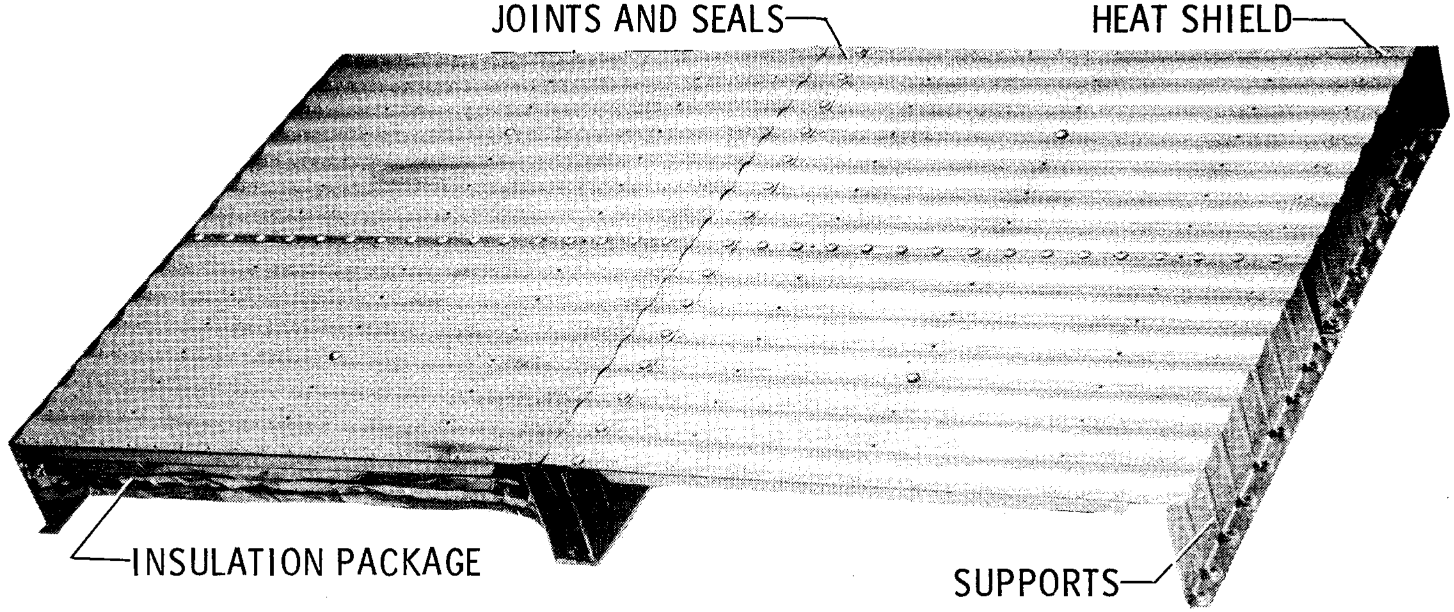

- ENVIRONMENTAL UNCERTAINTIES
- MATERIALS DATA BASE
- DESIGN CONCEPTS - PANEL CONFIGURATIONS
- TESTING AND EVALUATION
  - MATERIALS
  - PANELS AND THERMAL PROTECTION SYSTEMS

Figure 1

METALLIC THERMAL PROTECTION SYSTEM EVALUATION STUDIES

(Figure 2)

Where is the technology program now? Figure 2 gives a general indication of the evaluation studies which the technology program has either sponsored or is conducting in-house at NASA research centers. The first item, insulation packaging, is a completed study which showed that packaged low-density fibrous insulation could withstand simulated shuttle mechanical, vibration, and thermal environments with excellent reuse capability at shield temperatures above 1365 K (2000° F) whereas TD Ni-20Cr foil showed good reusability at 1480 K (2200° F) as a packaging material. In the area of advanced materials development, NASA sponsorship has made the dispersion-stabilized alloy TD Ni-20Cr available in reproducible, reliable, large-size sheet for shuttle TPS studies. Another program has shown field repair of silicide coating on columbium to be feasible. The materials evaluation work at or under contract to four research centers has answered many questions about the behavior of a range of metallic materials. The studies, in general, indicated that the maximum proposed use temperatures, which will be discussed subsequently, are feasible for the orbiter mission. Stability of superalloy, dispersion-stabilized-alloy, and coated-columbium emittance in high-speed-airflow tests has been demonstrated. Other results in this area will also be described. The design criteria work which contributes to the shuttle design criteria document (NASA SP-8057) is applicable to metallic TPS as well as metallic structures. The two final items are comprehensive multienvironment tests of full-size hardware for available materials and advanced materials. These will be described subsequently.

Considerable other work in metallic TPS evaluation is also being conducted in the shuttle Phase B auxiliary program, under sponsorship of other government agencies and in industry IRAD programs. The scope of this work reaches (in general terms) from elemental-specimen tests to subsize-panel and joint tests to panel tests in the Air Force Flight Dynamics Laboratory's 50 Megawatt Facility. The materials under study run the gamut from titanium to tantalum.

METALLIC THERMAL PROTECTION SYSTEM EVALUATION STUDIES
SPACE SHUTTLE TECHNOLOGY PROGRAM

SCOPE OF WORK	MATERIALS	NASA CENTER
INSULATION PACKAGING DEVELOPMENT AND VERIFICATION	FIBROUS INSULATIONS, METAL FOILS	MSFC
ADVANCED MATERIALS DEVELOPMENT, FIELD REPAIR OF COATINGS	D.S. ALLOYS, REF. MET. COATINGS	LeRC, MSFC
MATERIAL EVALUATION IN MISSION SIMULATION TESTS, PRELIMINARY DESIGN PROPERTIES	TITANIUM ALLOYS, SUPERALLOYS, DISPERSION STAB-ILIZED ALLOYS, COATED Cb ALLOYS	ARC, LeRC, MSFC, LaRC
DESIGN CRITERIA STUDIES		LaRC
COMPREHENSIVE MULTIENVIRONMENT EVALUATION OF FULL-SIZE PANELS	TITANIUM ALLOYS, SUPERALLOYS	LaRC
DEVELOPMENT OF CONCEPTS AND COMPREHENSIVE EVALUATION OF FULL-SIZE PANELS	COATED COLUMBIUM, DISPERSION STAB-ILIZED ALLOYS	LaRC

Figure 2

ORBITER THERMAL-PROTECTION-SYSTEM MATERIALS USAGE

(Figure 3)

In consideration of the materials-data-base situation, it is recognized that design-property-data generation for a large number of materials which must operate in a complex environment is expensive and time consuming. Thus, the materials mix and the maximum allowable use temperature must be considered and evaluated. Figure 3 shows the effects of maximum use temperature and materials mix on orbiter TPS materials usage. For a typical 1770 km (1100 mi.) cross-range orbiter, the two plots show percentage of surface area above the indicated surface temperature. Two maximum use temperatures are given for each material. The solid vertical line shows maximum use temperature projected by most assessors of the data base for multimission shuttle flight reusability. The dashed vertical line is the material cutoff temperature if the most conservative use temperatures are considered. Thus, the range of uncertainty in use temperature is indicated by the shaded area. The actual heat-shield area for a given material, such as H-188, changes significantly if the materials mix allowable changes from three to six materials or if use temperatures change from projected to conservative.

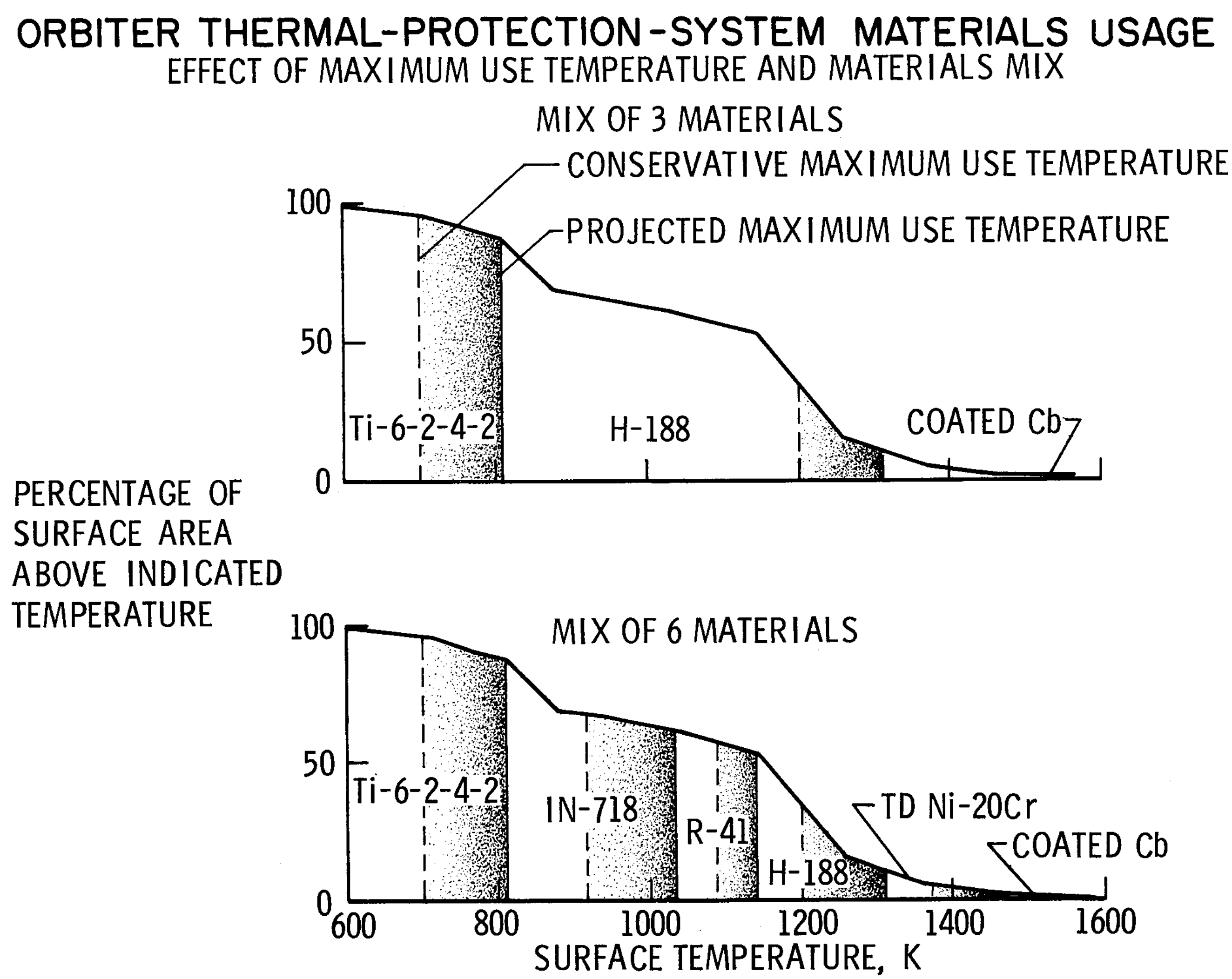
ORBITER THERMAL-PROTECTION-SYSTEM MATERIALS USAGE
EFFECT OF MAXIMUM USE TEMPERATURE AND MATERIALS MIX
MIX OF 3 MATERIALS
CONSERVATIVE MAXIMUM USE TEMPERATURE
PROJECTED MAXIMUM USE TEMPERATURE
100
50
0
Ti-6-2-4-2
H-188
COATED Cb
PERCENTAGE OF
SURFACE AREA
ABOVE INDICATED
TEMPERATURE
MIX OF 6 MATERIALS
Ti-6-2-4-2
IN-718
R-41
H-188
TD Ni-20Cr
COATED Cb
600
800
1000
1200
1400
1600
SURFACE TEMPERATURE, K

Figure 3

THERMAL-PROTECTION-SYSTEM WEIGHT IMPACTS
(Figure 4)

Figure 4 gives an indication of the weight penalties involved. The relative area from figure 3 has been converted into relative TPS weights by estimating heat shield, support, and insulation weights per unit area. Since the bar graphs shown are the additive relative weights of each materials system used, the top of each bar is an estimate of total relative TPS weight. On the left is the impact of the materials mix for the conservative maximum use temperature limits. In this case, the six-materials mix reduces relative TPS weight by 17 percent from the three-materials mix. This must be qualified by noting that if the comparison was made on the basis of projected use temperatures, the difference would be 10 percent. On the right is shown the impact of maximum use temperature allowable for the three-materials mix. The reduction in weight from conservative use temperature to projected maximum use temperature is also about 10 percent. Thus, the sensitivities involved are clearly indicated.

THERMAL-PROTECTION-SYSTEM WEIGHT IMPACTS

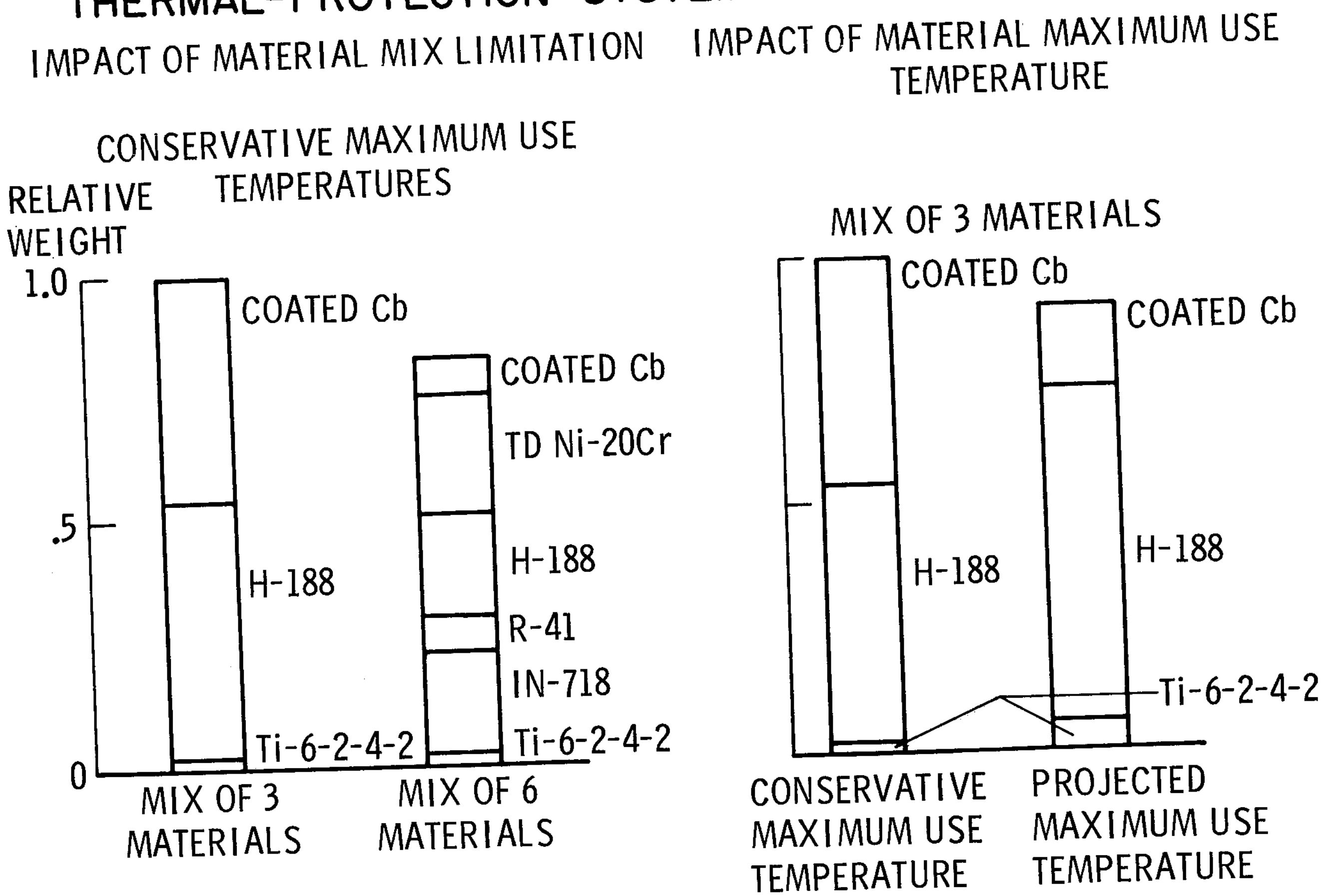

Figure 4

CYCLIC-CREEP PREDICTION LIMITATIONS

(Figure 5)

The prediction of the cyclic-creep behavior of heat-shield alloys is one universally recognized area where technology development is needed. Figure 5 considers the shuttle mission and current predictive capability for elemental specimen creep under conditions of the type shown at the top of the figure where temperature, load, and external pressure are varied in each test cycle to simulate boost, reentry, and cruise portions of an orbiter mission. A materials test under such conditions is referred to as a multiparameter materials test. The lower plots show cumulative creep strains as a function of the number of these simulated shuttle missions for coated columbium and René 41 nickel-base alloy. In both cases, the experimental data exhibited considerably more creep than had been predicted by using existing techniques. Designs must account for both the unconservative prediction and the typical creep-data scatter. These cases are also typical of those for other alloys. But this information must be put into context. Since creep is a power function of stress and an exponential function of temperature, a relatively small reduction in either will reduce creep significantly. Furthermore, heat-shield creep deformation is a "benign" problem in that it occurs slowly and is detectable by visual inspection between flights. Panels which exceed allowable deformation should be readily replaceable.

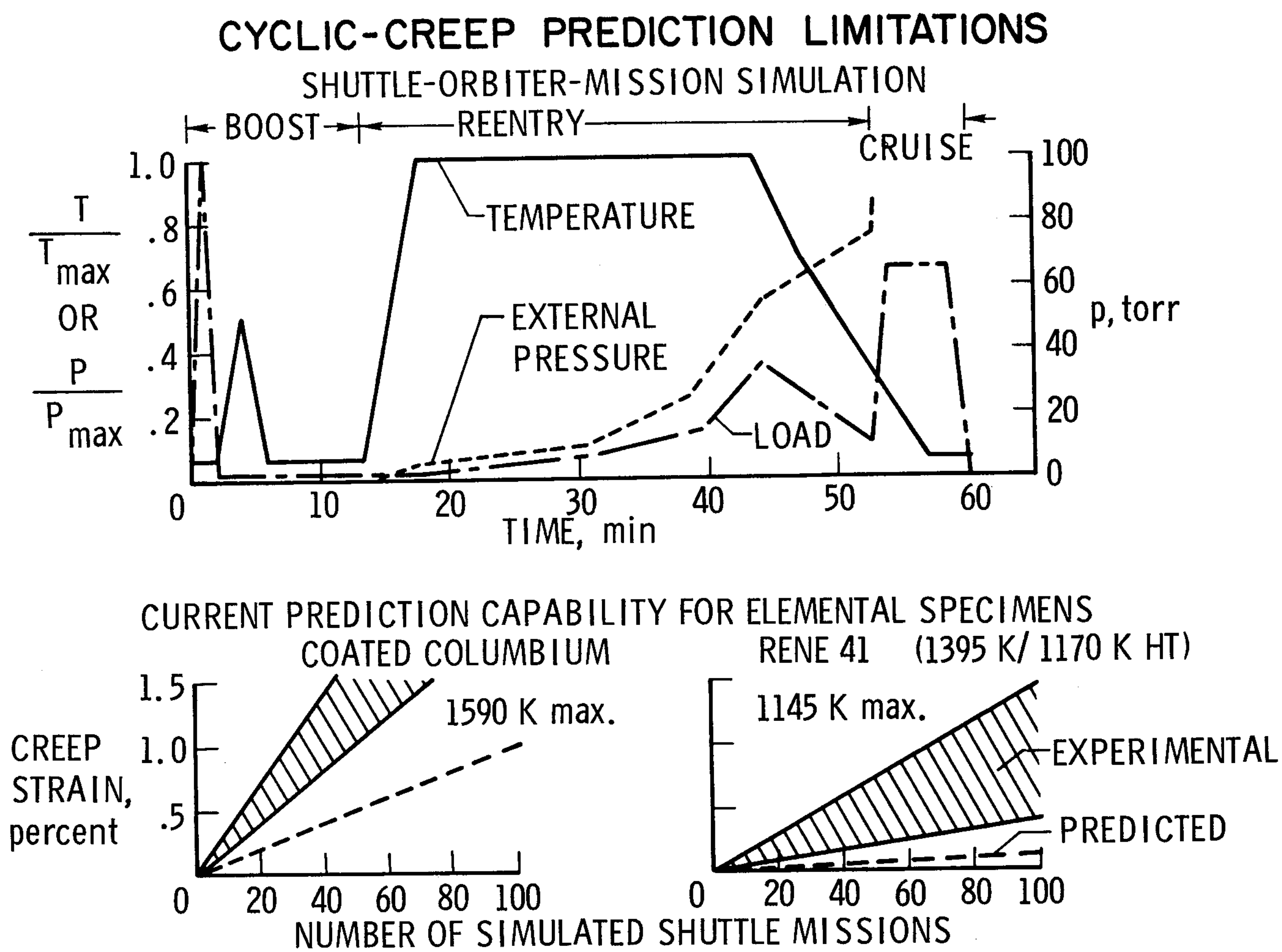
CYCLIC-CREEP PREDICTION LIMITATIONS
SHUTTLE-ORBITER-MISSION SIMULATION
BOOST
REENTRY
CRUISE
T/T max OR P/P max
1.0
.8
.6
.4
.2
0
10
20
30
40
50
60
TIME, min
100
80
60
40
20
0
p, torr
TEMPERATURE
EXTERNAL PRESSURE
LOAD
CURRENT PREDICTION CAPABILITY FOR ELEMENTAL SPECIMENS
COATED COLUMBIUM
1590 K max.
RENE 41 (1395 K/ 1170 K HT)
1145 K max.
CREEP STRAIN, percent
1.5
1.0
.5
0
20
40
60
80
100
EXPERIMENTAL
PREDICTED
NUMBER OF SIMULATED SHUTTLE MISSIONS

Figure 5

HYPERSONIC-AIRFLOW OXIDATION TEST RESULTS

(Figure 6)

The next two figures indicate that oxidation uncertainties have been largely resolved in the technology program. Figure 6 shows the effects of hypersonic-airflow oxidation tests on TD Ni-20Cr sheet specimens. The curves show substrate thickness decrease as a function of the number of $\frac{1}{2}$-hour test cycles at 1480 K (2200° F) and Mach 5. Information such as that shown by the upper curve has been generated at several laboratories and the data have been presented at several recent meetings. In comparison to static test data, they indicate that this alloy oxidizes faster in flowing airstreams at an oxygen partial pressure of 3 torr. However, when the partial pressure was lowered to 0.3 torr, oxidation rate was minimal. Both pressures (3 and 0.3 torr) are in the possible range of heat-shield operation. Two observations are to be made from these data: First, even in the worst case, substrate thickness loss was less than 0.050 mm (0.002 inch) in 50 test cycles; therefore, this material is certainly promising. Second, testing in simple static tests is not adequate to define the detailed behavior of the material for the proposed application.

HYPERSONIC-AIRFLOW OXIDATION TEST RESULTS

0.5-mm-THICK TD Ni-20Cr SHEET SPECIMENS; 1480 K; 0.5-hr TEST CYCLES

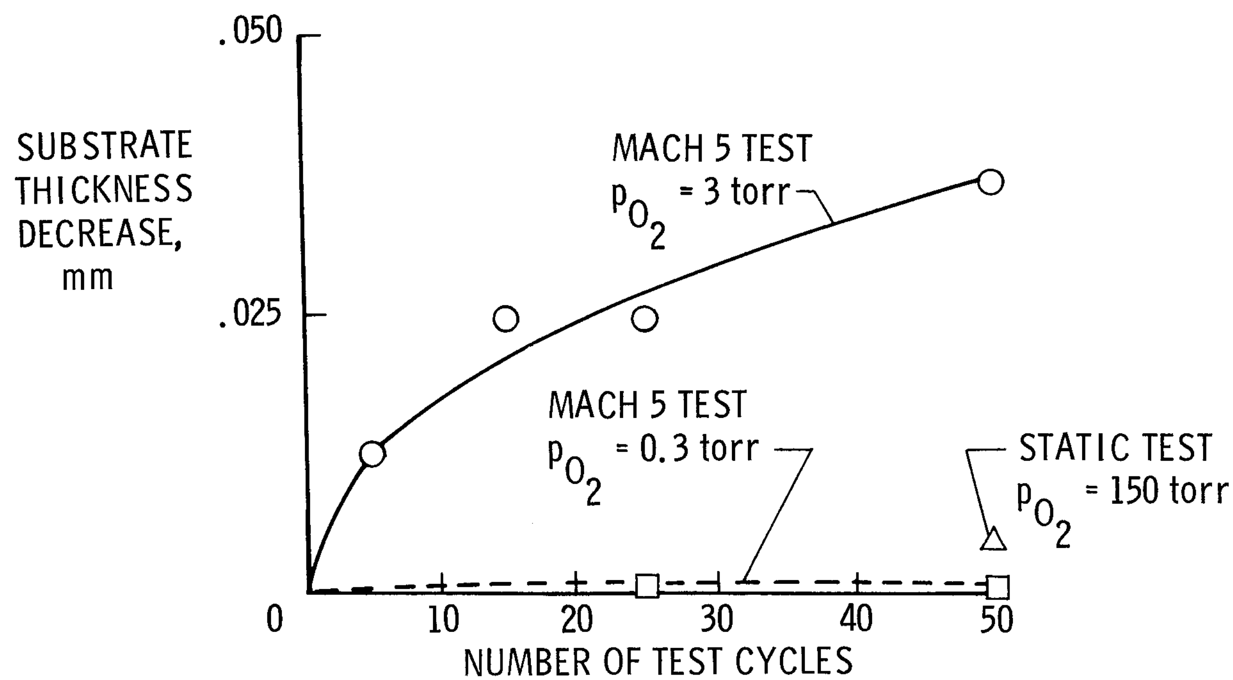

Figure 6

EFFECT OF DYNAMIC AIRFLOW ON FLAW GROWTH RATE

(Figure 7)

Another of the significant materials uncertainties has been the effect of coating flaws on columbium alloys during reentry. Figure 7 highlights research in this area. At the top of the figure are photographs of small coated Cb specimens tested in hypersonic airflow at Langley Research Center. The intentional defect is a 3-mm-diameter (1/8-inch) hole drilled through the specimen before the test. After the 10-cycle test at the conditions noted, the coating defect had shown negligible growth. At the bottom of figure 7 is a plot of flaw growth rate as a function of temperature. The data were generated under contract to NASA and were obtained under the conditions noted. It shows that at the maximum proposed use temperature 1590 K (2400° F), flaw growth rate is exceedingly small. Even for overshoots at temperatures up to 1700 K (2600° F), flaw growth rate is not excessive. More importantly, flaw sites on the exposed surface are easily visible many flight cycles before they are structurally significant.

EFFECT OF DYNAMIC AIRFLOW ON FLAW GROWTH RATE

COATED COLUMBIUM ; INTENTIONAL DEFECT

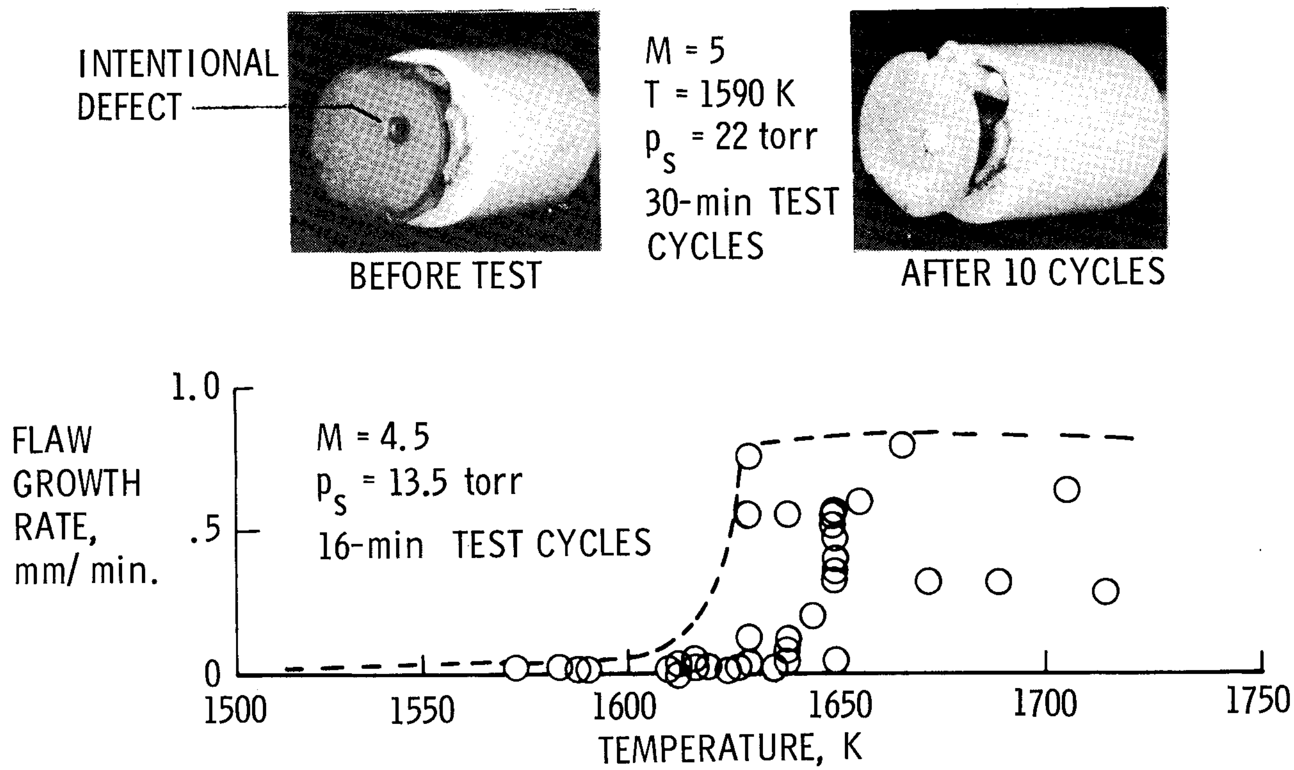

Figure 7

TYPICAL METALLIC TPS CONFIGURATIONS

(Figure 8)

The next part of this assessment concerns design concepts and configurations. Figure 8 indicates some of the diverse solutions proposed in current metallic TPS concepts. Illustrated are concepts under evaluation at NASA. At the upper left is a corrugation stiffened, lightly corrugated-surface panel supported on clips with spring-loaded overlapping joints. This panel is fabricated of a cobalt-base superalloy. At the upper right is a corrugation stiffened panel with beaded surfaces on post supports, of nickel-base superalloy. The tie-down joint utilizes the pi-strap concept. The panel at the lower left is fabricated of a titanium alloy and consists of a flat surface corrugation stiffened and on clip supports. Two kinds of joints are detailed, omega seals and overlapping sliding seals. At the lower right is a nickel-base alloy panel with a simple corrugated skin design. There are clip supports and a simple overlapping joint, but it is backed by a full bellows seal if hot gas intrusion through the joint becomes significant. Inspection methods for any of these concepts do not appear to be beyond the state of the art and refurbishment by removal and replacementof mechanical fasteners, joint seals, and shields seems straightforward.

TYPICAL METALLIC TPS CONFIGURATIONS

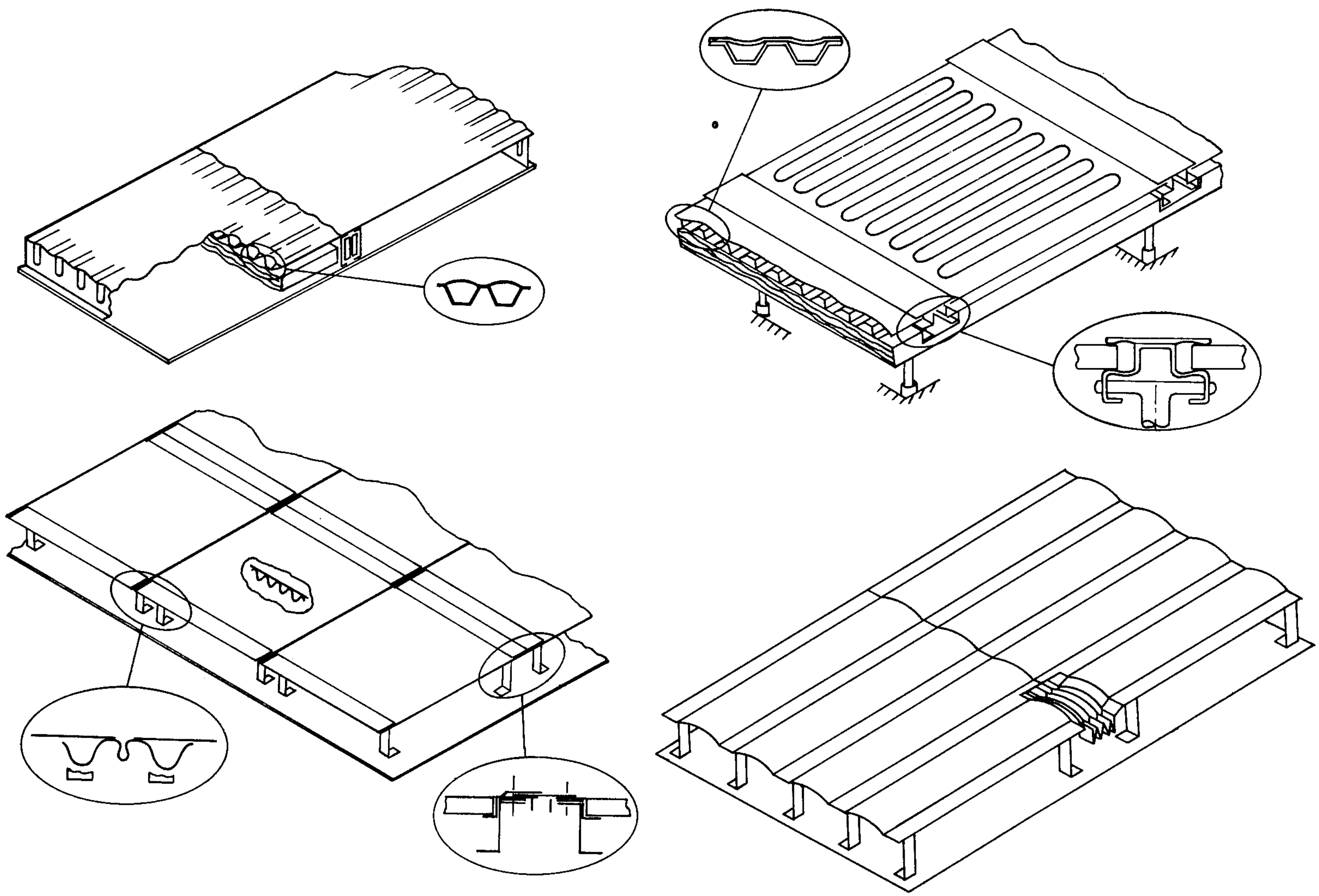

Figure 8

MICRO-QUARTZ (64 kg/m^3) INSULATION PACKAGES
(Figure 9)

Lightweight fibrous insulations such as Micro-Quartz, Dyna-Flex, and Zircar, depending on maximum TPS use temperature, have been shown to be adequate for these systems. In figure 9 are insulation packaging concepts using 64 kg/m^3 (4 lb/ft^3) Micro-Quartz, 5 cm (2 inches) thick. The quartz cloth envelope, inconel foil envelope, and stainless-steel screen envelope packages have similar unit weights. The inconel foil envelope will prevent moisture ingress whereas the quartz cloth and screen envelopes will not perform this function. The basic mass of the insulation without the packaging is 3.26 kg/m^2 (0.667 lb/ft^2). Now that the concepts for the various TPS components have been shown, examples of panels will be shown in figures 10 and 11 to indicate the status of realistic hardware fabrication.

MICRO-QUARTZ (64 kg/m^3) INSULATION PACKAGES

PACKAGE WEIGHTS BASED ON 5-cm THICKNESS

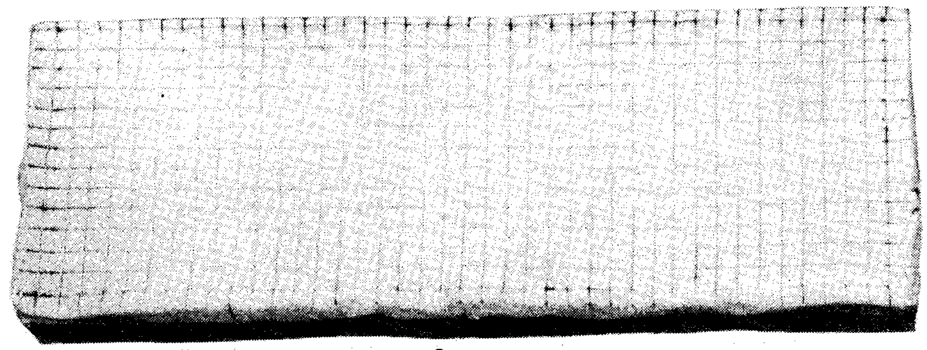

4.2 kg/ m^2 WITH
QUARTZ CLOTH ENVELOPE

4.4 kg/ m^2 WITH
INCONEL FOIL ENVELOPE

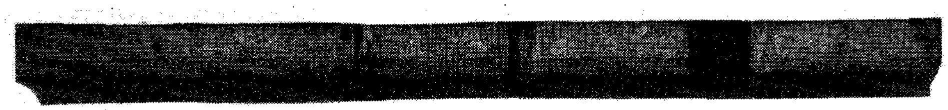

4.0 kg/ m^2 WITH STAINLESS-STEEL
SCREEN ENVELOPE

Figure 9

RENÉ 41 NICKEL-BASE-ALLOY TPS PANELS

(Figure 10)

Figure 10 shows a montage of two similar 107 cm × 152 cm (42" × 60") René 41 nickel-base-alloy corrugated-surface panels with single and double clip supports and inconel foil packaged insulation. These panels were designed and fabricated in-house at NASA and are being subjected to a variety of evaluation tests, which will be described subsequently. These panels (including insulation, supports, seals, and fasteners) weigh 10.74 kg/m^2 (2.20 lb/ft^2).

RENÉ 41 NICKEL-BASE-ALLOY TPS PANELS

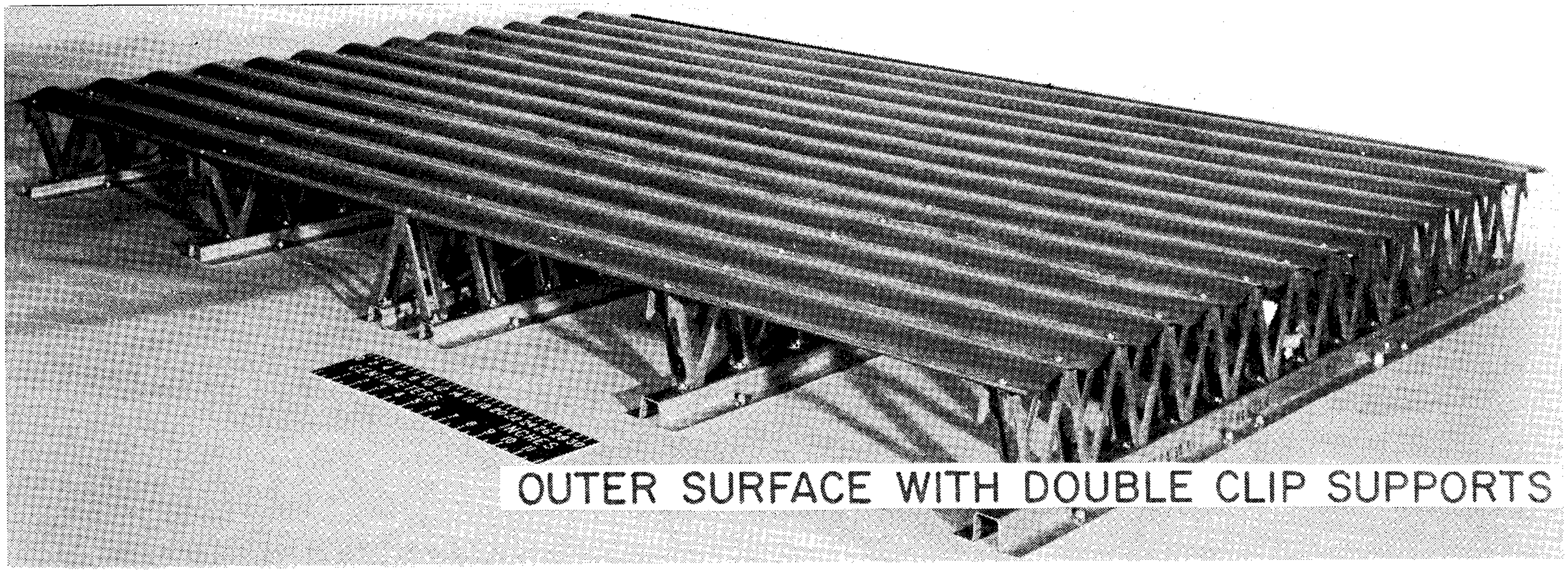

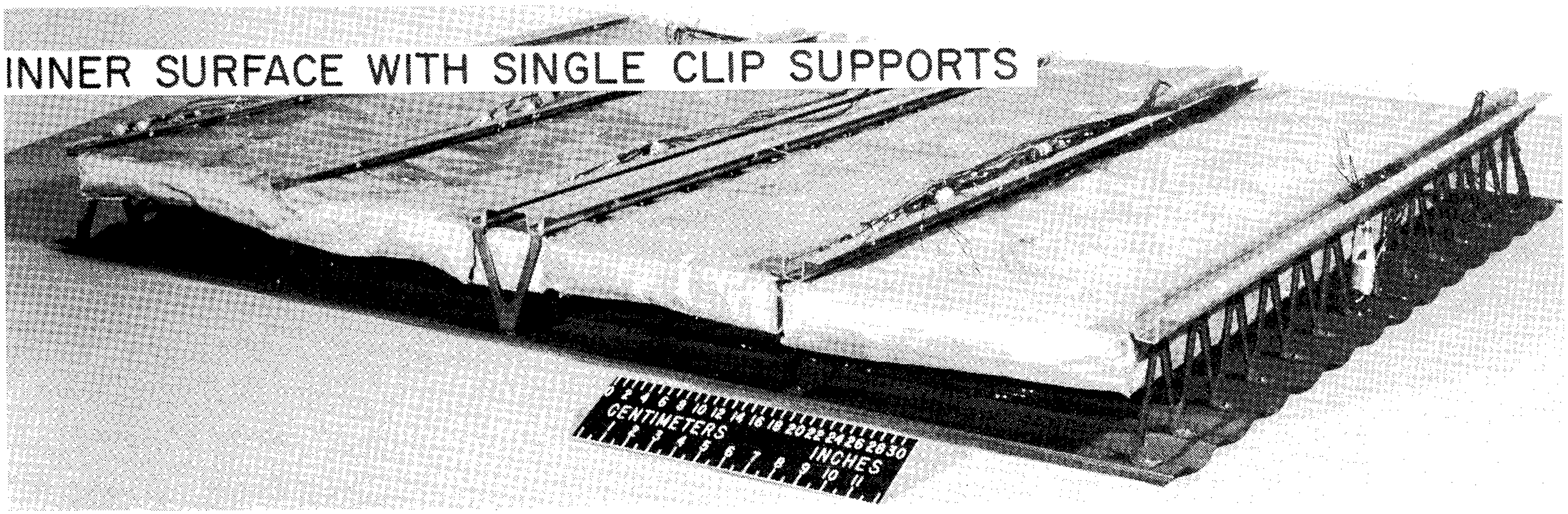

Figure 10

L-605 COBALT-BASE-ALLOY TPS PANELS

(Figure 11)

Figure 11 shows an L-605 cobalt-base-alloy panel array fabricated by a contractor for NASA tests. Panels of this design have successfully withstood 20 simulated shuttle heating and loading tests to 1255 K (1800° F) plus five tests to 1310 K (1900° F). These panels, again including everything from heat shield to substructure, weigh 12.94 kg/m^2 (2.65 lb/ft^2).

To summarize this design concept part of the assessment, it appears that configurations and fabricated flight-weight hardware are available for metallics. Elemental-specimen, subsize-panel, and system-concept evaluation tests, currently in progress, should reveal the most promising systems and design details.

L-605 COBALT-BASE-ALLOY TPS PANELS

Figure 11

SHUTTLE SURFACE PANEL EVALUATION PROGRAM

(Figure 12)

The last part of the assessment covers testing and evaluation. It was previously indicated that complex materials tests are being conducted under the technology program. Multiparameter simulation tests are also being conducted on small heat-shield segments. However, systems tests for concept evaluation are much more complex.

Figure 12 outlines the shuttle surface panel evaluation program at Langley. Full-scale panels such as the one illustrated in the center of this figure and those in figures 10 and 11 will be subject to cyclic boundary-layer noise tests, vibration tests, varied analyses, flutter tests, Mach 7 wind-tunnel integrity tests, and service-life tests in the facilities shown in figure 12. This program will provide data (1) to evaluate TPS performance in multiple discipline areas, (2) to assess validity of complex analytical tools, and (3) to define problem areas in existing designs and to perturb the design concepts to solve these problems. NASA and industry TPS configurations are presently undergoing pre-tunnel tests to determine panel vibration modes and frequencies and to define panel stiffness and support characteristics for use in correlating data with theory.

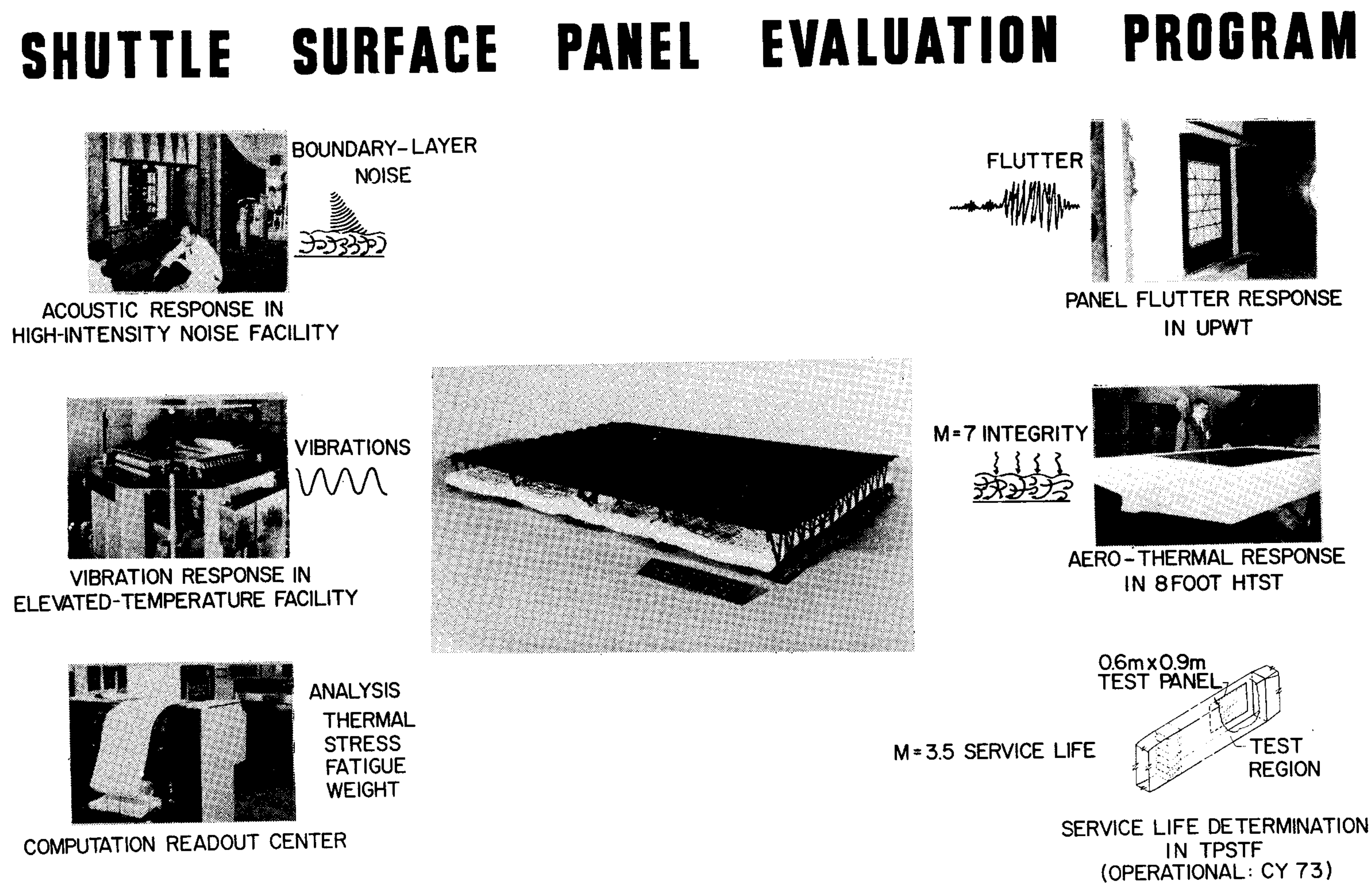
SHUTTLE SURFACE PANEL EVALUATION PROGRAM
BOUNDARY-LAYER NOISE
ACOUSTIC RESPONSE IN HIGH-INTENSITY NOISE FACILITY
VIBRATIONS
VIBRATION RESPONSE IN ELEVATED-TEMPERATURE FACILITY
ANALYSIS
THERMAL
STRESS
FATIGUE
WEIGHT
COMPUTATION READOUT CENTER
FLUTTER
PANEL FLUTTER RESPONSE IN UPWT
M=7 INTEGRITY
AERO-THERMAL RESPONSE IN 8FOOT HTST
0.6m x 0.9m TEST PANEL
M=3.5 SERVICE LIFE
TEST REGION
SERVICE LIFE DETERMINATION IN TPSTF (OPERATIONAL: CY 73)

Figure 12

THEORETICAL FLUTTER BOUNDARIES FOR TWO METALLIC TPS DESIGNS

(Figure 13)

In the area of panel flutter, considerable progress has been made in theoretical development, and work is underway to define the potential benefits of boundary-layer thickness in preventing flutter at transonic speeds. One of the most critical problems in metallic TPS design from the panel-flutter standpoint is the adverse effects of flow orientation. This is indicated in figure 13, which plots the dynamic pressure at flutter q over the Mach number parameter as a function of flow orientation for the corrugation-stiffened design in figure 11 and the single-skin TPS design in figure 10. Corrugation-stiffened panels are inherently weak at the supports and the measured value of the deflectional spring constant k_D is used in the flutter theory.

The capability to resist flutter is shown by the solid curves. At zero flow angle, both panels have flutter margins of more than two orders of magnitude when compared with the maximum value of the dynamic-pressure parameter for shuttle ascent.

For any arbitrary flow orientation, the corrugation-stiffened panel has ample capability to resist flutter within the dynamic-pressure envelope of shuttle; however, the single-skin concept penetrates the envelope even at small flow angles. The influence of boundary layer, as well as structural and aerodynamic damping, will raise the flutter boundary curve; but the flutter margin desired may not be possible without a structural weight penalty.

These theoretical trends are planned to be evaluated in an extensive experimental study this summer at the Langley Unitary Plan wind tunnel.

THEORETICAL FLUTTER BOUNDARIES FOR TWO METALLIC TPS DESIGNS

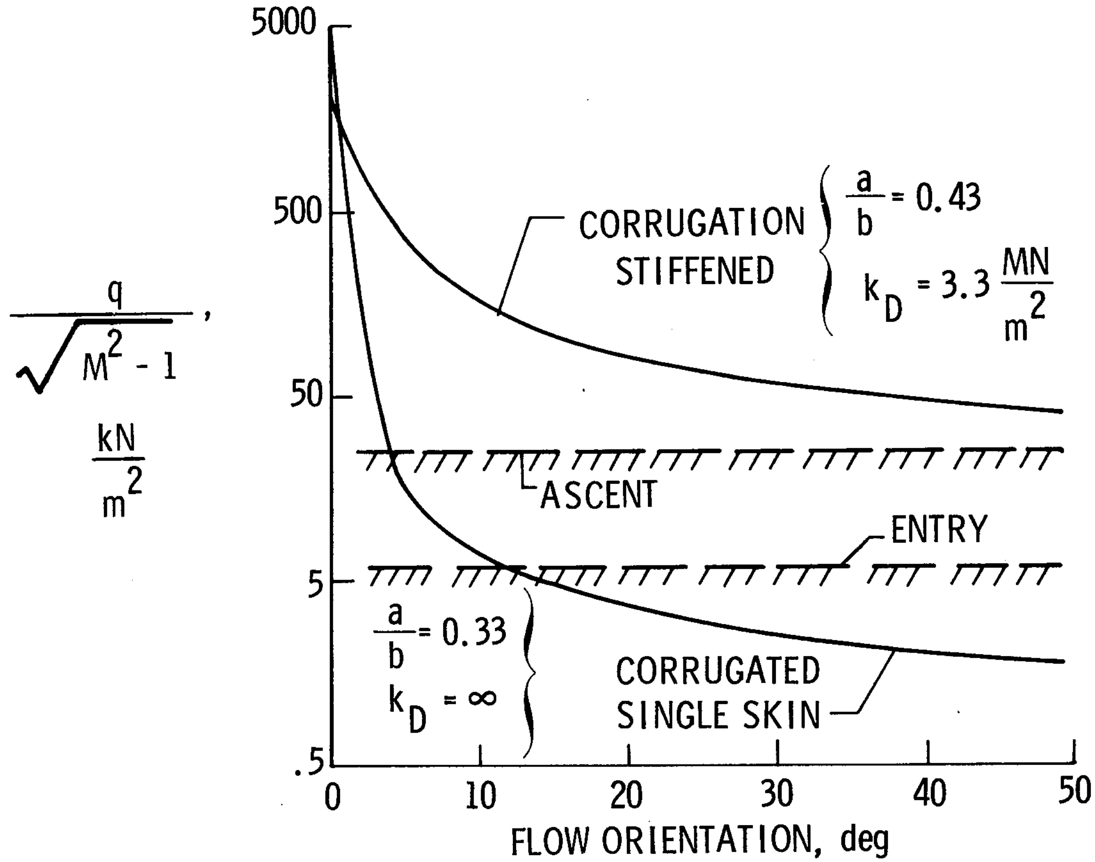

Figure 13

STRUCTURES-TPS TEST FACILITY CAPABILITIES

(Figure 14)

The structural integrity tests will be run in the Langley 8-foot high-temperature structures tunnel (HTST). The operating envelope of this facility is shown in figure 14, which is a plot of panel surface pressure as a function of panel equilibrium temperature.

A short film was made to illustrate the nature and complexity of these structural integrity tests. The panel fixture for these tests accommodates TPS panels or arrays of panels 107 cm (42 inches) wide by 152 cm (60 inches) long. As shown in the film, just ahead of the leading edge of the panel, a row of small spheres trips the boundary layer to generate fully turbulent flow over the test surface. Aerodynamic fences extending 7.6 cm (3 inches) above the surface provide uniform one-dimensional flow. Spring-loaded flapper valves vented to the cavity behind the panel maintain pressure differential within 3.4 kN/m^2 (1/2 psi) during rapid tunnel startup and shutdown. The cavity pressure is also controlled during a test to simulate the trajectory pressure loading history. Prior to tunnel startup, the panel is below the test section being preheated with banks of quartz lamps to a prescribed temperature history. The tunnel is started, the lamps extracted, and the panel fixture inserted into the stream and pitched to an angle of attack to provide appropriate heating rate and differential pressure loading. After the Mach 7 test is completed, the fixture is withdrawn from the stream and the controlled cooling cycle begins. Although test time in the HTST is limited to 200 seconds per Mach 7 cycle, these tests provide data on local hot spots, hot-gas flow at joints, heat shorts, insulation efficiency, and life expectancy. Temperatures measured over the panel surface, around heat sinks, and through the insulation provide data for supporting thermal analysis and thermal stress analysis.

Service-life verification tests of full-scale TPS will be conducted in the Langley thermal protection system test facility (TPSTF). Its operating envelope is also indicated in figure 14. The TPSTF will accommodate panels up to 0.61 m (2 ft) by 0.91 m (3 ft) and will simulate heating rate, static pressure, and differential pressure over the entire entry trajectory. Running time will be up to 2000 seconds. This facility (which is expected to be operational in the fall of 1973) should provide the environment for verification of TPS designs.

STRUCTURES – TPS TEST FACILITY CAPABILITIES

LaRC

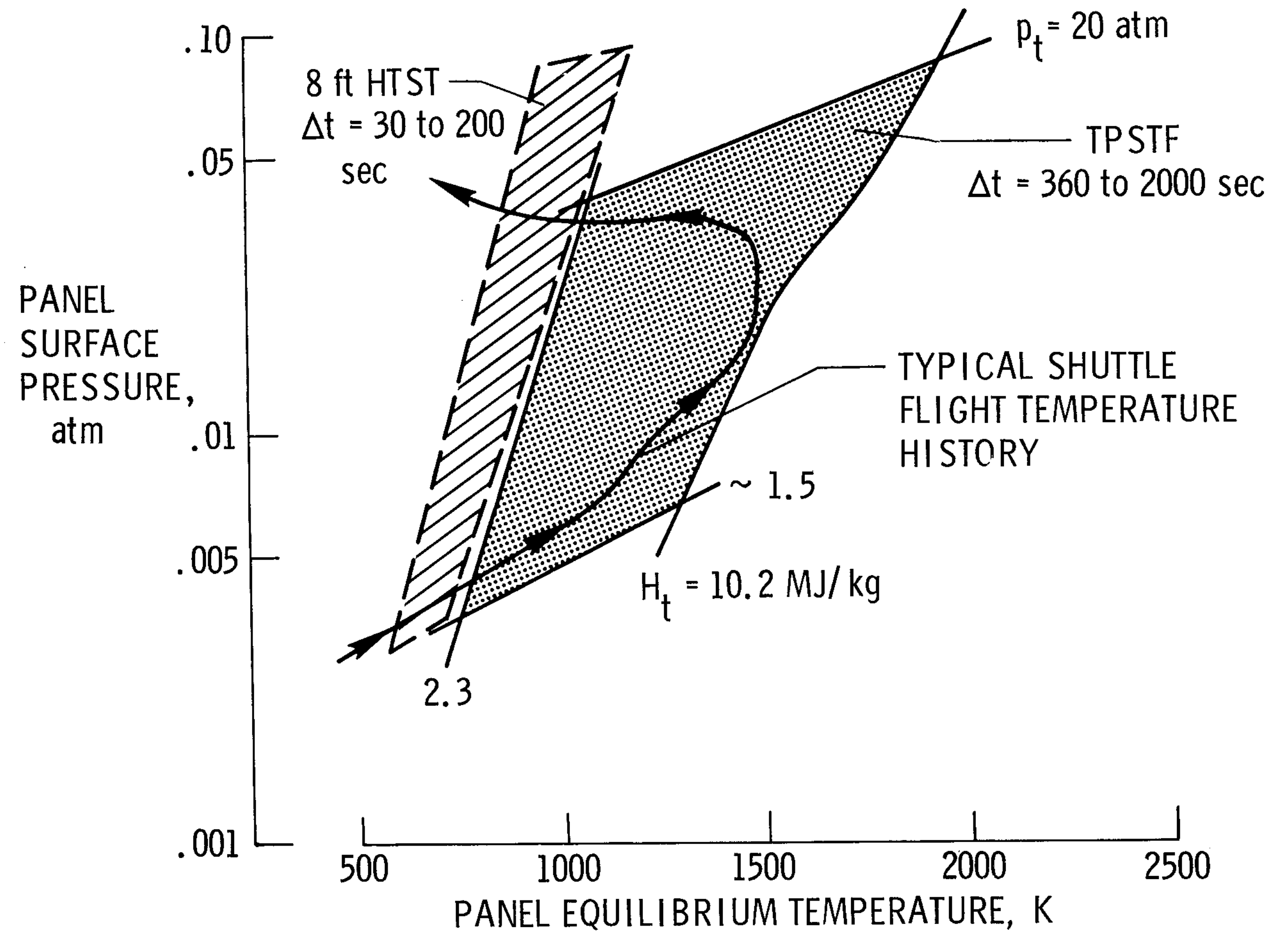

Figure 14

TPS DEVELOPMENT AND EVALUATION PROGRAMS FOR ADVANCED HEAT-SHIELD MATERIALS

(Figure 15)

In addition to the in-house NASA evaluation work on TPS of currently available materials systems just described, NASA is funding efforts to develop optimized TPS of advanced materials. Figure 15 outlines these programs. The materials under study are coated columbium alloys and TD Ni-20Cr. The approach includes (1) analytical and experimental studies of materials behavior to provide preliminary design properties, (2) design, fabrication, and testing of small-size TPS assemblies to select the best configuration and verify the design, and (3) full-size, full-scale design, fabrication, and test to demonstrate proof of concept and generate cost and performance information. The scope of the evaluation tests includes materials mechanical properties, multiparameter simulation, creep, and residual properties; special tests such as lightning and micrometeoroid exposure; and the last three items (TPS vibration and acoustics, TPS thermostructural, and TPS in hypersonic airflow), which are similar to the ones previously described in figure 12.

In summing up this part of the assessment, testing methods and facilities appear adequate except in one area, full-size qualification tests.

TPS DEVELOPMENT AND EVALUATION PROGRAMS FOR ADVANCED HEAT-SHIELD MATERIALS

MATERIALS

- COATED COLUMBIUM ALLOYS
- TD Ni - 20Cr

APPROACH

- MATERIALS STUDIES - PRELIMINARY DESIGN PROPERTIES
- SMALL-SIZE TPS - CONFIGURATION SELECTION AND DESIGN VERIFICATION
- FULL-SIZE TPS - PROOF OF CONCEPT DEMONSTRATION

SCOPE OF EVALUATION TESTS

- MATERIALS MULTIPARAMETER SIMULATION AND RESIDUAL PROPERTY
- LIGHTNING AND MICROMETEOROID EXPOSURE
- TPS VIBRATION AND ACOUSTICS
- TPS THERMOSTRUCTURAL
- TPS IN HYPERSONIC AIRFLOW

Figure 15

ASSESSMENT OF REMAINING UNCERTAINTIES IN RADIATIVE METALLIC TPS FOR SHUTTLE (Figure 16)

Figure 16 turns to the future in an assessment of the remaining uncertainties in radiative metallic thermal protection systems for shuttle. These are listed under the areas covered in this paper. In the current technology program, efforts are underway to establish preliminary design properties, to improve our ability to predict cyclic creep, to assess structural integrity of TPS concepts, and in concept evaluation testing.

The items listed under future requirements are dependent on the final vehicle design and therefore are not considered to be part of a technology program although they will need attention. They include better definition of environmental factors, materials design data base for the actual materials used, structural fasteners, joints and seals for specific designs, and systems qualification testing.

ASSESSMENT OF REMAINING UNCERTAINTIES IN RADIATIVE METALLIC TPS FOR SHUTTLE

UNCERTAINTY AREA	CURRENT TECHNOLOGY PROGRAM	FUTURE REQUIREMENT
ENVIRONMENT		●
MATERIALS		
DESIGN DATA BASE	●	●
PREDICTION OF CYCLIC CREEP	●	
STRUCTURAL INTEGRITY		
CONCEPTS	●	
FASTENERS	●	●
JOINTS AND SEALS		●
EVALUATION AND TESTING		
CONCEPT EVALUATION	●	
SYSTEM QUALIFICATION		●

Figure 16

CONCLUDING REMARKS

The objective of the technology program was to generate enough information to permit designers to make rational decisions on materials and the structural integrity of configurations through concept evaluation and testing studies. It is believed that the previous work and continuation of the present programs will satisfy that objective.

TPS TRADE STUDIES ON ABLATORS AND REUSEABLE SURFACE INSULATION

By George Strouhal and Donald M. Curry
NASA Manned Spacecraft Center
Houston, Texas

INTRODUCTION

The Space Shuttle Thermal Protection System (TPS) must be designed to perform multiple missions involving the environments of launch, orbit, entry, and ground handling. The successful development of a minimum weight/low cost reuseable shuttle vehicle is highly dependent on a TPS that will achieve a balanced performance with respect to thermal insulation efficiency, load-carrying capability, reuse, and sensitivity to entry heating environments for different mission profiles. The total TPS weight is the most significant design parameter.

Analytical trade studies are presented that consider passive TPS configurations using the following material categories:

a. Reuseable Surface Insulation (RSI) - surface-coated rigidized ceramic fiber.

b. Low-density charring ablators.

c. Carbon-carbon and high-density ablators for leading edge areas.

It is emphasized that this paper explores how TPS weight is affected by variations in entry trajectories and material thermal characteristics. Thermal-physical properties used in the analyses were obtained from available reports and the trajectory data was furnished by the Mission Planning and Analysis Division, Manned Spacecraft Center.

SPACE SHUTTLE ORBITER ANALYSIS BASELINE (Figure 1)

The shuttle orbiter vehicle selected as the analysis baseline is characterized by a 60° leading edge-sweep delta-wing planform with a straight side wall fuselage. This vehicle is a variation on MSC's 040A configuration with a fuselage length of 33.5 m (110 ft) and a wing span of 22.6 m (74 ft). Vehicle systems were sized for the following requirements:

a. External propellant tanks

b. 4.6 m (15 ft) diameter by 18.3 m (60 ft) cargo bay

c. 29 484 kg (65 000 lb) payload in due-east orbit

d. 18 144 kg (40 000 lb) payload in polar orbit

e. Aerodynamic flyback and landing

f. 2037 km (1100 N. Mi.) cross-range capability

This figure also illustrates major surface areas which require thermal protection.

SPACE SHUTTLE ORBITER ANALYSIS BASELINE

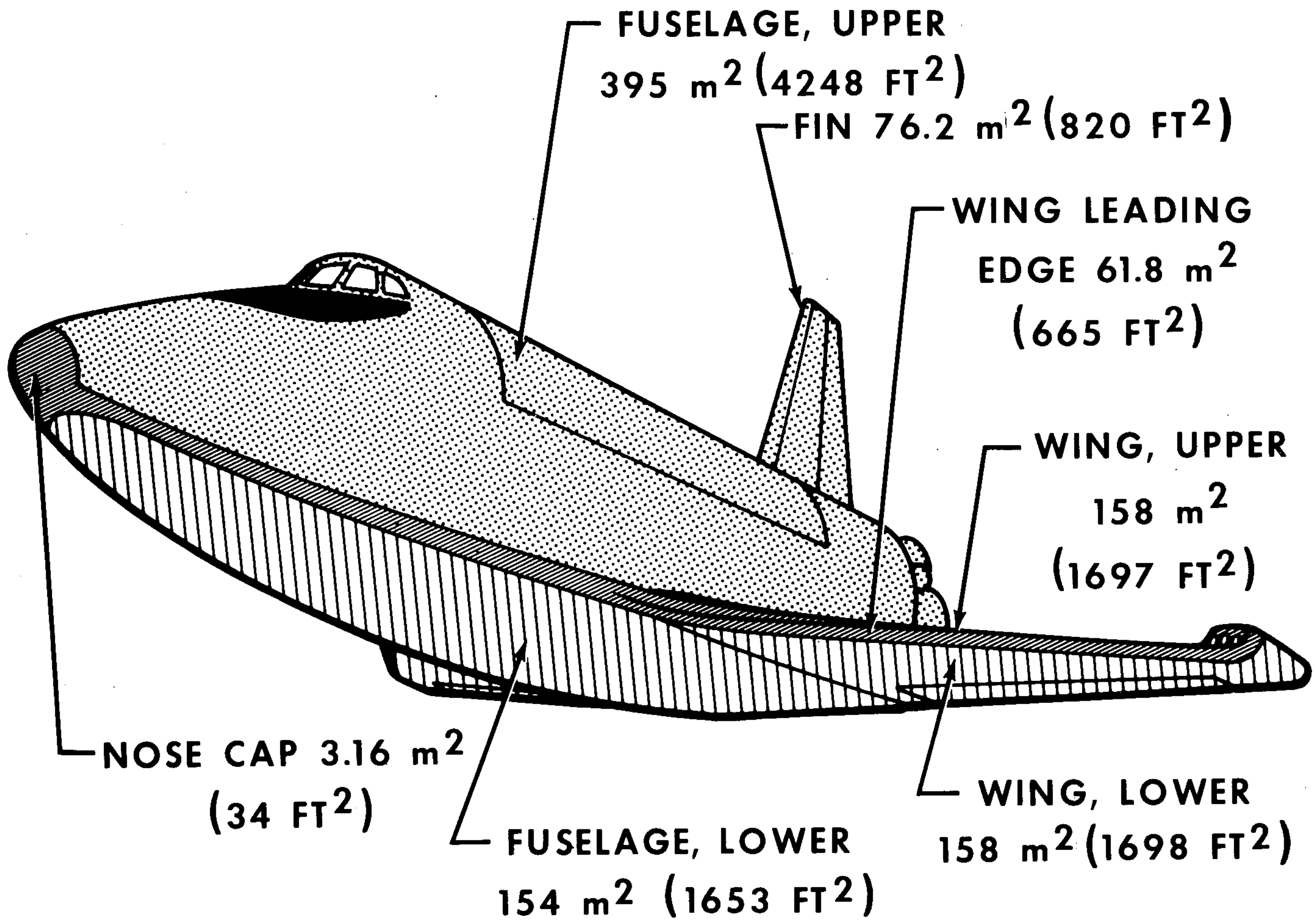

Figure 1

HEATING-RATE HISTORY FOR TEMPERATURE-CONSTRAINT-SHAPED TRAJECTORIES (Figure 2)

Heating-rate histories (based on a 0.305 m [1 ft.] radius sphere) for a long down-range and a short down-range trajectory illustrate the variation in heating-rate level, duration of entry, and total heat loads investigated in this study. Variation in heating rate as a function of down-range distance was obtained by generating temperature constrained, "g" load limited, entry trajectories for a constant cross range of 2037 km (1100 N. Mi.). Entry guidance logic was based on a constant 30° angle of attack with a modularized bank angle to achieve cross range without exceeding specified heating and load limits. Temperature constraints of 1367K (2000°F) and 1645K (2500°F) were applied to a lower surface and located near the nose at $X/L = 0.12$. All trajectories were initiated from a 185 km (100 N. Mi.) polar orbit at a flight path angle of -1.45° and constrained to a "g" load limit of 1.5.

HEATING-RATE HISTORY FOR TEMPERATURE-CONSTRAINT-SHAPED TRAJECTORIES

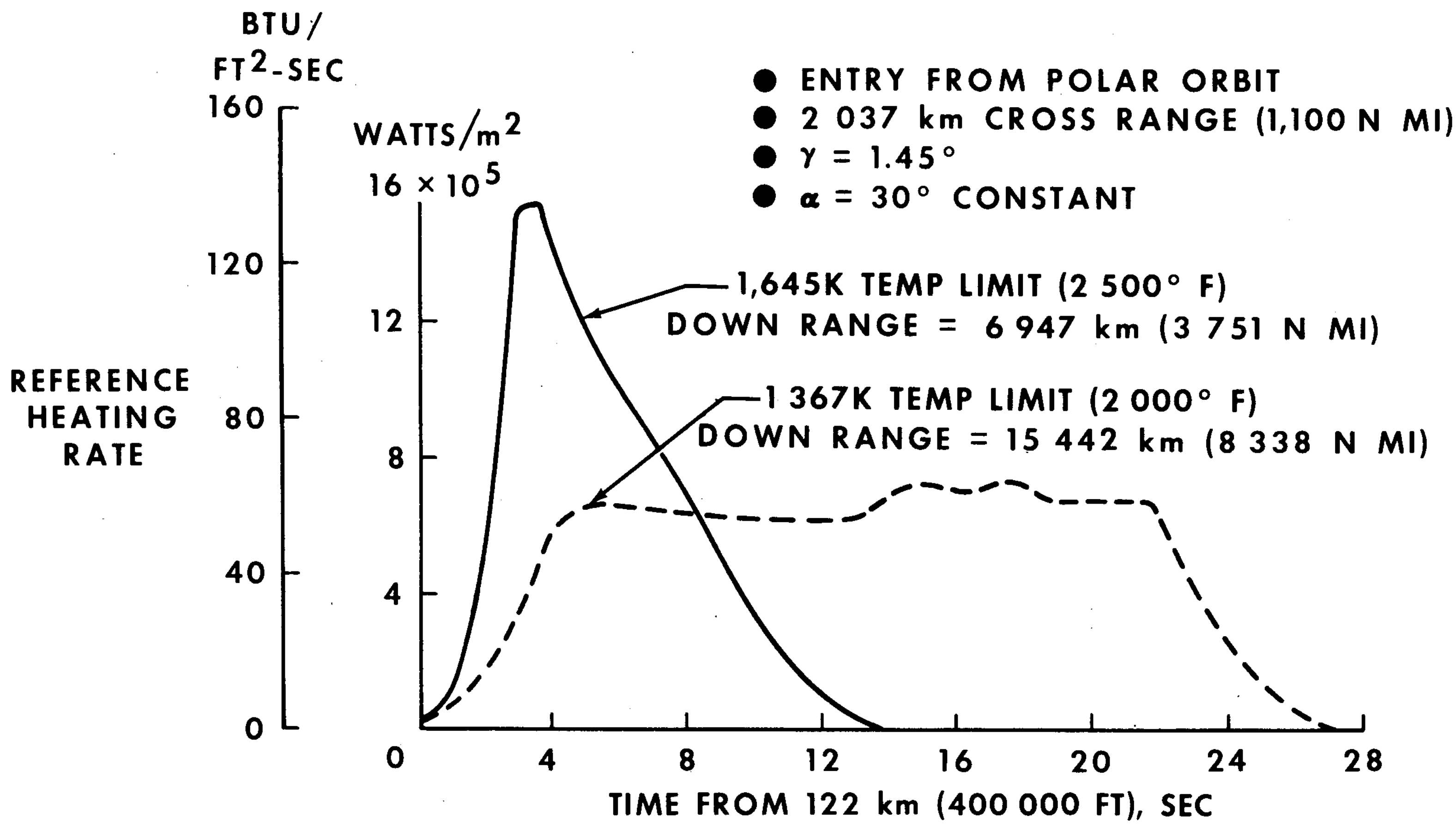

Figure 2

NORMALIZED HEATING-RATE DISTRIBUTIONS (Figure 3)

Local heating-rate distributions over the orbiter wetted surface for a 30° angle-of-attack entry are shown. Local heating rates have been normalized to a 0.305 m (1 ft) radius sphere and represent the distribution for laminar flow during hypersonic flight.

In order to perform TPS weight predictions, the vehicle area was divided into appropriate regions so that an average local heating rate could be assigned to each surface region.

NORMALIZED HEATING-RATE DISTRIBUTIONS

REFERENCE - .305 m (1 FT) RADIUS SPHERE

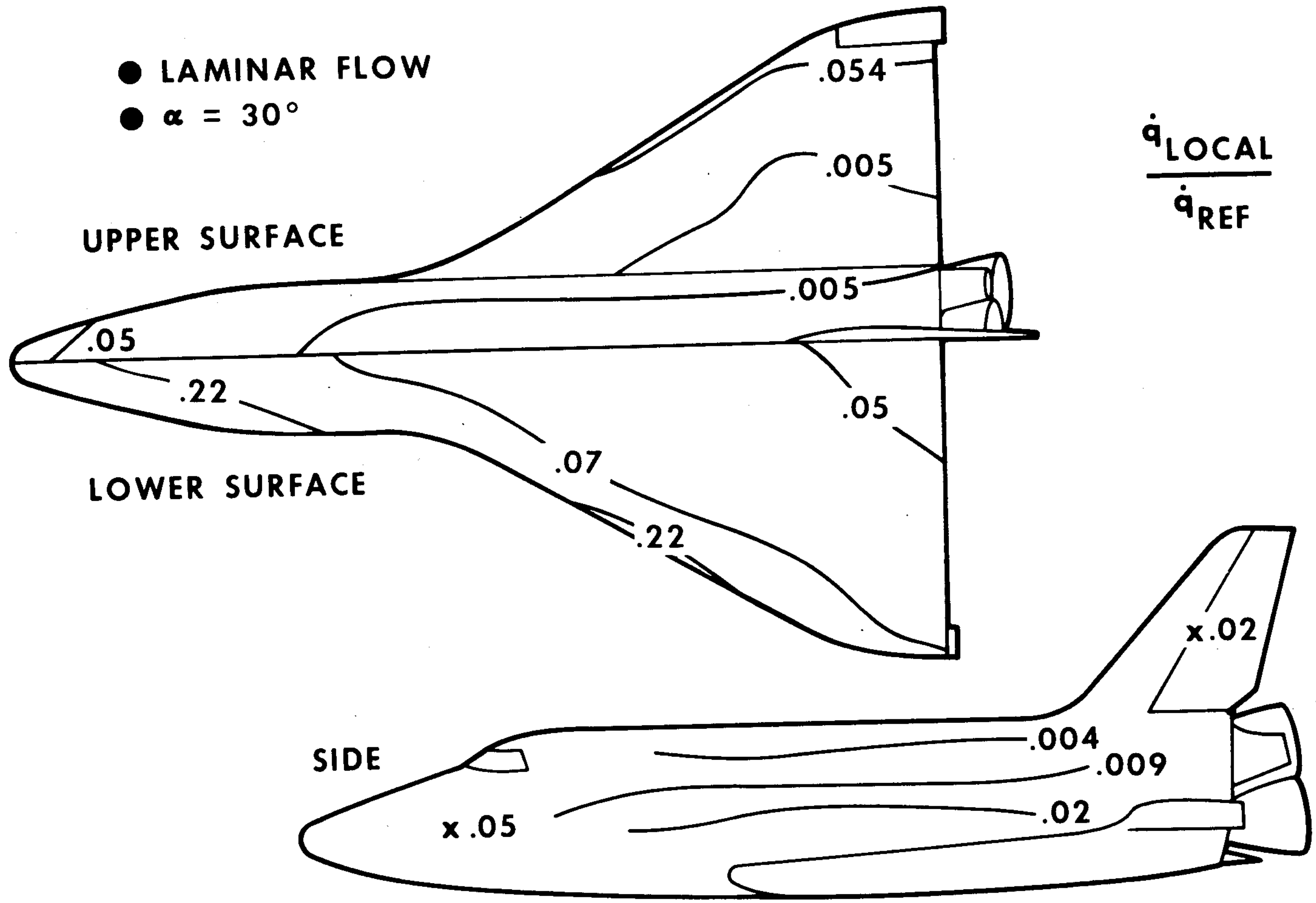

Figure 3

HEATING RATE/AREA DISTRIBUTION (Figure 4)

Data shown in the previous figure are plotted in terms of surface area and heating-rate ratios. The major surface areas; upper, side, and lower, are shown in relation to the percent of area at or above a $\dot{q}_{local}/\dot{q}_{ref}$ ratio.

Although peak heating rates are of importance in establishing material reuseability, the TPS weight is more sensitive to material performance in the moderate and low heating-rate environments. As can be seen, only 30 percent of the surface experiences a heating-rate ratio greater than approximately 0.06.

HEATING RATE/AREA DISTRIBUTION

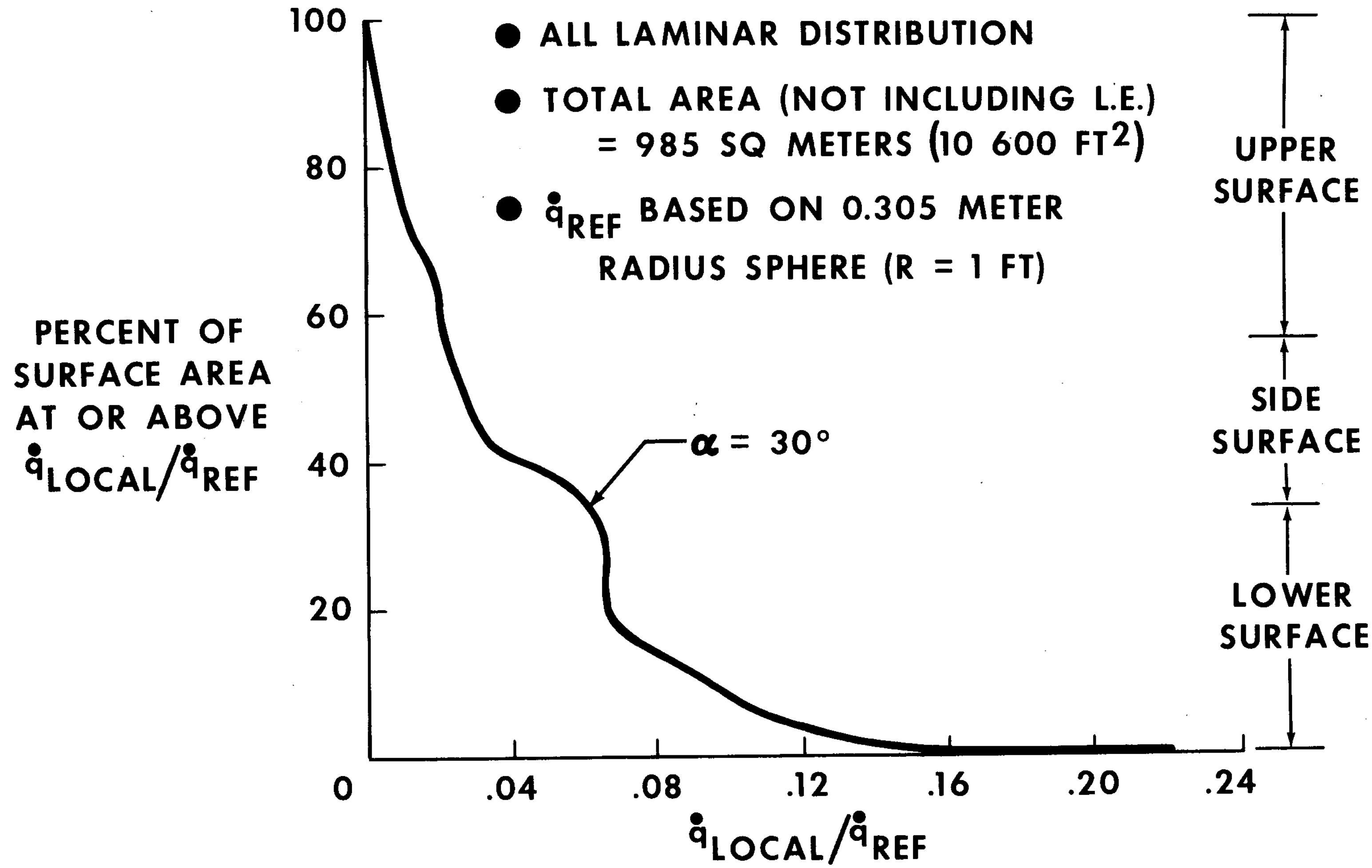

Figure 4

FLIGHT BOUNDARIES FOR CONSTANT 30° ANGLE OF ATTACK (Figure 5)

To minimize the weight of the TPS, it is desirable to minimize heat load or entry time without exceeding prescribed surface temperature or "g" load limits. A typical operational corridor on a h-V plot is shown for entries from a 185 km (100 N. Mi.) orbit with an inclination of 55° to the equatorial plane. The overshoot boundary is defined by the equilibrium glide which represents a trajectory stability limit. The undershoot boundary is a composite of two constraints defined by a temperature limit at the high entry velocity and by the "g" load limit at lower velocities. Temperature boundaries of 1478K (2200°F) and 1645K (2500°F) were chosen as being representative of RSI reuse temperature limits. A lower fuselage location, X/L = 0.12, was determined to be the most restrictive of the 22 body locations investigated.

The flat portion of the temperature boundary at constant altitude represents flight conditions where transition from laminar to turbulent flow occurs for the two temperature limits selected.

Changing the TPS surface temperature constraint from 1645K (2500°F) to 1478K (2200°F) reduces the altitude depth of the entry corridor by approximately 6096 m (20 000 ft.).

Although the thermal boundaries shown are configuration dependent, the basic trends are applicable to other configurations.

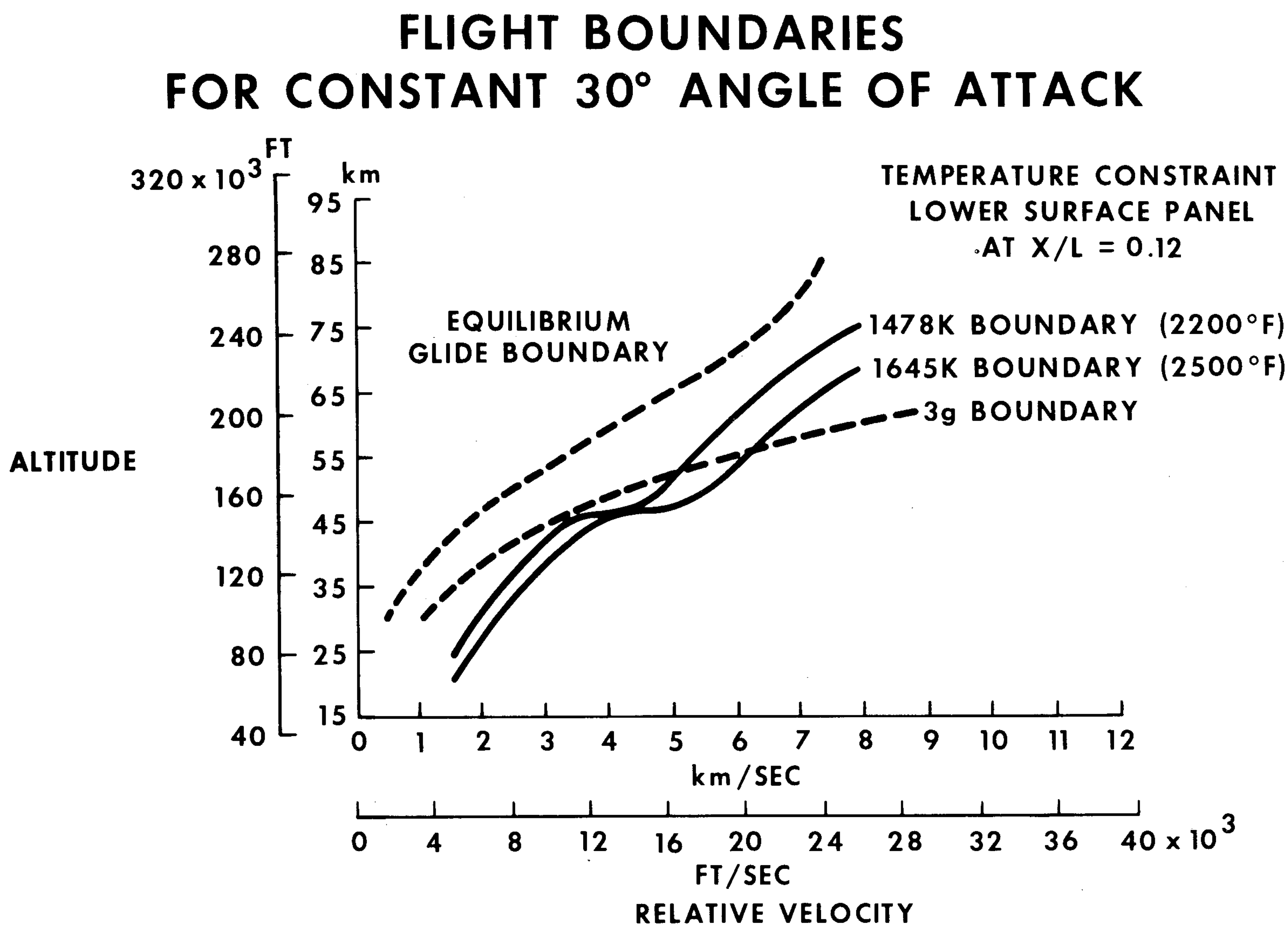
FLIGHT BOUNDARIES
FOR CONSTANT 30° ANGLE OF ATTACK
ALTITUDE
FT
320 x 10³
280
240
200
160
120
80
40
km
95
85
75
65
55
45
35
25
15
EQUILIBRIUM
GLIDE BOUNDARY
TEMPERATURE CONSTRAINT
LOWER SURFACE PANEL
AT X/L = 0.12
1478K BOUNDARY (2200°F)
1645K BOUNDARY (2500°F)
3g BOUNDARY
0 1 2 3 4 5 6 7 8 9 10 11 12
km/SEC
0 4 8 12 16 20 24 28 32 36 40 x 10³
FT/SEC
RELATIVE VELOCITY

Figure 5

THERMAL PROTECTION SYSTEM CONFIGURATIONS (Figure 6)

The TPS configurations utilized in this study for leading edges and major surface areas are shown. Only oxidation inhibited carbon-carbon, RSI, and ablators were considered. The leading edge is an aerodynamic fairing attached to the wing front spar and consists of a low-temperature structural shell protected by an ablator or a carbon-carbon high-temperature structural shell attached to an intermediate metallic structure. As shown, the TPS for the major surface areas consisted of ablator or RSI attached by silicone elastomeric bond to an aluminum primary structure. An elastomeric foam pad serves to isolate the RSI from strain in the primary structure.

Although TPS weight depends on the material capabilities coupled with interactions to primary structures, vehicle configuration, and mission profiles, this study considers only material and entry trajectory variables.

THERMAL PROTECTION SYSTEM CONFIGURATIONS

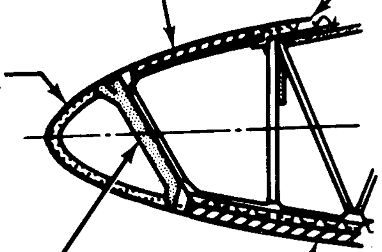

LEADING EDGE

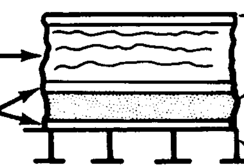

DIRECT ATTACHMENT

MAJOR SURFACE AREA

TRADE STUDY

VARIABLE	LEADING EDGE	MAJOR SURFACE AREA
MATERIAL SELECTION	X	X
PRESSURE DEPENDENT PROPERTIES		X
INITIAL TEMPERATURE		X
TRAJECTORY	X	X

Figure 6

RSI WEIGHT SENSITIVITY TO PRESSURE (Figure 7)

RSI material is a low-density porous insulation containing 90 percent or more void space wherein heat is transported simultaneously by gas conduction, solid-to-solid conduction, and radiation. Accordingly, bulk thermal conductivity of RSI exhibits a dependence on pressure as well as temperature. This reduction in conductivity with a reduction in pressure is well characterized for each material, and has been included in the thermal simulation model of this study.

The effect of a reduced pressure environment on RSI unit weight is shown as a function of heat load for three typical pressure conditions. RSI material weights were calculated for a number of body points and correlated as a function of total heat load for a typical 2037 km (1100 N. Mi.) cross range entry. This correlation, in turn, can be used to estimate weight at any other location which can be described by a total heat load. As indicated, a rather significant reduction in unit weight is achieved by reducing pressure from a constant 1 atm. condition to an altitude pressure variation taken from the entry trajectory. Altitude pressure was taken to be the lowest pressure that the vehicle would experience on the upper surface. A pressure ratio ($p_{local}/p_{t,2}$) of 0.25 was taken as the highest local RSI surface pressure expected during a 30° angle-of-attack entry.

It is evident from the figure that reduced pressure effects must be included in a TPS weight estimate, while surface pressure variation over the vehicle produces a small effect and can be ignored in most cases.

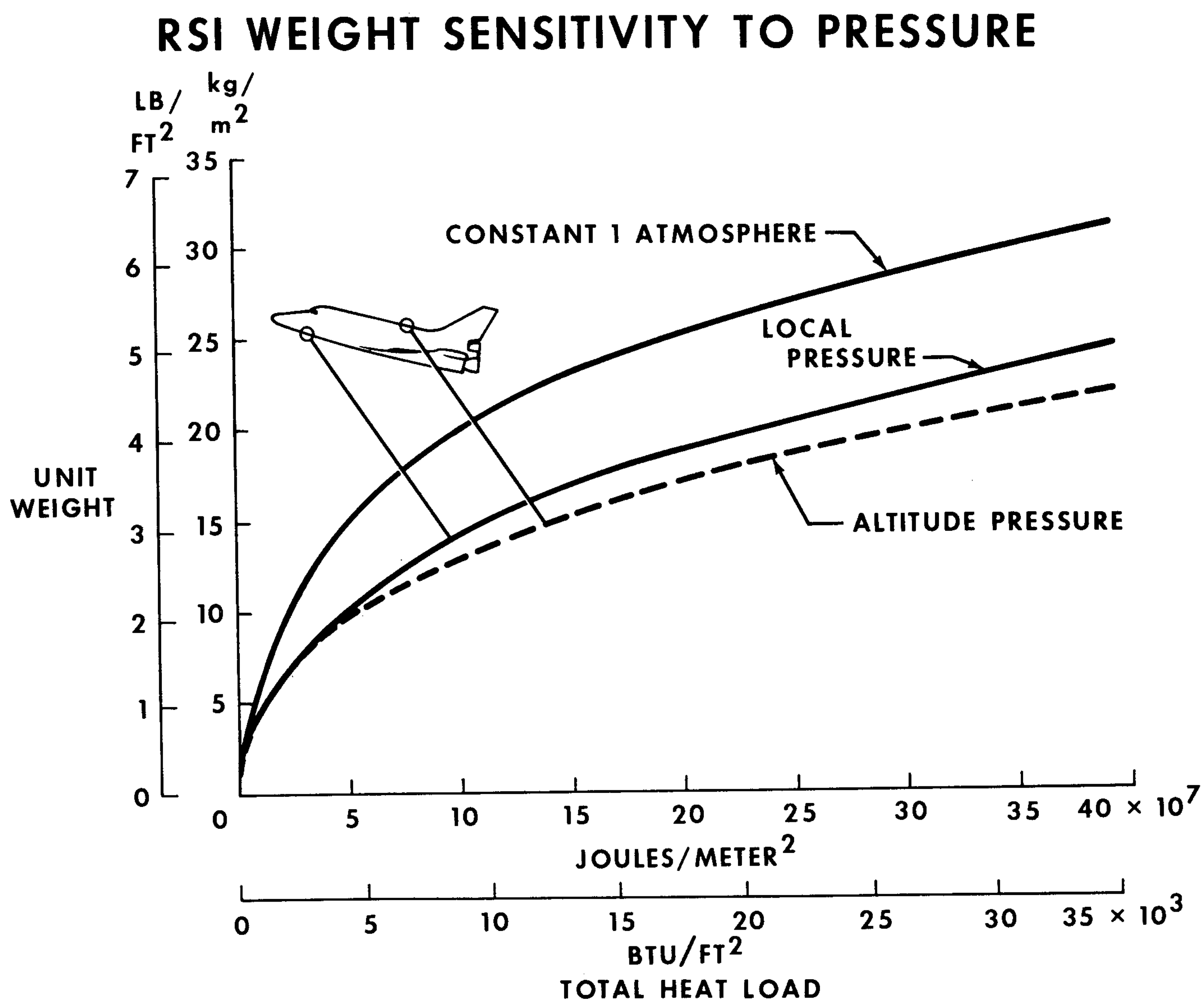

RSI WEIGHT SENSITIVITY TO PRESSURE
LB/FT2
kg/m2
UNIT WEIGHT
CONSTANT 1 ATMOSPHERE
LOCAL PRESSURE
ALTITUDE PRESSURE
0 5 10 15 20 25 30 35 40 × 10^7
JOULES/METER^2
0 5 10 15 20 25 30 35 × 10^3
BTU/FT^2
TOTAL HEAT LOAD

Figure 7

RSI WEIGHT SENSITIVITY TO INITIAL BONDLINE TEMPERATURE (Figure 8)

Maximum initial bondline temperatures which might result from different on-orbit conditions are illustrated. The effect of initial temperature at start of entry on TPS unit weight for several locations with their associated heat load are presented. An initial temperature of 311K (100°F) was used in TPS sizing; however, an initial temperature of 394K (250°F) is possible for a hot soak condition on a TPS surface without external coating whose absorptance-to-emittance ratio can be as high as 1.0.

RSI WEIGHT SENSITIVITY TO INITIAL BONDLINE TEMPERATURE

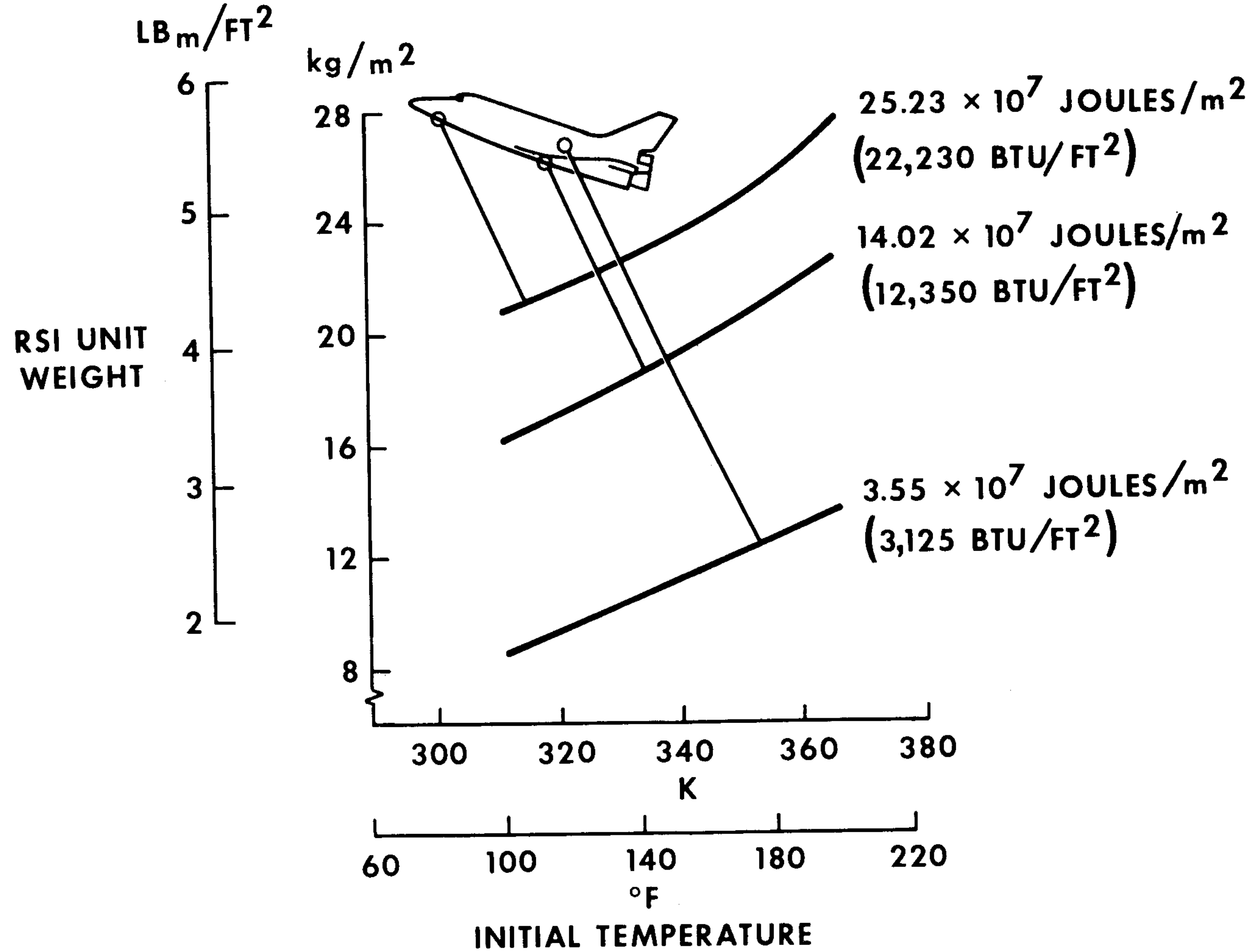

Figure 8

RSI UNIT AREA WEIGHTS (Figure 9)

As has already been shown in the previous figures, it is possible to correlate both the RSI and ablative material unit weights as a function of total heat load. Such a set of correlations for various down ranges and, therefore, entry times for the RSI material are presented. These curves were generated by simply multiplying the reference entry heating rate by several factors of q/q_{ref}. Also shown in this figure are typical constant heating-rate ratios for increasing down range. Using a similar set of data for the ablative material, it is possible to define the heat load for a particular down range at which the RSI and ablator unit weights are equal.

A comparison of the RSI and ablator unit weight results showed that the RSI was more efficient at the lower heat loads as a result of its lower thermal conductivity. However, the ablator is more efficient at the higher heating rates and associated heat loads. Both RSI classes of materials (silica and mullite) gave comparable weights for the down-range conditions shown in this figure.

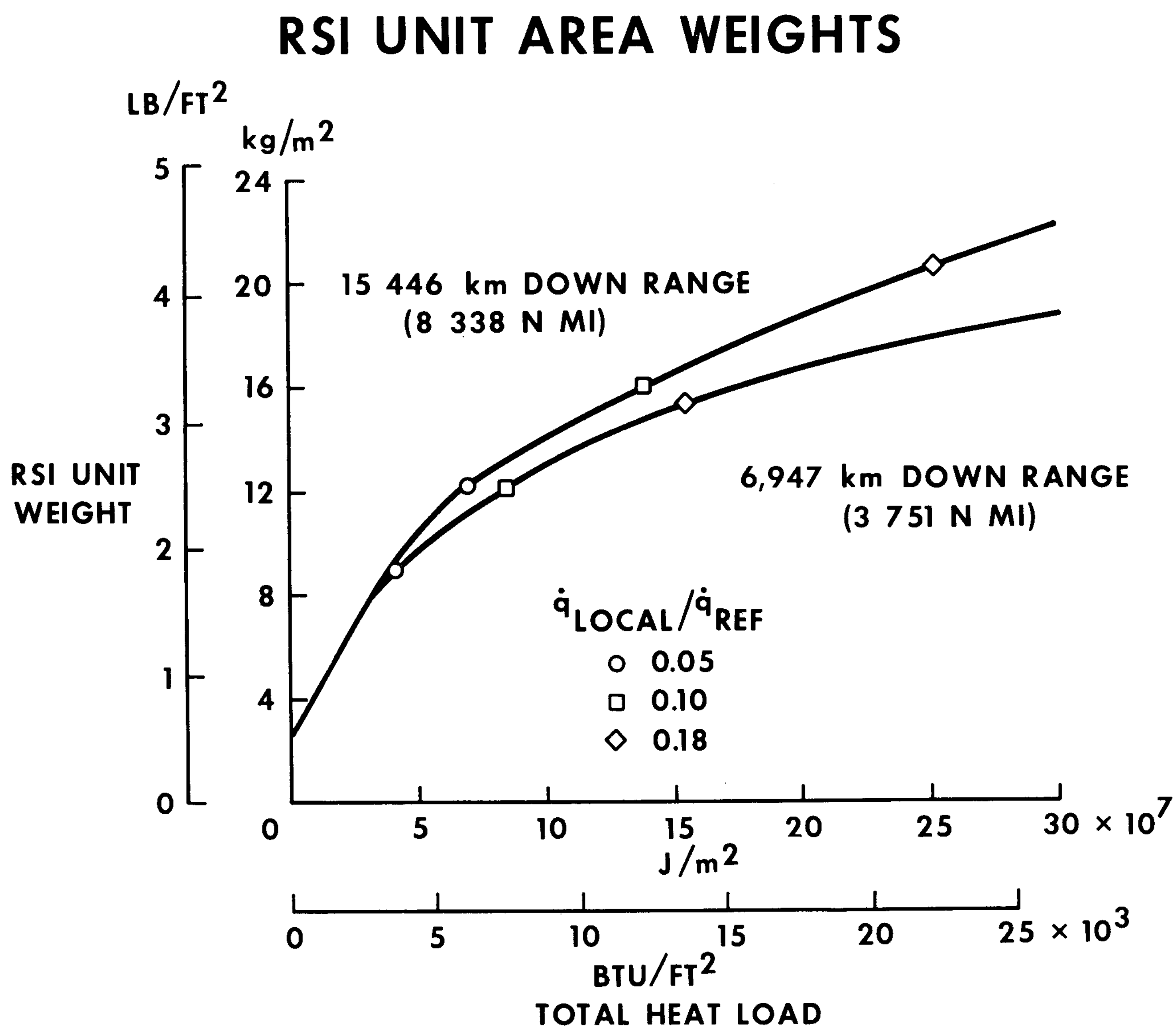
RSI UNIT AREA WEIGHTS
LB/FT2
kg/m2
RSI UNIT WEIGHT
5
4
3
2
1
0
24
20
16
12
8
4
15 446 km DOWN RANGE
(8 338 N MI)
6,947 km DOWN RANGE
(3 751 N MI)
q̇LOCAL/q̇REF
0.05
0.10
0.18
0
5
10
15
20
25
30 × 10^7
J/m2
0
5
10
15
20
25 × 10^3
BTU/FT2
TOTAL HEAT LOAD

Figure 9

TPS MATERIAL WEIGHT SENSITIVITY TO DOWN–RANGE VARIATION (Figure 10)

Using the results shown in the previous figure for RSI and a similar set of data for ablator, TPS material weights were calculated for the orbiter vehicle as a function of down range (or entry time). Two structural bondline peak temperature limits were considered: 422K (300°F), and 450K (350°F). As shown, the ablative system weight is lighter for down ranges less than 10 835 km (5850 N. Mi.) for the 422K (300°F) limit case, and for down ranges less than 8334 km (4500 N.Mi.) for the 450K (350°F) limit case. The crossovers between the RSI and ablator material weight are partially a result of the higher ablator efficiency at the high heating rates associated with the shorter down–range cases. It should be emphasized that the weights shown are based on thermal considerations only.

TPS MATERIAL WEIGHT SENSITIVITY TO DOWN-RANGE VARIATION

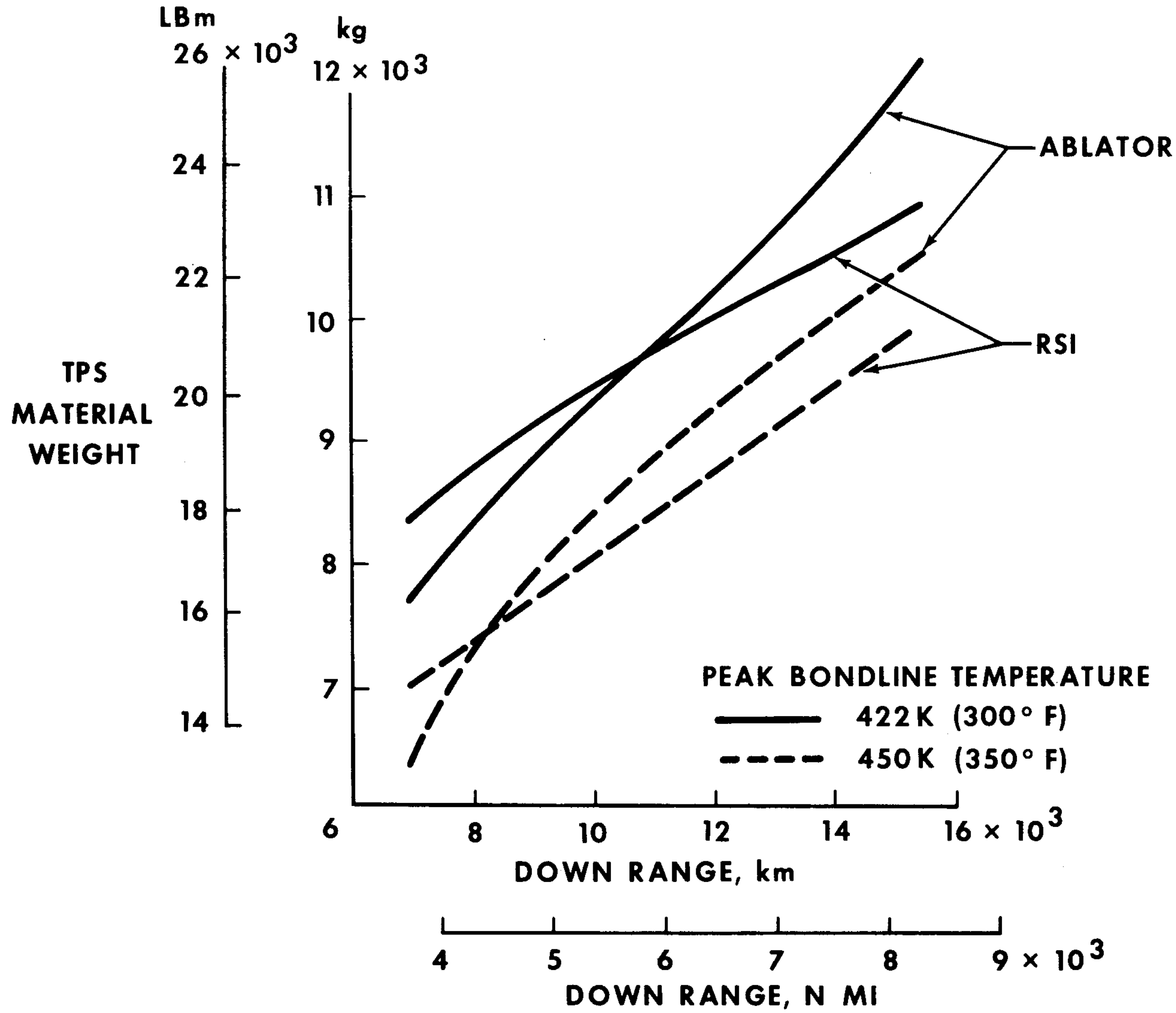

Figure 10

MATERIAL THERMAL CONDUCTIVITY/TPS IN-DEPTH TEMPERATURE DISTRIBUTION (Figure 11)

The effect of material thermal conductivity on the thermal soak is also an important factor in the weight crossover shown in the previous figure. The in-depth temperature profiles for the RSI and ablator are shown at peak heating and at touchdown. At peak heating, the ablator temperature is lower as a result of the ablation process. In addition, these curves indicate the importance of the coupled interaction of the material thermal conductivity and entry trajectory. As shown for the short down range, the major temperature level is around 811K (1000°F), and the higher conductivity associated with an ablative char provides an increase in heat rejection to space during the latter stages of entry and the landing phase.

EFFECT OF CONDUCTIVITY ON TEMPERATURE DISTRIBUTION

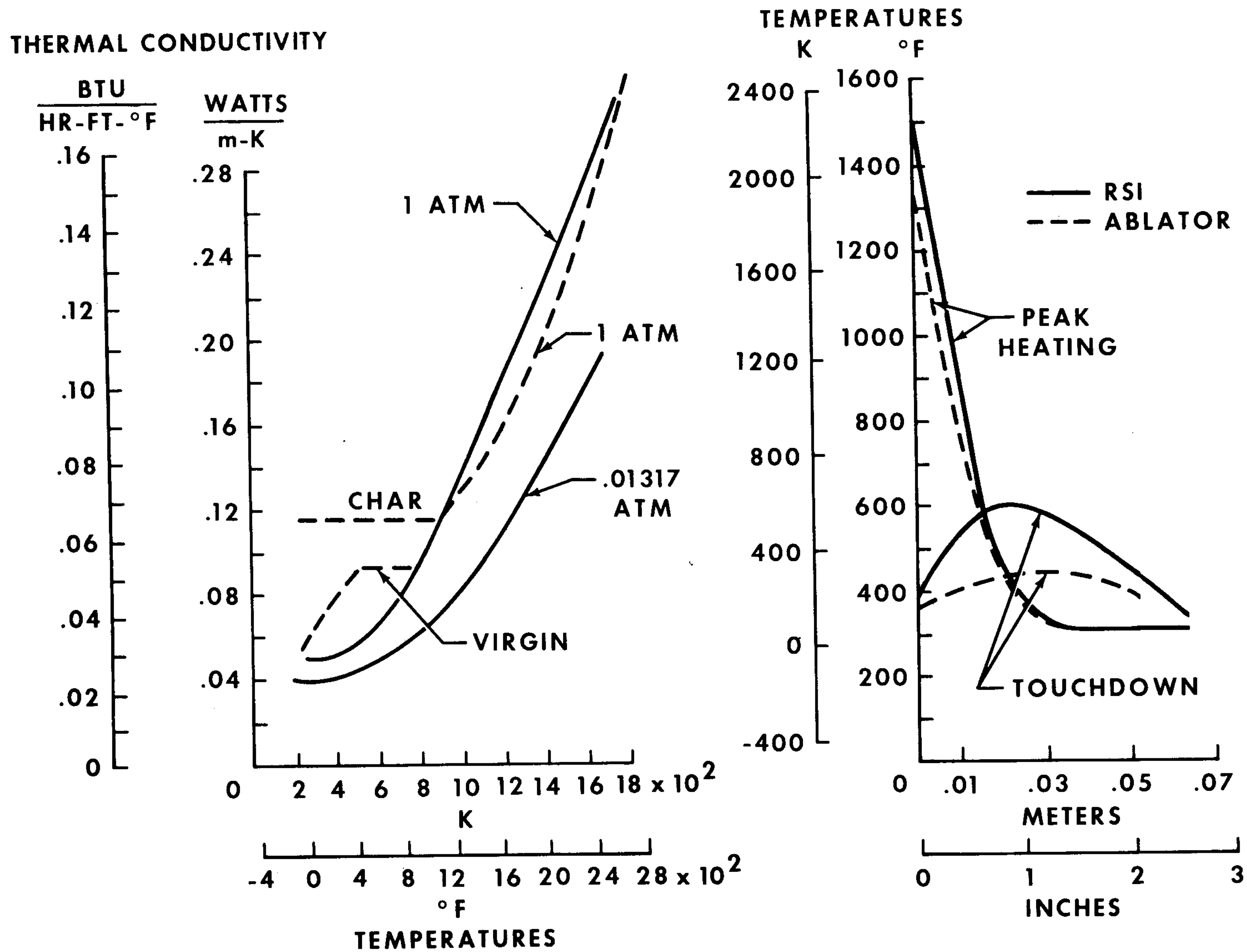

Figure 11

THERMAL PROTECTION SYSTEM WEIGHT SENSITIVITY TO DOWN-RANGE VARIATION (Figure 12)

Combining the results of the previous figure with the tare weights associated with the RSI and ablator coating and adhesive, a total TPS weight can be computed for RSI and ablative systems as a function of down range. A comparison of these weights are shown for three structural temperature constraints: 422K (300°F), 422/450K (300/350°F), and 450K (350°F). For the second case, a 422K (300°F) limit is maintained during flight and allowed to increase to 450K (350°F) after landing. A comparison of the 422K (300°F) and 422/450K (300/350°F) RSI weight curve shows a weight difference of approximately 907 kg (2000 lb) constant with down range. Corresponding ablator weight curves show little weight difference between the two cases. The 422/450K (300/350°F) RSI weight becomes lighter for down ranges greater than 1352 km (7300 N. Mi.). A comparison of the 422/450K (300/350°F) and 450K (350°F) RSI curves show a maximum weight savings of 454kg (1000 lb). The corresponding ablator weight savings possible is 1361 kg (3000 lb).

THERMAL PROTECTION SYSTEM WEIGHT SENSITIVITY TO DOWN-RANGE VARIATION

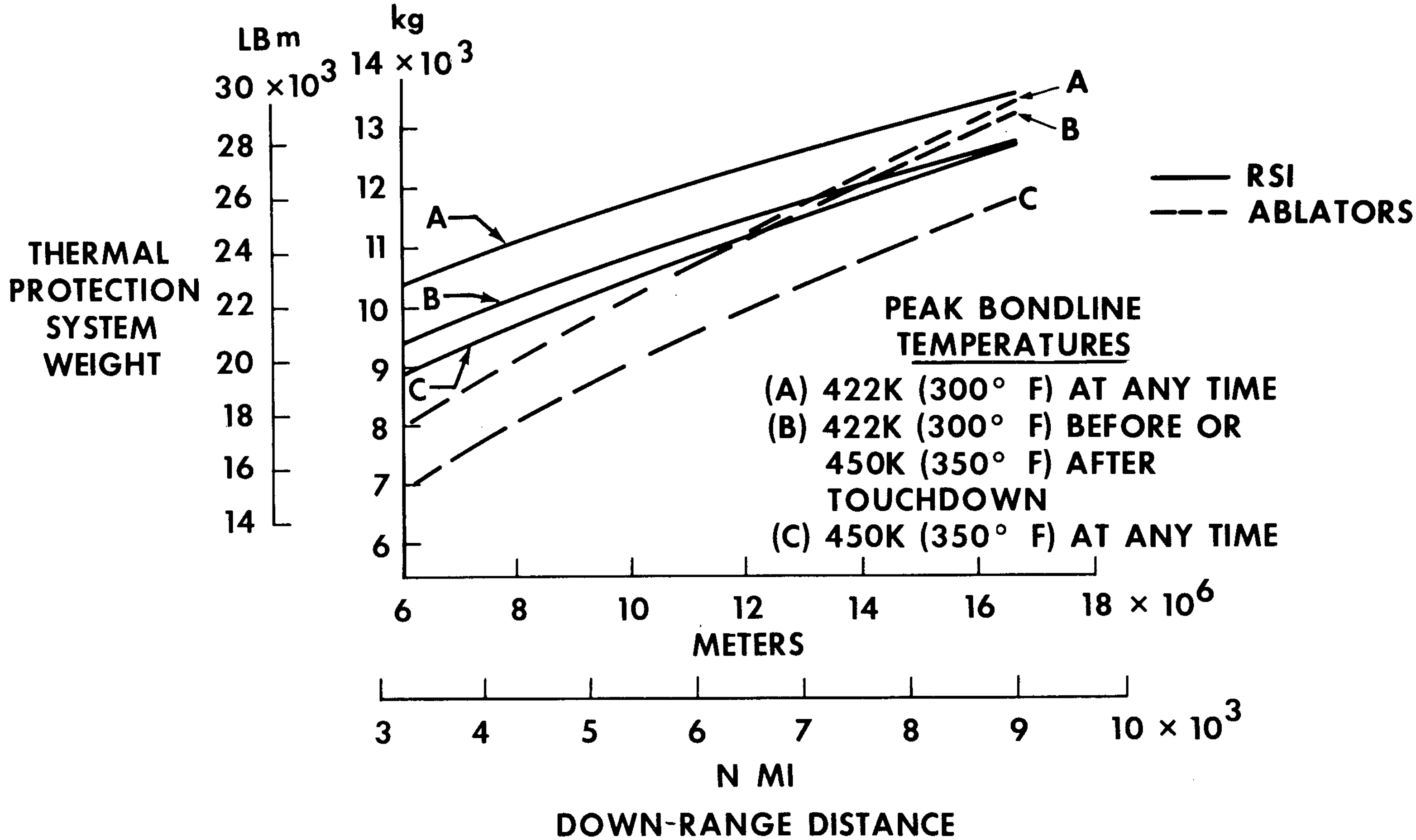

Figure 12

EFFECTS OF RSI TEMPERATURE CONSTRAINTS ON LEADING-EDGE TEMPERATURE. (Figure 13)

The previous figures have discussed the major surface areas. The results of constraining these major surface-area temperatures to specified limits [namely, 1645K (2500°F) and 1367K (2000°F)] on leading-edge temperature is shown. For a 1367K (2000°F) panel temperature constraint, a completely reuseable carbon-carbon leading edge is feasible for the range of radii shown. However, for a 1645K (2500°F) panel temperature the wing leading-edge temperature exceeds the carbon-carbon reuse temperature over a significant portion of the span.

These results indicate a minimum leading-edge radius of 0.098 m (3.85 in.) is required for reuse capability for the higher temperature trajectories.

EFFECTS OF RSI TEMPERATURE CONSTRAINTS ON LEADING-EDGE STAGNATION TEMPERATURE

● LOWER SURFACE PANEL AT X/L = 0.12

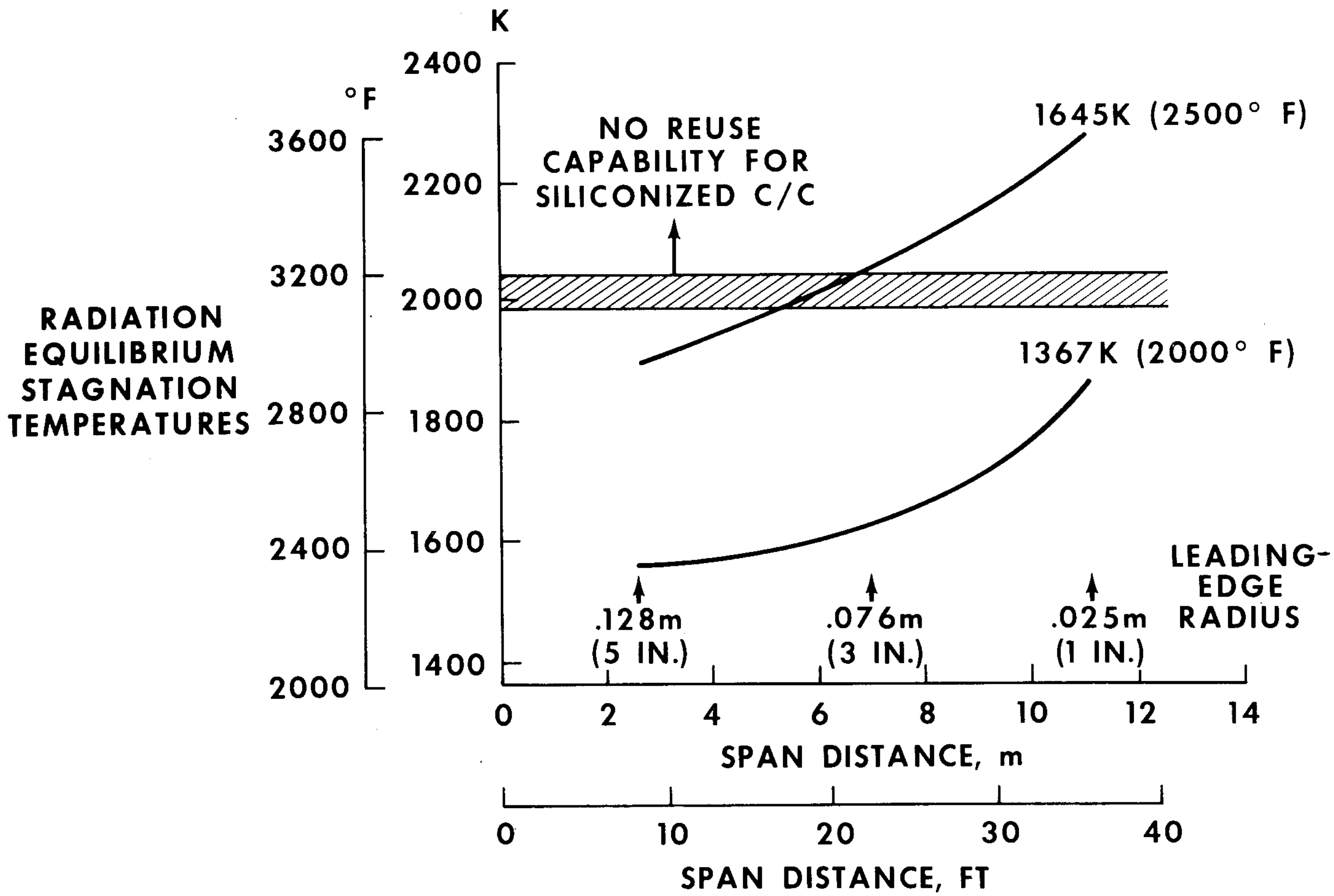

Figure 13

WING-LEADING-EDGE TPS WEIGHT DISTRIBUTION (Figure 14)

The entry trajectories shown on the previous figure indicate that for radii less than 0.098 m (3.85 in.), a fully reuseable carbon-carbon leading edge is not attained. However, the results do indicate that a 0.127 m (5 in.) radius leading edge would be fully reuseable over the trajectory conditions investigated. This figure presents weight per unit length for an ablative and carbon-carbon leading edge of 0.127 m (5 in.) radius. Weights are shown for both a "fail-safe" and "safe-life" carbon-carbon system. As shown, the weights for the ablative and carbon-carbon "fail-safe" designs are comparable. For these calculations, a leading-edge design which covers the wing to 2.4 percent chord on the upper surface and 5.8 percent chord on the lower surface and a substrate temperature limit of 422K (300°F) was assumed.

The "safe-life" design was developed under the carbon-carbon technology program; the "fail-safe" design is similar, but includes adequate carbon thickness to accomplish one safe entry without the oxidation-inhibited coating.

WING-LEADING-EDGE TPS WEIGHT DISTRIBUTION

- 0.128 m (5 IN.) CONSTANT RADIUS
- 6802 km (3673 N MI) DOWN RANGE TRAJECTORY

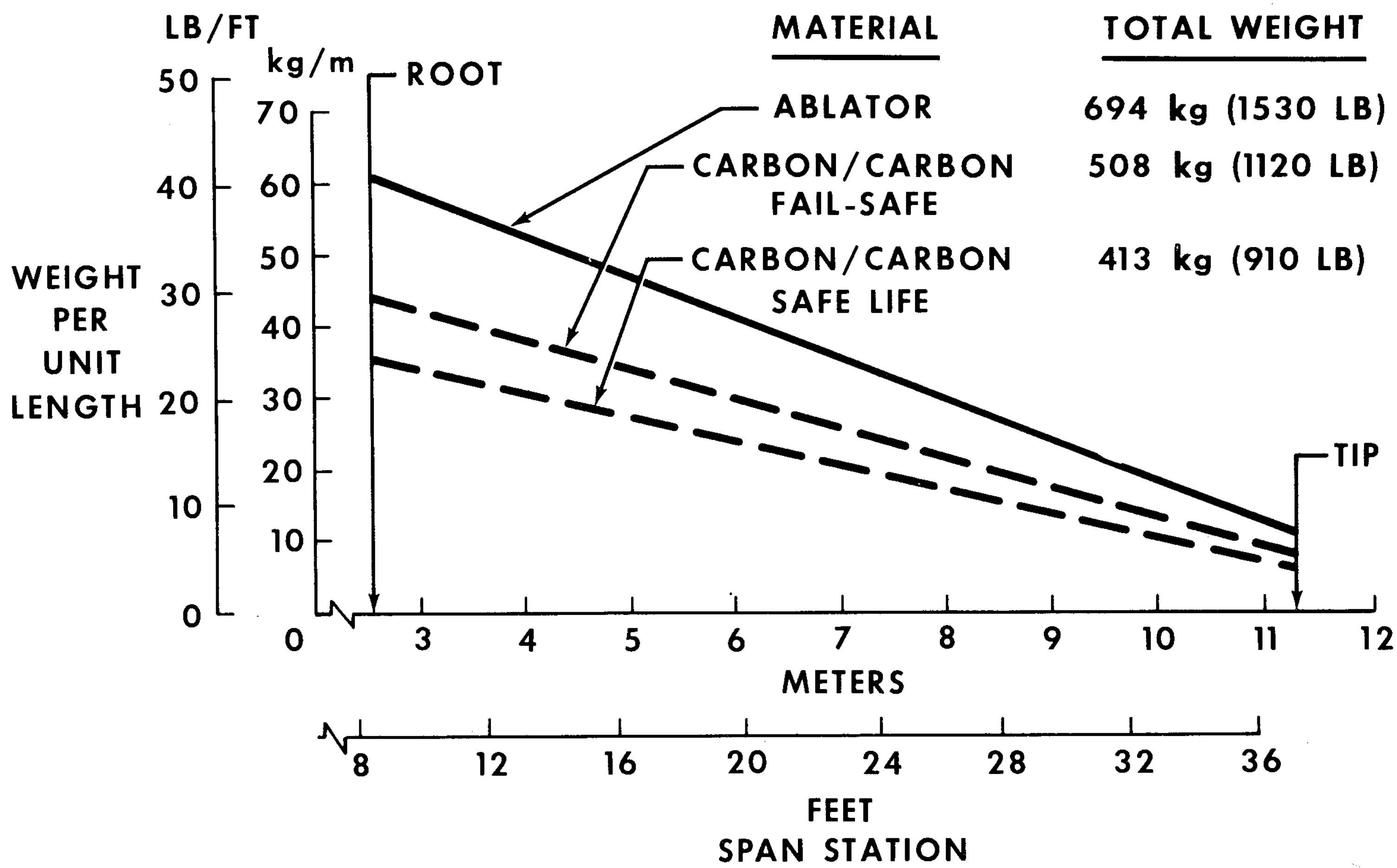

Figure 14

TRAJECTORY SHAPING EFFECTS ON TPS WEIGHT AND LEADING-EDGE REUSE (Figure 15)

A summary of the trajectories investigated with their associated peak reference heating rates and heat loads, and the resulting RSI material weights are shown. Also shown is an assessment of the percent of reuseable carbon-carbon leading edge. The leading-edge radius-span station relation [namely, 0.025 m (1 in.) at tip, 0.076 m (3 in.) at midspan, 0.128 m (5 in.) at root] shown previously was used in making this assessment.

TRAJECTORY SHAPING EFFECTS ON TPS WEIGHT AND LEADING-EDGE REUSE

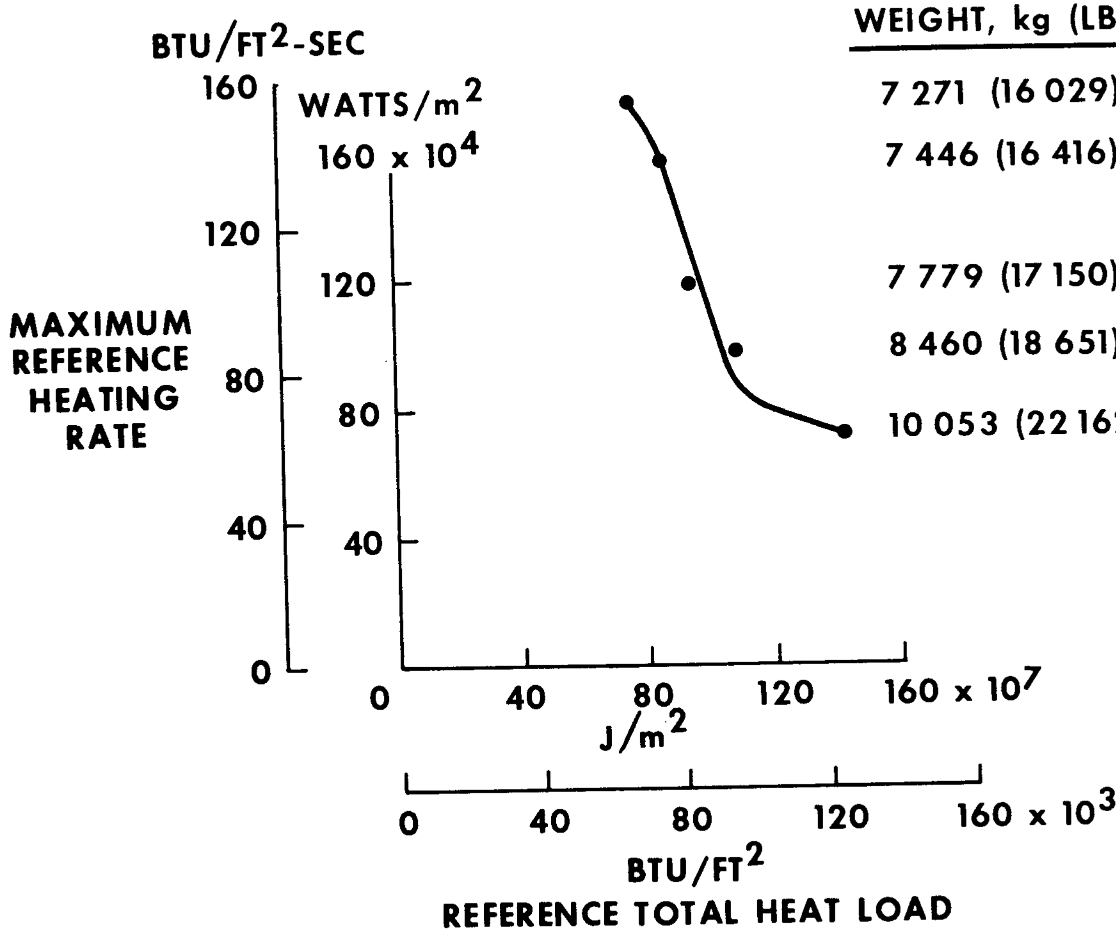

RSI MATERIAL WEIGHT, kg (LB)	C/C LEADING EDGE PERCENT REUSEABLE
7 271 (16 029)	0
7 446 (16 416)	50
7 779 (17 150)	70
8 460 (18 651)	95
10 053 (22 162)	100

Figure 15

CONCLUDING REMARKS

Trade study results presented herein indicate the importance of material thermal characteristics and trajectory shaping on entry TPS weights. Unit weight of RSI and ablators are similarly dependent upon both total heat load and duration of entry heat pulse. TPS weights calculated for RSI and ablators are comparable for all trajectories considered, in that weights increase with down range as result of longer entry times.

The use of a 422K (300°F) flight/450K (350°F) post-touchdown peak bondline temperature constraint results in a weight saving for the RSI material; corresponding temperature constraints did not show a weight saving for the ablative system. For the short down-range entry trajectories which resulted in the lowest weight TPS, a specified minimum leading-edge radius is required in order to maintain a reuseable carbon/carbon system.

OXIDATION PROTECTED CARBON-CARBON

by

James E. Pavlosky

Leslie G. St. Leger

Manned Spacecraft Center

INTRODUCTION

Pyrolized carbon-carbon has one unique advantage over other materials that makes its application to the space shuttle thermal protection system very attractive. This unique characteristic is the increase in material strength and modulus with increase in temperature up to about 2500K (4040°F). Offsetting this unique advantage are disadvantages which include brittleness, high cost, and the tendency of the material to react with oxygen, particularly at high temperatures.

The material has been under "low key" development for several years and its only application (which was relatively minor) in a space program was on the Apollo command module where it was used as a cover for the astro-sextant and telescope windows. Serious development of carbon-carbon was undertaken by the NASA - Manned Spacecraft Center in February 1970 as part of the shuttle technology program. The emphasis has been on the development of an oxidation inhibitor for the material and the definition of fabrication processes for selected full-scale components. The highlights of this development program are the subject of this presentation.

13

TYPICAL SHUTTLE LEADING EDGE TEMPERATURES

The locations of interest for potential application of carbon-carbon composite material on the orbiter are shown, along with associated peak temperatures for a typical shuttle entry trajectory.

TYPICAL SHUTTLE LEADING EDGE TEMPERATURES

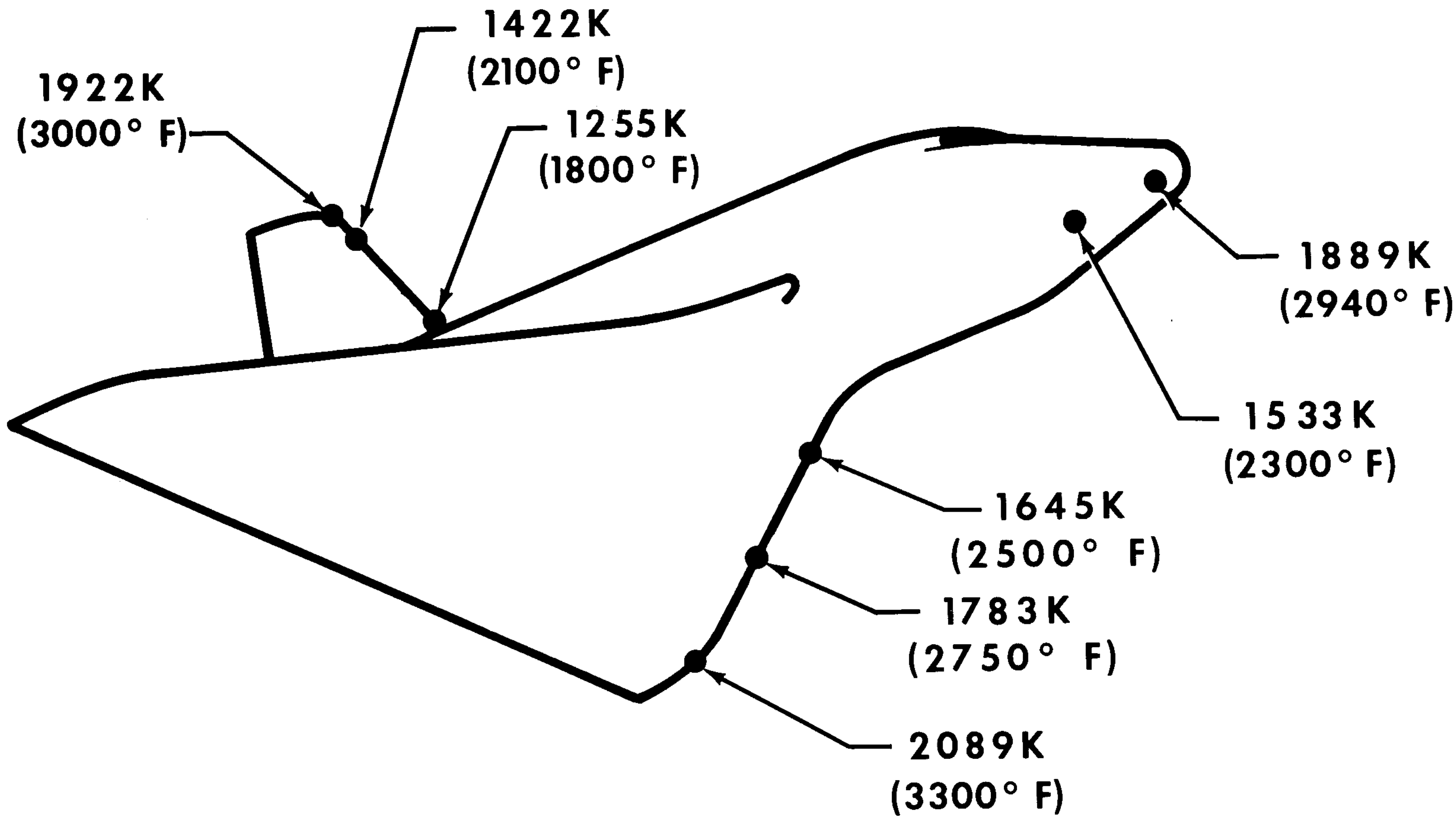

VARIATION OF STRENGTH WITH TEMPERATURE OF CANDIDATE TPS MATERIALS

The variation of structural efficiency with temperature of several candidate reuseable TPS panel materials is shown. It can be seen that above 1500K (2240°F) the selection of reuseable TPS materials is restricted to columbium and carbon-carbon, both of which are prone to oxidation above 700K (800°F) and must be protected for use above this temperature. Above 1700K (2600°F) the only TPS choice, besides an ablative material, is oxidation inhibited carbon-carbon. The strength of this material actually increases with increasing temperature and has a tensile strength-to-density ratio of 50 000 newton-m/kg (200 000 lb_F-in/lb_M) at 1800K (2780°F), based on 13-ply inhibited material with a specific gravity of 1.41.

VARIATION OF STRENGTH WITH TEMPERATURE OF CANDIDATE TPS MATERIALS

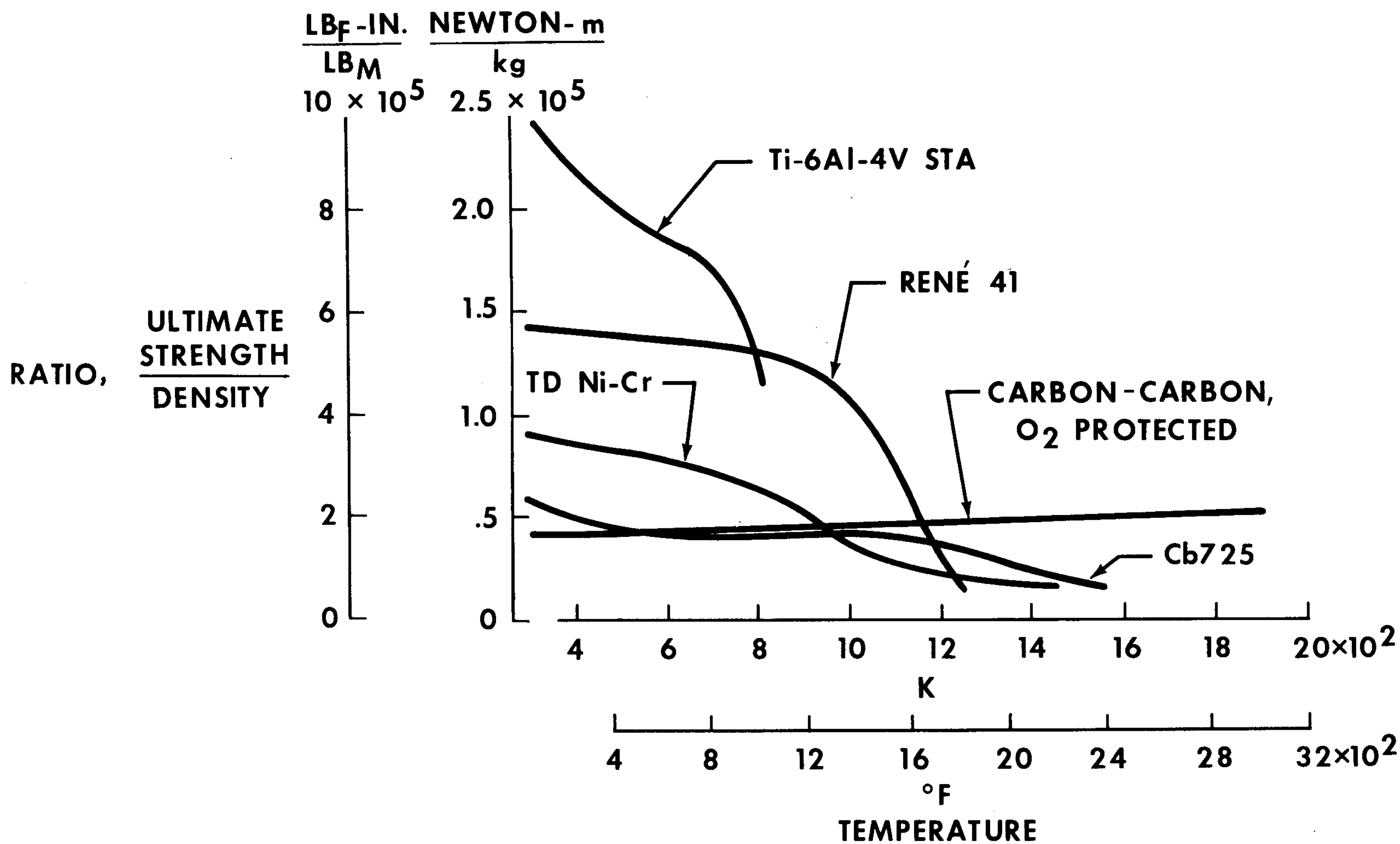

INHIBITED CARBON-CARBON MATERIALS SELECTION

Substrates, binders, and oxidation inhibitors were investigated separately to ultimately develop a compatible system. Substrates employing graphite or carbon filaments, high and low modulus fibers in cloth, yarn, or tapes, were evaluated for strength, fabricability, and coating compatibility.

Phenolics, epoxies, furfuryl alcohol, pitch, and chemical vapor deposition were studied to identify the binder which resulted in the highest strength substrate.

Exploration of oxidation inhibitors involved carbides and oxides of a number of metals applied by diffusion, chemical vapor deposition, and flame sprayed overlays; inhibitors added into the resin during initial makeup of the laminate were also investigated.

Materials evaluation included tests for strength, oxidation resistance in a furnace, and extensive plasma arc exposure simulating the entry environment.

It was found that solid laminate designs employing graphite cloth with a phenolic binder and furfuryl alcohol for reimpregnation were less sensitive to strength degradation from the coating system. The diffusion process was found to be superior in that the inhibitor could be diffused into the substrate to a controlled depth to provide multi-mission capability without weakening the interlaminar strength of the composite.

Inhibitor systems based on silicon carbide with alumina were found to offer the highest temperature reuse capability of all systems examined and to provide good strength at all temperatures.

INHIBITED CARBON-CARBON MATERIALS SELECTION

SUBSTRATES

- √ GRAPHITE CLOTH
- CARBON CLOTH
- CARBON YARN
- GRAPHITE FILAMENTS
- CARBON FILAMENTS

BINDERS

- √ PHENOLIC
- EPOXY
- √ FURFURYL
- PITCH
- CHEMICAL VAPOR DEPOSITION

INHIBITORS

- √ DIFFUSION
  - √ SILICON - $SiC-Al_2O_3$
  - ZrB_2 - SILICON
  - Ta - SILICON
  - Ti - SILICON
  - Hf - SILICON
  - Hf - TANTALUM
- ADMIXTURE
  - ABOVE MATERIALS MIXED IN BINDER
- COMBINED
  - ABOVE MATERIALS ADDED TO BINDER PLUS DIFFUSION
- OVERLAY
  - LAMINATED OR SPRAYED ON OXIDES

FABRICATION FLOW CHART

The baseline process for the siliconized carbon-carbon process is illustrated. The carbon substrate processing is, through the cure operation, similar to conventional practices with fiberglas-reinforced plastic parts. Resin degradation to produce the carbon char matrix binder phase occurs in the pyrolysis step [422K (300°F) for three hours], and volatile matter escapes. Repyrolysis requires an 80 hour treatment at 1089K (1500°F). This step is sensitive to the size, shape, and thickness of the part. The repyrolysis, reimpregnation, and repyrolysis steps are repeated to progressively densify and strengthen the parts in controlled increments. Following a cleaning, trim, and machining operation, the part is ready for application of the diffusion coating.

The oxidation inhibitor process starts with blending of the constituent powders, (alumina-10 percent, silicon-30 percent, and silicon carbide-60 percent) which are then packed surrounding the part in a graphite retort. The pack-diffusion process for oxidation protected carbon-carbon is carried out at a temperature of about 1977K (3100°F) for two to three hours. The powder characteristics, constituent formulations, and the manner in which the powders are packed around the part are important factors which govern the chemical reactions at the high processing temperature and the degree of consolidation and sintering of the powders.

FABRICATION FLOW CHART

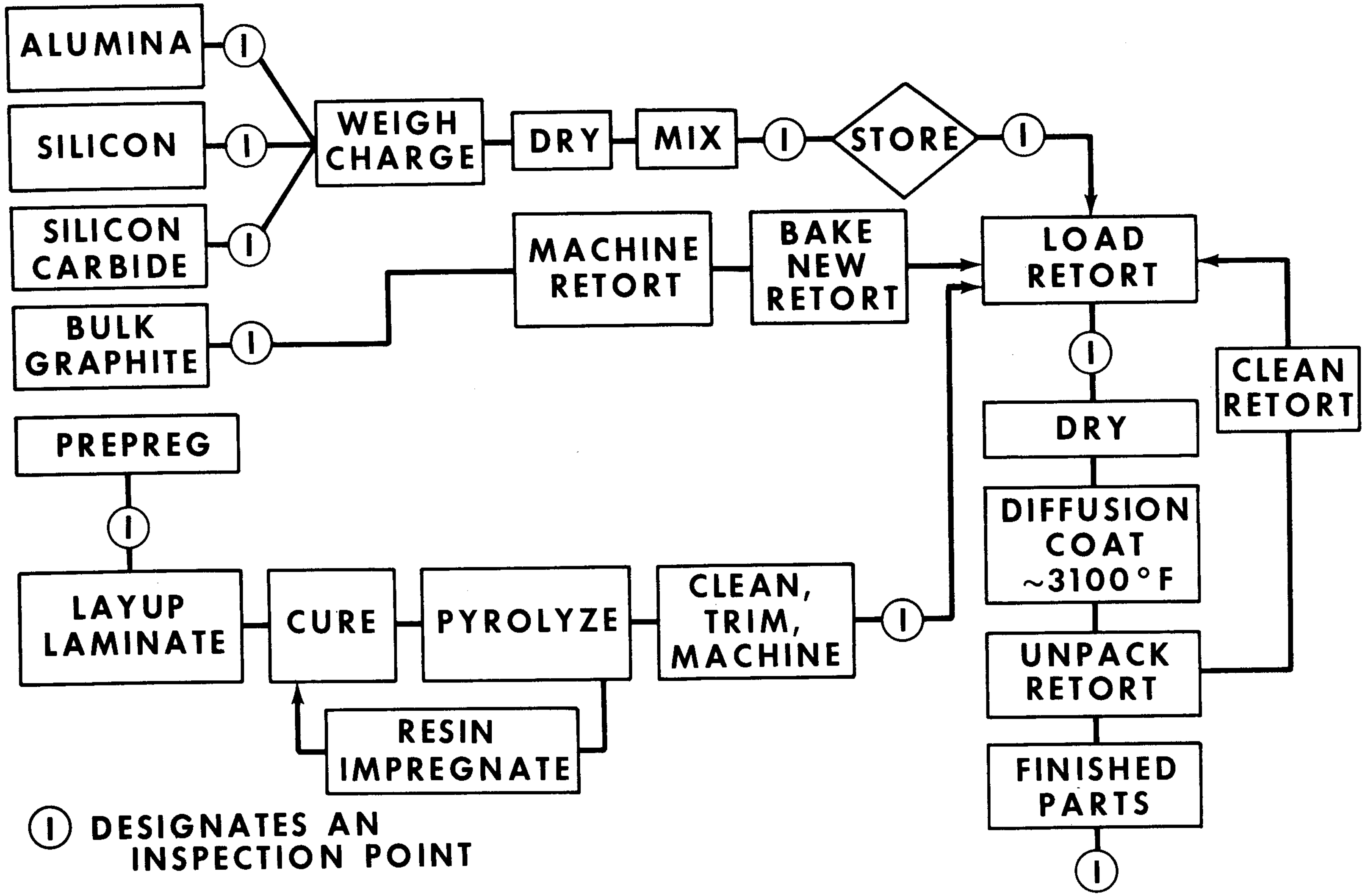

CROSS SECTION OF INHIBITED CARBON-CARBON - 40X

The nature of the oxidation inhibited carbon-carbon laminate material is shown enlarged 40 times. Indicated on the photograph is the oxidation protection area, nominally 5×10^{-4} m (20 mil) thick, which is a silicon carbide matrix integrally formed with about 2 plys of the graphite cloth. The carbon substrate is the graphite cloth formed with a carbon binder.

CROSS SECTION OF INHIBITED CARBON-CARBON

40X

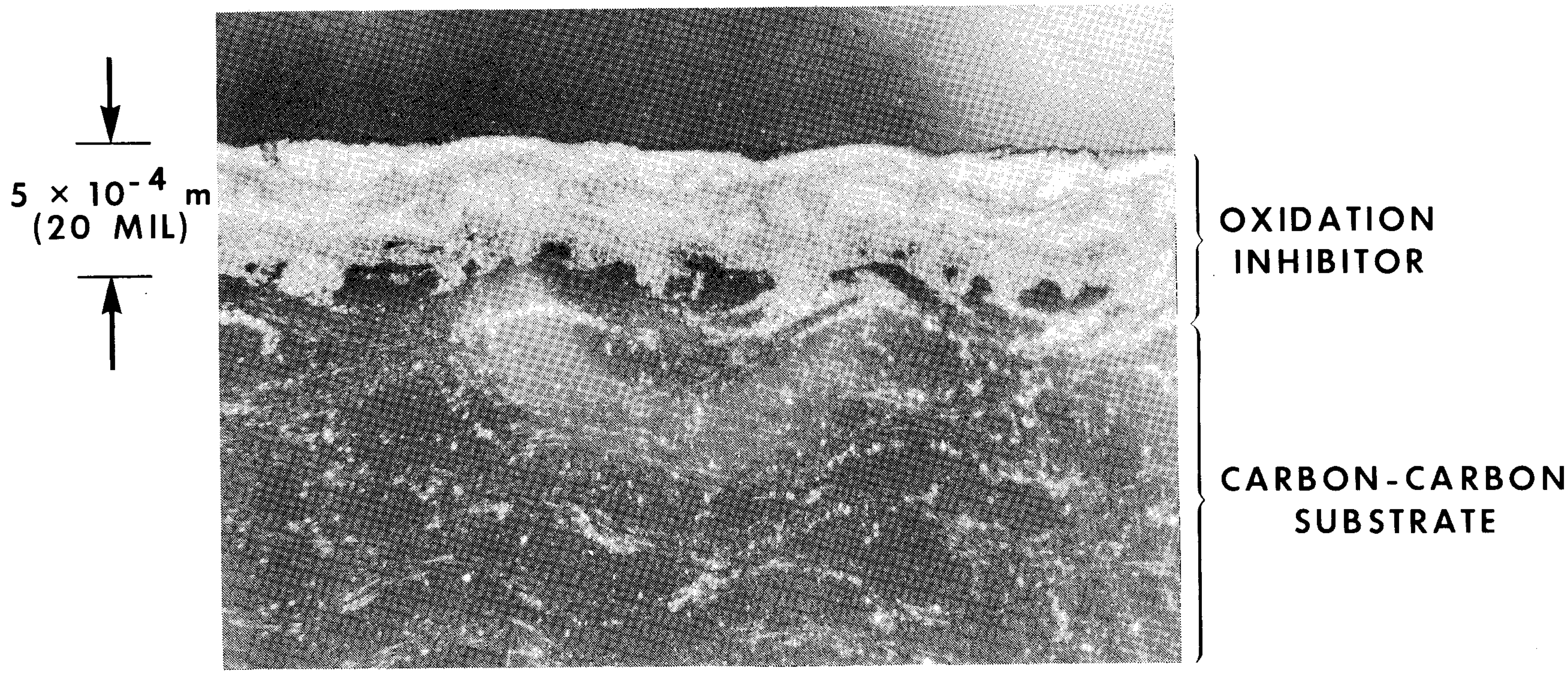

WING LEADING EDGE MISSION LIFE PREDICTED CAPABILITY

Predicted mission life is shown as a function of peak radiation equilibrium temperature during entry based on the mass loss rate and time at temperature for a particular entry trajectory. These predictions include the effect of internal cross radiation and the actual coating emittance.

Two mission life curves are shown for internal cross-radiation conditions, one for the current 5×10^{-4} m (20 mil) and one for 10×10^{-4} m (40 mil) coating thickness. These curves were obtained from actual mass loss of specimens exposed to plasma arc heating. The time at temperature for a particular entry trajectory is determined and a mass loss history is predicted for one mission. Predictions are then made of the number of missions which would result in reduction of coating thickness to 2.5×10^{-4} m (10 mil) which was chosen as the coating thickness for reuse capability. The third mission life curve shown is for no internal cross radiation and is typical of data obtained in arc-jet facilities with insulation behind the specimen. Symbols shown in terms of equivalent number of missions indicate the actual total exposure durations that individual plasma arc specimens have accumulated at a given temperature. A different trajectory would give different mission life capability.

WING LEADING EDGE
MISSION LIFE PREDICTED CAPABILITY

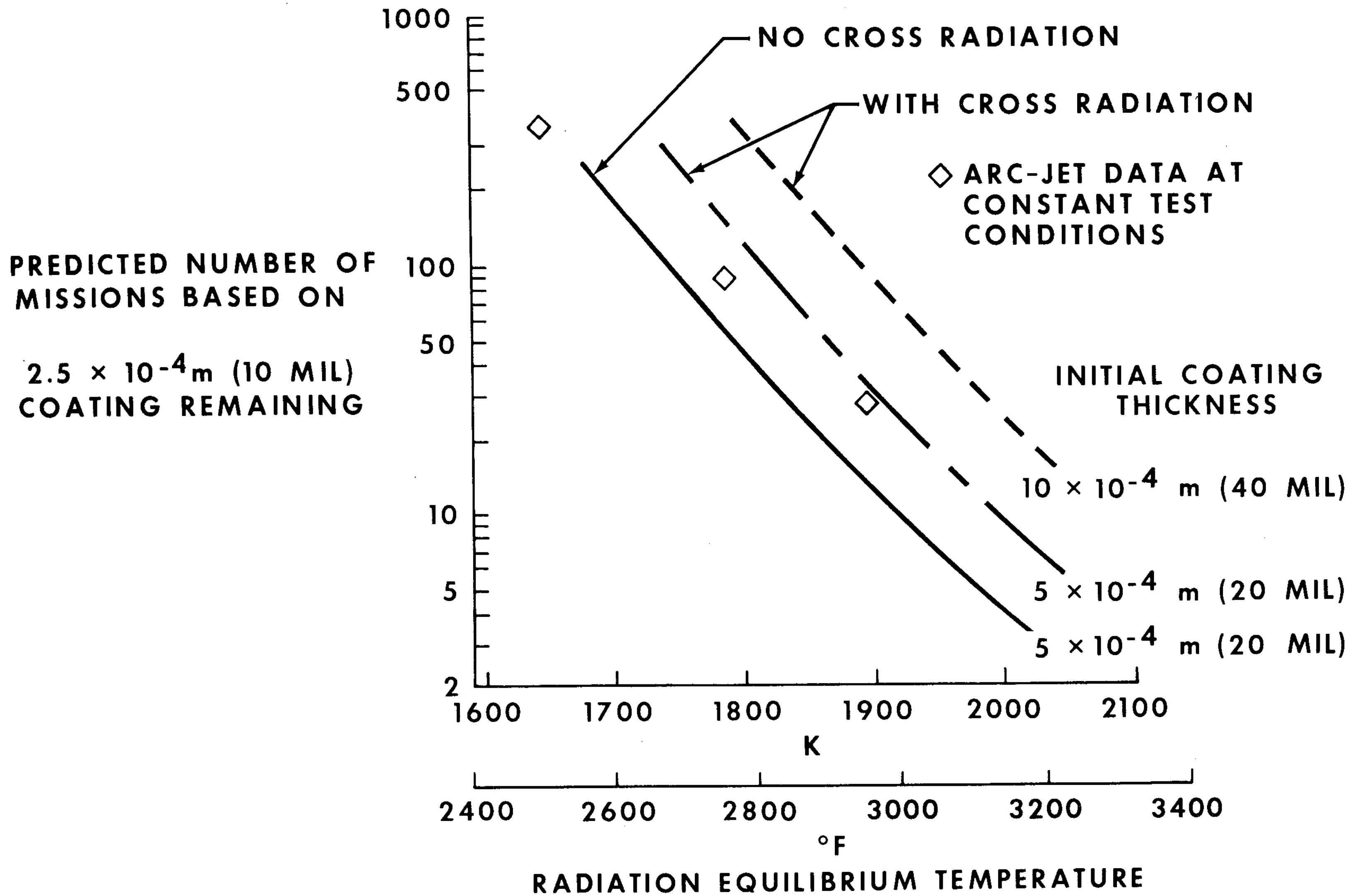

THERMAL PROPERTIES - SILICONIZED CARBON-CARBON

Thermal expansion, conductivity, emittance, and specific heat of 13-ply siliconized carbon-carbon are shown at room temperature and 1645K (2500°F). Properties have been obtained over the complete temperature range. The composite material is relatively stable in thermal expansion over the temperature range tested and other property data are typical of carbon composites.

THERMAL PROPERTIES
SILICONIZED CARBON-CARBON

PROPERTY	296 K (72° F)		1645 K (2500° F)	
THERMAL EXPANSION	K^{-1}	$°F^{-1}$	K^{-1}	$°F^{-1}$
WARP DIRECTION	3.06×10^{-6}	1.7×10^{-6}	3.06×10^{-6}	1.7×10^{-6}
FILL DIRECTION	1.80×10^{-6}	1.0×10^{-6}	2.70×10^{-6}	1.5×10^{-6}
CONDUCTIVITY	$\frac{\text{WATTS}}{\text{m-K}}$	$\frac{\text{BTU-IN.}}{\text{HR-FT}^2\text{-°F}}$	$\frac{\text{WATTS}}{\text{m-K}}$	$\frac{\text{BTU-IN.}}{\text{HR-FT}^2\text{-°F}}$
PARALLEL	9.52	66	14.71	102
PERPENDICULAR	4.76	33	6.78	47
EMITTANCE	0.82		0.93	
SPECIFIC HEAT	$\frac{\text{JOULES}}{\text{kg-K}}$	$\frac{\text{BTU}}{\text{LB-°F}}$	$\frac{\text{JOULES}}{\text{kg-K}}$	$\frac{\text{BTU}}{\text{LB-°F}}$
	753.6	0.18	1716.5	0.41

VARIATION OF EMITTANCE WITH TEMPERATURE

Total normal emittance is shown as a function of surface temperature to 2000K (3140°F). Emittances as high as 0.94 have been measured.

VARIATION OF EMITTANCE WITH TEMPERATURE

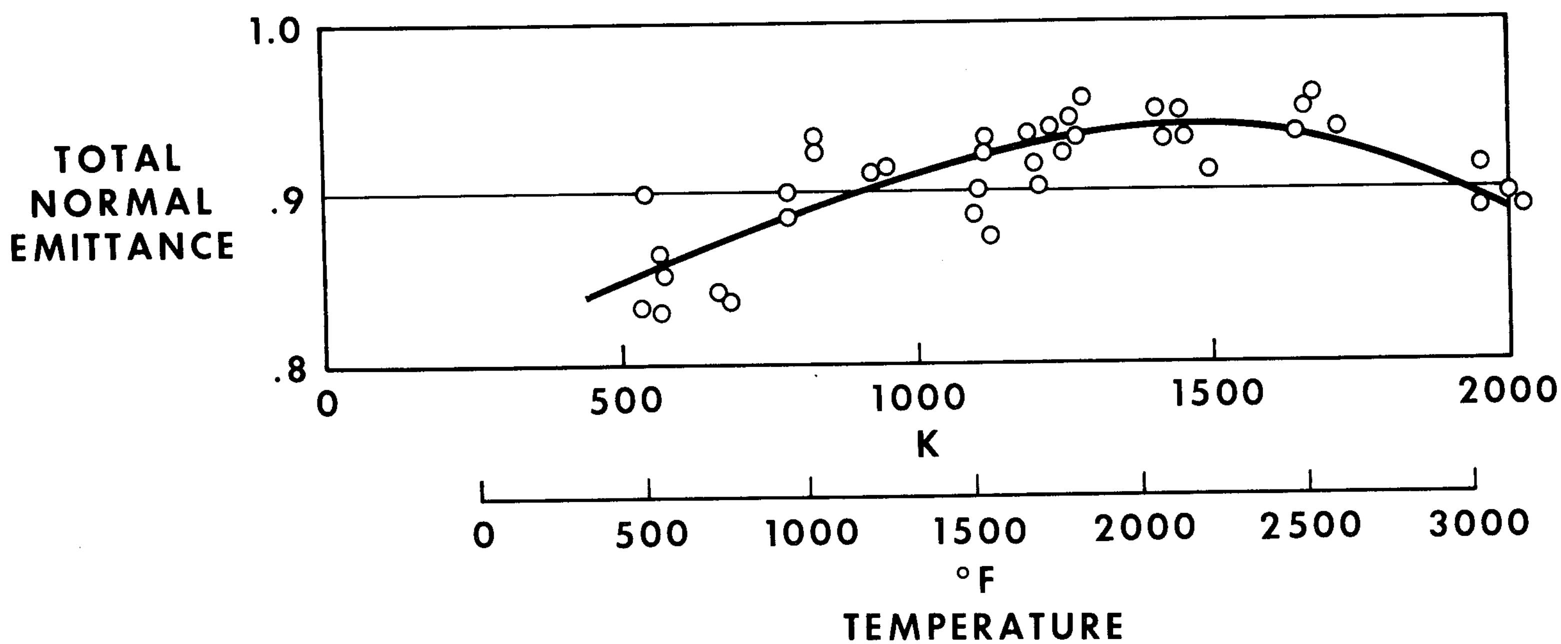

AVERAGE STRENGTH AT ROOM TEMPERATURE

The mechanical properties of 13-ply siliconized carbon-carbon have been obtained at room temperature and at elevated temperatures up to 2000K (3140°F). The material is anisotropic and consequently the strengths in each of the principal coordinate directions must be separately defined. Typical values for the strengths at room temperature are shown on the chart opposite. The values shown represent the average of three data points. For design purposes, these average values were arbitrarily reduced by 30 percent in order to allow for the scatter in the test data. The strength of the material in the interlaminar direction is comparatively low so that care must be taken during design to minimize interlaminar shear and tension stresses.

The strength data shown are not applicable to material thickness other than 13 ply, since the specific contributions of the silicon carbide coating and the carbon-carbon substrate to the measure composite strength were not determined.

AVERAGE STRENGTH AT ROOM TEMPERATURE
SILICONIZED 13-PLY CARBON - CARBON

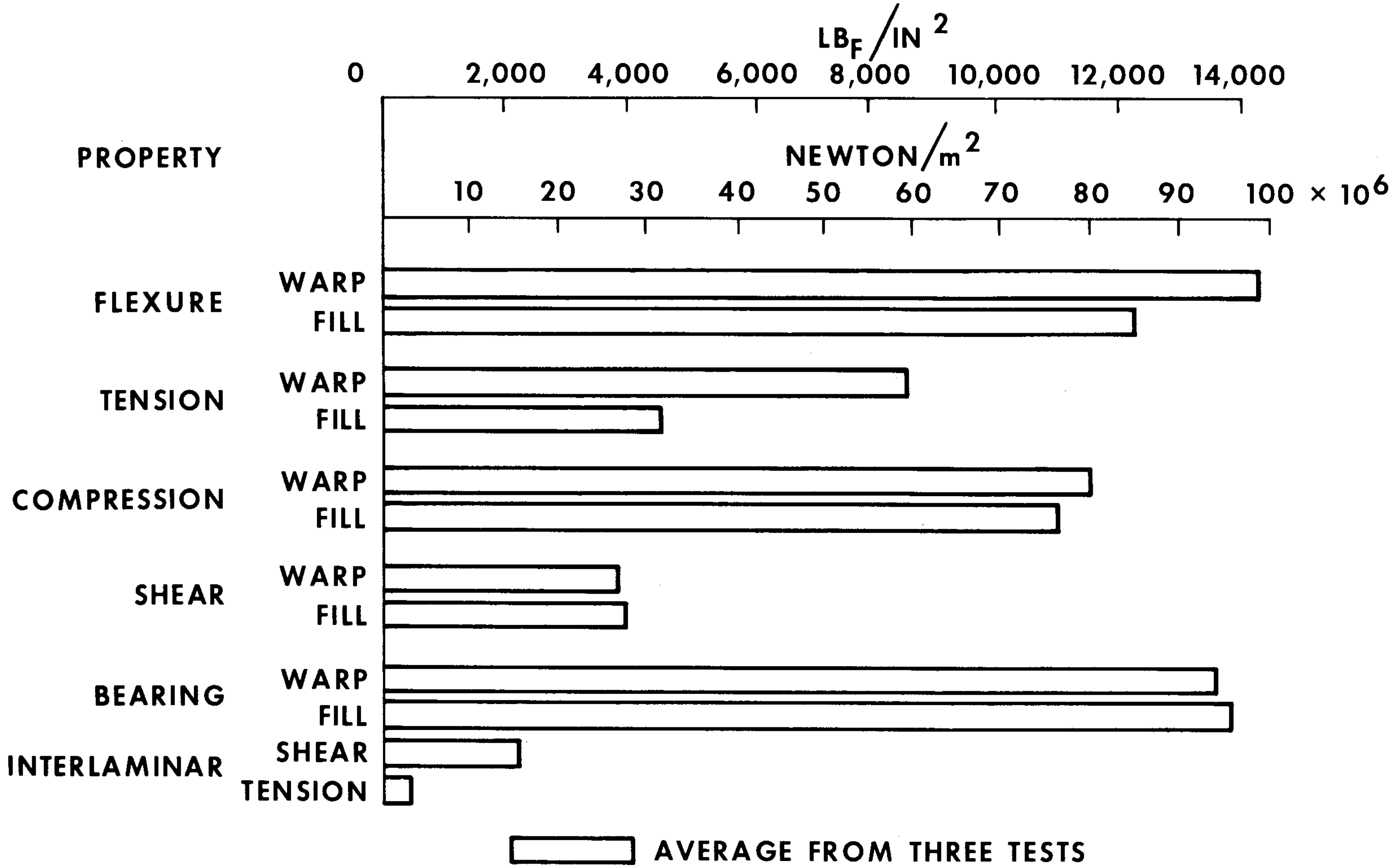

VARIATION OF FLEXURAL STRENGTH WITH TEMPERATURE

The temperature variation of flexural strength for the 13-ply composite is shown for both the warp and fill directions. A flexure bar, 0.013 m (0.50 in.) wide, 0.127 m (5.0 in.) long, and 0.004 m (0.17 in.) deep, and four point loading were used to obtain the data. It is noted that the composite strength appears to be relatively constant between 1645K (2500°F) and 1922K (3000°F) in the warp direction. These data are typical of increased strength with increasing temperature for all the strengths shown on the previous figure.

VARIATION OF FLEXURAL STRENGTH WITH TEMPERATURE 13-PLY SILICONIZED CARBON-CARBON

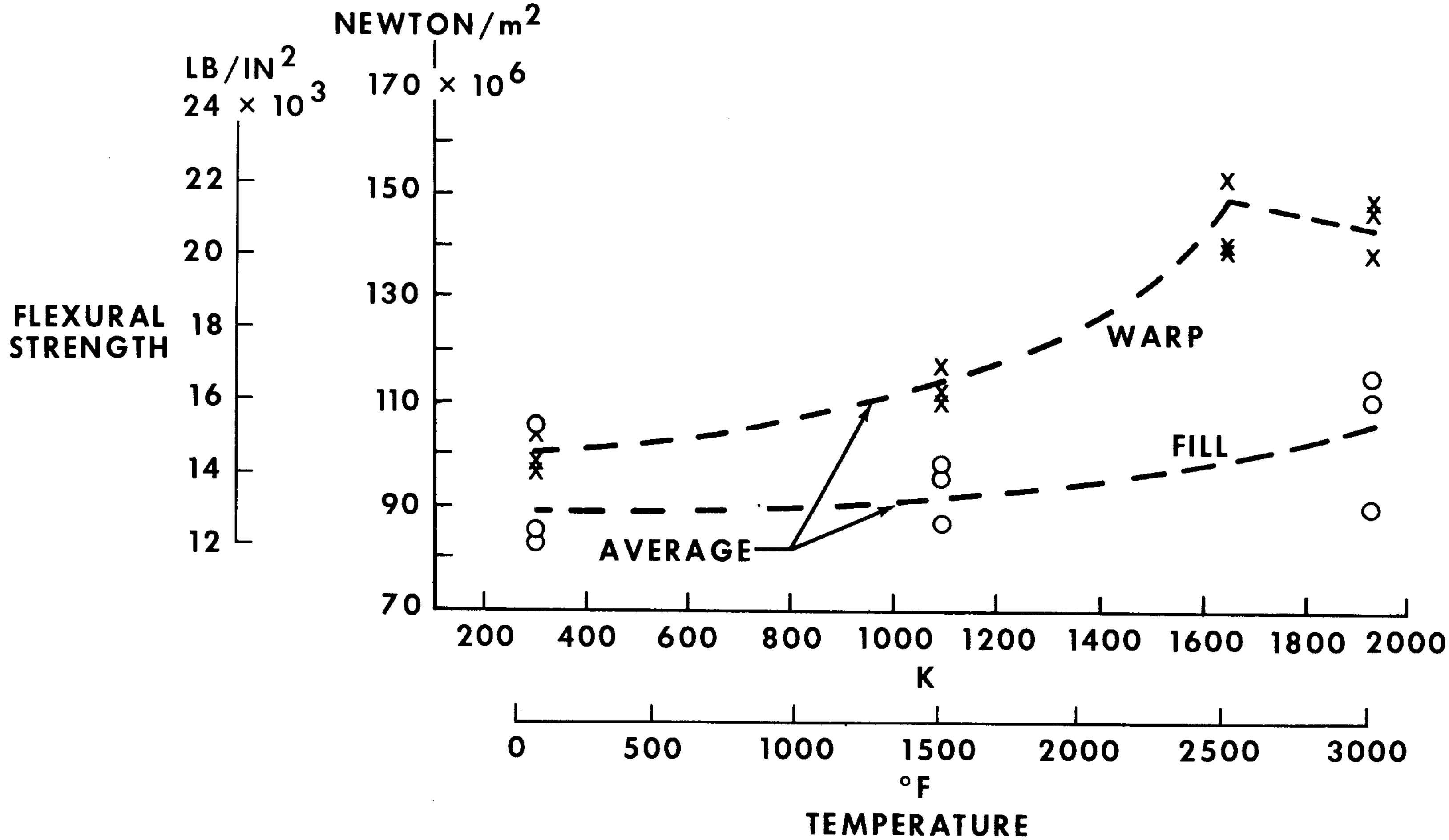

DESIGN STUDIES

Two applications for oxidation inhibited carbon-carbon have been pursued in the technology program and the phase "B" shuttle studies. The most promising application is to the leading edge regions, and wing tip and mid span designs have been developed. In addition, a fuselage panel was fabricated and tested.

DESIGN STUDIES

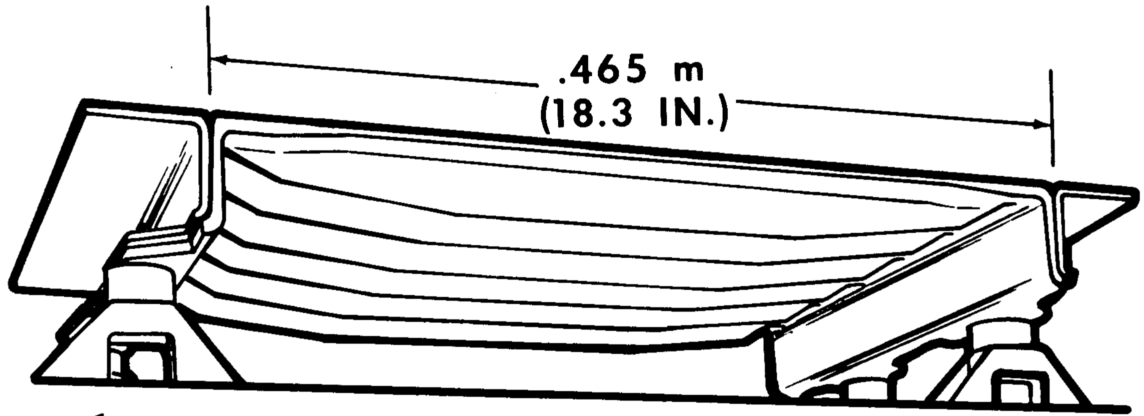

FUSELAGE PANEL

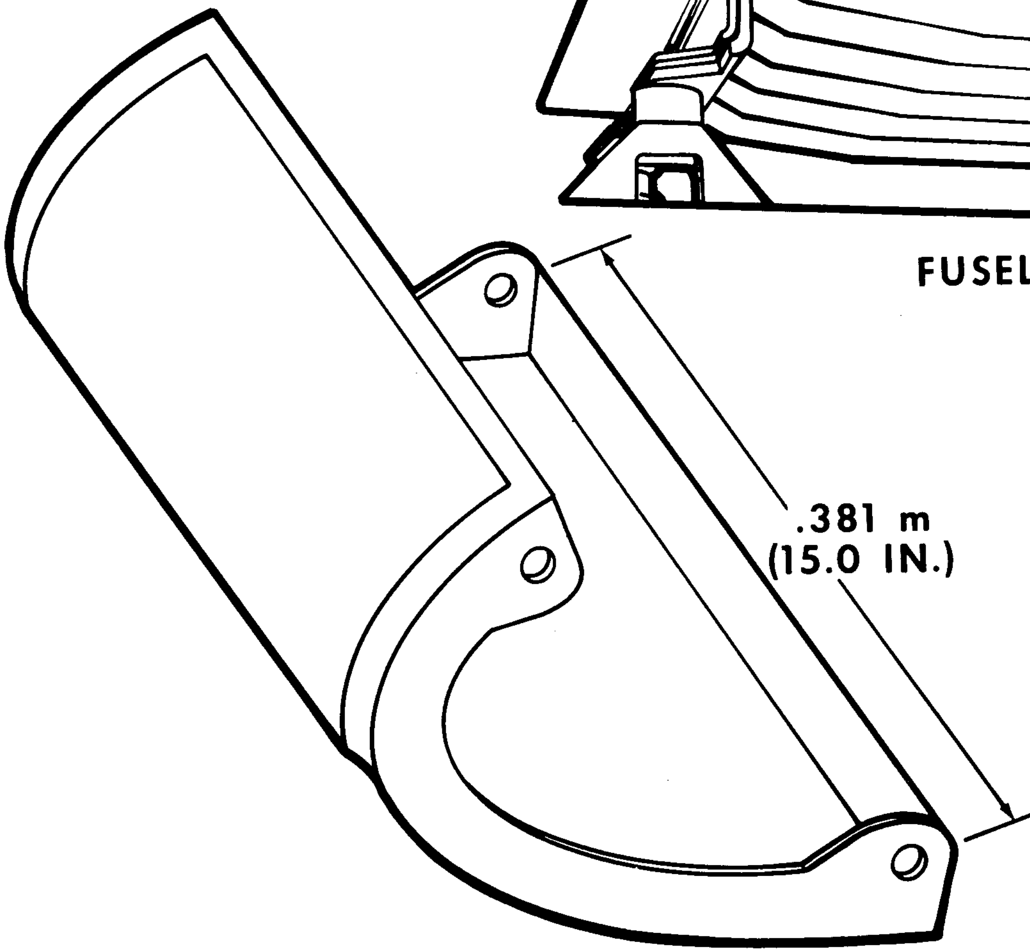

WING LEADING EDGE PANEL

WING LEADING EDGE DESIGN CRITERIA

The design criteria used for the wing leading edge are summarized. The maximum equilibrium temperature at the stagnation point, based on an emittance of 0.85, is 1783K (2750°F) and occurs 420 seconds after entry from 122 km (400 000 ft) altitude. No loads or pressures are assumed to act on the structure during the entry heating phase of the mission. The maximum pressures on the leading edge occur at maximum "q" during boost when the structure is still at room temperature. The ultimate pressures shown include a factor of safety of 1.4 and the design burst pressure includes an internal limit ΔP of 10.35 kN/m^2 (1.5 psig) to allow for a venting lag during boost. The ultimate collapse pressure of 19.31 kN/m^2 (2.8 psig) assumes a zero pressure differential due to venting. Also shown in the figure are the vibration and acoustic environments which will be used during tests of full-scale leading edge segments.

WING LEADING EDGE DESIGN CRITERIA

- MAXIMUM EQUILIBRIUM TEMPERATURE, $\epsilon = 0.85$ ---------- 1783 K (2750° F)
- BOOST PRESSURE
  - BURST (INCLUDES VENTING LAG) ---- 27.58×10^3 NEWTON/m^2 ULT (4.0 PSI)
  - COLLAPSE -------------------- 19.31×10^3 NEWTON/m^2 ULT (2.8 PSI)
- RANDOM VIBRATION -------------- 32 'g' RMS
- ACOUSTIC NOISE ----------------- 163 DB OA
- ENTRY TIME -------------------- 2400 SEC

THERMAL ENVIRONMENT - WING LEADING EDGE

The temperature of the leading edge at 75 percent span is shown as a function of entry time for a typical delta wing high cross range vehicle.

Radiation equilibrium temperatures were computed using a surface emittance of 0.85 to provide an upper limit of expected temperatures on the leading edge.

THERMAL ENVIRONMENT
WING LEADING EDGE

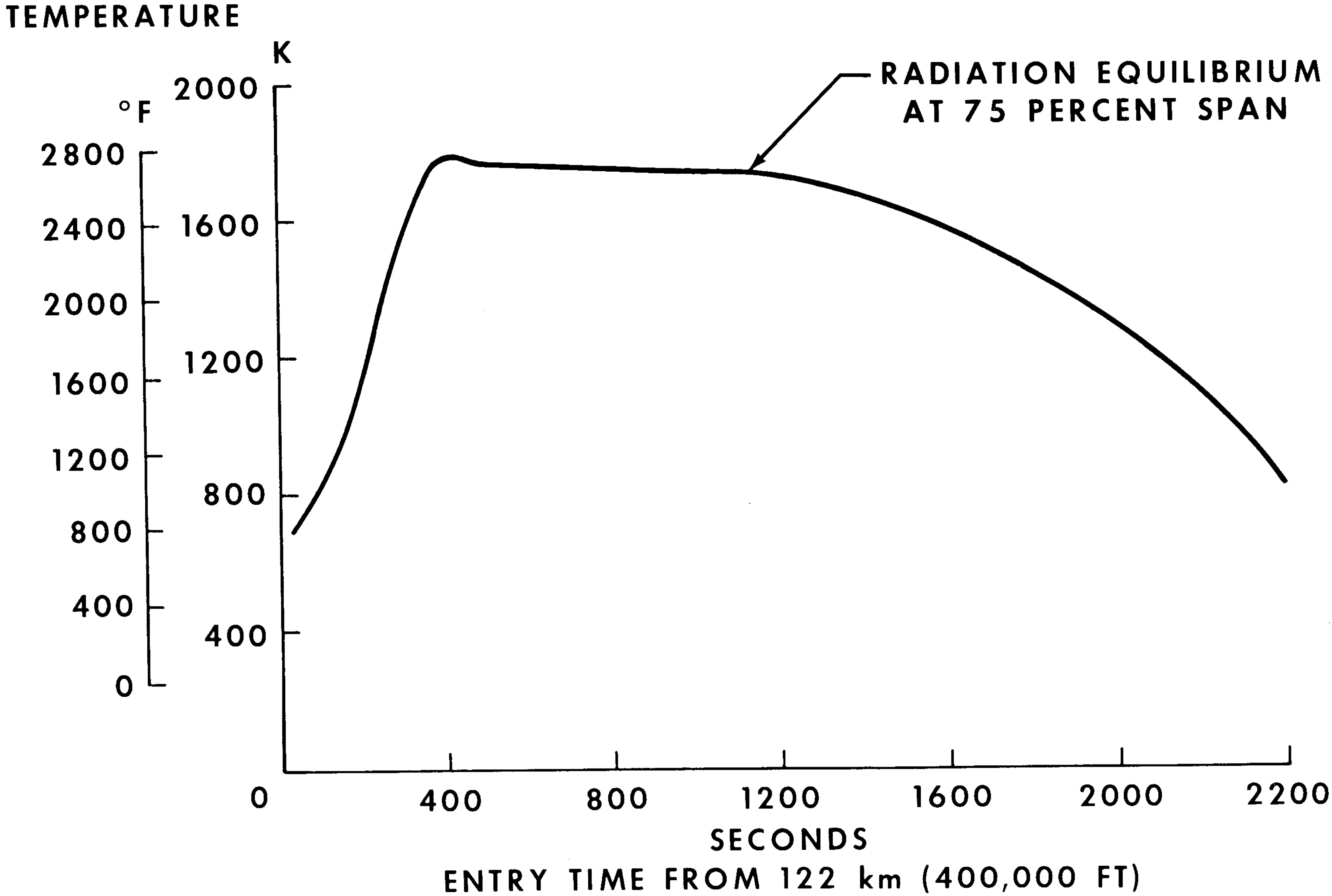

TEMPERATURE DISTRIBUTION AROUND LEADING EDGE

The temperature distribution around the leading edge at 420 seconds after start of entry is compared with maximum radiation values. A two-dimensional analysis was performed to determine the combined effects of internal cross radiation. Heat conduction through the skin in both circumferential and thickness directions was included in the analysis. The back plane of the leading edge was assumed to be adiabatic to represent insulation over the wing support structure and support joints. A portion of the skin interior surface near both windward and leeward support joints was assumed to be covered by insulation material to protect the joints. These surfaces were also assumed to be adiabatic. The remaining interior nodes were permitted to cross-radiate. The point of peak circumferential temperature gradient in the radiation equilibrium analysis was near the geometric leading edge centerline. In the cross-radiation analysis the maximum gradient shifts to the location on the leeward side where the wing support insulation begins. The peak gradient is also reduced from the radiation equilibrium value of 2.12×10^4 K/m (513°F/in.) to 1.72×10^4 K/m (325°F/in.) which is significant from a thermal stress standpoint.

TEMPERATURE DISTRIBUTION AROUND LEADING EDGE

PEAK TEMPERATURES AT 420 SECONDS
AFTER START OF ENTRY, K (°F)

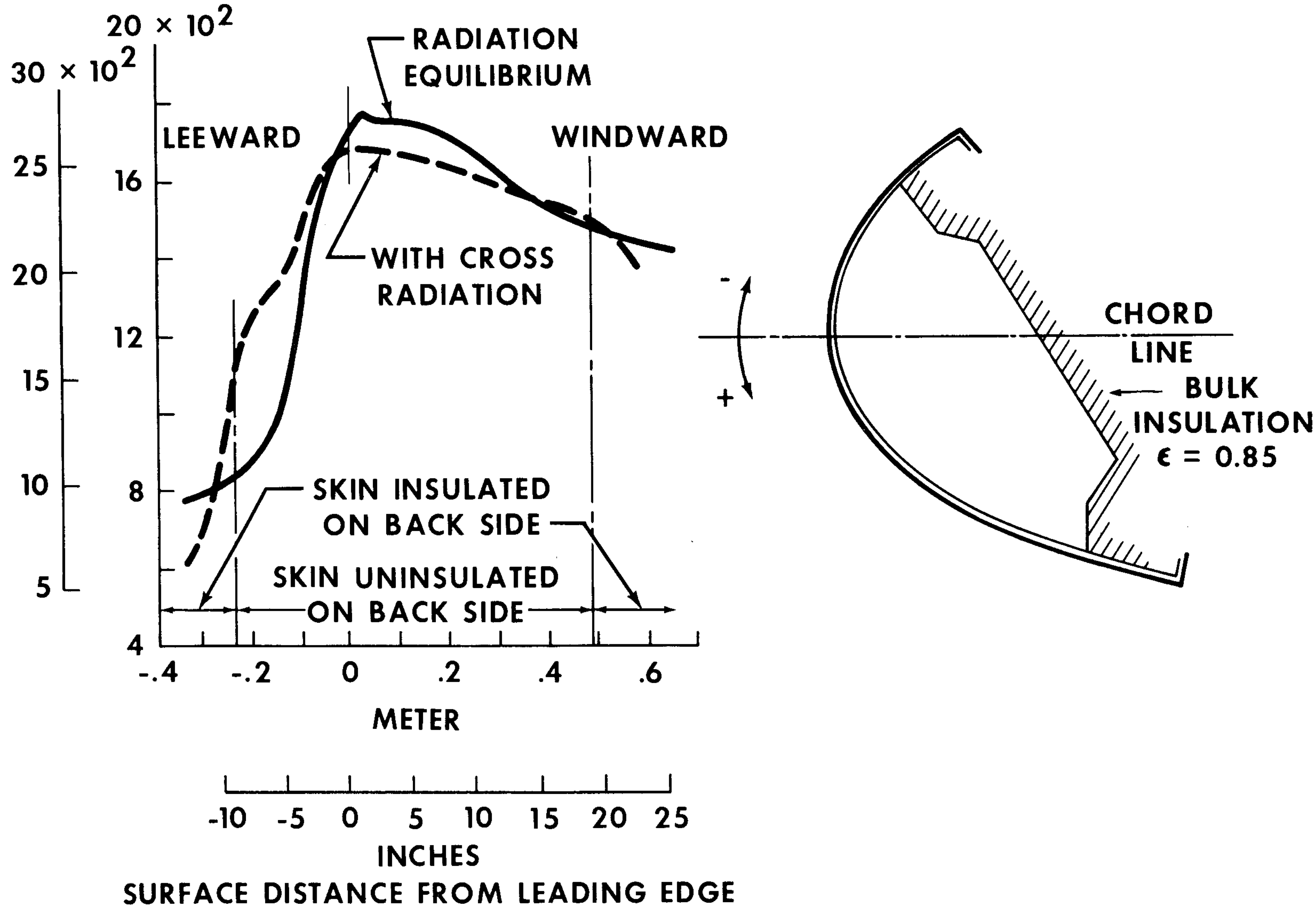

WING LEADING EDGE DESIGN

The current preliminary design for a delta wing vehicle leading edge is shown. The design is comprised of five integrally fabricated structural elements: an airload panel, two ribs with integral attachment lugs, and an upper and lower cross beam at the aft edges of the airload panel. These cross beams serve to support the airload panel against flutter and reduced airload panel thickness and weight. Wing interface geometry is typical of support structure that could be employed to attach the leading edge to the wing. The design is 0.609 m (24 inches) high by 0.469 m (18.42 inches) chord by 0.38 m (15 inches) span. Coating furnace limitations dictated a span of 0.38 m (15 inches) for test hardware. A typical section of the thickened lug area together with the stiffened beam is shown. The in-board lugs of each leading edge segment are fixed against side movement, while the out-board lugs are free to slide on the insulators to accommodate thermal expansion. Nominal weight of the inhibited carbon-carbon leading edge based on surface area is 9.47 kg/m^2 (1.94 lb/ft^2).

WING LEADING EDGE DESIGN

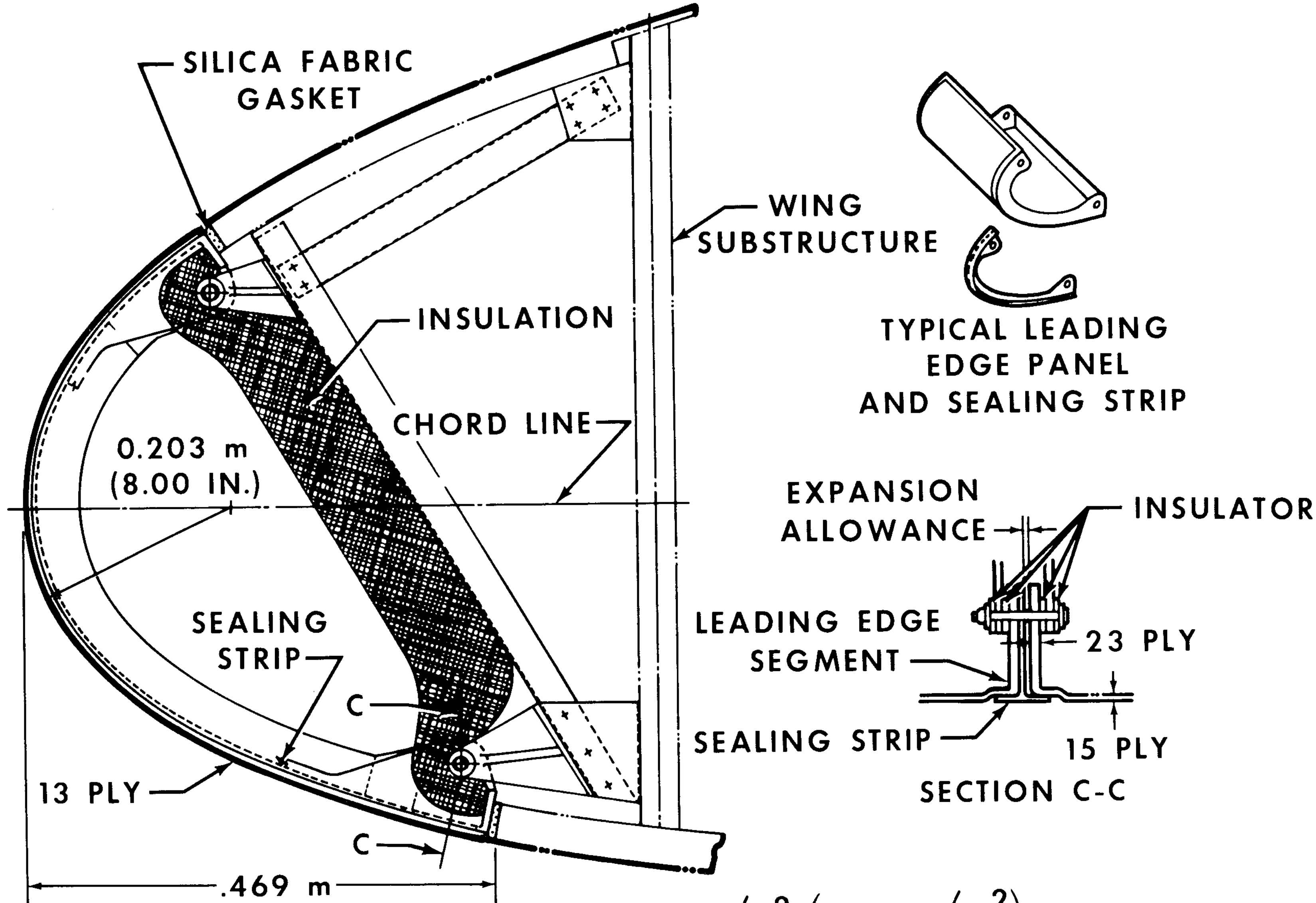

UNIT WT = 9.47 kg/m^2 ($1.94\ LB/FT^2$) OF SURFACE AREA

PROTOTYPE CARBON LEADING EDGE SEGMENTS

Photographs are shown of the leading edge test segments. The photograph on the left is the prototype leading edge and seal strip prior to application of the oxidation inhibitor. On the right are shown two oxidation inhibited leading edges and a seal strip ready for the thermal test.

PROTOTYPE CARBON LEADING EDGE SEGMENTS

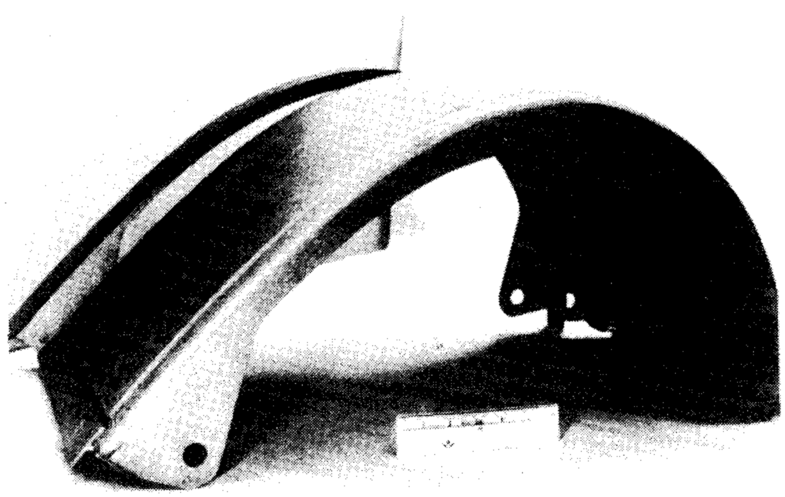

LEADING EDGE BEFORE INHIBITOR APPLICATION

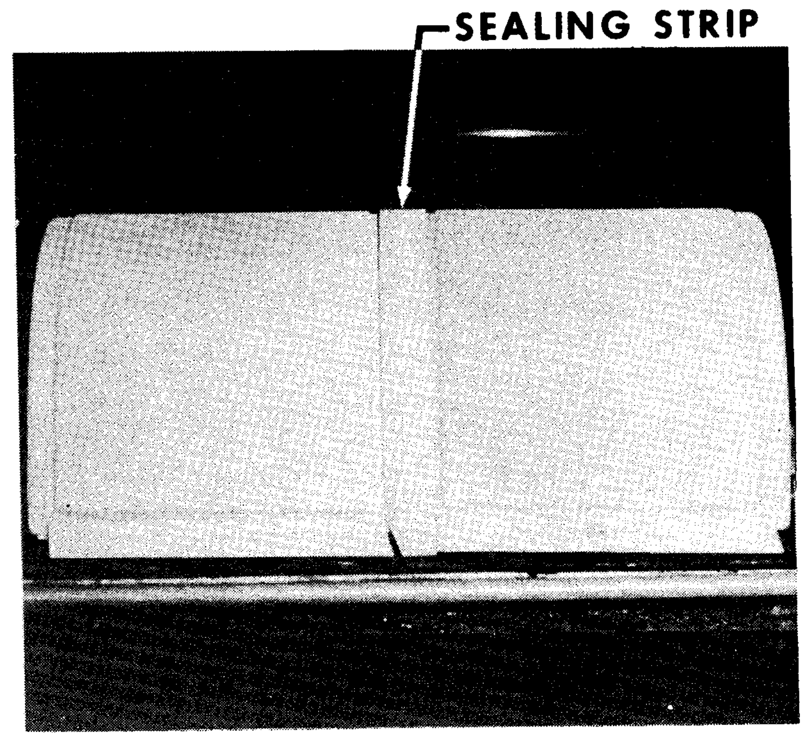

SILICONIZED LEADING EDGES IN TEST FIXTURE

PROTOTYPE LEADING EDGE TESTS

The testing that has been done on the leading edge prototype specimens consists of an airload proof test at room temperature, and a thermal cycle test in an argon atmosphere. For the airload proof test a single .38 m (15 inches) span segment was supported at the four corners to a test fixture, and a constant pressure of 17.94 kN/m^2 (2.6 psi) was applied over the bottom surface only of the leading edge segment. This test condition represented the limit air pressure at max q (headwind) during boost and includes an internal pressure of 10.35 kN/m^2 (1.5 psig) to allow for an assumed venting lag. Strain gauges at 35 different locations were used to monitor stresses during this test and to compare with the analyses. A comparison of the measured stresses on the inside of the rib flanges with the analytically predicted stresses using the Nastran finite element computer program is shown. A value of 9650 MN/m^2 (1.4 x 10^6 psi) for Young's modulus in tension was used to convert the measured strains into stresses. No anomalies or failures were observed after this test.

The thermal cycle test was performed in a large chamber filled with argon gas. The test specimen consisted of two .38 m (15 inches) span adjacent segments with a carbon-carbon sealing strip representative of the flight article design. The objective of the test was to verify the structural integrity of the leading edge for design entry temperatures and temperature gradients. The maximum temperature at the stagnation point for the test was 1695K (2592°F). Twenty-four thermocouples were used to measure the temperatures during the test. Posttest visual examination of the test segments revealed no cracks or failures.

PROTOTYPE LEADING EDGE TESTS
AIRLOAD PROOF TEST AT ROOM TEMPERATURE

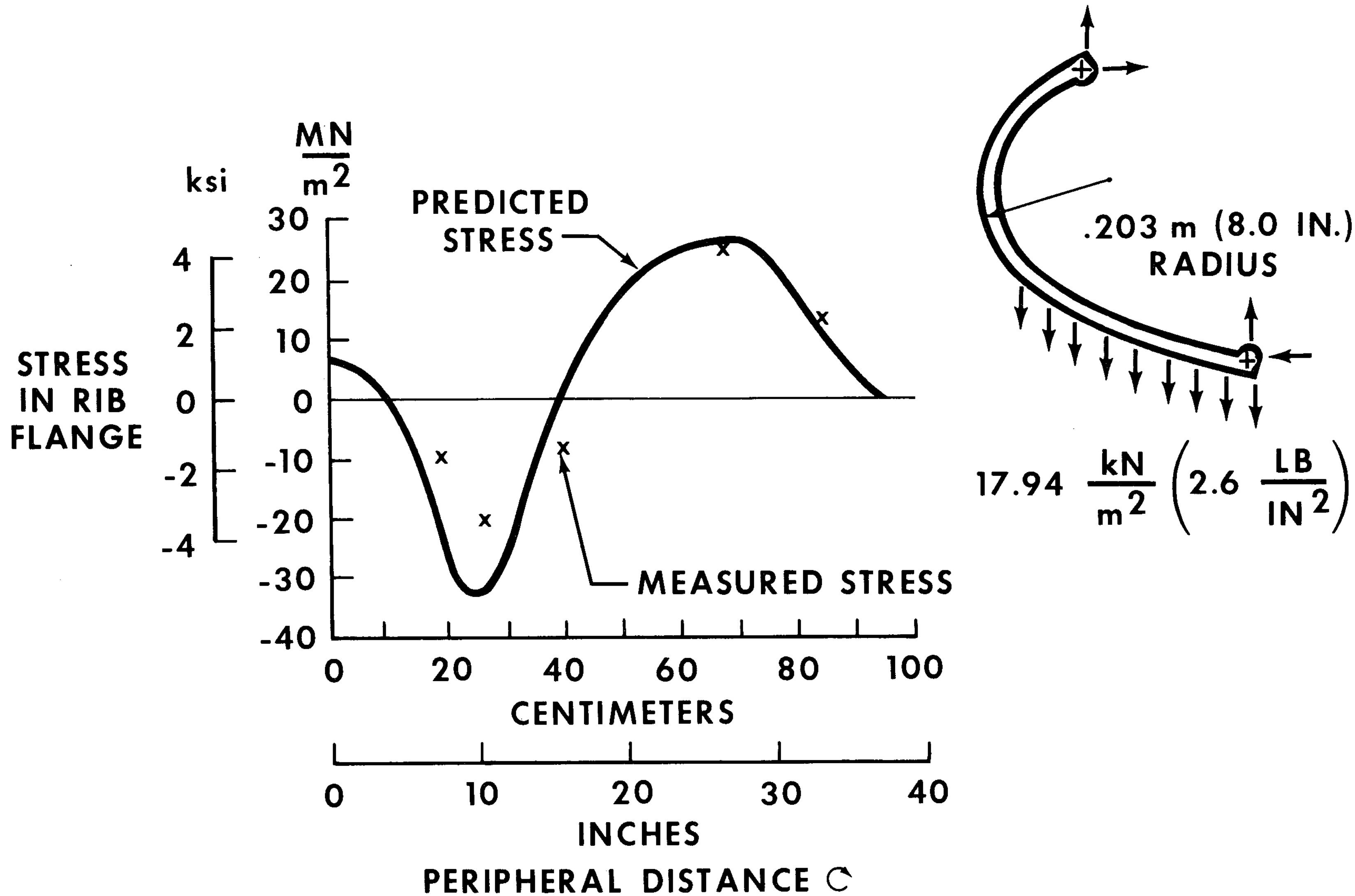

FUSELAGE TEST PANEL - SILICONIZED CARBON-CARBON

In addition to the wing leading edge segments, two fuselage panels have been fabricated. These panels were made in order to check the feasibility of using inhibited carbon-carbon for the TPS on the bottom surface of the orbiter fuselage and to obtain actual weight values.

Maximum temperature capability required was 1645K (2500°F) with a life requirement of 100 missions. Design limit pressures, which occur during boost when the surface temperature is below 338.7K (150°F), were 21 kN/m^2 (3.2 psi) burst and 18 kN/m^2 (2.6 psi) collapse. These pressures include venting lag and establish the sizing of the panel and support structure. A maximum acceleration of 3.3 "g" and acoustic noise requirement of 167 dB overall were also used to size the panel.

The design concept configuration shown is a "T" panel with an integrally fabricated flexure support joint. The overall panel size is 0.305 m (12 inches) by 0.465 m (18.3 inches). Weight of the basic panel is 1.25 kg (2.76 lb), corresponding to approximately 7.8 kg/m^2 (1.6 lb/ft^2).

Tests have been completed on the panels. The first test on the concept was a limit burst pressure test to 21.06 kN/m^2 (3.2 lb/in^2) with no visible structural damage and deflections slightly lower than predicted. Next was the limit collapse static pressure test to 17.94 kN/m^2 (2.6 lb/in^2) with no visible structural damage and deflections slightly lower than predicted. The next test was 100 thermal cycles of a complete entry temperature profile that reached a maximum of 1645K (2500°F). Inspection after the 100 cycles did not reveal any structural damage to the panel. Finally, to determine if any degradation in stiffness occurred after completion of the 100 thermal cycles an ultimate static burst pressure test to 31.1 kN/m^2 (4.5 lb/in^2) was performed. The panel concept successfully completed the test program.

FUSELAGE TEST PANEL
SILICONIZED CARBON-CARBON

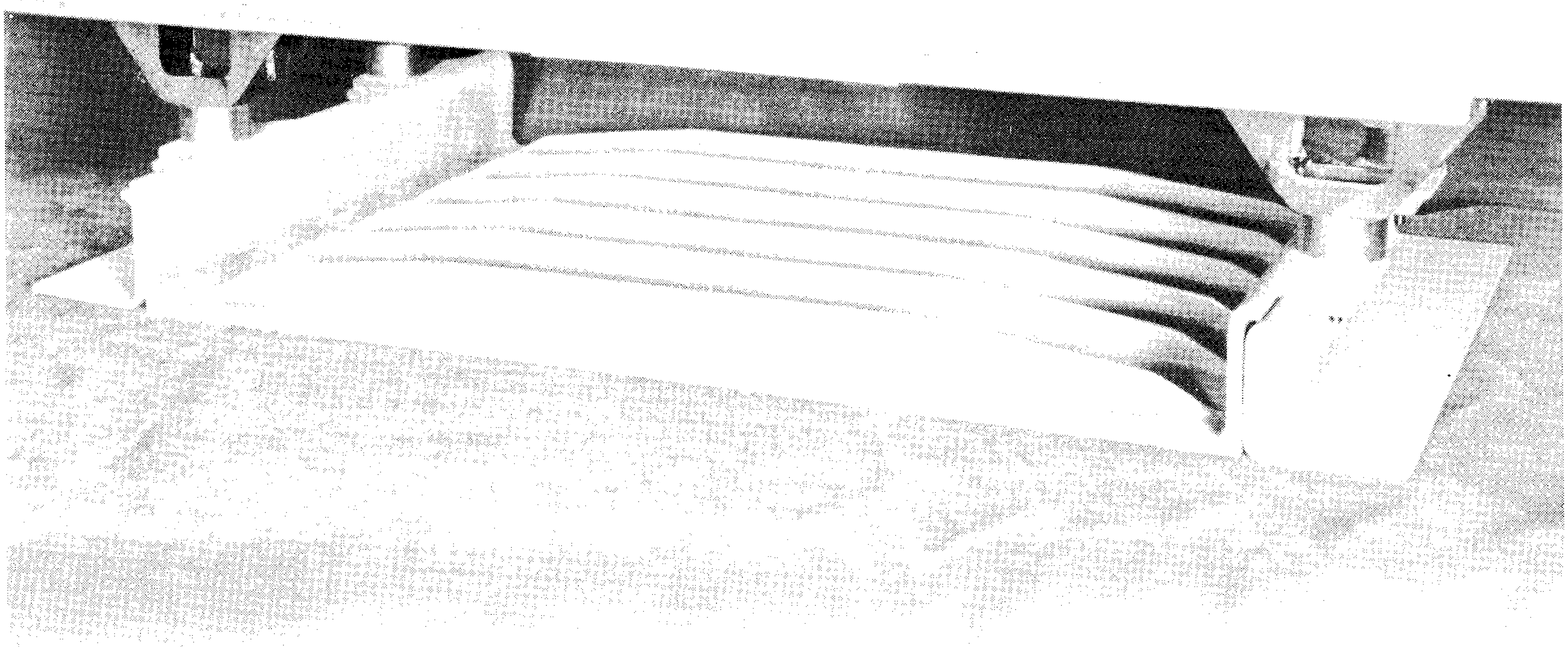

CONCLUDING REMARKS

SUMMARY

- MATERIAL FABRICATION PROCESSES AND THERMAL AND MECHANICAL PROPERTIES (13-PLY) DEFINED
- THREE FULL-SCALE LEADING EDGES AND TWO FUSELAGE PANELS FABRICATED AND TESTED, AND TWO SUBSCALE LEADING EDGE SPECIMENS UNDERGOING TESTS AT MSC
- 100 MISSION REUSE CYCLES PROJECTED FOR 1811K (2800° F) MAXIMUM SURFACE TEMPERATURE

FUTURE TASKS

- DESIGN AND FABRICATION OF FAIL-SAFE LEADING EDGE ASSEMBLIES INCLUDING INSULATION
- TESTING OF LEADING EDGE ATTACHMENTS AND HOT GAS LEAKAGE BETWEEN LEADING EDGE SEGMENTS
- DESTRUCTIVE AND NONDESTRUCTIVE EVALUATION METHODS AND PROCEDURES FOR IN-PROCESS AND REUSE ANALYSIS

REUSABLE SURFACE INSULATION MATERIALS RESEARCH AND DEVELOPMENT

Howard E. Goldstein
NASA Ames Research Center, Moffett Field, California

John D. Buckley
NASA Langley Research Center, Hampton, Virginia

Harry M. King
NASA Marshall Space Flight Center

Hubert B. Probst
NASA Lewis Research Center, Cleveland, Ohio

Ivan K. Spiker
NASA Manned Spacecraft Center, Houston, Texas

INTRODUCTION

(Figure 1)

Reusable Surface Insulation (RSI) is currently considered a prime candidate for heat shielding large areas of the Space Shuttle Vehicle (SSV). This class of materials has been under development by NASA and its contractors for approximately two years. Rapid progress has been made in both development and characterization of RSI. The objectives of this paper are to describe the state of technology of RSI, indicate the improvements that have been made and discuss the current effort aimed at further improvement. Mr. Greenshields et al.[1] discuss the systems applications of RSI and the system evaluation tests by MSC; so that work will not be discussed in this paper. Because of the restrictions that must be observed during PHASE C/D proposal preparation much of the data discussed in this paper cannot be attributed to its source. When this quiet period is ended, the authors will be happy to supply references for the data presented to all interested parties.

The composition and fabrication of RSI materials will be discussed first, followed by evolution of RSI and current problems, physical and thermal properties, arc plasma test data and results, and material improvement research. Finally, a summary of RSI technology status is presented.

---

[1]Paper no. 15 of this compilation.

REUSABLE SURFACE INSULATION (RSI) MATERIALS RESEARCH AND DEVELOPMENT

- RSI MATERIALS AND FABRICATION
- RSI EVOLUTION
- PHYSICAL PROPERTIES
- THERMAL PROPERTIES
- ARC PLASMA TESTING
- IN-HOUSE NASA RSI RESEARCH
- SUMMARY

Figure 1

RSI Materials Problems
(Figure 2)

RSI materials problems can be broken down into three general categories: those related to the state of development of RSI; those related to the systems requirements for the Space Shuttle Vehicle; and those related to the inherent physical properties of this class of materials. The state of development problems are primarily caused by its immature status and the rapid development of RSI. For engineering applications it is considered essential that sufficient property data be available to determine statistical variations of properties to properly define design allowable limits. Available data on even the best characterized materials are generally based on no more than a dozen duplicate tests. Added to this is the great difficulty in determining valid physical testing techniques. Most of the data available on thermal and mechanical environmental tests have been obtained on materials that are no longer being manufactured. There is no current agreement on the failure modes for RSI materials in thermal and mechanical stress environments. Finally, the RSI materials are changing so rapidly that it is quite likely that none have really reached their optimum state of development. Therefore, design work being done, based on the current properties, may not be pertinent to application of the final RSI materials.

The systems requirements are discussed in detail by Mr. Greenshields. Listed are three systems problems that are directly related to materials development. The optical properties that will be optimum for each region of the SSV heat shield are not completely defined. It is quite likely that in certain areas a balance between high temperature emittance and solar absorptance is desirable, which gives adequate in-orbit temperature control as well as sufficiently low surface temperatures during reentry. The reentry environment is still not completely defined, particularly the turbulent heating effects in gaps and on protuberances and the general heating levels that can be expected over many regions of the shuttle. Another environmental problem is probable exposure to salt spray and its attendant effects. The present ground rule states that the heat shield shall be continuously waterproof, for 100 flights. If this ground rule can be relaxed to some degree, many of the difficult problems such as coating strain to failure and coating tile interface failure can be more easily solved.

The problems with the physical properties of RSI materials are not subject to complete solution. The materials are inherently weak and brittle because they are low density ceramics. Design studies have shown that the current RSI properties are marginal and require unusual design solutions such as strain isolation to permit their use on the shuttle. Significant improvement in the physical properties could drastically simplify design. Thermal stress problems of the RSI materials are, of course, closely related to these marginal physical properties.

The problems listed above have evolved from the many studies that have been carried out over the last two years. As the shuttle program proceeds and the RSI materials are better understood, it is likely that many of the above problems will be solved and others defined.

RSI MATERIALS PROBLEMS

- STATE OF DEVELOPMENT
  - INSUFFICIENT PHYSICAL AND THERMAL PROPERTY DATA
  - INSUFFICIENT THERMAL AND MECHANICAL ENVIRONMENTAL RESPONSE DATA
  - DEFINITION OF FAILURE MODES NEEDED
  - MATERIALS NOT OPTIMIZED
- DEFINITION OF SYSTEM REQUIREMENTS
  - OPTICAL PROPERTIES
  - SYSTEM ENVIRONMENTS
  - WATERPROOFING REQUIREMENTS
- PHYSICAL PROPERTIES
  - WEAK
  - ANISOTROPIC
  - LOW STRAIN TO FAILURE

Figure 2

RSI COMPOSITION

(Figure 3)

The RSI materials have been evolving so rapidly that the compositions shown in this figure are probably obsolete. These compositions are considerably changed from what was reported six months ago. Silica RSI is fabricated from a purified grade of silica, 1.0 μm fiber, using a colloidal silica binder. The coating consists of a densified sub-layer with a borosilicate glass sealer layer. The additive material for emittance in the coating is silicon carbide. The tile composition has been the same for nine months, while the coating is a recent innovation.

The mullite A is fabricated from 4.7 μm mullite fiber. The binder is colloidal silica with organic additives, to promote dispersion of the binder and control migration during processing. Zircon powder is added to improve opacity and silica microspheres are included for density control and for added strength. The coating is multilayered having a dense sub-layer, a diffusion barrier of $AlPO_4$ and chromium oxide and an emittance pigment P700, containing iron, cobalt, and chromium oxides. Next there is a borosilicate glass layer with a silicate bonded P700 layer on the outside. The tile composition was changed recently by improving the binder, using the smaller diameter fiber and adding an opacifier. The coating has gone through a number of variations and is apparently still in a rapid state of development.

Mullite B is also fabricated using the 4.7 μm fiber. The binder is a ternary Al_2O_3-SiO_2-B_2O_3 glass. This material is significantly changed from the earlier version mullite which was bonded with a complex organo-metallic binder system. The coating system is made up of a densified layer and an outer coating of Kyanite/Petalite in a glass matrix. Both layers have the same composition. Nickel oxide is added as an emittance agent.

RSI COMPOSITION

MATERIAL DESIGNATION	FIBER	BINDER	FILLERS	COATING
SILICA	SILICA FIBER 1.0 μm	COLLOIDAL SILICA		— BOROSILICATE GLASS — SILICON CARBIDE EMITTANCE AGENT
MULLITE A	MULLITE (ALUMINUM SILICATE) FIBER 4.7 μm	SILICA	SILICA MICROSPHERES ZIRCON (OPACIFIER)	— SILICATE BONDED P700 EMITTANCE AGENT — BOROSILICATE GLASS — $AlPO_4 + Cr_2O_3$ + SILICATE BONDED P700 — MULLITE FIBER + Al_2O_3 CEMENT
MULLITE B	MULLITE (ALUMINUM SILICATE) FIBER 4.7 μm	TERNARY $Al_2O_3-SiO_2-B_2O_3$ GLASS		— KYANITE / PETALITE MULTIPHASE GLASS — DENSIFIED LAYER OF THE SAME COMPOSITION

Figure 3

RSI-MANUFACTURING FLOW CHART
(Figure 4)

Though silica and mullite are similar in final form they are fabricated by different techniques as shown by the accompanying figure. The silica is made by dispersing the silica fibers in water and casting, by gravity or centrifugal force, onto a screen. The unbonded felt is dried, fired, and impregnated in a controlled environment. To make mullite A the fiber and microsphere filler is dispersed in a binder solution and the impregnated felt is vacuum cast on a screen. The manufacturer of mullite B disperses the fiber in a slurry containing the binder and a fiber matt is formed by molding with a gravity drain of the excess slurry liquid. The drying, firing, and machining for all the fiber based RSI materials are similar. All the materials are fired at temperatures ranging from 1260° to 1370° C (2300° to 2500° F). Firing cycles are apparently fairly complex in that a controlled slow rate of temperature rise is required to obtain optimum tile properties. The detailed firing cycles are considered proprietary by some of the manufacturers.

Coating processes vary greatly from material to material. It is worth noting that all these coating systems are unique in that they are meant to be essentially soft at their upper operating temperatures. Silica tile coating is applied in two layers with the outer borosilicate glass applied as an overspray. The coating is then fired. The mullite A coating is applied in alternate layers with drying and firing cycles between. The mullite B coating is applied in two layers, a densified layer that is dried and fired and an outer layer which is sprayed on and again fired.

All the above processing procedures have been changing rapidly. A number of changes are likely in the near future. Of particular interest is the possibility of the mullite materials going to smaller diameter fibers which could both improve their strength and decrease thermal conductivity of the finished tile. Binder systems and tile processing for both of the mullite systems are also likely to be modified. Changing emittance additives, modifying the thermal expansion and softening characteristics of the coatings, and going to more simplified coating systems (fewer number of layers) are areas of likely improvement to existing coating systems. All the manufacturers are considering the use of refurbishable organic coatings if the glassy coatings are not adequate for the order of 100 flights.

All three manufacturers have put pilot plant-sized facilities into operation. Their current production capabilities are on the order of 92.9 to 464.5 m^2 (1000 to 5000 ft^2) of coated RSI per year. Each manufacturer feels that increasing production to the rate necessary for fabrication of shuttle heat shields should be easily accomplished. The present cost of both silica and mullite coated tile is $7535 to $9150/$m^2$ ($700 to $850/$ft^2$) and is expected to decrease to about $3767/$m^2$ ($350/$ft^2$) when full-scale production is reached. This cost does not include installation on the vehicle, capital costs, NDE, or design of the heat shield.

RSI-MANUFACTURING FLOW CHART

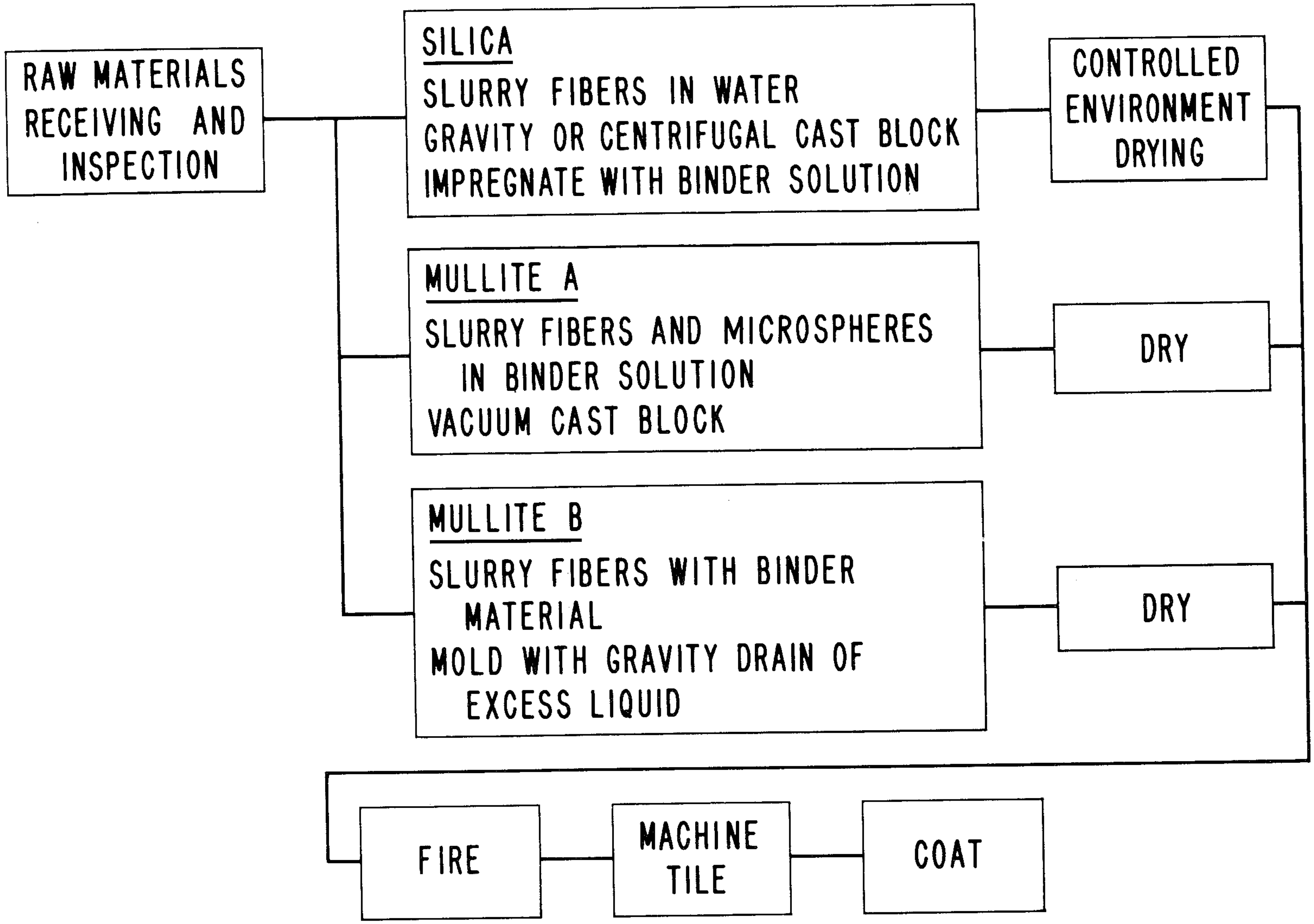

Figure 4

EVOLUTION OF REUSABLE SURFACE INSULATION
(Figure 5)

This figure illustrates the evolution of the RSI materials. Initial development can be traced to requirements for base-heating protection of large boosters and composite insulation-ablation materials for lifting reentry bodies. Early in its development the silica material was shown to have reuse potential. In early 1970, MSC initiated a screening program to evaluate this class of materials for possible use on the Space Shuttle Vehicle. A large number of concepts and material variations were initially considered by NASA and its contractors. Silica fibers were selected early by one contractor. Among the other materials considered were mullite, other alumino-silicates, zirconia, and silicon carbide coated carbon. Numerous coating and binding systems were considered and discarded. By mid-1970 one contractor had chosen mullite and in early 1971 a second contractor picked mullite.

Late in 1970 MSC initiated a second phase of development with contracts going to those contractors whose RSI materials appeared to have the most promise. During this period the first nominally, waterproof coating was developed for a mullite RSI material. In 1971 a significant improvement in the silica tile was obtained by incorporating a highly purified silica fiber, allowing higher firing temperatures which allowed a waterproof coating for the silica RSI to be developed. In mid-1971 MSC initiated a Phase II procurement of the RSI materials. During the same time period RSI development and improvement contracts were let by MSC for silica and by MSFC and LRC for mullite. Through these contracts significant improvements in coatings and binders of the mullite systems have been accomplished.

In the last three months each contractor has fabricated materials with significantly improved physical properties. A 240 kg/m^3 mullite material with much higher and more uniform strength characteristics, a 192 kg/m^3 mullite, and a 144 kg/m^3 silica are being supplied to NASA. These materials are currently being assessed. Unfortunately, they have been available for such a short time that only very limited data are available. In subsequent sections of this paper these are the materials discussed, where data are available.

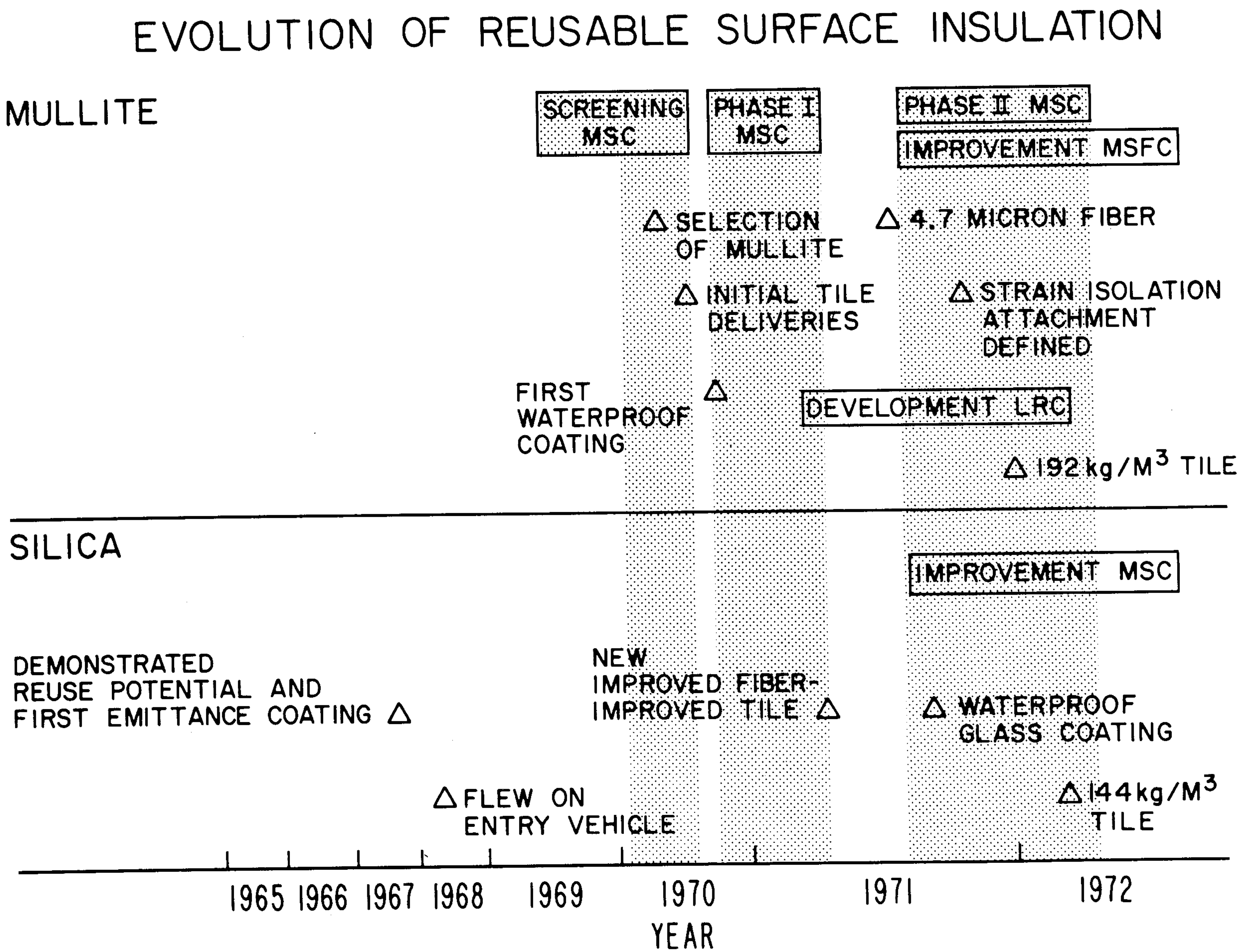
EVOLUTION OF REUSABLE SURFACE INSULATION
MULLITE
SCREENING MSC
PHASE I MSC
PHASE II MSC
IMPROVEMENT MSFC
SELECTION OF MULLITE
4.7 MICRON FIBER
INITIAL TILE DELIVERIES
STRAIN ISOLATION ATTACHMENT DEFINED
FIRST WATERPROOF COATING
DEVELOPMENT LRC
192 kg/M3 TILE
SILICA
IMPROVEMENT MSC
DEMONSTRATED REUSE POTENTIAL AND FIRST EMITTANCE COATING
NEW IMPROVED FIBER-IMPROVED TILE
WATERPROOF GLASS COATING
FLEW ON ENTRY VEHICLE
144 kg/M3 TILE
1965 1966 1967 1968 1969 1970 1971 1972
YEAR

Figure 5

TENSILE PROPERTIES OF RSI

(Figure 6)

This figure illustrates the improvements that have been accomplished in RSI physical properties over the last four years. Only tensile properties are shown, but the same trends exist for other properties. The mullite RSI has improved rapidly with NASA funding over the last two years, probably because the state of the art was less advanced for mullite than for silica. At the present time the mullite has essentially equaled the physical properties of the silica. The longitudinal strength of both materials is greater than the transverse strength. The difference is much greater for silica than for mullite. The increase in modulus of the silica is a result of improved fiber and processing, but also may result partially from changes in testing techniques that have occurred during the last two years. It is quite likely that this type of strength improvement will continue for the next year since it is generally agreed that considerable improvements are desirable and possible.

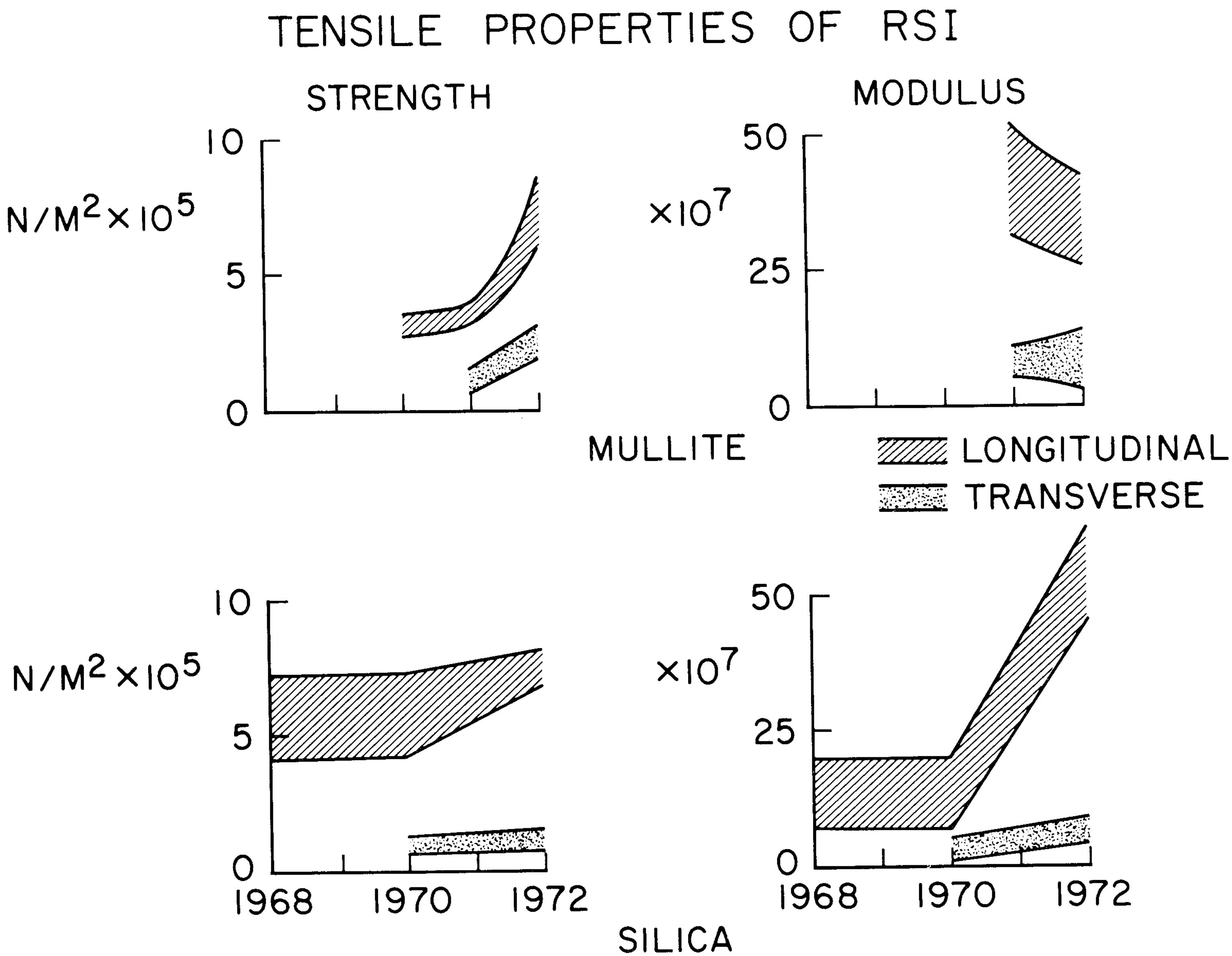
TENSILE PROPERTIES OF RSI
STRENGTH
MODULUS
N/M2×105
×107
10
5
0
50
25
0
MULLITE
LONGITUDINAL
TRANSVERSE
SILICA
1968
1970
1972

Figure 6

CURRENT RSI PHYSICAL PROPERTIES
(Figure 7)

Presenting valid comparative mechanical properties for the RSI materials is extremely difficult. This difficulty arises for a number of reasons. For one, varying testing methods and sample geometries are used. Also, mechanical properties are strongly dependent on sample density, fiber size, and processing variables. Finally, the major source of difficulty is the rapid evolution that the RSI materials are experiencing. It has often been the case that when numerical data were published in a contractor's report they were soon made obsolete by new data being generated on a revised version of the material. In 1971 Battelle compared properties of the then available RSI materials under identical test conditions. Unfortunately, the data were rapidly made obsolete as materials and processing were changed. Thus, these limitations have to be fully realized when comparisons are attempted.

In this table, room temperature physical properties (manufacturers' data) for a 240 kg/m^3 silica and a 192 kg/m^3 mullite and a 240 kg/m^3 mullite are compared. In terms of design, tensile strength is probably the most significant property. A comparison between tensile strengths of the three current materials indicates that the high density mullite is strongest in both the longitudinal and transverse directions. The longitudinal (strong) direction is parallel to the fiber's long axis and the transverse (weak) direction is perpendicular to the same axis. The silica shows the greatest difference between longitudinal and the transverse directions, nearly a factor of five difference compared with a factor of three for the mullite. Tensile modulus in the transverse direction of the silica is generally higher than the mullite materials and the strain to failure of the mullite materials is higher than that of silica. The values shown here are a significant improvement in strain to failure values over the earlier mullite materials. The high density mullite has the highest compressive strength of the materials. Comparability of physical test data between materials will be discussed subsequently.

In general, there is good agreement between the manufacturers' and Ames Research Center data (not shown) considering the variations that can be expected between different measuring techniques and the possible variability of materials from tile to tile. Perhaps the only significant difference between the results are that the densities of the denser mullite and the silica samples measured by ARC were higher than the manufacturers' specifications by about 15 percent.

CURRENT RSI PHYSICAL PROPERTIES

	SILICA	MULLITE
DENSITY, kg/M^3	240	192 240
TENSILE STRENGTH, $N/M^2 \times 10^5$		
LONGITUDINAL	4.8	5.9 6.6
TRANSVERSE	1.0	1.9 2.5
COMPRESSIVE STRENGTH, $N/M^2 \times 10^5$		
LONGITUDINAL	10	6.5 15
TRANSVERSE	2.8	2.9 4.3
SHEAR STRENGTH, $N/M^2 \times 10^5$		
LONGITUDINAL	2.6	2.1 3.9
TENSILE MODULUS, $N/M^2 \times 10^7$		
LONGITUDINAL	41	29 39
TRANSVERSE	4.1	6.3 13
TENSILE STRAIN TO FAILURE, percent	0.09	0.23 0.17

Figure 7

COMPRESSIVE STRESS STRAIN FOR RSI

(Figure 8)

The reason that valid comparative physical property data are so difficult to obtain is illustrated by this figure. Initially compressive tests were performed on 2.54 cm cubes in the transverse (weak) direction. The stress-strain curves shown on the left were obtained. The actual yield point was extremely difficult to define for the mullite materials. In fact, these materials simply crushed at the surface and never failed at any other point in the sample, while the silica broke cleanly in a plane, nearly perpendicular to the load direction. In a subsequent test series the materials were tested with the coating on one surface and bonded to a substrate on the other surface giving the results shown on the right. In this case, the break occurred in the sample and not at the surface. Finally, it was found that by bonding both surfaces of the sample and measuring the strong direction compressive strength, no crushing occurred and a clean break was always obtained. More important was the fact that the silica gave essentially the same result bonded or not, whereas the mullite materials gave a factor of two higher strength when bonded on both sides. It appears, therefore, that it is important how these tests are run and even identical test techniques may not give truly comparable data on the materials.

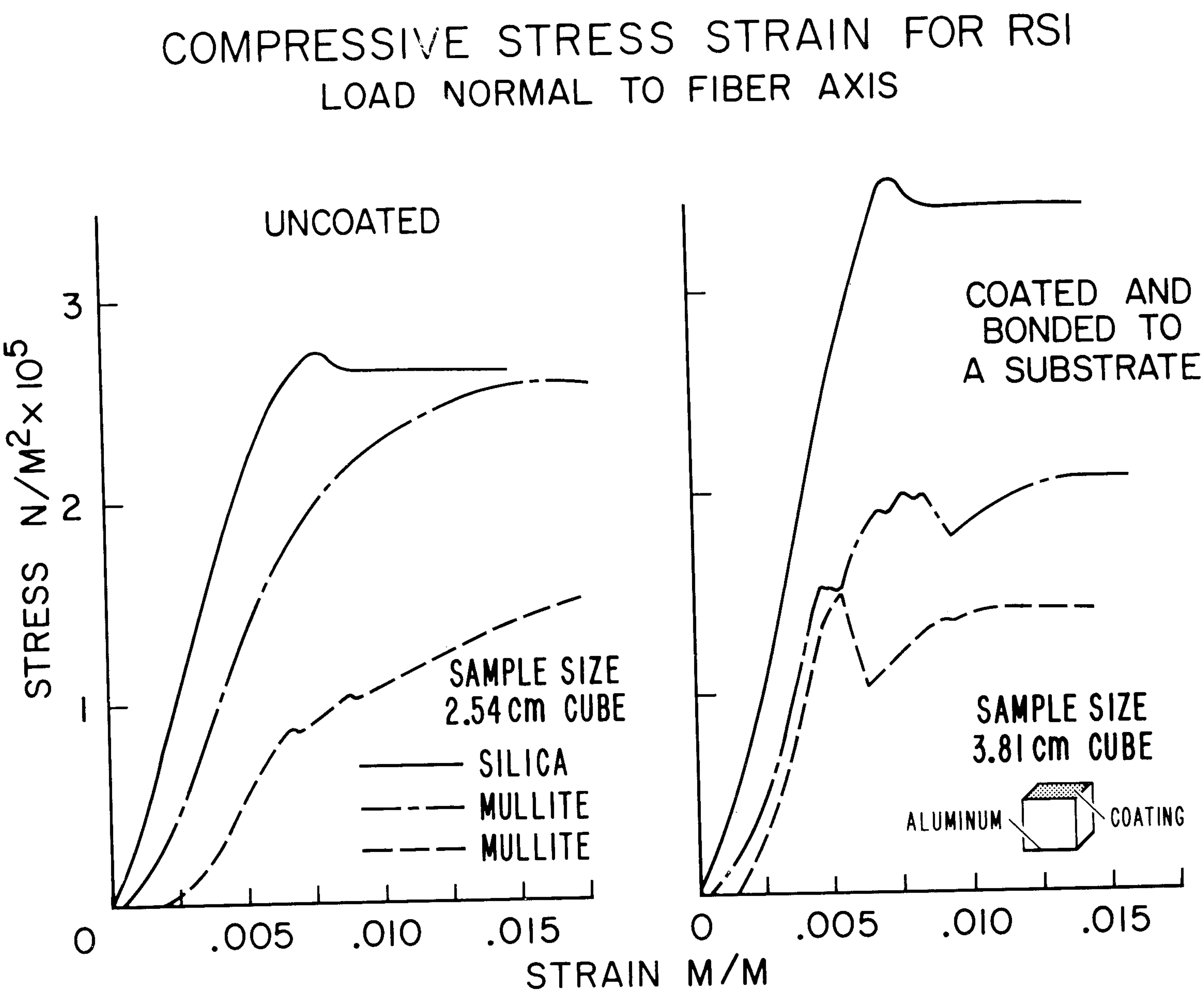
COMPRESSIVE STRESS STRAIN FOR RSI
LOAD NORMAL TO FIBER AXIS
UNCOATED
COATED AND BONDED TO A SUBSTRATE
STRESS N/M² × 10⁵
3
2
1
0
.005
.010
.015
STRAIN M/M
SAMPLE SIZE 2.54 cm CUBE
SILICA
MULLITE
MULLITE
SAMPLE SIZE 3.81 cm CUBE
ALUMINUM
COATING

Figure 8

CURRENT COATING PHYSICAL PROPERTIES

(Figure 9)

This figure shows contractor reported physical properties of a mullite and a silica RSI coating. The coatings are quite strong in comparison with the tiles due to their higher density. Since they are fully dense glass they have low strains to failure and a high modulus. Because of the low strain and high modulus and their high thermal expansion coefficient (shown in the next figure) mullite materials are particularly sensitive to thermal stress failure. The manufacturers have been devoting a considerable effort to improve these properties, so far with limited success. A promising approach to circumventing the problem has been to stress relieve the surface by notching and gapping. This approach, however, makes the waterproofing problem somewhat more difficult to solve. Another approach to coating improvement has been to use refurbishable organic coatings. Only limited data are available on this type of coating to date.

CURRENT COATING PHYSICAL PROPERTIES

	SILICA	MULLITE
DENSITY OF GLASS SEALER COATING, kg/m^3	2200	2200
TENSILE STRENGTH, $N/M^2 \times 10^5$	165	124
TENSILE MODULUS, $N/M^2 \times 10^8$	131	600
TENSILE STRAIN TO FAILURE, percent	0.12	0.03

Figure 9

THERMAL AND THERMOPHYSICAL PROPERTIES OF RSI
(Figure 10)

This table shows some of the thermal and thermophysical properties of the current RSI materials. The most important property in terms of material survival in thermal stress environments is the thermal expansion coefficient. This table shows that silica has a much lower thermal expansion coefficient than the mullite materials. Therefore, the thermal stress will be higher for an equivalent thermal gradient in the mullite than in the silica. This problem is significant for design of the SSV heat shield and is being studied at this time. In arc-plasma testing it is also a significant problem and will be discussed subsequently.

Specific heat is essentially equivalent among the materials. From the emittance and solar absorptance values tabulated one can see that α/ϵ is nearly 1.0 for all materials. For the final SSV design it is likely that α and ϵ of the surface should be tailored for both optimum thermal control in orbit and optimum surface emittance during entry.

The design maximum use temperature of all the RSI materials is 1350° C. Both the coatings and the tiles have no strength at this temperature according to the manufacturers' data. The reason that RSI is usable at these conditions is that there is a very steep temperature gradient in the RSI when the surface temperature is at its maximum. Therefore, only a very thin layer actually is at zero strength and it is sufficiently supported by the cooler substrate to prevent mechanical failure.

The overshoot temperature listed is the surface temperature quoted by the manufacturer at which significant damage will occur to a coated tile. The value is subject to interpretation. Silica is a very viscous melt at this temperature and will shrink and flow under shear. The glass coatings on the mullite materials will also flow. It is not clear whether a heat shield heated above this surface temperature would survive reentry or not. Survivability of the heat shield is dependent on the boundary-layer shear, pressure, acoustic, and mechanical loads to which the heat shield is subjected during the over-temperature period. Once a heat shield surface has reached this temperature it would probably have to be replaced after one flight.

THERMAL AND THERMOPHYSICAL PROPERTIES OF RSI

	SILICA	MULLITE
THERMAL EXPANSION COEFFICIENT, M/M - °C × 10^6		
TILE	0.5	5.0
COATING	0.7	5.0
SPECIFIC HEAT, cal/g - °C	0.24	0.25
TOTAL HEMISPHERICAL EMITTANCE OF COATING	0.90	0.70-0.85
SOLAR ABSORPTANCE OF COATING	0.77	0.72
TEMPERATURE OF ZERO STRENGTH, °C		
TILE	1260	>1260
COATING	1100	750-1240
DESIGN USE TEMPERATURE, °C	1350	1350
OVERSHOOT TEMPERATURE, °C	1600	1600-1700

Figure 10

THERMAL CONDUCTIVITY OF RSI

(Figure 11)

The most critical property in terms of heat shield section weight requirements is thermal conductivity. This figure illustrates the differences between the measured values of conductivity for the RSI materials. These measurements were made, by the manufacturers, using a conventional guarded hot plate apparatus. At the same density the silica material has a lower conductivity at 1.01×10^5 N/m^2 (1.0 atm) and 1.01×10^3 N/m^2 (10^{-2} atm) pressure. This results mainly from the amorphous nature and the smaller fiber diameter of the silica fibers, 1.0 μm compared to 4.7 μm. The smaller fiber size results in smaller pores, therefore less convective and radiative heat transfer. Because of the many more interfaces between fiber and binder in the silica contact resistance increases and solid conduction also decreases. The two 240 kg/m^3 mullite materials have fairly comparable conductivities as would be expected. The 192 kg/m^3 mullite has conductivities comparable to the silica material. Insufficient correlation of either arc plasma data or radiant test data has been performed to fully authenticate the conductivities shown. Correlations by the manufacturer seem to indicate that lower than measured conductivities are required to predict performance of silica in an arc plasma test; and one mullite manufacturer has reported that higher than measured conductivities are required to predict the material response of their mullite in radiant heating tests.

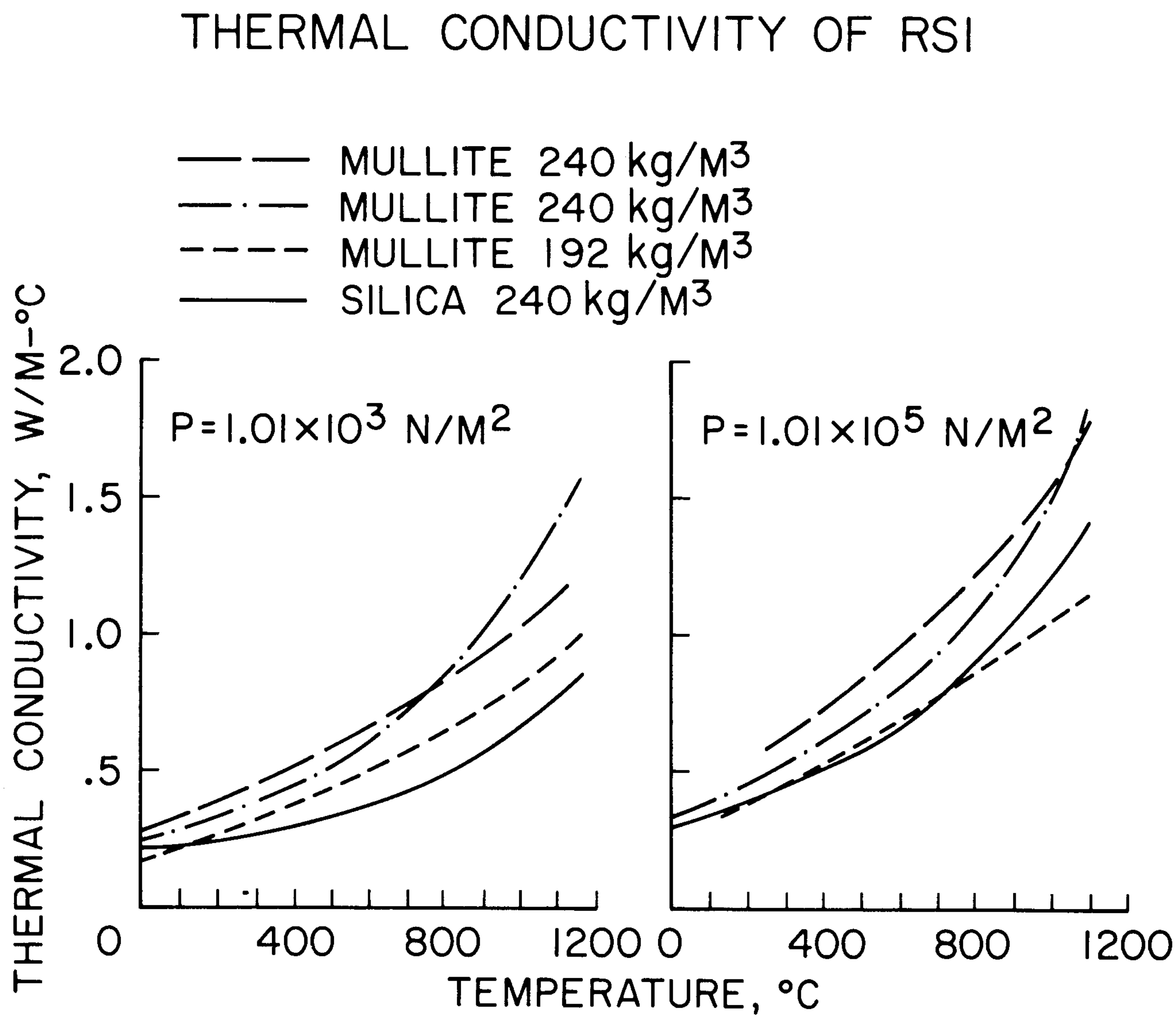
THERMAL CONDUCTIVITY OF RSI
MULLITE 240 kg/M3
MULLITE 240 kg/M3
MULLITE 192 kg/M3
SILICA 240 kg/M3
P=1.01×10^3 N/M^2
P=1.01×10^5 N/M^2
THERMAL CONDUCTIVITY, W/M-°C
2.0
1.5
1.0
.5
0
400
800
1200
0
400
800
1200
TEMPERATURE, °C

Figure 11

ARC PLASMA MODEL CONFIGURATIONS

(Figure 12)

Arc plasma testing is required to more fully characterize the performance of RSI materials. Only in the arc plasma stream can the reentry heating environment be reasonably well simulated. This figure shows three model configurations that are used for this type of testing. Each has its advantages. The stagnation model has a uniform heating distribution over the model surface, a subsonic laminar boundary layer, and very low shear forces. This type of environment is excellent for obtaining accurate surface and internal temperature response data, measuring noncatalytic wall effects and for examining the chemical changes in coatings due to convective heating. The wedge model has a thin supersonic laminar boundary layer and a controlled heating rate gradient on the surface. This type of model can be used to obtain data on the effects of laminar shear and the effects of heating rate differences, across a surface, for surface and internal temperature response and can generally be used to test larger models than can be tested using a stagnation model in the same facility. It can also be used to investigate laminar convective heating in joints and gaps. The duct configuration provides a thick turbulent supersonic boundary layer. This type of facility can be used to test nearly full sized heat shield panels under conditions that simulate large regions on the shuttle. Of particular interest in such a facility are studies of the response of gaps and joints.

Most data on RSI that has been obtained has been from stagnation and wedge model configurations on small samples of earlier materials. Joint tests in turbulent environments, RSI/ablator interactions, and large scale tests of realistic panel configurations have not yet been performed. In this section we will discuss what arc plasma testing to date has determined.

ARC PLASMA MODEL CONFIGURATIONS

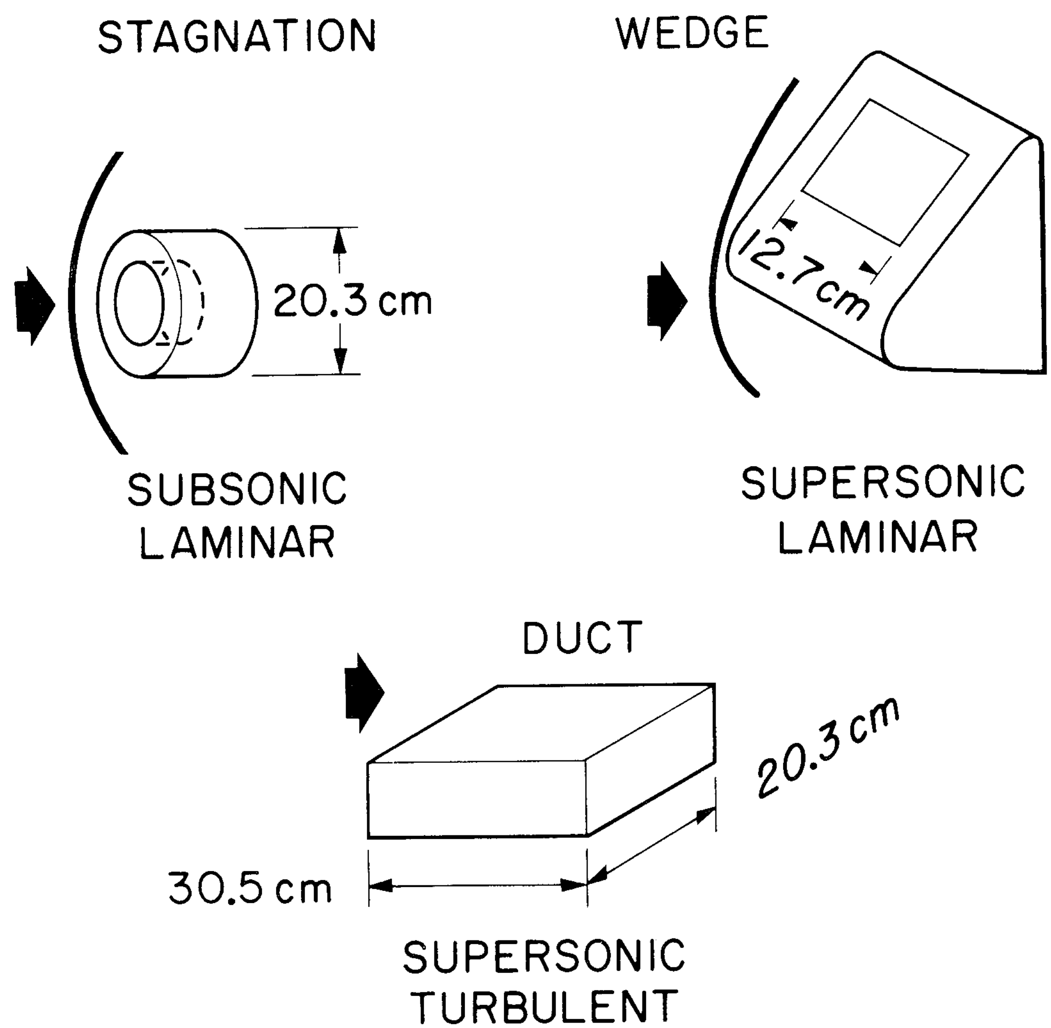

Figure 12

ARC PLASMA TESTING OF RSI MATERIALS

(Figure 13)

This figure lists the organizations, type of test, sample size, and the hours of testing that have been accomplished. The very nature of arc plasma testing makes it very difficult to do a large number of test cycles on any material. There have been on the order of 700 arc plasma tests but no more than thirty on any one sample. As the table also shows, most of these tests have been stagnation tests and nearly all the others have been on wedges and therefore had laminar flow. Recently tests have been run by Stewart at ARC where the sample is preheated before and postheated after the model is placed in the plasma stream, to better simulate the Space Shuttle environment. In the near future both LRC and MSC will also begin to use preheaters in their RSI tests. Tests in turbulent flow have been run on the very early silica and mullite RSI in a 2.5 × 12.7 cm (1" × 5") turbulent duct at ARC. In the near future large turbulent ducts will be used to test 20.3 × 50.8 cm (8" × 20") panel models at ARC and 30.5 × 30.5 cm (12" × 12") panel models at MSC. In these test facilities it is hoped that realistic data on joints in turbulent flow can be obtained. In their 30.5 × 30.5 cm (12" × 12") wedge MSC has recently obtained data on joints in supersonic laminar flow. Of the latest RSI materials only silica has been subjected to any extensive cyclic testing. It has been cycled twenty times with preheating at ARC, nineteen times at LRC, twenty-five times at MSC, and thirty times by a contractor. Minimal cracking occurred in these tests.

ARC PLASMA TESTING OF RSI MATERIALS

ORGANIZATION	TYPE OF TEST	SAMPLE SIZE	TOTAL HOURS OF TESTING
AMES RESEARCH CENTER INHOUSE			
	STAGNATION	4"D X 2" DISK	55
	STAGNATION + PREHEATER	4"D X 2" DISK	17*
	TURBULENT DUCT	3" X 5"	15
	TURBULENT DUCT	8" X 20"	
AEROTHERM			
	STAGNATION	4" X 1 1/2" DISK	112
	WEDGE	4" X 4 3/8"	0
LANGLEY RESEARCH CENTER			
	STAGNATION	3"D ISOQUE	3
	WEDGE	3 1/2" X 3 1/2"	2
	WEDGE	5" X 5"	9
MANNED SPACE CENTER INHOUSE			
	STAGNATION	2", 3", 4", 5" DISKS	17
	WEDGE	6" X 6"	5
	WEDGE	12" X 12"	1
	TURBULENT DUCT	12" X 12"	
BATTELLE MEMORIAL INSTITUTE			
	WEDGE + PREHEATER		

* CONVECTIVE HEATING TIME, TOTAL HEATING TIME INCLUDING RADIANT HEATING 76 HOURS

Figure 13

ARC TUNNEL TEST CONDITIONS FOR 5-INCH-SPAN WEDGE

(Figure 14)

Arc plasma tests at LRC to evaluate both reuse capability and thermal response have been carried out using 12.6 × 12.6 cm (5" × 5") samples in a wedge configuration. Tests were performed so that the nominal heating condition would correspond to the heating conditions (100 to 300 kW/m^2) on several areas of the orbiter. The conditions are shown in this figure. The heating pulse was a square pulse and the criteria for test termination was that the backface of the sample reach 150° C. The three RSI materials, two mullites and a silica, were tested. The backwall of each model was isolated from the structure of the test fixture by an air gap. For one mullite material (240 kg/m^3) a 500-second exposure was required to reach 150° C, for a second mullite material (192 kg/m^3) a 650-second exposure was required, and for the silica material a 2400-second exposure was required. Since the densities of the materials were not identical an exact comparison cannot be made. However, an order of magnitude comparison does indicate that the silica does show superior insulation efficiency.

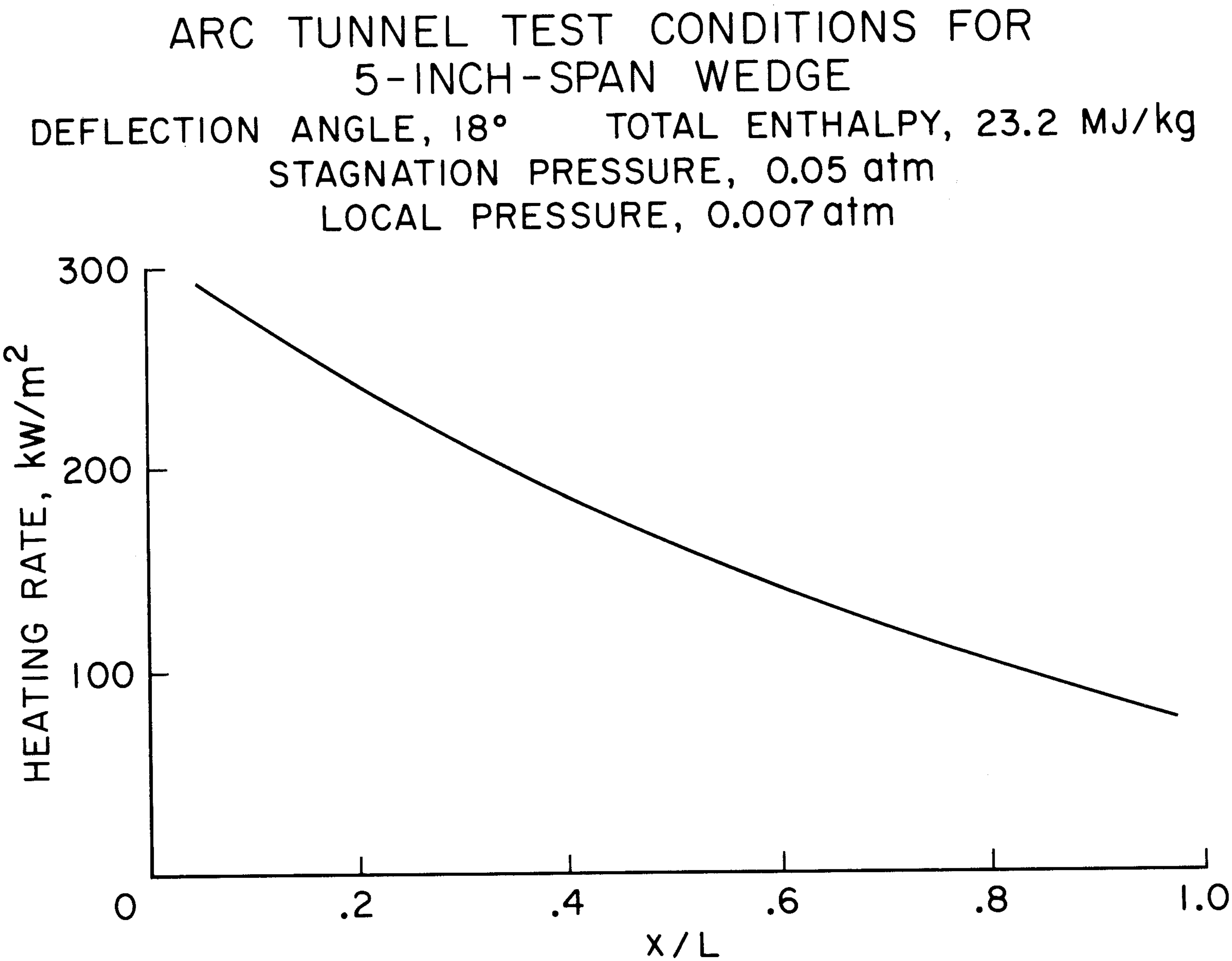
ARC TUNNEL TEST CONDITIONS FOR
5-INCH-SPAN WEDGE
DEFLECTION ANGLE, 18°
TOTAL ENTHALPY, 23.2 MJ/kg
STAGNATION PRESSURE, 0.05 atm
LOCAL PRESSURE, 0.007 atm
HEATING RATE, kW/m2
300
200
100
0
.2
.4
.6
.8
1.0
X/L

Figure 14

ARC TUNNEL TESTS OF REUSABLE SURFACE INSULATION

(Figure 15)

This figure shows one of the mullite samples tested as described in the previous figure after one and again after two test cycles. Before testing the coating was dark and had a pitted texture. After the first cycle one could observe a gradation in color and texture across the coating surface. The coating was fused along a narrow strip in the high heat-transfer area. One could deduce the heating rate distribution from the pattern on the surface. After the second test cycle the general appearance was still the same except that there was a large crack extending from the leading edge about two-thirds the length of the tile. The coating appeared to be pervious to water after this cycle based on the fact that a drop of water placed on the surface was absorbed. A similar test on a 192 kg/m^3 mullite showed cracking after three cycles and some bubbling in the higher heat rate areas. It also was found to be pervious to water. The three cycle test on silica showed no visible cracks, but the coating was pervious to water. Microscopic examination showed a fine crack about two-thirds the length of the tile. Subsequent to these tests the silica tile was run for nineteen cycles without further change.

Tests at MSC, at ARC, and at a contractor facility in stagnation model configurations have shown essentially the same type of results, that is significant cracking of mullite occurs early in the tests while silica shows only minor cracking, if any, after as many as twenty-five to thirty cycles. All materials appear to be pervious to water after multiple tests.

ARC TUNNEL TESTS OF REUSABLE SURFACE INSULATION

MULLITE

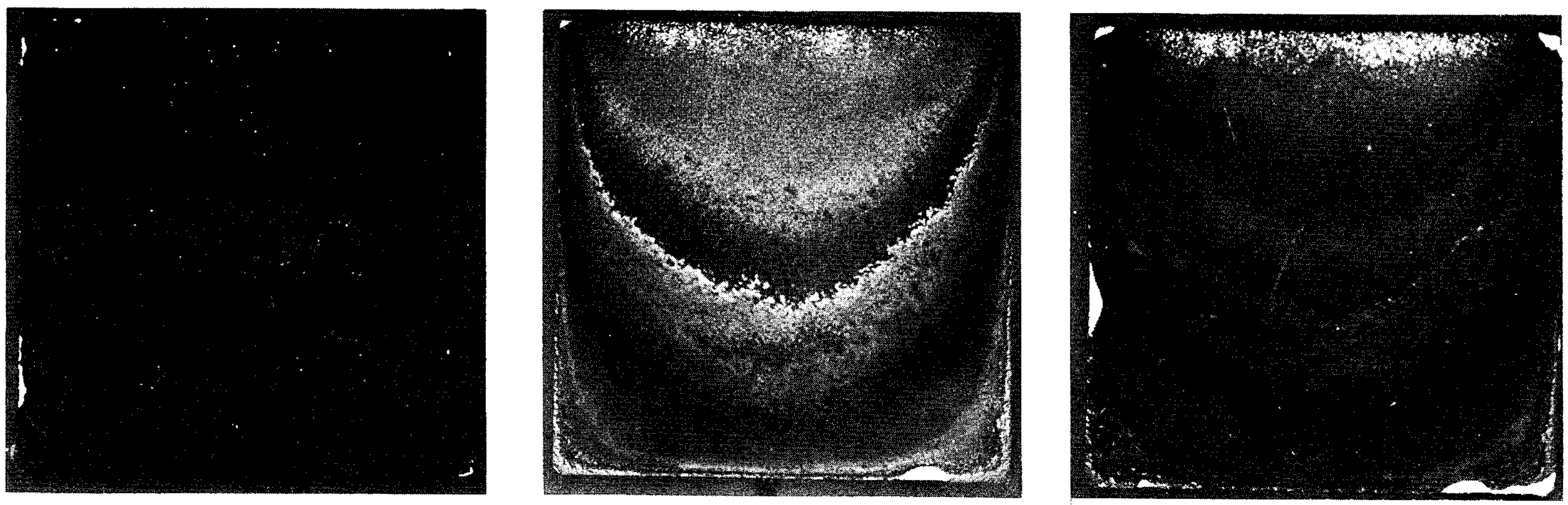

BEFORE TEST

CYCLE I
500 sec

CYCLE 2
1049 sec

Figure 15

ARC HEATER FACILITY WITH PREHEATER IN PLACE

(Figure 16)

Because of the extensive cracking due to thermal shock that has been observed in arc plasma testing of RSI materials it has become clear that preheating of the samples in order to more realistically simulate the Space Shuttle entry heating environment is required. This figure shows a preheater system developed by Stewart at ARC. It consists of heating element mounted on the back of a cone. The heating element radiates directly on the model and is protected by the cone from the arc plasma stream. The cone and preheater assembly is moved in and out of the stream independently of the model. Using this system the model can be preheated to about 1250° C before it is exposed to the arc plasma stream and after arc plasma exposure can be slowly cooled to room temperature, again simulating the total entry environment.

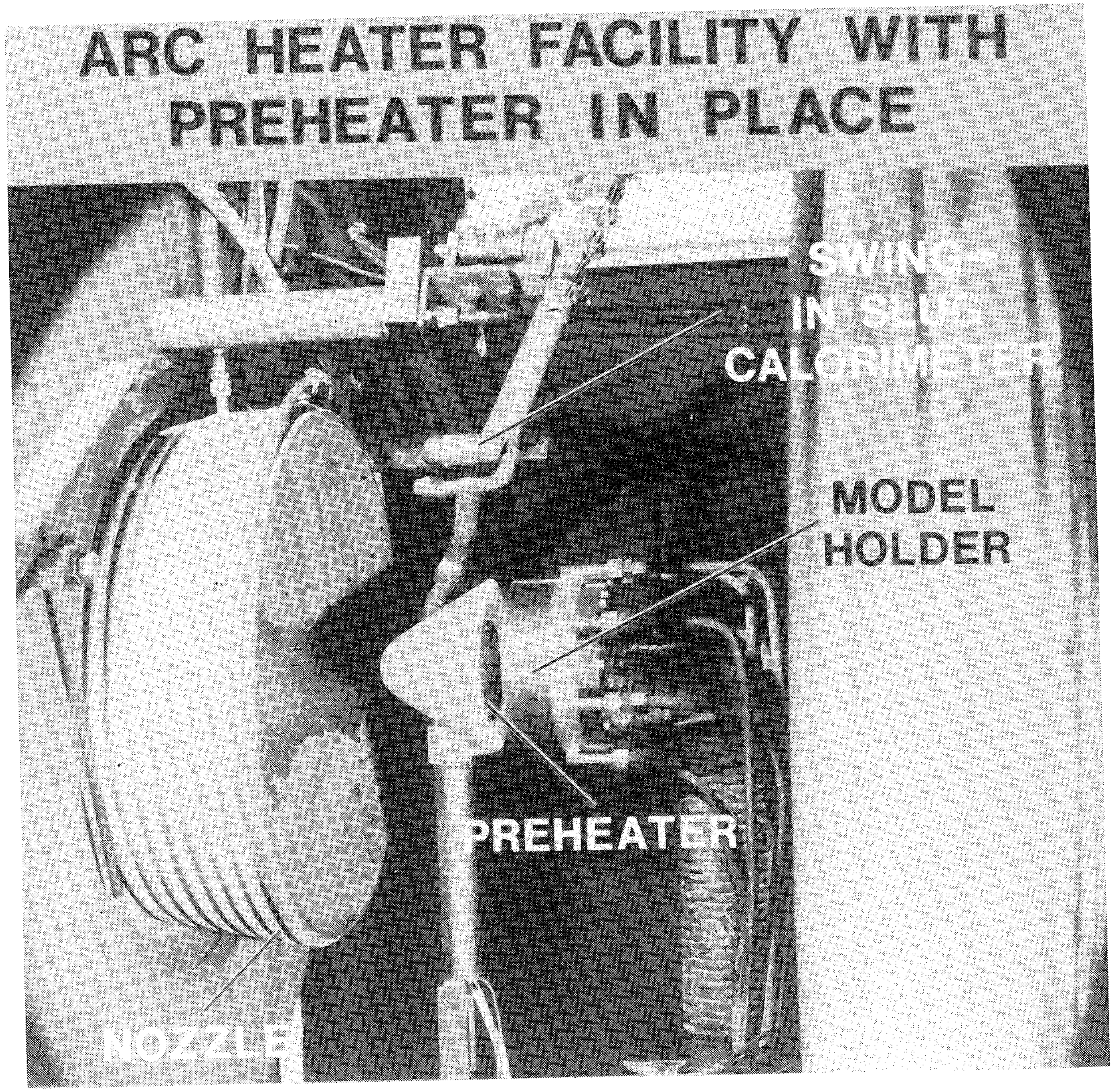
ARC HEATER FACILITY WITH
PREHEATER IN PLACE
SWING-
IN SLUG
CALORIMETER
MODEL
HOLDER
PREHEATER
NOZZLE

Figure 16

MULLITE MODEL BEFORE AND AFTER ARC PLASMA TESTING

(Figure 17)

This figure shows a mullite model before and after ten arc plasma test cycles using the preheater system. This model showed no cracking after thirty-two cycles. In other thirty cycle test series on a different mullite material only a small crack was observed to occur at the edge of the sample coating, and silica had no cracks. This result shows that by better simulation of the Space Shuttle environment cracking of mullite RSI can be significantly reduced.

The surface coating on this mullite material has been changed significantly by the test. It appears that the binder for the emittance material on the surface has been removed leaving a friable layer of emittance material. Detailed chemical analysis has not yet been performed to determine if this is the case. In the same test series the other mullite material's coating became a much lighter green after thirty cycles and the silica coating became a slightly lighter grey.

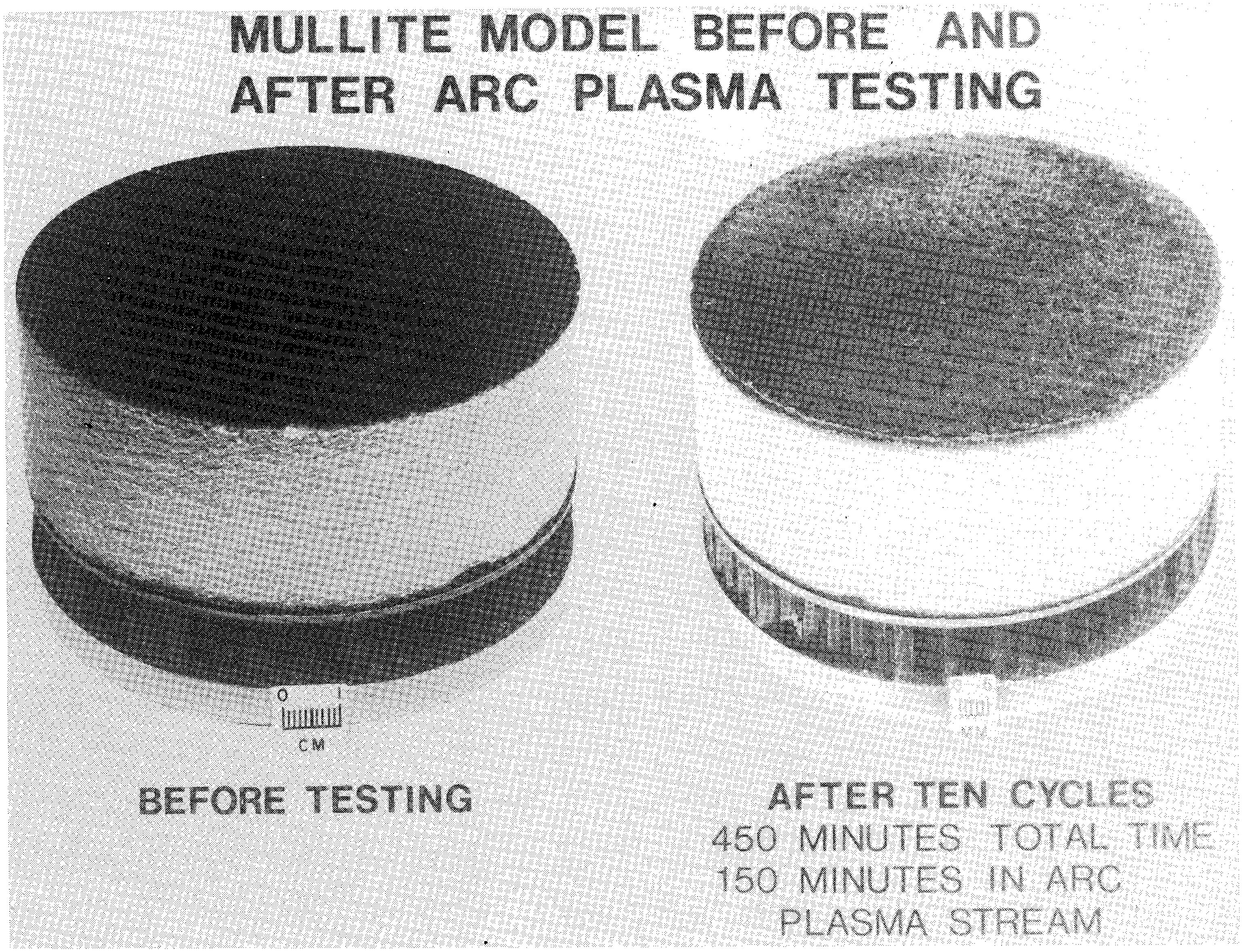
MULLITE MODEL BEFORE AND
AFTER ARC PLASMA TESTING
0 1
CM
BEFORE TESTING
AFTER TEN CYCLES
450 MINUTES TOTAL TIME
150 MINUTES IN ARC
PLASMA STREAM

Figure 17

TEMPERATURE TIME HISTORY DURING ARC PLASMA TEST OF MULLITE RSI

(Figure 18)

This figure shows a typical temperature response of a mullite model exposed to a simulated shuttle environment obtained using the preheater shown in figure 16. The surface temperature was brought up to 600° C with the preheater and then the arc plasma stream was used for ten minutes at a heating rate of 235 kW/m^2. At the end of the run the preheater was used to bring the temperature down slowly. Temperature response data for other 240 kg/m^3 mullite models having the same configuration was essentially identical. A silica model of the same type had much lower internal temperatures. The peak backface temperature of the silica was about 75° C compared to roughly 180° C of mullite. The internal temperature response of the materials tested was not changed by as many as thirty-two test cycles with heating rates from 235 to 480 kW/m^2.

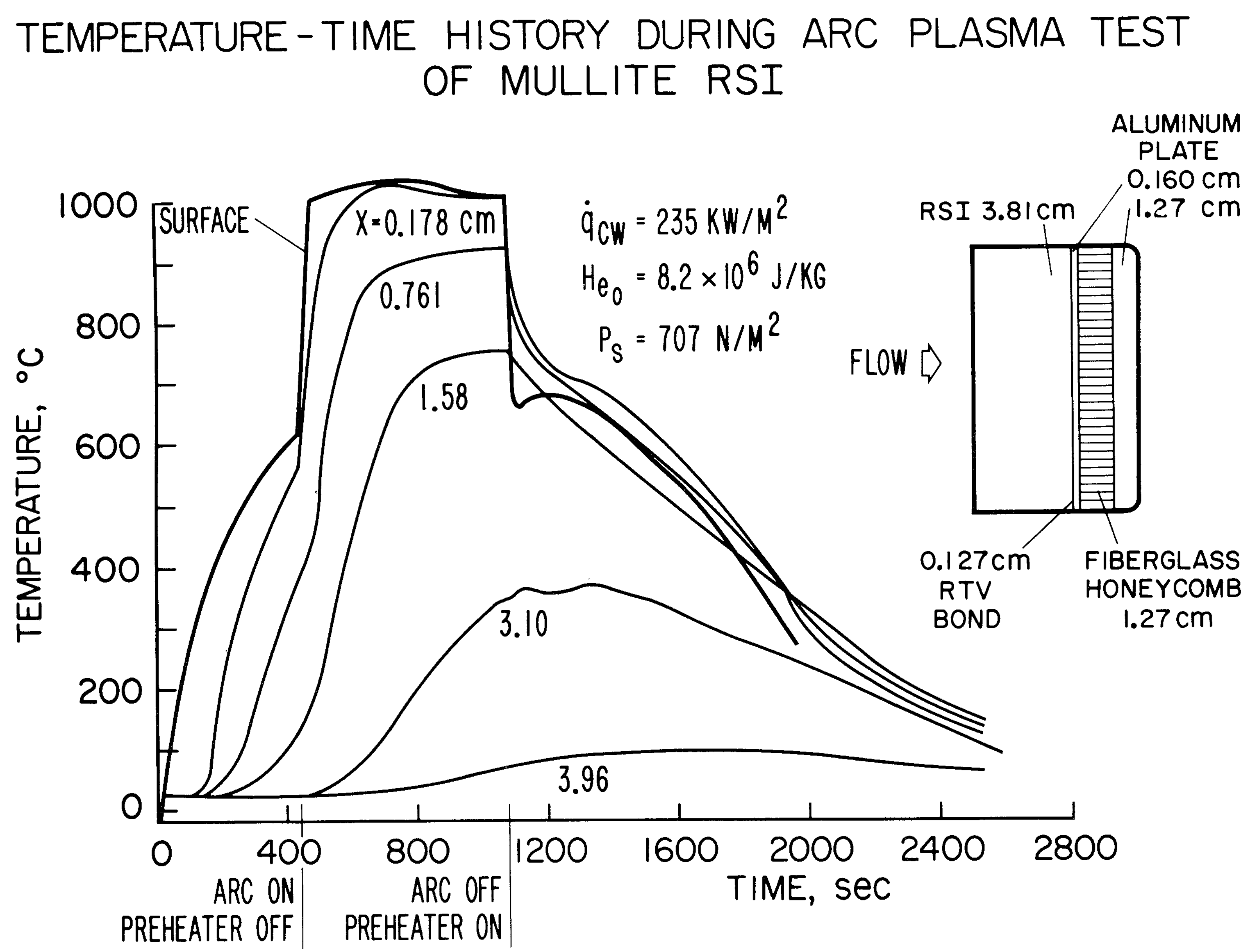
TEMPERATURE - TIME HISTORY DURING ARC PLASMA TEST
OF MULLITE RSI
TEMPERATURE, °C
1000
800
600
400
200
0
SURFACE
X=0.178 cm
0.761
1.58
3.10
3.96
$\dot{q}_{CW}$ = 235 KW/M^2
He_0 = 8.2 × 10^6 J/KG
P_S = 707 N/M^2
0
400
800
1200
1600
2000
2400
2800
TIME, sec
ARC ON
PREHEATER OFF
ARC OFF
PREHEATER ON
FLOW
RSI 3.81 cm
ALUMINUM
PLATE
0.160 cm
1.27 cm
0.127 cm
RTV
BOND
FIBERGLASS
HONEYCOMB
1.27 cm

Figure 18

RSI TEST SAMPLES BEFORE AND AFTER ARC PLASMA TESTING

(Figure 19)

As noted previously a large number of arc plasma tests on mullite and silica have been conducted under an ARC directed contract. Since these tests were performed and reported the samples have been returned to ARC for detailed posttest analysis. This figure shows two mullite samples and a silica sample before and after thirty half-hour arc plasma test cycles. The test conditions are noted in the figure. These three samples have received more arc plasma exposure under identical conditions than any other samples yet tested. Both of the mullite samples show significant cracking. In handling it was found that the one coating was not as well adhered to the insulation surface as it was prior to test. The other mullite and the silica coatings were still well adhered. The most interesting thing to note in this figure is the change of color that has occurred. All the coatings appear to be grey after test. While the change was small for the silica it was a considerable change for the other materials. In the next figure these surface changes are discussed.

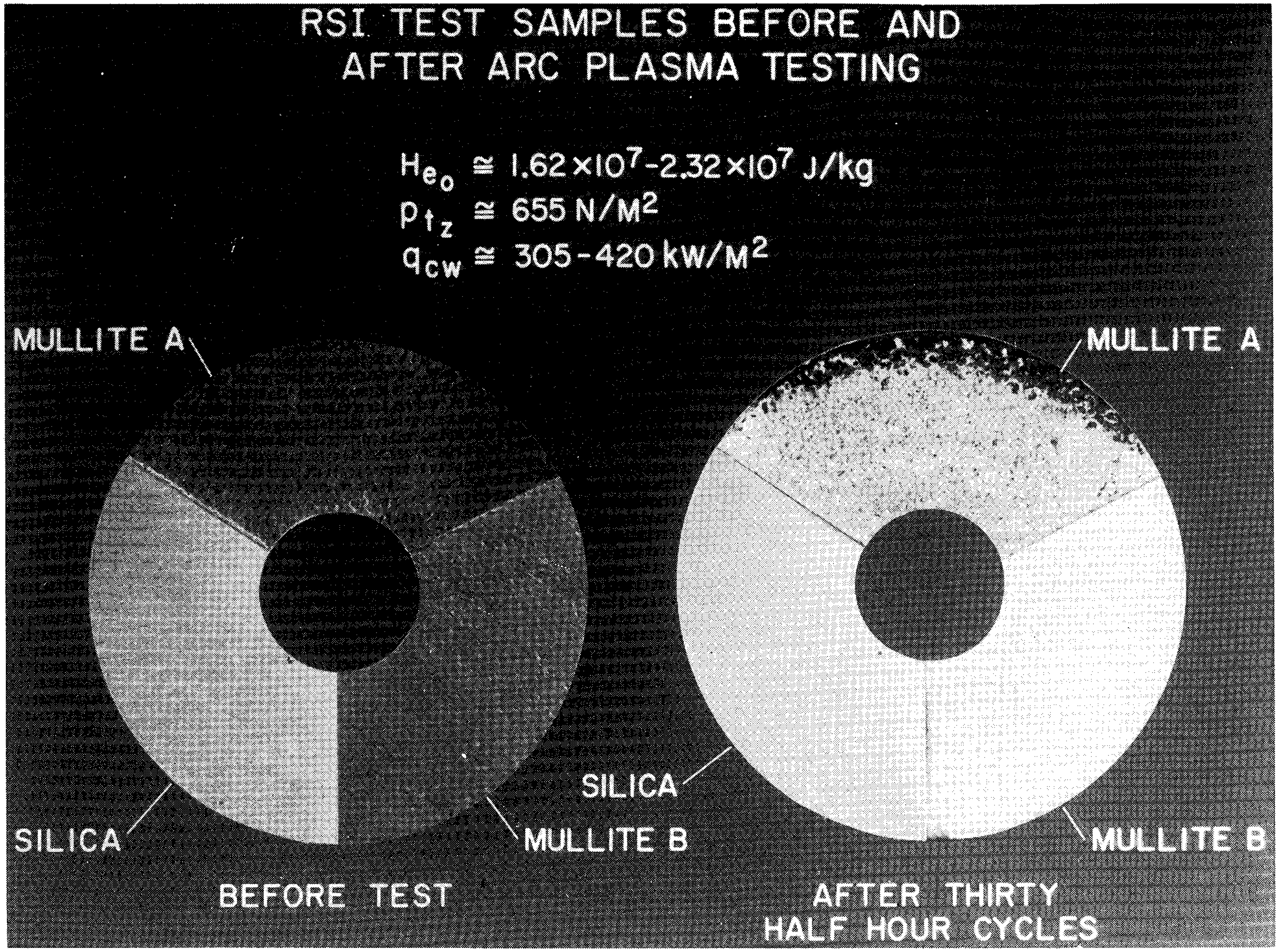
RSI TEST SAMPLES BEFORE AND
AFTER ARC PLASMA TESTING
$H_{e_o} \cong 1.62 \times 10^7 - 2.32 \times 10^7$ J/kg
$p_{t_z} \cong 655$ N/M^2
$q_{cw} \cong 305-420$ kW/M^2
MULLITE A
SILICA
MULLITE B
BEFORE TEST
MULLITE A
SILICA
MULLITE B
AFTER THIRTY
HALF HOUR CYCLES

Figure 19

TOTAL NORMAL EMITTANCE BEFORE AND AFTER ARC PLASMA TESTING

(Figure 20)

The spectral emittance at room temperature of the coatings shown previously was measured in the range 0.3 to 25 μm. This figure shows the total normal emittance calculated from these room temperature measurements, plotted as a function of temperature for a silica and a mullite RSI. The figure shows that total emittance after test has decreased significantly from the pretest values. The largest decrease was for one of the mullite materials. While this change is significant it is probably not a critical factor in terms of the backface temperatures that would be experienced during reentry. The most important effect of this change may be on the requirements for orbital thermal control because the changes in solar absorptance are also significant as shown by the figure. In order to optimize the design of the Space Shuttle and to accurately measure surface temperatures in arc plasma tests, precise measurements of both spectral and total emittance at temperature are required. D. Dicus at LRC is carrying out a study to try and accomplish this. At ARC Roy Wakefield is attempting to measure both spectral and total emittance of the RSI materials in an arc jet facility using a unique Barnes multichannel radiometer.

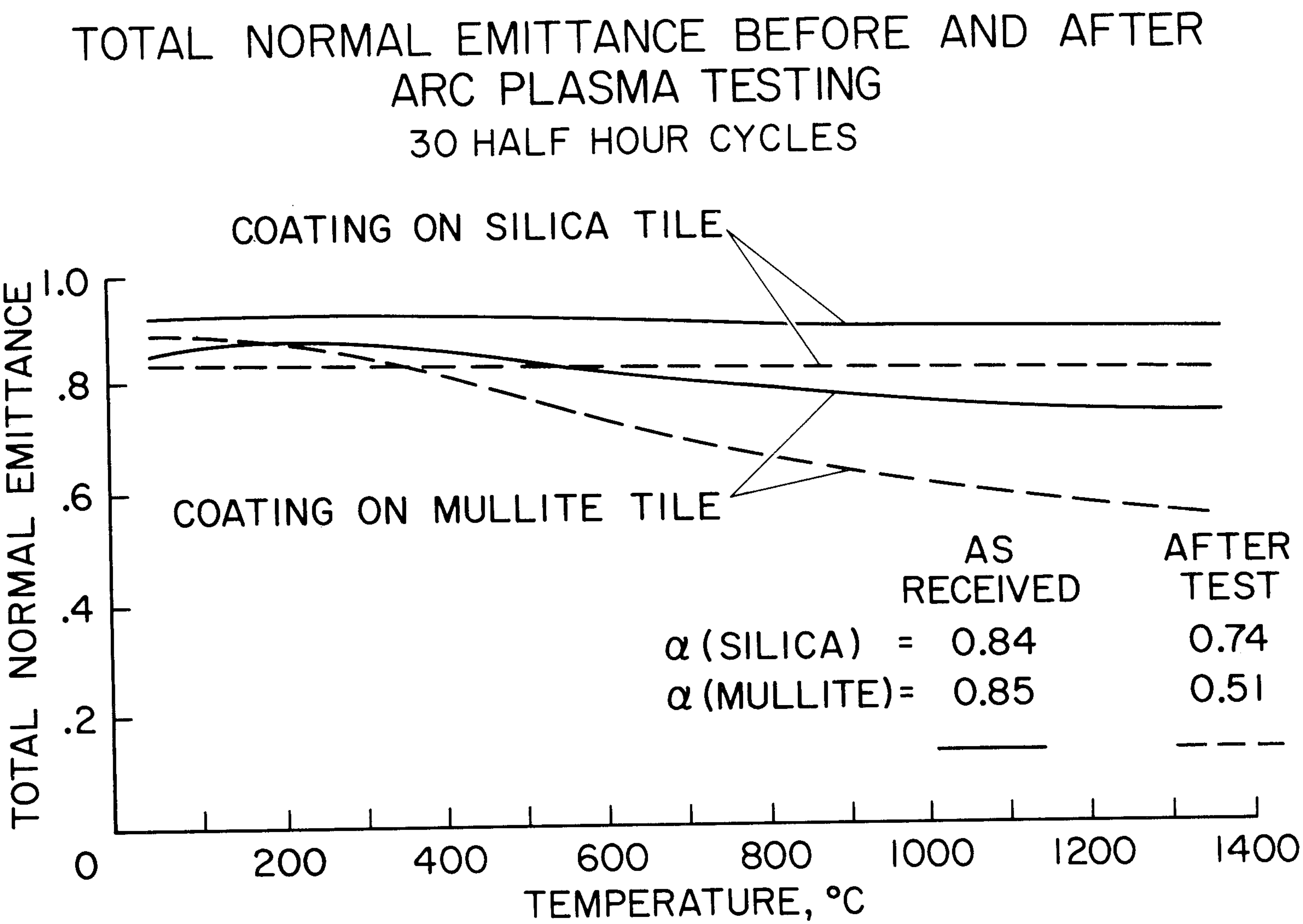
TOTAL NORMAL EMITTANCE BEFORE AND AFTER
ARC PLASMA TESTING
30 HALF HOUR CYCLES
COATING ON SILICA TILE
COATING ON MULLITE TILE
TOTAL NORMAL EMITTANCE
1.0
.8
.6
.4
.2
0
200
400
600
800
1000
1200
1400
TEMPERATURE, °C
AS RECEIVED
AFTER TEST
α (SILICA) = 0.84
0.74
α (MULLITE) = 0.85
0.51

Figure 20

SCANNING ELECTRON MICROGRAPHS OF MULLITE RSI, BEFORE AND AFTER 30 HALF-HOUR ARC PLASMA TEST CYCLES

(Figure 21)

This figure shows scanning electron micrographs of one mullite surface before and after the thirty arc plasma cycles described in the previous figures. The major change in the coating seems to be that the outer layer of phosphate bonded emittance agent has been partially removed and the layer of borosilicate glass under it has been exposed. Before test a rather uniform but rough surface is observed. X-ray fluorescence analysis showed that this material was a phosphate bonded emittance material. After test analysis showed that nearly all the phosphorus had been removed and that the outer surface was mostly silica. Most of the emittance material had been removed, although patches remained. Similar analyses are being carried out on the other mullite and the silica material. The changes in chemistry that occur due to arc plasma heating affect other properties of the coatings as shown in the next figure.

SCANNING ELECTRON MICROGRAPHS OF MULLITE RSI, BEFORE AND AFTER 30 HALF HOUR ARC PLASMA TEST CYCLES

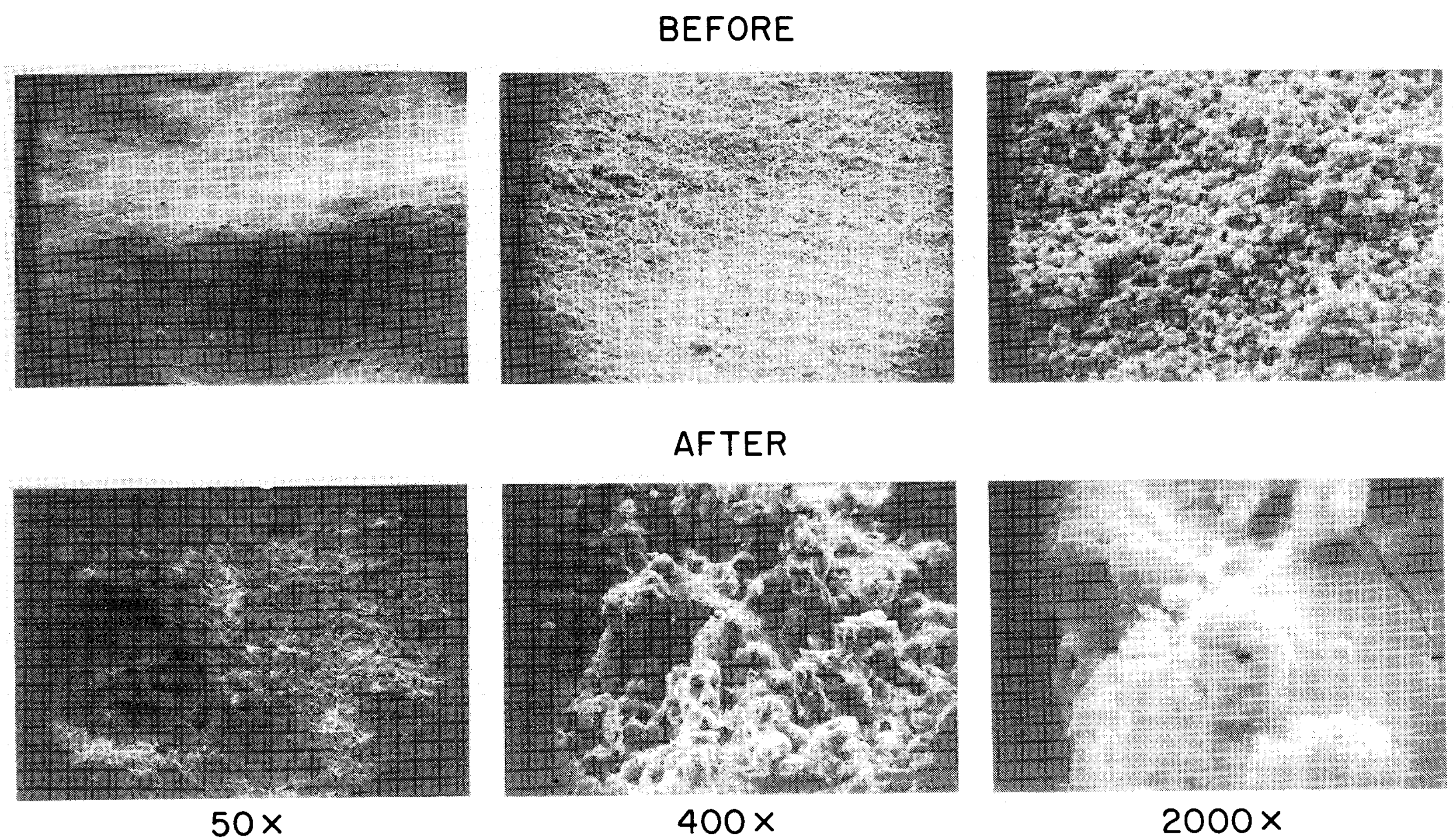

Figure 21

EFFECT OF SURFACE CATALYTIC ACTIVITY ON SURFACE TEMPERATURE

(Figure 22)

This figure illustrates the noncatalytic character of the RSI coatings. The surface temperature is plotted against hot wall heating rate for the cases of a wall that is catalytic to recombination of atoms of nitrogen and oxygen and one that is noncatalytic to the recombination. Superimposed on the theory curves are regions that summarize the data obtained at ARC on early mullite and silica RSI's. These data show that the coatings are catalytic at low heating rates and noncatalytic at the higher heating rates. The new RSI coatings tested by ARC are in most cases also noncatalytic at the higher heating rates. However, one new mullite coating is nearly catalytic at the higher heating rate.

This noncatalytic effect may be significant in design of a Space Shuttle heat shield. Therefore, development of the most noncatalytic coating possible is a desirable goal. The catalytic efficiency of a number of possible coating materials has been studied by Cole of MSC at room temperature and studies at elevated temperatures have recently been initiated at Stanford Research Institute by ARC. At both ARC and MSC studies of the catalytic efficiency of these coatings in arc jets are continuing. The data indicate that all the glassy RSI coatings are noncatalytic to some extent.

EFFECT OF SURFACE CATALYTIC ACTIVITY
ON SURFACE TEMPERATURE OF RSI

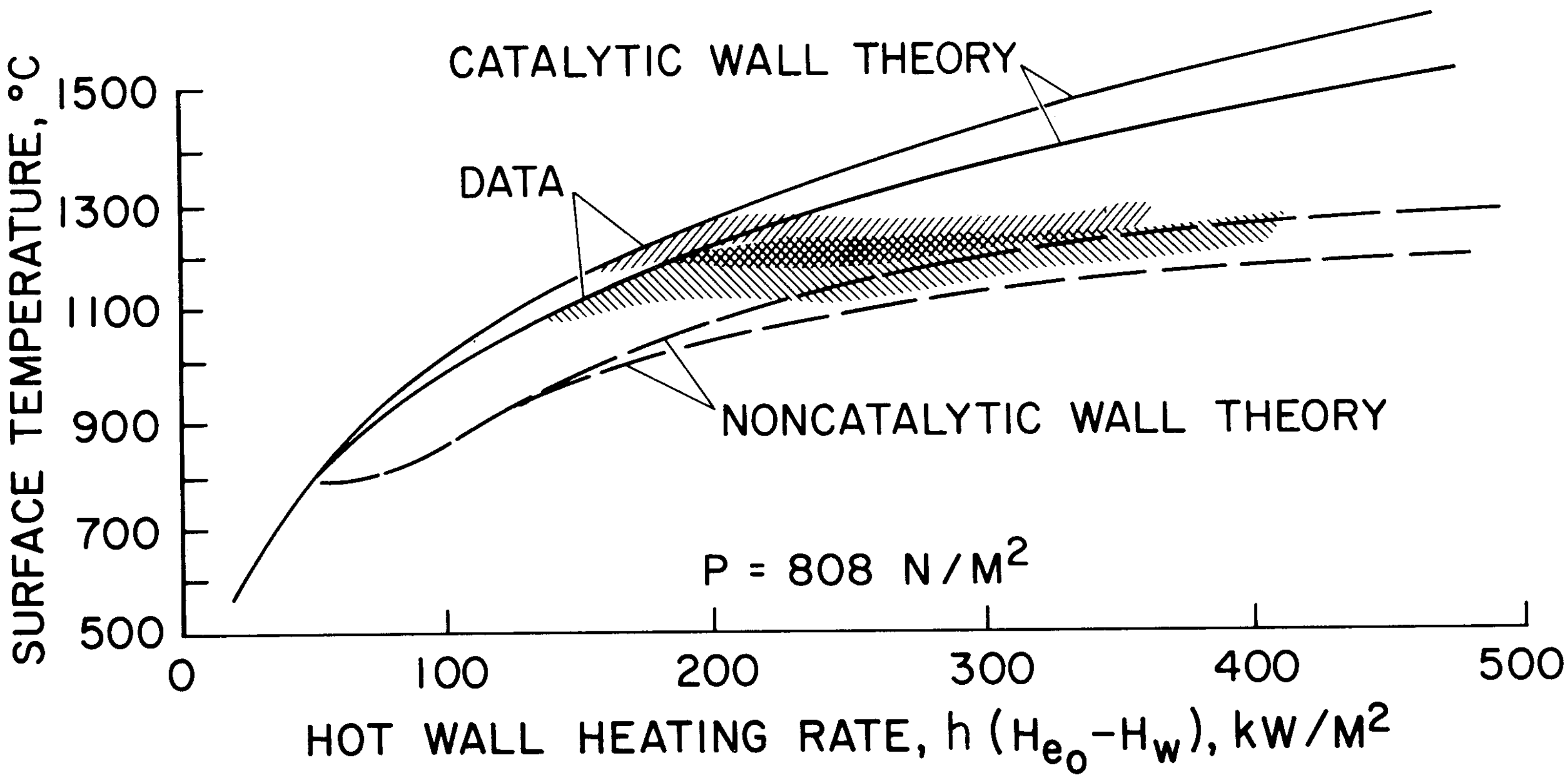

Figure 22

ARC PLASMA TEST RESULTS

(Figure 23)

The results of arc plasma testing to date are summarized in the accompanying figure. Much more arc plasma testing is still required. Only limited data on the newest mullite materials have been obtained and there are no data on panels larger than 15.2 × 15.2 cm yet. Particular emphasis in the future will be on tests in turbulent flow facilities on large panel configurations to obtain accurate data on heating in joints and gaps, the effect of RSI failure on survivability, and the effect of surface roughness on heat transfer to the surfaces. More cyclic tests using preheaters are required to determine if the mullite RSI's can survive repeated realistic entry heating tests and to obtain more complete internal temperature response data so that the design thermal conductivities can be verified. The thermochemistry of coatings exposed to many arc jet cycles must be studied more thoroughly to determine the optimum materials in terms of component removal by convective heating and in terms of surface catalytic effects. The effect of arc plasma testing, using preheaters, on the waterproofness of coatings must be evaluated.

ARC PLASMA TEST RESULTS

- RADIATION HEATING COMBINED WITH PLASMA GIVES MORE REALISTIC SIMULATION
- COATINGS LOSE VOLATILE SPECIES DURING TESTS
- COATINGS OF ALL RSI MATERIALS DECREASE IN EMITTANCE AFTER MULTIPLE TESTS
- WATERPROOF CAPABILITY OF ALL COATINGS AFTER MULTIPLE TESTS IS QUESTIONABLE
- SILICA IS A BETTER INSULATOR THAN MULLITE AT THE SAME DENSITY
- ALL GLASSY OUTER COATINGS ARE NONCATALYTIC TO SOME DEGREE

Figure 23

RSI RESEARCH AT NASA CENTERS

(Figure 24)

The accompanying figure lists the varied research efforts on RSI being carried out by the NASA centers and their contractors. The major systems responsibility rests with MSC, of course, and the results of these efforts are discussed by Mr. Greenshields et al. in another paper. Each center listed has taken on one or more specific research areas. These complement each other although in some areas parallel efforts are being pursued. The arc plasma testing work being carried on by ARC, LRC, MSC, and their contractors has been discussed in the previous section. Material fabrication and improvement research efforts are being carried out in-house at both MSFC and ARC. Some of the results of these efforts will be discussed in the subsequent section. LeRC is sponsoring work to improve on the currently available fibers. Basic research on the fibers and fabricated tiles is being carried out at LeRC and at ARC in-house and under contract. Physical and thermophysical characterization of the RSI materials is being carried out at the centers listed in several specialized areas. MSC is also sponsoring detailed characterization work. Emittance measurements are of special interest and are being carried out by ARC, LRC, and MSFC both in-house and under contract.

The effect of salt corrosion of RSI is being studied in particular depth at LRC and will be discussed in this section. Material improvement programs with each of the RSI manufacturers have been funded by MSFC, LRC, or MSC. Most of the work to be discussed in this section was only begun in the last seven months so that the results are preliminary in nature. Only highlights of each center's efforts are presented.

RSI RESEARCH AT NASA CENTERS

IN-HOUSE	CONTRACT
AMES RESEARCH CENTER	
ARC PLASMA TESTING	BASIC RESEARCH (U OF WASHINGTON)
MATERIAL AND PROCESS IMPROVEMENT	ARC PLASMA TESTING (AEROTHERM)
PHYSICAL, CHEMICAL AND THERMOPHYSICAL PROPERTIES	MICROSTRUCTURAL EFFECTS (U OF MARYLAND)
ACOUSTIC TESTING IN SUPERSONIC FLOW	EMITTANCE MEASUREMENTS (LMSC)
EMITTANCE MEASUREMENTS	
LANGLEY RESEARCH CENTER	
ARC PLASMA TESTING	REI IMPROVEMENT (G. E.)
SALT CORROSION STUDIES	CPI IMPROVEMENT (GRUMMAN)
RADIANT HEATING TESTS	3DSX RESEARCH (AVCO)
EMITTANCE MEASUREMENTS	
VIBRATIONAL AND SONIC TESTING	
LEWIS RESEARCH CENTER	
PHYSICAL AND CHEMICAL CHARACTERIZATION	MULLITE FIBER IMPROVEMENT (BABCOCK AND WILCOX)
RSI IMPROVEMENT	SILICA FIBER IMPROVEMENT (JOHNS MANVILLE)
COATING IMPROVEMENT	
GEORGE C. MARSHALL SPACE FLIGHT CENTER	
MATERIAL AND PROCESS IMPROVEMENT	HCF IMPROVEMENT (MDAC)
MOISTURE ABSORPTION	
RADIANT HEATING TESTS	
MANNED SPACECRAFT CENTER	
ARC PLASMA TESTING	HCF DEVELOPMENT (MDAC)
WATER ABSORPTION	LI-1500 DEVELOPMENT (LMSC)
FLIGHT SIMULATION	REI DEVELOPMENT (G. E.)
	CPI DEVELOPMENT (GRUMMAN)
	3DSX DEVELOPMENT (AVCO)
	PHYSICAL AND THERMOPHYSICAL CHARACTERIZATION (BATTELLE)

Figure 24

PHOTOGRAPHS OF THERMAL CYCLIC TESTS ON RSI
(Figure 25)

Langley Research Center is carrying on detailed studies of RSI both in-house and under contract. Among the programs underway in-house are the arc plasma testing ahd characterization previously discussed, salt corrosion studies, high temperature emittance measurements, radiant heating tests, and vibrational and sonic testing. Improvement of mullite RSI is being accomplished and development of a nonrigid fibrous insulation and a closed pore ceramic insulation is being pursued under contract.

Since it is quite likely that the Space Shuttle will be launched and recovered from a seacoast location where the heat shield would be exposed to a sea salt environment, LRC has run extensive tests to determine what the effect of this environment would be on RSI materials. This figure shows two mullite and a silica RSI before and after being exposed to alternate cycles of sea water spraying and thermal cycling at LRC. The sample size is approximately 3 cm square. The sea water was applied as an atomized spray and the thermal cycle used was a radiant heat simulation of a typical 1400 n. mi. cross-range, Phase B trajectory. Maximum temperature reached was approximately 1300° C but it was about 900° C for most of the 2700 second test cycle. The mullite material shown at the top of the figure appears to have melted and been absorbed into the tile after ten heating cycles without salt spray. When sea salt was sprayed on the coating between thermal cycles, holes appeared in the black surface coating exposing a white dense layer under the outer coating after ten cycles. An earlier coating, not shown, remained free of cracks or holes and was waterproof after fifty sea salt and thermal cycles. Scanning electron micrographs of fractured cross sections of this coating indicated that the coating exposed to sea salts was actually densified and the initially present porosity had disappeared. The coating was somewhat pitted and roughened after test.

The second set of mullite samples shown in the figure show no change in texture after ten cycles without sea salt; but the color has changed from brown to green. After ten cycles with sea salts, the color has changed to a lesser extent from brown to green and the surface has become glassy looking.

After twenty cycles without sea salt the silica specimen shown at the bottom of the page looked essentially the same as the pretest specimen shown in the figure. No change in color or texture had occurred. After ten cycles with sea salts the color change is very noticeable and the surface appears splotchy. After twenty cycles with sea salts the coating has cracked and spalled. Initial failure of the specimen occurred at the fifteenth cycle. No sea water was sprayed on after the initial failure. In another twenty cycle test with sea salt spray, failure occurred on the ninth cycle.

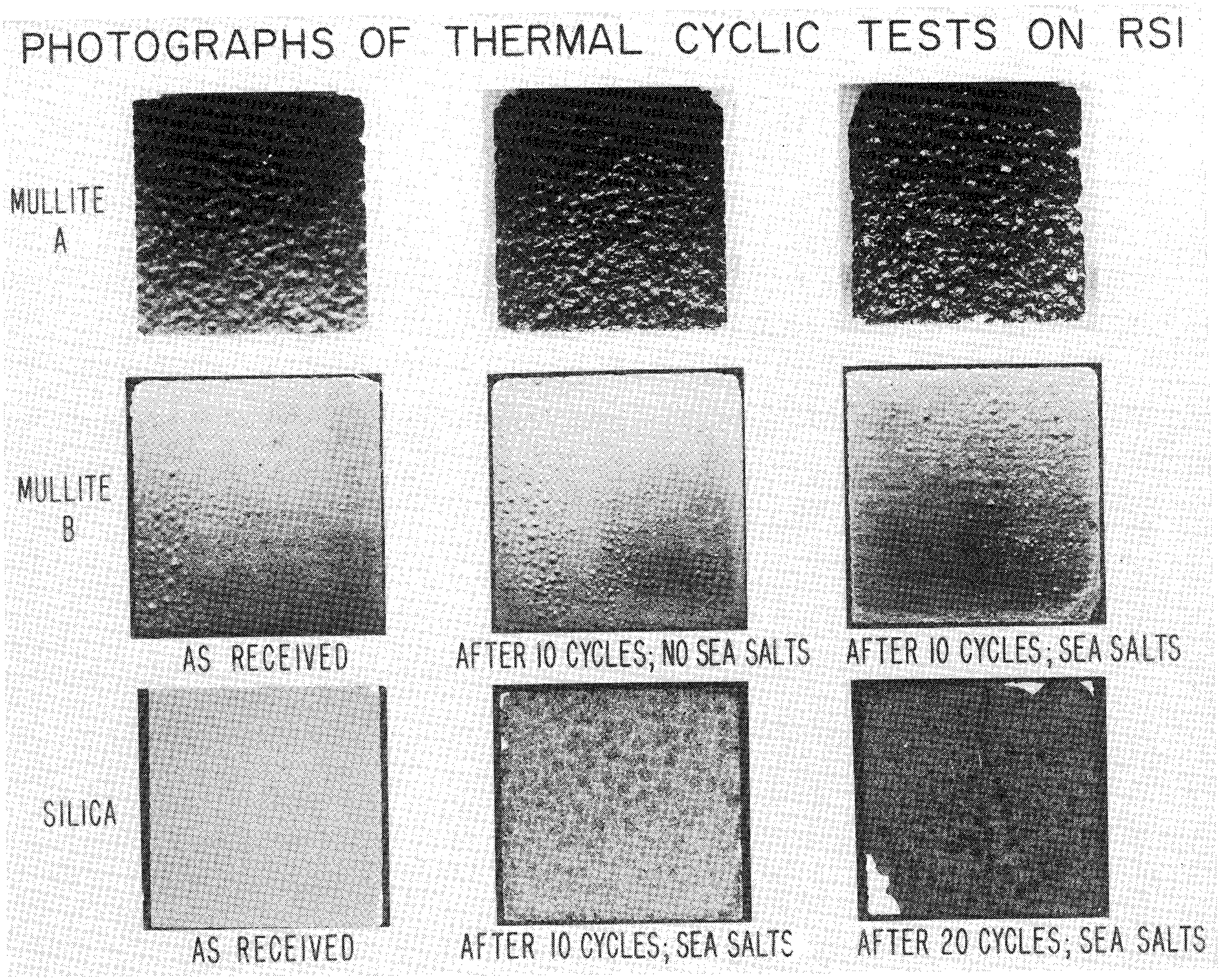
PHOTOGRAPHS OF THERMAL CYCLIC TESTS ON RSI
MULLITE A
MULLITE B
SILICA
AS RECEIVED
AFTER 10 CYCLES; NO SEA SALTS
AFTER 10 CYCLES; SEA SALTS
AS RECEIVED
AFTER 10 CYCLES; SEA SALTS
AFTER 20 CYCLES; SEA SALTS

Figure 25

EFFECT OF DENSITY ON COMPRESSIVE STRENGTH AND WEIGHT GAIN DUE TO EXPOSURE TO THE NATURAL ENVIRONMENT

(Figure 26)

RSI fabrication studies at MSFC have utilized a combination of molding and vacuum slurry casting to produce higher density, and stronger mullite RSI. With this processing and in work done under contract, the properties of higher density RSI are being determined. The accompanying plot is typical of the strength variation with density that has been observed. While the program is not complete, the following tentative conclusions have been reached: A small density increase has a strong effect on strength, a very weak effect on strain-to-failure, and a negligible effect on thermal conductivity.

Moisture studies indicate it may be dangerous to rely upon the glassy, ceramic coatings for waterproofing. The data show the weight variation due to absorbed moisture for coated mullite and silica tiles bonded to a substrate and exposed to the natural environment (rain, dew) at Huntsville. Neither tile was treated with a hydrophobic material.

Processing studies of mullite on contract have produced better methods for and better control of the dispersion and casting operations, resulting in reduced density gradients in the fabricated tile and reduced dispersion in tile strength values. In the coating improvements, the investigation of alternates to the glassy coatings and of methods to reduce the modulus of the glassy coatings has not resulted in coatings greatly different from the earlier coatings. Some improvement in the processing and properties of the glassy coatings has been realized.

Reinforced RSI studies have concentrated on methods to prevent the loss of a tile, or substantial portions of a tile, in the event of cracking. The casting of mullite RSI into a 3-D matrix of wires has been demonstrated. A specimen with FS-80 columbium wire reinforcement is now being fabricated, with a secondary insulation package. Due to the efficiency of the low density thermal insulation, no weight penalty for this reinforced concept is predicted.

Thermal conductivity reduction work initially stressed the effect of opacifiers; however, the opacifiers have had little effect on thermal conductivity and infrared transmission studies have indicated the opacifiers have little effect on the optical absorption coefficient. These studies are continuing in order to derive the radiation component of total thermal conductivity so that effective means of thermal conductivity reduction may be obtained.

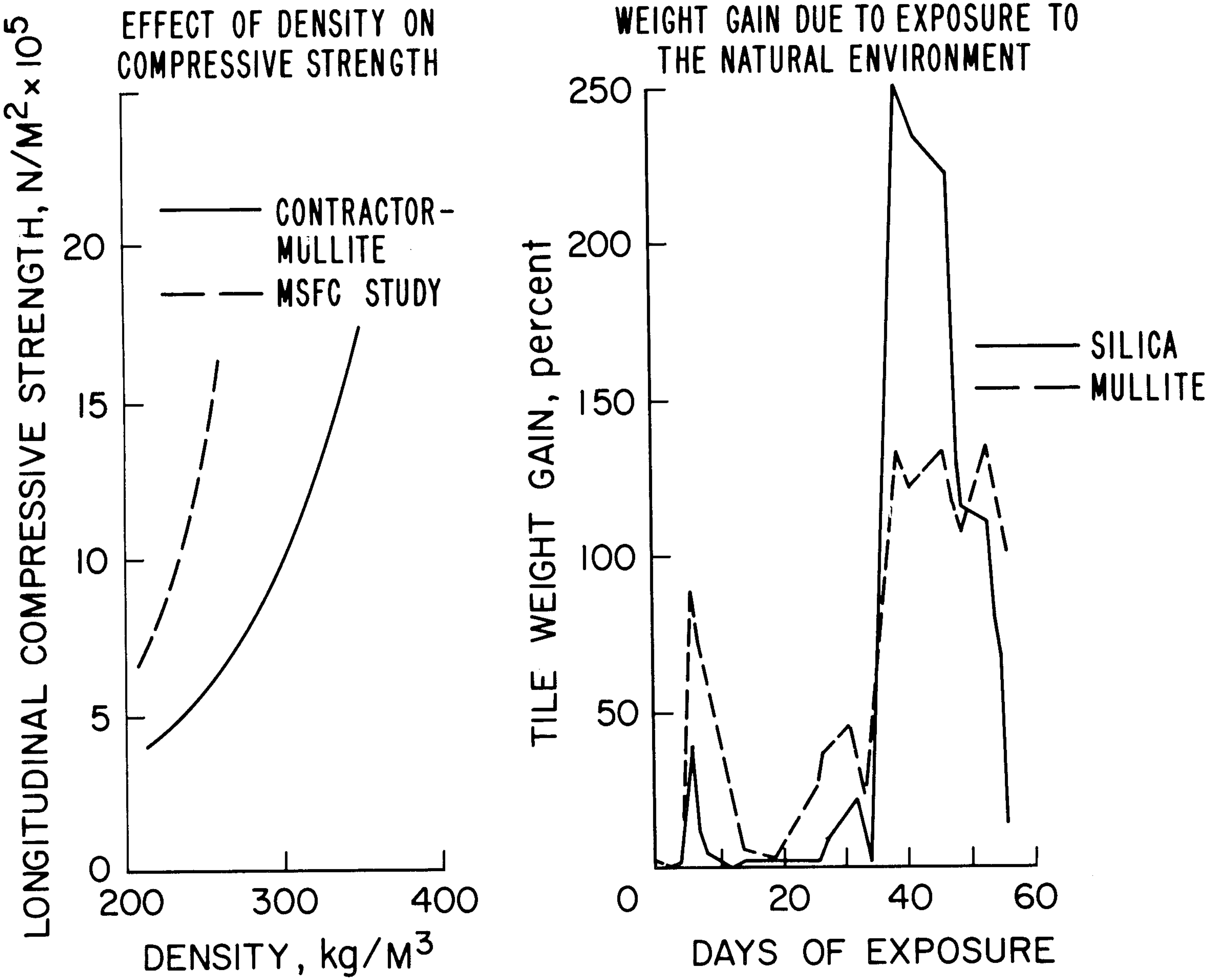
EFFECT OF DENSITY ON COMPRESSIVE STRENGTH
LONGITUDINAL COMPRESSIVE STRENGTH, N/M^2 x 10^5
CONTRACTOR-MULLITE
MSFC STUDY
DENSITY, kg/M^3
0
5
10
15
20
200
300
400
WEIGHT GAIN DUE TO EXPOSURE TO THE NATURAL ENVIRONMENT
TILE WEIGHT GAIN, percent
SILICA
MULLITE
DAYS OF EXPOSURE
0
50
100
150
200
250
20
40
60

Figure 26

MICROSTRUCTURES OF SPUN MULLITE FIBERS

(Figure 27)

The LeRC in-house RSI effort is concerned with silica and mullite fibers and rigidized tiles made from these fibers. It is concentrated in three areas:

(1) Characterization of fibers and tiles, in terms of chemistry, macrostructure, microstructure, phase identification, and phase morphology.

(2) Improvement of mechanical properties of rigidized tiles by techniques that are independent of tile rigidizing processes. Examples of approaches to these problems include efforts to stabilize new phases at fiber surfaces, eliminate fiber surface flaws, and increase the number of fiber-to-fiber bonds.

(3) Improvement of tile surface qualities such as improved moisture resistance and thermal emittance glazes by particular additives.

This figure shows mullite microstructures obtained by a cathodic etching technique developed by LeRC. In this technique the fibers are subjected to bombardment by ionized argon for times up to 30 minutes. The features noted in the micrographs show a general coarsening of the microstructure caused by thermal exposures. This apparently is the result of grain growth; however, the complete identification of the observable features is not yet possible. These features may represent true grain boundaries, low angle sub-boundaries, and/or boundaries between regions of varying phase composition. Although the potential is great, in-depth studies are required in order to increase our ability to interpret the many features observable and relate these to mechanical behavior and thermal stability.

It has been shown that the thermal stability of silica fibers is strongly dependent on the chemistry of the fibers which in turn depends on the leaching steps in the process by which the fibers are made. Comparisons of fibers made in 1969 with those currently being made show that the total impurities have been significantly decreased, particularly the alkaline elements. Further purification, which is possible, should enhance the resistance to crystallization. Recent results at LeRC suggest that major shrinkage occurs by viscous flow which could be retarded by some controlled crystallization. The effects of both surface and combined water and the spatial distribution of elemental impurities on devitrification behavior are important but are yet to be fully investigated.

A contract with the silica fiber manufacturer seeks to minimize the variability of silica fibers through control of process variables. In particular, control over leaching process parameters is being sought.

MICROSTRUCTURES OF SPUN MULLITE FIBERS

MAGNIFICATION = 65,000 ×

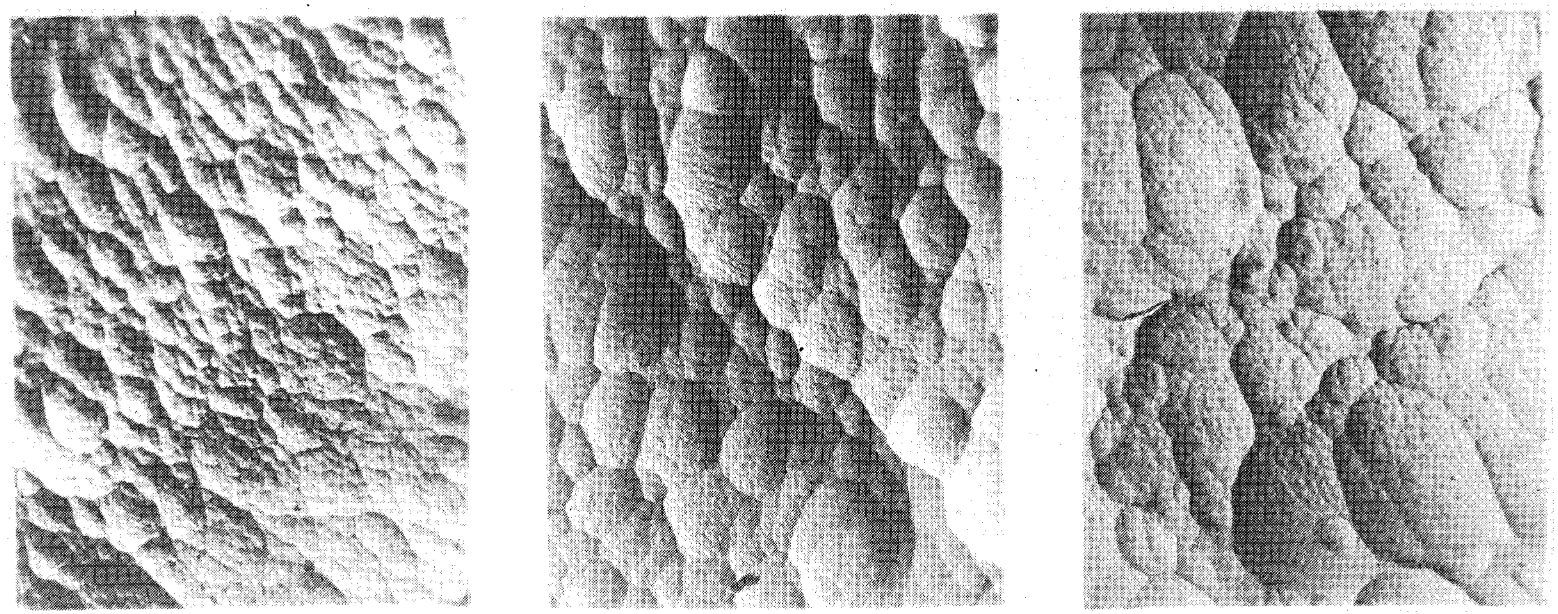

AS MANUFACTURED
XRD: α-Al_2O_3

EXPOSED IN 1 atm
AIR 2200° F 1 hr
XRD: MULLITE

EXPOSED IN 1 atm
AIR 2600°F 16 hrs
XRD: MULLITE
PLUS UNIDENTIFIED PHASE

Figure 27

THE LOSS OF ADDITIVES FROM MULLITE FIBERS

(Figure 28)

In the production of mullite fibers, additives are made to the basic SiO_2-Al_2O_3 composition for two purposes. These are, first, to act as a mineralizer and promote the mullite formation reaction at low temperatures and, second, to act as high temperature stabilizers and prevent excessive grain growth during firing and subsequent exposures. The presently used additives, B_2O_3 and P_2O_5, are lost from the fiber during thermal exposures as illustrated in the accompanying figure. More stable additives that would be lost at a lower rate would certainly increase the high temperature stability of mullite fibers. The more stable additives are particularly important when one considers the smaller diameter (4 μm) mullite fibers which will be even more susceptible to additive loss and its accompanying strength degradation.

LeRC, in a contract with the fiber manufacturer, seeks to establish strength, shrinkage, thermal stability, and microstructural relationships for the mullite-type fibers. Composition (silica rich and alumina rich) and firing schedule are major variables. It appears that major compositional variations from the "standard" composition do not offer a high potential for fiber property improvement. On the other hand, obtaining improved thermal stability seems possible by minor chemistry changes.

THE LOSS OF ADDITIVES FROM MULLITE FIBERS

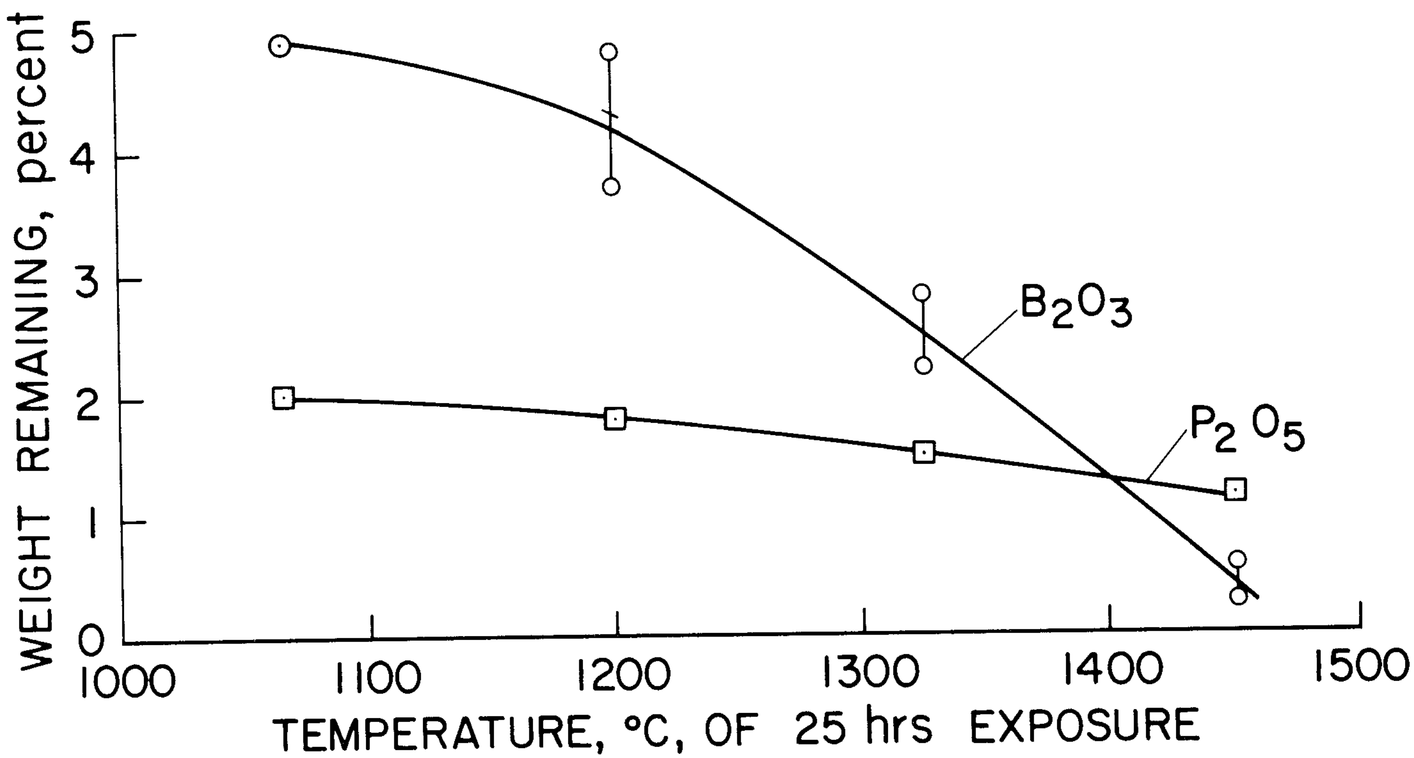

Figure 28

EFFECT OF MULTIDIRECTIONAL PRESSING ON SILICA RSI STRENGTH

(Figure 29)

ARC is working on a number of areas of RSI characterization and improvement both in-house and on contract. The specific areas of research are listed below.

(1) Materials and Process Improvement: This work encompasses studies of binder improvements, processing parameters, unique fiber/binder combinations, effects of crystallinity on tile properties, coating improvement, and opacification of the tile.

(2) Environmental Response of RSI in Arc Plasma Facilities: Both contractor supplied RSI and Ames fabricated RSI are being exposed to repeated laminar and turbulent arc plasma tests to characterize the materials response to convective heating, study the noncatalytic wall effects on glass coatings, and to study chemical changes that occur in coatings.

(3) Pretest and Posttest Chemical, Thermal and Physical Analysis of RSI: Physical properties, detailed chemical analysis, X-ray diffractions, scanning electron microscopy, and spectral emittance are being measured on both the Ames fabricated and contractor supplied materials.

(4) Basic Fiber and Tile Characterization and Research: This research being sponsored by ARC is meant to provide a more detailed understanding of the morphology, crystallinity, and thermophysical response of RSI materials and their component fibers.

Other work being sponsored by ARC includes studies of the catalytic efficiency of glass surfaces, studies of the effects of microstructure on thermostructural response and, in-house, the response of RSI materials to acoustic environments created by supersonic boundary layers.

This figure illustrates a result that was obtained in the ARC materials and process improvement research. Shown are physical properties measured on a silica RSI tile molded by pressing in one direction, those measured on a tile made by pressing in two directions, and for comparison the properties of a contractor-supplied silica tile. These results show that the transverse or weak direction tensile strength can be significantly increased by two directional pressing without adversely affecting the other physical properties of the RSI tile. A comparison with the contractor's material shows that the two directional pressing provides a much higher ratio of weak to strong direction strength than has been obtained in the commercial product. It is possible that by techniques such as this or isostatic pressing that isotropic RSI can be fabricated.

EFFECT OF MULTIDIRECTIONAL PRESSING ON SILICA RSI STRENGTH

	SINGLE DIRECTION PRESS		TWO DIRECTION PRESS		CONTRACTOR SILICA*	
DENSITY, kg/M^3	240		240		240	
	TRANSVERSE	LONGITUDINAL	TRANSVERSE	LONGITUDINAL	TRANSVERSE	LONGITUDINAL
TENSILE, $N/M^2 \times 10^5$	$\boxed{1.2}$	4.2	$\boxed{2.5}$	5.6	0.9	8.3
TENSILE MODULUS, $N/M^2 \times 10^7$	2.1	19	6.2	22	8.3	55
COMPRESSIVE, $N/M^2 \times 10^5$	2.2	6.5	2.8	5.2	5.1	11
COMPRESSIVE MODULUS, $N/M^2 \times 10^7$	2.1	11.1	4.4	8.8	3.5	17

* MEASURED AT ARC

Figure 29

RSI TECHNOLOGY STATUS

(Figure 30)

This paper has presented data on test results, shown that the properties of RSI are changing and in many cases are poorly defined but also has indicated that significant progress has been made in RSI technology. Coatings are now available that are at least nominally waterproof. Some coatings have survived multiple arc plasma and radiant heating cycles. Physical properties have been improved in some cases by a factor of four. The manufacturers have shown that they can manufacture tile in pilot plant quantities. It appears that scaling up is feasible and that the projected price of the base RSI tile is not prohibitive.

There are, of course, many problems that remain. A great deal more data on all aspects of RSI, that is, thermal response, thermal and physical properties, reproducibility, cost, and all the many aspects of its systems applications are required. The materials that have come out of the MSC Phase II program and the RSI improvement efforts must be fully characterized and compared. It is likely that significant improvements in basic fiber properties, in binding systems and in coatings can be accomplished. The anisotropy and low strength of RSI is likely to be improved by better processing techniques.

RSI TECHNOLOGY STATUS

- MATERIALS GREATLY IMPROVED IN LAST YEAR
  - BETTER COATINGS
  - STRONGER TILE WITH HIGHER STRAIN TO FAILURE
  - DEMONSTRATED REUSE CAPABILITY
  - PILOT PLANTS PUT INTO OPERATION
  - DEMONSTRATED INCREASED PRODUCTION RATE OF REPRODUCIBLE MATERIAL
- PROBLEMS REMAIN
  - NOT ENOUGH TEST DATA!
  - RSI COATINGS NOT PROVEN ADEQUATE FOR 100 FLIGHTS
  - STRONGER, MORE ISOTROPIC TILES AND COATINGS DESIRABLE
  - ADEQUACY OF MULLITE THERMAL SHOCK AND THERMAL STRESS RESISTANCE
  - RSI'S RESPONSE TO CONTAMINANTS NOT COMPLETELY UNDERSTOOD

Figure 30

STATUS OF RSI TPS TECHNOLOGY PROGRAMS

David H. Greenshields, Andre J. Meyer, and Donald J. Tillian
NASA Manned Spacecraft Center, Houston, Texas

INTRODUCTION

NASA has sponsored the development of three low-density rigidized insulation materials for the shuttle TPS application. These materials consist of one high-purity silica system and two systems based on mullite, an aluminum silicate. Both systems consist of fibers joined together with appropriate binders to obtain a rigidized insulation composite. Both material systems require the application of a glassy coating to provide a wear resistant, high emittance surface and to prevent the absorption of water by the fiber matrix.

The technology program has addressed the development of water impervious coatings, methods of assembling the materials in design concepts while minimizing the thermal stress in the insulation, achieving compatibility between the RSI material and the structural system, and test evaluations to demonstrate the feasibility of the surface insulation concept.

ENTRY TRAJECTORY LIMITS FOR A TYPICAL SPACE SHUTTLE

(Figure 1)

A specific entry trajectory for the space shuttle has not been selected; however, the trajectory will lie between the equilibrium glide established by aerodynamic design and 3g limits shown here. If the lower surface of the vehicle is limited to 1367K, the entry corridor will be very narrow, while an increase to 1644K provides a significantly wider entry corridor at the higher velocities; primarily for this reason, 1644K has been used as a target reuse temperature in the RSI development program.

ENTRY TRAJECTORY LIMITS FOR A TYPICAL SPACE SHUTTLE

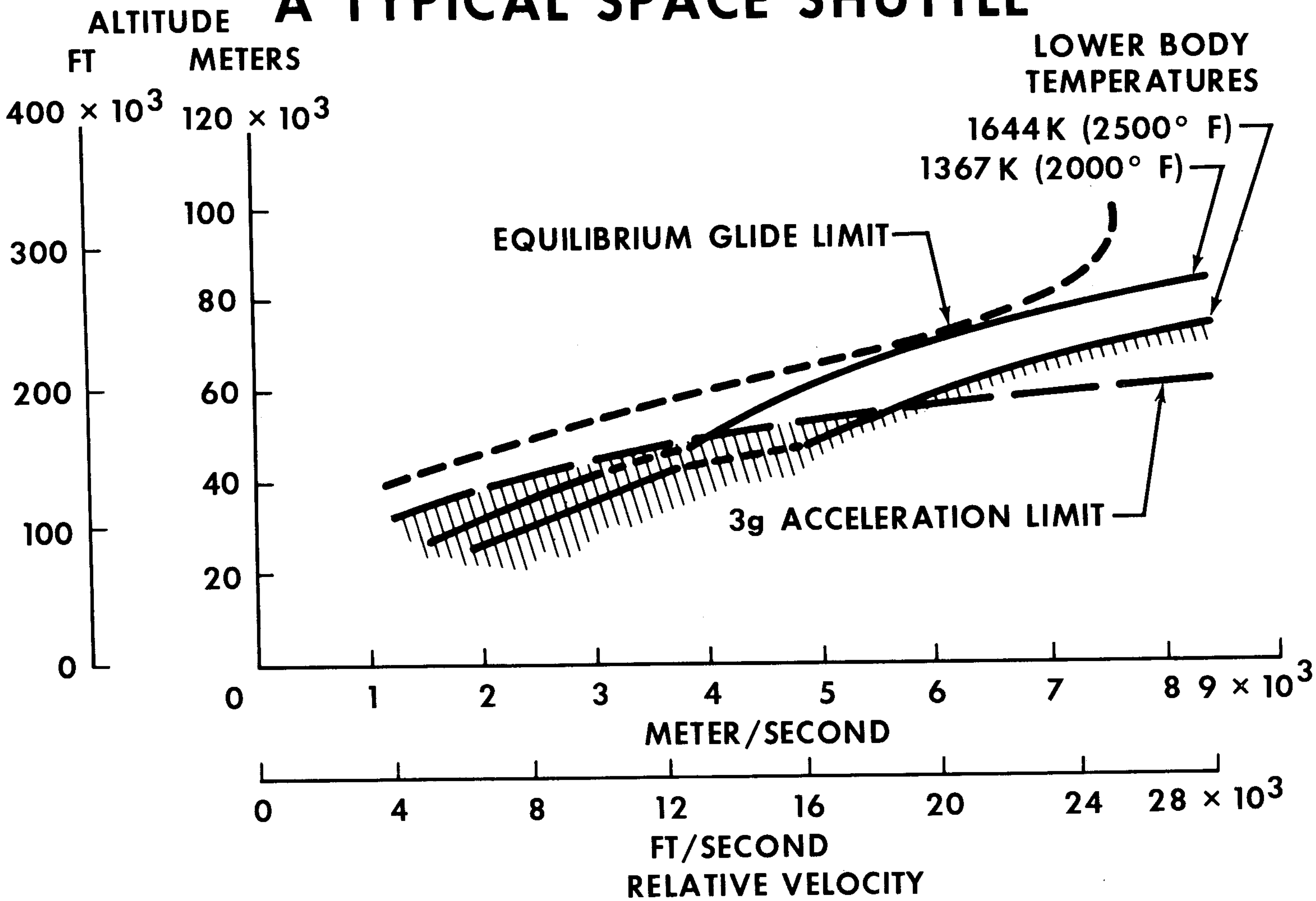

Figure 1

DISTRIBUTION OF PEAK SURFACE TEMPERATURES

(Figure 2)

This figure illustrates the peak temperatures expected on the under side of the shuttle for the trajectory selected as a baseline for RSI development. The two areas that were considered for prototype hardware designs are designated Areas 1 and 2. Area No. 2, near the leading edge, is the portion of RSI that would see the maximum temperature approaching 1644K. The Area No. 1 is more representative of the general acreage under the orbiter and reaches a peak temperature of approximately 1035K.

DISTRIBUTION OF PEAK SURFACE TEMPERATURES

RSI TECHNOLOGY BASELINE

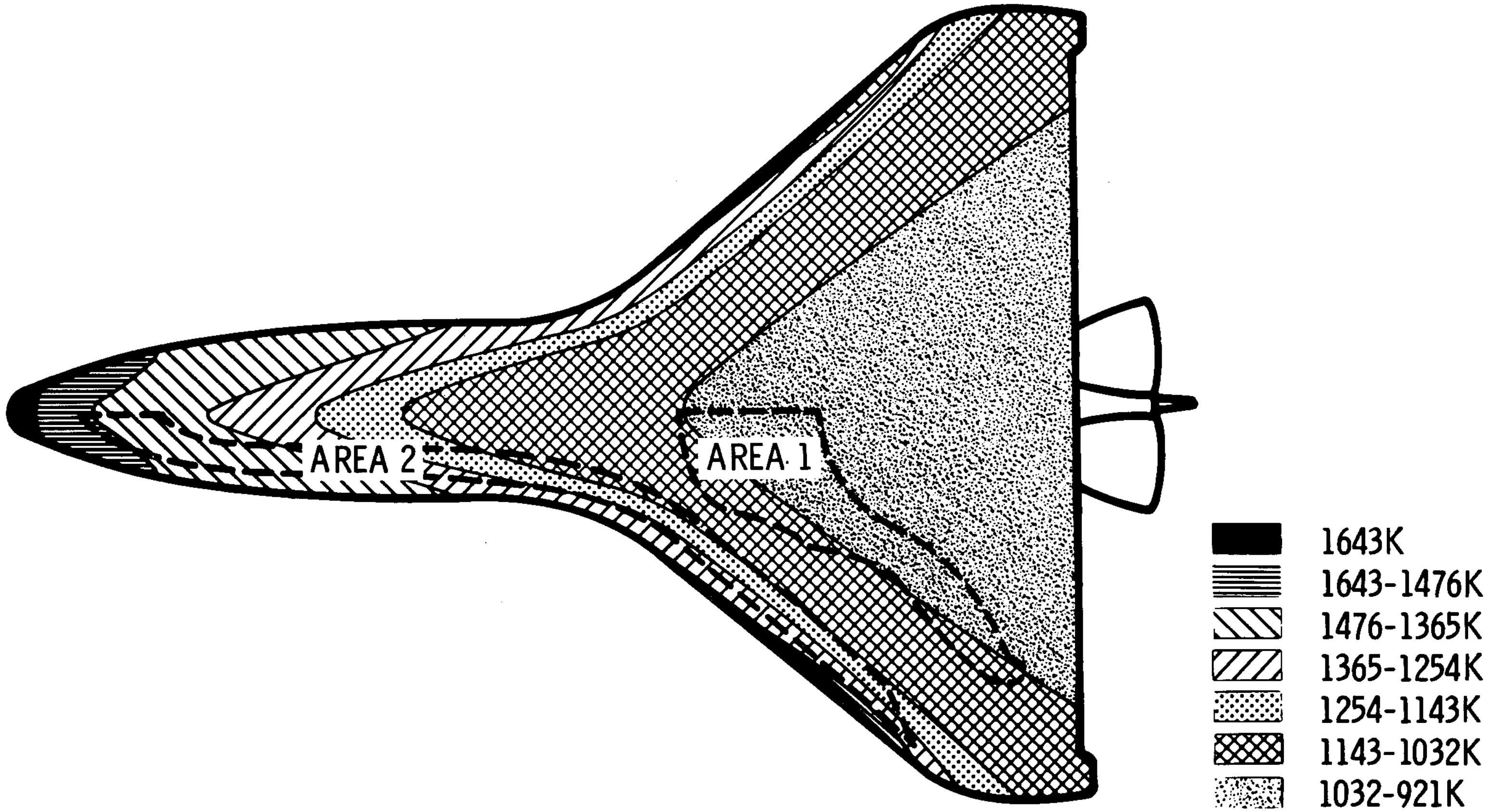

Figure 2

DESIGN REQUIREMENTS FOR PROTOTYPE TPS HARDWARE

(Figure 3)

This graph shows the design surface temperature and aerodynamic load histories used in the technology program. It is evident that when the peak temperatures are encountered, the loads are relatively low, and after the heat pulse, higher loads are encountered. The loads spikes after reentry heating are due to maneuvers and gusts encountered before touchdown.

DESIGN REQUIREMENTS FOR PROTOTYPE TPS HARDWARE

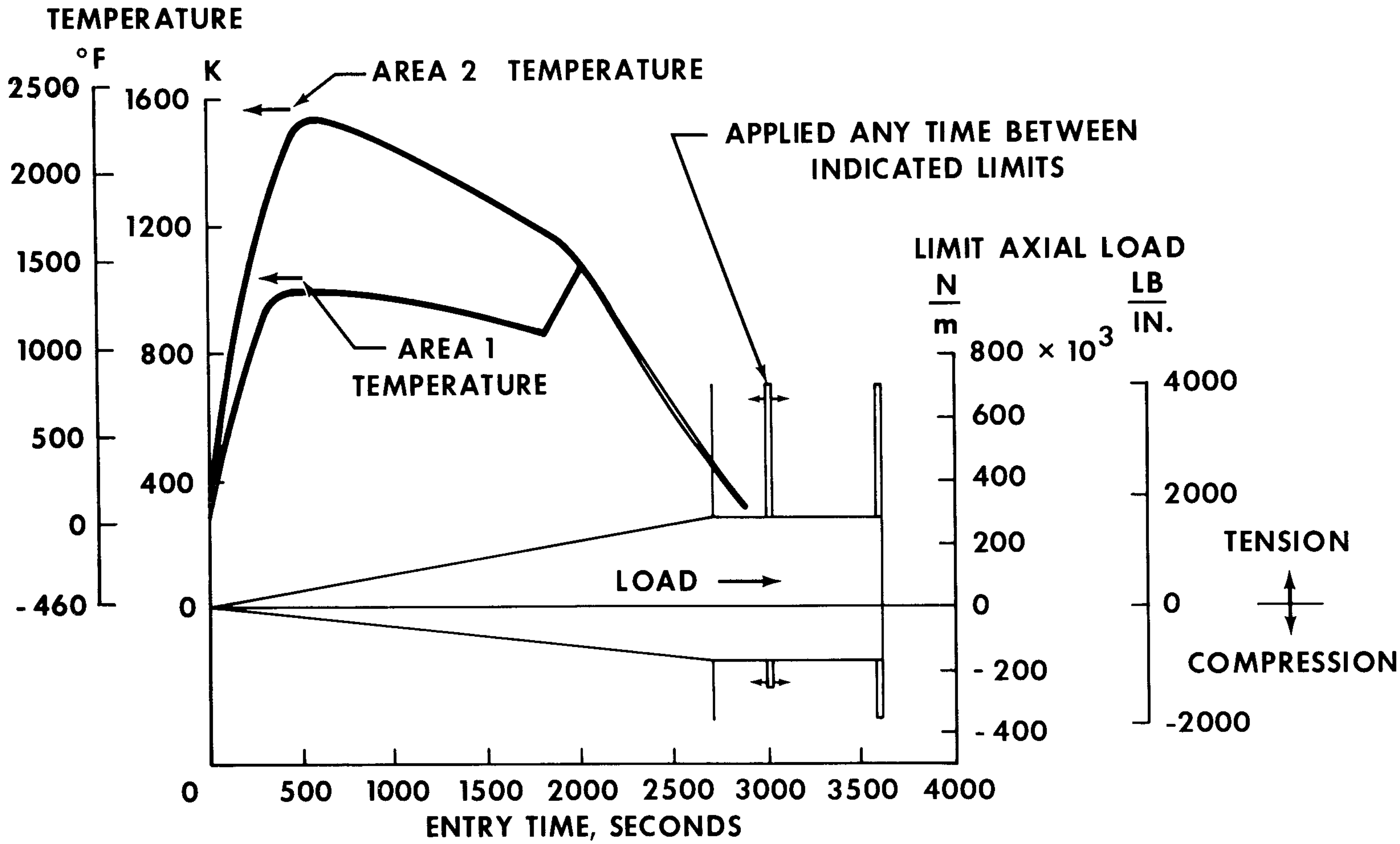

Figure 3

CROSS SECTION OF SILICA SURFACE INSULATION

(Figure 4)

A scanning electron photomicrograph of the silica material cross section including its coating is shown. The dense, glassy seal coat is readily detectable immediately below the more porous high emissivity silicon carbide coating. The anisotropic characteristic or layering of the rigidized fiber insulation substrate is also obvious.

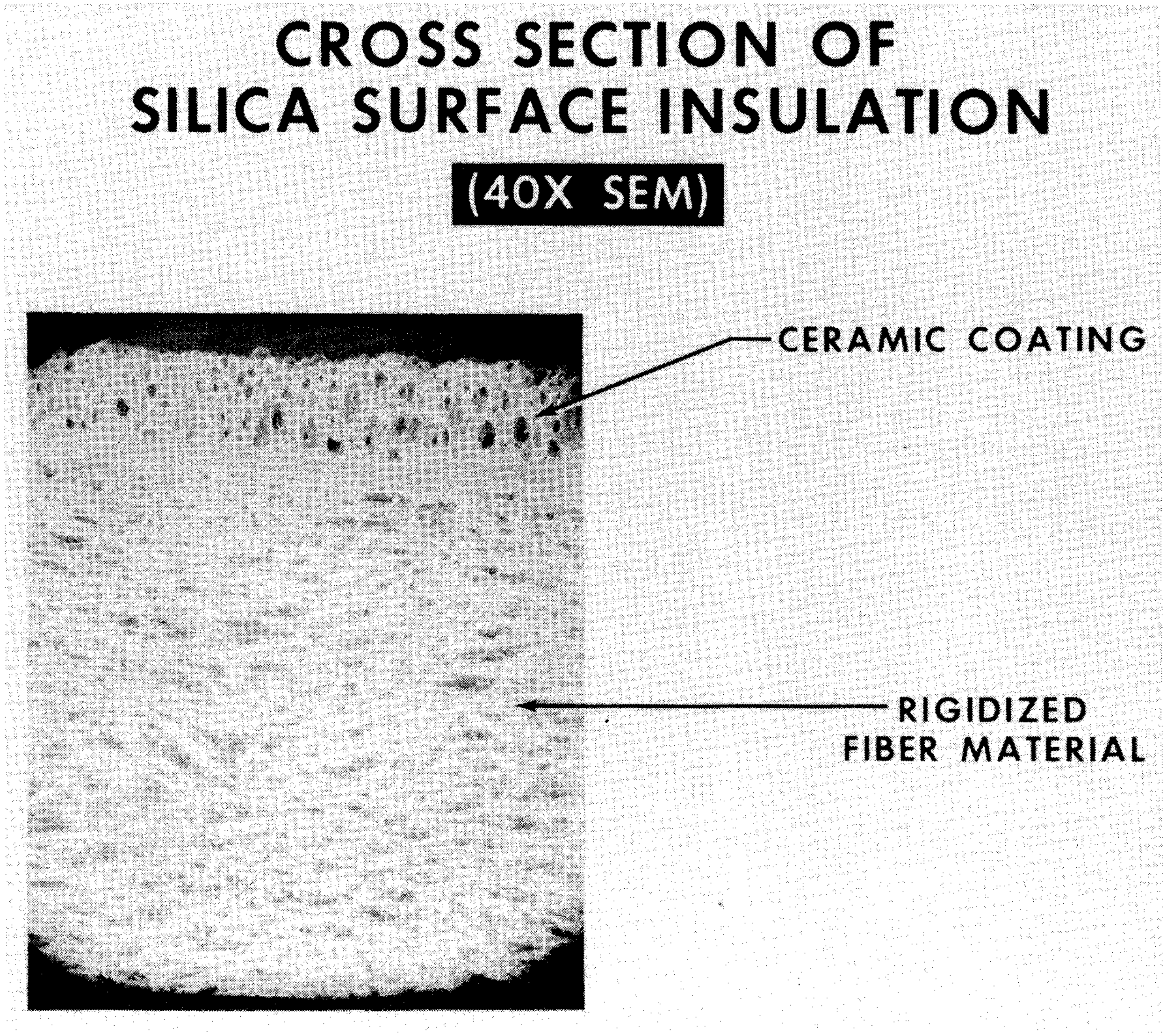
CROSS SECTION OF
SILICA SURFACE INSULATION
(40X SEM)
CERAMIC COATING
RIGIDIZED
FIBER MATERIAL

Figure 4

CROSS SECTION OF MULLITE SURFACE INSULATION
(Figure 5)

Two different mullite systems have been under development. Both systems use the same mullite fibers; however, one employs a silica binder, and the other an aluminum silicate. This SEM photograph is representative of the mullite material which contains silica microspheres in the binder. The thick glassy external coating is characteristic of both mullite systems.

CROSS SECTION OF
MULLITE SURFACE INSULATION
(40X SEM)

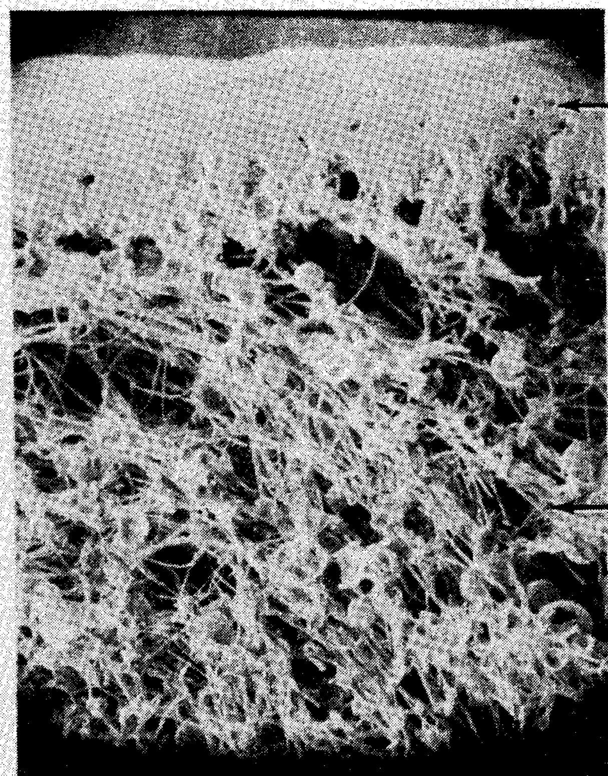

Figure 5

DESCRIPTION OF MATERIALS USED IN TPS PANEL DELIVERABLES

(Figure 6)

The table shows the basic composition of the rigidized fiber, binder, and the coating. The raw fiber for the mullite composites are not yet available in the small size used for the silica. Smaller fiber diameter should improve the strength and the thermal properties of the mullite material. One of the mullite materials contains an opacifier to reduce radiative heat transport. Basically, all coatings are variations of a borosilicate glass with pigment consisting of metallic oxides and carbides.

DESCRIPTION OF MATERIALS USED IN TPS PANEL DELIVERABLES

FIBER	MULLITE	MULLITE	SILICA
AVG DIA	4.7 μm	4.7 μm	1 μm
BINDER	SILICA	Al_2O_3-SiO_2-B_2O_3	SILICA
FILLER	SILICA ECCOSPHERES	-	-
OPACIFIER	ZIRCON	-	-
COATING	OXIDES, BOROSILICATE GLASS ($Al_2O_3SiO_2$-Cr_2O_3)	OXIDES, MULLITE PHASE GLASS (Li_2-Al_2O_3-SiO_2)	SILICON CARBIDE, BOROSILICATE GLASS (SiC/SiO_2-B_2O_3)

Figure 6

REUSABLE SURFACE INSULATION TPS DESIGN CONCEPTS

(Figure 7)

In the technology development program, two approaches have evolved for application of the RSI material to the shuttle structure. One concept is direct attachment of the RSI material to the primary structure; the other involves the application of the RSI materials to subpanels which are mechanically attached to the primary structure. In both cases, bonding is the primary method of attaching the RSI to the substrate studied. This figure shows the subpanel and primary structure variations developed in the technology program for the specified load conditions.

REUSABLE SURFACE INSULATION TPS DESIGN CONCEPTS

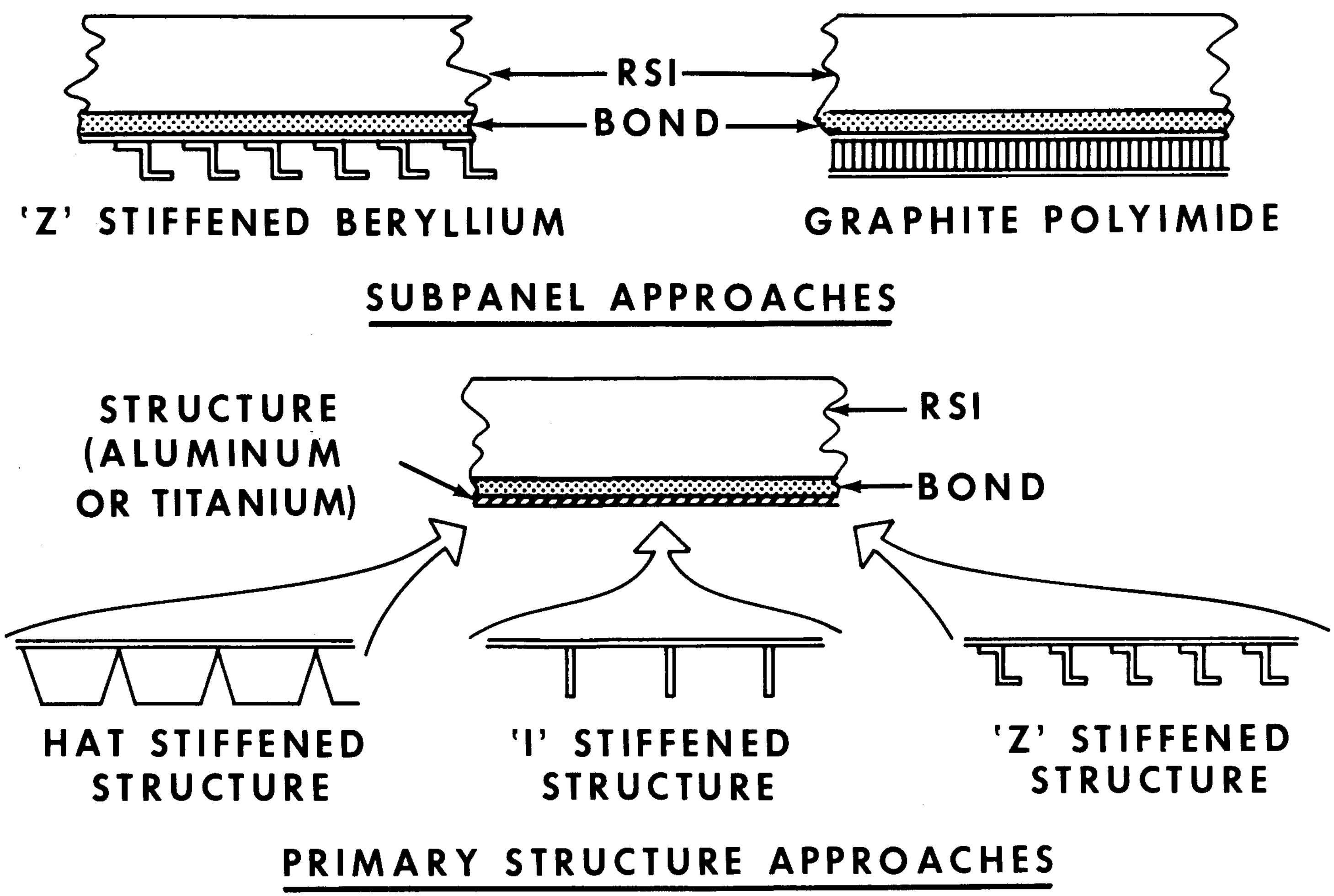

Figure 7

STRAIN ISOLATION PROVIDED BY FOAM BOND PADS

(Figure 8)

One of the primary mechanical design problems posed by the RSI concept is the isolation of the brittle ceramic materials from strains induced in the structure or subpanel. This graph illustrates the strain isolation provided by foamed elastomer pads. The solid lines show the strain in the coating produced by various strains in the aluminum airframe structure when the foamed pad is not used. The dashed lines show the reduction in strain to within acceptable limits using the pad. The same pad also reduces the stresses induced by differential thermal expansion between the RSI and structure.

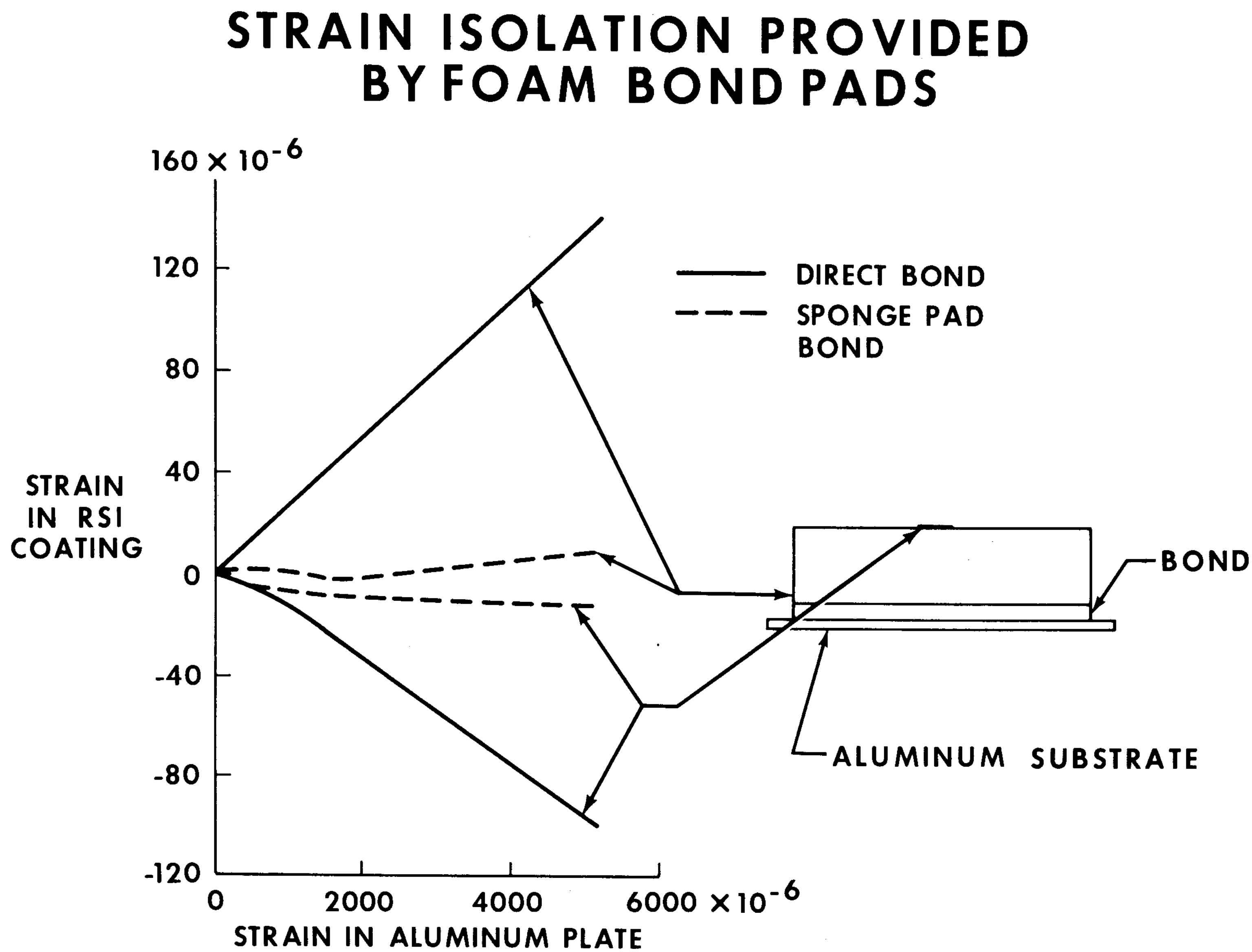
STRAIN ISOLATION PROVIDED BY FOAM BOND PADS
160 × 10^-6
120
80
40
0
-40
-80
-120
STRAIN IN RSI COATING
0
2000
4000
6000 × 10^-6
STRAIN IN ALUMINUM PLATE
DIRECT BOND
SPONGE PAD BOND
BOND
ALUMINUM SUBSTRATE

Figure 8

COMPARISON OF BONDLINE TEMPERATURE AND LOAD HISTORIES

(Figure 9)

This figure shows the effect of initial bondline temperature on the temperature history of the bond. Superimposed on the figure are the loads. The properties of the soft bond and foam pad materials are functions of the bond temperature. The temperature of the bond next to the RSI reaches its maximum value when the bond has a high initial temperature, and the TPS experiences maximum design heating. However, when the bond initial temperature is the minimum value, and the heating is lower than design values, as indicated by the dashed line on the figure, loads may occur while the bondline is below 172K.

Since the glass transition temperature for elastomers considered approaches minus 172K, a potential problem is indicated when significant deflection loads are imposed on the bond before it becomes elastic.

COMPARISON OF BONDLINE TEMPERATURE AND LOAD HISTORIES

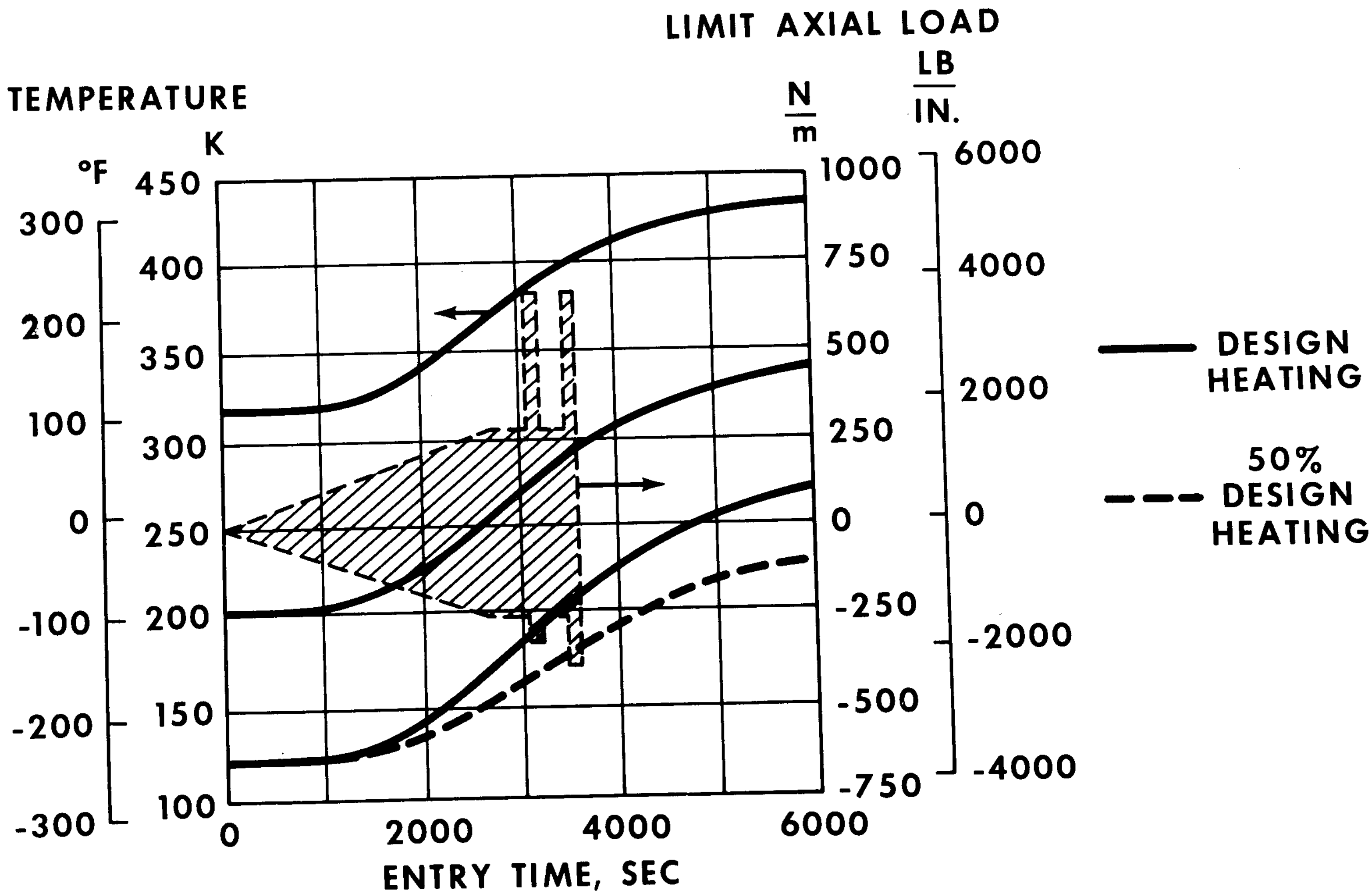

Figure 9

RSI PREDICTED FAILURE MODES
(Figure 10)

This sketch illustrates the thermal stress failure modes which effect tile size and foam bond thickness limits. The two critical conditions are (1) when the external coated surface is initially heated and (2) after heat soak through the tile when the bondline reaches its peak temperature. In the first case, combined shear and tensile failure occurs through the thickness of the RSI above the bond interface. Inplane tensile failure of the coating on the sidewalls of the tile are possible due to the high thermal gradient through the coating from the hot exterior surface to the cold bondline. The thermal soak failures possible are combined shear and tension due to the mismatch in expansion between the elastomeric strain isolation system and the RSI. The other critical case is a tensile failure in the ceramic coating at the outer surface due to stretching of the tile caused by expansion of the strain isolator.

RSI PREDICTED FAILURE MODES

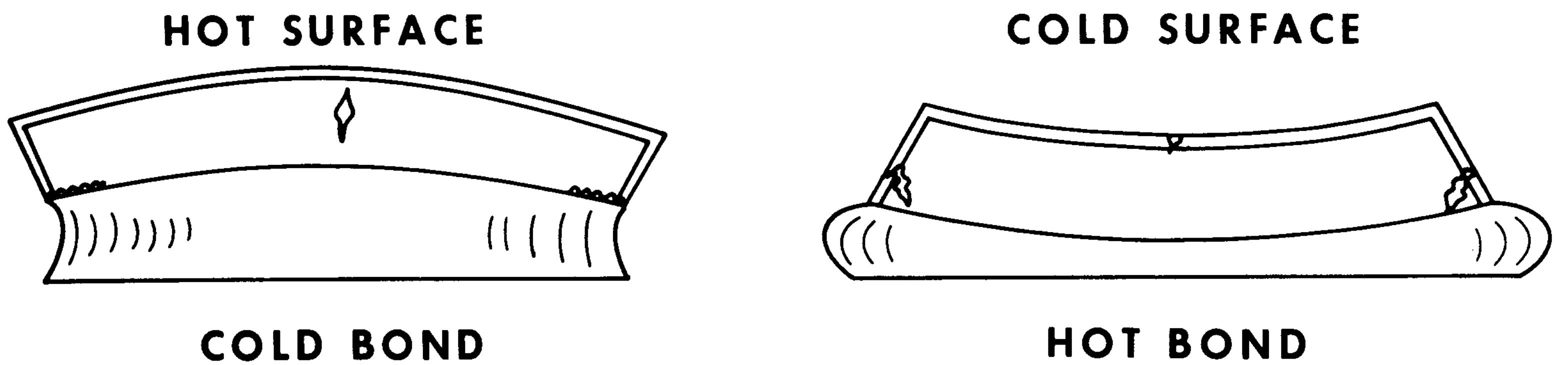

Figure 10

ACOUSTIC TEST OF TPS PANELS AFTER THERMAL TESTS

(Figure 11)

A RSI TPS panel is shown in the test facility used to simulate launch acoustics. Sound levels up to 164 dB were produced after thermal/load tests.

The white areas shown are considered to be examples of the thermal stress failures illustrated on the preceding figure which were propagated as a result of the acoustic exposure.

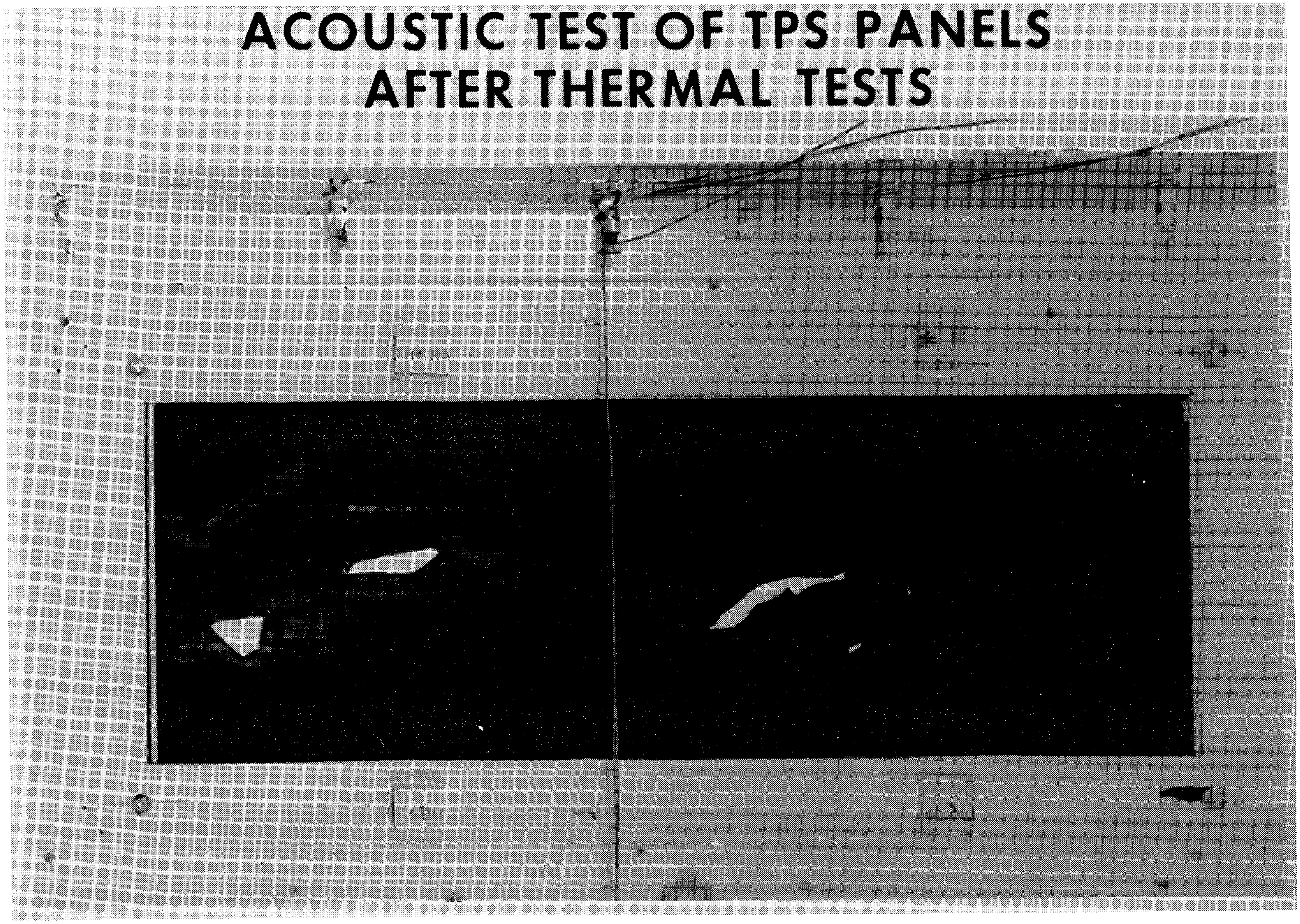

Figure 11

PROTOTYPE TPS HARDWARE WEIGHT SUMMARY - AREA 2
(Figure 12)

This bar graph shows the total and component weights for three designs for the area which reaches 1533K. The advantage of lower thermal conductivity is evident for the silica material. The weights for the primary structure are all approximately the same as indicated by the cross-hatched area below the zero line. The TPS weights reflect the use of foam bonds to alleviate thermal stress and provide strain isolation. In the case of the heaviest bond shown, the bond is used to minimize the thickness of RSI to prevent thermal stress failure, and provides part of the insulation required for the structure.

PROTOTYPE TPS HARDWARE WEIGHT SUMMARY

AREA 2 - 1533K (2300° F)

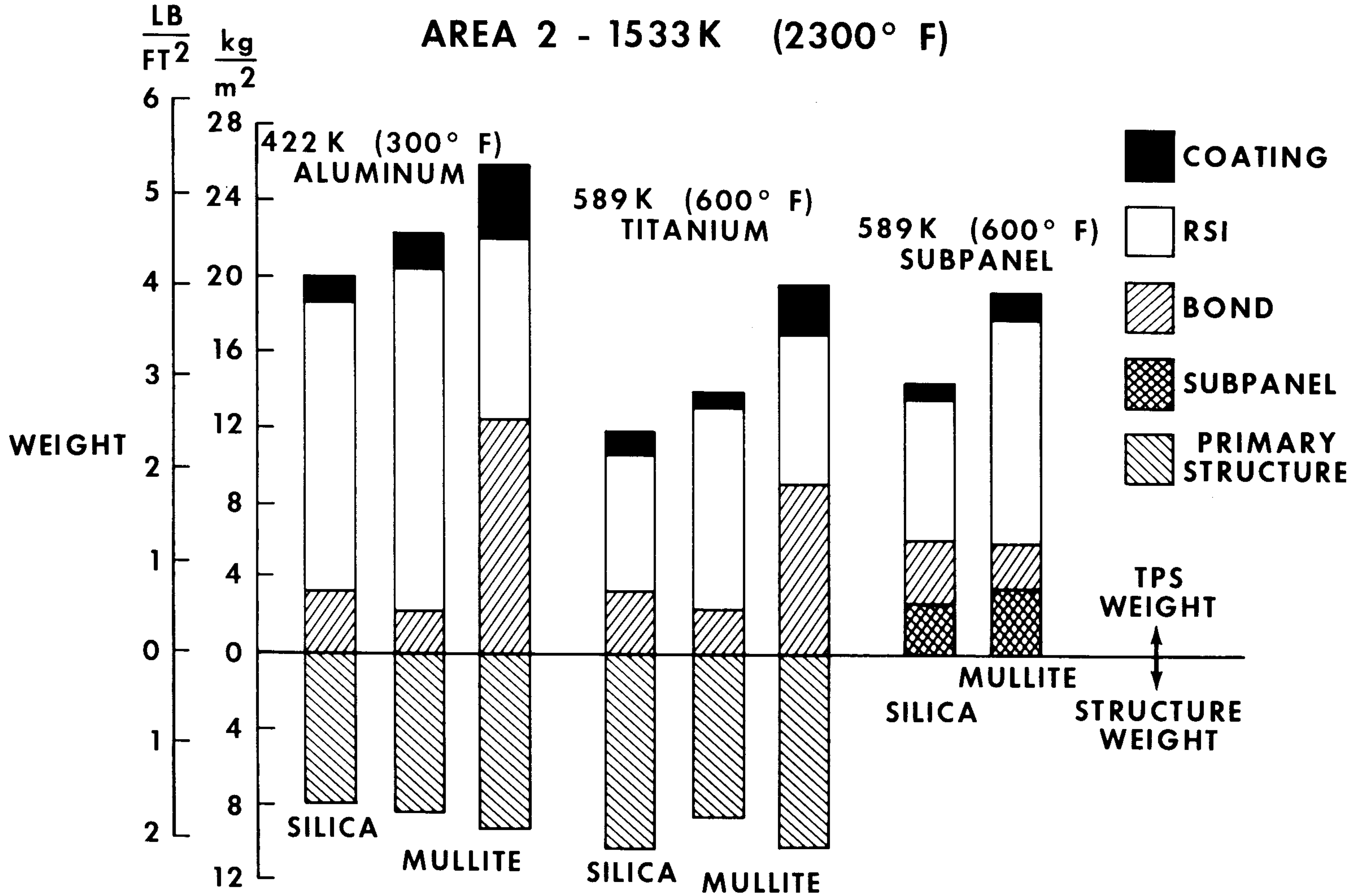

Figure 12

PROTOTYPE TPS HARDWARE WEIGHT SUMMARY - AREA 1

(Figure 13)

There is very little difference in the total TPS weight for the three materials designed for Area 1, which reaches 1033K. This is significant in that Area 1 is representative of about 3/4 of the total area requiring RSI thermal protection.

PROTOTYPE TPS HARDWARE WEIGHT SUMMARY

AREA 1 1033K (1400° F)

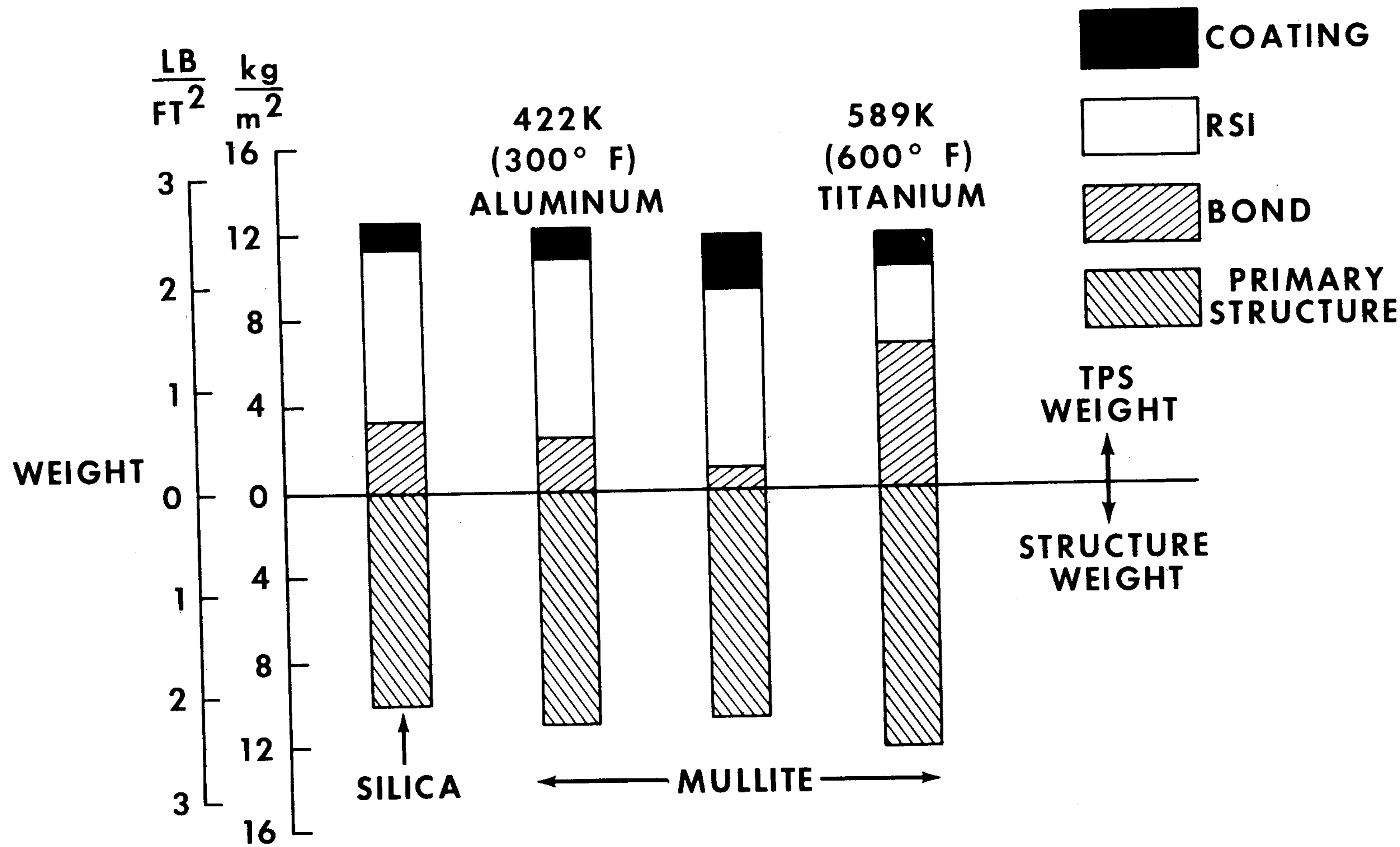

Figure 13

RSI GAP REQUIREMENTS
(Figure 14)

One of the design problems associated with RSI is the sizing and shaping of gaps between the tiles to minimize heat shorts and prevent excessive heating to the tile sides, while allowing adequate clearance for thermal expansion and accommodation of tile size tolerances.

This photograph shows gap test specimens of two of the RSI materials. The gap dimensions required to accommodate thermal expansion and deflection loading for the two basic materials are shown. Gap size for the mullite is dictated by thermal expansion while that for the silica is controlled by structural deflections. Two gap designs are shown; one is merely a butt joint filled and unfilled, while the other is a step joint designed to reduce heating of the bond material. Realistic accommodation of manufacturing tolerance has not been included.

RSI GAP REQUIREMENTS

MULLITE

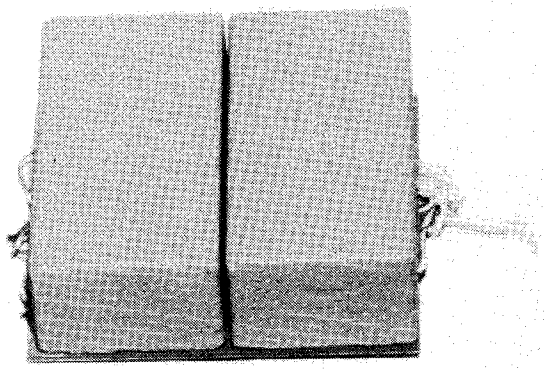

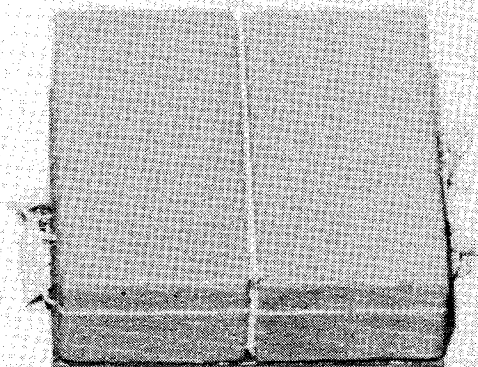

SILICA

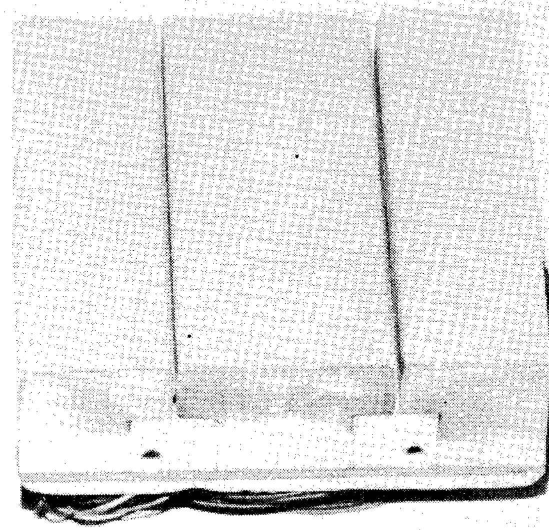

MULLITE

	mm	(IN.)
EXPANSION	2.3	(.092)
LOADING	.56	(.022)
COLD SOAK	.46	(.018)
TOLERANCE	+.25 -.0	(+.010 -.000)
NOMINAL GAP	2.5	(.100)

SILICA

	mm	(IN.)
EXPANSION	.10	(.004)
LOADING	.89	(.035)
COLD SOAK	.36	(.014)
TOLERANCE	±.25	(±.010)
NOMINAL GAP	1.1	(.045)

Figure 14

GAP HEATING EVALUATION OF SURFACE INSULATION TEST PANEL

(Figure 15)

The figure is a view of a gap test panel in MSC's 10 Megawatt Arc Facility. The model is mounted in a wedged configuration at 22.5° angle of attack. This particular model permits adjustment of the gap width to evaluate the effect on temperatures near the bondline. Configurations with gaps perpendicular and parallel to the flow are being evaluated. It will be noted that, for the relatively wide gap being tested here, the temperature in the gap exceeds that of the adjacent external surfaces. However, for narrower gaps at the same test condition, the RSI temperatures were lower near the sidewalls than in the center of the tiles.

GAP HEATING
EVALUATION OF
SURFACE INSULATION
TEST PANEL

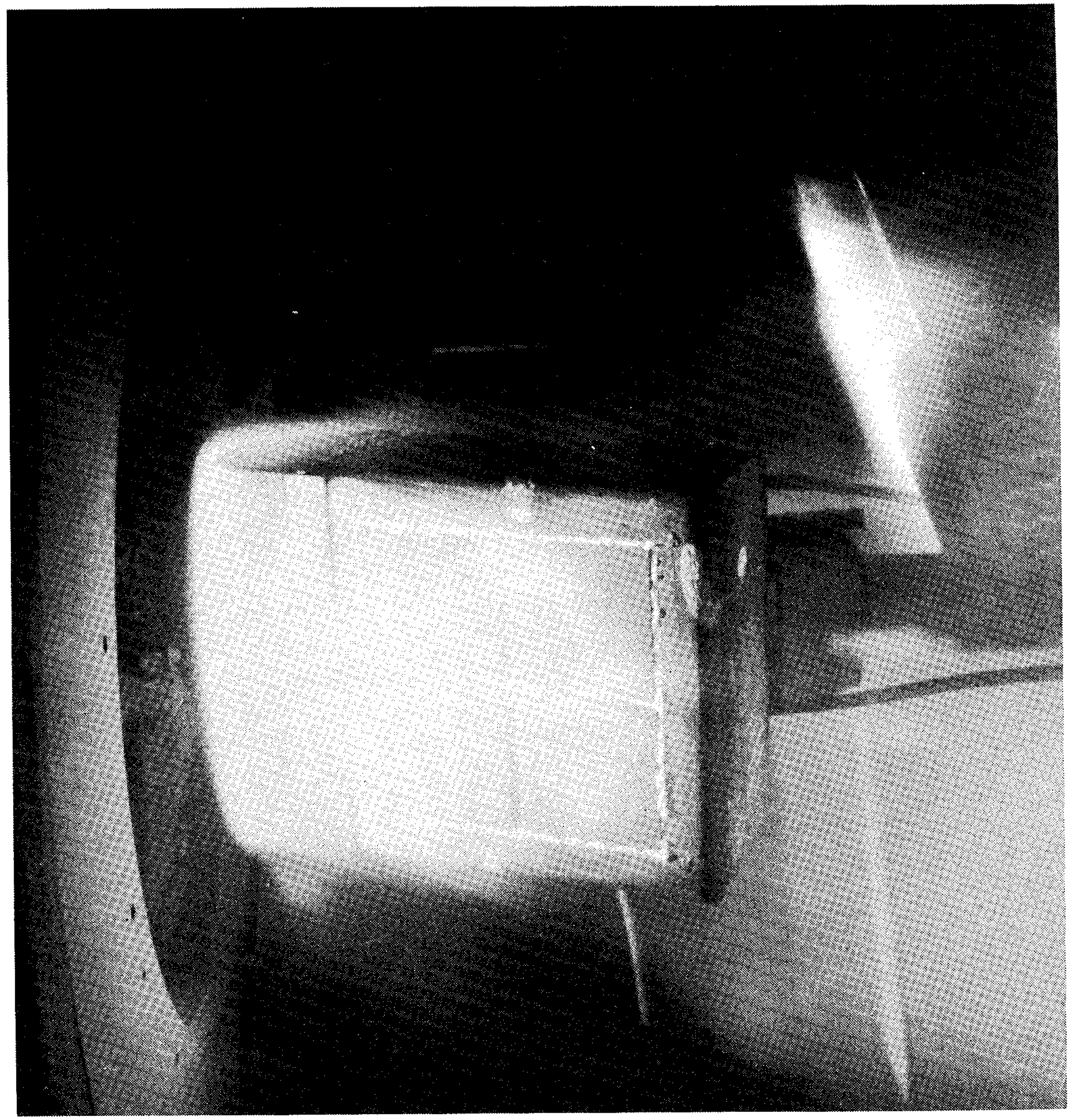

Figure 15

RADIANT HEATING AND LOADING TEST OF SURFACE INSULATION BONDED TO STRUCTURE

(Figure 16)

Prototype TPS panels (~2' x 2') have been fabricated as part of the technology program. The test program consists of subjecting the panels to sequential and combined environments of ascent acoustic loading, ascent mechanical loading, cold soak, entry heating, and cruise mechanical loading at maximum bondline temperature. This figure shows a test article supplied on previous contracts being simultaneously subjected to radiant thermal heating and axial loading representing wing deflections. These tests are being conducted in the Thermal Structural Test Laboratory at NASA/MSC.

RADIANT HEATING AND LOADING TEST
SURFACE INSULATION BONDED TO STRUCTURE

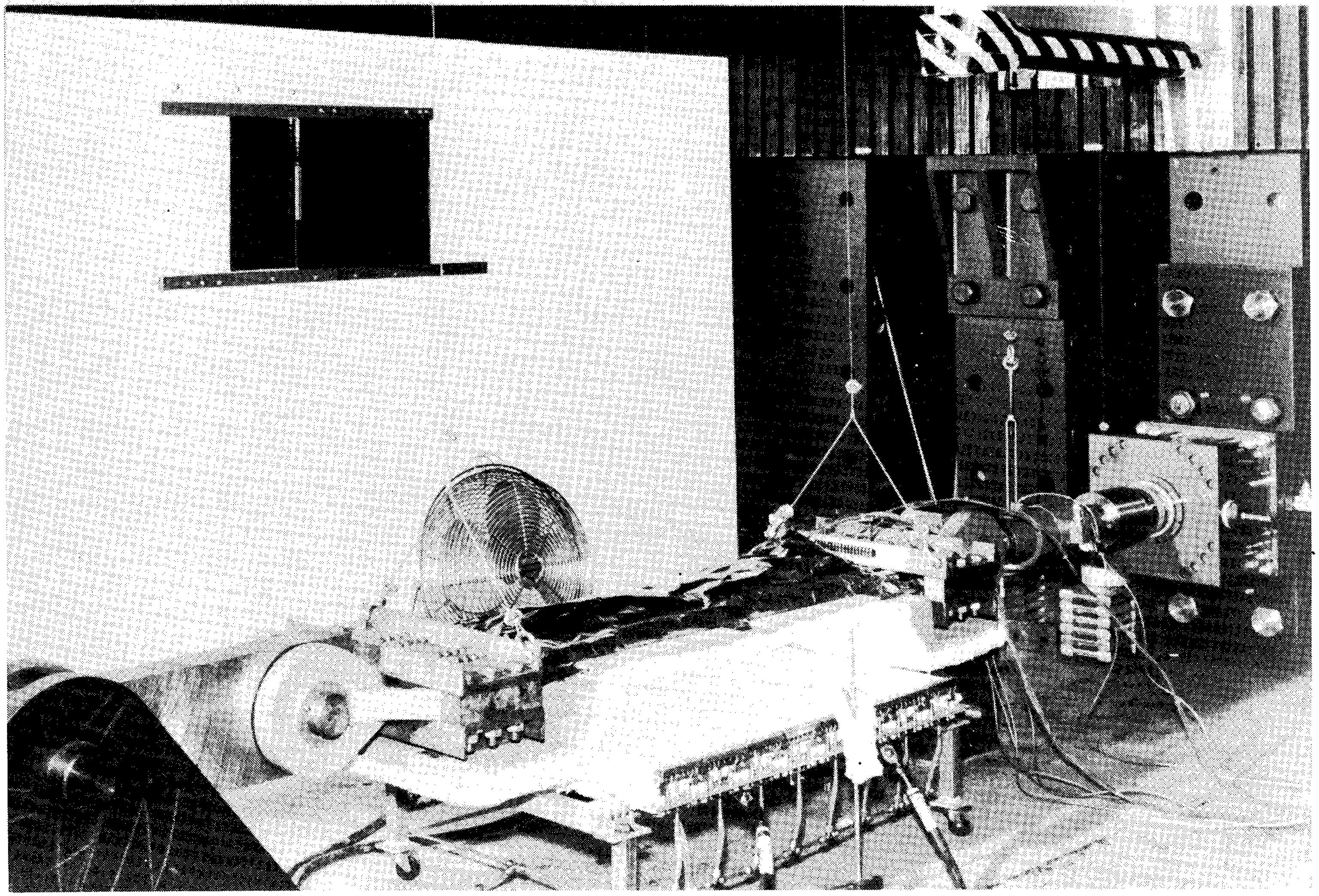

Figure 16

SILICA RSI TEST PANEL

(Figure 17)

The silica thermal test panel designed for the higher temperature region (Area 2) is shown in this photograph. Six-inch-square tiles are bonded with solid RTV 560 to an aluminum simulated primary structure. The grey silicon carbide coating is apparent.

SILICA RSI TEST PANEL

ALUMINUM PRIMARY STRUCTURE
AREA 2 DESIGN

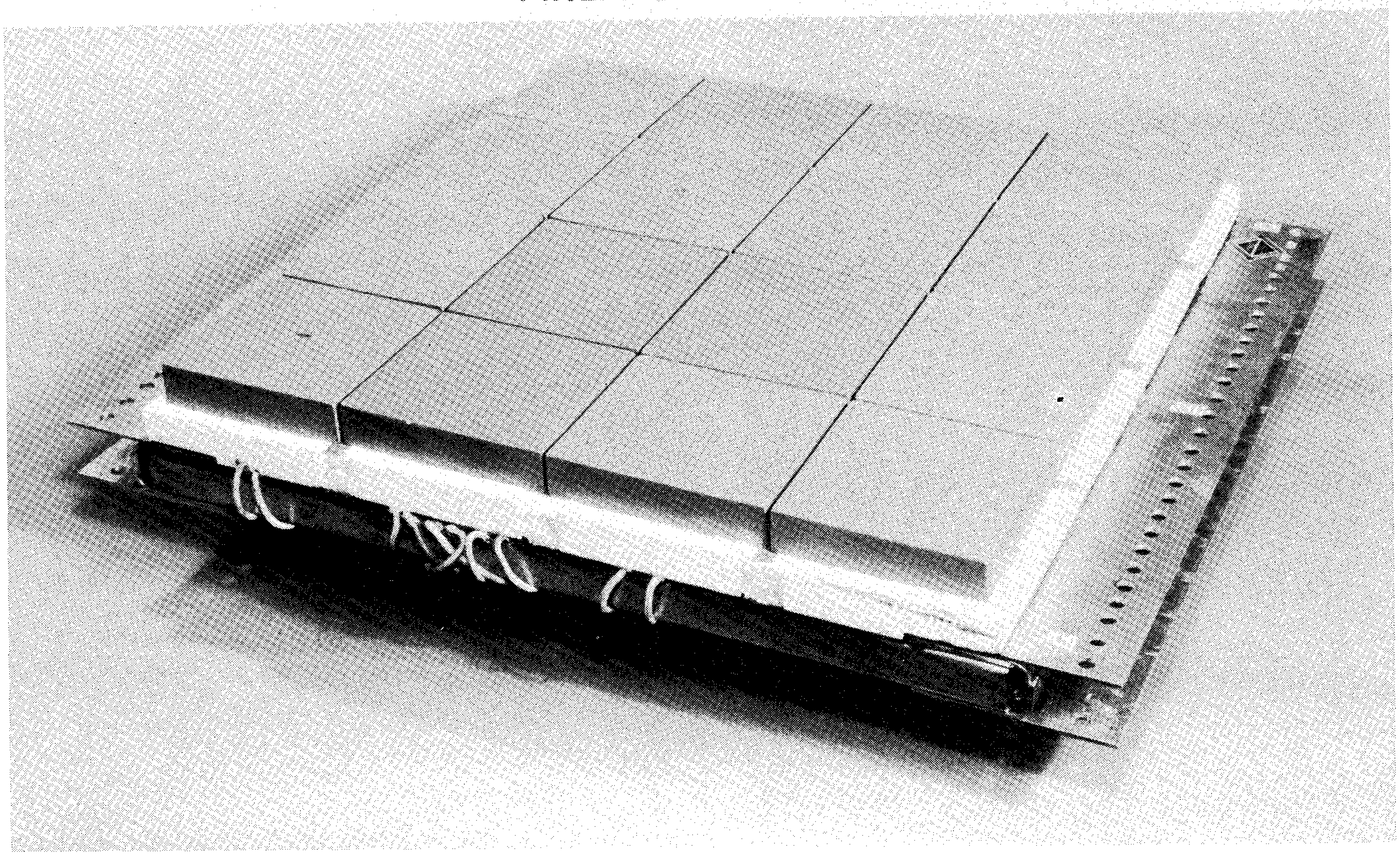

Figure 17

MULLITE RSI TEST PANEL
(Figure 18)

This figure shows a similar mullite test article which incorporates two means of tile attachment. One is direct bonding to primary structure including a thick foam strain isolation pad and the other incorporates fish barbs through bonded metallic screen as in mechanical attachment concept. These panels and others representing Area 1 designs, designs for titanium primary structure, and limited subpanel concepts will be subjected to a series of tests including all mission phases. The test articles are extensively instrumented with thermocouples and strain gages to measure thermal performance and substrate strains.

MULLITE RSI TEST PANEL

ALUMINUM PRIMARY STRUCTURE
AREA 2 DESIGN

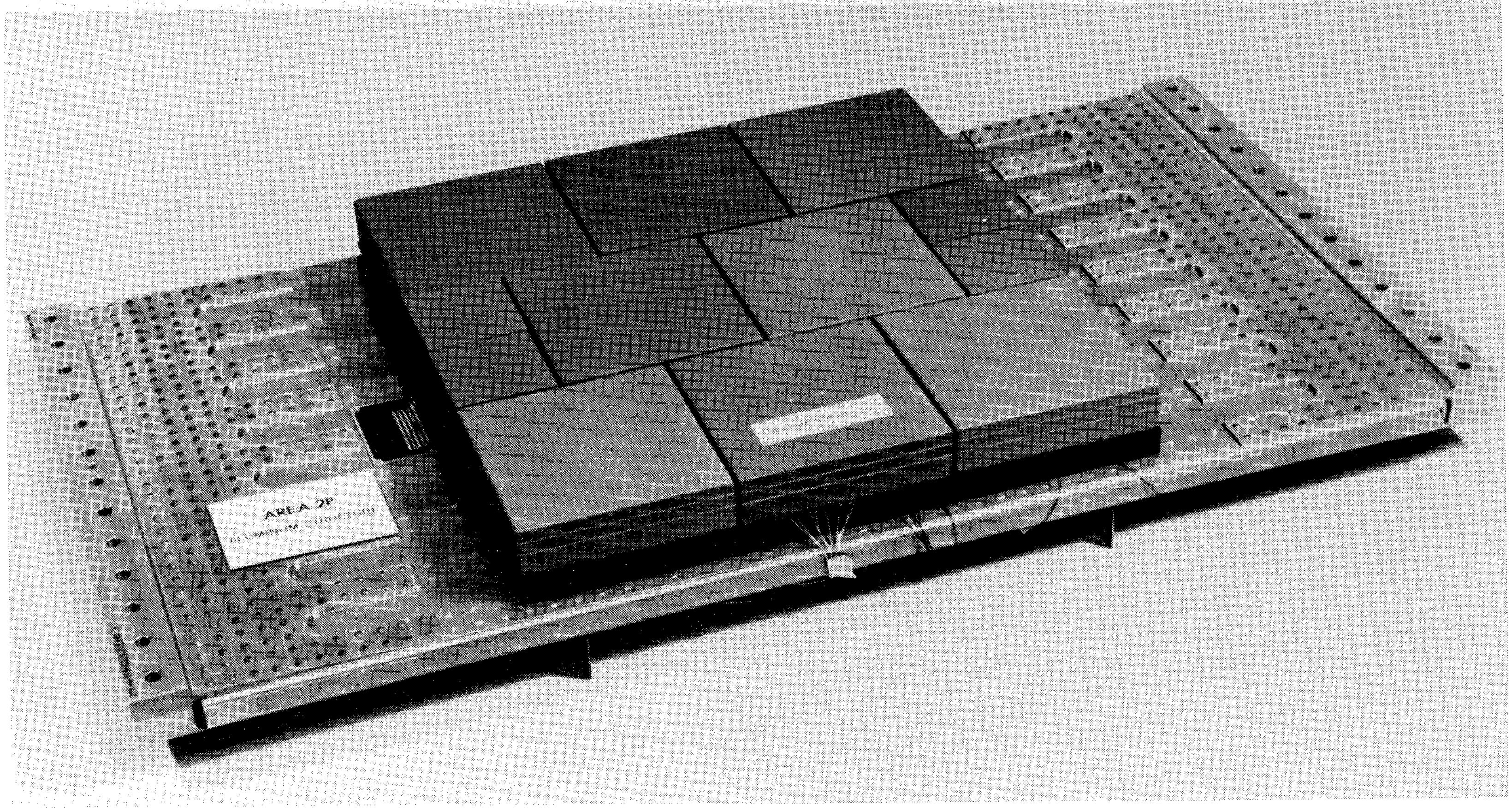

Figure 18

ENVIRONMENTAL EXPOSURE OF SURFACE INSULATION MATERIALS

(Figure 19)

In addition to the system tests, extensive material evaluation test programs are being conducted at various NASA Centers over a wide range of shuttle environmental conditions. Test programs include detailed material morphology, material property characterization and arc-jet thermal evaluation. These test programs have been discussed previously in paper no. 14.

This figure shows a rack at Cape Kennedy near the ocean shore to determine the effects and amount of salt accumulation on and within each of the materials, both coated and uncoated, for various lengths of exposure. The specimens are returned to MSC and subjected to thermal cycles to establish any degradation in thermal stability resulting from material contamination. Initial specimens exposed for one month showed no degradation in properties as a result of these tests.

ENVIRONMENTAL EXPOSURE OF SURFACE INSULATION MATERIALS

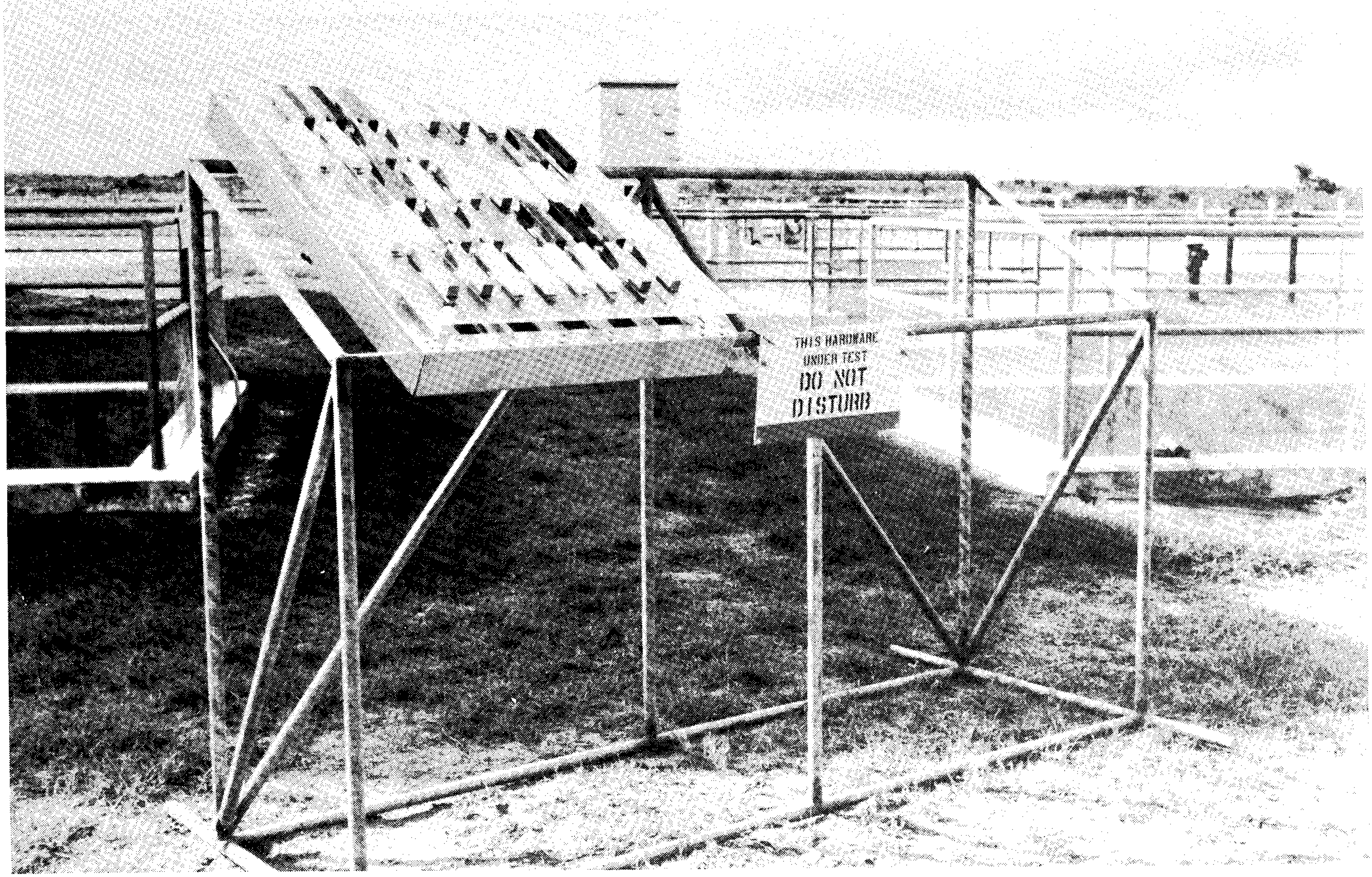

Figure 19

CONCLUDING REMARKS

Over the past two years, reusable surface insulation (RSI) thermal protection systems have been brought from little more than a concept to the point of a viable design option. A detailed understanding of the thermal and structural performance of each system is emerging, and extensive testing of prototype systems and the basic materials is well underway. Although some design aspects, such as attachment cold soak performance and gap design, require intensive evaluation and development, the technology of RSI should be adequately developed this calendar year to support the shuttle program.

ABLATOR MANUFACTURING

By Claud M. Pittman and William D. Brewer
NASA Langley Research Center
Hampton, Virginia

INTRODUCTION

Ablators have been used extensively on flight vehicles and have proven to be efficient and reliable thermal protection systems. However, the cost of ablators has typically been very high and must be reduced substantially if ablators are to be considered for use on space shuttle vehicles. To attack this problem, several low-cost fabrication procedures were developed under contract and large-size heat shields were fabricated by using these low-cost processes (refs. 1 to 5). Cost estimates for large quantities of panels were then derived from the actual fabrication costs obtained. Various techniques for further reducing fabrication costs are being investigated under follow-on contracts (refs. 6 and 7 and work being done by Brunswick Corp. under contract no. NAS1-10864 and by Fansteel Inc. under contract no. NAS1-11004).

As part of the overall low-cost ablator program, studies are being conducted to determine how manufacturing-induced defects affect the performance of ablative heat shields (ref. 8). If commonly occurring defects do not affect material performance, simpler manufacturing techniques can be used, quality control requirements can be relaxed, repair and rework operations can be held to a minimum, and thus the total manufacturing cost can be reduced.

The results, to date, of the low-cost fabrication studies and the defect studies are discussed in this paper.

ORBITER PANEL CURVATURE

(Figure 1)

One of the most important factors influencing panel fabrication costs is the curvature of the panels. As would be expected, flat panels are the least expensive to fabricate, single curvature adds to panel costs, and double curvature adds further cost. Figure 1 shows a typical array of panels on a shuttle vehicle. Flat and single-curvature areas comprise over two-thirds of the total vehicle area. Although most of the wing panels have single curvature, the curvature is very small. Even the single-curvature panels on top of the vehicle have a radius of curvature of at least 2.4 meters. The importance of this discussion is that flat-panel fabrication procedures can probably be used effectively to fabricate curved panels with large radii of curvature.

ORBITER PANEL CURVATURE

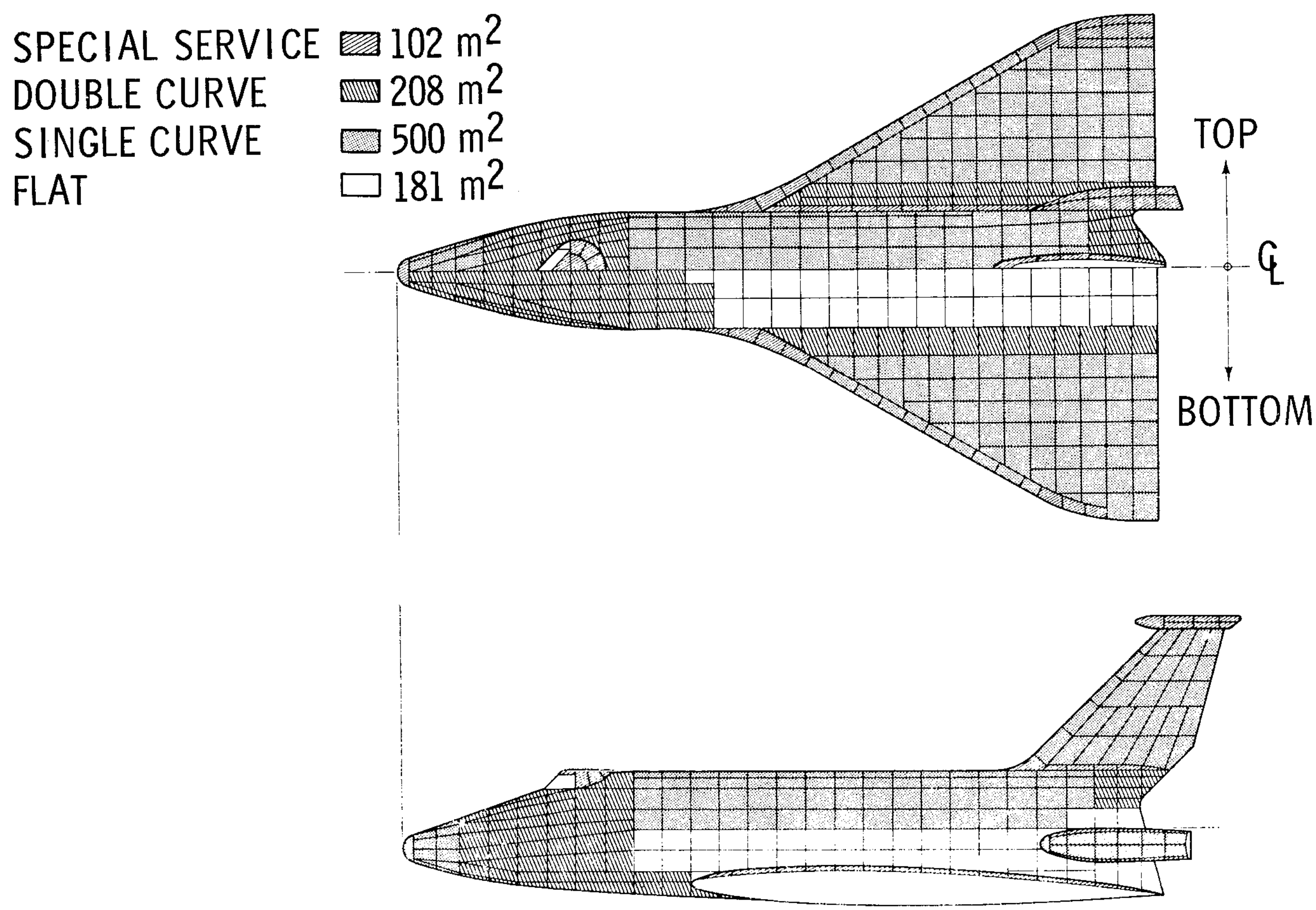

Figure 1

240 kg/m^3 ELASTOMERIC HEAT-SHIELD PANELS

(Figure 2)

Typical panels, made under the initial fabrication contracts, are shown in figure 2. The panels are 0.61 by 1.22 by 0.051 m thick. The curved panel has a radius of 0.61 m. The panels consist of a phenolic-glass honeycomb core bonded to a phenolic-glass facesheet and filled with an elastomeric ablator. The ablator is a representative formulation with handling characteristics similar to more refined compositions. The overall panel density is approximately 240 kg/m^3. In this concept, the panel would be mechanically attached to the vehicle through the holes in the panel and then the plugs would be bonded in the holes.

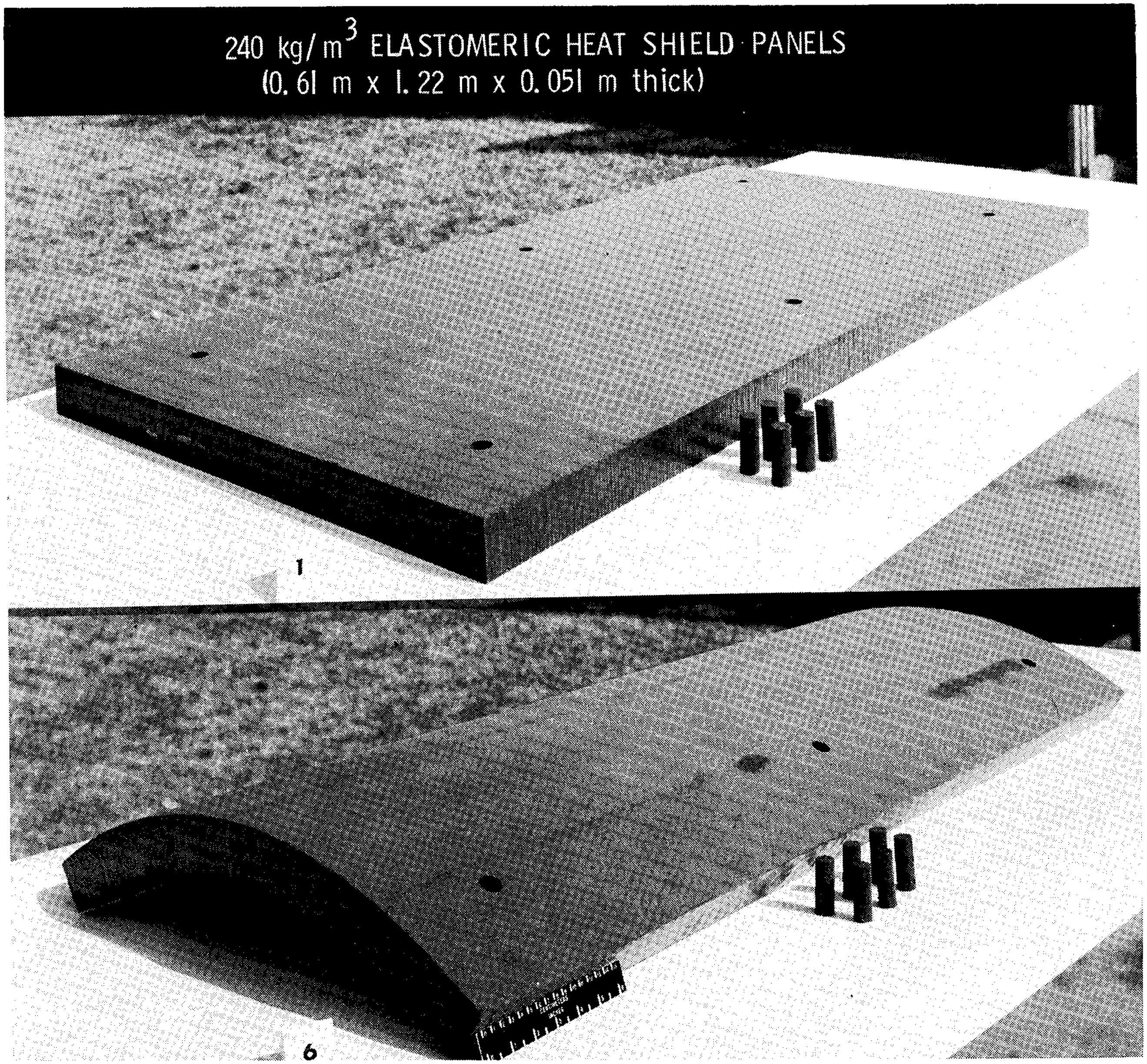
240 kg/m3 ELASTOMERIC HEAT SHIELD PANELS
(0.61 m x 1.22 m x 0.051 m thick)
1
6

Figure 2

PROCESS SUMMARY FOR FABRICATION CONTRACTS

(Figure 3)

A summary of the fabrication processes used to make these panels is shown in figure 3. The methods for making the honeycomb-core/facesheet subassembly, the material used to prime the honeycomb, the extent of ablator precompaction, the method of putting the ablator into the honeycomb, and the curing method are given.

Fabricators A, B, and C prebonded the core to the facesheet. Fabricator A used a porous facesheet and fabricator B drilled small holes in the facesheet beneath each cell. Both of these modifications were incorporated to provide an outlet for air trapped in the cells when the ablator is inserted. Fabricator C made no provisions for this, and his panels showed a higher incidence of voids near the facesheet.

Two fabricators used silicone honeycomb primers and two used phenolic primers. Use of the phenolic primers resulted in a more effective bond between the ablator and the core. Only one fabricator precompacted the ablator before inserting the material into the honeycomb. Methods used for inserting the ablator into the cells included "cookie cutting" the core into the precompacted material, hand troweling with small-area impacting, and hand troweling and autoclaving. In both honeycomb filling and panel curing, vacuum bags were used and the panels were oven cured.

Fabricator D used compression molds and reduced the entire fabrication process to essentially one step. Thus, he used expensive tooling to simplify the fabrication process.

The next two figures contrast the simple tooling used by fabricator A with the expensive molds used by fabricator D.

PROCESS SUMMARY FOR FABRICATION CONTRACTS

FABRICATOR	PREBONDING	HC PRIMER	ABLATOR PRECOMPACT	HC FILLING	PANEL CURING
A	POROUS FACE-SHEET PRE-BONDED TO HC	DC-1203 SILICONE PRIMER	ABLATOR PRECOMPACTED IN PRESS	HC COOKIE CUT INTO ABLATOR	VACUUM BAG; OVEN CURE
B	FACESHEET PREBONDED TO HC AND PERFORATED	DC-1200 SILICONE PRIMER	NONE	HAND TROWEL-ING; SMALL-AREA IMPACT-ING	VACUUM BAG; OVEN CURE
C	FACESHEET PREBONDED TO HC	SC-1008 PHENOLIC RESIN	NONE	HAND TROWEL-ING; AUTO-CLAVE	VACUUM BAG; AUTO-CLAVE (4hr; OVEN (20hr)
D	HC PRIMED WITH BRL-1100 PHENOLIC RESIN FACESHEET BOND, HC FILL, AND PANEL CURE DONE IN ONE-STEP COMPRESSION MOLD PROCESS				

Figure 3

CURVED-PANEL CURE FIXTURE

(Figure 4)

The basic tool used by fabricator A to make the curved panel is shown in figure 4. The tool base was simply a curved aluminum sheet. Rails were used to frame the panel. The curved end rails were made of a flexible silicone material. In the actual fabrication process, the panel frame was placed on a flat surface and the facesheet/core subassembly was filled with ablator. The filled panel was pressed down on the curved surface and cured. After curing, the panel held its curved shape with very little springback. This method is now being tried on double-curvature panels.

CURVED-PANEL CURE FIXTURE

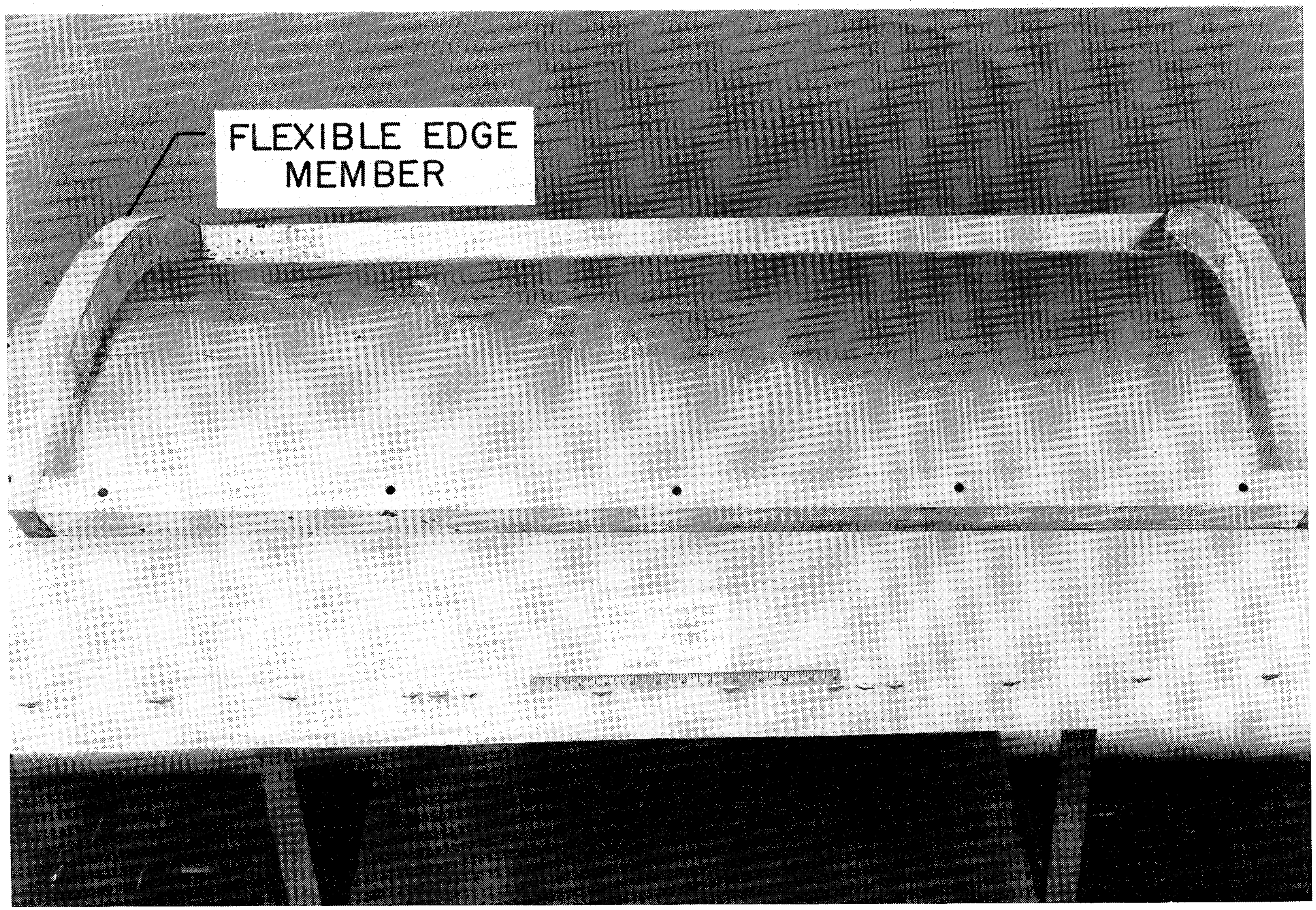

Figure 4

COMPRESSION MOLDING OF CURVED PANEL
(Figure 5)

Figure 5 shows a schematic of the curved-panel compression mold used by fabricator D. Approximately 10 percent of the ablator was screeded into the mold. The honeycomb core was pressed into this material and the remaining ablator was screeded over the honeycomb. The mold was closed to force the material into the cells. The mold was then opened, the B-staged facesheet applied, the mold closed, and the panel cured.

COMPRESSION MOLDING OF CURVED PANEL

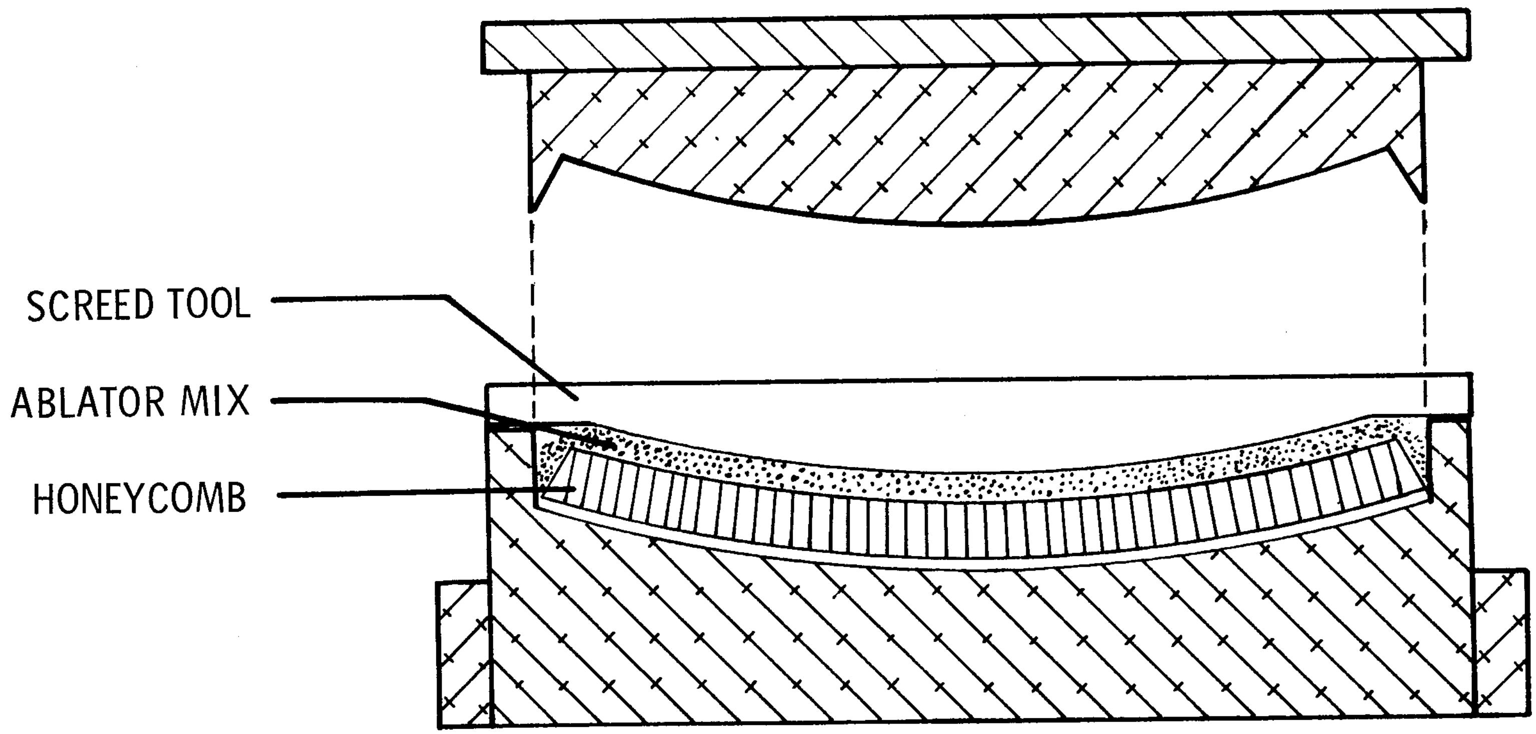

Figure 5

COST AND EFFICIENCY OF ABLATIVE PANELS

(Figure 6)

All fabricators obtained actual fabrication costs for the panels they made. They then used this cost as a basis for estimating costs for various panel lot sizes. A summary of these costs is shown in figure 6. Although panel costs vary significantly, especially for one panel, the percentage cost decrease for larger sized lots is consistent. The third bar, which represents the cost when the compression mold is used, shows a steeper cost reduction than the others. This sharp reduction indicates that the initial mold cost is amortized very rapidly.

Specimens were taken from each of the panels and tested in an arc-jet facility to obtain relative efficiencies of the materials. The results are shown on the right side of the figure. The efficiencies shown are comparable to efficiencies of specimens made with laboratory techniques. The panels made in the compression mold show the highest efficiency. The second best efficiency was obtained by the fabricator who was most familiar with ablative-heat-shield fabrication procedures for flight vehicles. This is reflected in his consistently highest fabrication costs. The efficiency of the least expensive panels is not much lower than that of the most expensive panels, a result which indicates that too much quality assurance in ablative-heat-shield fabrication may not be cost effective. This subject will be discussed later in this paper.

COST AND EFFICIENCY OF ABLATIVE PANELS

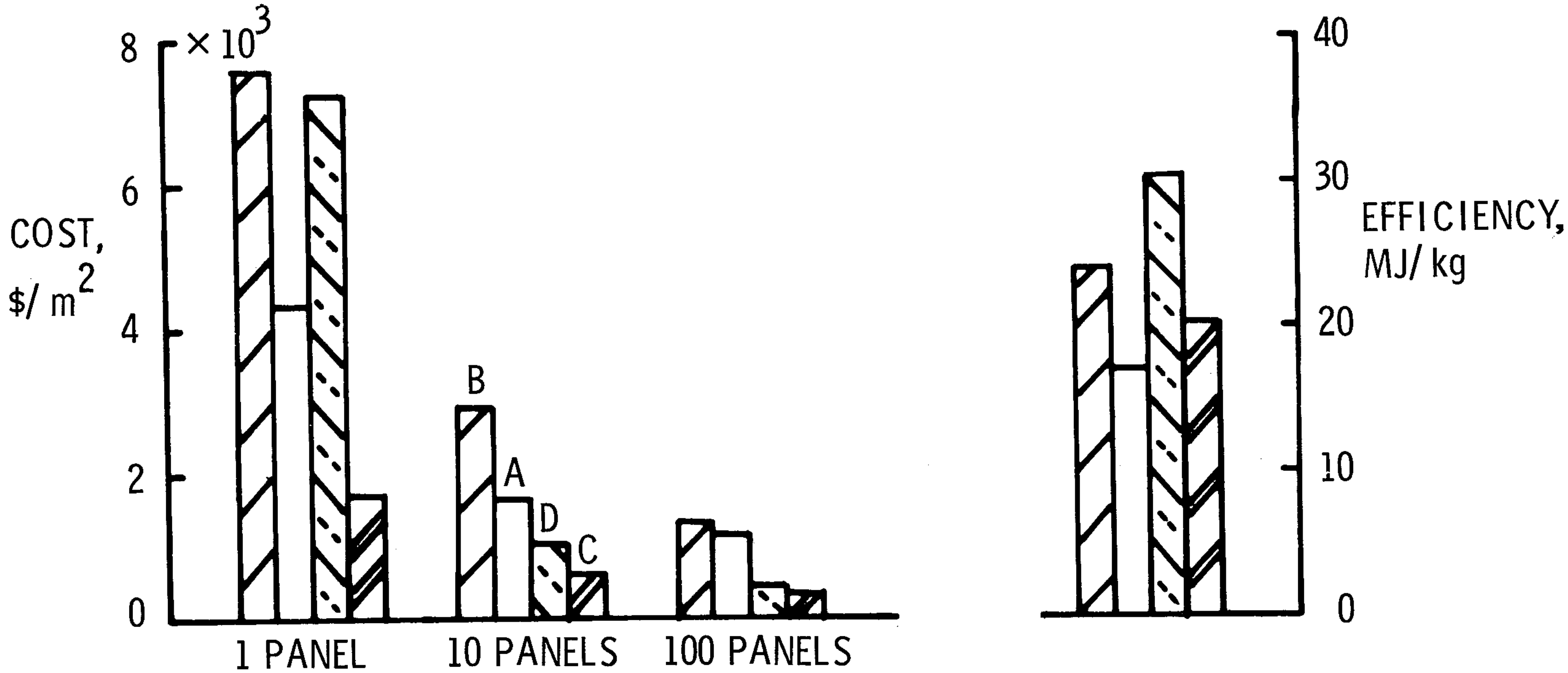

MANUFACTURING COST OF 0.6-m × 1.2-m PANELS

THERMAL EFFICIENCY OF 13-cm × 13-cm SPECIMENS

Figure 6

ABLATIVE-HEAT-SHIELD PANEL COST DISTRIBUTION

(Figure 7)

The four fabricators discussed in the previous figures were awarded follow-on contracts to develop methods which will further reduce fabrication costs and to establish better base lines for large-lot cost estimating. One contractor examined the previous contracts to identify large cost items. A breakdown of panel fabrication costs is shown in figure 7. The shaded area in the figure shows that at least 25 percent of the panel cost is associated with the honeycomb-core reinforcement. One-half of the material costs and more than one-third of the manufacturing costs are directly attributed to the honeycomb.

This contractor has investigated ways to replace the honeycomb with other reinforcing materials without sacrificing heat-shield performance or reliability.

ABLATIVE-HEAT-SHIELD PANEL COST DISTRIBUTION

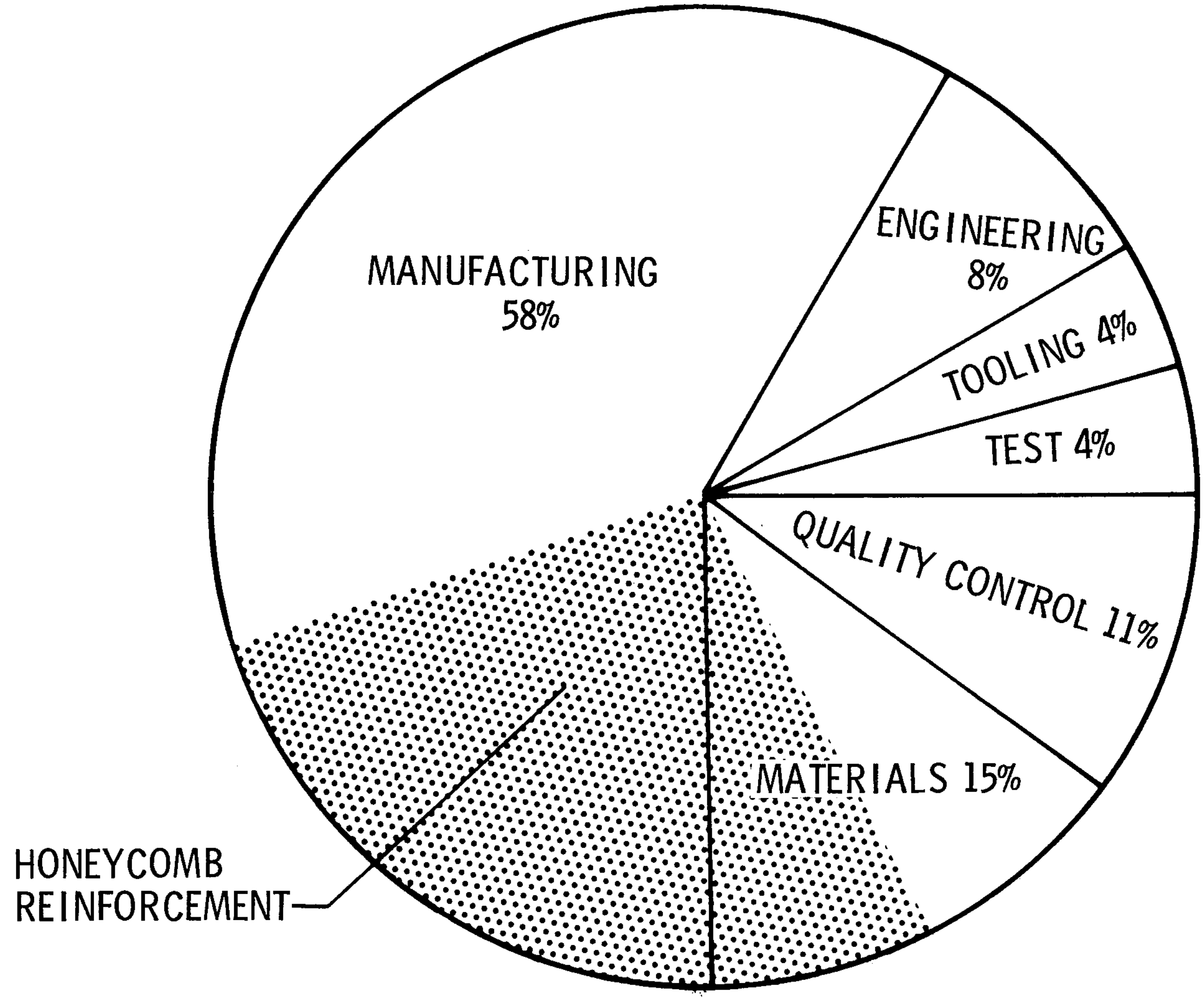

Figure 7

RIBBON REINFORCEMENT

(Figure 8)

One of the most promising reinforcement concepts is shown schematically in figure 8. In this concept, phenolic-glass ribbons are laminated between 1.3-cm-thick strips of ablator. The ablator is reinforced with 10 percent silica fibers to stop crack formation along the ablator strip.

Specimens of this material have been fabricated and tested in arc-jet facilities. Whether the ribbons were parallel or perpendicular to the flow made no discernible difference. The specimens showed good char layer integrity, and thermal performance was unchanged. It is estimated that fabrication costs can be reduced by one-third if this concept is used.

RIBBON REINFORCEMENT

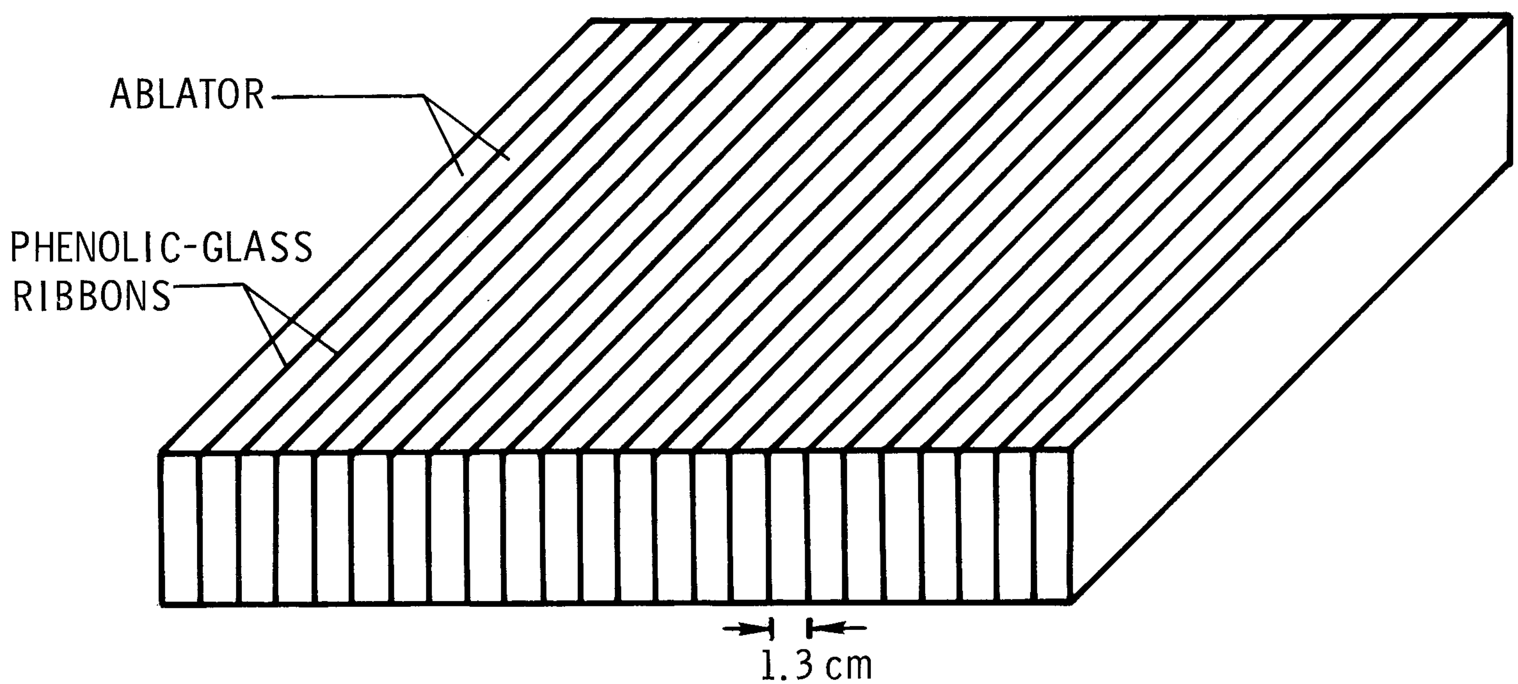

Figure 8

MULTIPLE PANEL BONDING FACESHEET/CORE

(Figure 9)

Another contractor has investigated methods of further reducing the fabrication costs of honeycomb-reinforced panels. He has established a simplified mass-production process for bonding the honeycomb to the facesheet. Figure 9 shows a schematic of the apparatus used. This is a heated, multiple-platen press used for making plywood. The contractor was able to make facesheet/core subassemblies for 12 heat-shield panels in one operation. Each of the six panels shown being made was cut in half to make two heat-shield panels.

MULTIPLE PANEL BONDING FACESHEET/CORE

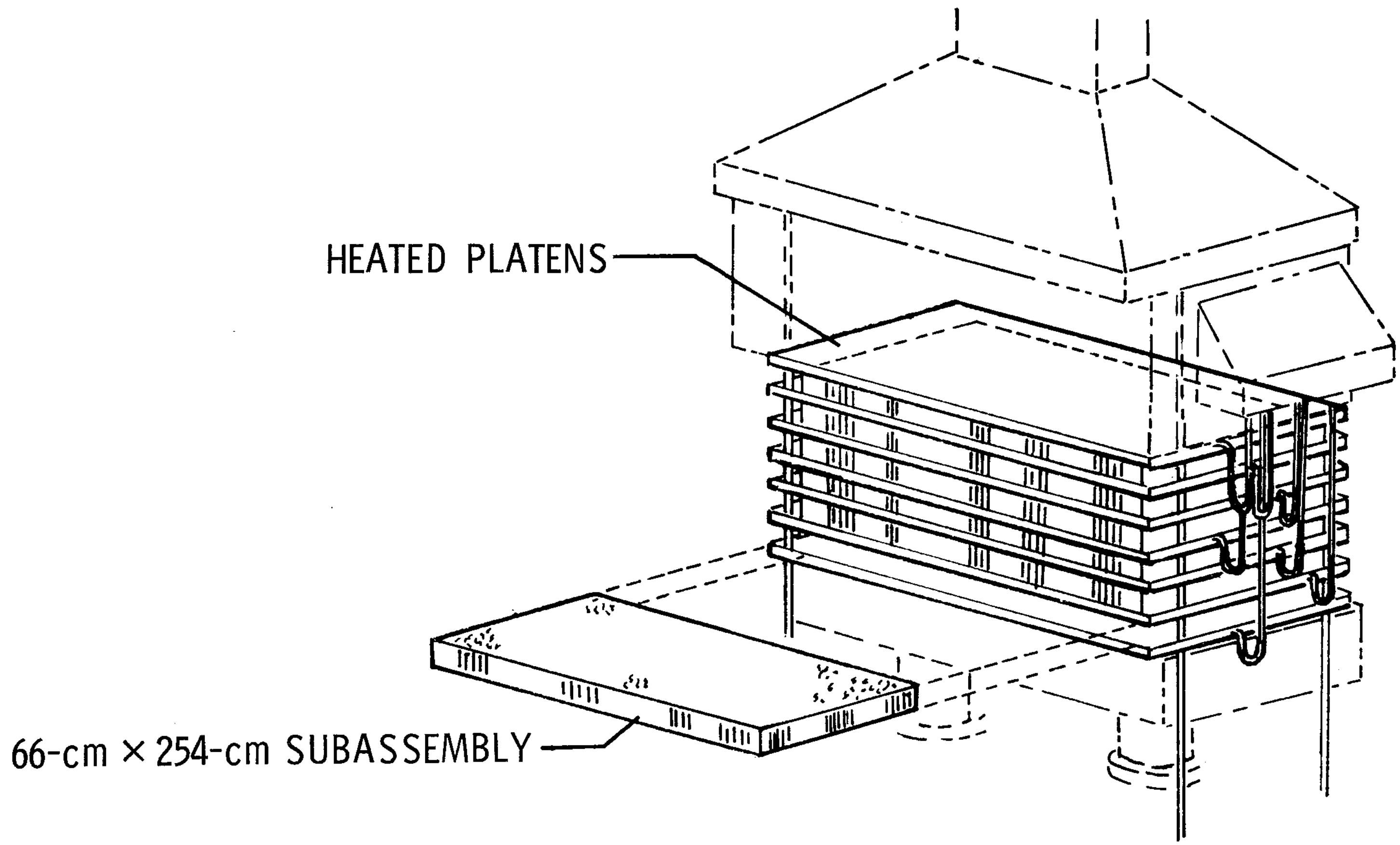

Figure 9

ABLATIVE-PANEL COST REDUCTION

(Figure 10)

Results have been obtained from two of the four follow-on contracts (phase 2). Both of these fabricators were major aerospace contractors. Figure 10 shows a summary of the cost reductions obtained with improved fabrication processes. In 100-panel lots, both contractors show a reduction of about 50 percent in panel costs. Estimates were also made for 1000-panel lots on the follow-on contracts. These costs are probably approaching the point where material costs will inhibit much further cost reduction.

ABLATIVE-PANEL COST REDUCTION

NO. OF PANELS	COST, $\$/m^2$			
	FABRICATOR A		FABRICATOR B	
	PHASE 1	PHASE 2	PHASE 1	PHASE 2
1	4295	3391	7621	6234
100	1152	624	1335	764
1000	---	452	---	484

Figure 10

THE INFLUENCE OF DEFECTS ON PERFORMANCE AND COST

(Figure 11)

As mentioned previously, extensive quality assurance procedures on ablative heat shields may not be cost effective. A contract was established to study the influence of common manufacturing defects on ablative-heat-shield performance and cost. An outline of this study is shown in figure 11. The heat-shield configuration investigated had a honeycomb reinforcement and a facesheet. The defects considered are shown in the left column. The heat-shield properties and cost factors, which could be affected by the defects, are shown in the center. The quantities in the center column would, in turn, affect heat-shield thermal and mechanical performance and cost. The first phase of this study was an investigation of performance in the entry environment. The second phase, which is currently underway, is to investigate the ascent and orbit flight environments.

Specimens, with each of the defects listed, were fabricated and tested in an arc-jet facility. Large voids were the only defect which was found to have a significant effect on material performance in the entry environment.

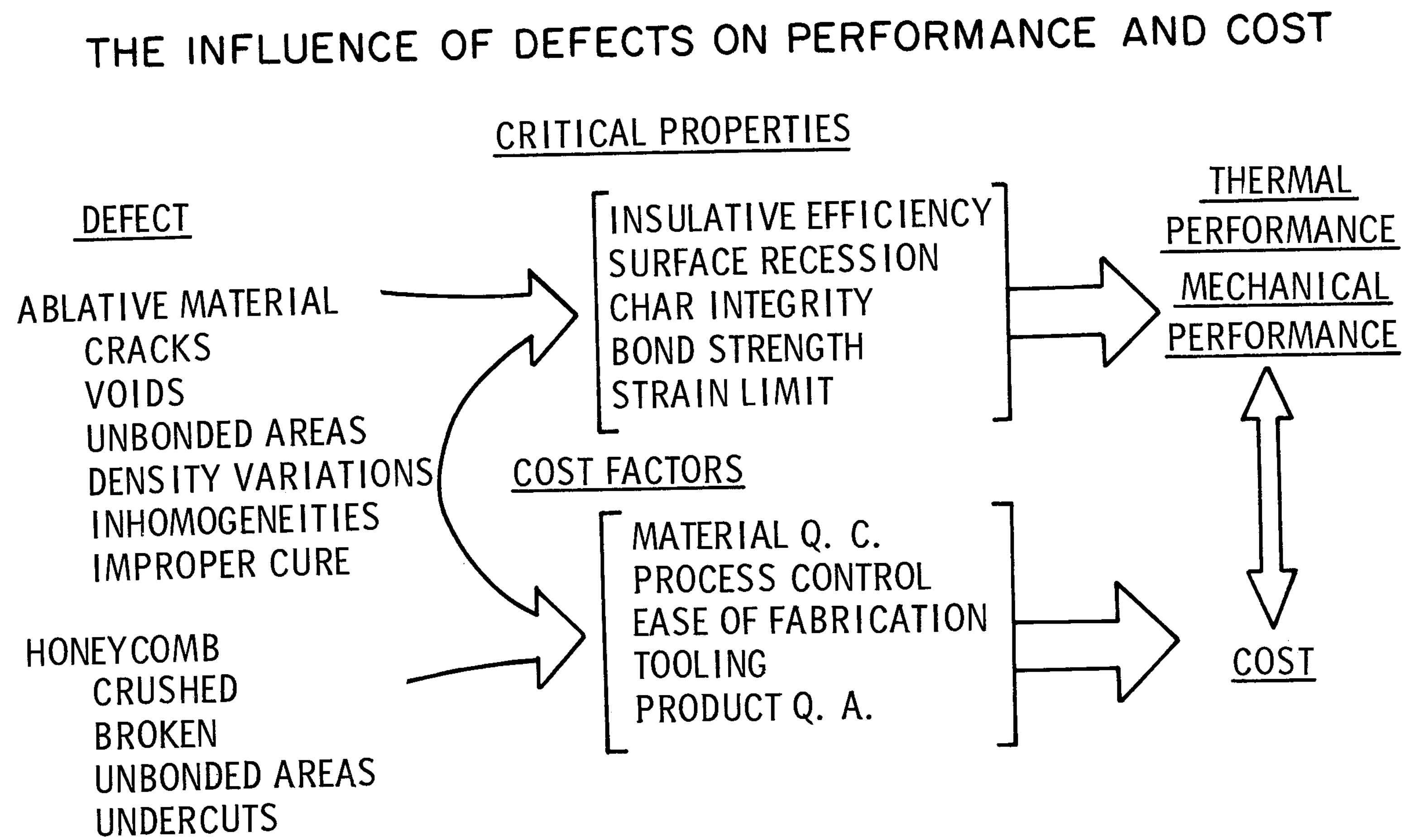
THE INFLUENCE OF DEFECTS ON PERFORMANCE AND COST
CRITICAL PROPERTIES
DEFECT
ABLATIVE MATERIAL
CRACKS
VOIDS
UNBONDED AREAS
DENSITY VARIATIONS
INHOMOGENEITIES
IMPROPER CURE
HONEYCOMB
CRUSHED
BROKEN
UNBONDED AREAS
UNDERCUTS
INSULATIVE EFFICIENCY
SURFACE RECESSION
CHAR INTEGRITY
BOND STRENGTH
STRAIN LIMIT
COST FACTORS
MATERIAL Q. C.
PROCESS CONTROL
EASE OF FABRICATION
TOOLING
PRODUCT Q. A.
THERMAL PERFORMANCE
MECHANICAL PERFORMANCE
COST

Figure 11

EFFECT OF VOIDS ON BACK-SURFACE TEMPERATURE

(Figure 12)

The specimens used to evaluate void effects are shown schematically in figure 12. The back-surface temperature rise for each specimen is given in terms of the reference back-surface temperature rise ΔT_{ref}. The void area was equal to 25 percent of the material thickness and extended more than halfway across each specimen. The top of each specimen was subjected to the heating rate q, and three different void locations were investigated. It was found that the presence of these voids increased the back-surface temperature rise by approximately 50 K and that voids closest to the back surface were more detrimental.

Although the voids shown here did have a significant effect on back-surface temperature rise, the 25 percent void thickness is unrealistically large and it would, obviously, take very little process control to insure that voids of this size did not occur.

EFFECT OF VOIDS ON BACK-SURFACE TEMPERATURE

$q = 0.3\ MW/m^2$

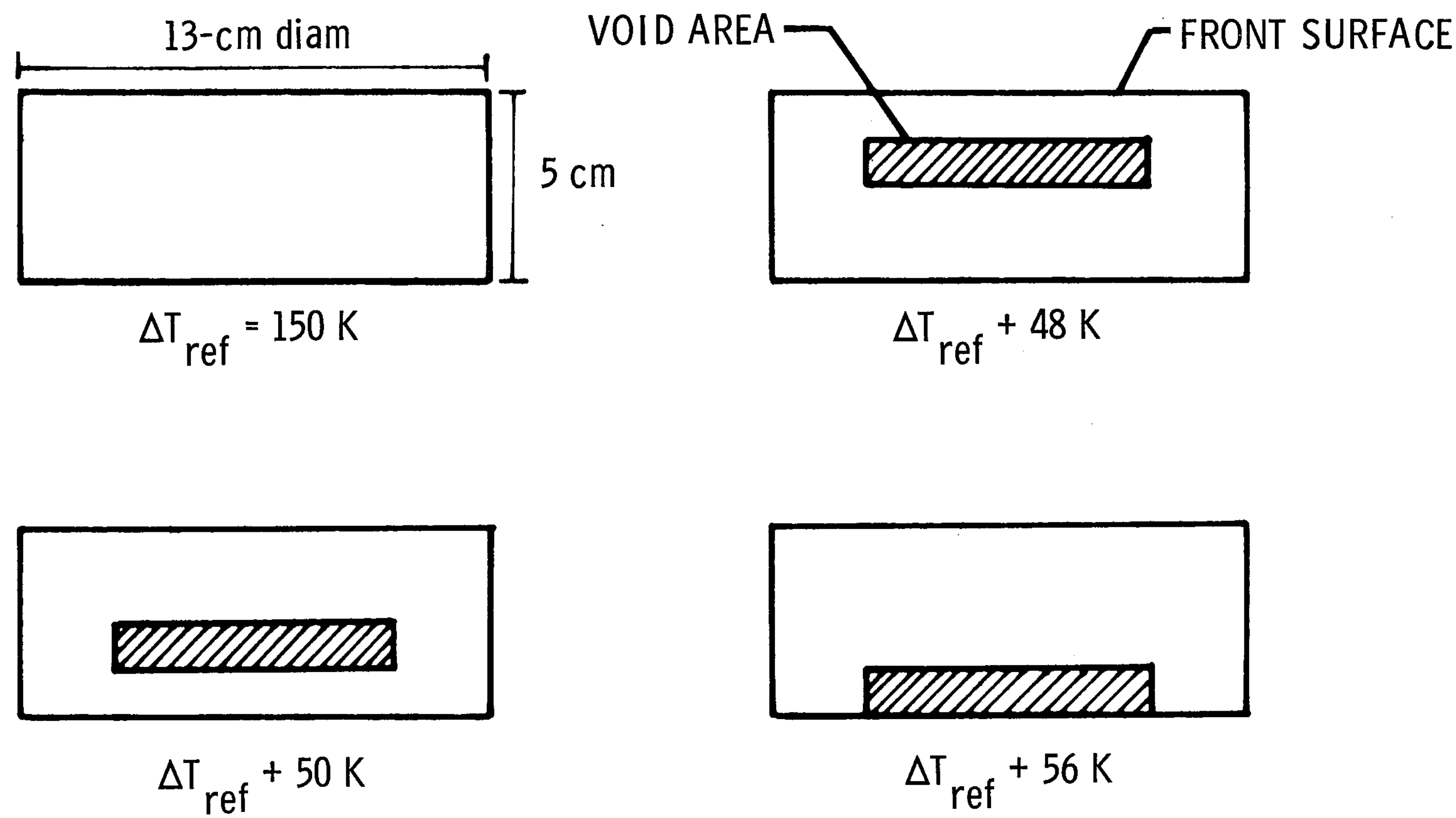

Figure 12

DEFECTED LOW-DENSITY ABLATOR PANEL AFTER TEST

(Figure 13)

One ablator panel (20 by 35 by 5 cm thick) with a number of intentional defects has been subjected to a sequence of environmental tests. A post-test photograph of this panel is shown in figure 13. Besides the defects shown in the figure, the panel also contained crushed core, undercut core, a high-density area, a low-density area, metal inclusions, and facesheet/core disbonds around two of the attachment points beneath the plugs. The through holes stopped at the facesheet. The panel was subjected to acoustic levels of 156 dB for 15 seconds and 159 dB for 50 seconds, a hot vacuum (420 K front surface, 300 K back surface, 10^{-4} N/m^2 for 72 hours), a cold vacuum (170 K front surface and back surface, 6×10^{-4} N/m^2 for 24 hours), and a simulated entry heat pulse in an arc-jet facility. None of the defects had any significant effect on the mechanical or thermal performance of the panel.

DEFECTED LOW-DENSITY ABLATOR PANEL AFTER TEST

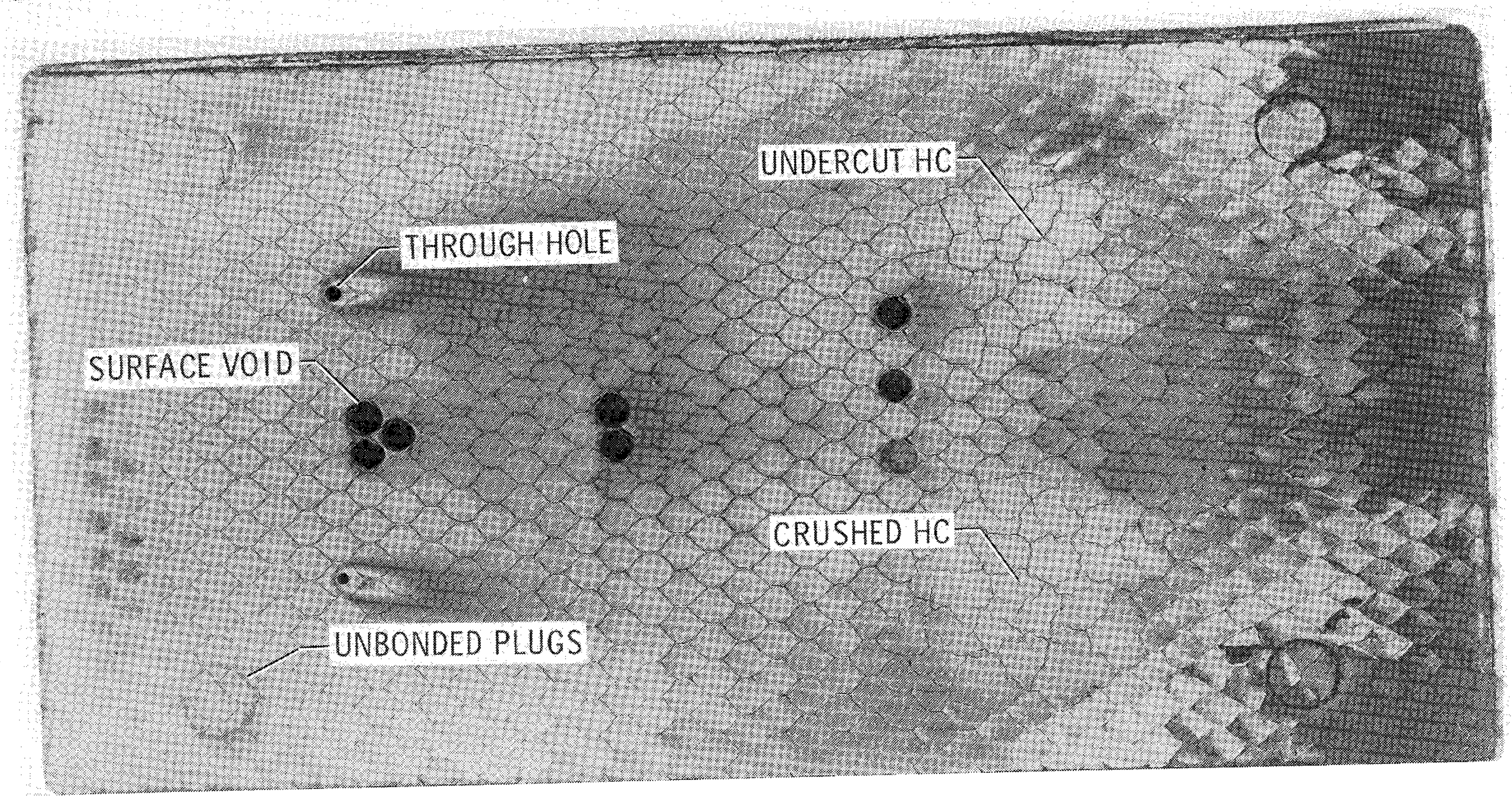

Figure 13

SUMMARY

(Figure 14)

A summary of the most important results of these ablator manufacturing studies is shown in figure 14. Several low-cost ablative-heat-shield fabrication processes have been used successfully. Since a large part of the shuttle thermal protection system (TPS) area is either flat or has a large radius of curvature, flat-panel fabrication processes can be used. An investigation is currently underway to determine whether flat panels can be reformed to curved shapes by using procedures compatible with production processes.

If the honeycomb-core reinforcement can be replaced, a substantial further reduction in fabrication costs can be obtained. Ablative-heat-shield performance is very insensitive to manufacturing defects. Our current estimate is that ablative-heat-shield costs, when flight hardware is actually fabricated, will be less than $1000/m^2$.

SUMMARY

- LOW-COST ABLATIVE-HEAT-SHIELD FABRICATION PROCESSES HAVE BEEN ESTABLISHED
- APPROXIMATELY TWO-THIRDS OF THE SHUTTLE TPS AREA IS EITHER FLAT OR HAS A LARGE-RADIUS SINGLE CURVATURE. THIS CONFIGURATION ALLOWS FLAT-PANEL FABRICATION PROCESSES TO BE USED
- ELIMINATION OF THE HONEYCOMB-CORE REINFORCEMENT COULD REDUCE FABRICATION COSTS BY 30 TO 40 PERCENT
- LOW-COST FABRICATION PROCESSES AND COMMONLY OCCURRING MANUFACTURING DEFECTS DO NOT SIGNIFICANTLY AFFECT MATERIAL PERFORMANCE
- ABLATIVE-HEAT-SHIELD COSTS FOR ACTUAL FLIGHT VEHICLES SHOULD AVERAGE LESS THAN $1000/ m^2

Figure 14

REFERENCES

1. Production Engineering and Development Department: Final Report on Low-Cost Ablative Heat Shield for Space Shuttles. SD 70-400 (Contract NAS 1-9943), North American Rockwell, Nov. 20, 1970. (Available as NASA CR-111795.)
2. Chandler, Huel H.: Low-Cost Ablative Heat Shields for Space Shuttles. Contract No. NAS1-9946, Martin Marietta Corp., [1970]. (Available as NASA CR-111800.)
3. Dulak, R. E.; and Cecka, A. M.: Low Cost Ablative Heat Shields for Space Shuttles. Contract No. NAS 1-9947, Fansteel Inc. – Reflective Laminates Division, 1970. (Available as NASA CR-111814.)
4. Abbott, Harry T.: Low-Cost Fabrication Method for Ablative Heat Shield Panels for Space Shuttles. Contract No. NAS1-9945, Brunswick Corp., [1970]. (Available as NASA CR-111835.)
5. Freeder, Herman; and Smith, Wilson N.: Final Report on Low Cost Ablative Heat Shields for Space Shuttles. Contract No. NAS 1-9944, Aerospace & Defense Products, B. F. Goodrich Co., [1970]. (Available as NASA CR-111874.)
6. Norwood, L. B.: Final Report on Study of Low-Cost Fabrication of Ablative Heat Shields. SD 72-SH-0005 (Contract NAS1-10708), North American Rockwell, Mar. 31, 1972. (Available as NASA CR-112036.)
7. Chandler, Huel H.: Investigation of Low-Cost Ablative Heat Shield Fabrication for Space Shuttles. Contract No. NAS1-10793, Martin Marietta Corp., 1972. (Available as NASA CR-112045.)
8. Thompson, R. L.; Rummel, W. D.; and Driver, W. E.: Study of Critical Defects in Ablative Heat Shield Systems for the Space Shuttle. NASA CR-2010, 1972.

MATERIALS AND DESIGN FOR ABLATIVE HEAT SHIELDS

By Marvin B. Dow and Stephen S. Tompkins
NASA Langley Research Center, Hampton, Virginia,
and Frank Coe
NASA Manned Spacecraft Center, Houston, Texas

17

INTRODUCTION

Since its beginning the space-shuttle technology program has included a program for ablative thermal protection systems (TPS). The goal of the ablation technology program is to bring ablation research and development to a high state of readiness for application to space shuttle vehicles. This paper reports some recent results and current work in the areas of materials, designs, and refurbishment for ablative TPS. Future research and development needs are also presented.

SYMBOLS

E	effectiveness parameter
$\bar{E}$	normalized effectiveness
H_e	total enthalpy at edge of boundary layer
$\vec{L}$	lift
p_t	total pressure
Q_t	total heat input
q	convective heat-transfer rate
ΔT	change in temperature
t	thickness
$\vec{V}$	velocity
ΔV	change in velocity
α	angle of attack
ρ	density
τ	time

SPACE-SHUTTLE ABLATIVE-HEAT-SHIELD TECHNOLOGY

Figure 1 shows that the ablation technology program is able to draw upon an extensive background of technology and flight experience while focusing on three major areas: materials, design, and refurbishment.

For space shuttle applications, minor modifications to ablation materials may be desirable in order to "tune the technology," but a major materials development program is not required. The available materials must, however, be subjected to screening tests, and the best materials must be selected. Finally, complete thermal and physical characterization of the selected materials must be performed.

To accomplish the required thermal protection with the selected materials, practical designs must be developed and evaluated. These designs must consider materials application (that is, how the characteristics of materials can be best utilized to meet the vehicle requirements), attachment methods, and seals and joints.

Ablative heat shields on a multimission vehicle will require extensive refurbishment. Data which can be used to assess the cost and techniques required for refurbishment must be available as input to the design process.

SPACE-SHUTTLE ABLATIVE-HEAT-SHIELD TECHNOLOGY

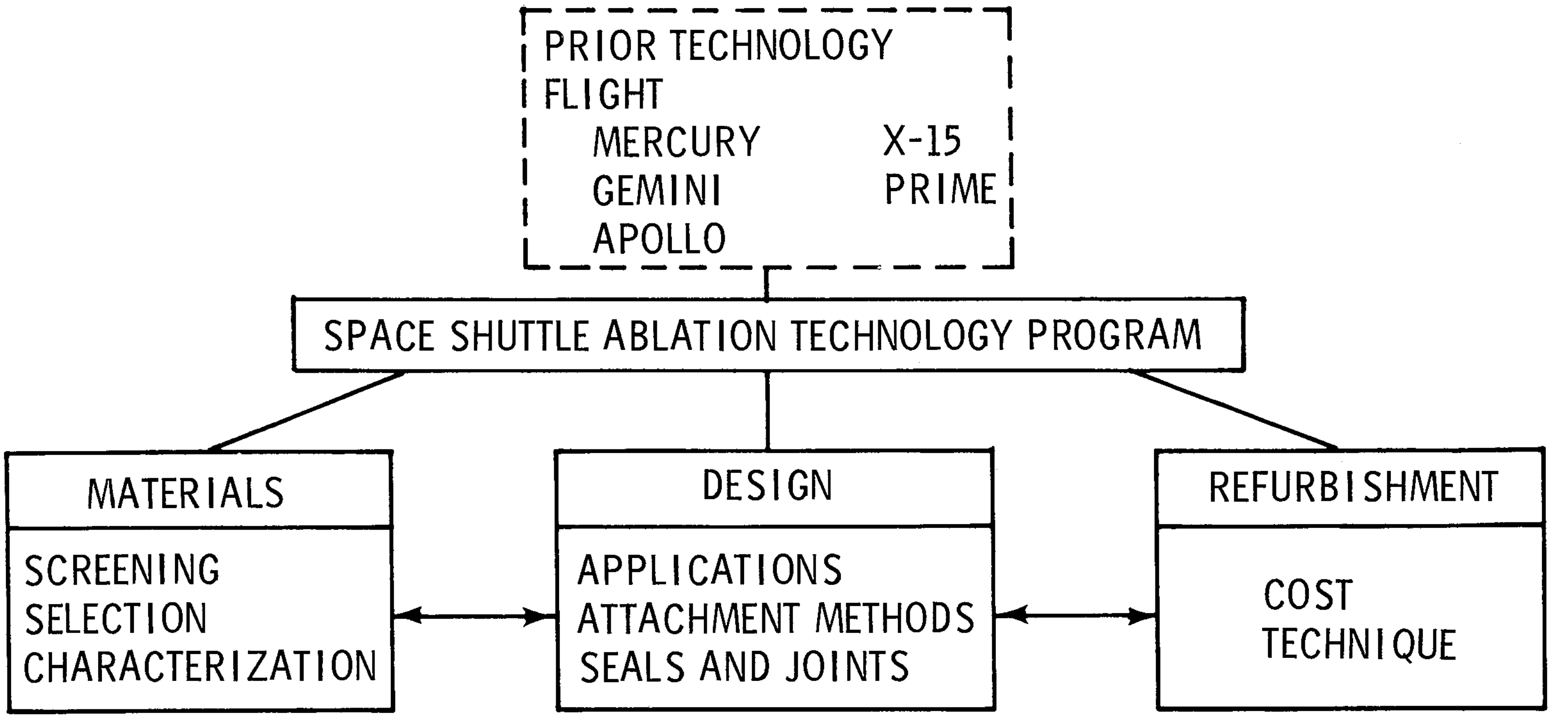

Figure 1

CANDIDATE ABLATORS FOR THE SPACE SHUTTLE ORBITER

Figure 2 is a partial listing of ablation materials which are candidates for screening tests to select materials for space shuttle applications. This figure shows that there are many available materials from which to make selections. Figure 2 is not intended to imply that these are the only materials which should be considered. Except for NASA SS-41, the composition of which is given in reference 1, the listed materials are proprietary.

The materials in figure 2 are grouped to show the orbiter region for which each material is probably most applicable. The leading-edge materials have roughly twice the density of the surface-area materials.

All the listed materials are included in screening tests being performed at various NASA centers.

CANDIDATE ABLATORS FOR THE SPACE SHUTTLE ORBITER

VEHICLE REGION	CANDIDATE ABLATORS
NOSECAP AND LEADING EDGES	MM ESA-5500 MM ESA-3560 AVCOAT 5026-39 AVCO MOD-7
SURFACES OF WINGS AND FUSELAGE	NASA SS-41 MM SLA-561 AVCO 480 SERIES MDAC ULD 100 SERIES GE FSA 1040 ULTRA-LOW-DENSITY FOAMS (LEEWARD SURFACES) GDC LOW-DENSITY ELASTOMERS

Figure 2

SPECIMEN HOLDERS AND TEST ENVIRONMENTS

The specimen holders and test environments used in material tests at two NASA centers are shown in figure 3. The specimen holders are both water-cooled metal wedges which expose ablator specimens to the hot gas stream produced by electric-arc heaters. The test environments used at the two NASA centers are similar, and both provide good simulation of the heating rate and enthalpy associated with an actual orbiter entry. The test pressures are, however, lower than the predicted pressure for an actual entry.

At one NASA center materials are evaluated on the basis of an effectiveness parameter E, which is a function of heat input and unit area mass. This parameter provides a measure of overall ablative performance, and its determination requires a minimum amount of specimen instrumentation since only the specimen back-surface temperature is measured. At the other NASA center the material specimens are instrumented with internal thermocouples, and the materials are evaluated on the basis of data obtained during exposure to a prescribed total heat input. In addition, other aspects of thermal performance can be investigated by using the data provided by more extensive instrumentation.

SPECIMEN HOLDERS AND TEST ENVIRONMENTS

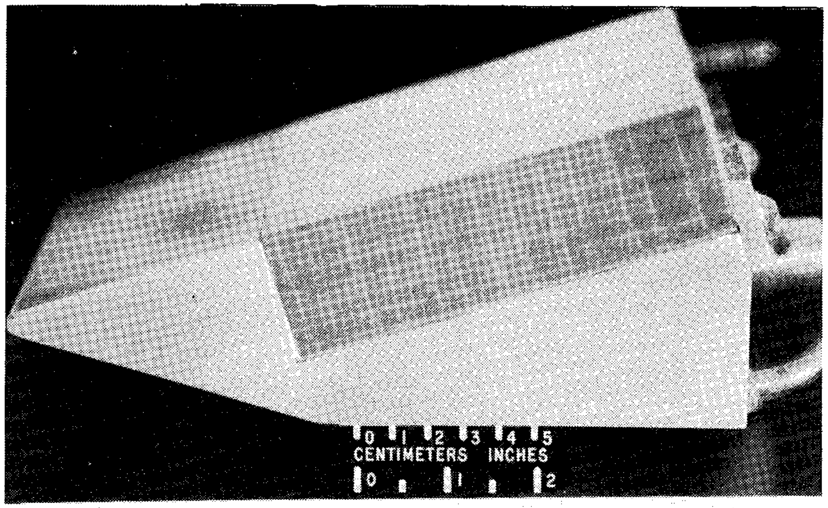

NOMINAL TEST ENVIRONMENT
AT PANEL MIDPOINT

α, rad	0.314
q, MW/m^2	0.11 AND 0.18
H_e, MJ/kgm	14 AND 23
p_t, atm	0.004 TO 0.005
TEST STREAM	SIMULATED AIR

$\left(\text{ABLATIVE EFFECTIVENESS PARAMETER, } E = \frac{q\tau}{\rho t}\right)$

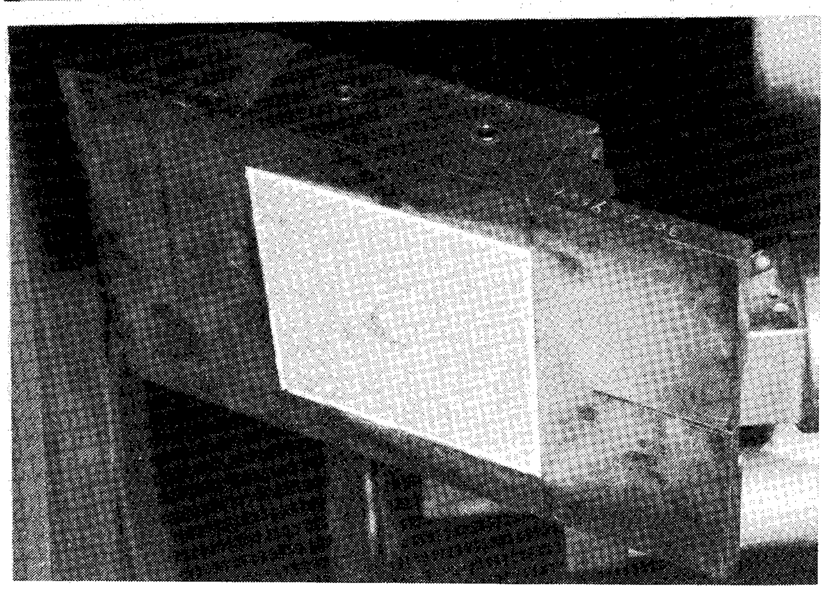

α, rad	0.262 TO 0.524
q, MW/m^2	0.07 TO 0.25
H_e, MJ/kgm	7 TO 23
p_t, atm	0.003 TO 0.005
TEST STREAM	SIMULATED AIR

(TOTAL HEAT INPUT, 12 MJ/m^2)

Figure 3

ABLATION PERFORMANCE DATA FOR CANDIDATE MATERIALS

Ablative performance data are shown in figure 4 for four ablation materials which were exposed to the given test conditions. For presenting these data, the density and the thermal effectiveness E of each material have been normalized with respect to the NASA SS-41 material.

A comparison of the normalized effectiveness $\bar{E}$ shows that for these test conditions, the two materials with a high volatile fraction had a higher thermal effectiveness than the two materials with a low volatile fraction. These results were expected because it has long been known that the production of gas, which blocks convective heating, is an important ablative heat protection mechanism, particularly at high enthalpy levels.

Posttest observations about the heated surface of each specimen are shown in the remarks column. It is noted that the SS-41 material was the only material which had honeycomb reinforcement.

ABLATION PERFORMANCE DATA FOR CANDIDATE MATERIALS

13×13-cm PANEL TEST RESULTS; $q \approx 0.170$ MW/m^2; $H_e \approx 23$ MJ/kgm;

$p_t = 0.005$ atm; SIMULATED-AIR TEST STREAM

ABLATOR	RELATIVE DENSITY	$\bar{E}$	REMARKS
NASA SS-41	1.00	1.00	SMOOTH, TOUGH CHAR SURFACE (MATERIAL IN HONEYCOMB)
MM SLA-561	0.93	0.88	SMOOTH, TOUGH CHAR SURFACE
AVCO 480-1M	1.00	0.58	SURFACE CRACKS; TOUGH CHAR SURFACE
MDAC ULD 100-4	1.28	0.45	ROUGH SURFACE; EXTREMELY TOUGH CHAR LAYER

Figure 4

RIBBON-REINFORCED ABLATOR

The ablator manufacturing studies reported in references 1 to 5 show that the use of honeycomb reinforcement is a major contributor to ablator manufacturing costs. Therefore, large manufacturing cost reductions might be achieved by the elimination of honeycomb; however, the resulting ablation materials must demonstrate good thermal performance, char-layer integrity, and handling qualities. Figure 5 shows a material which demonstrates the required characteristics without honeycomb reinforcement. Except for the addition of fibers, this material is the SS-41 material with a novel fiberglass-ribbon reinforcement. The details of this material are discussed in paper no. 16 by Claud M. Pittman and William D. Brewer.

The upper photograph in figure 5 shows the posttest appearance of the ribbon-reinforced SS-41 material without fibers. This photograph shows the char-layer cracking and separation, which has led to the widespread use of honeycomb reinforcement to achieve char-layer integrity. The lower photograph shows the marked improvement in char-layer integrity which is achieved by adding 10 percent by weight of fibers to the SS-41 formulation. This material has no char-layer cracking, and the char layer is firmly attached to the uncharred material. Furthermore, tests of the ribbon-reinforced SS-41 with fibers demonstrated a thermal effectiveness equal to the best materials.

RIBBON-REINFORCED ABLATOR

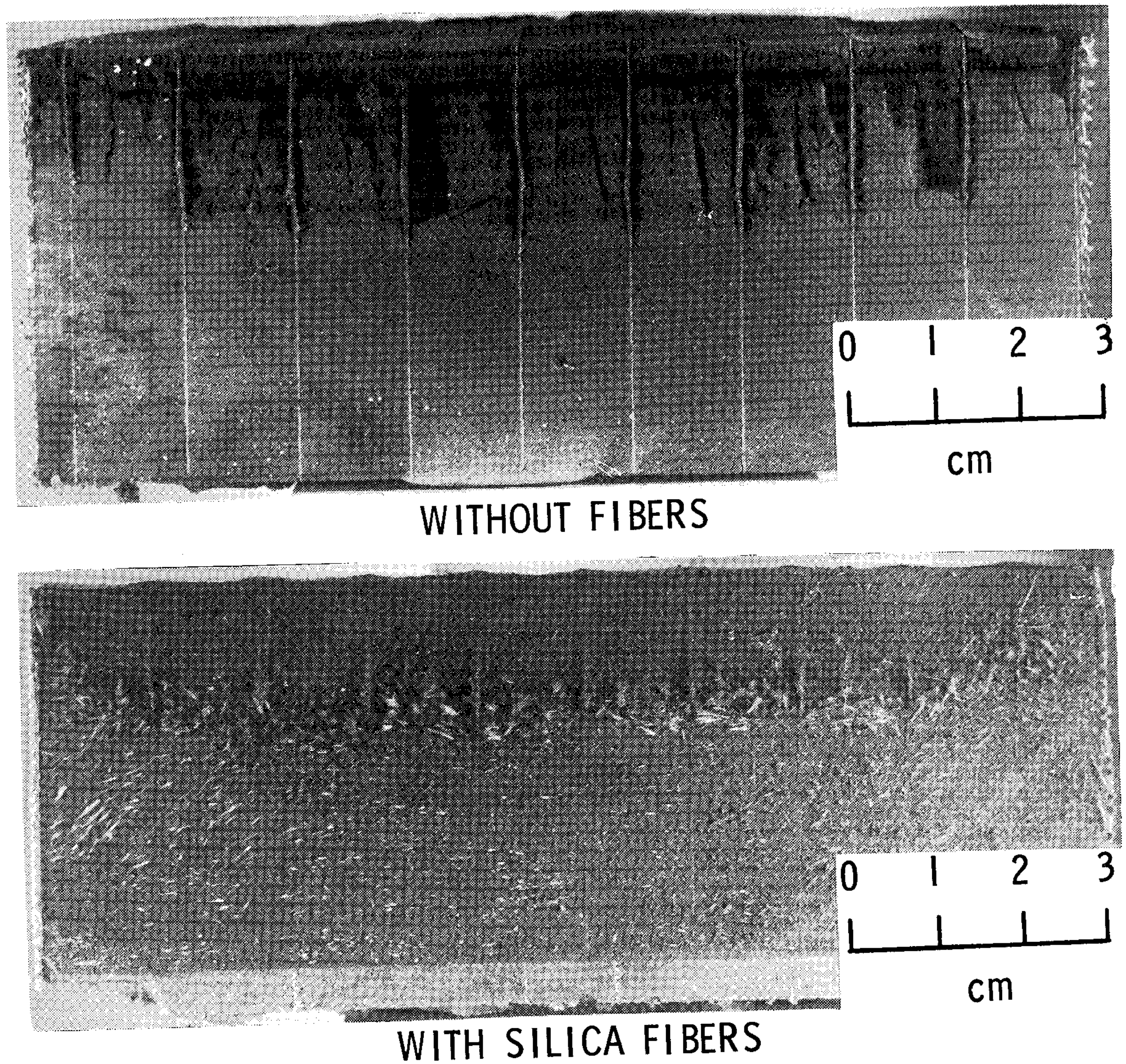

Figure 5

ABLATIVE-LEADING-EDGE RESEARCH

The development and evaluation of TPS designs are goals of the space-shuttle ablation technology program. Ablation materials are viable candidates for application to orbiter leading edges and offer a means to solve that particular TPS design problem. Figure 6 shows the objective and the approaches to be followed in a technology contract to perform ablative-leading-edge research. A contract (NAS1-11416) to perform this research was recently let, and the work is now underway.

ABLATIVE-LEADING-EDGE RESEARCH

OBJECTIVE

DESIGN AND DEMONSTRATE AN ABLATIVE LEADING EDGE FOR AN ORBITER

APPROACH

- DEFINE ENVIRONMENT
- CHOOSE ABLATION MATERIAL
- DESIGN LEADING EDGE
- FABRICATE LEADING-EDGE MODELS
- PERFORM THERMOMECHANICAL TESTS
- STUDY EFFECTS OF SHAPE CHANGE AND ROUGHNESS ON AERODYNAMIC PERFORMANCE
- ESTIMATE DDT & E AND OPERATIONAL COSTS

Figure 6

ABLATIVE-HEAT-SHIELD DESIGN STUDIES

In addition to ablative-leading-edge design, there is a need to develop ablative-heat-shield designs that apply to the major surface areas of the orbiter. Figure 7 shows the objective and a combination of the approaches to be followed in several related heat-shield design studies. This work, to be performed under contracts, will begin shortly.

These design studies will provide valuable information relative to the efficient application of ablative TPS to the space shuttle orbiter. Thermal-control and moisture-proof coatings are design items which will be considered in these studies. However, coatings have received little attention thus far, and therefore, additional study of coating requirements and designs may be needed.

ABLATIVE-HEAT-SHIELD DESIGN STUDIES

OBJECTIVE

DEVELOP OPTIMIZED ABLATIVE HEAT SHIELDS FOR AN ORBITER

APPROACH

- DEFINE ENVIRONMENT AND OPTIMIZE ENTRY TRAJECTORY
- DEMONSTRATE LOW-COST MANUFACTURING AND REFURBISHMENT TECHNIQUES
- DESIGN HEAT SHIELDS FOR SEVERAL VEHICLE LOCATIONS
- VERIFY DESIGNS THROUGH TESTS
- CALCULATE WEIGHT AND WEIGHT DISTRIBUTION
- ESTIMATE MANUFACTURING AND OPERATIONAL COSTS

Figure 7

EFFECTS OF ROLL ANGLE ON ENTRY HEATING

The heat-shield design studies require the contractors to define the entry heating environment and to examine optimized entry trajectories. Figure 8 presents the results of an entry trajectory optimization study performed at a NASA center. The results from previous studies had shown that for a given cross range, substantial reductions in heat input and ablative TPS weight could be achieved by increasing the deorbit ΔV. However, these studies also showed that the TPS weight savings did not compensate for the additional deorbit fuel required to increase the deorbit ΔV. Therefore, the present study was restricted to a low value of deorbit ΔV, but reductions in total heat input were achieved by beginning the entry with the orbiter inverted.

The sketch shows that the inverted entry involves an initial roll about the velocity vector and that the orbiter windward and leeward surfaces maintain their relative positions. The orbiter lift is utilized to increase the entry angle during the inverted entry.

The curves in figure 8 show, for three cross ranges, the reduction in total heating which was obtained by an inverted entry. For each cross range, the entries are made at a constant angle of attack.

These results indicate that a reduction in total heating and therefore a reduction in ablative TPS weight might be achieved by inverted entry. However, a more comprehensive optimization analysis, which considers such items as the orbiter guidance and control capabilities, is needed to obtain definitive information.

EFFECTS OF ROLL ANGLE ON ENTRY HEATING

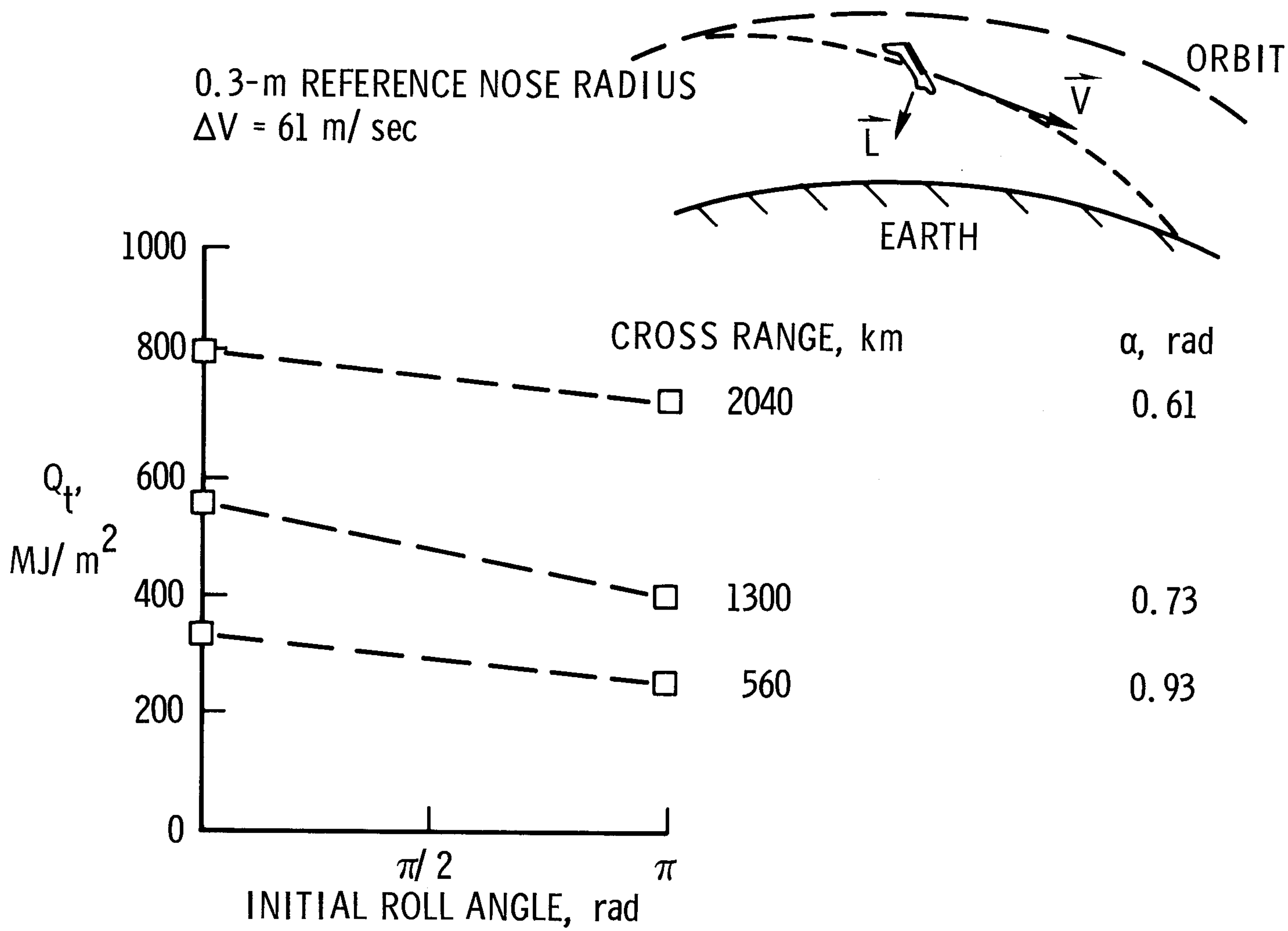

Figure 8

DIRECT-BOND AND CARRIER-PANEL WEIGHTS

Two design concepts for ablative heat shields are to bond the ablator directly to the structure and to bond the ablator on a carrier panel which is mechanically attached to the structure. Figure 9 gives a weight comparison of these two approaches for the design conditions shown, which are typical of a forward location on the bottom fuselage. For these conditions, there is no weight penalty associated with the carrier-panel concept. The graphite polyimide (G/Pi) carrier panel can operate at high temperature, and therefore the weight of the required ablation material is reduced. Fibrous insulation between the carrier panel and the vehicle structure maintains the structure at its design temperature. The carrier panel would be salvaged and refurbished.

Because the carrier-panel concept offers important advantages (ease of inspection, rapid replacement, and off-site refurbishment), it merits consideration in TPS design studies, particularly for highly heated regions on the orbiter. For highly heated regions, which will require extensive TPS replacement, the design studies may show that the advantages of the carrier-panel concept are obtainable with an insignificant weight penalty.

DIRECT-BOND AND CARRIER-PANEL WEIGHTS

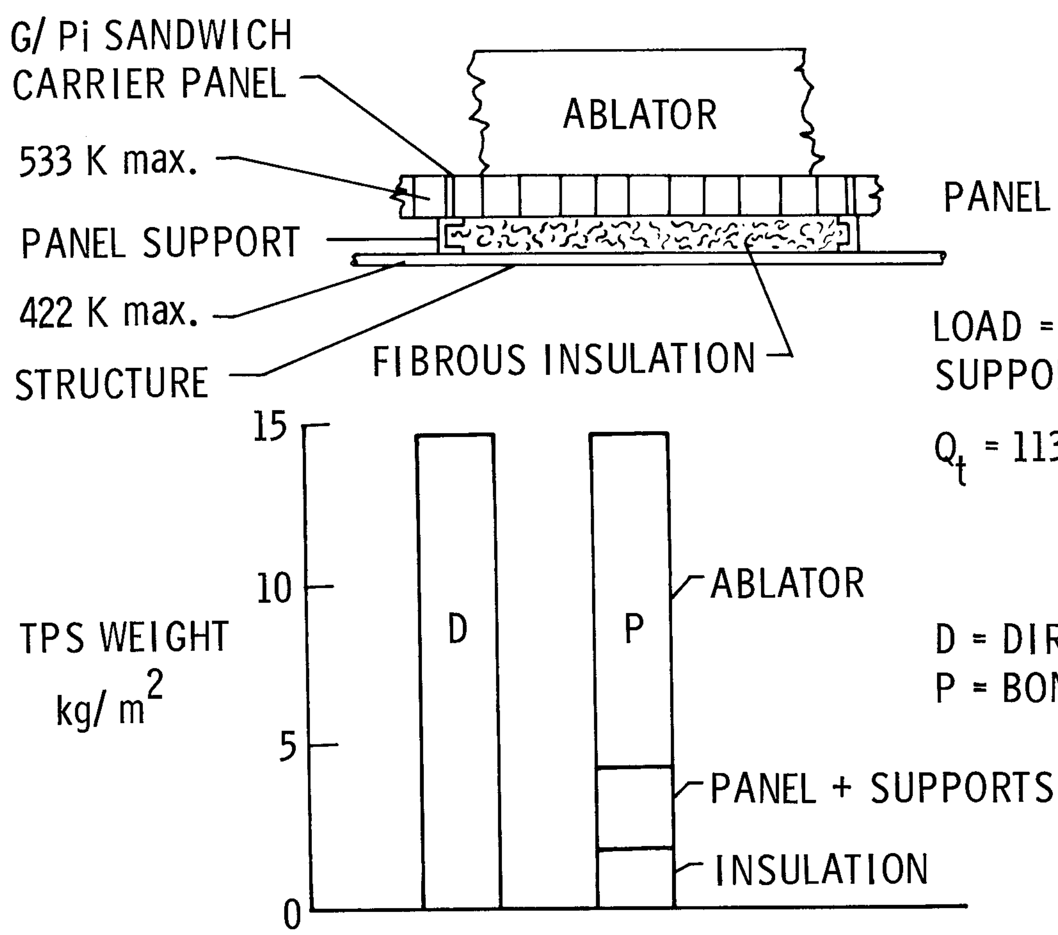

PANEL DESIGN CONDITIONS:

LOAD = ± 19.3 kN/ m^3
SUPPORT SPAN = 0.508 m
Q_t = 113.49 MJ/ m^2

D = DIRECT BOND
P = BONDED ON CARRIER PANEL

Figure 9

REUSE TESTS OF AN ABLATION MATERIAL

Relatively large areas of the orbiter will experience maximum temperatures below 650 K during entry. For these areas, unlike the highly heated areas, reusable ablative TPS may be feasible. Figure 10 presents the results from a preliminary evaluation of ablator reuse.

The sketch at the top of the figure shows the test apparatus. A quartz-lamp radiator, radiating to a heater plate, which rested on the ablator surface, was used to provide a controlled ablator surface temperature. The ablation material was adhesively bonded to an aluminum plate which represented the orbiter structure. The fibrous insulation thermally isolated the aluminum plate. Thermocouples were used to measure the temperature of the heater plate and the aluminum plate.

During the tests the ablator surface was maintained at a fixed temperature. Measurements of the time required to obtain a ΔT of 111 K in the aluminum plate were made in repeated tests. After each heating cycle, the specimens were allowed to cool and the ablator mass loss was determined from weight measurements.

The curves show that the time to produce a ΔT of 111 K generally decreased over the first two heating cycles. Thereafter, the time did not change. During these tests the major part of the total mass loss occurred in the first one or two heating cycles. Over the range of surface temperatures examined, there was no evidence of severe thermal degradation.

Ablator reuse could produce significant cost savings, but further tests are needed to establish ablator reuse potential.

REUSE TESTS OF AN ABLATION MATERIAL

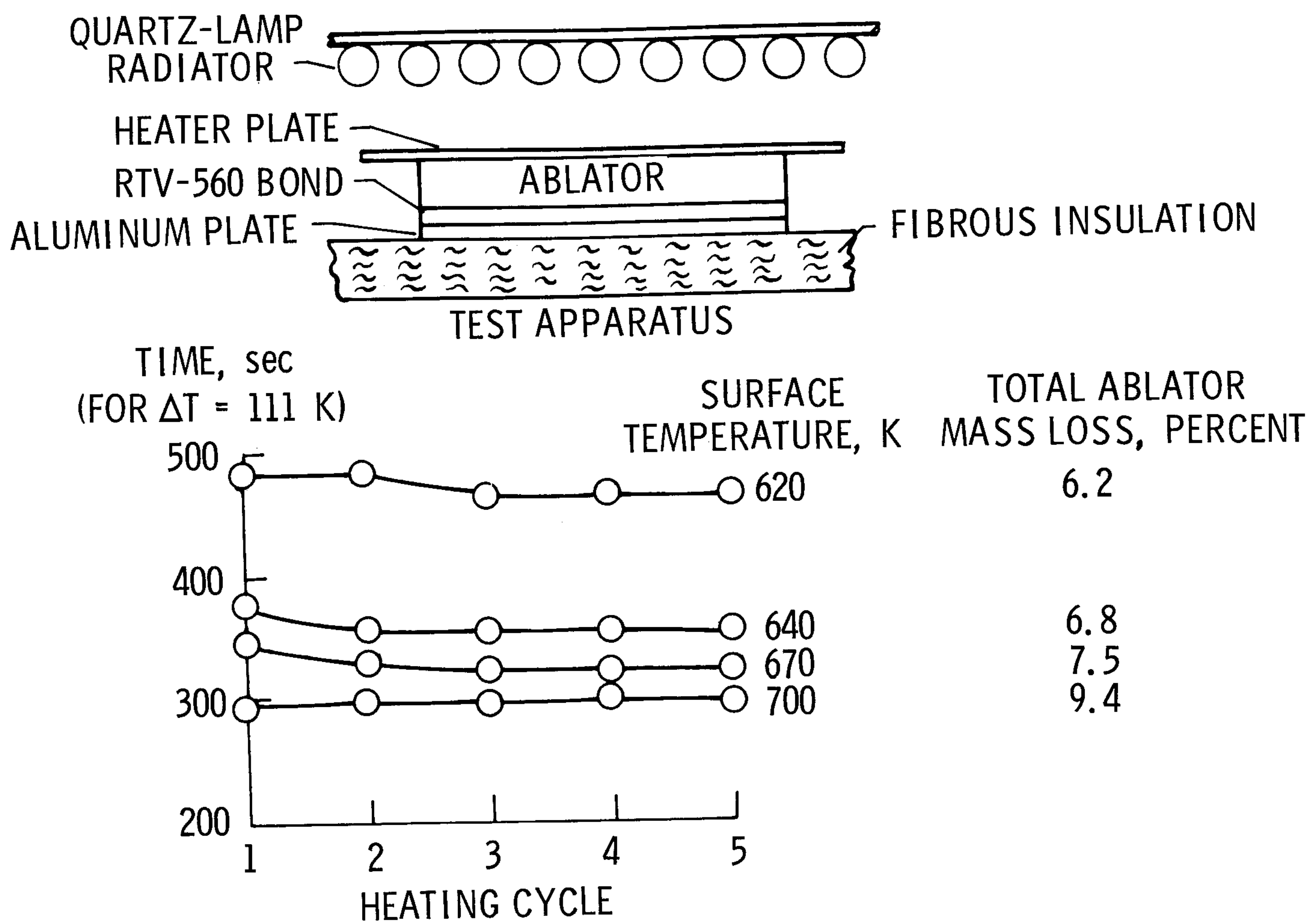

Figure 10

TPS REFURBISHMENT STUDIES

The space-shuttle ablation technology program has also included TPS refurbishment studies. Figure 11 shows a large space shuttle mockup with various TPS concepts attached, which is located at a NASA center and has been used in refurbishment studies. Also shown are some details of the various TPS concepts which were tested and some results from these studies (refs. 6, 7, and 8).

Two reusable surface insulation (RSI) and two ablator concepts were studied. (See refs. 7 and 8 for details.) The multiple mechanical fastener ablative concept consists of an ablator panel which is attached to the vehicle structure by closely spaced attachments. In the pi-strap concept, the ablator is attached to a carrier panel, which is, in turn, mechanically attached to the structure. The pi-strap is a closure strip which provides access to the carrier-panel attachments.

Prior to the performance of actual refurbishment operations, refurbishment labor estimates (in man-hours/m^2) were obtained from analytical studies performed by two contractors (refs. 6 and 7). The estimates differed widely. For the ablator concepts, comparison of the labor estimates and the test data shows that the actual refurbishment work on the mockup took much less time than either contractor estimated. The conclusion is that refurbishment labor is not a major cost item for the mechanically attached ablative TPS concepts which were used.

Further refurbishment studies of various TPS concepts, particularly for single and compound curvature surfaces, are needed. These studies should also concentrate on the inspection and NDE (nondestructive evaluation) requirements — a significant requirement that was not included in the scope of the current studies.

TPS REFURBISHMENT STUDIES

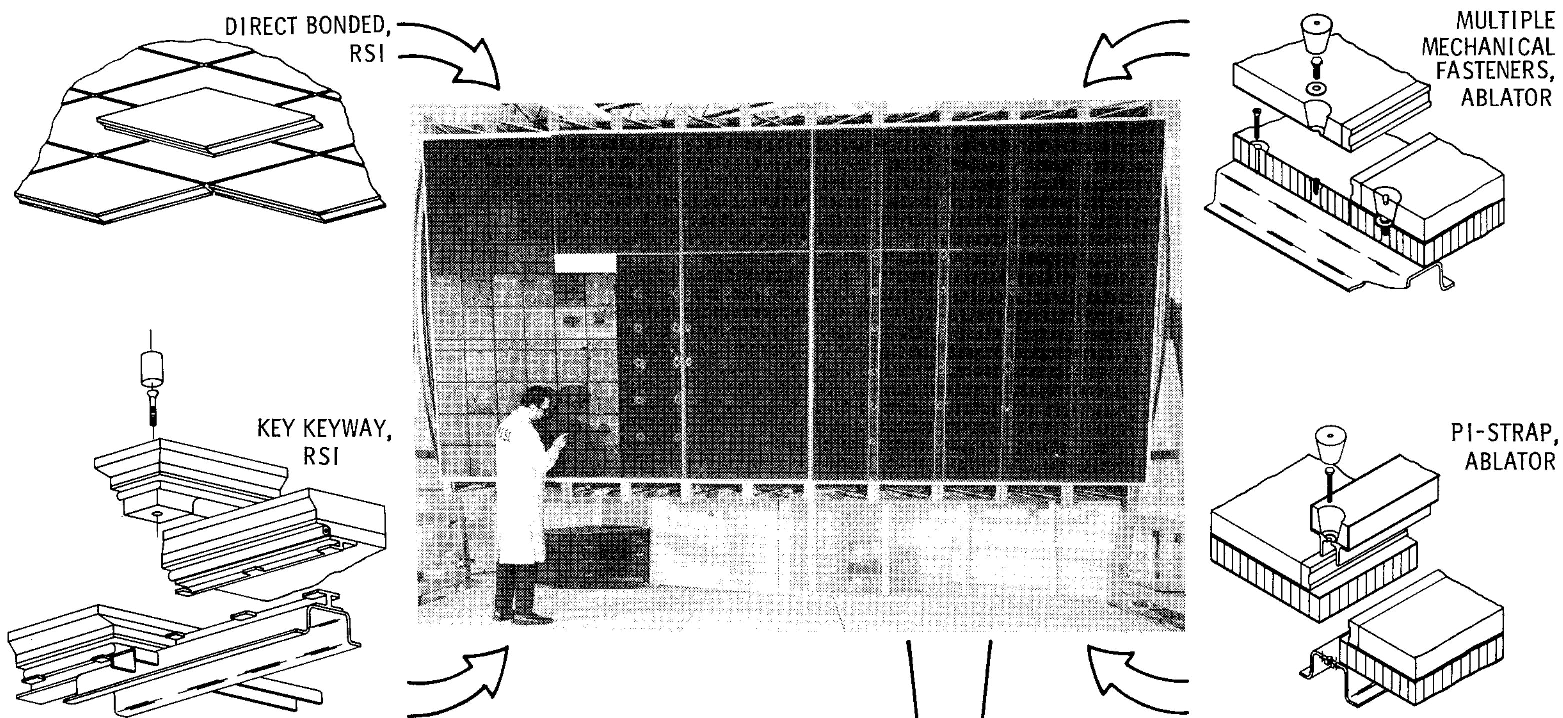

DIRECT LABOR TIME	KEY KEYWAY, RSI	DIRECT BONDED, RSI	PI-STRAP, ABLATOR	MULTIPLE MECH. FASTENERS, ABLATOR
ESTIMATES m-hr/m^2	5.06 - 40.58	13.99 - 45.21	5.81 - 40.58	10.23 - 50.70
TEST DATA m-hr/m^2	5.80	32.87	1.00	1.17

RESULTS

- DEMONSTRATED REFURBISHMENT TECHNIQUES & FIELD REPAIR METHODS
- OBTAINED TIME & COST DATA
- DETERMINED ADDITIONAL RESEARCH REQUIREMENTS

Figure 11

DIRECT-BOND AND CARRIER-PANEL TPS COSTS

The low refurbishment costs for ablator plus carrier-panel TPS may provide a means to secure some important advantages provided by the carrier-panel approach (inspection, rapid refurbishment, etc.) without significant changes in the total program cost. Figure 12 shows a total program cost comparison between direct-bond and carrier-panel ablative TPS for 100 and 60 percent refurbishment after each flight. This figure, based on the cost assumptions given in figure 13, shows that the labor cost for direct bonding can be traded for the increased material costs of the carrier-panel concept. Figure 12 also shows that refurbishment material costs are the major cost item for both concepts. It therefore follows that it is material costs which must be reduced to make significant reductions in the total cost of a refurbishable TPS.

The cost assumptions used in preparing this figure can be debated. A major cost element – inspection and recertification – is not included in this figure because there are no cost data. Not only are there no cost data, but, particularly for the direct-bond approach, there is little understanding of how to perform these operations.

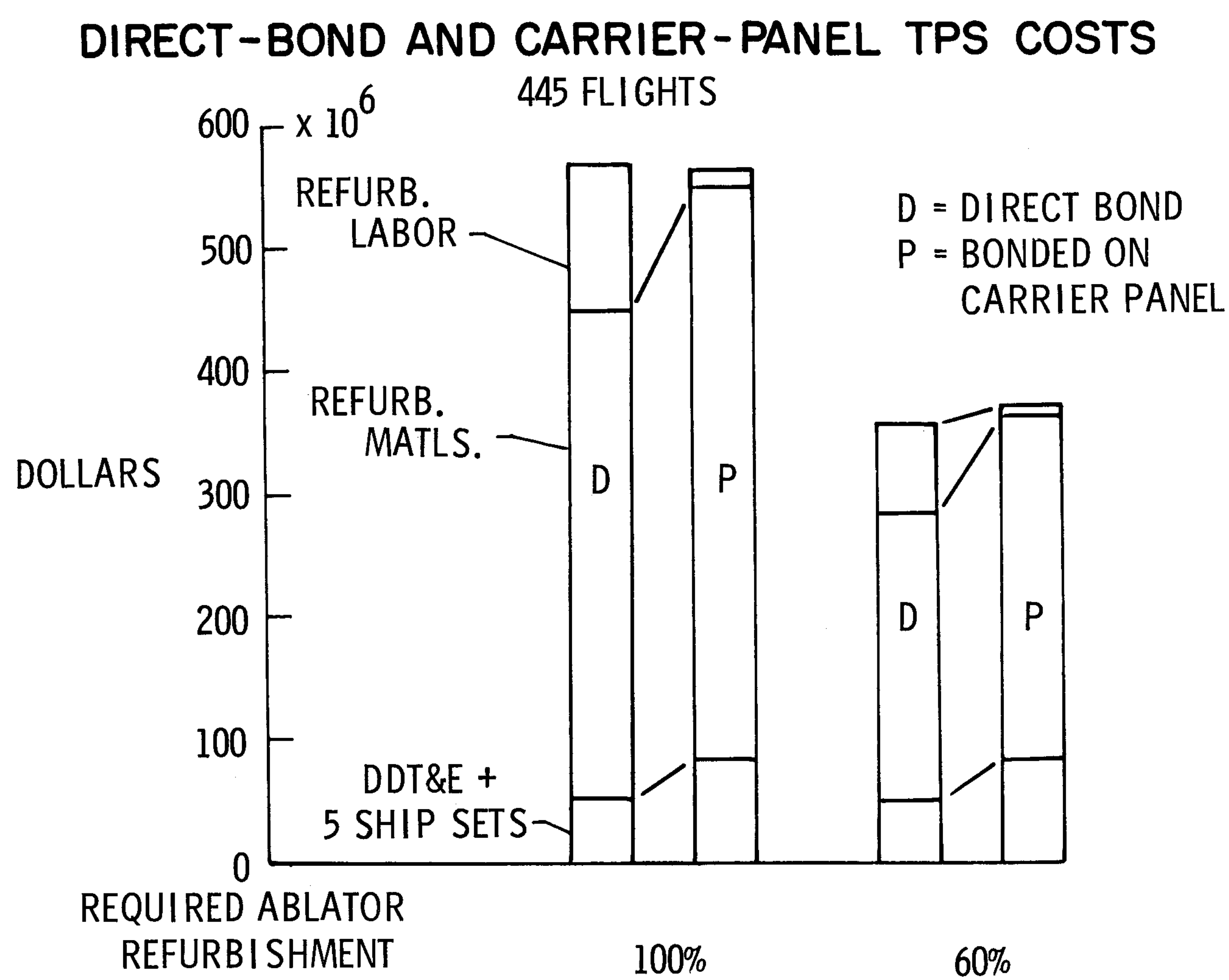
DIRECT-BOND AND CARRIER-PANEL TPS COSTS
445 FLIGHTS
DOLLARS
x 10^6
600
500
400
300
200
100
0
REFURB. LABOR
REFURB. MATLS.
DDT&E + 5 SHIP SETS
D = DIRECT BOND
P = BONDED ON CARRIER PANEL
D
P
D
P
REQUIRED ABLATOR REFURBISHMENT
100%
60%

Figure 12

ASSUMPTIONS FOR TPS COST COMPARISONS

Figure 13 shows the assumed values for each cost element used in figure 12. The values for DDT&E (design, development, testing and evaluation) and the carrier-panel costs are estimates. The ablation material costs are based on low-cost fabrication studies. The refurbishment labor cost for the direct-bond ablator was assumed to be equal to the labor costs given in reference 8 for direct-bond, reusable insulation TPS. The refurbishment labor cost for carrier-panel TPS was also obtained from reference 8. The items listed at the bottom of figure 13 are the other assumptions used in preparing figure 12.

ASSUMPTIONS FOR TPS COST COMPARISONS

	COST ELEMENT	AMOUNT
ABLATOR	DDT&E	\$46 MILLION
	MATERIAL	\$861/ m^2
	REFURB. LABOR (DIRECT-BOND ABLATOR)	\$269/ m^2
CARRIER PANEL	DDT&E	\$20 MILLION
	MATERIAL	\$3229/ m^2
	REFURB. LABOR (ABLATOR ON CARRIER PANEL)	\$26.9/ m^2

INITIAL COSTS INCLUDE FIVE SHIP SETS

5% ATTRITION OF REFURBISHED PANELS

NO SPARE SETS

445 FLIGHTS

Figure 13

FUTURE RESEARCH AND DEVELOPMENT NEEDS

The needs for future research and development of ablative TPS under the space-shuttle technology program are listed in figure 14. Elimination of honeycomb reinforcement from ablation material can lead to substantial manufacturing cost reductions; however, careful consideration must be given to test programs which will help insure acceptance of materials without honeycomb. Trajectory shaping offers a means to minimize TPS weight, but the feasibility and practicality of various approaches must be established. The requirements for thermal-control and moisture-proof coatings for ablative TPS must be established because these coatings could influence design, manufacturing, and materials selection. The reuse of ablation materials applied to lightly heated vehicle areas could lead to significant reductions in materials and refurbishment costs. Better definition of the time and cost required to refurbish various ablative TPS, particularly for single and compound curvature surfaces, is required for realistic cost estimates. Studies to obtain these data should be carefully related to the shuttle operational requirements, and particular concern needs to be given to establishing the requirements and procedures for inspection and NDE of all types of ablative TPS.

FUTURE RESEARCH AND DEVELOPMENT NEEDS

- INVESTIGATE ELIMINATION OF HONEYCOMB REINFORCEMENT
- DETERMINE FEASIBILITY OF TRAJECTORY SHAPING TO MINIMIZE TPS WEIGHT
- ESTABLISH REQUIREMENTS FOR THERMAL-CONTROL AND MOISTURE-PROOF COATINGS
- DETERMINE REUSE CAPABILITY OF ABLATORS FOR SPECIAL AREAS
- BETTER DEFINE REFURBISHMENT TIME AND COST
- ESTABLISH REQUIREMENTS AND PROCEDURES FOR INSPECTION AND NDE

Figure 14

REFERENCES

1. Norwood, L. B.: Final Report on Study of Low-Cost Fabrication of Ablative Heat Shields. SD 72-SH-0005 (Contract NAS1-10708), North American Rockwell, Mar. 31, 1972. (Available as NASA CR-112036.)

2. Production Eng. & Develop. Dep.: Final Report on Low-Cost Ablative Heat Shield for Space Shuttles. SD 70-400 (Contract NAS1-9943), North American Rockwell, Nov. 20, 1970. (Available as NASA CR-111795.)

3. Chandler, Huel H.: Low-Cost Ablative Heat Shields for Space Shuttles. Contract No. NAS1-9946, Martin Marietta Corp. (Available as NASA CR-111800.)

4. Dulak, R. E.; and Cecka, A. M.: Low Cost Ablative Heat Shields for Space Shuttles. Contract No. NAS 1-9947, Fansteel Inc. – Reflective Laminates Division, 1970. (Available as NASA CR-111814.)

5. Abbott, Harry T.: Low-Cost Fabrication Method for Ablative Heat Shield Panels for Space Shuttles. Contract No. NAS1-9945, Brunswick Corp. (Available as NASA CR-111835.)

6. Peterson, Robert J.: Final Report for Refurbishment Cost Study of the Thermal Protection System of a Space Shuttle Vehicle. Contract NAS 1-10094, Lockheed Missiles & Space Co., 1970. (Available as NASA CR-111830.)

7. Haas, D. W.: Summary Refurbishment Cost Study of the Thermal Protection System of a Space Shuttle Vehicle. Contract No. NAS1-10093, McDonnell Douglas Astronautics Co. – East, 1971. (Available as NASA CR-111833.)

8. Haas, D. W.: Refurbishment Cost Study of the Thermal Protection System of a Space Shuttle Vehicle. Final Report – Phase II. Contract No. NAS1-10990, McDonnell Douglas Corp., Apr. 1, 1972. (Available as NASA CR-112034.)

ADVANCED DESIGN CONCEPTS FOR SHUTTLE AIRFRAME STRUCTURE

By Michael F. Card, John G. Davis, Jr., and John L. Shideler

NASA Langley Research Center
Hampton, Virginia

SUMMARY

A review of a Langley Research Center program to develop weight-saving advanced design concepts for shuttle airframe structure is presented. Design concepts under investigation employ selective composite reinforcement and/or efficient geometric arrangements. An effort to develop metallic panel designs which exploit the relaxation of smooth external-surface requirements for skin structure is reviewed. Available highlights from research and development studies which investigated the application of composite reinforcement to the design of two types of fuselage panels, a shear web, a large fuselage frame, and a landing-gear-door assembly are presented. Preliminary results from these studies suggest weight savings of 25 percent can be obtained by using such concepts.

18

ADVANCED CONCEPTS

(Figure 1)

The purpose of this paper is to review results from a Langley Research Center program to develop advanced design concepts for shuttle airframe structure. The program was initiated in April 1971 and will be completed by the end of 1972. This report will review the elements of the program and represents a progress report on technical achievements and problem areas.

As indicated in figure 1, the Langley program encompasses two types of structural concepts: metallic panels which have structurally efficient geometric forms and composite-reinforced structures in which Langley's concept of selective composite reinforcement is exploited. For the metallic panels, problem areas are to establish a rational design methodology, to demonstrate a practical fabrication procedure, and to design end closures for such a construction. For composite-reinforced structures, a need for sound design methodology also exists. Load-introduction problems and methods of minimizing thermal stresses introduced by coupling materials with differing coefficients of expansion are also problem areas.

ADVANCED CONCEPTS

METALLIC

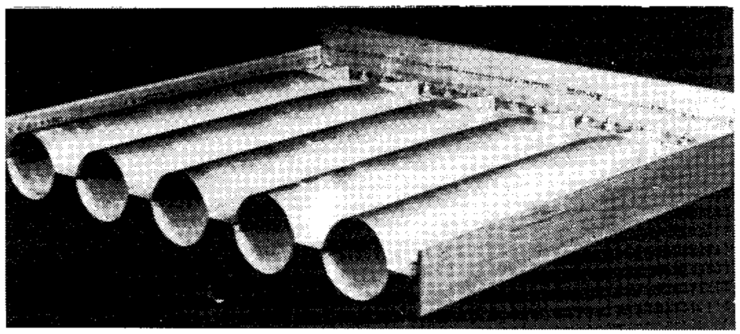

PROBLEM AREAS

- DESIGN METHODOLOGY
- FABRICATION
- END CLOSURE

COMPOSITES

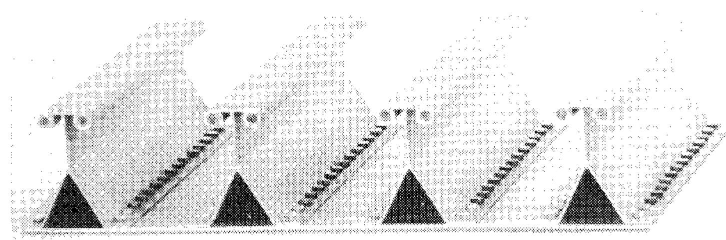

PROBLEM AREAS

- DESIGN METHODOLOGY
- LOAD INTRODUCTION
- THERMAL STRESS

Figure 1

BEAD-STIFFENED METAL PANEL

(Figure 2)

Because certain areas of the shuttle airframe structure require external thermal insulation, concepts which do not employ smooth external surfaces can be considered for the load-bearing substructure. A concept for fuselage and wing panels which exploits this characteristic is under development by The Boeing Company (under NASA Contract NAS1-10749). As indicated in the photograph in figure 2, geometrical efficiency of the concept is obtained by forming curved beads in metallic flat panels. The concept evolved from hypersonic wing studies to provide an efficient means to cope with thermal expansion, lateral pressure, and combined in-plane loadings. The objective of the present program is to develop and substantiate design theory with experimental results.

The structural efficiency of aluminum beaded-panel configurations is indicated in the graph in figure 2. The mass of various beaded-panel designs under compression loadings N_x of 0.175 to 0.900 MN/m (1000 to 5143 lb/in.) combined with shear loadings N_{xy} that are one-third the applied compressive load and a fixed lateral pressure p of 6.9 kN/m^2 (1 psi) are compared. Values for conventional Z-stiffened panels under combined compression and pressure loadings but without shear are shown for reference. The most efficient beaded-panel designs can be seen to be roughly one-half the weight of the conventional panels over the whole loading range. Thus, this type of construction appears to have considerable potential for efficient structural design.

BEAD-STIFFENED METAL PANEL

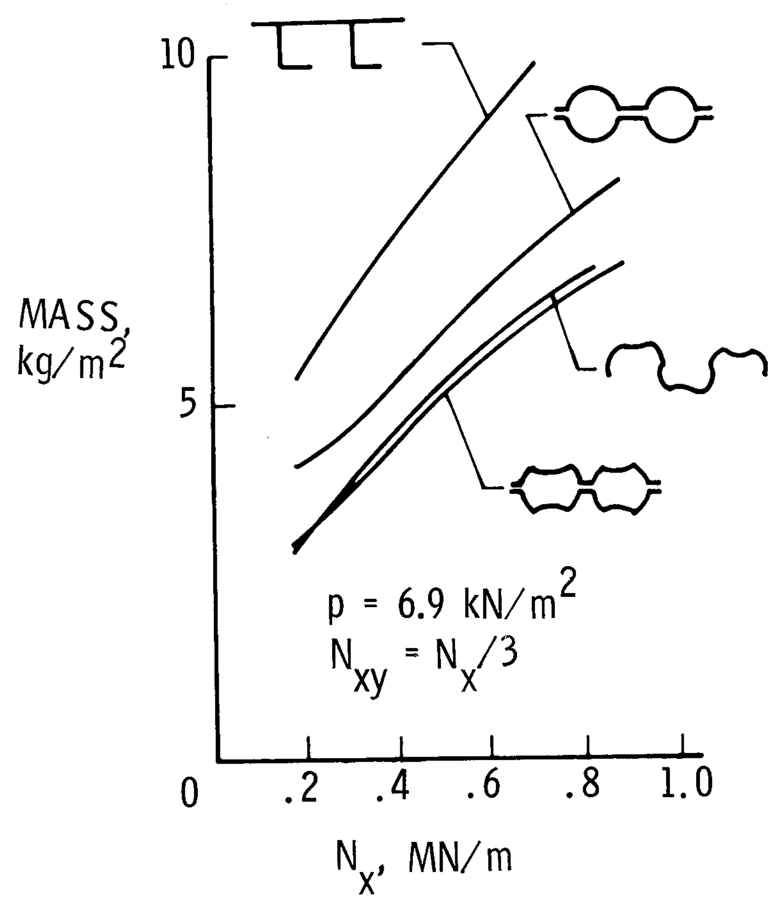

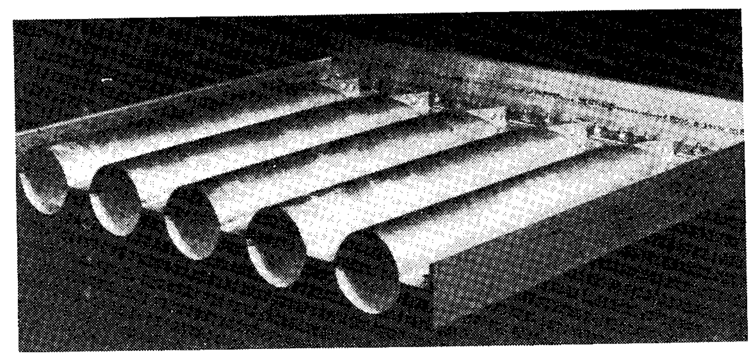

- EVOLVED FROM HYPERSONIC WING STUDIES
- EXPLOITS EFFICIENCY OF CURVED ELEMENTS
- DEVELOP DESIGN THEORY AND MODIFY WITH EXPERIMENTAL RESULTS

Figure 2

LOCAL BUCKLING RESULTS FOR BEAD-STIFFENED METAL PANELS

(Figure 3)

The photograph in figure 3 shows a bead-stiffened panel which has buckled locally under compression loading. The panel is about 51 cm square (20 inches square) and was used in a series of 30 tests to investigate local buckling of curved elements under various combinations of compression, bending, and shear loads. The table below the photograph shows a comparison of preliminary test results with theory for several load conditions. As can be seen, theory and experiment are in fair-to-good agreement with the greatest differences occurring for pure shear and pure bending tests. Plans are to modify the theory semiempirically (as is usually done for shell stability design) and to generate sufficient data to substantiate the analytical modifications. The panel-development program encompasses fabrication studies as well as other design investigations including tests of end closures and studies of the overall instability of larger panels under combined loads. A substantial body of experimental and theoretical design information will be generated to provide a technical base for this design concept.

LOCAL BUCKLING RESULTS

BEAD-STIFFENED METAL PANEL

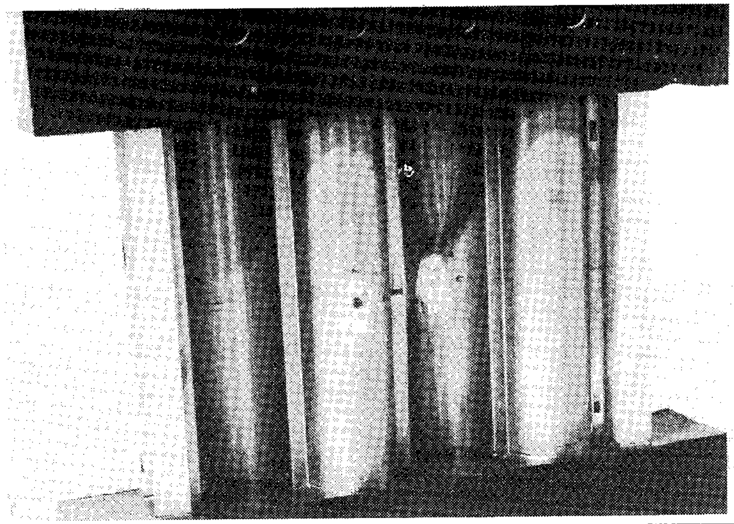

LOAD CONDITION	THEORY*	EXPERIMENT
COMPRESSION	0.918 MN/m	0.905 MN/m
SHEAR	0.250 MN/m	0.337 MN/m
BENDING	10.4 kN m/m	14.7 kN m/m
COMP. + SHEAR	0.815 MN/m + 0.171 MN/m	0.735 MN/m + 0.155 MN/m
COMP. + BENDING	0.450 MN/m + 4.6 kN m/m	0.470 MN/m + 4.75 kN m/m

*UNMODIFIED

Figure 3

PROGRAM TO EVALUATE COMPOSITE-REINFORCED-METAL STRUCTURES FOR SPACE SHUTTLE APPLICATION

(Figure 4)

As mentioned previously, the advanced concepts program for composite structures is focused on the application of the Langley concept of selective composite reinforcement of all-metal structures. This concept was judged to have the best near-term payoff for shuttle structure. The structural elements included in the program are listed in figure 4 and consist of elements of a booster thrust-structure truss, two types of fuselage-skin-panel construction, a thrust-structure shear web, and internal fuselage frame, and a landing-gear-door assembly. The truss structure is discussed in detail in reference 1 and, therefore, will not be considered herein except to note that the program was highly successful and demonstrated that weight savings of 25 percent for full-scale truss structures are feasible.

For each of the elements in this program, the approach was to design both an all-metal and a composite-reinforced-metal structure to representative shuttle loadings. Detail design of the composite-reinforced structures was supported by element tests to verify the integrity of the structural concept. When a suitable concept has been developed, the component will be constructed and tested. Because of budgetary constraints, most of the elements are scaled; however, the components are large enough to have representative fabrication details. Highlights from five of the component programs are discussed subsequently.

PROGRAM TO EVALUATE COMPOSITE-REINFORCED-METAL STRUCTURES FOR SPACE SHUTTLE APPLICATION

- COMPONENTS
  - TRUSS
  - SKIN PANELS
  - SHEAR WEB
  - FRAME
  - DOOR ASSEMBLY
- APPROACH
  - DESIGN (ALL METAL VERSUS COMPOSITE-REINFORCED METAL)
  - FABRICATION
  - TEST

Figure 4

PANEL CRIPPLING TESTS FOR INFILTRATED STRINGER SECTIONS

(Figure 5)

A joint program by NASA and AVCO Corporation (under NASA Contract NAS1-9938) to develop a panel design concept for cold shuttle structure using conventionally stiffened construction is underway. The photograph in the lower left of figure 5 shows the type of construction being investigated. Conventional aluminum extrusions are fabricated with hollowed recesses; these recesses are filled with epoxy-coated boron fibers that are postcured in place to form a composite-infiltrated structural section. Compression-panel design studies indicate that panels with Y-stiffeners may be 25 percent lighter than optimally designed all-metal panels from comparable alloys.

The photographs in the right of the figure show a short crippling panel that has been tested in axial compression. The panel test was successful, and inelastic stresses were developed in the aluminum material. As indicated, agreement between the theoretical buckling load P_{calc} and the experimental buckling load P_{exp} was excellent.

PANEL CRIPPLING TESTS
INFILTRATED STRINGER SECTIONS

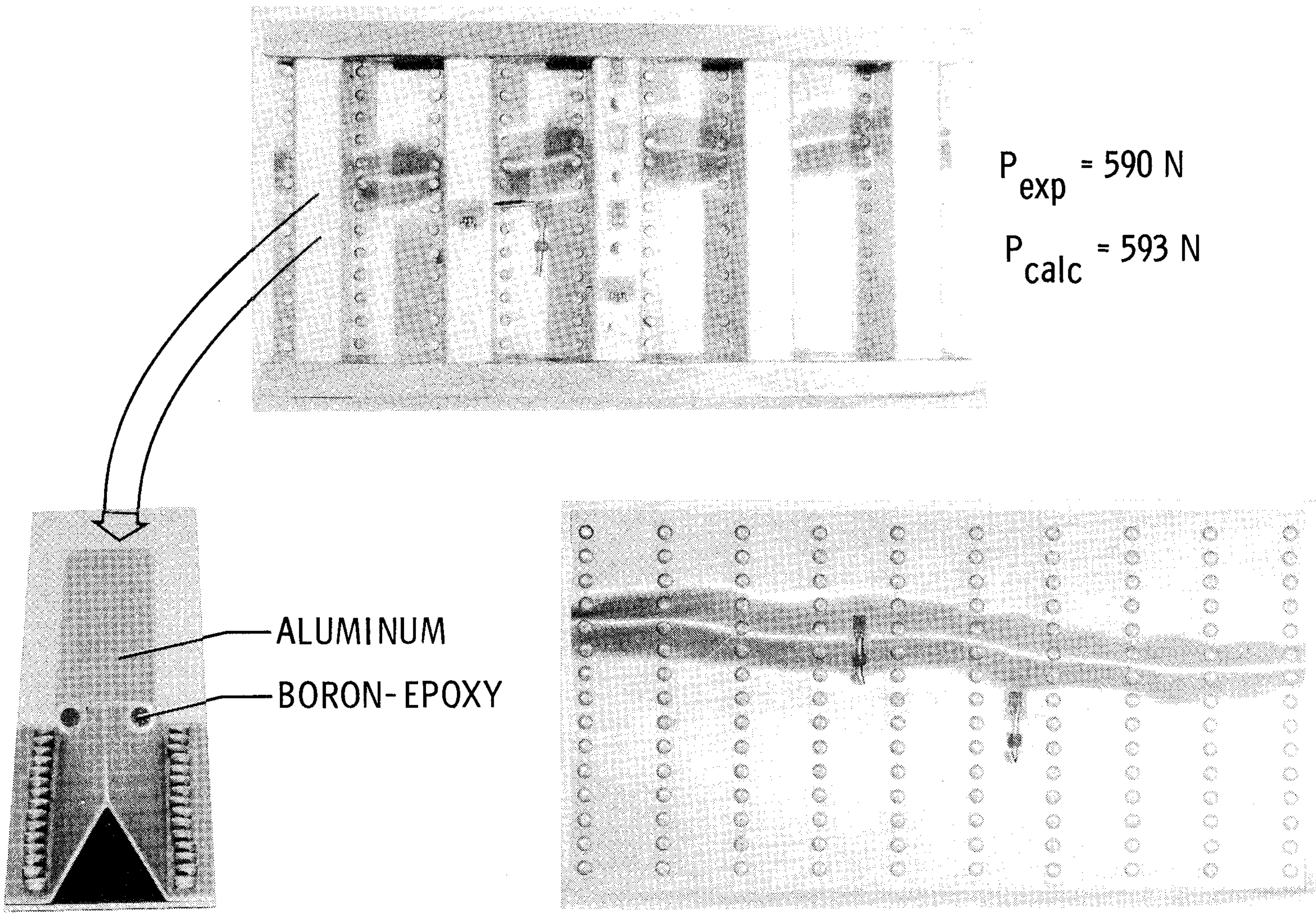

Figure 5

PANEL INSTABILITY TESTS OF INFILTRATED STRINGER SECTIONS

(Figure 6)

In this program a panel-instability test has also been conducted with somewhat less success. The 0.91- by 1.2-meter (3- by 4-foot) panel shown in the figure was tested in compression and failed prematurely at 64 percent of its ultimate design load. As shown in the detail insets in figure 6, the third stringer from each edge appeared to have rolled, and boron rods can be seen protruding from the ends of these stringers. The second stringer from each edge was found to have experienced a tensile rupture in the vertical web of the Y-stiffener. Strain-gage data indicated debonding of one of the rolled stringers, and it is believed this debonding may have precipitated the premature failure of the panel. The panel also contained an undesirable sinusoidal imperfection developed during riveting. A second panel is to be constructed under more stringent manufacturing controls and tested. The present test results illustrate the need for more precise manufacturing controls and inspection for composite-reinforced structures.

PANEL INSTABILITY TESTS
INFILTRATED STRINGER SECTIONS

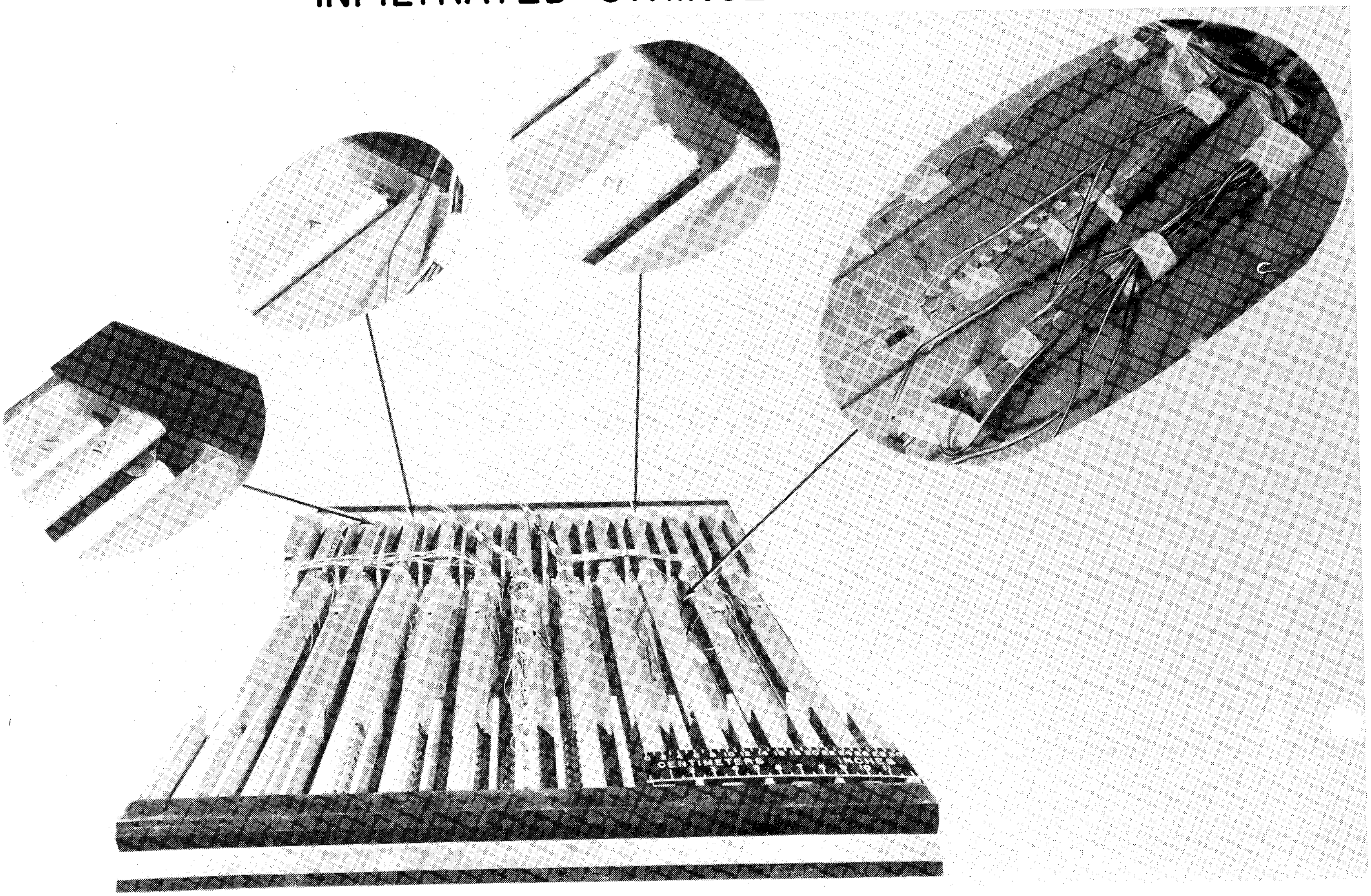

Figure 6

ORBITER FUSELAGE PANEL

(Figure 7)

A panel concept under investigation by the General Dynamics Corporation (under NASA Contract NAS1-10766) is for a lightly loaded fuselage panel. Composite-reinforced panels have been designed to withstand representative combined compression and shear loadings occurring in the lower aft fuselage of an early orbiter design. As shown in figure 7, the configuration under study is a panel stiffened by closely spaced hat sections and conventional frames. Buckling of the panel skin was not permitted, since it could impair the performance of surface insulation bonded to the panel skin.

In this study, weight trade-offs were made between hot and cold structural concepts and thermal insulation requirements. The maximum structural skin temperature considered was 589 K (600° F). The panels were found to be so lightly loaded that selective reinforcement of metal stiffeners proved ineffective. The concept of all-composite stiffeners on metal skin was, therefore, investigated. Relative panel efficiencies are summarized in figure 8.

ORBITER FUSELAGE PANEL

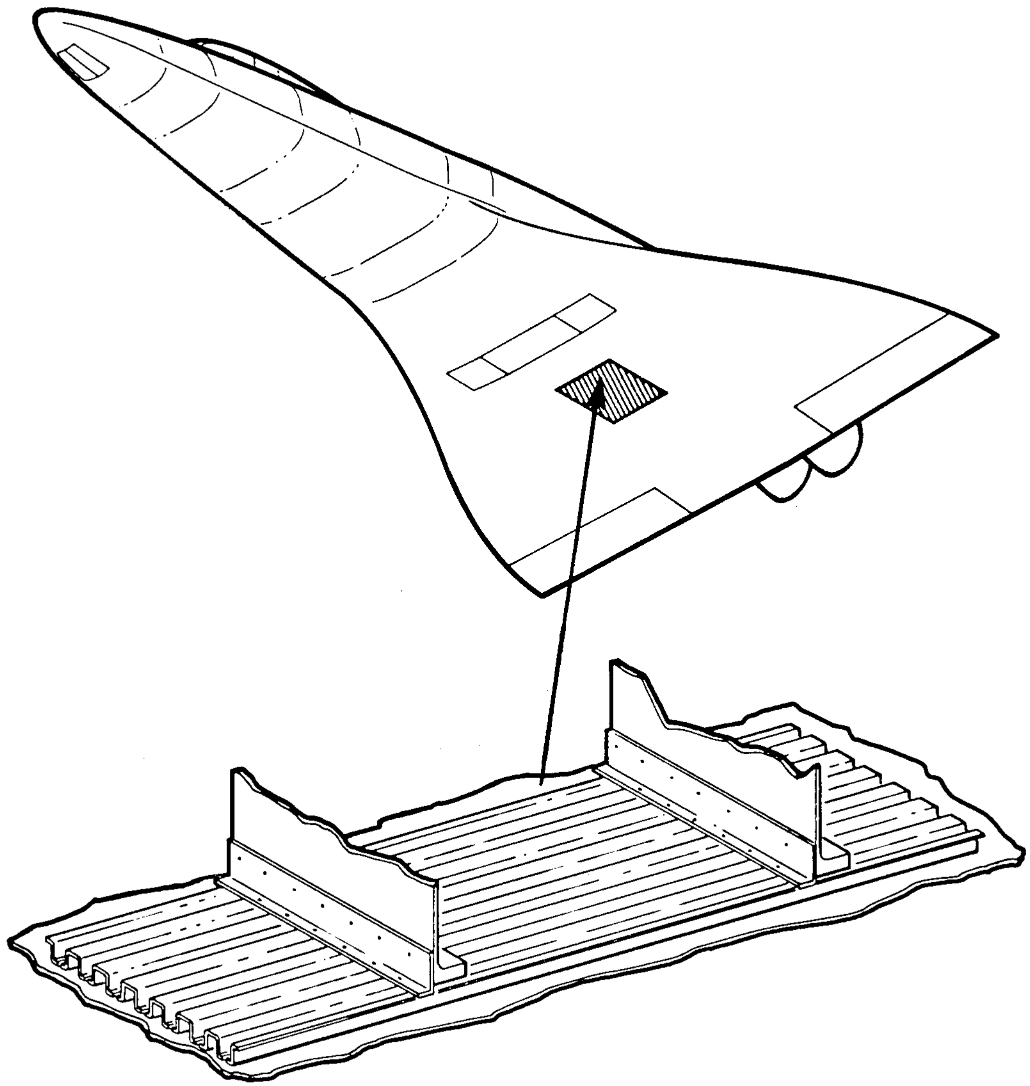

Figure 7

WEIGHTS OF HAT-STIFFENED FUSELAGE PANELS

(Figure 8)

The relative weights of all-metal panels and panels reinforced by composite stiffeners are shown in figure 8. In the aluminum (Al) panel design, 2024–T3 alloy was selected to operate at 450 K (350° F) and this design required additional insulation to compete with designs operating at the maximum structural temperature of 589 K (600° F). Boron-epoxy (B/E)-reinforced aluminum panels and graphite-epoxy (G/E)-reinforced titanium (Ti) panels operating at the same temperature can be seen to have a lighter structural weight and to yield 20- to 23-percent overall weight savings. Boron-polyimide (B/Pi)- or boron-aluminum (B/Al)-reinforced titanium panels both offer substantial weight savings because of minimum insulation requirements. These designs are significantly lighter than the all-titanium hot-structure design, which was the orbiter baseline structure.

Based on these studies, the boron-aluminum-reinforced titanium-panel concept has been adopted and two 0.6- by 1.2-meter (2- by 4-foot) panels will be designed and tested at temperature.

WEIGHTS OF HAT-STIFFENED FUSELAGE PANELS

MATERIAL HAT SKIN	OPERATING TEMP. K	OPERATING TEMP. °F	STRUCTURAL WEIGHT*	ADDITIONAL INSULATION WEIGHT*	TOTAL WEIGHT*
Al	450	350	0.69	0.31	1.00
B/E Al	450	350	.49	.31	.80
G/E Ti	450	350	.46	.31	.77
B/Pi Ti	561	550	.51	.06	.57
Ti	589	600	.84	0	.84
B/Al Ti	589	600	.54	0	.54

*ALL WEIGHTS NORMALIZED BY TOTAL WEIGHT OF ALUMINUM PANEL

Figure 8

THERMAL-CYCLING TEST RESULTS

(Figure 9)

In an early part of this panel design program, the effects of thermal cycling on composite-to-metal bonds were investigated. As shown in figure 9, a laminated specimen was used to perform short-beam interlaminar shear tests. The test specimens were exposed to 200 cycles of a representative orbiter-mission temperature history. The interlaminar shear-strength results for boron-epoxy- and graphite-epoxy-reinforced titanium laminates are shown in the bar graph in figure 9. Test results indicate that no degradation in strength occurred because of thermal cycling. In fact, a slight increase in strength over unexposed specimens occurred. Tests such as these are also being performed on boron-aluminum-reinforced titanium laminates to establish their integrity under thermal loading.

THERMAL-CYCLING TEST RESULTS

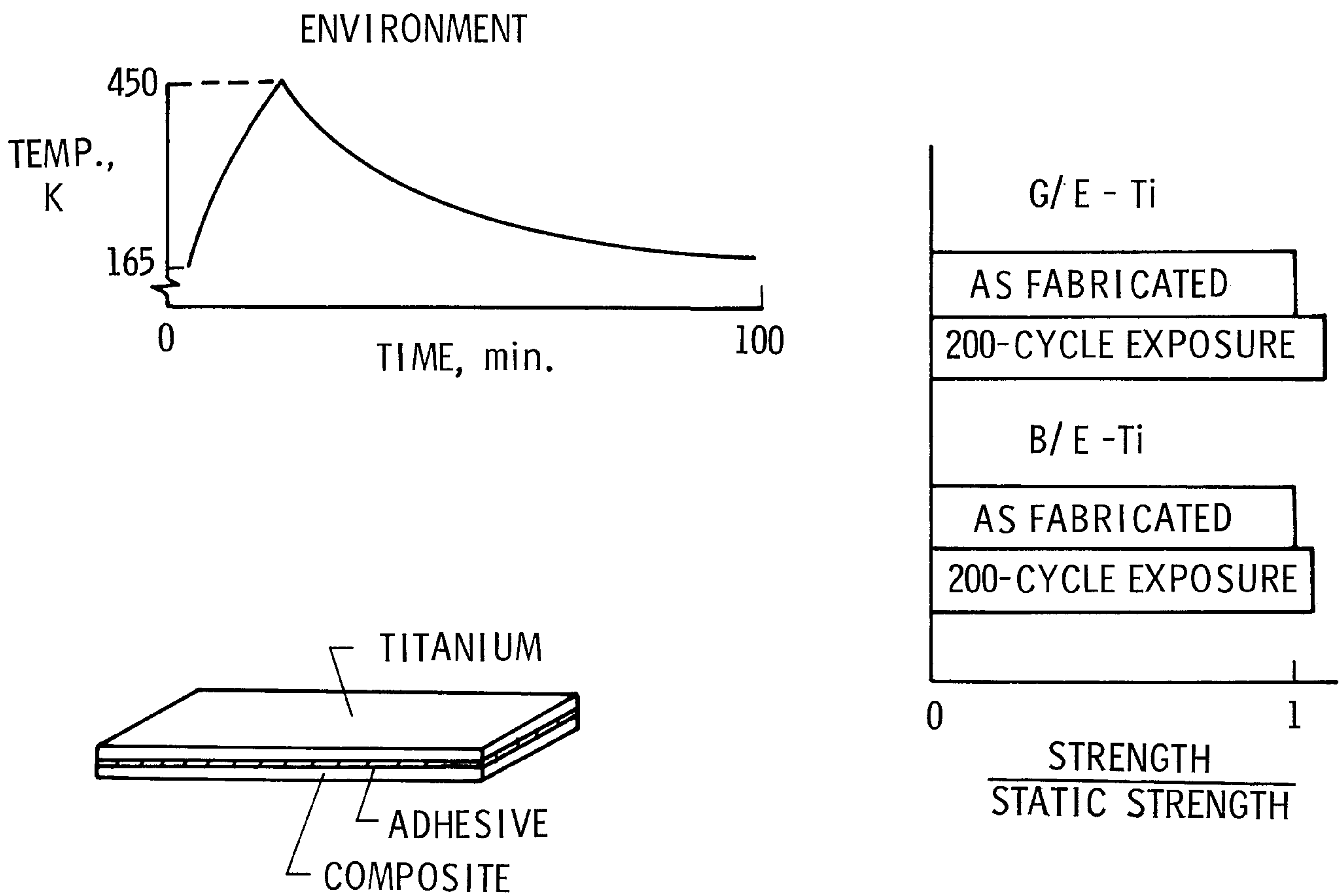

Figure 9

CRIPPLING TESTS ON TITANIUM SHEET REINFORCED WITH BORON-ALUMINUM HAT STIFFENERS

(Figure 10)

As part of the development of the panel-design concept, a series of crippling tests on titanium sheet reinforced with a unidirectional boron-aluminum hat stiffener has been conducted. The hat stiffener shown in the photograph has been spot-bonded to the titanium. The specimen shown has been buckled in compression. In contrast to boron-epoxy and graphite-epoxy stiffeners which splinter and debond at failure, the boron-aluminum has metallike buckling deformations develop at failure.

The table in figure 10 shows theoretical and experimental data from tests made at ambient temperatures of two types of stiffeners with different thicknesses. Agreement is satisfactory, and preliminary data from similar tests conducted at elevated temperature suggest the design concept will prove reliable at these temperatures also.

CRIPPLING TESTS

B/Al HAT SECTION STIFFENERS; Ti SKIN

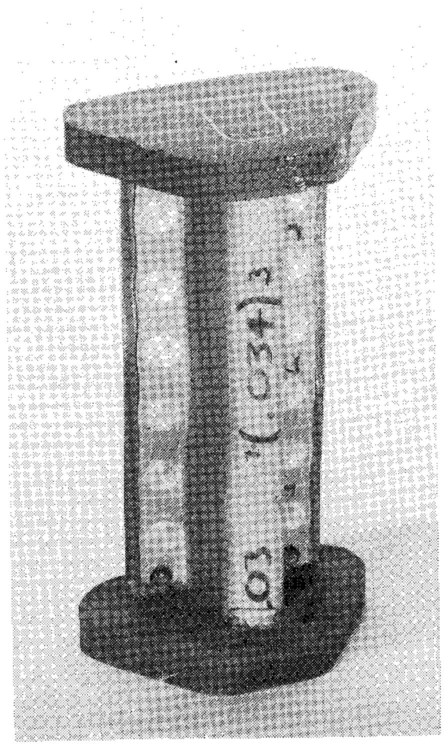

SPECIMEN	THICKNESS, mm	FAILURE LOAD, kN	PREDICTED LOAD, kN
1	6.9	43.8	50.8
2	6.9	49.5	50.8
3	8.6	73.0	67.3
4	8.6	76.4	67.3

Figure 10

ORBITER SHEAR WEB

(Figure 11)

A composite-reinforced shear web is being designed to withstand representative orbiter loadings by The Boeing Company (under NASA Contract NAS1-10860). A guideline for this study was consideration of solid, nonbuckling, shear-carrying webs, rather than open truss-work webs which were already under investigation. In preliminary studies, shear webs in the vehicle wing-root spars were found to be too lightly loaded to make selective reinforcement very effective. A heavily loaded web in the orbiter thrust structure was considered a more suitable candidate.

Figure 11 shows an early design concept and the vehicle location where representative loadings were determined. The concept shown is a titanium plate reinforced with skewed boron-epoxy-reinforced aluminum stiffeners. The concept is a "one-way" shear web which exploits the nature of thrust loading in the vehicle. Results of weight trade-offs between this construction and other concepts are shown in figure 12.

ORBITER SHEAR WEB

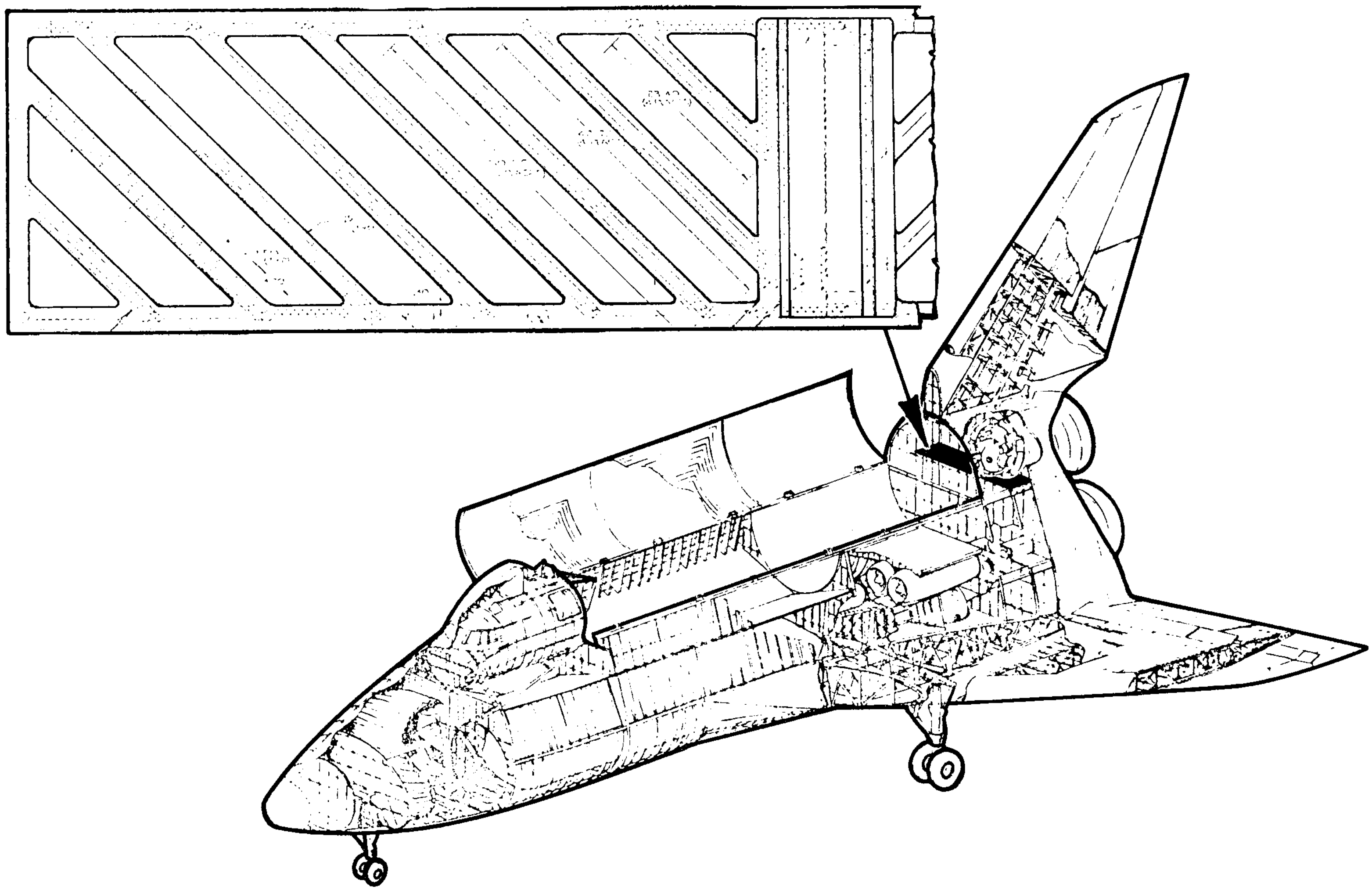

Figure 11

COMPOSITE-REINFORCED SHEAR-WEB CONCEPTS

(Figure 12)

In figure 12 the relative weights of various shear-web concepts are shown. Weights are based on design of a 1-meter-deep (40-inch), 2.5-meter-long (100-inch) shear web carrying a shear load of 1.3 MN/m (7.6 kips/in.). The concept shown in the left of the figure is the baseline all-metal design, a nonbuckling titanium web reinforced with aluminum T-stiffeners. Weights of other designs shown are normalized with respect to the metal design. The adjacent design shown is the skewed-stiffened (one-way) shear web discussed previously. The design was found to be about 11 percent lighter than the all-metal design and was not as efficient as anticipated. The next adjacent design shown is an improvement to the skewed-stiffener design obtained by employing a solid $\pm 45^{\circ}$ boron-epoxy web sandwiched between thin titanium face sheets. This configuration was the lightest weight design investigated. As a practical compromise, the more conventional design with reinforced T-stiffeners and a boron-epoxy titanium-clad web shown in the right of the figure was investigated. Its weight was found to be competitive with the best skew-stiffened design; thus, the boron-epoxy web appears to be supplying the major efficiency for the construction. Currently, the detail design and construction of this latter design is proceeding and, as shown, weight savings of roughly 30 percent are projected.

COMPOSITE-REINFORCED SHEAR-WEB CONCEPTS

CONCEPT

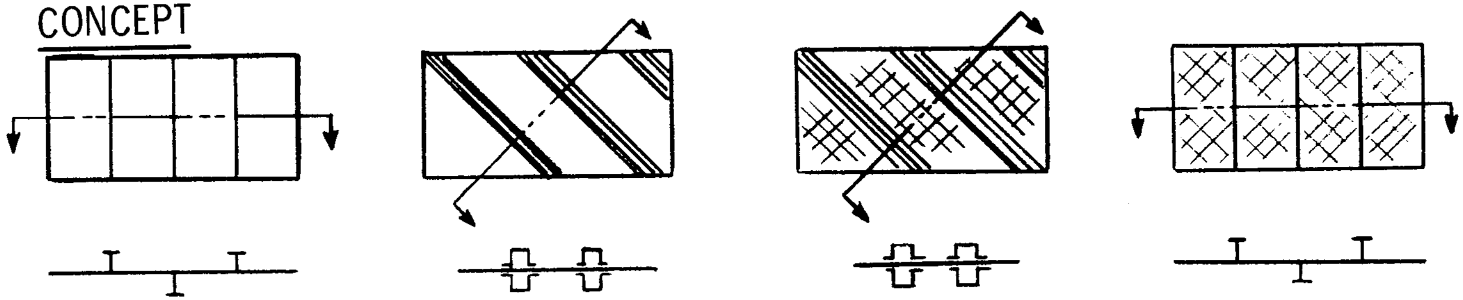

MATERIAL			
Ti WEB Al STIFFENERS	Ti WEB B/ E-REINFORCED Al STIFFENERS	B/ E WEB CLAD WITH Ti B/ E-REINFORCED Al STIFFENERS	
WEIGHT*			
1.00	0.89	0.69	0.71

*ALL WEIGHTS ARE NORMALIZED TO THE WEIGHT OF THE ALL-METAL SHEAR WEB

Figure 12

ORBITER FUSELAGE FRAME

(Figure 13)

A large fuselage frame is being designed by The Boeing Company (under NASA Contract NAS1-10797). As shown in figure 13, a frame in the cargo bay has been selected. Because of the payload space requirements, the frame is very large with a 9.1-meter (30-foot) base and a 3.9-meter (12.7-foot) height. The structural function of the frame is to provide adequate deflectional constraint to the fuselage panels, the cargo door, and, in some instances, the cargo. As shown, the configuration being studied is an I-frame with a metal web and a solid tension flange and sandwich compression flange. The construction is largely titanium with tapered composite strips used to reinforce the tension and compression flanges. The present design has achieved a 29-percent weight saving over an optimized all-titanium design. Plans are to construct a 1/3-scale model (1.5 by 1.2 meters (5 by 4 feet)) of half of the frame for test.

ORBITER FUSELAGE FRAME

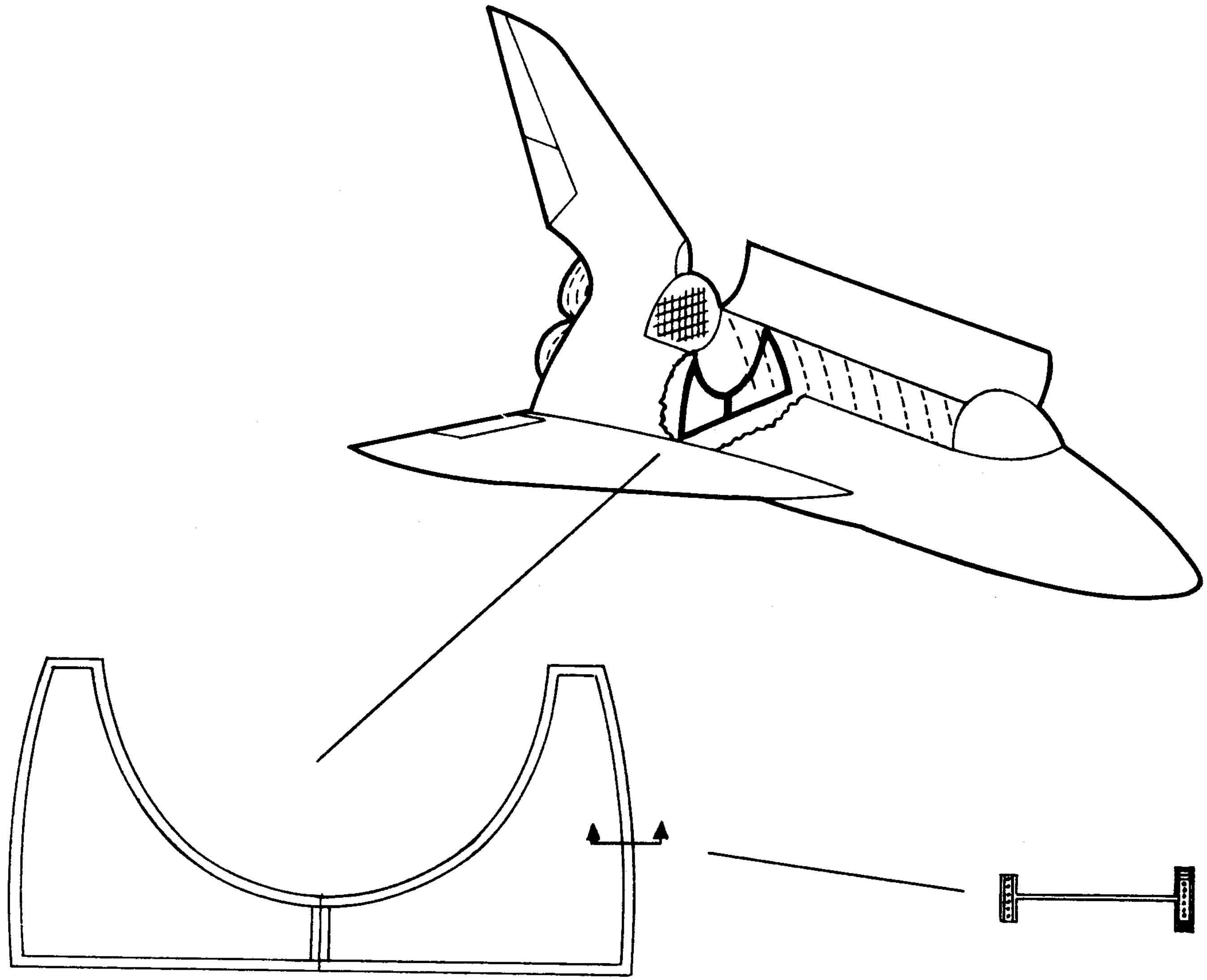

Figure 13

METAL-COMPOSITE LOAD TRANSFER

(Figure 14)

To evaluate design details in the frame construction, an investigation of the stepped titanium-boron-epoxy joint shown in figure 14 was conducted. The effects of including or excluding adhesive between the titanium and boron-epoxy was investigated by a series of static joint tests. Results for static tests at ambient and elevated temperatures are shown in the figure. The adhesive was found to improve the joint performance substantially.

This system was adopted and fatigue tests at ambient and elevated temperatures were conducted. Results are summarized in the bar graph in the figure. Cyclic tests at ambient temperatures in which 400 cycles of two-thirds ultimate static strength were applied showed only a slight decrease in residual fiber strength. Similar tests at elevated temperature showed that an adequate strength was retained.

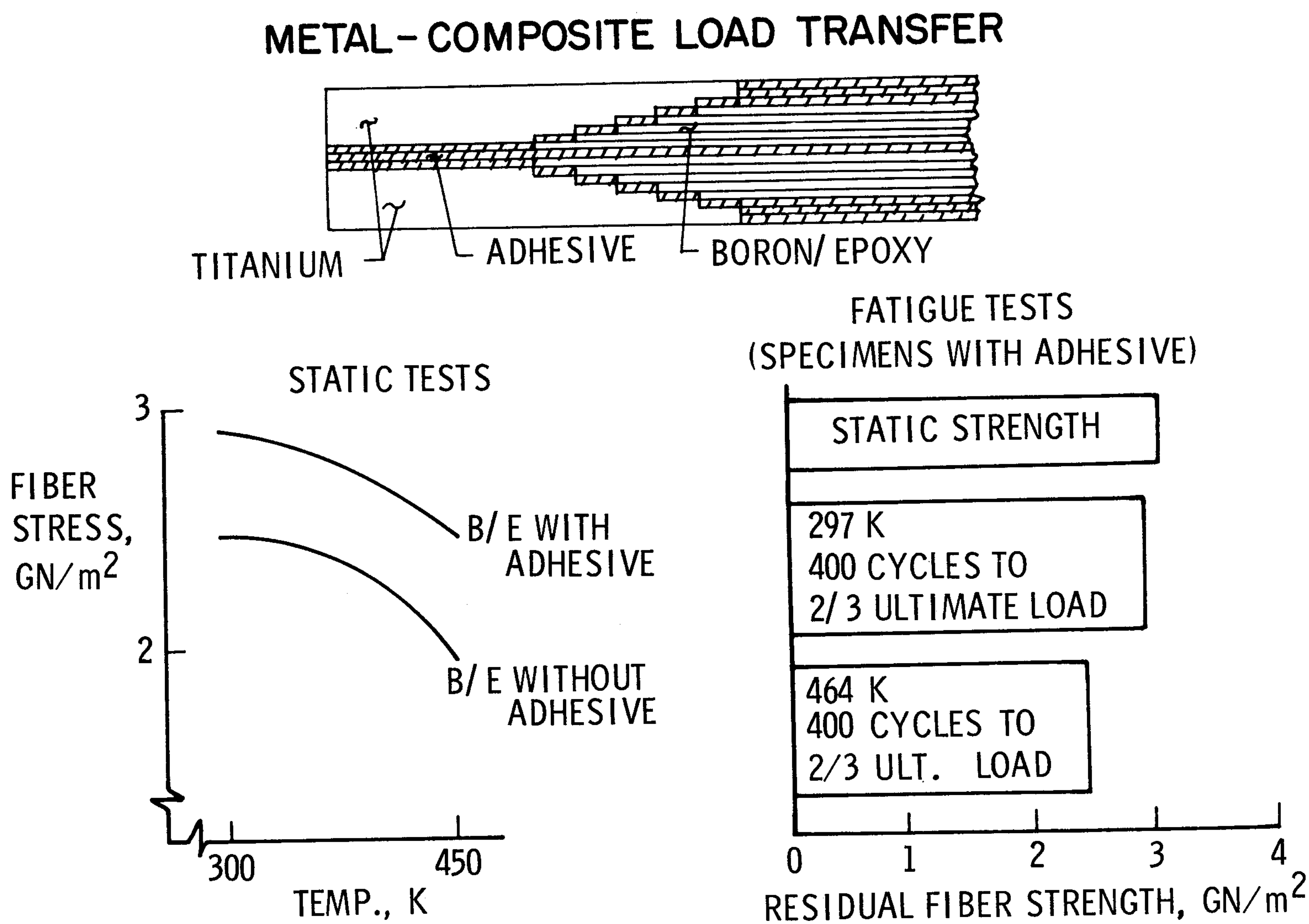
METAL-COMPOSITE LOAD TRANSFER
TITANIUM
ADHESIVE
BORON/EPOXY
STATIC TESTS
FIBER STRESS, GN/m2
3
2
300
450
TEMP., K
B/E WITH ADHESIVE
B/E WITHOUT ADHESIVE
FATIGUE TESTS
(SPECIMENS WITH ADHESIVE)
STATIC STRENGTH
297 K
400 CYCLES TO
2/3 ULTIMATE LOAD
464 K
400 CYCLES TO
2/3 ULT. LOAD
0
1
2
3
4
RESIDUAL FIBER STRENGTH, GN/m2

Figure 14

ORBITER LANDING-GEAR DOOR

(Figure 15)

A study by McDonnell Douglas Astronautics Company (under NASA Contract NAS1-10785) of the design of an orbiter landing-gear-door assembly is near completion. Composite reinforcement of the door together with an actuator mechanism is being considered. As shown in figure 15, the actuator consists of a triangular shaped beam and a tubular rod. The door dimensions are approximately 4.5 by 1.5 meters (15 by 5 feet). In order to satisfy tire temperature limitations, the door structural temperature must not exceed 366 K (200° F). Design loads for the door come from external aerodynamic pressures together with concentrated loadings on a "jammed" door introduced by the actuator. Various structural concepts for the door have been investigated, and results are summarized in figure 16.

ORBITER LANDING-GEAR DOOR

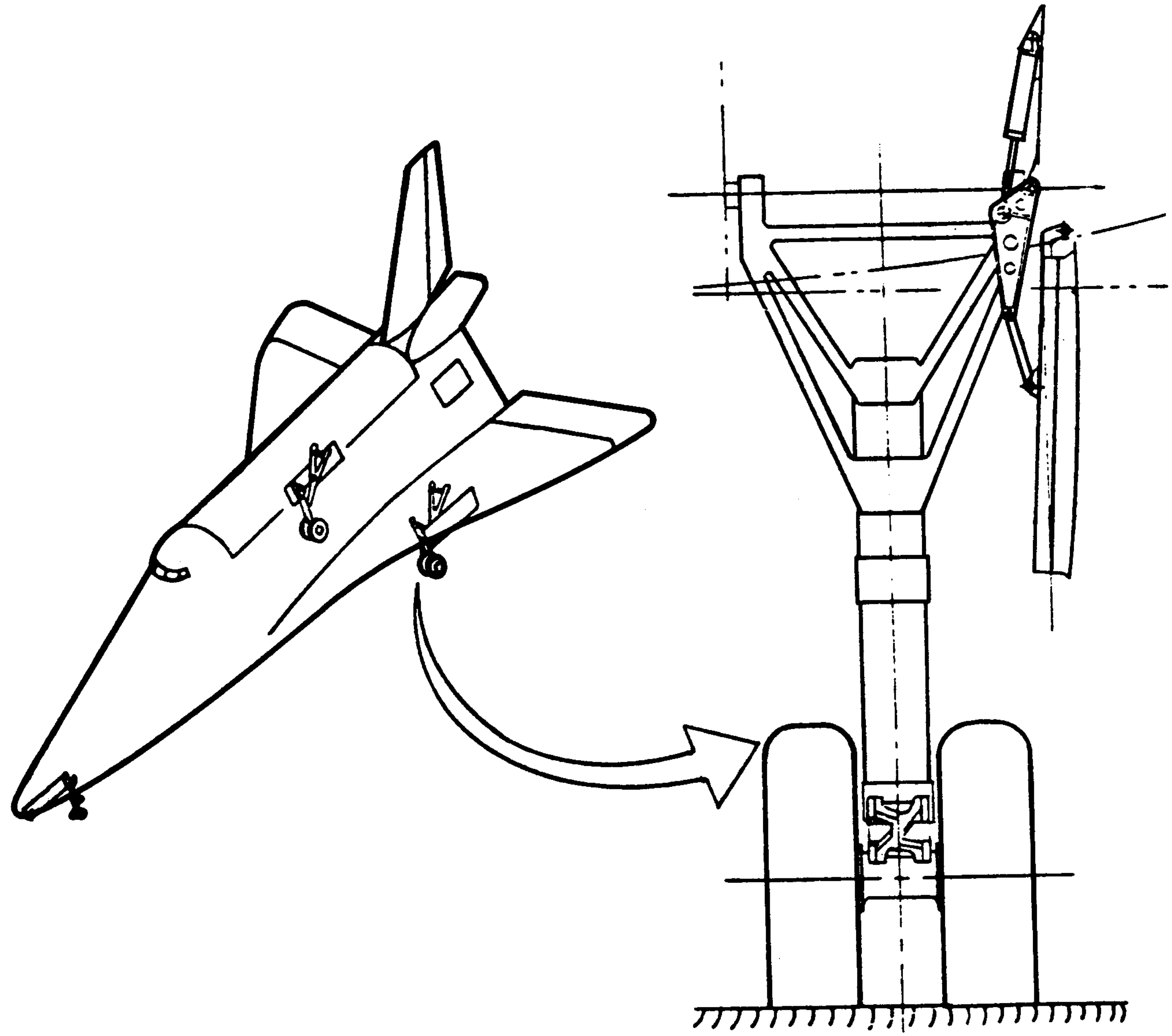

Figure 15

COMPARISON OF LANDING-GEAR-DOOR DESIGN CONCEPTS

(Figure 16)

Total weights of various design configurations are shown in figure 16. The baseline metal design was a titanium channel-stiffened plate. Selective composite reinforcement of this plate yielded weight savings of about 15 percent. This saving was not considered adequate, so more exotic types of construction were investigated. An aluminum honeycomb sandwich was found to be significantly lighter, and a graphite-epoxy sandwich with a metallic honeycomb core was judged to be the superior design. Detail design of this latter concept has been completed, and a 1.4- by 0.8-meter (4.5- by 2.75-foot) door section has been constructed and will be tested.

COMPARISON OF LANDING-GEAR-DOOR DESIGN CONCEPTS

MATERIALS	ALL TITANIUM	B/E - Ti	Al HONEYCOMB	G/E HONEYCOMB
DESIGN	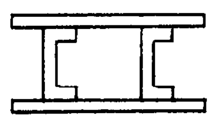	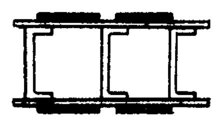		
WEIGHT	156 kg	133 kg	89 kg	82 kg

Figure 16

CONCLUDING REMARKS

(Figure 17)

Current results from a program to develop advanced structural concepts for shuttle airframe structure have been reviewed. Results of these studies suggest that weight savings of the order of 25 percent are feasible with such concepts. Metallic beaded panels for fuselage and skin structure appear to have good structural efficiency when compared with conventional construction. In order to achieve such efficiency, however, new design methods must be developed and careful attention must be paid to detail design problems. Studies of several composite-reinforced-metal components also suggest that weight savings can be achieved with only modest amounts of reinforcement. Manufacturing quality control for tnis type of construction appears to be the most serious obstacle to success.

CONCLUDING REMARKS

- STUDY OF ADVANCED CONCEPTS INDICATE 25% WEIGHT SAVINGS
- ANALYTICAL STUDIES ON METALLIC BEADED PANELS
  - STRUCTURALLY EFFICIENT DESIGN
  - REQUIRE FURTHER DEVELOPMENT
- COMPOSITE-REINFORCED-METAL STRUCTURAL COMPONENTS
  - MODEST USE OF COMPOSITES - LIGHTER STRUCTURE
  - QUALITY CONTROL STILL OF CONCERN

Figure 17

REFERENCE

1. Corvelli, N.; and Carri, R. L.: Evaluation of a Boron/Epoxy Reinforced Titanium Tubular Truss for Application to a Space Shuttle Booster Thrust Structure. AIAA Paper No. 72-393, Apr. 1972.

APPLICATION OF COMPOSITE MATERIALS TO SPACE SHUTTLE TANKS

By James R. Faddoul
NASA Lewis Research Center
Cleveland, Ohio

APPLICATION OF COMPOSITE MATERIALS TO SPACE SHUTTLE TANKS

The definitions necessary to this composite tank technology discussion are presented in the first slide. A tank as discussed here is a closed vessel that contains fluid under pressure. Tanks can then be broken down into two categories: pressure vessels, those tanks that carry primarily pressure loads; and structural tanks, those tanks that carry structural loads such as thrust or bending in addition to pressure. A significant portion of the Shuttle orbiter structure will be tanks and in order to minimize both weight and cost growth on these Shuttle tank structures, NASA has expended a considerable effort on composite tanks of both types. This presentation is a review of the status of the technology that has resulted from those efforts and begins with a discussion of the pressure vessel type tanks. The next slide will then provide an overview of what a composite pressure vessel is and what some of the problems associated with them are.

APPLICATION OF COMPOSITE MATERIALS TO SPACE SHUTTLE TANKS

DEFINITIONS:

TANK - A CLOSED VESSEL USED FOR CONTAINMENT OF FLUIDS UNDER PRESSURE

PRESSURE VESSEL - A TANK IN WHICH THE ONLY SIGNIFICANT LOADS CARRIED ARE DUE TO PRESSURE

STRUCTURAL TANK - CONTAINS FLUIDS UNDER PRESSURE AND CARRIES SIGNIFICANT STRUCTURAL LOADS

GLASS FIBER FILAMENT WOUND PRESSURE VESSEL

Due both to early development and many commercial applications, the state-of-the-art of glass fiber technology has become well advanced and virtually all the work covered by this presentation has used glass fibers. However, the actual problem shown here is typical of all filamentary composites--glass or otherwise.

In the typical makeup of a composite pressure vessel, the pressure loads are primarily carried by filaments embedded in a resin matrix. Stressing of the composite results in the formation of small cracks that can permit the contained fluid to leak out--usually an unacceptable situation. In order to prevent this, a liner is required. Polymeric materials can be, and indeed, have been, used for room temperature applications and where permeability is not a problem. However, for cryogenic temperatures where polymerics become brittle and exhibit insufficient entensibility, or at high pressures where permeation is a problem, metal liners must be used. A strain mismatch problem does however exist between a metal liner and the glass composite. The liner and glass composite have significantly different elastic strain characteristics: ≈ 2 percent elastic for the composite and only 0.5 percent elastic for metals. NASA efforts to solve this problem have resulted in two different solutions, one of which is illustrated in the next slide.

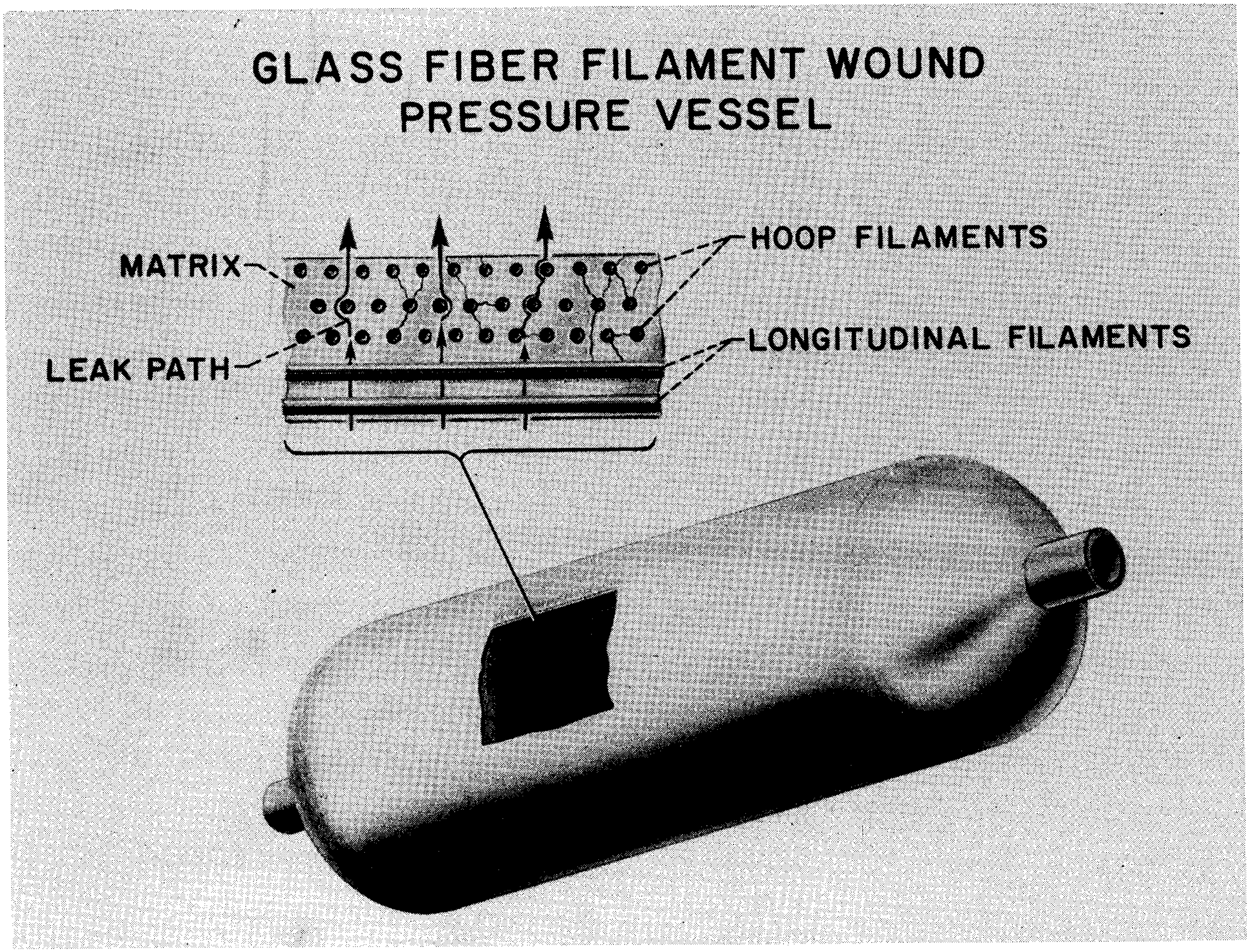
GLASS FIBER FILAMENT WOUND
PRESSURE VESSEL
MATRIX
LEAK PATH
HOOP FILAMENTS
LONGITUDINAL FILAMENTS

STRESS-STRAIN CURVE FOR FILAMENT-OVERWRAPPED METALLIC PRESSURE VESSELS

The mismatch in the stress-strain curves for the metal liner and filament overwrap is readily apparent in this figure. The filament curve is linearly elastic out to the proof strain and even beyond to burst. On the first cycle, the metal stress-strain curve shows an early yield and plastic flow at about 1/5 of the required proof strain. As the vessel proof pressure is released, the liner which has taken on a permanent plastic set is forced into compression by the filaments trying to return elastically to their original size. Thus, at zero pressure after proof, the metal is in compression and the filaments in tension. From that time on, the metal operates elastically from compression to tension while the filaments operate in a tension-tension mode. The terminology used to refer to this type of tank is a GFR (glass fiber reinforced) or load bearing metal liner concept. This concept has been demonstrated on various liner materials including Inconel, aluminum, cryoformed 301 stainless steel, and 4130 steel. Feasibility has been demonstrated with titanium. A more simple version of this concept, the overwrapping of the cylindrical section of a pressure vessel, has been demonstrated on aluminum; maraging, D6ac, and 4130 steels; and Inconel. The next slide shows the programs and documentation which have supported this technology.

STRESS-STRAIN CURVE FOR FILAMENT-OVERWRAPPED METALLIC PRESSURE VESSEL

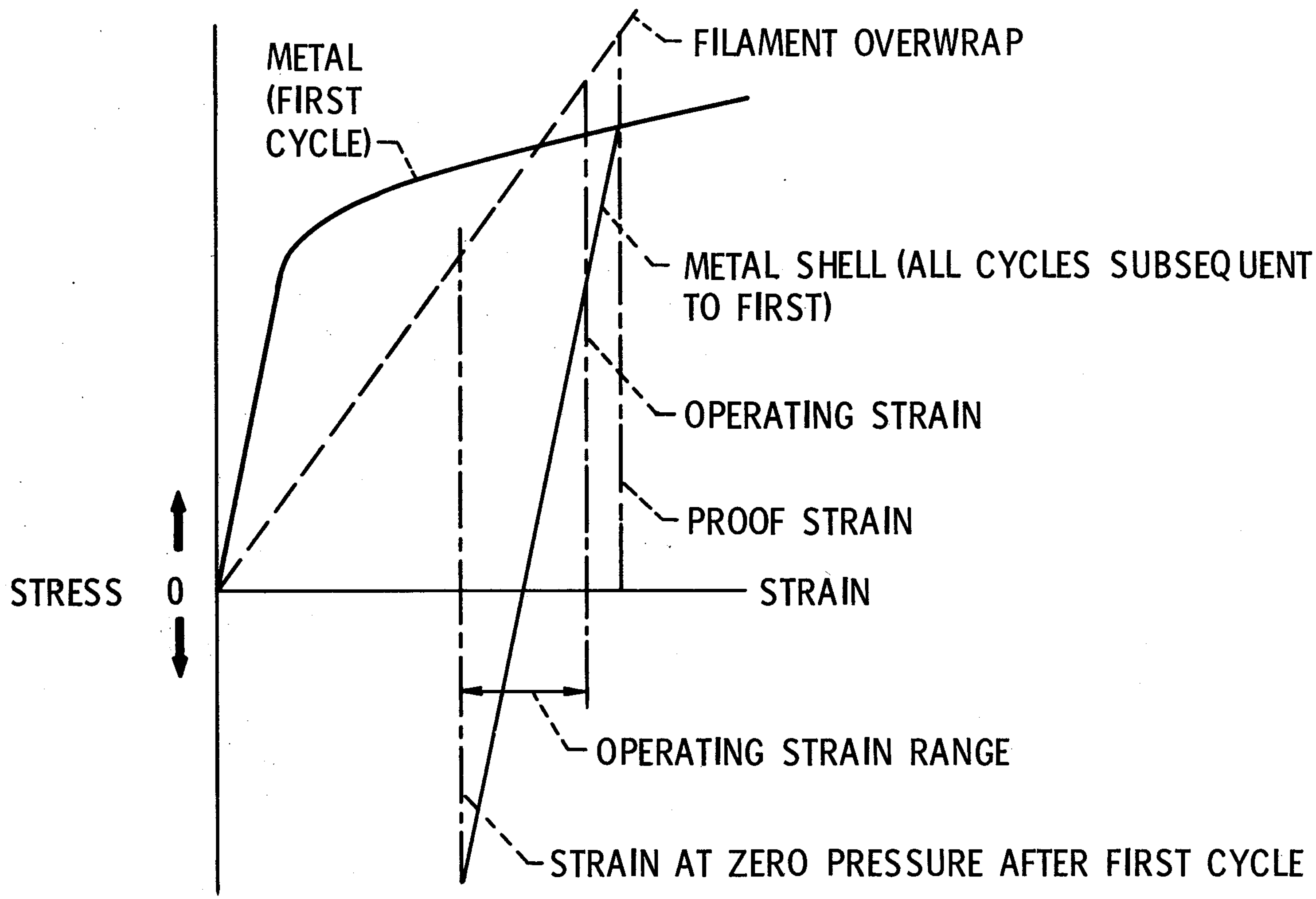

579

LOAD BEARING LINER DEVELOPMENT PROGRAM HISTORY

As the slide indicates, a number of different liner materials have been investigated in support of the load bearing liner technology. In each case, the weight savings shown in the conclusion column compares the resulting composite vessel to a similar homogenous metal vessel. Also, in the program objective column, H.W. refers to hoopwrapped and those programs that do not carry the H.W. designation are completely overwrapped.

REPORTS:

1. The Filament-Reinforced Motor Case. C. N. Odell, Aerospace Eng. Mag., April 1962.
2. Prestressed Fiber-Metal Cylindrical Pressure Vessels. F. Wolff, ASME Paper 63-AHGT-70, 1963.
3. Glass Filament Reinforced Homogenous Chambers. Aerojet General Report MF-546, 25 March 1964.
4. Fabrication and Test of Steel Lined Glass Filament-Wound Tanks. Aerojet General Report 2994, January 1965.
5. Filament-Overwrapped Metallic Cylindrical Pressure Vessels. Johns and Kaufman, NASA-LeRC AIAA/ASME Seventh Structures and Materials Conference Proceedings, April 1966, p. 52. (Also NASA TM X-52171.)
6. Parametric Study of Glass-Filament-Reinforced Metal Pressure Vessels. Morris et al, Aerojet General; Contract NAS3-6292; NASA CR 54-855; April 1966.
7. Glass-Fiber-Reinforced Metallic Tanks for Cryogenic Service. E. E. Morris, Aerojet General; Contract NAS3-6292; NASA CR-72224; June 1967.
8. Composite Tankage Developments. Aerojet General/SCI Report 3697, January 1969.
9. Development of a Filament-Overwrapped Cryoformed Metal Pressure Vessel. D. Gleich, Arde Inc.; Contract NAS3-11194; NASA CR-72753; January 1971.
10. Composite Overwrapped Metallic Tanks. Feldman and Holston, Martin/Denver; Contract 12023; NASA CR-72765; October 1971.
11. Fiberglass Overwrapped 2219-T87 Al Alloy Low-Pressure Cryogenic Tankage. B. Aleck, Grumman Aerospace; SAMPE Technical Conference; Vol. 3, p. 131; October 1971.

LOAD BEARING LINER DEVELOPMENT PROGRAM HISTORY

LINER MATERIAL	PROGRAM OBJECTIVES	CONCLUSION	REPORTS
7178-T6 Al	HOOP WRAP (HW), DESIGN FAB & TEST (DF&T) (15.24cm)	35% LIGHTER	1. AERO.ENG.MAG. 1962
4130 STEEL	HW DF&T (16.76 cm)	30% LIGHTER	2. ASME PAPER #63-AHGT-70
4130,D6ac & MARAGING STEEL	HW DF&T (20.32 & 45.72 cm)	40% LIGHTER	3. AEROJET GEN RPT#MF-546
4130 STEEL	DF&T (45.72 x 144.78 cm)	40% LIGHTER	4. AEROJET/SCI RPT#2994
2014-T6 Al	HW DF&T (14.2 cm)	50% LIGHTER	5. NASA TMX 52171
INCONEL X750	PARAMETRIC STUDY & DEMONSTRATION (45.72 cm)	15% LIGHTER	6-7. NASA CR's 54-855 AND 72224
TITANIUM 5Al-2.5Sn	DF&T (40.64 x 68.58 cm)	EQUAL WT (FEASIBILITY)	8. AEROJET/SCI RPT#3697
INCONEL 718/6061-T6 Al	DF&T (45.72/16.76 cm)	30%/25% LIGHTER	8. AEROJET/SCI RPT#3697
CRYOFORMED 301 (ARDEFORM)	DF&T (33.02 cm)	15% LIGHTER	9. NASA CR 72753
TITANIUM 5Al-2.5Sn	DF&T (625 cm)	EQUAL WT (FEASIBILITY)	10. NASA CR 72765
2219 Al/INCONEL/ARDEFORM	FLAW GROWTH PROGRAM	-----	*
2219 Al	QUALIFICATION DEMONSTRATION (3 SHAPES)	15 TO 45%	*
2219-T87 Al	HW DF&T (33.02 cm)	20% LIGHTER	11. SAMPE VOL 3 1971

*Programs currently active with no formal reports available

PRESSURE VESSEL PERFORMANCE FACTOR FOR HOMOGENOUS AND GFR METAL PRESSURE VESSELS

Since the potential for composite pressure vessels to minimize weight growth has been one of the main reasons for pursuing the technology, the information presented in this chart provides a comparison of the pressure vessel efficiency of GFR concepts to the corresponding homogenous metal vessel design. This efficiency is expressed in terms of a performance factor P_oV/W where P_o is the operating pressure, V is volume and W is weight. For a homogenous metal, the efficiency is directly proportional to the strength-to-density ratio with the proportionality constant being a function of shape. As indicated in the figure, the most efficient all-metal shape is a sphere where $\frac{P_oV}{W} = \frac{2}{3}\frac{\sigma}{\rho}$, while the least efficient all-metal shape is a long cylinder where $\frac{P_oV}{W}$ approaches $\frac{1}{2}\frac{\sigma}{\rho}$. The reverse is generally true for the GFR concept since the composite is most efficient as a unidirectional circumferential reinforcement. Note that in the case of 2219 Al, only a cylindrical wrap is shown by the GFR bar since due to both the strain mismatch and aluminum buckling allowable, it is not always advantageous to use a complete overwrap. Also, since the processing of a GFR-cryoformed 301 cylinder will present problems which have not yet been addressed, only the spherical GFR shape is shown. The main point is, however, that in all cases, appreciable efficiency increases or weight reductions are possible through application of composite technology. The magnitude of these advantages and the effect of shape on weight is shown more vividly on the next slide.

PRESSURE VESSEL PERFORMANCE FACTOR FOR HOMOGENOUS AND GFR METAL PRESSURE VESSELS

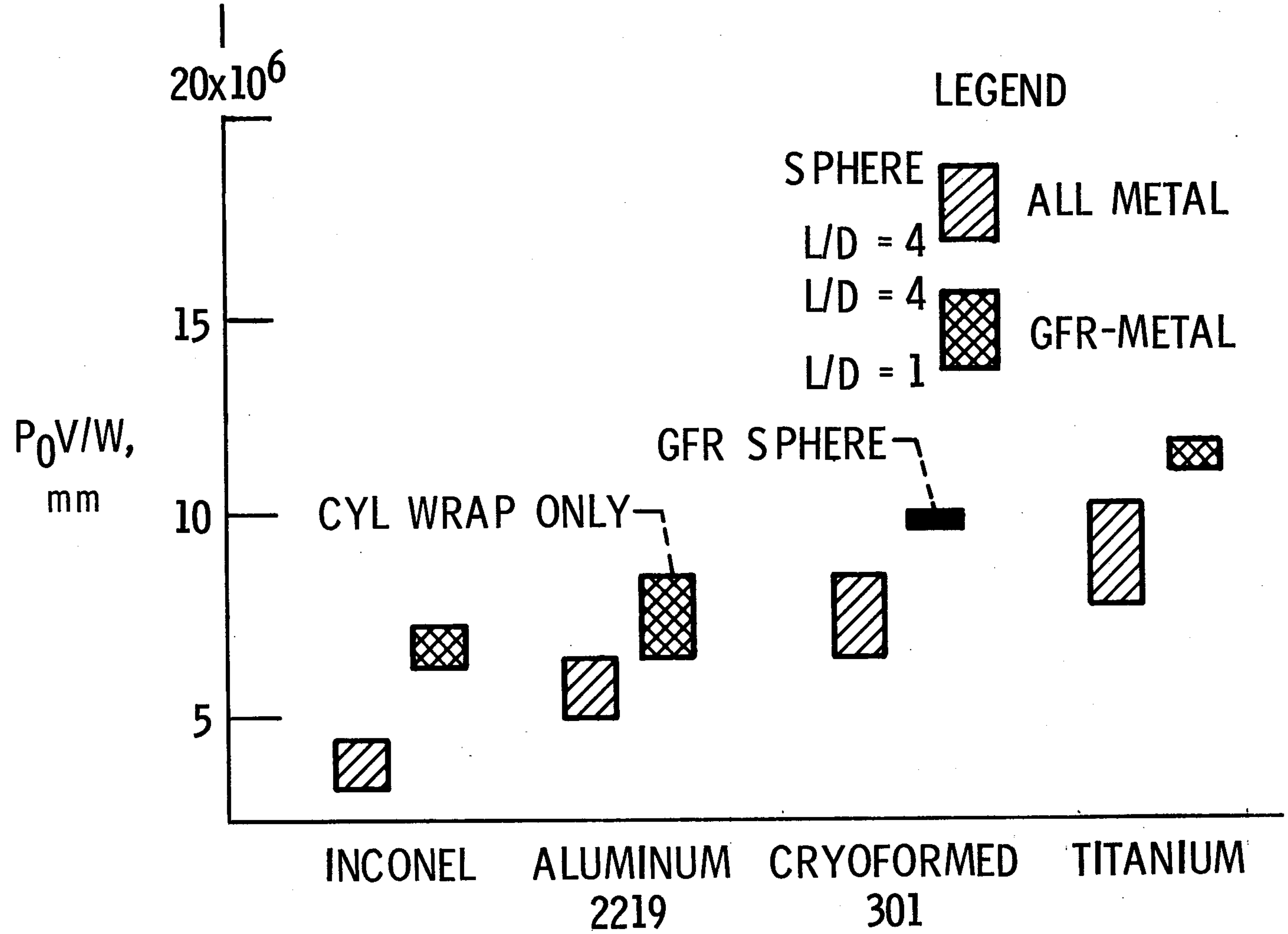

SUPERCRITICAL TANK WEIGHTS

The upper curve on this graph represents the weight of an all-aluminum pressure vessel operating at 2.758 MN/m^2 (400 psi) as a function of the length to diameter ratio. The L/D = 1 represents a sphere with a 1.27 m (50.8 in) radius or a volume of 8.9 m^3 (314 ft^3). The curve in the center represents the weight of a circumferentially wrapped aluminum cylinder. The bottom line represents the limiting case of composite pressure vessels, i.e., an all-composite tank with thin permeation barrier type liner. Referring to the righthand scale, the all-aluminum sphere with L/D = 1 has a weight of about 650 pounds. If a cylinder with an L/D = 4 were required due to envelope constraints, the weight of the cylindrical all-aluminum vessel would be 27 percent or 175 pounds greater than the equivalent sphere. Designing the same L/D = 4 cylinder with a hoopwrapped glass composite allows a savings of 115 kg (250 lb) or 30 percent and the hoopwrapped cylinder (even a short cylinder) weighs appreciably less than the all-aluminum sphere. The all-composite tank has a potential for a minimum 46 percent weight saving over the aluminum sphere.

The potential weight and packaging advantages of composite pressure vessels have been shown in the preceding slides, but another and perhaps even greater potential advantage of composite vessels is shown in the next slide.

SUPERCRITICAL TANK WEIGHTS

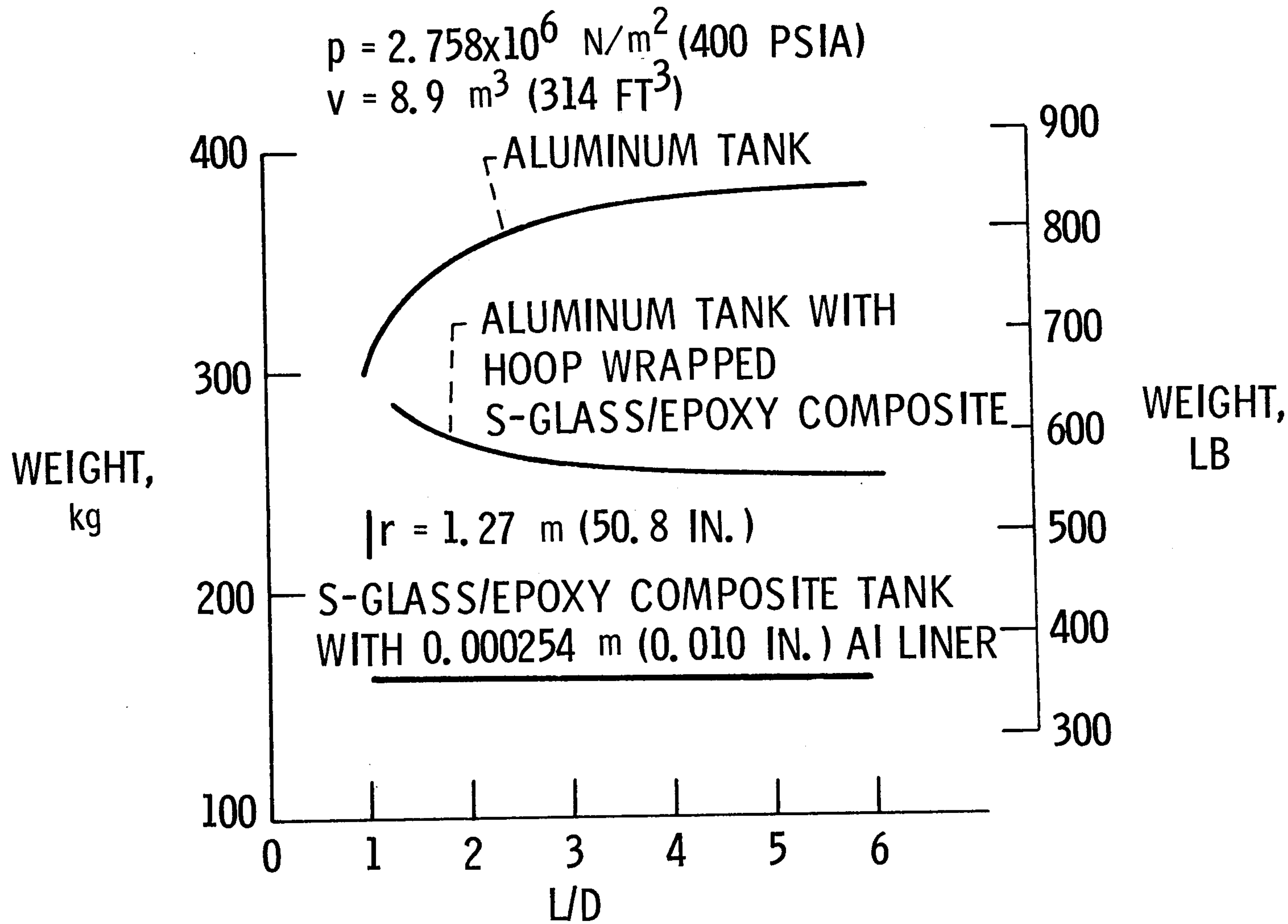

COMPOSITE PRESSURE VESSEL FAILURE MODE CONTROL

Two pictures of the same failed pressure vessel are shown here. The picture on the left was taken after the tank was removed from the burst test fixture. The tank was then sectioned for examination of the shattered metal liner as shown in the righthand photo. The composite overwrap completely contained all these fragments and the only evidence of failure was the rapid pressure loss. Had this been an all-metal tank, the metal fragments would have had an effect on surrounding structures (or personnel) similar to a hand grenade. Thus, composite tanks can provide a means of minimizing the probability of loss of a vehicle because of the loss of a tank.

As shown in this and previous slides, the GFR concept has a number of potential advantages and there have been numerous technology efforts directed at exploiting those advantages. Thus, the GFR concept has rapidly moved to an advanced state of development. However, one area of this technology which requires extensive study concerns the effect of the plastic sizing cycle on the resulting metal properties. Of primary concern is the effect of the high plastic strain on flaws in the metal, and since analytical techniques are insufficiently developed, an empirical program has been undertaken. The primary objective of this program is to determine how flaws in the metal liner will respond to the plastic sizing cycle and subsequent operational cycles at various stress levels. Liner materials of 2219-T62 Al, Inconel X-750, and Cryoformed 301 stainless steel are currently being investigated. The specific data being generated includes mechanical properties, critical flaw sizes at proof and operating, and flaw growth rates at various stress levels. When this data is then applied to pressure vessel designs, the typical results shown in the next slide result.

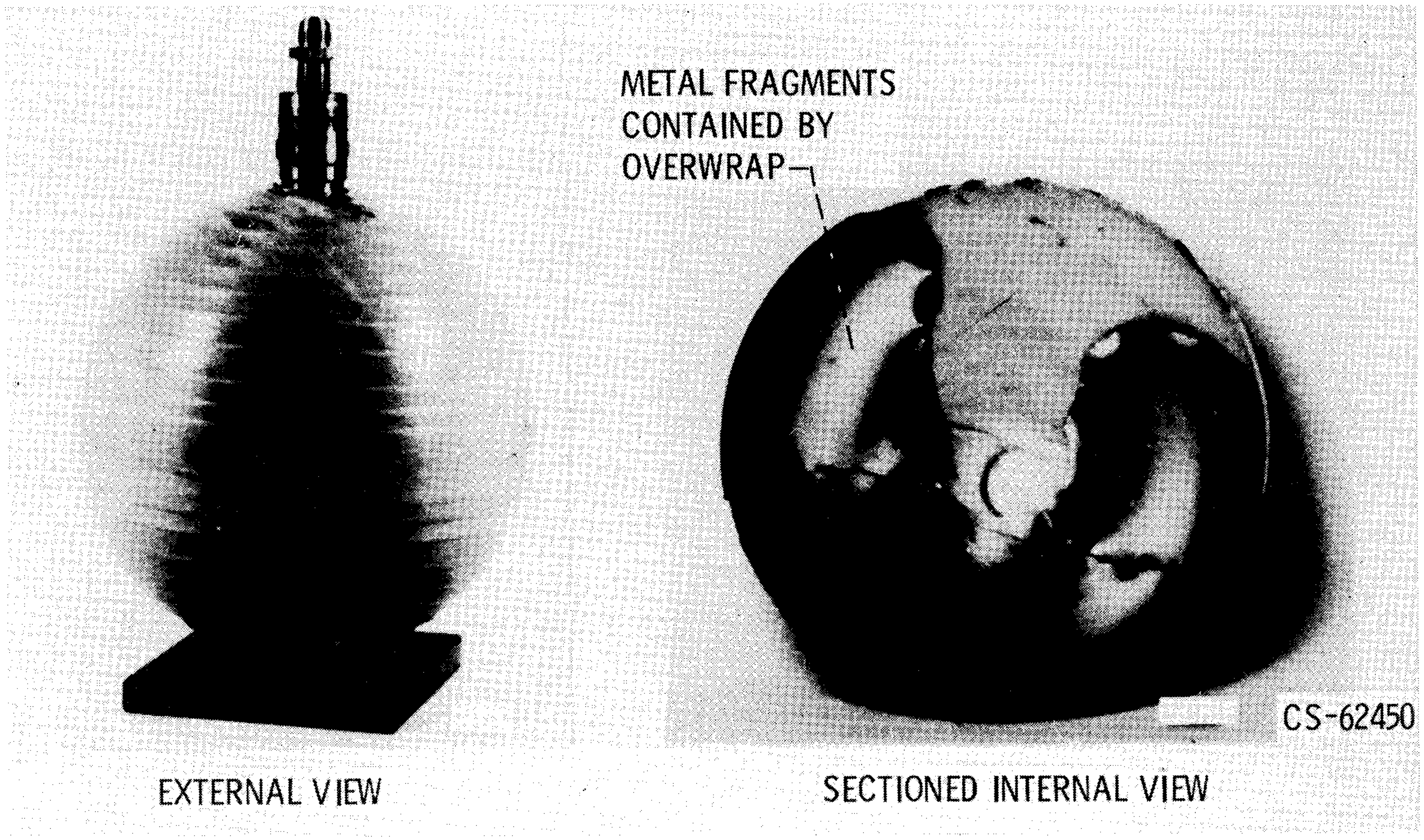

Composite pressure vessel failure mode control.

2219-T62 Al CYLINDER DESIGNS BASED ON FRACTURE PROGRAM RESULTS

Shown here are the more important parameters for a GFR and a homogenous 16.5 cm (6.5-in) 2219-T62 Al cylinder designed for 2000 cycles at 12.7 MN/m^2 (1840 psi). The first two items shown are the proof to operating pressure and metal (liner or homogenous) stress ratios. For the homogenous aluminum, they are identical while the GFR design permits a higher liner stress ratio for a lower vessel pressure ratio. This condition develops because the deflection versus pressure relations of the liner and overwrap are different as illustrated in the third figure. However, due to the high liner proof stress inherent in the GFR concept to achieve the required liner compressive stress, the operating stress is about 33 MN/m^2 (5 ksi) higher than the all-metal cylinder. Because of the high proof stress the flaw size (a_{cr}) screened by proof is .117 cm (.046-in) for the GFR case and about three times as large, .325 cm (.128-in) for the all-metal case. In both vessels, the critical flaw size is large enough to suggest that the proof failure rate will not be unreasonably high. The ratio of the critical flaw size to the wall thickness (t) is 11 percent less for the GFR vessel. This means that as operating pressure or diameter requirement is allowed to decrease, other factors remaining constant, the all-metal design will reach a point where cyclic life cannot be guaranteed more rapidly than the equivalent GFR design. Or to express it another way, there will be a greater number of applications where the proof of the homogenous vessel will only demonstrate that there is no through-the-thickness flaw but leakage may occur on the next cycle while the equivalent GFR concept would proof out a finite number of cycles prior to leak or burst. The final entry to be noted is that the relative efficiency ϵ_r of the GFR design is potentially 70 percent greater than the all-metal design. This slide concludes the section on the GFR pressure vessel concept. The second concept for solving the liner problem in a glass composite pressure vessel is then illustrated in the next slide.

2219-T62 Al CYLINDER DESIGN BASED ON FRACTURE PROGRAM RESULTS

DIAMETER = 16.5 cm (6.5 IN.)

OPERATING PRESSURE = 12.7 MN/m^2 (1840 PSI)

CYCLES REQUIRED = 2000

	HOOPWRAPPED ALUMINUM DESIGN	HOMOGENOUS ALUMINUM
P_p/P_o	1.25	1.35
σ_p/σ_o	1.43	1.35
σ_o	231 MN/m^2 (33.6 KSI)	198 MN/m^2 (28.7 KSI)
a_{cr}	0.117 cm (.046 IN.)	0.325 cm (.128 IN.)
a_{cr}/t	51%	62%
ϵ_r	1.7	1.0

TYPICAL STRESS-STRAIN CURVE FOR FILAMENT-WOUND VESSEL WITH A THIN BONDED LINER

This approach, referred to as the thin bonded liner, uses the glass composite to carry all the loads and a thin metal liner only to prevent leakage. This is in contrast to the GFR concept where the metal liner carries a significant portion of the pressure loads. In the bonded liner approach, the liner is forced to flow plastically on both the pressurization and depressurization. Aluminum is currently being used as the liner since it is lightweight, readily available, and provides minimum fabrication problems. Since the liner is thin, it has little buckling stability. Buckling of the liner on depressurization is prevented, however, by bonding the liner to the composite wall. The capability of the bond has been demonstrated both by in-house and contracted NASA efforts. This technique produces the lightest weight glass filament-wound pressure vessels since the basic weight of the vessel consists of the highly efficient composite. However, the cyclic life of these vessels is severely limited by the high plastic strain cycle required for the thin bonded liner. In addition, local areas such as cylinder-to-dome junctures, and boss areas exhibit higher strains and even shorter cyclic life than the general membrane area. The use of high modulus filaments such as Boron or graphite, or PRD-49, which has a modulus twice that of glass, looks attractive for this concept since the total strain range of the liner would be greatly reduced and cyclic life should be increased appropriately. But even for a limited cyclic life requirement, there is still a need for further technology development on glass or high modulus composites before this concept could be used reliably for application to the early Shuttle vehicle auxiliary system pressure vessels. However, application of the thin bonded liner concept to barrel sections of single cycle tanks as in the Shuttle disposable HO structural tanks is a possibility that will be discussed shortly. Before discussion of the structural tanks, however, a final summary of the status of the pressure vessel technology programs--both GFR and thin bonded liner, as shown in the next slide--is in order.

TYPICAL STRESS-STRAIN CURVE FOR FILAMENT-WOUND VESSEL WITH A THIN BONDED LINER

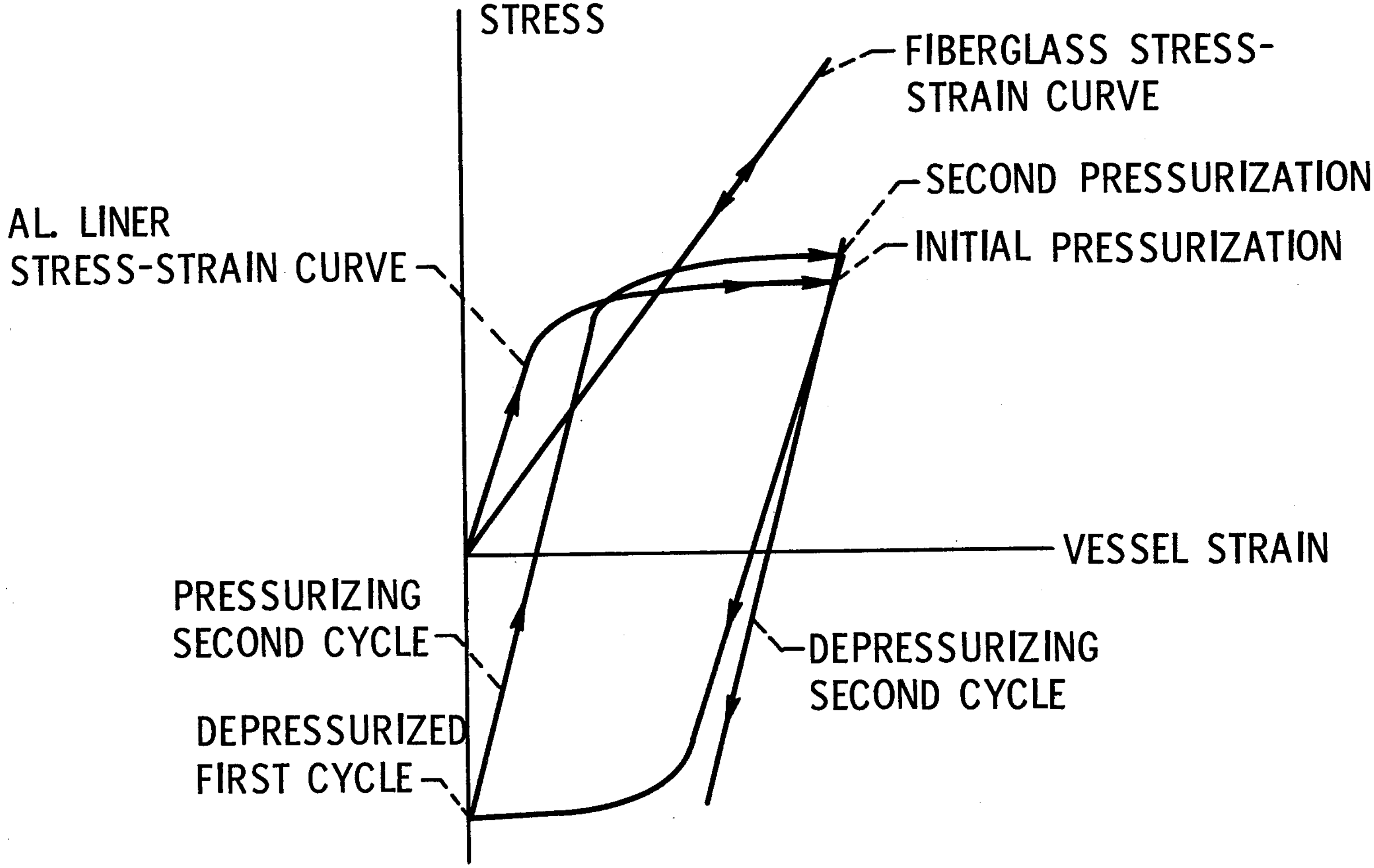

COMPOSITE PRESSURE VESSEL TECHNOLOGY STATUS

Here you see the past, present and future of composite pressure vessel technology. Note that for both the GFR and bonded liner concepts, there will be continuing efforts to obtain, extend, interpret, and improve the properties of the composite, including advanced fibers and matrix materials. Also, NDI applications for both the thin bonded liner and GFR concepts are currently being investigated. Techniques such as acoustic emission are being applied and this type of information will be a continuing output from future programs which will hopefully result in a complete NDI philosophy for failure prediction. Looking specifically at the GFR concept, the design concept has been verified and a number of specific configurations have been successfully tested. This has led to a current program which is just getting underway, that will design, fabricate, and test three configurations (one spherical and two different cylinders) to meet the pressure, volume, and cyclic environment requirements of a piece of real hardware. The fracture philosophy and design handbook are part of the current effort but a greater knowledge of fracture mechanisms will be required to fully optimize the GFR designs. This will require a continuing effort to obtain fracture data on specific materials and conditions. The final item of importance to the development of GFR technology would then be the development of a complete design philosophy to cover all materials and include items such as fracture, environmental effects, and factors of safety.

Looking specifically at the bonded liner concept, it is evident that since the liner bonding technique has been established, cyclic life is the main area of technical concern. Past programs have developed design techniques for boss and cylinder to dome transition areas that may potentially reduce much of the high local strains encountered. A current program is attempting to evaluate these techniques. However, it will still be necessary for future programs to demonstrate not only the reliability of the techniques but also improvements of designs and materials (such as PRD-49, boron and graphite fibers) that will provide increased cyclic life.

This ends the discussion of the pressure vessels; the next slide will thus provide an overview of structural tanks and highlight some of their attendant problems.

COMPOSITE PRESSURE VESSEL TECHNOLOGY STATUS

	TECHNOLOGY DEMONSTRATED THROUGH PAST PROGRAMS	CURRENT TECHNOLOGY PROGRAMS	FUTURE TECHNOLOGY REQUIRED
GFR CONCEPT:	COMPOSITE PROPERTIES	COMPOSITE PROPERTIES	COMPOSITE PROPERTIES
	DESIGN CONCEPT	FRACTURE PHILOSOPHY	FRACTURE DATA
	SPECIFIC CONFIGURATION	DESIGN HANDBOOK NDI TECHNIQUES FULL SCALE HARDWARE DEMONSTRATION	DESIGN PHILOSOPHY
THIN BONDED LINER CONCEPT:	COMPOSITE PROPERTIES	COMPOSITE PROPERTIES	COMPOSITE PROPERTIES
	LINER BONDING	NDI TECHNIQUES	NDI PHILOSOPHY
	HIGH STRAIN DAMPING TECHNIQUES	IMPROVED CYCLIC CAPABILITIES	HIGHER CYCLIC LIFE

STRUCTURAL TANKAGE (BUCKLING CRITICAL)

Shown in this slide is a series of typical all-metal configurations which may be candidates for a buckling critical orbiter LH_2 tank. Except for the monocoque shell, which is a simple concept but very weight inefficient in buckling, all of these concepts employ machined integral rings and/or stringers and are much more complex to fabricate than a pure pressure membrane type tank. Thus, all of these concepts are directly opposed to one or the other of the two primary requirements of the Shuttle orbiter disposable HO tanks: lightweight and low cost. A current NASA program is now exploring methods by which advanced composite technology may be applied to these complex tank structures as a possible means of minimizing both cost and weight growth.

STRUCTURAL TANKAGE (BUCKLING CRITICAL)

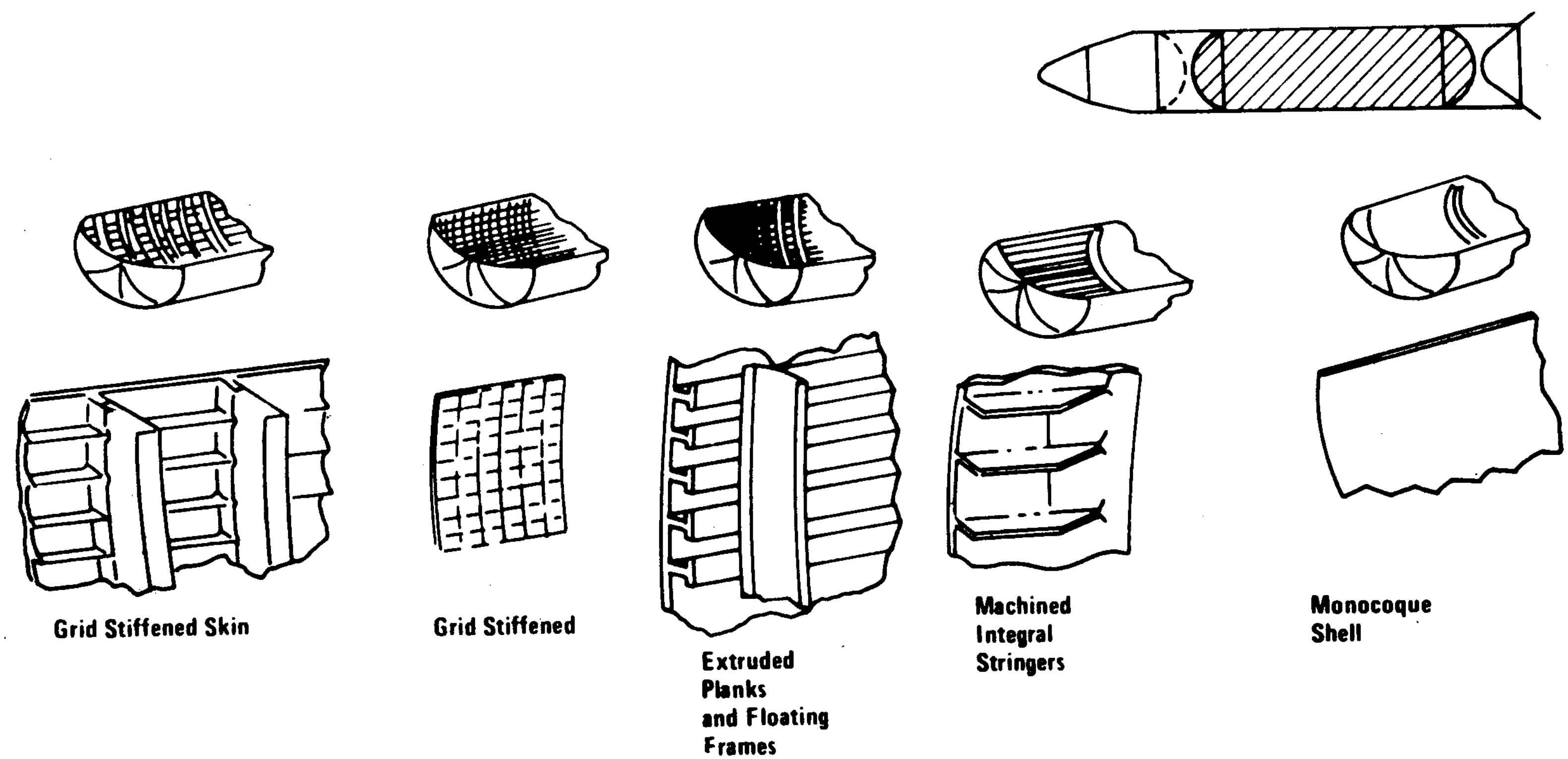

COMPOSITE REINFORCED PROPELLANT TANKS

The objective of this program has been to evaluate techniques whereby composite materials could be used efficiently on the Shuttle orbiter HO tanks. The primary emphasis has been to maximize the mass fraction since this will have a direct effect on payload. In addition, minimizing the fabrication costs has also been a driver and has led to almost exclusive use of glass fiber composites due to their low raw material cost. A third area where composites were believed to offer potential advantages was in providing cryogenic insulation. The approach used in evaluating composites for these applications was to initially select a number of potential configurations. Then, the most current loads data available from the prime Shuttle contract was used as input to automated structural analysis programs such as STARS II and BOSOR. Both static and stability conditions were evaluated to optimize the final configurations. Where materials properties input to the automated programs required an assumption, component tests of the materials or configurations in question were conducted to justify those assumptions. After the structural sizing of each concept, a comprehensive cost analysis was performed. This included all tooling and material costs along with quality control and management labor. The final structural sizing and costing is now complete and the Contractor is currently in the process of selecting a configuration for testing. Two 1.016 x 2.032 m (40 x 80-in) test sections will be fabricated and subjected to combined pressure, torsion, and bending, and shear loads at room and cryogenic temperatures. The next slide shows the composite configurations that resulted in potential cost or weight advantages.

COMPOSITE REINFORCED PROPELLANT TANKS

OBJECTIVE

ESTABLISH A BASIS FOR COMPOSITE APPLICATION TO THE DISPOSABLE H-O TANKS OF THE SHUTTLE ORBITER

CONSIDERATIONS

WEIGHT OF TANKS HAS DIRECT EFFECT ON PAYLOAD

MINIMUM FABRICATION COST IS ESSENTIAL

INSULATION EFFICIENCY OF COMPOSITE DESIGNS MAY BE AN ADDED ADVANTAGE

EVALUATION OF SEVERAL CONCEPTS WILL BE REQUIRED

SMALL SCALE COMPONENT TESTS USED TO SCREEN CONCEPT PRACTICALITY

1.016 x 2.032 m (40 x 80 IN.) COMBINED LOAD TEST MODELS OF SELECTED CONCEPT

CURRENT COMPOSITE HO TANK CONCEPTS

Shown here are four LH_2 tank composite concepts and one composite LOX tank concept. Each of these configurations has evolved through the Contractor cost and weight analyses of the previous program. Since the baseline LOX tank is designed by the high hoop loads produced by the fluid pressure during launch acceleration, the only composite configuration that applies is the simple GFR type hoopwrap to reduce the metal thickness. The potential advantage of this concept is shown to be a reduction of 20 percent in weight, but there is an attendant 90 percent penalty on cost due to the conical shape of this tank. The weights and cost savings for the LH_2 concepts are all compared to the integrally machined rings and stringers of the baseline concept shown. The most simple composite concept reduces the baseline membrane thickness by using a hoopwrap. This results in a slight weight advantage but costs more since all the fabrication of the metal remains and the overwrap must be added to that base. A more complex concept is the monocoque shell with overwrap stiffened by bonded rings and stringers. This concept has a potential advantage of 14 percent on weight and 49 percent on cost. The efficiency of bonding the reinforcement was initially assumed to be equal to riveted rings and stringers. This was later verified by a component test that carried more than 100 percent of the predicted failure load. The next LH_2 concept was a monocoque shell stabilized by a paper honeycomb with a composite outer face sheet. The potential advantages of this concept are -2 percent on weight and 65 percent on cost. The most complex composite concept replaces the monocoque aluminum of the honeycomb concept with a composite wall having a thin bonded aluminum liner. The technology required for successful application of a bonded liner for a single use cylinder has been demonstrated and was referred to in my discussion of the thin bonded liner pressure vessel concept. The projected advantages of this concept are 15 percent on weight and 75 percent on cost. For the honeycomb designs shown, the honeycomb was not considered a factor in the cryogenic insulation system. Further reduction in both weight and cost could be realized if the insulation effectiveness of the honeycomb was used to decrease the thickness of, or possibly eliminate, the required external foam.

On the basis of the potential advantages shown in this slide and the minimum technology development required, the honeycomb with aluminum inner face and composite outer face has been tentatively selected for testing. Should this testing be successful in demonstrating the potential of composite structural tank configurations, further research and development as outlined in the next slide may be warranted.

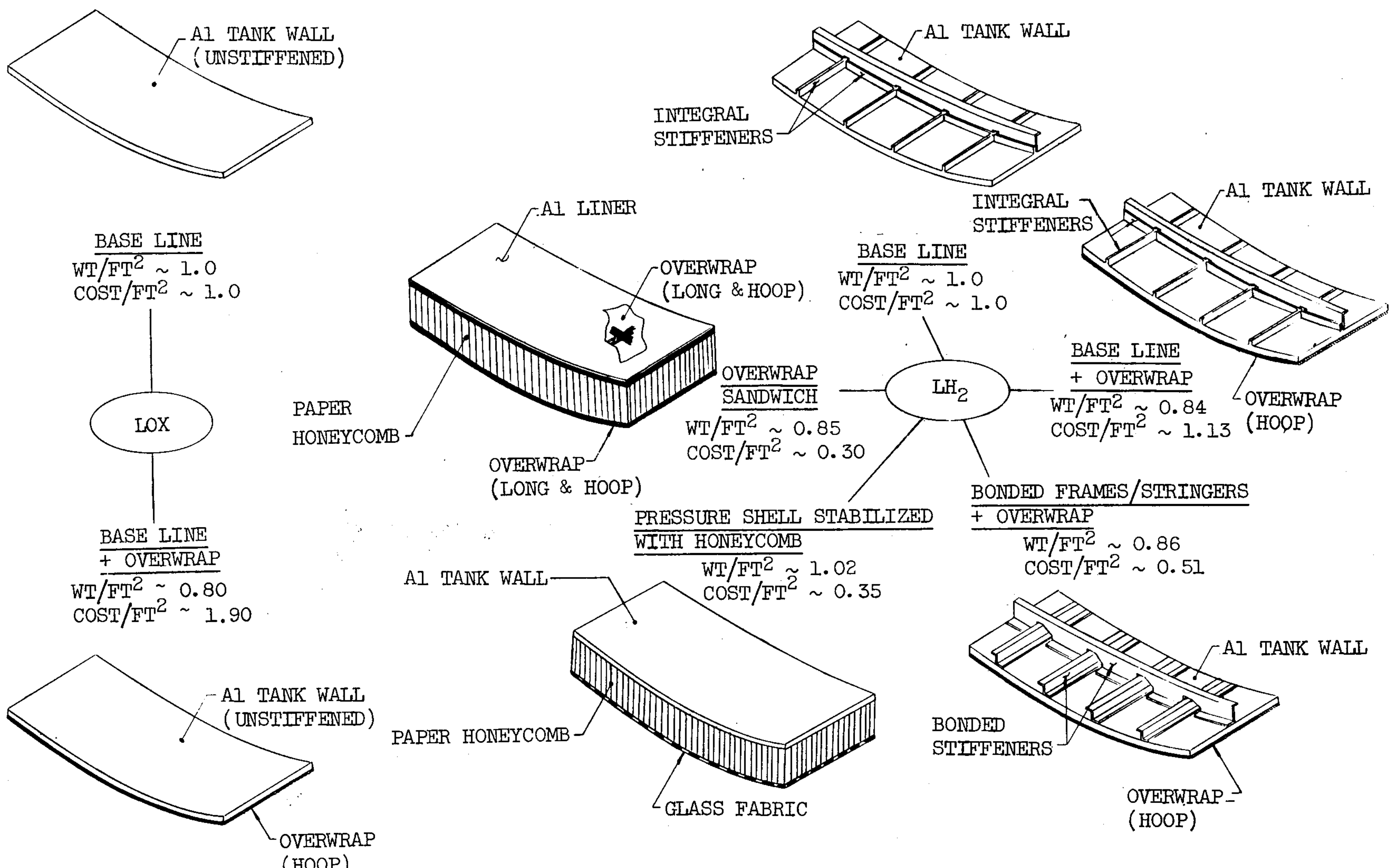

CURRENT COMPOSITE HO TANK CONCEPTS

KEYS TO APPLICATION OF COMPOSITES ON ORBITER DISPOSABLE MAIN PROPELLANT TANKS

This slide presents a roadmap of important stops between where the current technology stands and where it must go to be applied. In addition to the currently funded tests of the 1.016 m x 2.032 m (40 x 80-in) models, a preliminary composite design of a complete HO tank system would be necessary and must consider all load mechanisms and local discontinuities such as penetrations, attachment points, thickness changes, etc. The objective of this preliminary design would be to confirm that the potential weight and cost advantages are not cancelled by other design considerations. Component testing of advanced techniques could be carried out concurrently. Success of both the preliminary design and component tests would then warrant the fabrication and test of 2/5 scale HO tank models. The end result of this testing would be a finalized design of both the HO tank system and tooling. To accomplish this technology program the Contractor has estimated that a further commitment of $1.0 million to $2.0 million would be required and that this extended program would take 18 months to complete from the start of preliminary design.

KEYS TO APPLICATION OF COMPOSITES ON ORBITER DISPOSABLE MAIN PROPELLANT TANKS

CURRENT PROGRAM

- DESIGN, FABRICATION, & TEST OF 1.016 x 2.032 m (40 x 80 IN.) MODELS

NEW EFFORT REQUIRED

- PRELIMINARY DESIGN OF COMPLETE FULL SCALE SYSTEM TO INCLUDE SHEAR TRANSFER, END FITTINGS, & ATTACHMENT METHODS
- SUBSCALE & FULL SCALE COMPONENT TESTING
- DESIGN OF 2/5 SCALE 3.048 x 6.096 m (120 x 240 IN.) MODELS
- FABRICATION OF 2/5 SCALE MODELS
- TEST & ANALYSIS
- FINALIZED DESIGN OF TANKS & TOOLING

SUMMARY

In summary, this has been a review of the status of NASA technology programs for composite tanks. Several important points should be noted. First, the thin bonded liner concept appears to require further development before it could be used to reliably provide pressure vessels in reusable auxiliary systems. Second, the GFR pressure vessels offer a number of potential advantages and the technology appears to be ready for application to Shuttle auxiliary system tanks if needed. And third, the current study of disposable HO tanks has identified a significant potential for both cost and weight savings and has further indicated that the cost of obtaining the technology required to exploit the concept is in a favorable ratio with the potential savings.

SUMMARY

1. COMPOSITE PRESSURE VESSELS

   - THIN BONDED LINER HAS LIMITED CYCLIC LIFE CAPABILITY
   - GFR CONCEPT HAS A WELL ESTABLISHED BACKGROUND
   - POTENTIAL FOR GFR CONCEPT TO PROVIDE:
     - LOWER WEIGHT (UP TO 50% LIGHTER)
     - GREATER SAFETY (CONTROL OF FRAGMENTATION)
     - BETTER PACKAGING (CYLINDERS CAN WEIGH LESS THAN SPHERES)
     - LOWER COST (MINIMIZES METAL TECHNOLOGY)
   - HARDWARE DEMONSTRATION PROGRAM CURRENTLY ACTIVE

2. STRUCTURAL TANKAGE (BUCKLING CRITICAL)

   - NEW COMPOSITE TECHNIQUES CAN PROVIDE
     - LOWER WEIGHT (UP TO 16% LIGHTER)
     - LOWER COST (UP TO 65% LESS THAN INTEGRALLY MACHINED)
   - 1/10 SCALE TEST PROGRAM CURRENTLY ACTIVE
   - SHEAR LOAD TRANSFER, DISCONTINUITIES, AND HARD SPOTS NEED FURTHER STUDY
   - DESIGN AND DEMONSTRATION PROGRAM OF 2/5 SCALE MODEL MAY BE WARRANTED
   - RATIO OF DEVELOPMENT DOLLARS TO POTENTIAL PAYOFF IS ATTRACTIVE

COMPOSITE SYSTEMS UTILIZATION FOR SPACE SHUTTLE STRUCTURES

By E. E. Engler and O. D. Meredith
NASA Marshall Space Flight Center

INTRODUCTION

During the study phase, preceding the selection of a Space Shuttle configuration, an extensive effort in research and development of composite material systems was undertaken. The main goal of this work is twofold: to show applicability of these materials to shuttle structures and to demonstrate availability through a hardware development program. Composites were not included in the baseline structures.

The paper first describes the various configurations studied and potential areas of composite structures use. In the second part, an outline of ongoing composite programs, complementing the indicated feasible applications, including a typical cost study, is shown. Finally, an assessment of the composite program is given.

The following composite systems are investigated: Boron filaments with epoxy, polyimide, or aluminum matrix, and graphite filaments with epoxy or polyimide matrix .

Flyback TPS Booster

During phase B, a fully reusable LOX/LH_2 flyback booster and orbiter were studied. Shown in the slide is a typical booster configuration, staging at a velocity of approximately 3,650 m/sec. (12,000 ft/sec.). An external metallic or nonmetallic TPS system, attached to a primary structure, is utilized. Primary structure temperatures do not exceed 148° C. (300° F.). Areas of potential composite application, structural dry weight, and attainable weight savings are indicated.

FLYBACK TPS BOOSTER

STRUCTURAL WEIGHT (DRY) – 284,376 Kg (626,933 LBS.)

<u>POTENTIAL WEIGHT SAVINGS</u>

THRUST STRUCTURE BEAMS – 991 Kg (2,185 LBS.) 21%

THRUST STRUCTURE SKIRT – 605 Kg (1,335 LBS.) 15%

INTERTANK – 1,386 Kg (3,056 LBS) 26%

WING & STABLIZER – 1,639 Kg (3,614 LBS.) 16%

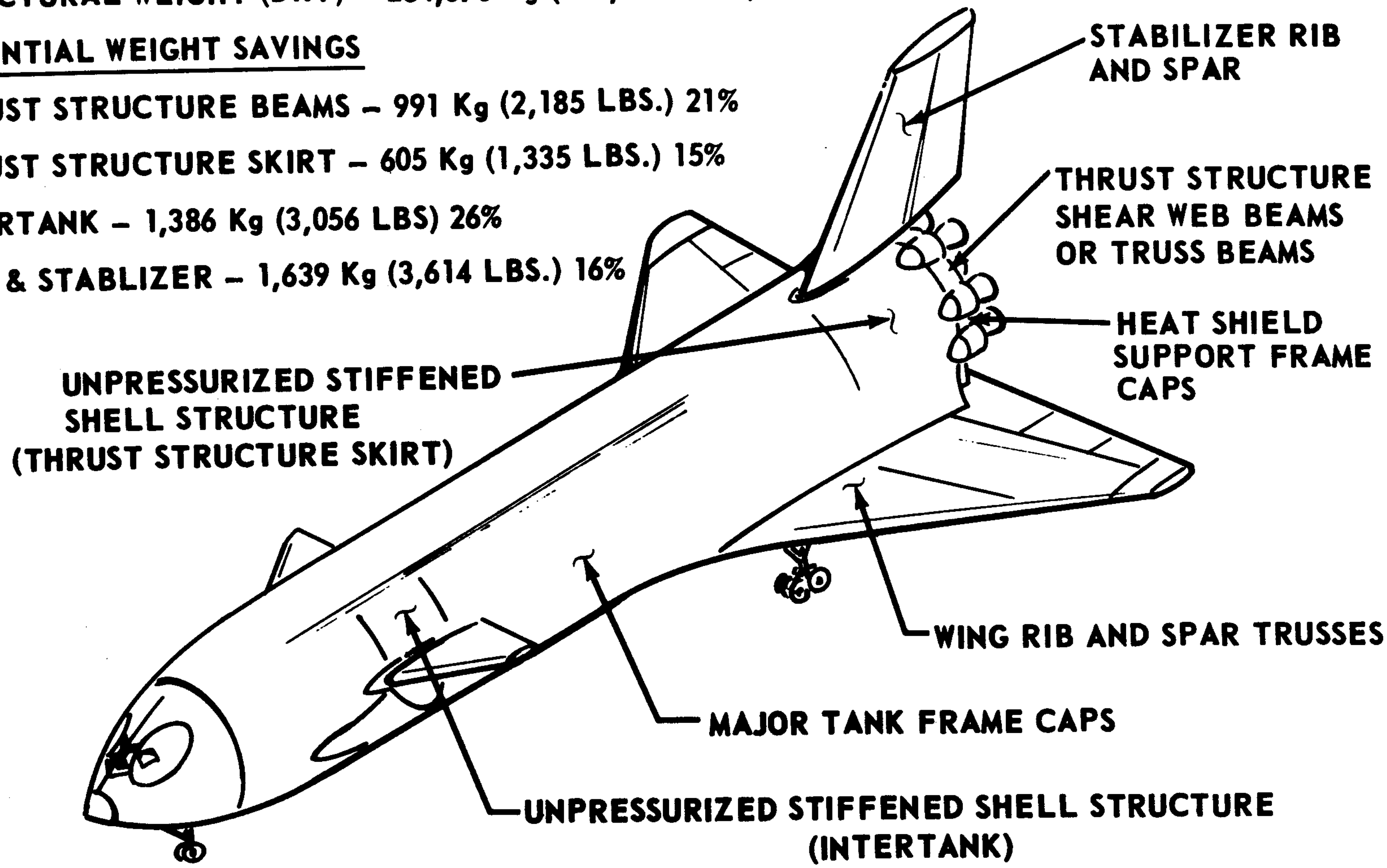

Flyback Heat Sink Booster

Space Shuttle configurations, using a LOX/LH_2 orbiter with expendable H/O tank, were investigated. The lower staging velocity in this approach, approximately 2,150 m/sec. (7,000 ft/sec.), allows a "heat sink" structure on most of the primary booster structure. This eliminates a separate TPS without raising the fuselage temperature over 148° C. (300° F.). Areas of potential composite application, structural dry weight, and attainable weight savings are indicated.

FLYBACK HEAT SINK BOOSTER

STRUCTURAL WEIGHT (DRY) – 156,880 Kg (345,856 LBS.)

<u>POTENTIAL WEIGHT SAVINGS</u>

THRUST STRUCTURE BEAMS – 585 Kg (1,289 LBS.) 21%

WING AND STABILIZER – 1,148 Kg (2,530 LBS) 16%

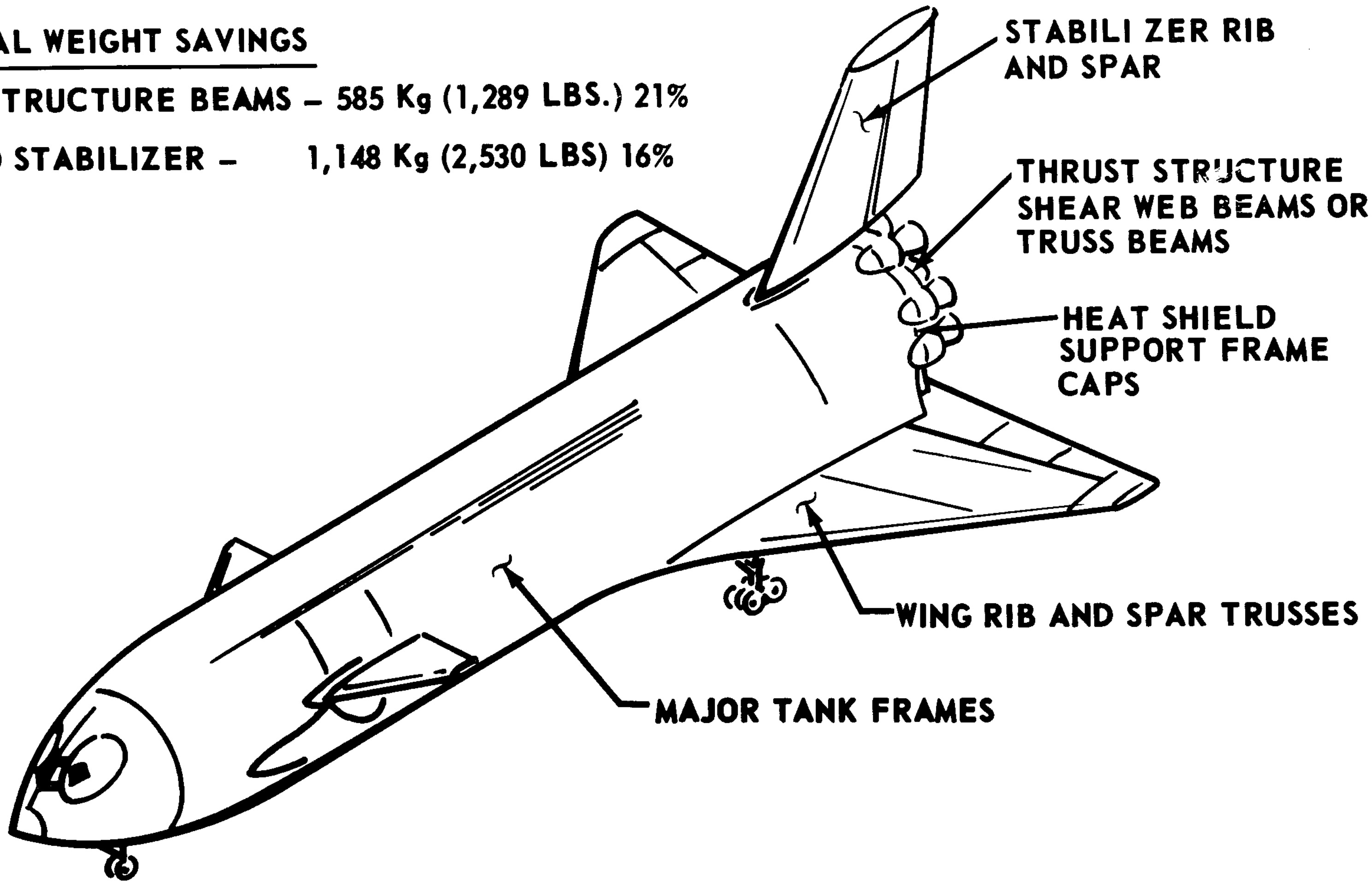

Ballistic Recoverable Booster

Another booster configuration, in conjunction with an H/O tank orbiter, is the ballistic recoverable booster. It reenters after separation from the orbiter ballistically and descends to the surface of the ocean by means of parachutes. After water impact, the booster is towed back to shore and refurbished. Staging velocity is between 1,520 m/sec. (5,000 ft/sec.) and 2,150 m/sec. (7,000 ft/sec.). Both pressure-fed and pump-fed rocket engines can be utilized in this configuration. Due to the required skin thicknesses on the fuselage, the "heat sink" principle is used, and no separate TPS is required. Areas of potential composite application, structural dry weight, and attainable weight savings are indicated.

BALLISTIC RECOVERABLE BOOSTER

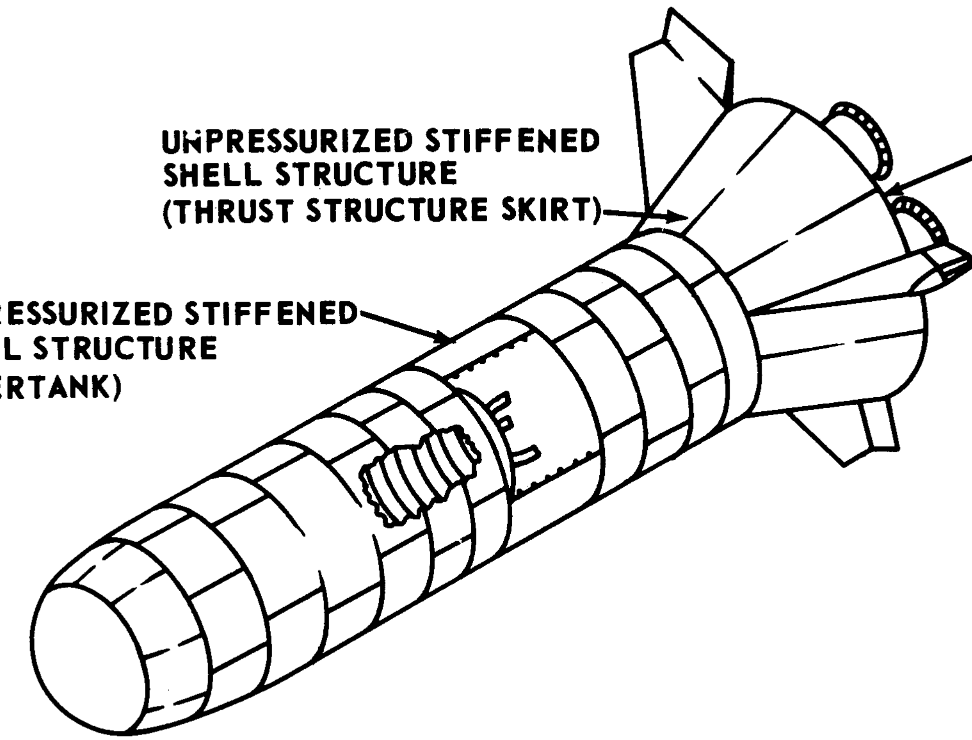

STRUCTURAL WEIGHT (DRY)–214,326 Kg (472,500 lbs)

POTENTIAL WEIGHT SAVINGS

THRUST STRUCTURE BEAMS	1,445 Kg	(3,186 lbs)	21%
THRUST STRUCTURE SKIRT	871 Kg	(1,921 lbs)	15%
INTERTANK	1,325 Kg	(2,922 lbs)	26%

Parallel Burn Solid Booster

A different configuration is the parallel burn configuration. Both the orbiter engines and the two SRM's are ignited on the ground and burn together. At SRM burnout, the empty cases are separated and reenter the earth atmosphere. Parachutes are deployed to lower the water impact velocity. Empty cases and parachutes are recovered for reuse. The application of composites is in the area of attach members between H/O tank, orbiter, and SRM's. System weights and attainable weight savings are indicated.

PARALLEL BURN SOLID BOOSTER

STRUCTURAL WEIGHT (DRY) 132,200 Kg (291,460 lbs)

POTENTIAL WEIGHT SAVINGS
RADIAL & ROLL LOAD MEMBERS – 156 Kg (343 lbs) 17%

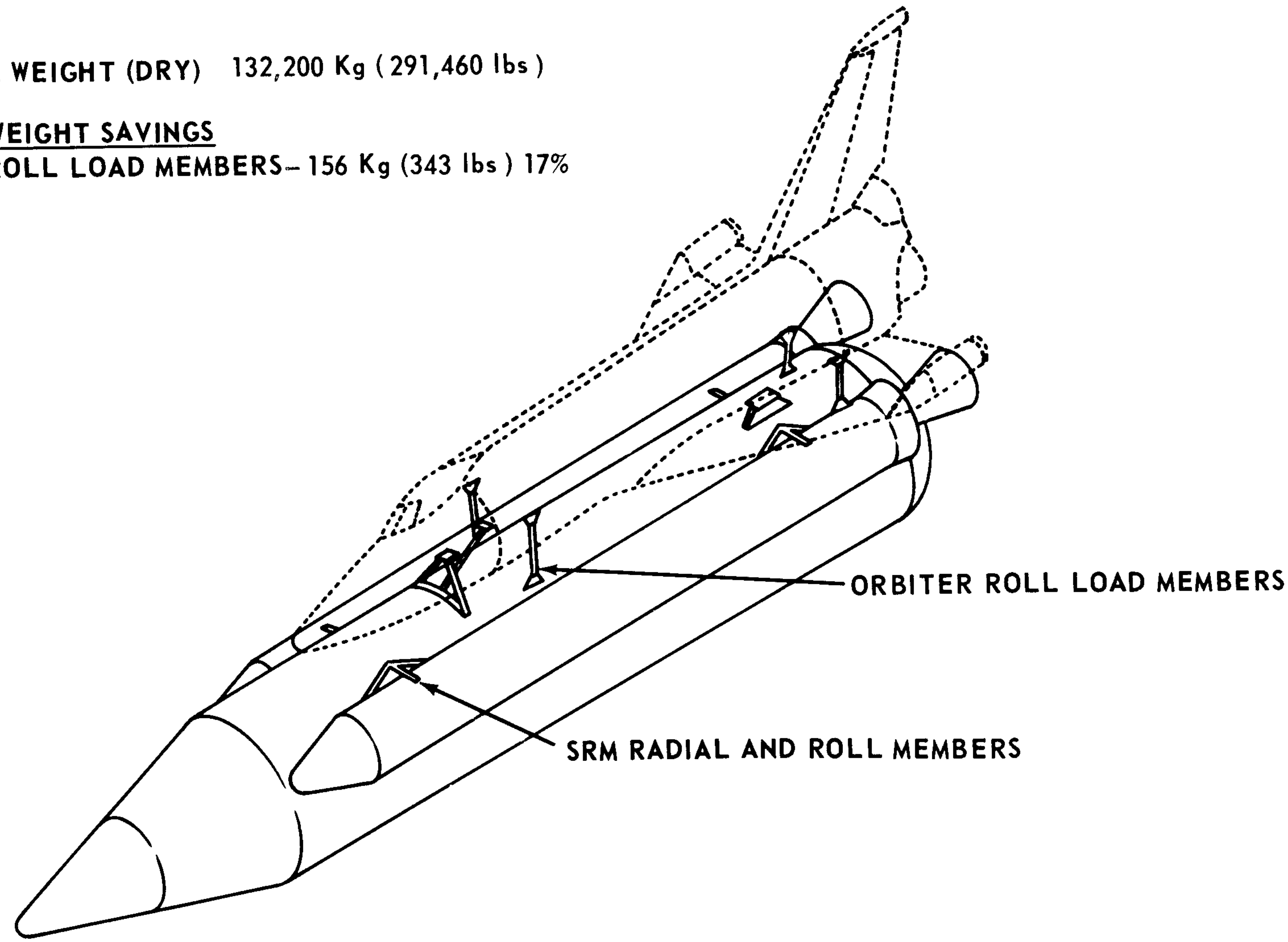

Orbiter

The orbiter primary structure offers a number of potential composite applications. A typical orbiter for configurations with external H/O tank (parallel and tandem staging) utilizes RSI (Reusable Surface Insulation) directly attached to the primary structure as TPS. Temperature of all structural elements does not exceed 148° C. (300° F.). Potential areas of composite application, structural dry weight, and attainable weight savings are indicated.

ORBITER

STRUCTURAL WEIGHT (DRY) –65,772 Kg (145,000 lbs)

<u>POTENTIAL WEIGHT SAVINGS</u>

THRUST STRUCTURE TUBES – 113 Kg (250 lbs) 21%

THRUST STRUCTURE & SKIRT PANELS – 143 Kg (315 lbs) 15%

WING – 271 Kg (598 lbs) 16%

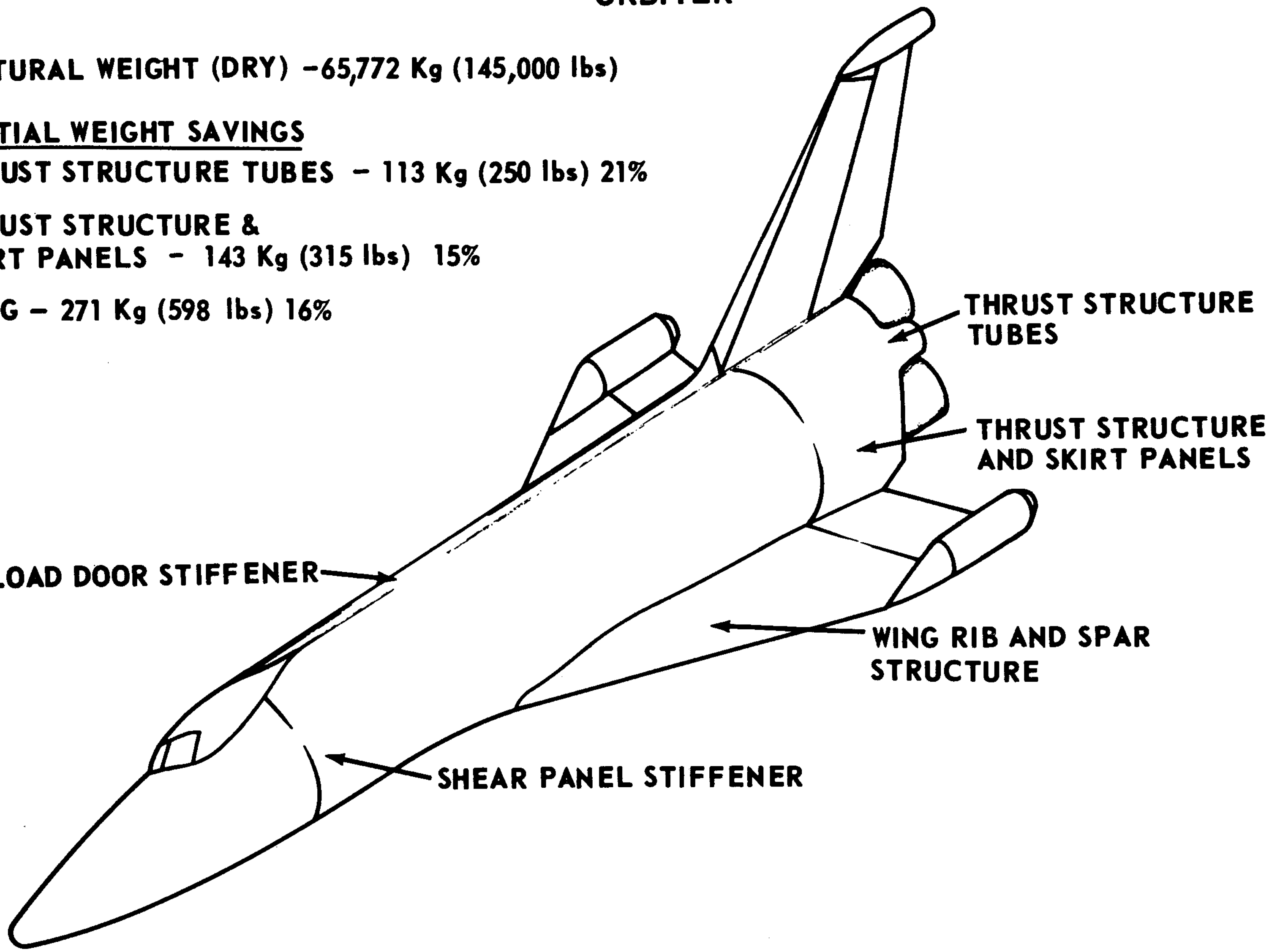

MSFC Composites Programs
(Resin Matrix)

All composites programs performed in support of the Space Shuttle program are listed. Composite work in the area of resin matrix materials is outlined.

MSFC COMPOSITES PROGRAMS (RESIN MATRIX)

PROGRAM	STATUS	COMPLETION DATE
1. DEVELOPMENT OF DESIGN DATA FOR GRAPHITE/EPOXY AND GRAPHITE/ POLYIMIDE (NAS8-26198)	TEST SPECIMENS BEING FABRICATED AND TESTED. EMPHASIS ON POLYIMIDE.	NOV. 1972
2. INVESTIGATION OF HIGH TEMPERATURE STRENGTH DEGRADATION OF FIBER REINFORCED RESIN COMPOSITES (NAS8-27435)	MOISTURE RELATED DEGRADATION TESTS FOR DIFFERENT RESINS AND FIBERS.	JULY 1972
3. DESIGN, FABRICATION, AND TEST OF BORON AND GRAPHITE/ POLYIMIDE BOX BEAMS (NAS8-24511)	BORON/POLYIMIDE BEAM TESTED AND FAILED PREMATURELY DUE TO BOND LINE FAILURE. GRAPHITE/ POLYIMIDE BEAM NOT ASSEMBLED.	JULY 1972
4. DESIGN AND FABRICATION OF GRAPHITE/EPOXY COMPRESSION PANELS (NAS8-26242)	FIRST PANEL SUCCESSFULLY TESTED TO 160% OF LIMIT LOAD. SECOND PANEL IN FABRICATION.	DEC. 1972

5. FABRICATION OF BORON/EPOXY TRUSS BEAM (NAS8-26675)	TESTS SUCCESSFUL ON INDIVIDUAL TUBES. NINE-ELEMENT BEAM ASSEMBLY IN FABRICATION.	AUG. 1972
6. STANDARDS FOR NON-DESTRUCTIVE EVALUATION (NAS8-26565)	PROGRAM COMPLETE.	COMPLETE
7. CONTINUOUS FORMING TECHNIQUES FOR ADVANCED COMPOSITE STRUCTURAL SHAPES	CURVED FIBERGLAS/EPOXY AND STRAIGHT GRAPHITE/EPOXY HAT SECTION SHAPES FABRICATED. TESTS PLANNED.	JUNE 1972
8. THERMAL DESIGN OF COMPOSITE MATERIAL HIGH TEMPERATURE ATTACHMENTS (NAS8-27041)	DESIGN CONCEPTS MADE AND TEST ITEMS PLANNED.	MAY 1972
9. DESIGN AND FABRICATION OF A GRAPHITE OR BORON/POLYIMIDE PANEL	CONTRACT AWARD IMMENENT.	18 MONTHS FROM AWARD
10. DESIGN, FABRICATION, AND TEST OF A BORON/EPOXY COMPRESSION PANEL, SHEAR WEB BEAM, AND RELATED COMPONENTS (IN-HOUSE)	PANEL AND BEAM COMPONENT TESTS PARTIALLY COMPLETE. PANEL ASSEMBLY NEAR COMPLETION.	FEB. 1973

MSFC Composites Programs
(Metal Matrix)

All metal matrix composite programs are listed.

MSFC COMPOSITES PROGRAMS (METAL MATRIX)

PROGRAM	STATUS	COMPLETION DATE
1. DESIGN AND FABRICATION OF BORON/ALUMINUM COMPONENTS (NAS8-27735)	PROGRAM IN DESIGN AND MATERIAL PROCESSING PHASE. FABRICATION OF A PANEL ASSEMBLY SCHEDULED.	OCT. 1972
2. DESIGN AND FABRICATION OF BORON/ALUMINUM COMPONENTS (NAS8-27738)	PROGRAM IN DESIGN AND SUBELEMENT TEST PHASE. FABRICATION OF BEAM COMPONENTS SCHEDULED.	OCT. 1972
3. DEVELOPMENT OF A METHOD FOR FABRICATING METALLIC MATRIX COMPOSITE SHAPES BY A CONTINUOUS MECHANICAL PROCESS (NAS8-27010)	PROCESSING STUDIES TO CONSOLIDATE SPIRAL WOUND BORON FILAMENTS INTO STRUCTURAL SHAPES.	SEPT. 1973
4. FABRICATION OF BORON/ ALUMINUM TEST COMPONENTS BY CONTINUOUS CASTING (NAS8-27132)	BORON/ALUMINUM HAT SECTIONS AND COUPONS FABRICATED. WILL BE TESTED AT MSFC.	JUNE 1972
5. FATIGUE OF BORON/ ALUMINUM COMPOSITES (NAS8-27437)	TESTING IN PROGRESS ON FATIGUE OF JOINTS.	JUNE 1972

Compression Panel (Graphite/Epoxy)

Objectives of this program are to demonstrate the weight savings and fabrication of stiffened panels under representative loading intensities and including load introduction provisions.

The first of two panels to be fabricated was tested at MSFC in late 1971. The panel sustained 160 percent of limit compression load (ultimate design was 140 percent of limit load). Weight saving demonstrated over a metallic panel design was approximately 18 percent as fabricated. Excess resin remained in the panel during cure. Process studies will be performed to remove excess resin in the second panel. Cyclic load testing of the second panel is planned.

COMPRESSION PANEL (GRAPHITE/EPOXY)

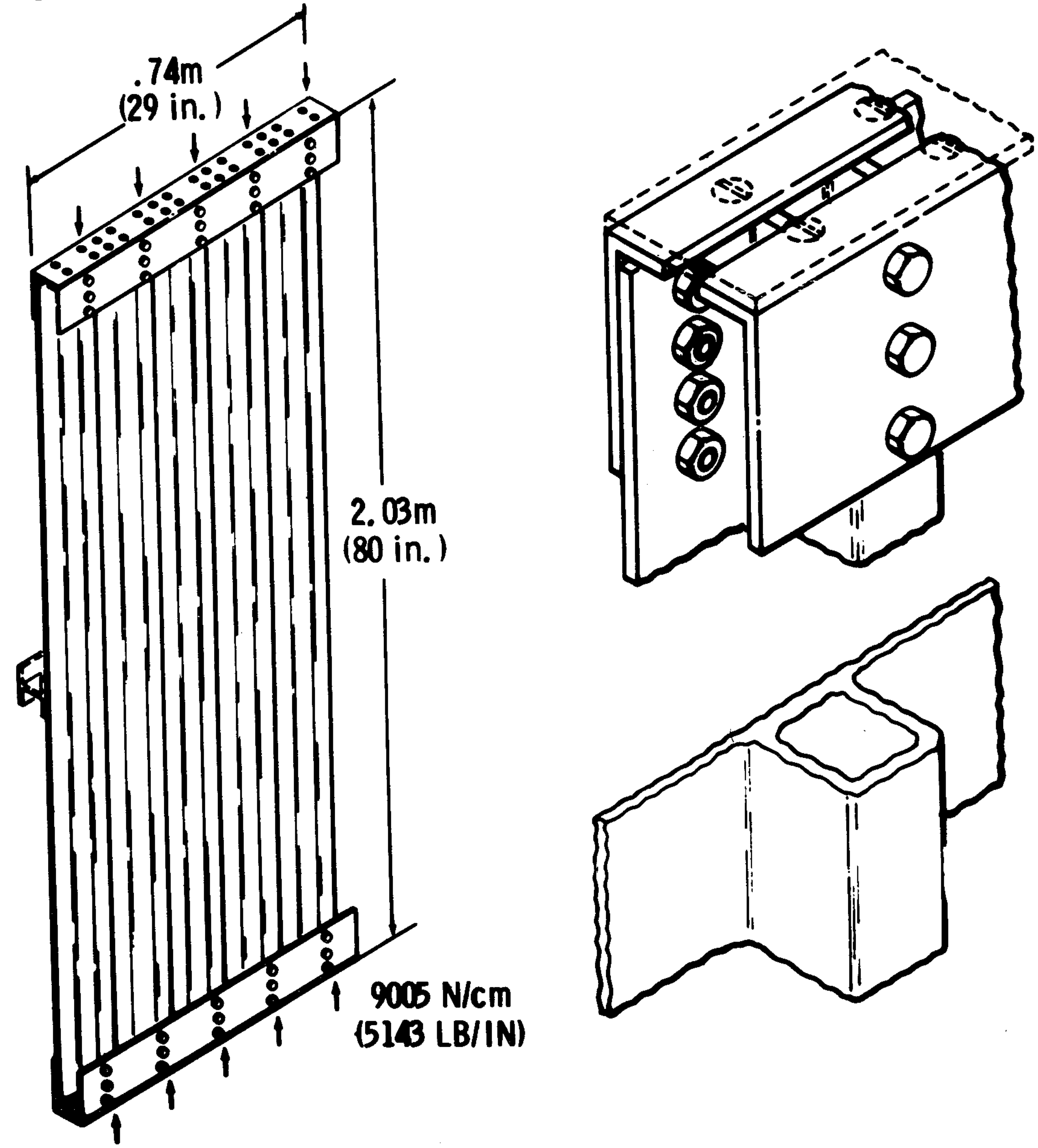

Boron/Epoxy Truss Beam

A one-third scale beam applicable to booster configurations is in fabrication. The center vertical tube in a thrust structure assembly was initially chosen for design, fabrication, and test. Based on this successful testing, the nine-element beam assembly is being fabricated for test at MSFC. Delivery is scheduled in May 1972.

An objective of this program is to demonstrate the potential weight savings of boron/epoxy thrust structure beams. Representative loads and joining methods are utilized. Weight savings over a metallic thrust structure of similar configuration are approximately 23 percent. Weight savings in a full scale thrust structure are even higher, as joints represent a lower weight percentage in the full scale design.

ENGINE THRUST BEAM
TRUSS BEAM

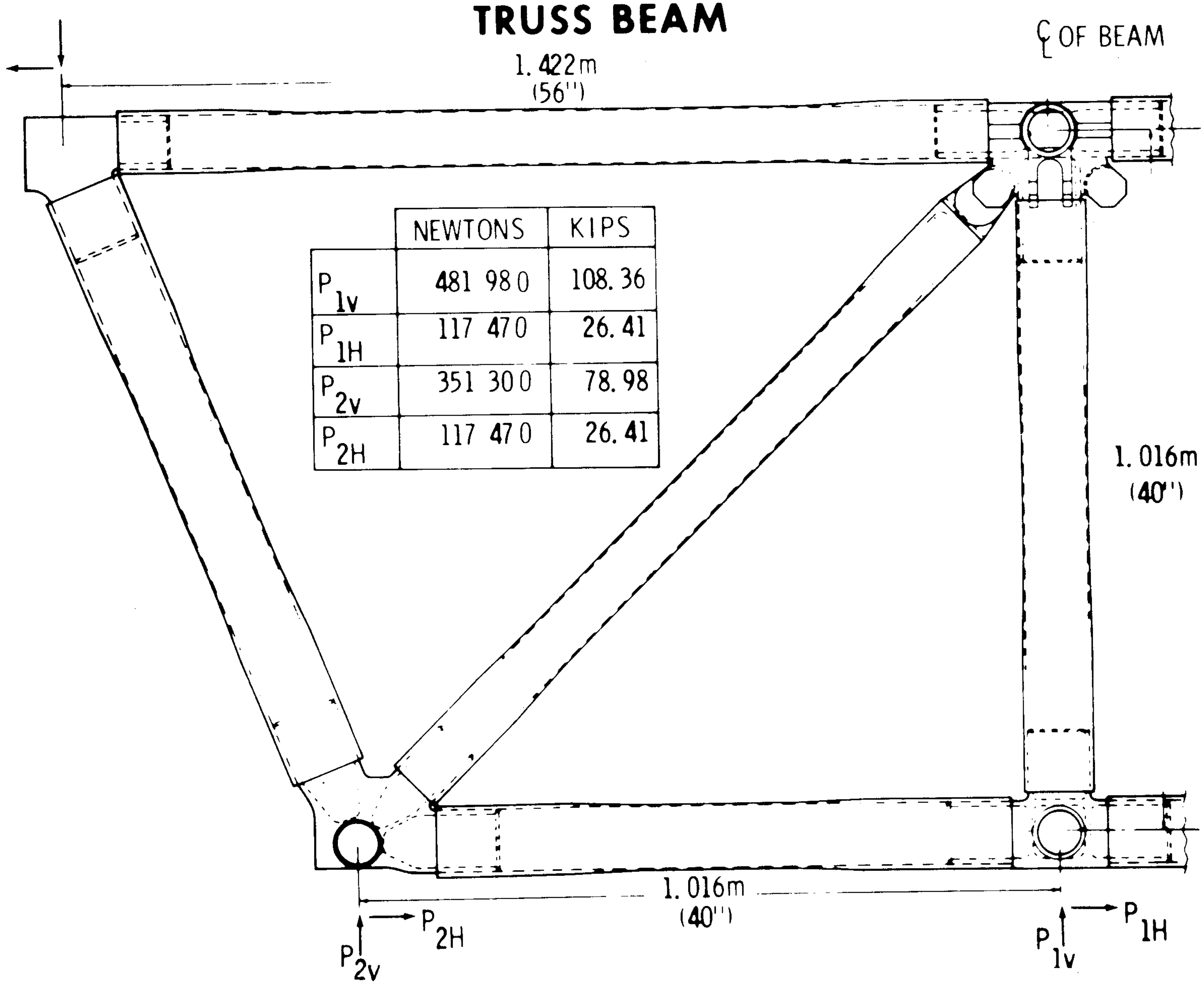

	NEWTONS	KIPS
P_{1v}	481 980	108. 36
P_{1H}	117 470	26. 41
P_{2v}	351 300	78. 98
P_{2H}	117 470	26. 41

Panel Assembly (Graphite/Polyimide or Boron/Polyimide)

This new program is designed to demonstrate the current potential for fabrication of large structures with polyimide resin and to explore potential weight savings. The panel to be designed and fabricated will be 3.05 by 3.05 meters (10' by 10') and will include introduction of a concentrated load. The panel includes a combination of shear and compression with tapered thicknesses for minimum weight. It is felt that this type panel combines the problems of composites utilization into one complex package. The panel is scheduled for delivery to MSFC in approximately 1 year.

PANEL ASSEMBLY–GRAPHITE OR BORON/POLYIMIDE

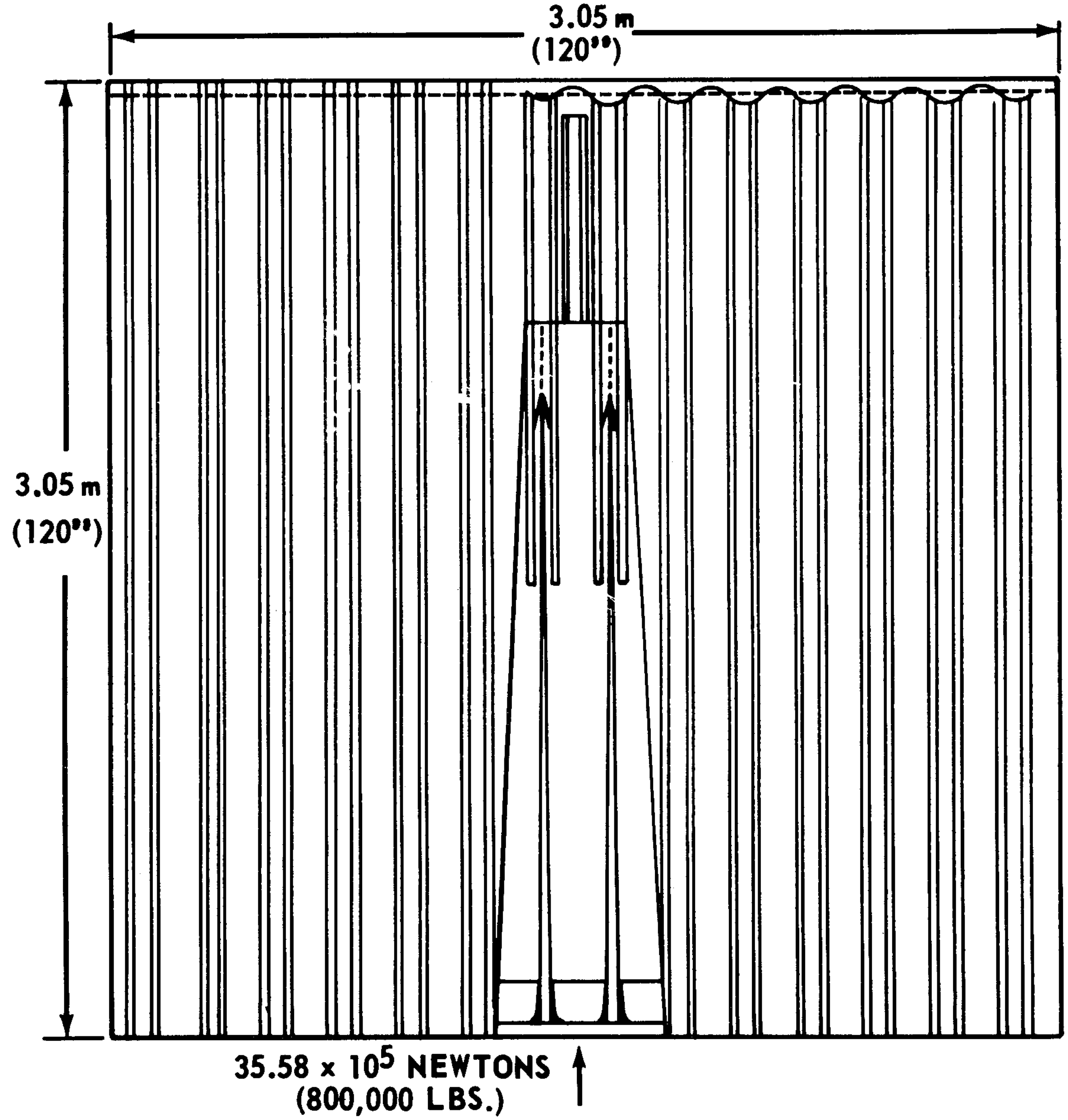

Panel Assembly (Boron/Aluminum)

Design and fabrication of the boron/aluminum panel as shown is under contract. The requirements of combined shear and compression with resultant heavy sections and tapered thicknesses compound many problems into one structure. The program is presently in the design and subelement test phase. Delivery to MSFC for test is scheduled in July 1972.

The contractor is also designing full size boron/aluminum thrust structure beams (truss and shear web). No fabrication of test hardware is planned.

PANEL ASSEMBLY-BORON/ALUMINUM

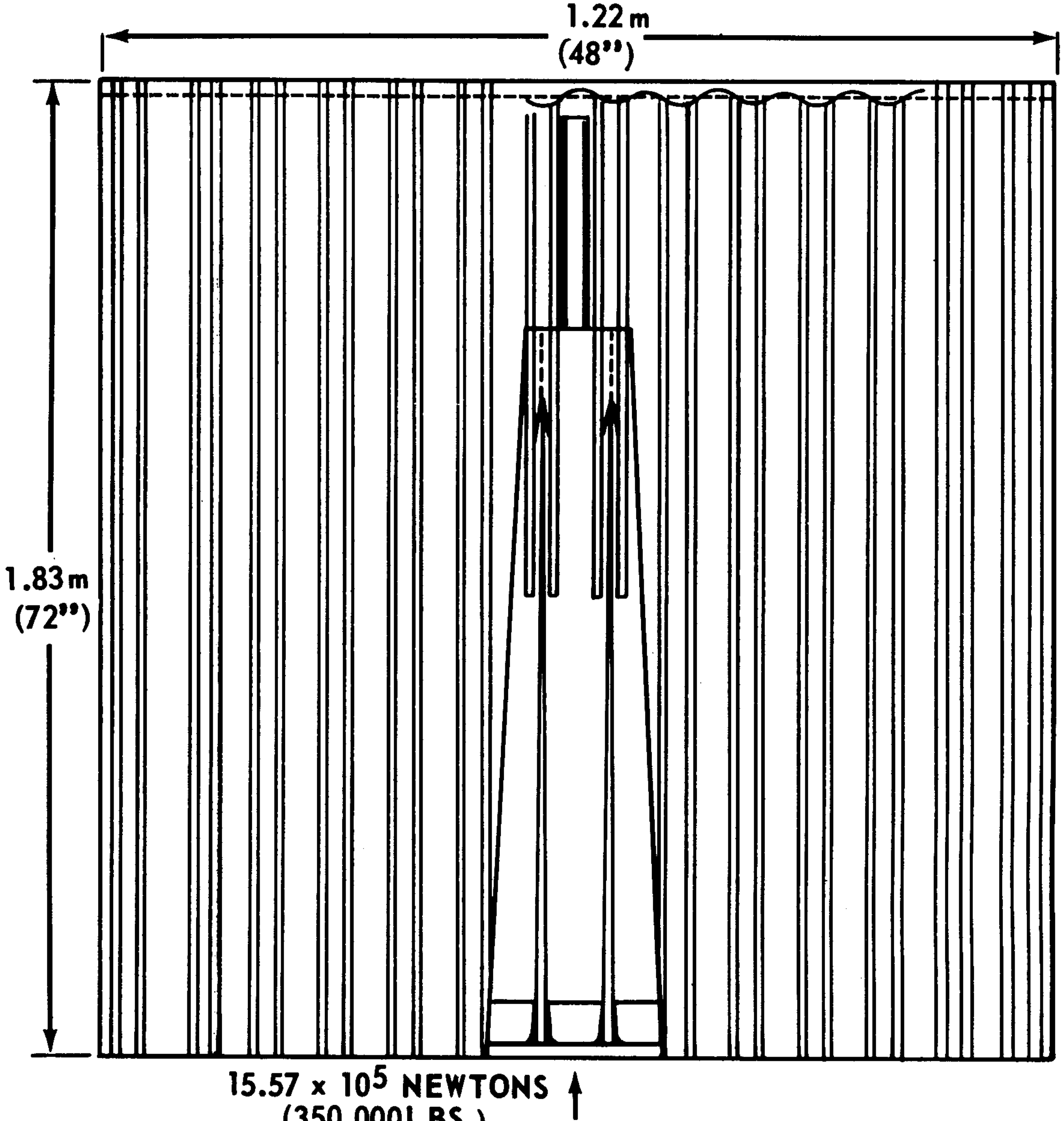

Compression Panel (Boron/Epoxy)

The panel shown has been designed and is being fabricated under an in-house program at MSFC. The boron/epoxy skins and stringers are cured and secondarily bonded. The design includes titanium load introduction fittings with mechanical fasteners.

Perforated titanium foil is incorporated in the laminate in areas of mechanical fasteners for increased properties. Stringer sections and load introduction fittings were tested satisfactorily.

Weight savings over a similar aluminum panel are projected at 25-30 percent. The panel has been designed to the same criteria as the graphite/epoxy panel under contract NAS8-26242. Testing will be performed in June 1972.

COMPRESSION PANEL (BORON/EPOXY)

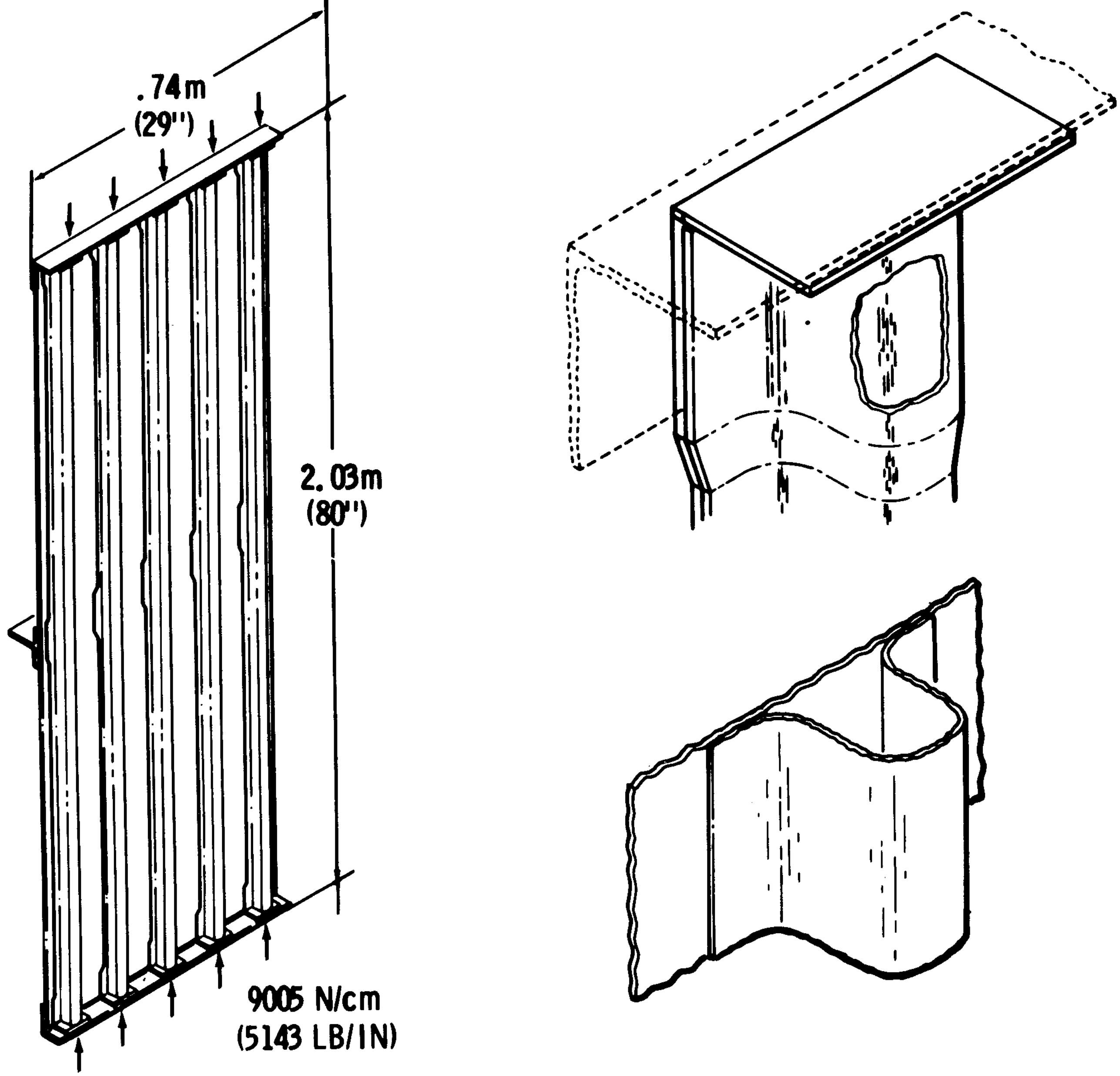

Shear Web Beam (Boron /Epoxy)

The beam assembly shown is representative of a one-third scale version of booster thrust structure beams. This MSFC in-house program is designed to investigate the potential of boron/epoxy for this type structure including representative joining and assembly methods. Considerable difficulty has been experienced in drilling combinations of titanium splice fittings and boron/epoxy. Significant redesign of the beam was necessary. Component tests for joints and shear webs are in progress, and test of the final beam assembly is planned for late 1972.

Full size weight saving comparisons are clouded by the contribution of joints to the total weight. The total beam weight in boron/epoxy is 185 kilograms (407 pounds) which represents slightly over 10 percent savings compared to a titanium design. This would increase for full size beams because the percentage of joints decreases. However, final assessment is not yet available.

ENGINE THRUST BEAM
SHEAR WEB BEAM

	NEWTONS	KIPS
P_{1v}	481,980	108.36
P_{1H}	117,470	26.41
P_{2v}	351,300	78.98
P_{2H}	117,470	26.41

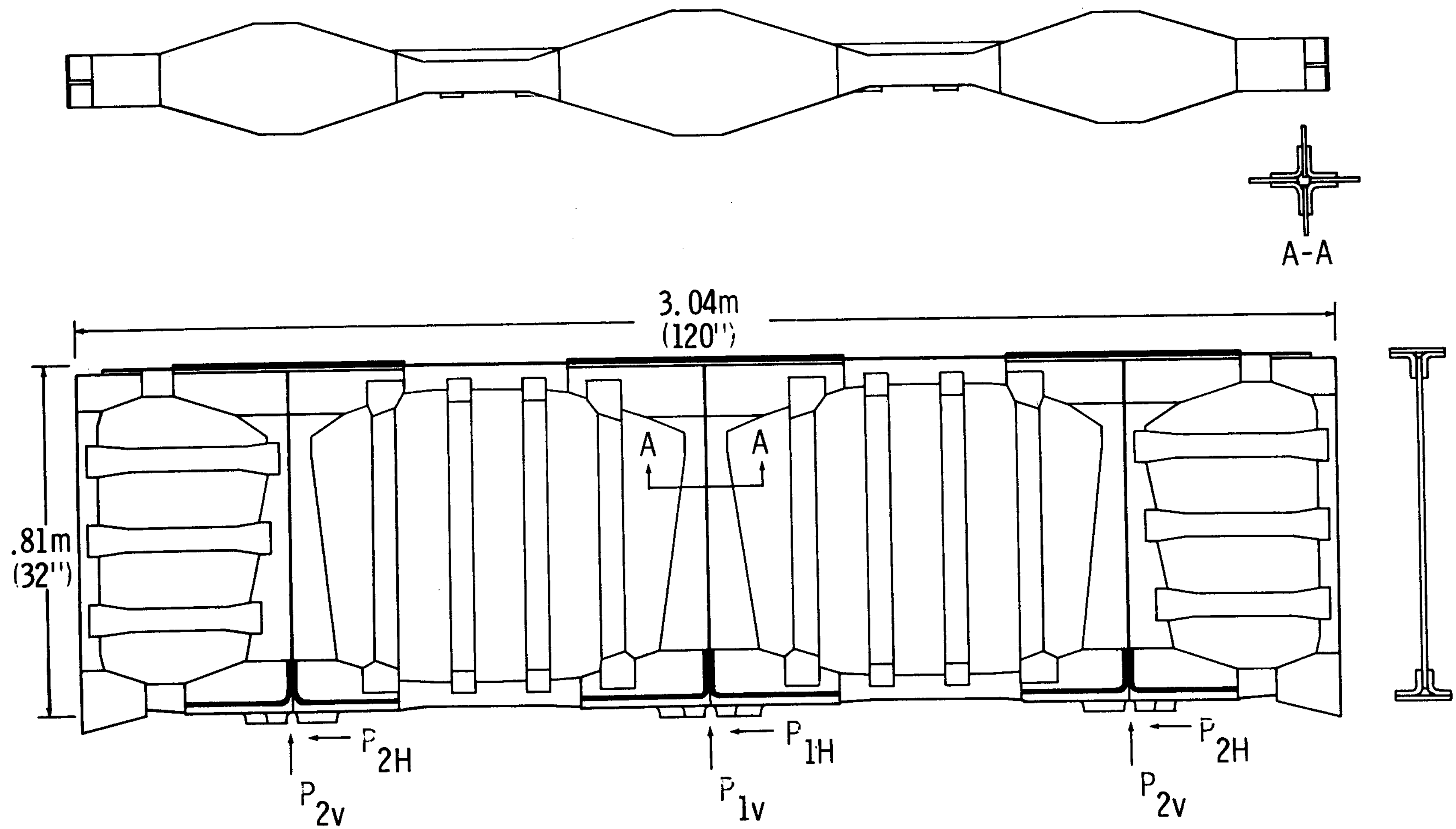

Thrust Structure Truss Beam (Boron/Aluminum)

Design and development of a typical booster truss beam (full size), utilizing diffusion bonded boron/aluminum, are in progress. Estimated weight for a square tube truss, as shown, is 485 kilograms (1,070 lb.). An all metal truss is being designed to establish weight comparison. Fabrication and testing of a tubular section are planned.

This program is intended to explore the potential of boron/aluminum for this type structure.

THRUST STRUCTURE TRUSS BEAM-BORON/ALUMINUM

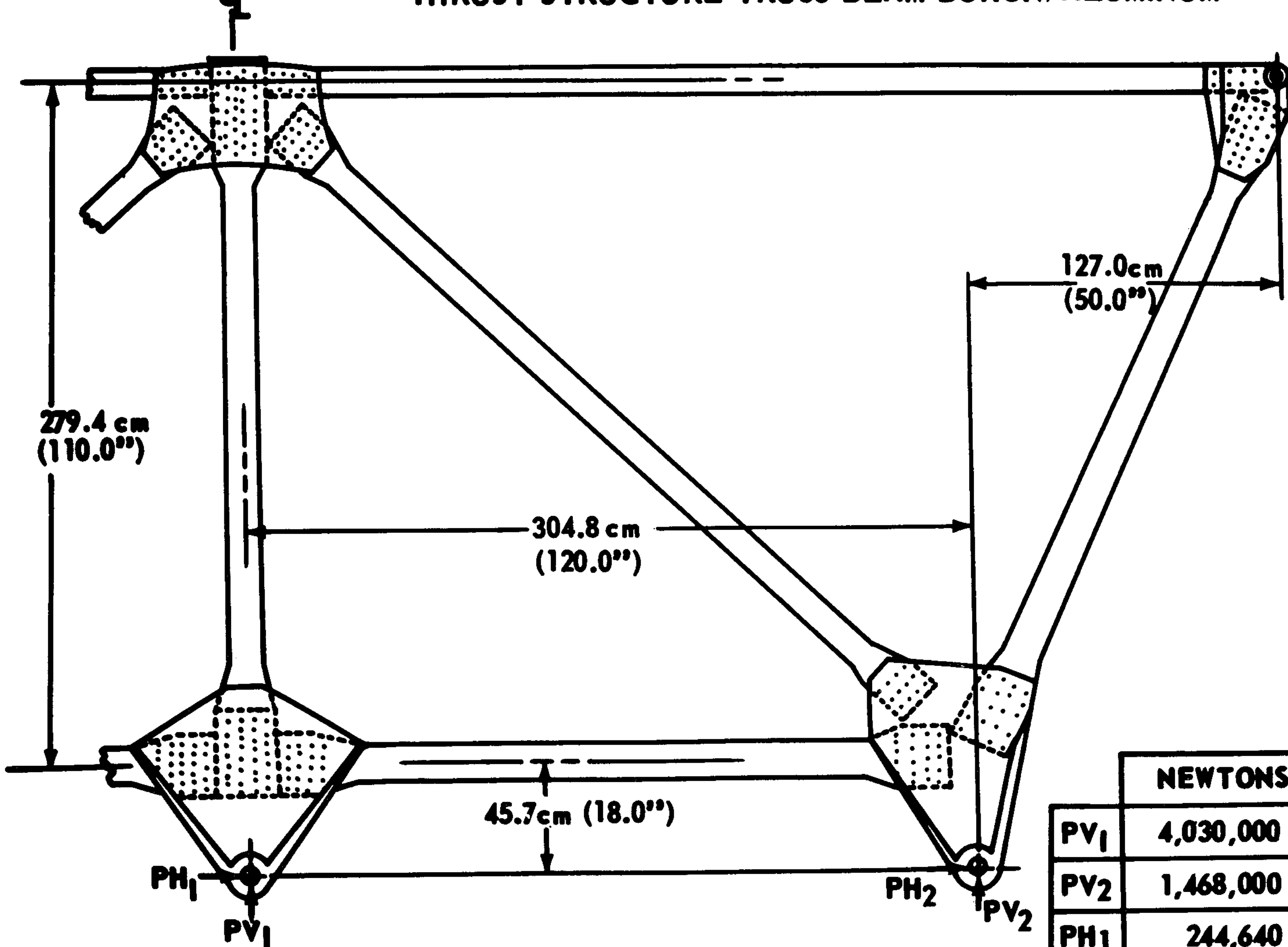

	NEWTONS	KIPS
PV_1	4,030,000	906
PV_2	1,468,000	330
PH_1	244,640	55
PH_2	489,300	110

Thrust Structure Shear Web Beam (Boron/Aluminum)

This design represents a full size booster thrust structure beam. The objectives are to investigate the potential of boron/aluminum for this type structure and to demonstrate fabrication. Weight advantage of boron/aluminum for the web has proven questionable, but the design is proceeding with it. The beam is designed with nonbuckled webs, but test items will include a tension field web. The weight estimate for the beam is 725 kilograms (1,600 pounds).

SHEAR WEB BEAM ASSEMBLY-BORON/ALUMINUM

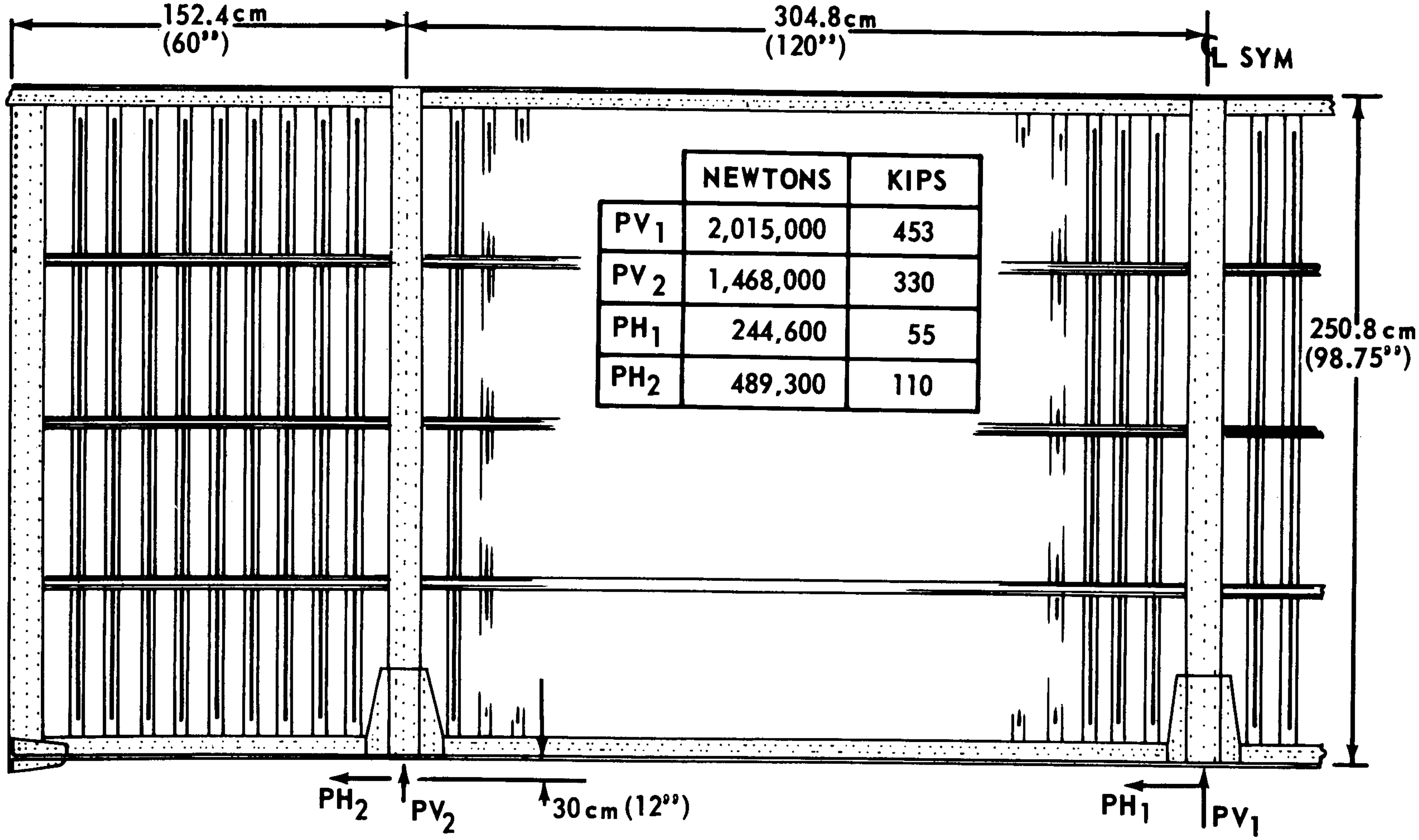

	NEWTONS	KIPS
PV_1	2,015,000	453
PV_2	1,468,000	330
PH_1	244,600	55
PH_2	489,300	110

Cost Comparison

A cost analysis of the various costs associated with fabrication of boron/epoxy tubes for the one-third scale booster thrust structure under contract NAS8-26675 is shown. Projected figures reflect the cost of boron/epoxy tubes with titanium end fittings, using an 80-percent learning curve for B/E layup and a 95-percent learning curve for the machining and EB welding operations on the titanium end fittings.

The relation of actual unit cost and average unit cost with the number of units is indicated. These curves and the actual man-hours recorded for tube fabrication have been used to generate the cost data for the center tube of the one-third scale structure presently under fabrication.

COST COMPARISON

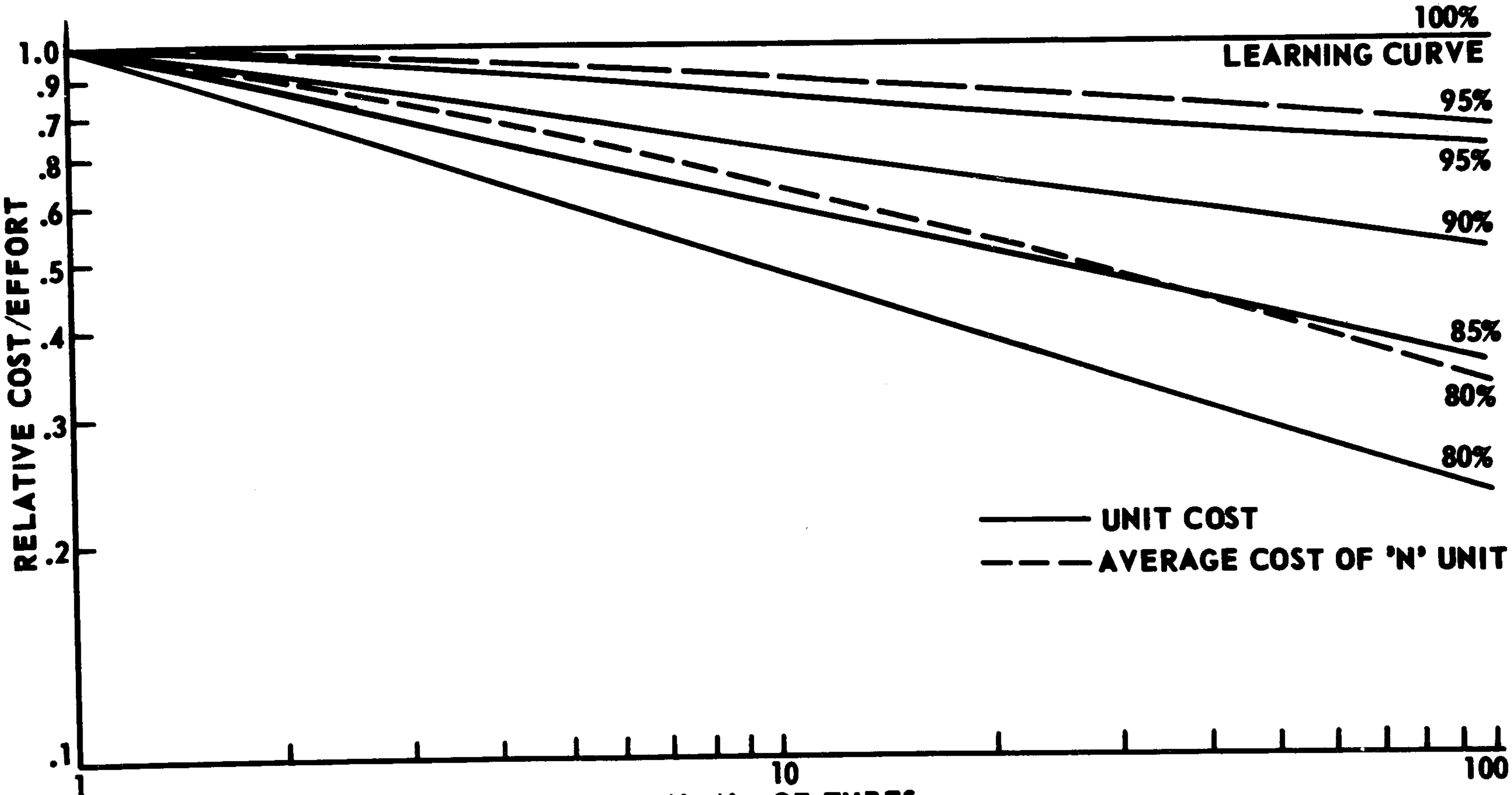

LEARNING CURVE (COST VS NO OF TUBES)

Cost Comparison
(Variation of Average Cost of B/E Tubes With Number of Units)

With amortized tooling costs, this tube becomes cost competitive with titanium at the 11th unit when the total cost of 11 B/E tubes equals the total cost of 11 titanium tubes, assuming a B/E prepreg cost of $1.58/ft ($5.18/m) or $107/lb ($235/kg).

The cost of the titanium tube was calculated on the assumption that the tube would be machined from solid stock. A previous cost analysis indicates that, for the small quantities required for the shuttle, tubes made from welded, hot formed plate or forgings would be more expensive.

COST COMPARISON
VARIATION OF AVERAGE COST OF B/E TUBES WITH NUMBER OF UNITS

1/3 SCALE PLANAR TRUSS
CENTER TUBE

P_{MAX} = 1,290,000 N (290,000 lb) COMPRESSION

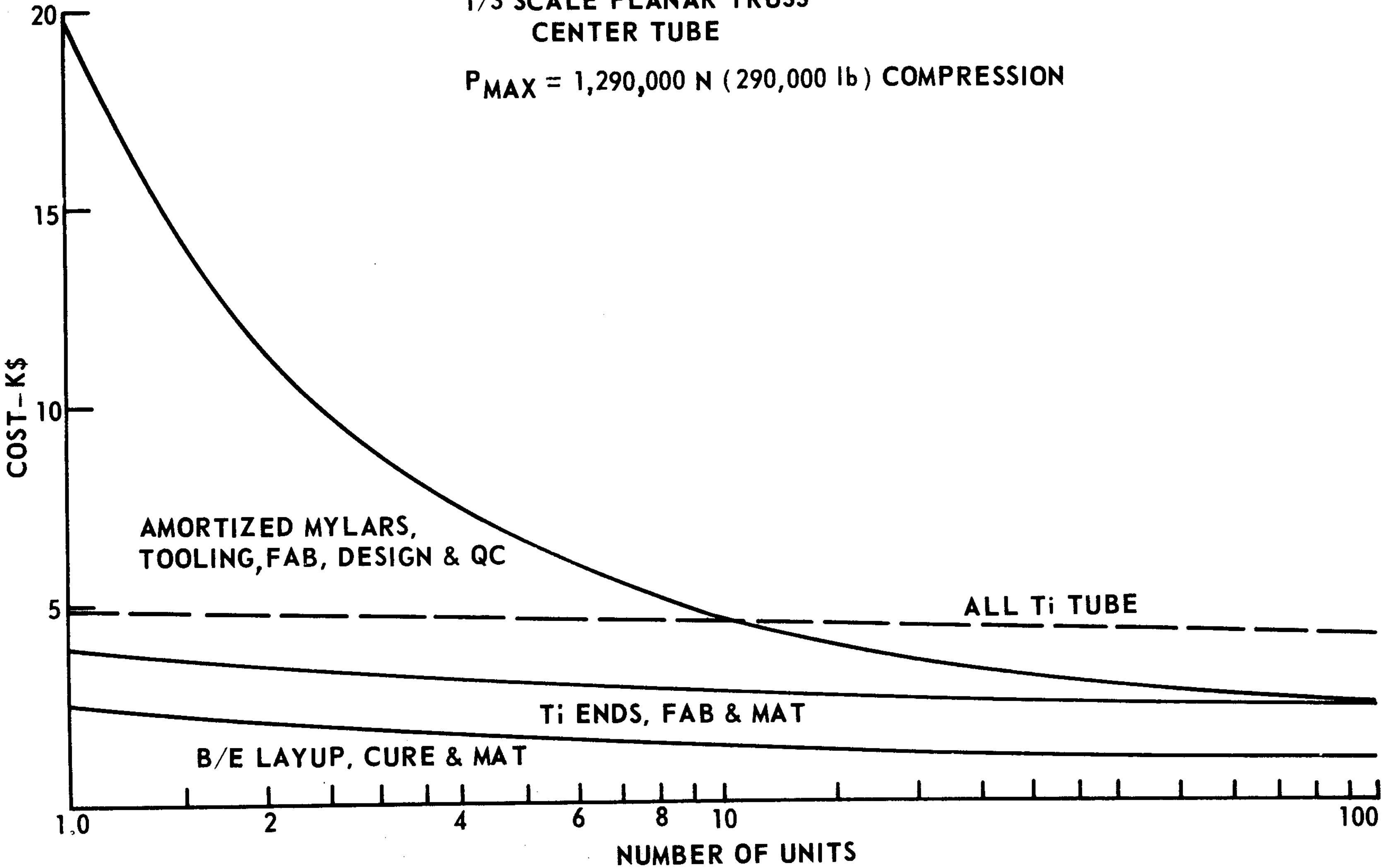

Weight Savings

Obtained and projected weight savings for different components under development are shown.

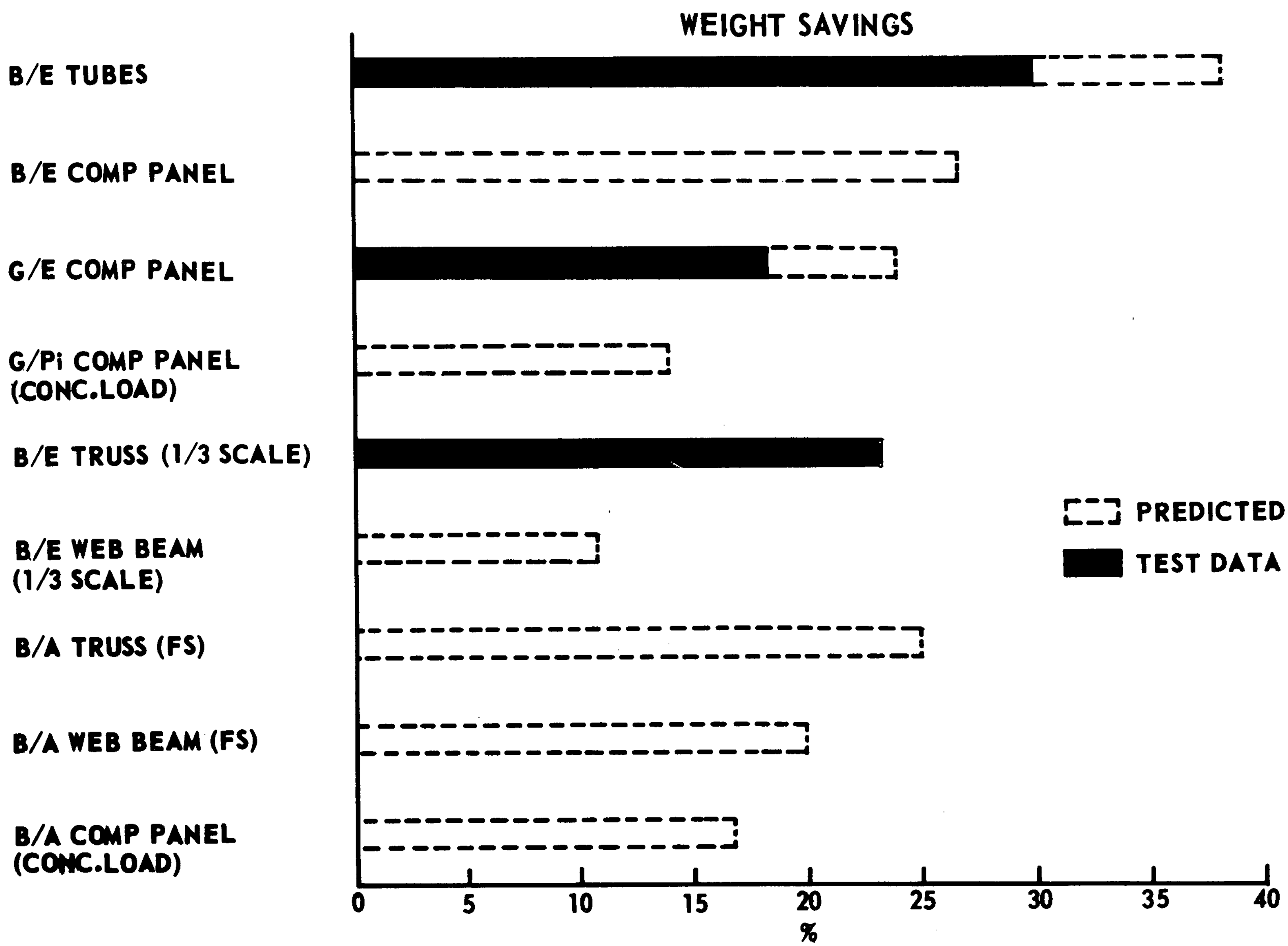
WEIGHT SAVINGS
B/E TUBES
B/E COMP PANEL
G/E COMP PANEL
G/Pi COMP PANEL
(CONC.LOAD)
B/E TRUSS (1/3 SCALE)
B/E WEB BEAM
(1/3 SCALE)
B/A TRUSS (FS)
B/A WEB BEAM (FS)
B/A COMP PANEL
(CONC.LOAD)
PREDICTED
TEST DATA
0
5
10
15
20
25
30
35
40
%

Program Results

A synopsis of major accomplishments is given. Problems encountered in the development program are indicated. Details and other data, such as detailed material properties, NDE method developments, and fabrication processes, are being reported in the regular publications and at appropriate symposiums.

PROGRAM RESULTS

I. PROGRESS

a. A .74 m BY 2.03 m GRAPHITE/EPOXY COMPRESSION PANEL WAS FABRICATED AND SUCCESSFULLY TESTED IN EXCESS OF DESIGN REQUIREMENTS. (114%)

b. BORON/EPOXY TUBULAR STRUTS WITH BONDED TITANIUM END FITTINGS HAVE BEEN FABRICATED AND SUCCESSFULLY TESTED. ASSEMBLY OF A NINE-MEMBER TRUSS BEAM IS NEARING COMPLETION.

c. HAT SECTION BORON/ALUMINUM STRINGERS USING BOTH HIGH AND LOW PRESSURE BONDING HAVE BEEN FABRICATED AND TESTED.

d. SPOT AND BRAZE JOINING OF BORON/ALUMINUM HAS BEEN SUCCESSFUL.

e. BORON/EPOXY BOLTED JOINT STRENGTH IS CONSISTENT BETWEEN SPECIMENS.

f. GRAPHITE/POLYIMIDE HAT SECTION STRINGERS WERE FABRICATED.

g. DESIGN ALLOWABLES ARE BEING GENERATED FOR GRAPHITE/POLYIMIDE.

2. <u>PROBLEM AREAS</u>

a. ELEVATED TEMPERATURE GRAPHITE/EPOXY AND BORON/EPOXY PROPERTY DEGRADATION WAS FOUND TO OCCUR DUE TO ROOM TEMPERATURE AGING.

b. DIFFICULTY IS ENCOUNTERED IN DRILLING IN A COMBINATION OF BORON/EPOXY AND METALLIC JOINTS.

c. BOLT LOAD EQUILIZATION IN MULTI-BOLT JOINTS REQUIRES FURTHER INVESTIGATION.

d. SIZE LIMITATIONS IN BRAZE JOINING TECHNIQUES FOR BORON/ALUMINUM.

Conclusion

Based on the outlined research and development effort, it is the opinion of the authors that application of composite structures in selected areas of the Space Shuttle System is feasible. Boron/epoxy structures, especially tubular members, are considered state-of-the-art and are cost effective. Shell and beam structures in resin and metal matrix composites require completion of the ongoing program to make final recommendations. Results to date indicate that the shown weight savings of composites can be utilized. Single flight application of composites in areas of the connecting struts between SRM's, H/O tank, and orbiter are also recommended.

In most areas of selected application, only a normal structural development and qualification program similar to customary ones for metal structures is required. However, boron/aluminum usage would require additional development.

EUROPEAN TECHNOLOGY ON COMPOSITE MATERIALS

By

J. Fray, Hawker Siddeley Dynamics

A. W. Kitchenside, British Aircraft Corporation

J. J. Cools, FOKKER-VFW (Netherlands Aircraft)

C. P. H. Hanselmann, Maschinenfabrik Augsburg, Nürnberg

R. J. Jonke, European Space Vehicle Launcher Development Organisation

ELDO SPONSORED COMPOSITE RESEARCH

(Figure 1)

A study program was initiated to evaluate the significance of the post-Apollo program for Europe, to ascertain European ability to participate in certain new technological areas, and generally to prepare European industry to participate in the program.

This report deals with studies which were conducted in Europe under the direction of the European Space Vehicle Launcher Development Organisation (ELDO) on behalf of the European Space Conference in the field of advanced composite materials, based on previous industrial experience with a view toward future Space Shuttle application.

Four contracts on fibre-reinforced composites were awarded to four European firms with a total amount of approximately $500,000. (See fig. 1.)

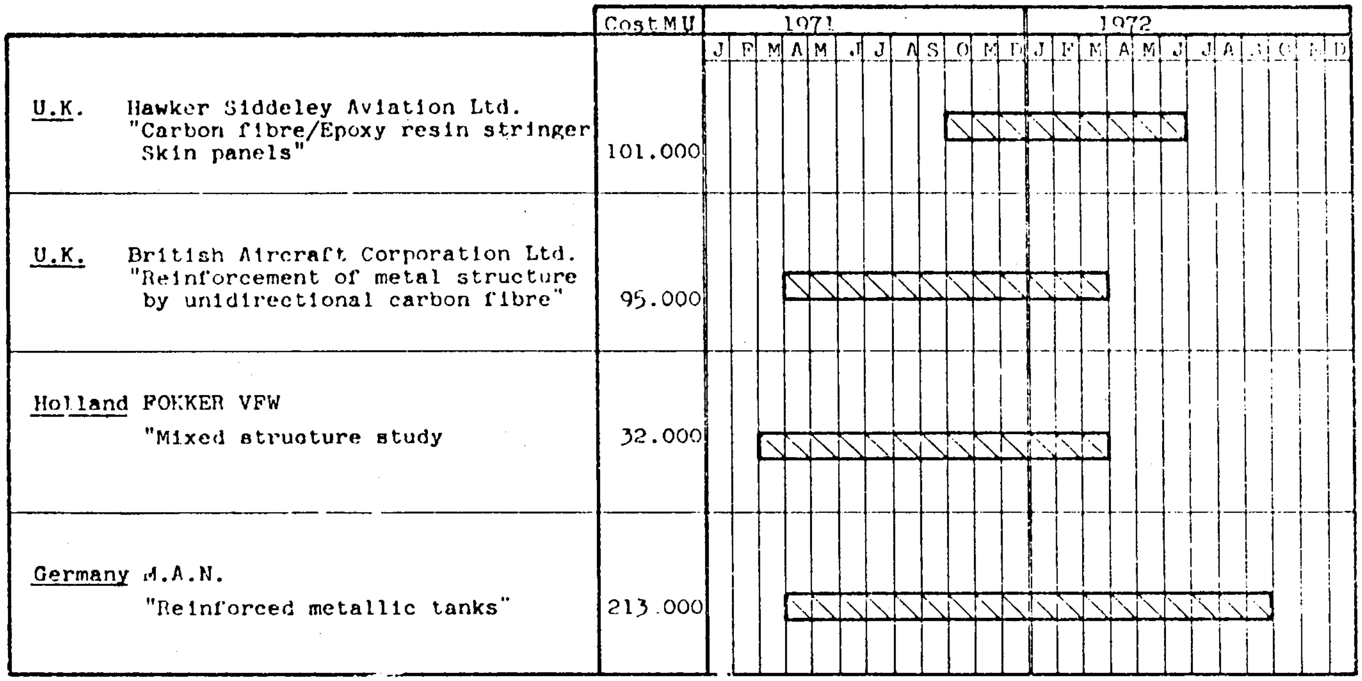

Figure 1.- ELDO sponsored composite research.

ELDO SPONSORED COMPOSITE RESEARCH

(Figure 2)

In selecting the program and in choosing firms which already have experience in this field, ELDO tried to cover, insofar as possible, future applications. Carbon and boron fibre components are manufactured and tested, using epoxy and polyimide as resins, with a view to extending the application field of the composite to 315° C (600° F). (See fig. 2.)

Hawker Siddeley Aviation (HSA), London, England, is working on carbon fibre and epoxy resin stringer and skin panels without any metallic part whereas British Aircraft Corporation (BAC), London, England, is concerned with reinforcement of metal structure by unidirectional carbon fibre in polyimide resin.

Maschinenfabrik Augsburg, Nürnberg (MAN), West Germany, is testing high-pressure steel tanks where the cylindrical part is reinforced by carbon fibre.

FOKKER-VFW (Netherlands Aircraft), Schipol-Oost, The Netherlands, has the task of manufacturing and testing a structural element of an orbiter cargo door in boron fibre and polyimide resin.

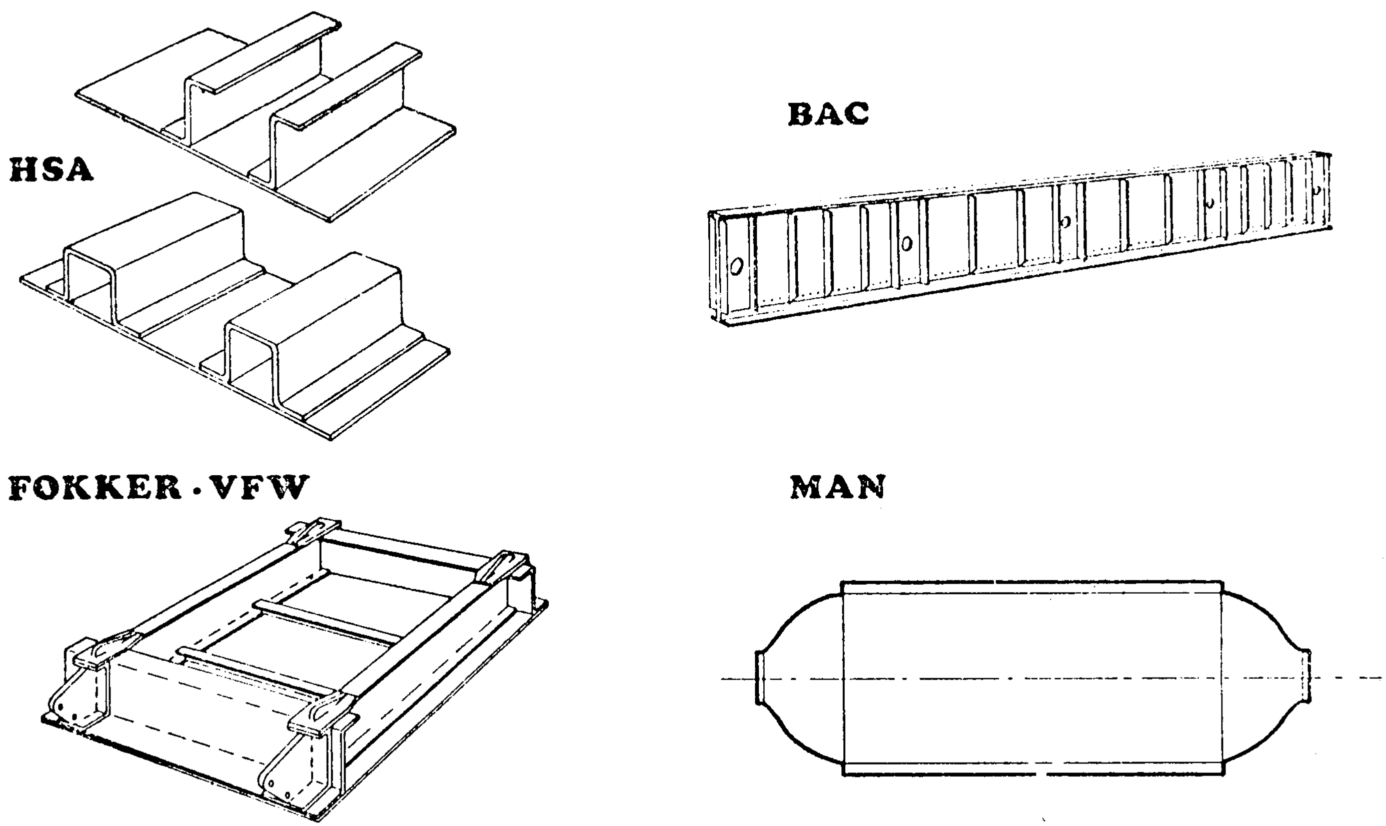

Figure 2.- ELDO sponsored composite research.

DEVELOPMENT OF CARBON FIBRE/EPOXY RESIN STRINGER/SKIN PANELS

(Figure 3)

The object of this program initially is to develop methods of analysis for carbon fibre in epoxy resin stringer and skin compression panels, and then to extend the work to the design and testing of a limited number of optimised panels. The work is divided into parts (a) and (b).

Part (a) covers the theoretical prediction of the initial compressive buckling stress of stringer skin panels made from high-strength carbon-fibre-reinforced plastic. Work has been carried out on a series of test panels having varying layups for both Z- and hat-section stringers in order to verify the theory. (See fig. 3.) In general, the layup of the stringers differed from that of the skin.

Part (b) entails the design and manufacture of optimum panels that make use of the theory developed in part (a). The panels have been optimised so that local torsional buckling and Euler buckling of the panel are coincident. The test work has yet to be completed.

The buckling analysis closely followed the method used in the RAeS Data Sheets 02.01.28 to 37 (ref. 1) and the optimisation work was based on that proposed by Farrar (ref. 2).

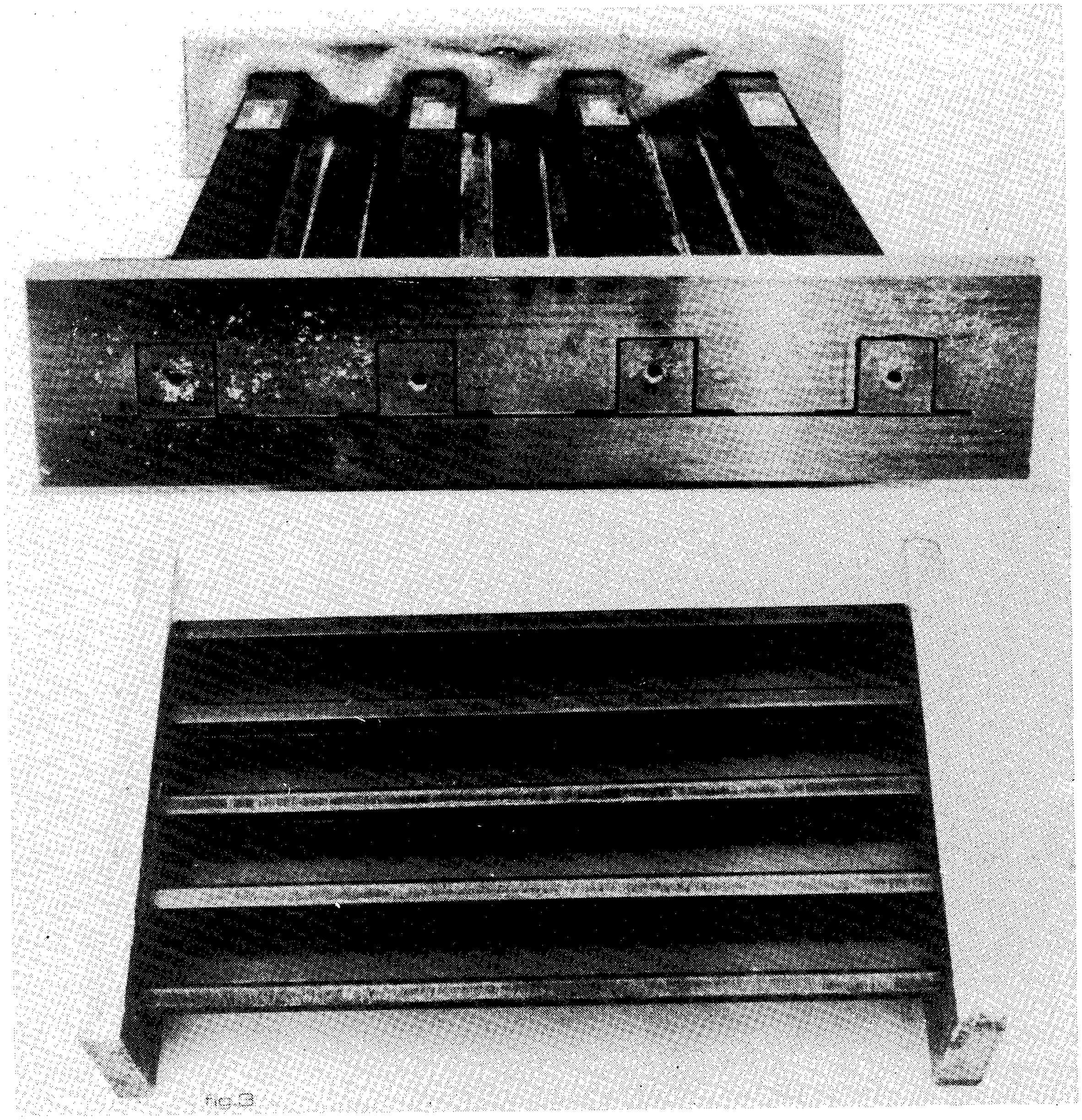

Figure 3.- Z- and hat-section stringers.

CROSS-SECTIONAL GEOMETRY OF HAT- AND Z-SECTION PANELS

(Figure 4)

For part (a) several panels (fig. 4) of constant geometry for each type were manufactured, with differing fibre orientations. These panels were tested in compression and, by means of electrical resistance strain gauges and dial gauges, the initial buckling stress of each panel was determined. There are four optimised panels in part (b) which have yet to be tested to see whether they achieve the buckling stresses predicted by theory.

In order to meet the simply supported condition for a given length of panel L, the panels which were actually tested were twice L in length and had the ends fully fixed against rotation; this arrangement gives effectively a simply supported section of length L in the centre of the panel.

In order that the panel would not fail by yielding of the material before the onset of buckling, "high-strength" fibre was used; thus, a greater margin between material failing load and buckling load is created.

Where resistance strain gauges were used, the dummy gauges were attached to a piece of material of identical layup to that being tested.

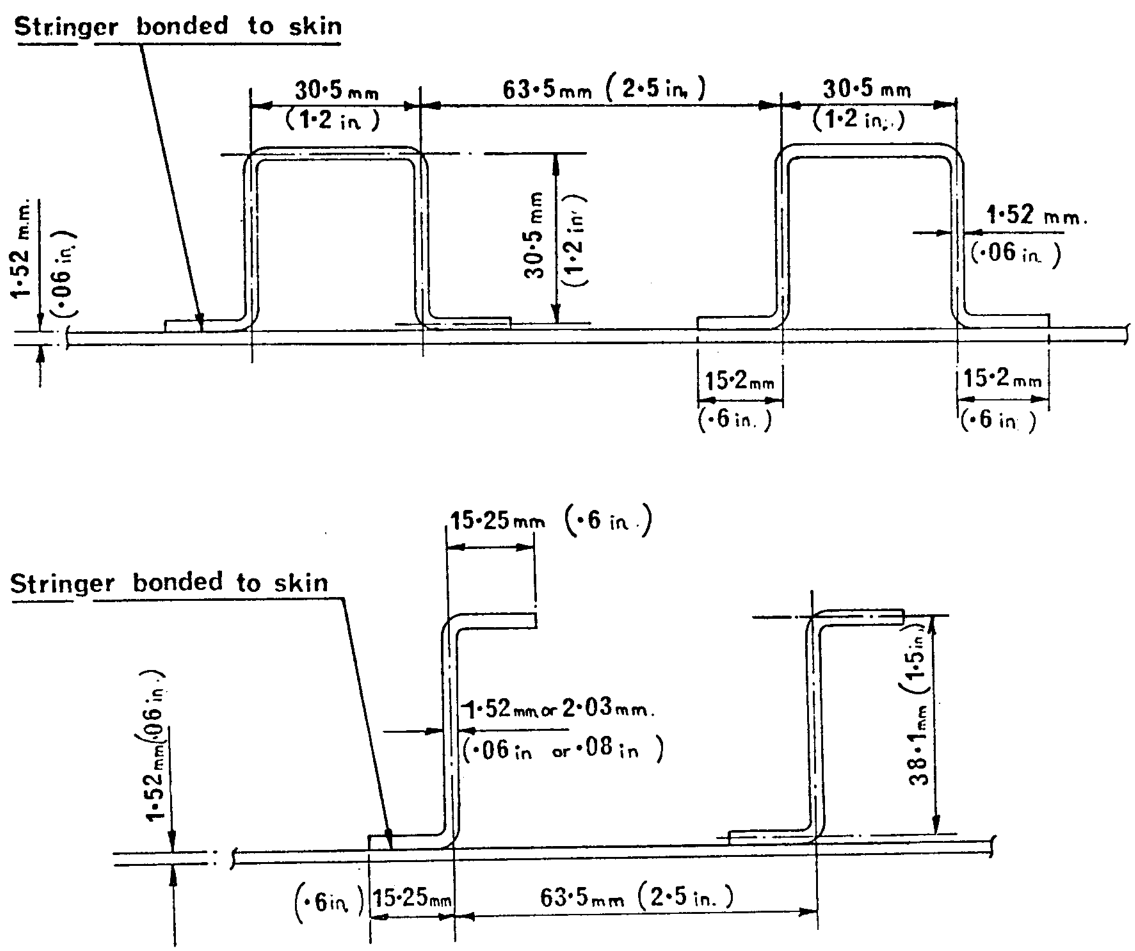

Figure 4.- Cross-sectional geometry of hat- and Z-section panels.

PANEL TESTING

(Figure 5)

All the panels in part (a) exhibited elastic properties up to buckling (fig. 5) and, in general, continued to carry up to 50 percent additional load before failure. The adhesive joint between stringers and skin remained intact up to panel failure, which was caused by failure of the composite rather than failure of the bond. All the Z-section panels buckled in a coupled local-torsional mode which was predominantly local buckling, with only small amounts of stringer roll. The hat-section panels buckled in a local mode. The buckled shape of the panels resembled that usually obtained from aluminum alloy panels, the half wavelength of the buckle being fractionally less than the stiffener pitch. The highest buckling stress achieved in part (a) was approximately 0.207 GN/m^2 (30 000 lb/in^2). This stress was for a hat-section panel with $\pm 15^\circ$ stringers and 0°, $\pm 45^\circ$ (33 percent at 0) skin.

One of the problems associated with optimised panels is obtaining the optimum plate thicknesses. Unless very thin sheets of "pre-preg" are used, it is often difficult to get a thermally balanced laminate of given layup and thickness. This limitation is a serious one and it may be necessary eventually to build certain constraints into the optimisation theory to produce practical panels. Since the optimum panels for part (b) have not yet been tested, the effect of slightly off-optimum thicknesses cannot be fully assessed.

Part (a) showed good comparison between theoretical and experimental buckling stresses for the panels and therefore the theory and assumptions used to predict the initial buckling stress of a given panel made from an isotropic material would seem to be valid. To establish the theory beyond doubt, however, would require a much larger number of panel tests and a large range of fibre orientations and cross-sectional geometries.

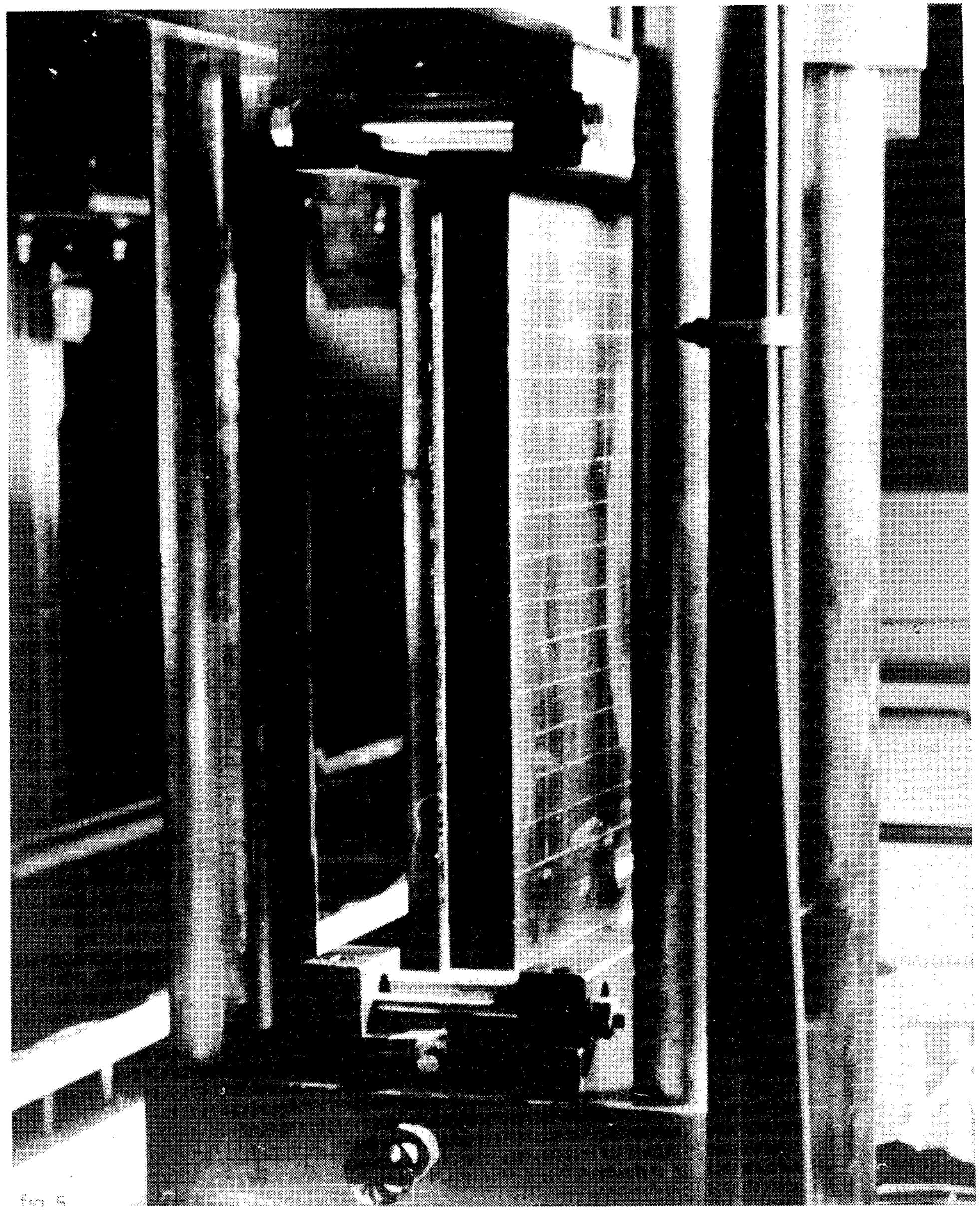

Figure 5.- Panel testing.

REINFORCEMENT OF METAL STRUCTURE BY UNIDIRECTIONAL CARBON FIBRE COMPOSITE

(Figure 6)

Unidirectional high-temperature carbon-fibre-composite reinforcement (CFRP) of metal structures under Space Shuttle environment was the programme at the British Aircraft Corporation that extended existing composite and adhesive research.

Design data for selected polyimide and epoxy matrix and adhesive systems (ICI QX13, Shell DX210, Cyanamid FM34 and 3M's AF 130) were derived by use of the specimens depicted in figure 6. Also shown is the final component, a test beam having a span of 1.2 meters (4 ft).

The following parameters were recognised as being of fundamental importance to the proposed application:

(a) Effective bonding temperature of the adhesive (governs thermal stresses, and was determined by using bimaterial strip curvatures)

(b) Composite shear modulus (term in flange stability, measured by torsion of strips)

(c) Basic shear strength of adhesive (measured by flexure shear specimen)

(d) Fatigue of compound specimens (composite and metal)

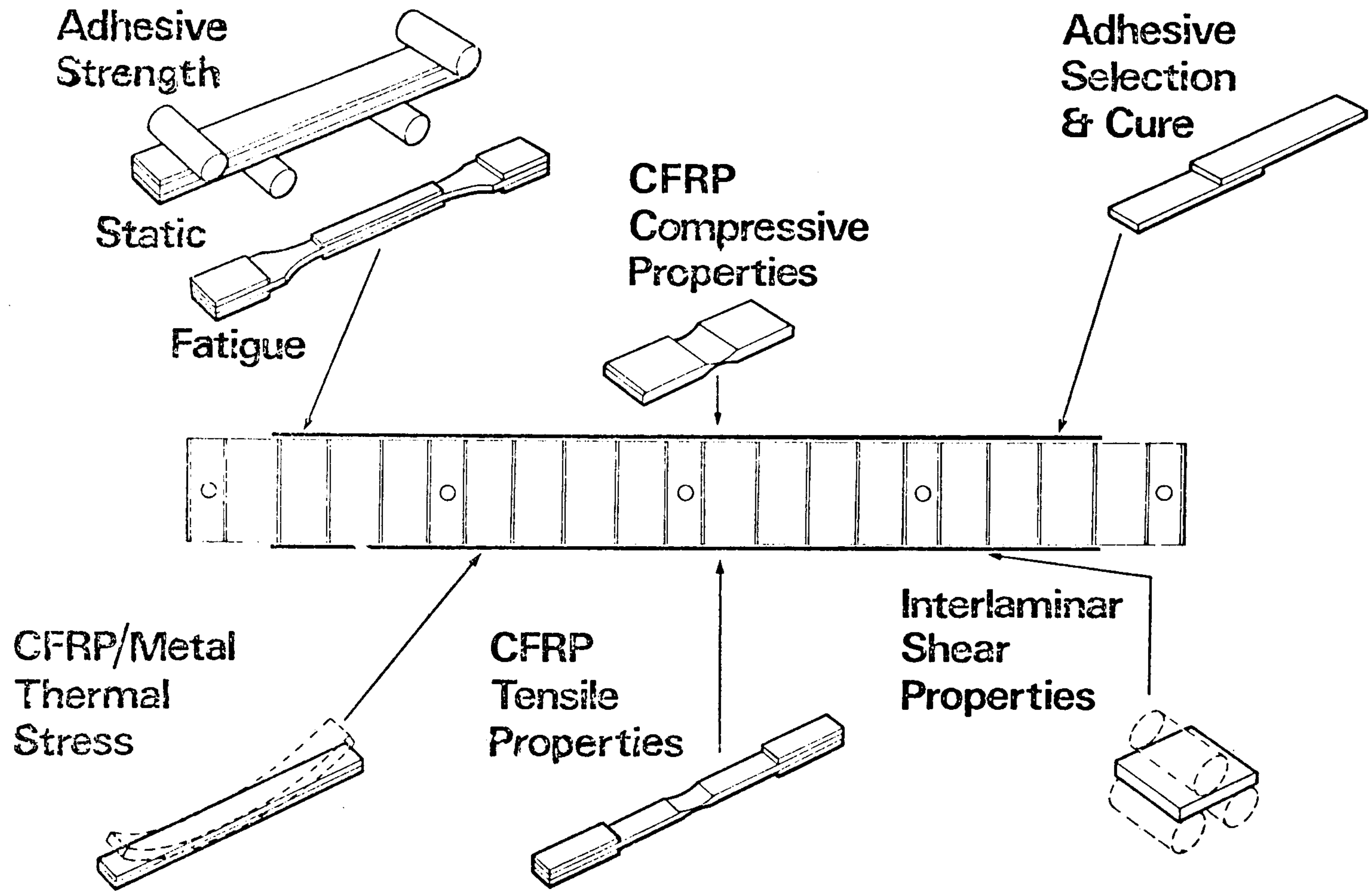

Figure 6.- Test specimens.

REPRESENTATIVE BEAM COMPONENT

(Figure 7)

Participation in the North American Rockwell Space Shuttle team aided the definition of task assumptions. At program initiation, the SSV baseline was a protected titanium structure, and a titanium alloy (6Al-4V) beam reinforced by polyimide composite strips was selected as the target structural component (fig. 7). Static testing and repeated load testing at the established maximum service temperature were used to establish beam performance. Epoxy composite systems with aluminum alloy and titanium alloy were included in data compilation work both as a fallback and as a possibility for crew compartment and payload module structure.

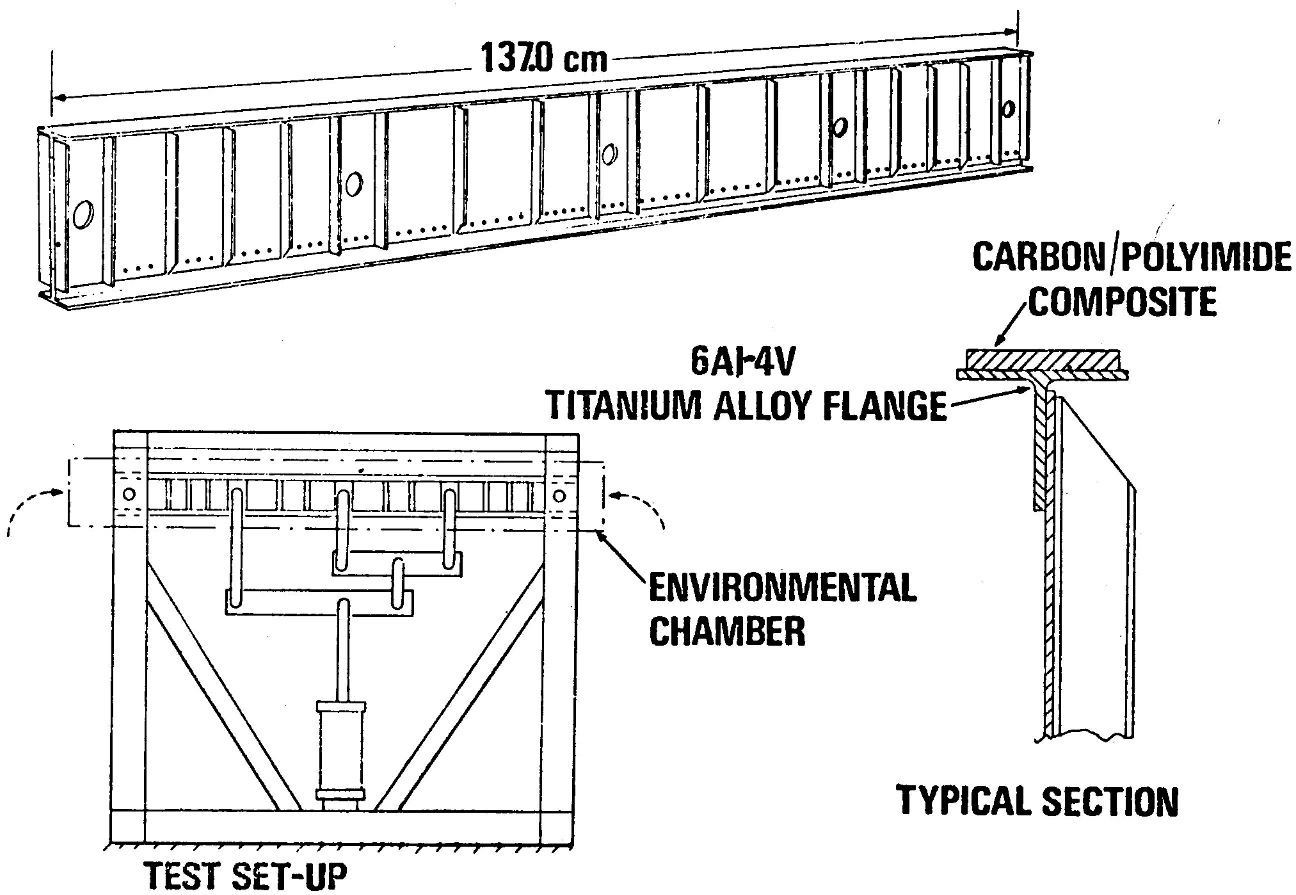

Figure 7.- Representative beam component.

INTERLAMINAR SHEAR STRENGTHS

(Figure 8)

Results for basic composite and adhesive properties were presented at the mid-term review in Paris in October 1971 (ref. 3). As an example, interlaminar shear strengths for the epoxy and polyimide systems are shown in figure 8. These and other results indicate that the polyimide matrix, although it has a greater usable temperature, was generally less satisfactory than the epoxy matrix. The epoxy matrix showed much reduced compressive and interlaminar shear strength above 100° C. Tensile strength was close to the anticipated value but the polyimide compressive strength was lower than that expected – about half the tensile strength up to 200° C and less above this temperature. A maximum usable temperature of 300° C was established for the polyimide matrix. Shear moduli were measured by a modified Greszczuk ring (ref. 4) for the epoxy composite and by flat strip torsion for the polyimide to alleviate moulding problems.

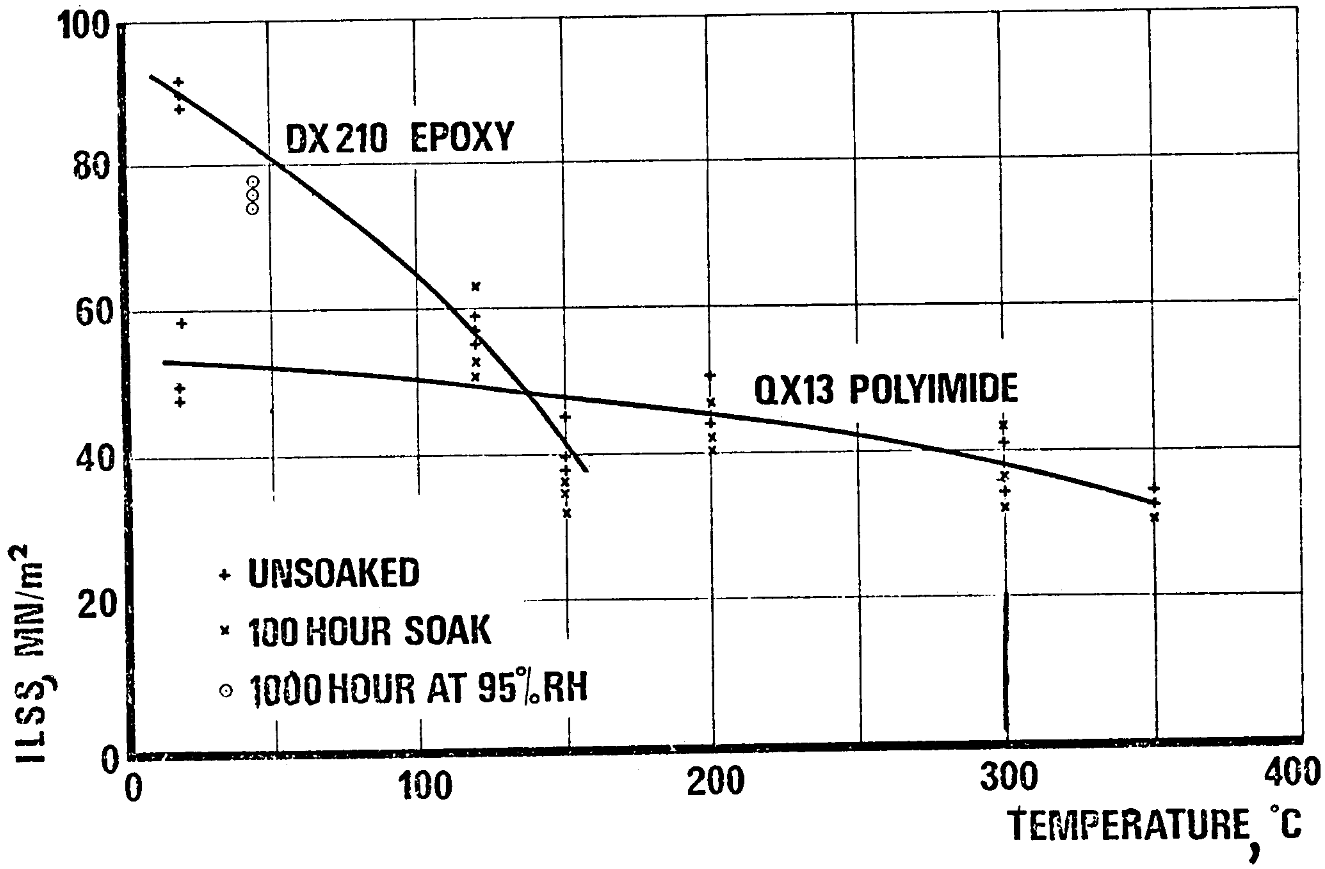

Figure 8.- Interlaminar shear strengths.

SHEAR STRENGTH OF FM34 ADHESIVE

(Figure 9)

Figure 9 compares flexure and lap shear strength results for FM34 adhesive and indicates the stress concentration in the lap joints. The zero thermal stress temperature was 200° C for a cure temperature of 350° C (for AF 130 corresponding values were 150° C and 177° C). At low temperature, a significant alleviation of thermal stress results, but at maximum temperature, thermal stresses not originally anticipated are produced.

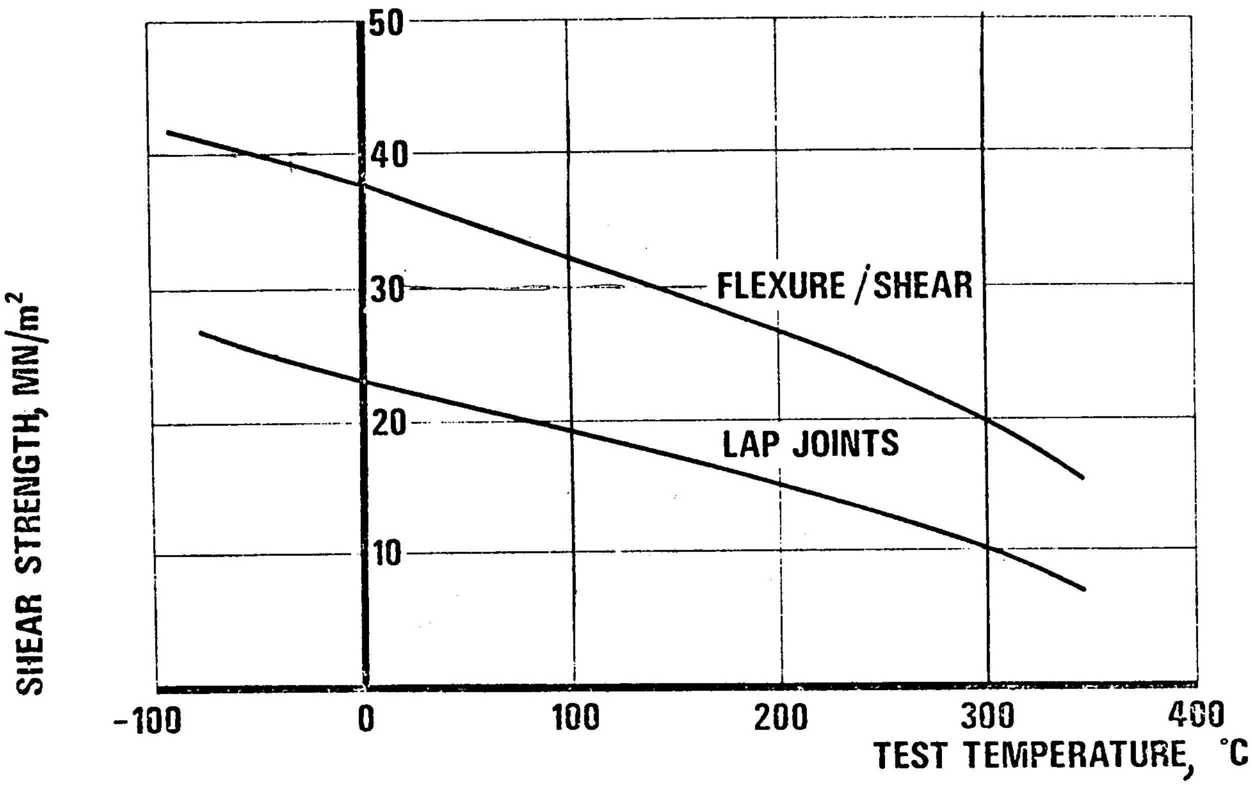

Figure 9.- Shear strength of FM34 adhesive. Composite/titanium.

COMPOUND FATIGUE TEST SPECIMEN
(Figure 10)

The compound fatigue test specimen (fig. 10) was designed to give a representative stress concentration in the adhesive. The effect of this stress concentration was clearly shown in the results obtained under cyclic thermal testing, particularly with the polyimide adhesive, where cracks formed in the adhesive at the ends and spread toward the centre.

Under repeated loading the shear stress in the adhesive is critical, and this effect was confirmed by the beam fatigue test at 300° C. The adhesive failed on the tension flange where thermally induced stresses were added to those due to the applied load, since the effective cure temperature was 100° C less than the test temperature.

The static test failure occurred in the compression flange at a composite stress consistent with test coupon results.

Minimisation of adhesive stress concentrations is a fundamental design problem in the reinforcement of metal structure by composite strips and would be greatly assisted by adhesives with greater flexibility.

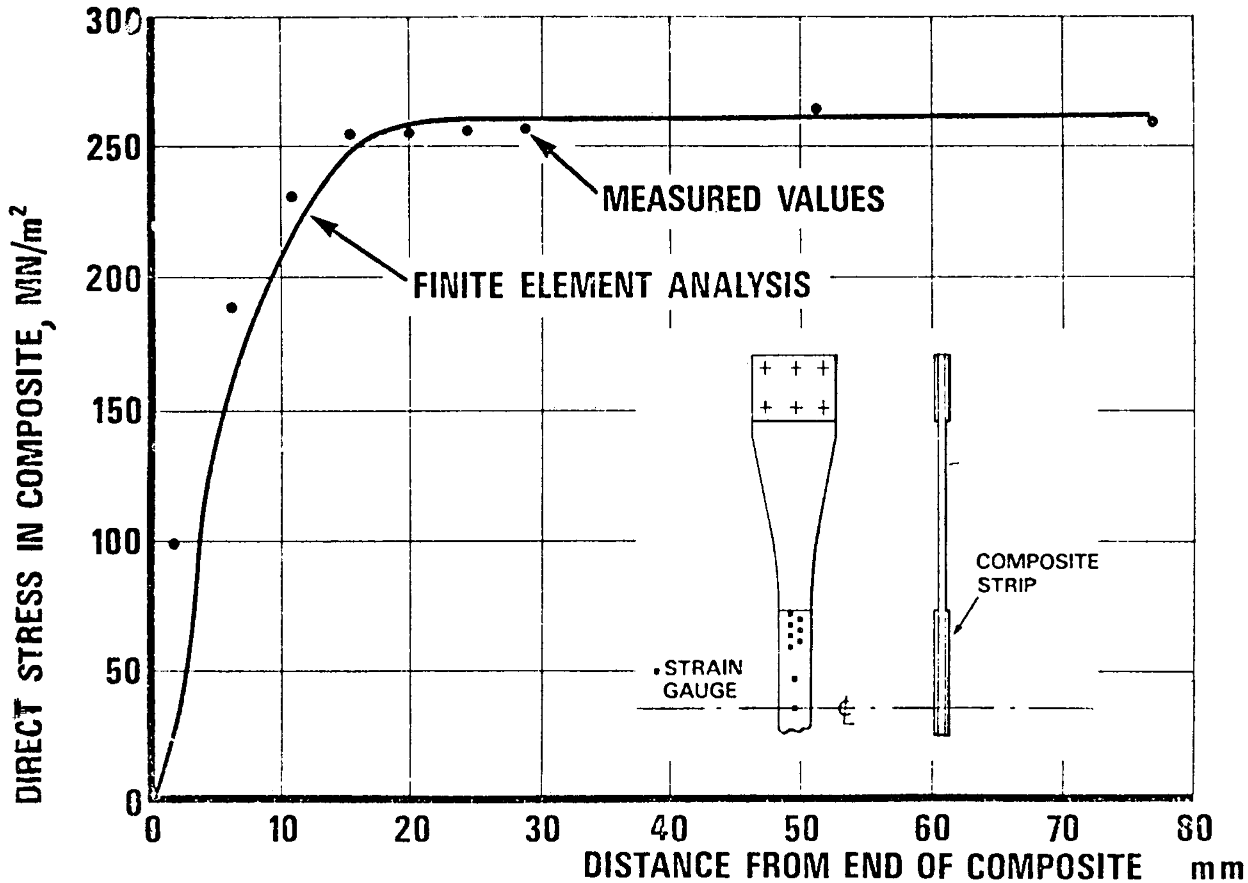

Figure 10.- Fatigue test specimen. Plain composite.

MIXED STRUCTURE STUDY FOR AN ORBITER CARGO DOOR

(Figure 11)

By use of design criteria supplied by McDonnell Douglas Corporation, a feasibility study of a mixed structure using boron/polyimide composite and titanium has been carried out. High-modulus boron composite is sandwiched between metallic sheets in order to (1) seal the polyimide resin matrix from oxidation effects, (2) improve transverse properties, and (3) provide an electrically conductive coating.

The maximum loads are encountered at ambient temperature during opening and closing of the door and at 150° C due to a pressure differential of ± 6.895 mN/m^2 (± 1 psi). The maximum temperature reached is 315° C.

The resin matrix must provide adequate adhesion to the metallic outer sheets and be able to withstand a maximum temperature of 315° C. Another important problem is the transfer of concentrated loads into mixed structural laminates which necessitates mechanical fastening.

The combination of boron composite and titanium was selected because of the thermal stresses which occur when the structure is subjected to extremely high and low temperatures relative to the cure temperature.

It can be concluded from figure 11 that the combination of boron composite and titanium is far more favourable than a mixed structural laminate with carbon composite material.

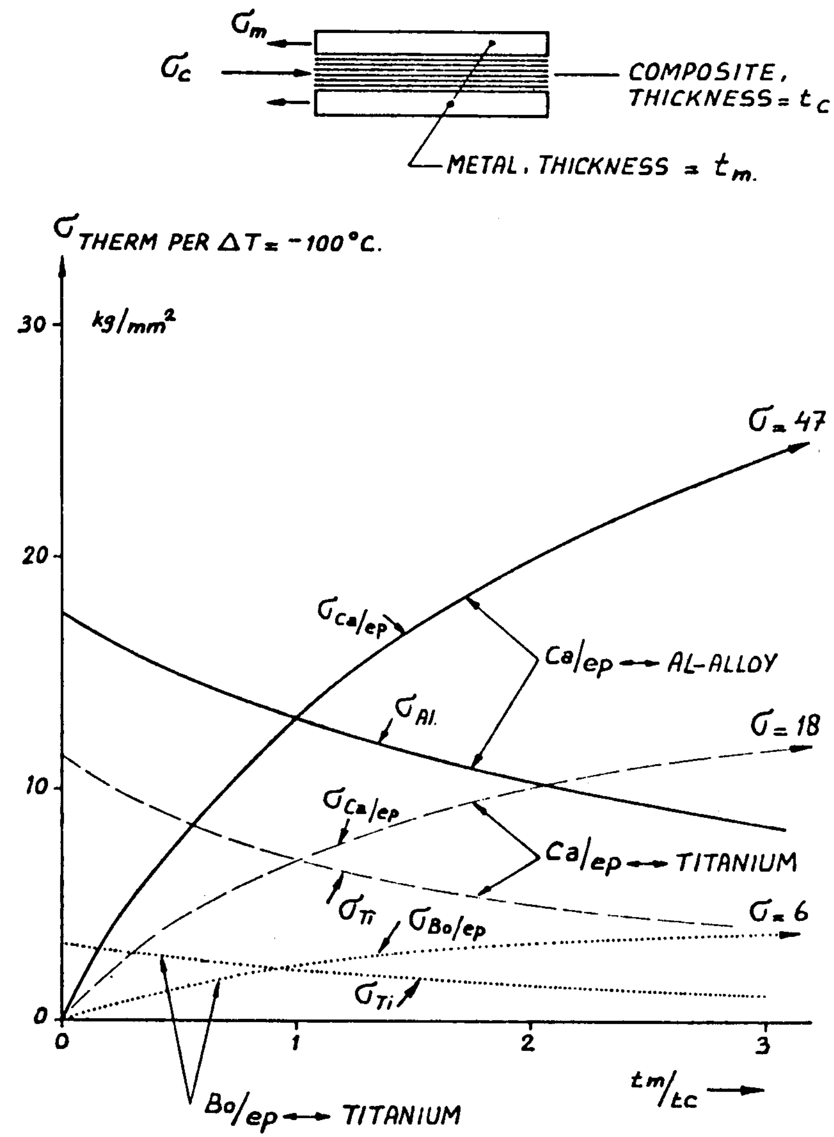

Figure 11.- Thermal stresses in mixed structural laminates.

FLEXURAL PROPERTIES OF BORON AND POLYIMIDE

(Figure 12)

The maximum temperature of 315° C requires a heat-resistant polyimide resin as matrix. The heat resistance of boron laminates was determined by using flexural specimens. These specimens were coated with aluminum foil during the postcure of the resin and heat-aging of the specimens. Prior to testing, the aluminum foil was removed.

Test results are given in figure 12. Failure of all specimens was initiated by interlaminar shear. In general, the composite material shows good strength retention with relative low scatter. The scatter in flexural strength increases considerably at 315° C and indicates that this temperature must be considered as the ultimate operating temperature.

Test temperature, °C	Aging temperature, °C	Aging time, hr	E_{FLEX} average, kg/mm²	σ_{FLEX} Minimum ⟷ Maximum, kg/mm² (a)	σ_{FLEX} Average, kg/mm²
22	---	---	17 500	58 to 65	60
150	---	---	15 670	41 to 45	42
315	---	---	13 540	[b] 42 to 72	58
22	315	50	16 870	104 to 123	115
		100	17 070	58 to 62	59
150	150	50	15 680	48 to 54	52
		100	16 400	49 to 53	51
315	315	50	14 300	[b] 43 to 105	70
		100	14 060	[b] 63 to 96	76

[a] Minimum and maximum values of three specimens.

[b] Great scatter when tested at 315° C.

Figure 12.- Flexural properties of boron and polyimide. Fibre orientation, parallel; fibre content, 55 to 60 percent by volume.

BONDED ASSEMBLY OF CARGO DOOR SPECIMEN

(Figure 13)

Figure 13 shows the bonded assembly of the developed door specimen, measuring about 550 mm by 750 mm. At the four corners of the panel will be attached brackets, shaped so that the panel can be tested in bending.

The normal loads from the brackets (representing the hinge brackets of the door) are directly transferred to the flanges of the I-frames by means of bolted gusset plates. The gusset plate on the skin side passes through a slot in the web of the Z-edge member.

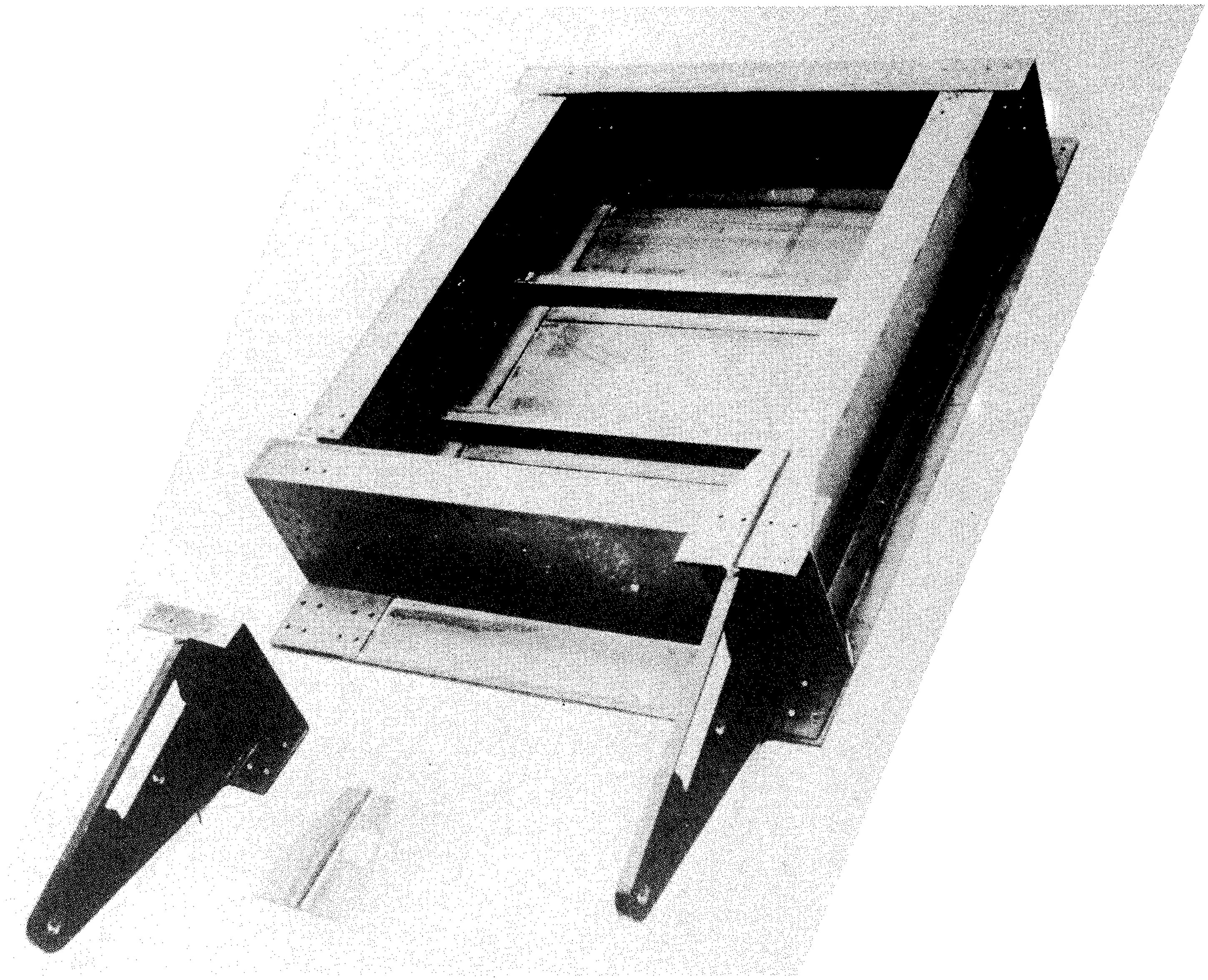

Figure 13.- Bonded assembly of cargo door specimen.

CONSTRUCTION OF I-FRAME
(Figure 14)

The mixed laminated structure of the I-frame is shown in figure 14. At the ends of the flanges the boron composite has been replaced by titanium reinforcing strips of staggered length for load introduction by means of bolts.

The condensation products which are formed during the cure of the polyimide necessitated a two-step process to avoid a porous boron laminate. First the boron laminate is cured using vertical bleeding to carry off volatiles and condensation products. Next the cured laminate is bonded between the titanium sheets with the heat-resistant adhesive Narmco 840. This adhesive was also used for assembly bonding of the door specimen. To facilitate production, a heat-resistant resin matrix which cures without forming condensation products is desirable. This resin matrix would also need to have good interlaminar shear strength and good adhesion to titanium. The two-stage manufacturing process could then be eliminated.

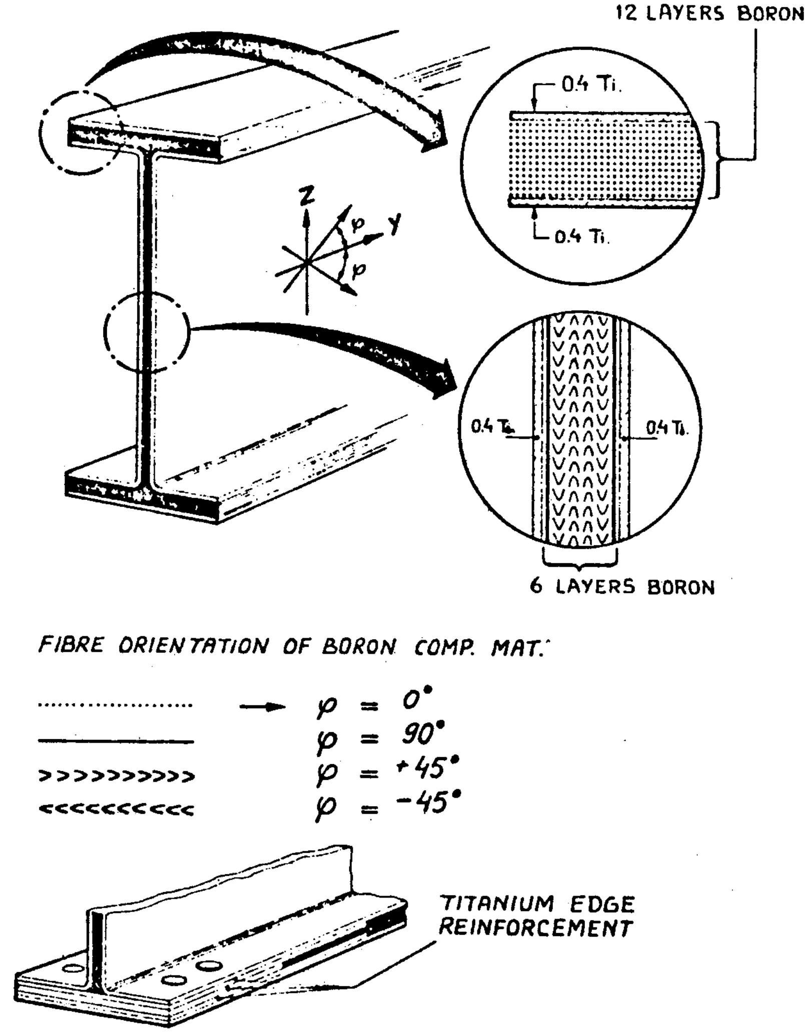

Figure 14.- Construction of I-frame.

PARTIALLY REINFORCED HIGH PRESSURE VESSEL

(Figure 15)

The partial reinforcement of a high pressure vessel by carbon-fibre-reinforced plastic (CRP) leads to a weightsaving of up to 20 percent when compared with a purely metallic vessel of the same geometry. On the other hand, the fabrication technique raises relatively few critical technological problems, especially in view of the required reusability of the vessel.

The applicability of carbon-fibre-reinforcement techniques has been demonstrated at MAN in a number of development projects, such as cryogenic storage vessels, totally reinforced pressure vessels, solid rocket motor cases, structural elements, and gas centrifuge rotors. (See fig. 15.)

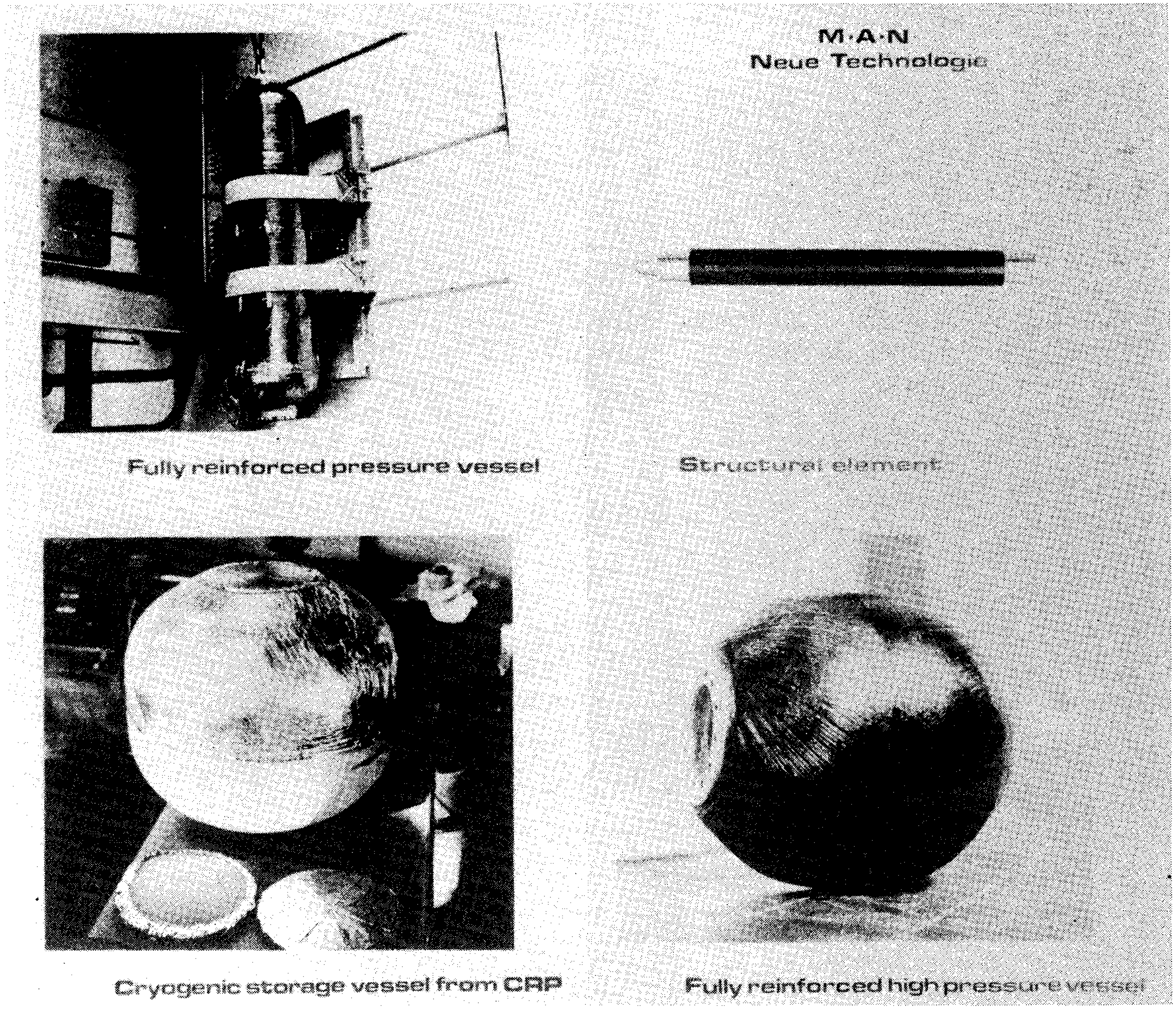

Figure 15.- Application of techniques.

TANK DESIGN

(Figure 16)

The vessel design is shown in figure 16. A metallic liner of constant thickness (1.7 mm) of high-strength steel ($\sigma_y = 170$ kg/mm^2) is reinforced circumferentially on the cylindrical section by CRP. The fittings are weight optimised. No provision for support has been provided yet. The carbon-fibre reinforcement extends over the cylindrical section into the caps, in order to decrease the tension gradually and thus to avoid fibre separation. The thickness of the CRP reinforcement was calculated to be 2.25 times the thickness of the metallic liner, the tensions in the longitudinal and circumferential directions in the liner being assumed to be of the same magnitude.

The CRP data were assumed to be

$$E = 1.1 \times 10^4 \text{ kg/mm}^2; \quad \sigma_y = 120 \text{ kg/mm}^2$$

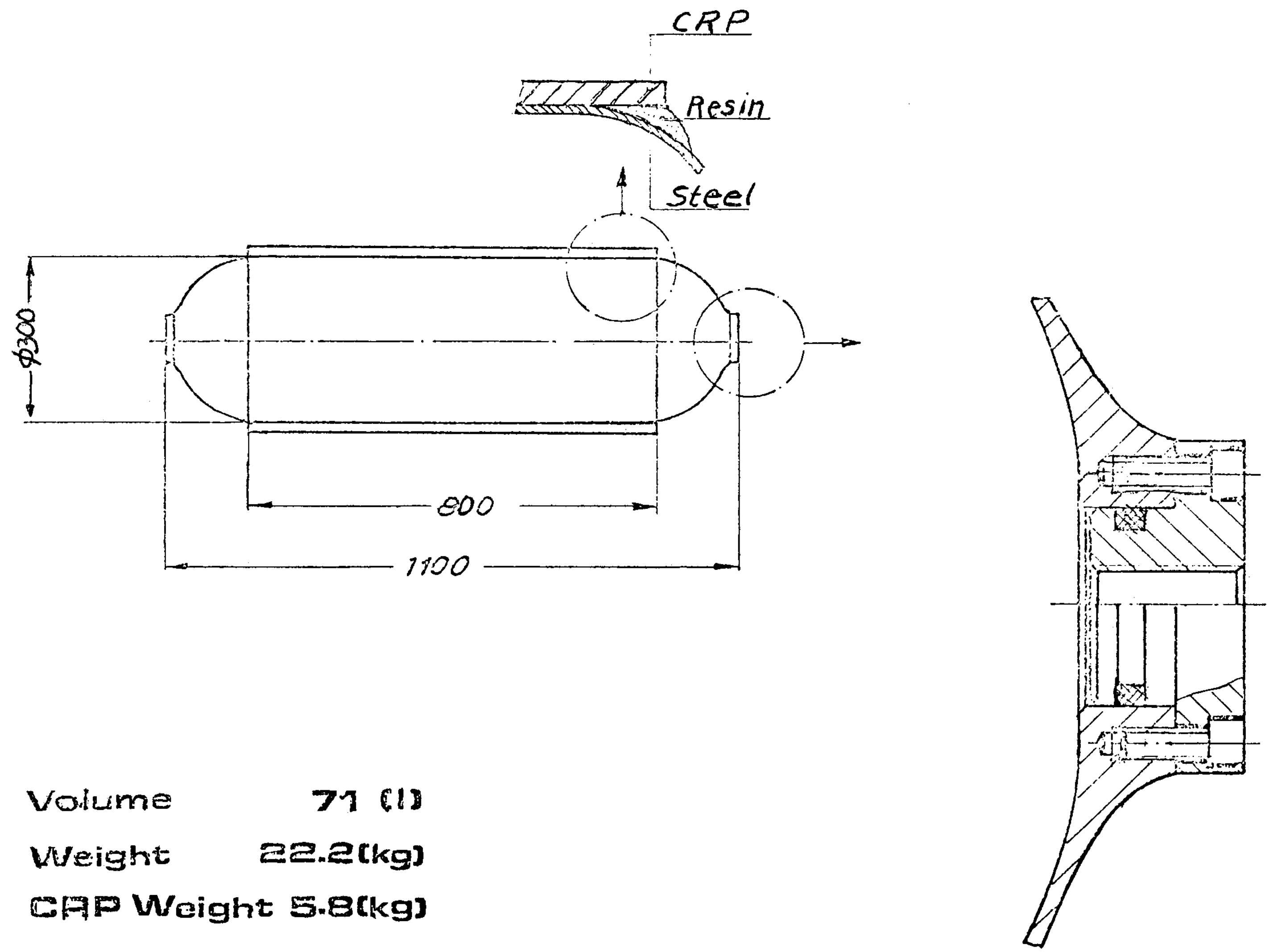

Figure 16.- Tank design.

FABRICATION OF METALLIC LINER

(Figure 17)

The metallic liner was manufactured from hot pre-formed parts. The caps and cylinder were cold rolled and turned to the final dimensions for welding. The latter was accomplished by EB welding in order to obtain a high reproducibility. The steps in the liner manufacture are listed in figure 17.

MAIN STEPS OF FABRICATION OF METALLIC LINER

INSPECTION OF RAW MATERIAL

HOT FORMING – ROLL FORMING OF HEMISPHERICAL SECTION (yet to be determined)

ROLL FORMING OF CYLINDRICAL SECTION

CRACK INSPECTION

TURNING OF COMPONENTS (in preparation for welding)

GEOMETRICAL CONTROL

CLEANING

ELECTRON BEAM WELDING

X-RAY INSPECTION OF WELDS

- surface cracks inspection
- Helium leakage detection

HARDENING (VACUUM OVEN)

SECOND CRACK INSPECTION

APPLICATION OF STRAIN GAUGES ON METALLIC SURFACE

Figure 17.- Main steps of fabrication.

FABRICATION STEPS
(Figure 18)

The CRP reinforcement was applied in circumferential wraps directly over the caps, using a fillet of resin to maintain the cylinder geometry. The yarn was routed through a heating device and wound onto the tank at a constant tension. The resin used was of the cold setting type (cure temperature 40° for 24 hours). Tests to obtain information about the difference in shrinkage between liner and CRP were previously performed with success.

Some of the fabrication steps are shown in figure 18.

The carbon fibres on the market exhibit variations in quality that cannot be tolerated for reproducible manufacturing processes. With funds from the German Government and working together with the carbon-fibre manufacturers, MAN has developed methods to ensure variations of acceptable magnitude. A method for continuous nondestructive testing of the carbon fibre is currently being developed. In the same government-sponsored programs, the factors influencing quality in the same manufacturing process of CRP have been determined and suitable manufacturing specifications have been established.

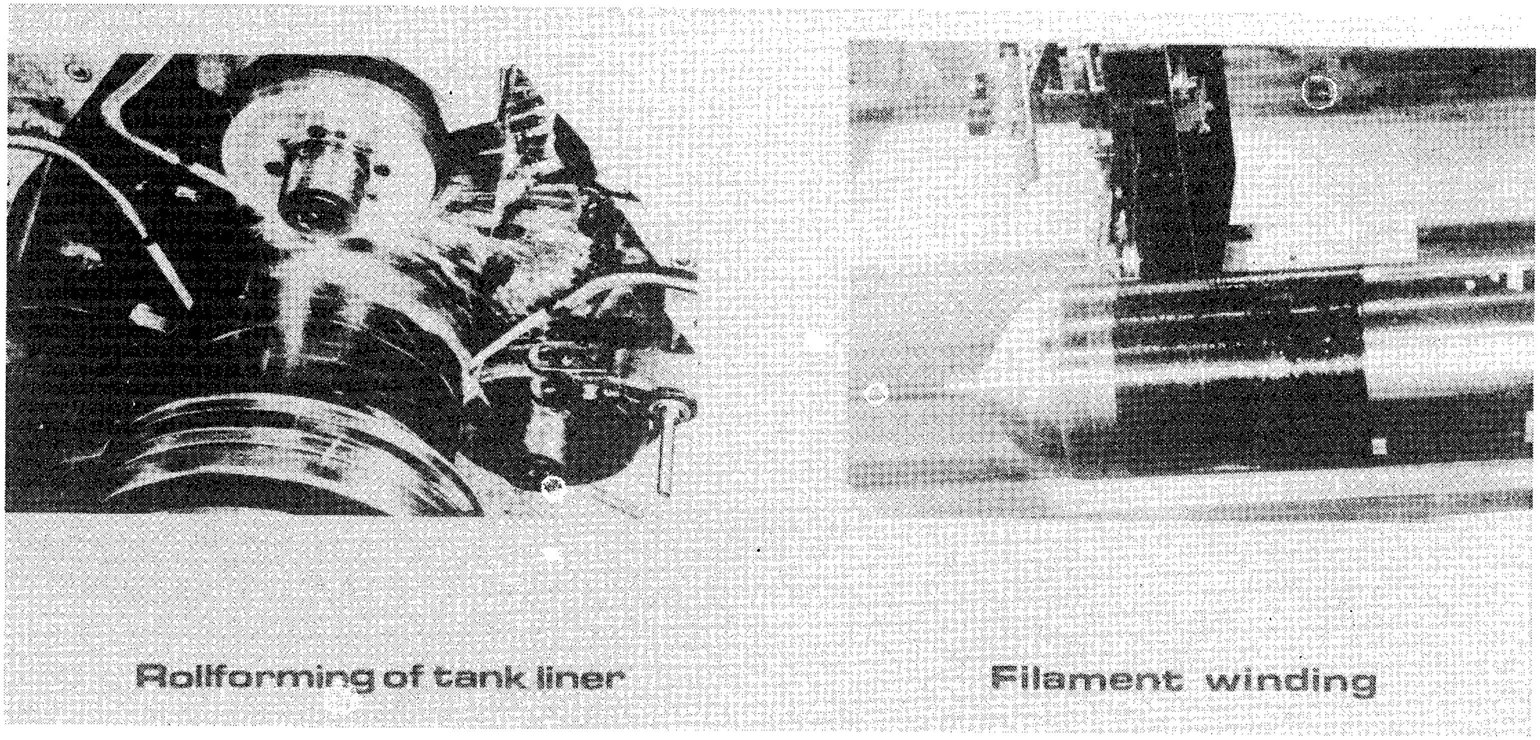

Figure 18.- Fabrication steps.

TESTBOX AND TANK

(Figure 19)

After manufacture and inspection, the pressure vessels were installed for testing and submitted to water pressure tests up to rupture (fig. 19). The results obtained with the "fabrication test models" were somewhat below the theoretical design values. A burst pressure of 365 atmospheres was obtained. (1 atmosphere = 1.013×10^5 N/m^2.)

The rupture of the vessel seems to have begun in the cylindrical section of the metallic liner, probably caused by an agglomeration of titanium carbide. The carbon-fibre reinforcement practically remained intact and confirmed the design results which indicated that the CRP was not submitted to its maximum load capability.

In the remaining program, 17 vessels are planned to be fabricated in order to obtain sufficient information on the fabrication reproducibility. Tests will include pressure cycling in order to demonstrate the reusability of the pressure vessel concept.

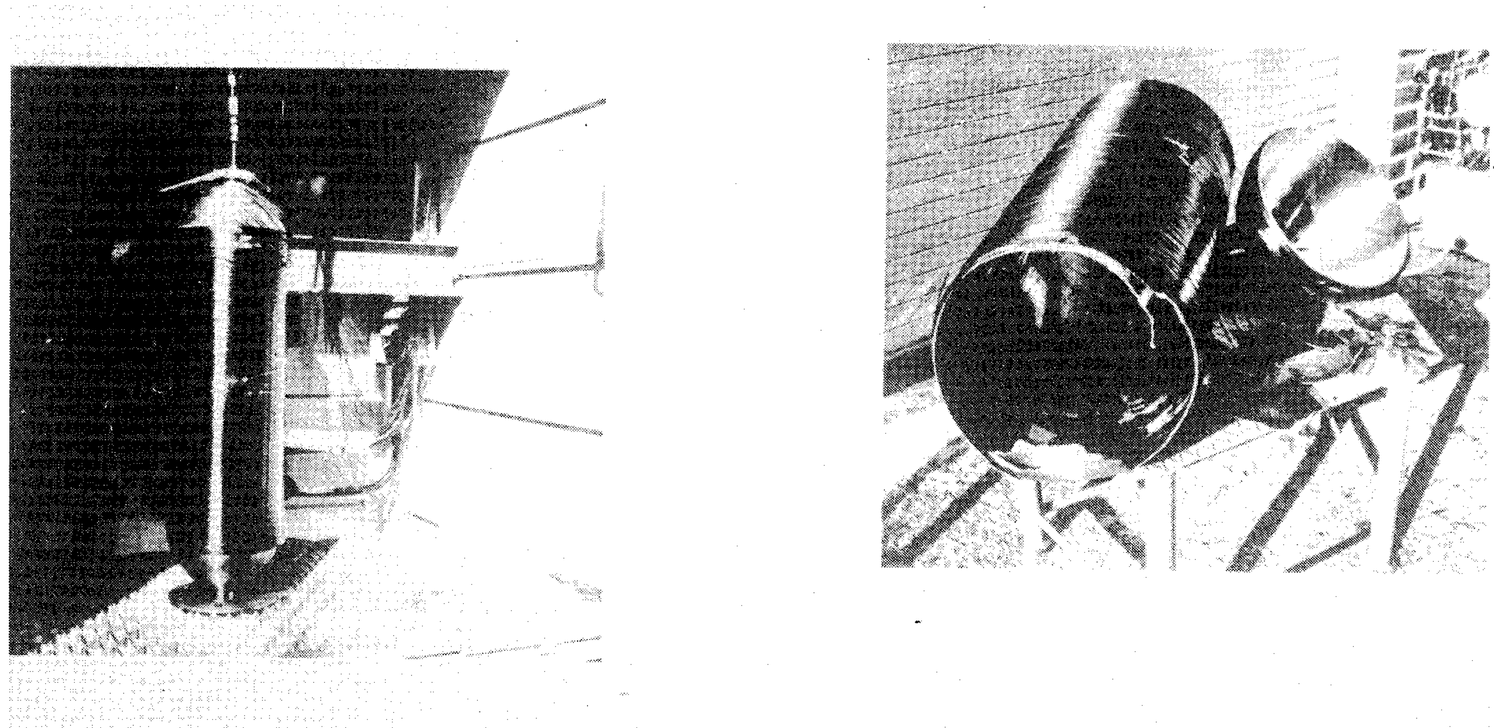

Figure 19.- Testbox and tank.

CONCLUDING REMARKS

The preliminary results of the European technology program on composite materials presented in this paper are encouraging. These analyses already indicate the direction in which further work could be undertaken but the continuation of this program will depend on decisions regarding the participation in the future. However, the choice by NASA of more conventional technologies for the Space Shuttle make the application of these techniques more remote.

If the definition of the space tug shows a major interest for this type of material, ELDO structure technology work could be oriented towards use for the space tug, if this element is selected as the key contribution of Europe to the post-Apollo program.

REFERENCES

1. Anon.: Engineering Science Data Aeronautical Series, Structures Subseries. Vol. II, Nos. 02.01.28 to 02.01.37, Roy. Aeronaut. Soc., 1954.
2. Farrar, D. J.: The Design of Compression Structures for Minimum Weight. J. Roy. Aeronaut. Soc., vol. 53, Nov. 1949, pp. 1041-1052.
3. Anon.: Reinforcement of Metal Structures by Unidirectional Carbon Fibre Composite. ELDO sponsored research at the British Aircraft Corporation. WSO/M/583, British Aircraft Corp., Oct. 12, 1971.
4. Greszczuk, L. B.: Shear-Modulus Determination of Isotropic and Composite Materials. Composite Materials: Testing and Design, Spec. Tech. Publ. No. 460, Amer. Soc. Testing Mater., c.1969, pp. 140-149.

ASSESSMENT OF ADVANCES IN STRUCTURAL ANALYSIS FOR SPACE SHUTTLE

By

Sidney C. Dixon, Melvin S. Anderson, and Wendell B. Stephens

NASA Langley Research Center
Hampton, Virginia

STRUCTURAL ANALYSIS PROGRAMS FOR SPACE SHUTTLE

The purpose of this paper is to review the latest technology for structural analysis in relation to the design tasks that lie ahead for the space shuttle. Consideration will be given to programs in the public domain which were developed or funded (completely or partially) by NASA. These programs are state-of-the-art in capability, are well documented, and are or will soon be available through COSMIC.*

The types of structures to be discussed herein are indicated in the figure. For shell-of-revolution structures, the analysis can be formulated as a one-dimensional problem which is readily solved by using finite-difference or numerical-integration techniques. Three excellent programs are available for analysis of this type of structure: SRA (refs. 1 to 4), BOSOR (refs. 5 to 8), and SALORS (ref. 9). The SRA system of programs currently has the most capability, and a problem illustrating recent extensions to this system will be discussed in some detail. For more general asymmetric shells, a two-dimensional formulation is required. However, the governing equations are readily formulated and are amenable to solution by finite-difference techniques. The STAGS program (refs. 10 to 12) is based on a two-dimensional finite-difference technique, and problems illustrating its capabilities will be discussed. For a completely general structural arrangement, such as structural frameworks, recourse is usually made to discretized formulations using finite elements. Of course, the finite-element programs could be used for shell structures, but at a loss in accuracy and increase in computer time compared with the special-purpose programs. In this paper, discussion will be restricted to the NASTRAN system (refs. 13 and 14) although numerous other programs exist and several are available for general use.

A comprehensive review of current analysis capability for shells of revolution is given in reference 9, and summaries of recent structural analysis and design developments are given in references 15 to 17. Some of the recent developments in automated design will be discussed later in this paper.

---

*Computer Software and Management Center, University of Georgia, Athens, Georgia.

STRUCTURAL ANALYSIS PROGRAMS FOR SPACE SHUTTLE

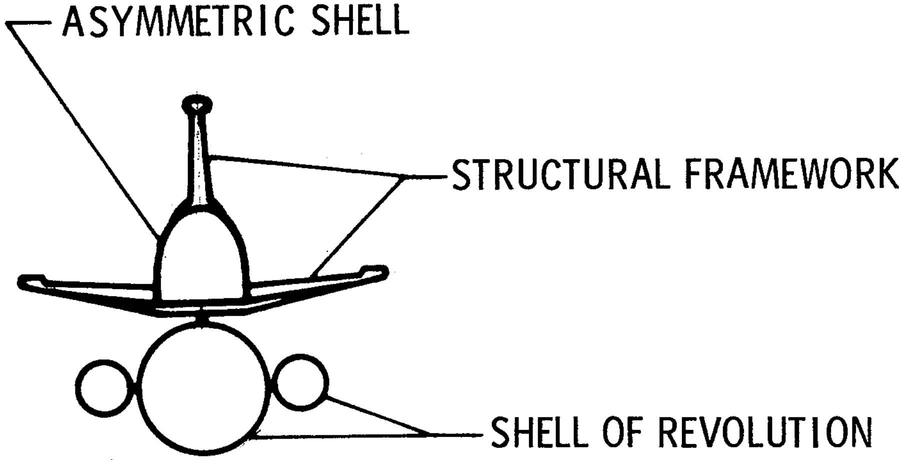

TYPE OF STRUCTURE	TYPE OF ANALYSIS	PROGRAM
SHELL OF REVOLUTION	ONE-DIMENSIONAL	SRA BOSOR SALORS
ASYMMETRIC SHELL	TWO-DIMENSIONAL	STAGS
STRUCTURAL FRAMEWORK	FINITE-ELEMENT	NASTRAN

SHELL-OF-REVOLUTION PROGRAM CAPABILITIES

Many structural components of the space shuttle can be approximated as shells of revolution with a high degree of accuracy. The shell geometry and stiffness are considered to be rotationally symmetric (hence stringers are smeared), and variables are expanded circumferentially in Fourier series to formulate a one-dimensional problem. The shell meridian is discretized by finite-difference stations or subintervals for numerical-integration schemes. The extensive stress, vibration, and buckling analysis capability that exists for shells of revolution was discussed at the 1971 NASA Space Shuttle Technology Conference (ref. 15). This capability includes the complexities shown in the figure, such as complex wall construction, discrete rings, and segmented and branched shells.

Recent advances in analysis capability will be illustrated by results obtained for the buckling of a segmented, branched HO tank under asymmetric mechanical loads. Currently, only the SRA system of shell-of-revolution programs can consider all these complexities. This system of programs is based on numerical-integration techniques. Typical of numerical-integration schemes is the "long subinterval" problem which requires that the shell meridian be integrated in short segments. The length of the short segment is dependent primarily on the shell radius and thickness. The SRA programs were originally dimensioned to handle 33 subintervals, and only a portion of the HO tank could be modeled with this restriction. These programs were extended at Langley to allow approximately a factor of three increase in the number of subintervals, which is adequate for an analysis of the entire HO tank.

SHELL-OF-REVOLUTION PROGRAM CAPABILITIES

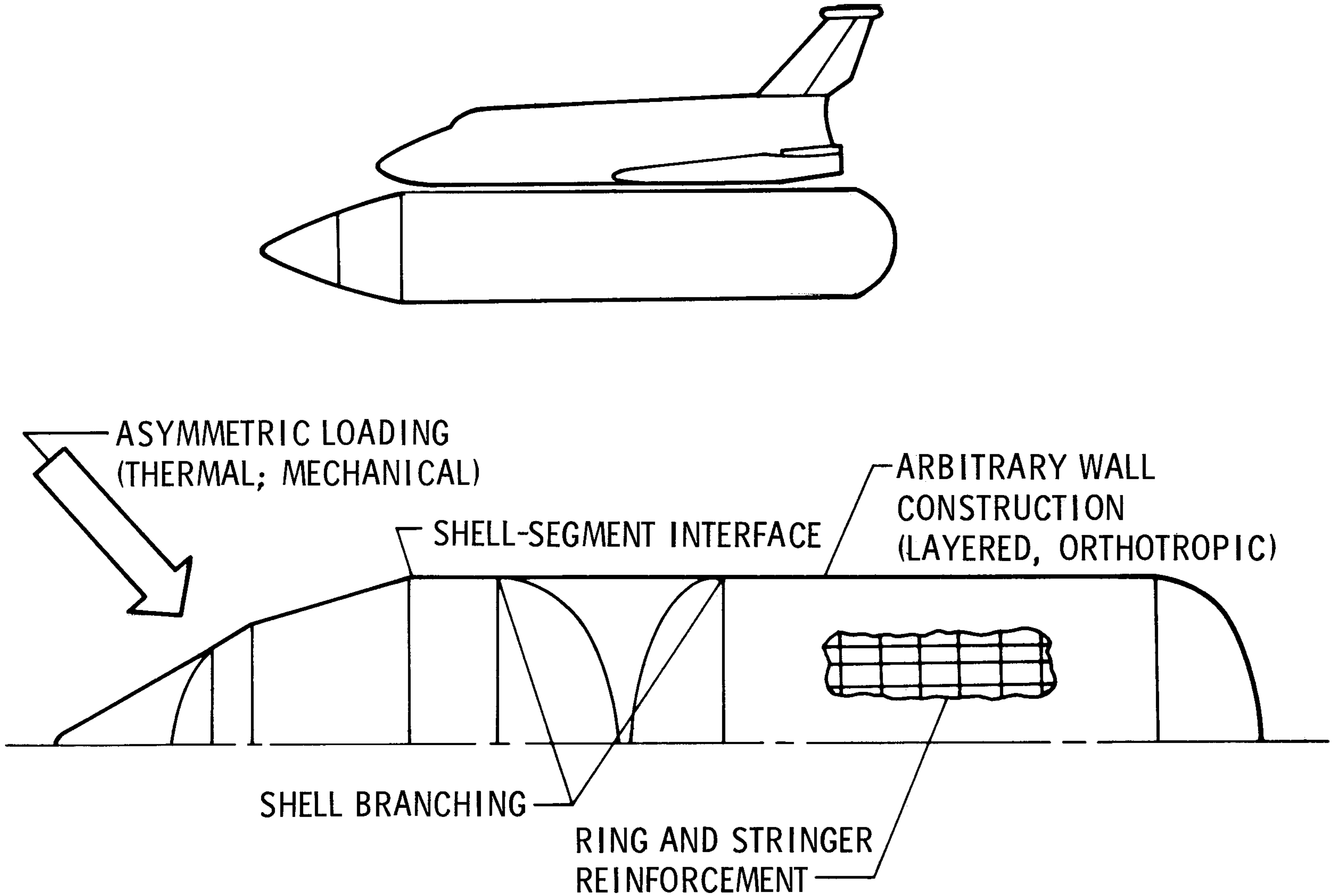

HO TANK ANALYZED WITH SRA PROGRAMS

The HO tank geometry and loading conditions considered in the analysis are shown in the figure. The structure has four components: (1) the LOX tank which has one spherical head and one elliptical head and which is enclosed by conical and cylindrical shell segments; (2) the ring- and stringer-stiffened cylindrical LOX-LH_2 interstage skirt; (3) the ring- and stringer-stiffened cylindrical LH_2 tank with elliptical heads; and (4) the aft ring- and stringer-stiffened LH_2 tank skirt. In addition, the structure is reinforced by 100-cm-deep frames at the three orbiter attachment points. All shell components are constructed of aluminum-alloy standard gage sheets. The LOX tank length is 1125 cm, the LH_2 tank length is 2570 cm, and the overall shell structure is approximately 4050 cm in length. The elliptical and spherical heads are all analyzed as open branches.

Values of the externally applied axial, shear, and moment loadings are shown in the figure along with the internal tank pressures, which correspond to a 3g flight condition. The concentrated loads are taken as point loads in the meridional direction and are assumed to be applied over a 20° arc in the circumferential direction. Fourier expansion is used to describe the variation of forces in the circumferential direction.

The buckling strength of this shell was determined by three different approaches. The simplest approach was to assume the shell to be simply supported between major frames (general instability) or between rings (panel instability), to have constant properties, and to have the loading determined from $P/A + Mc/I$. The strength was then determined from classical cylinder buckling equations that account for eccentric smeared rings and stringers (ref. 18). The second approach involved a complete stress analysis using the shell-of-revolution programs and considering the effects of the concentrated loads applied to the deep frames. Buckling was determined from a program capable of handling only a symmetric stress distribution, which is the usual case for shell-of-revolution analysis. In the region found critical for buckling, the largest compressive stresses were located in a meridian 90° from the meridian passing through the orbiter attachment point. A symmetric stress distribution of magnitude corresponding to the stress distribution along this meridian was used in the analysis. Since the actual stress distribution is less severe than this over much of the shell, this approach (called worst meridian) leads to conservative results. Finally, the shell was analyzed with the newly developed capability of the SRA program to consider buckling under a general asymmetrical loading. The results of the three analyses are shown in the next figure.

HO TANK ANALYZED WITH SRA PROGRAMS

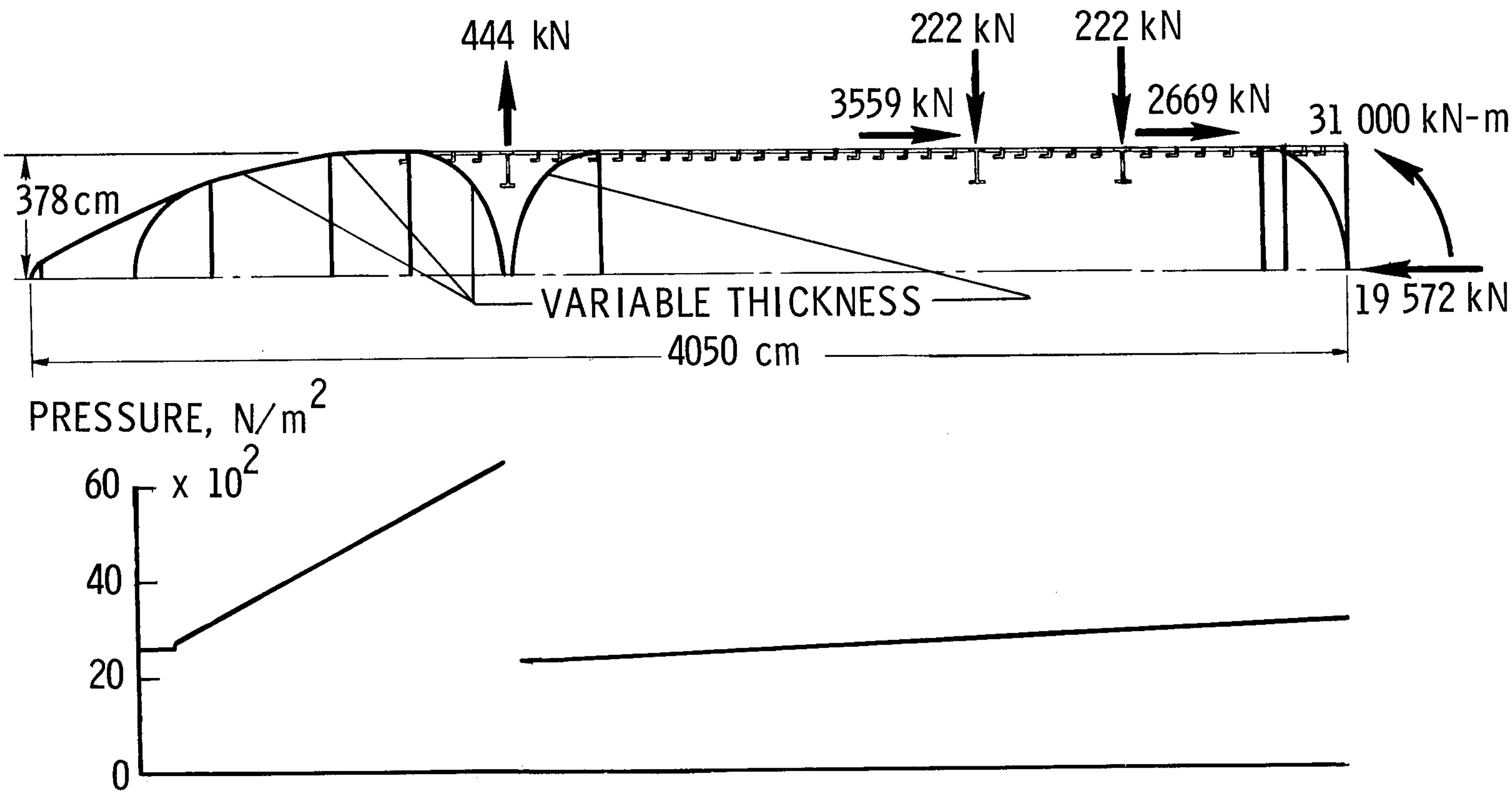

PRELIMINARY BUCKLING RESULTS FOR HO TANK

The figure shows preliminary values of the relative load level required for buckling of the HO tank; a relative load of 1.0 signifies buckling would occur when the magnitudes of the loads are equal to the values shown in the previous figure. Results from the classical solution indicated buckling occurs between rings in the interstage skirt. The axial compression in this portion of the structure results from the internal pressure loads on the aft dome of the LOX tank. Buckling occurred at a high number of circumferential waves ($n = 21$) at a relative load of 0.90.

For the calculations with the SRA programs, the complete shell was analyzed to determine the prestress state considering seven harmonics of the Fourier load representation. Initial calculations for the complete shell indicated that buckling again occurred in the interstage skirt. Hence, for the buckling calculations, the model was modified to include only the interstage skirt and sufficient portions of all the adjacent structure so that proper edge effects were obtained. The worst-meridian calculations indicated buckling at a relative load level of 1.30 at $n = 22$. Since the prestress state for this case is higher than that used in the simpler approach, this result indicates that the restraint imposed by the rings was greater than the simple support assumed in the classical solution.

Some difficulty was encountered in the buckling calculations with asymmetric prestress, as the structural arrangement and loading conditions were such that negative eigenvalues were obtained. It is standard procedure to avoid negative eigenvalues by use of eigenvalue shifts. However, when the prestress state is asymmetric, there are restrictions on the shifts that can be made, and for the present study, these restrictions prevented shifting sufficiently to avoid the negative eigenvalues. To avoid this difficulty, the prestress state used in the buckling calculations was altered by removing all tensile stresses in the tanks and the tensile hoop loads in the rings of the interstage skirt. This deletion of tensile stresses is a conservative approach in that the effect of these stresses would be to increase (probably slightly) the buckling load of the structure. Buckling about an asymmetric prestress does not occur at a distinct value of n but as a combination of harmonics. The harmonics used in the present study corresponded to values of n from 14 to 29. The value of the relative load level obtained was 1.53, which indicates the conservativeness of the worst-meridian approach.

The classical-solution approach typifies the analysis sophistication used for existing hardware. The worst-meridian approach typifies current analysis sophistication, and the asymmetric-prestress calculations represent the latest developments in shell-of-revolution buckling analysis capability. The results shown in the figure indicate that as the structural analysis becomes more sophisticated, the load-carrying capacity of the structure is better defined and, for the present problem, increases with analysis sophistication. Thus, use of the latest analysis technology should lead to lighter and more reliable designs.

PRELIMINARY BUCKLING RESULTS FOR HO TANK

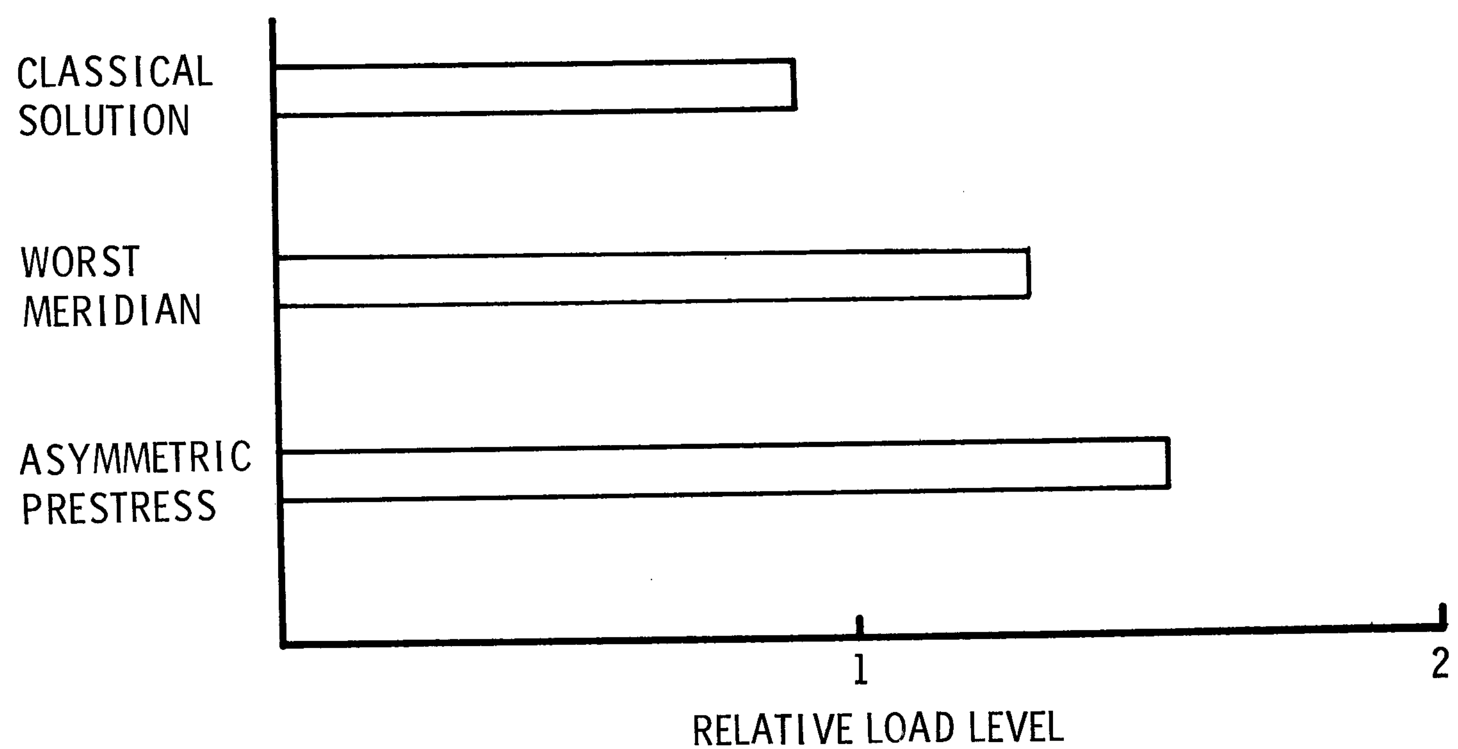

ANALYSIS OF ASYMMETRIC SHELLS

Many shell-type components for the space shuttle are highly asymmetric and thus are not amenable to analysis by shell-of-revolution programs except under certain circumstances using special and restricted techniques (ref. 19). For general asymmetric shells, the analysis must be based on two-dimensional techniques such as finite elements or two-dimensional finite-difference grids, such as shown in the figure. The STAGS program (Structural Analysis of General Shells) was developed specifically for the nonlinear static and collapse analysis of general shells under arbitrary static mechanical and thermal loads. It is based on an energy formulation and two-dimensional finite-difference techniques. STAGS has been under development by Lockheed Missiles and Space Company since 1963 and has been funded by LMSC, NSRDC, AFFDL, SAMSO, and NASA. The capabilities of the STAGS program were described in some detail at the 1971 NASA Space Shuttle Technology Conference (ref. 15).

Currently, NASA has a contractual effort to modify STAGS for shuttle application. The modified version, which will be completed in December 1972, will have the added capability of nonorthogonal coordinates, general boundary constraints, nonlinear bifurcation buckling, segmented and branched shells, improved computation efficiency, and designer-oriented input/output. The significance of nonlinear collapse analysis capability and the problem size and complexities an analyst or designer can consider in using STAGS will be illustrated in the next few figures by results obtained for the collapse of shells with cutouts and a bifurcation buckling analysis of the Skylab shrouds.

ANALYSIS OF ASYMMETRIC SHELLS

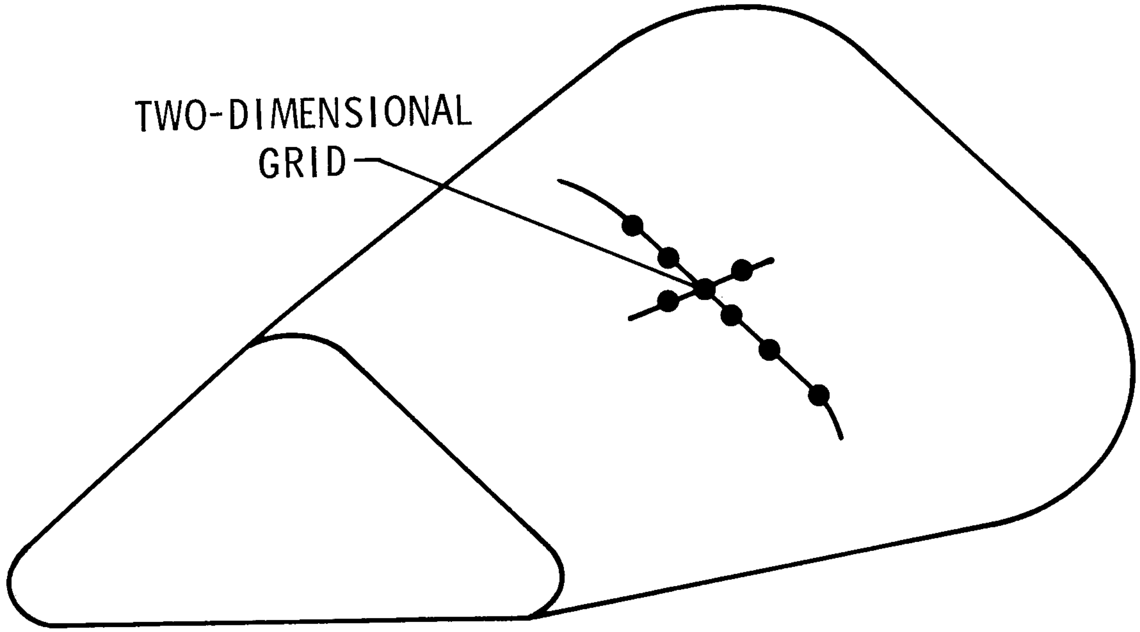

STRUCTURAL ANALYSIS OF GENERAL SHELLS - STAGS

PURPOSE: NONLINEAR STATIC AND COLLAPSE ANALYSIS OF GENERAL SHELLS UNDER ARBITRARY STATIC MECHANICAL AND THERMAL LOADS

THEORETICAL BASIS: ENERGY FORMULATION

METHOD OF SOLUTION: TWO-DIMENSIONAL FINITE-DIFFERENCE TECHNIQUES

COLLAPSE OF SHELLS WITH CUTOUTS

An analytical study of the collapse loads for cylinders with cutouts was recently conducted (ref. 12) with STAGS used as the analysis tool. Some of the results of this study are shown in the figure to illustrate the significant effects that nonlinear behavior can have on the collapse loads of shells. These results were obtained for a cylindrical shell with two diametrically opposite rectangular cutouts subjected to an axial load. The plot on the left is for an unreinforced cutout, whereas the plot on the right indicates the effects of reinforcing stringers added to the edges of the cutout. The symbols in the figure indicate buckling loads obtained from STAGS for bifurcation buckling about a linear prestress state for the shells including the effects of the cutouts and reinforcing stringers.

For the unreinforced cutout, the results of the nonlinear stress analysis revealed that the free edges of the cutouts start to bend immediately at application of load. However, as the area around the cutouts weakens, the stresses are redistributed so that more load is carried in the parts of the shell away from the cutouts. There is a tendency of the lateral displacement to become large at the bifurcation point. However, the shell continues to carry load, and collapse occurs at roughly twice the load required for bifurcation buckling. This effect could not be found with a linear analysis. The buckling mode is confined to the area of the cutout; however, the collapse mode extends over the entire shell surface. The maximum displacement in the collapse mode occurs at point A. When the edges of the cutouts are reinforced with stringers, the shells sustain more load and deflections are reduced. The stresses are rather uniformly distributed over the shell surface and buckling occurs in an area away from the cutout. The bifurcation buckling load in this case is somewhat higher than the collapse load. The maximum displacement in the collapse mode occurs at point B.

The salient point of the figure is that ignorance of the nonlinear collapse behavior of shells may lead to an overly conservative design with a corresponding weight penalty, or it may lead to an unconservative design and possible structural failure. With the aid of programs such as STAGS, the designer can investigate the sensitivity of a shell structure to nonlinear effects and can determine if more detailed analyses or redesign is required.

COLLAPSE OF SHELLS WITH CUTOUTS

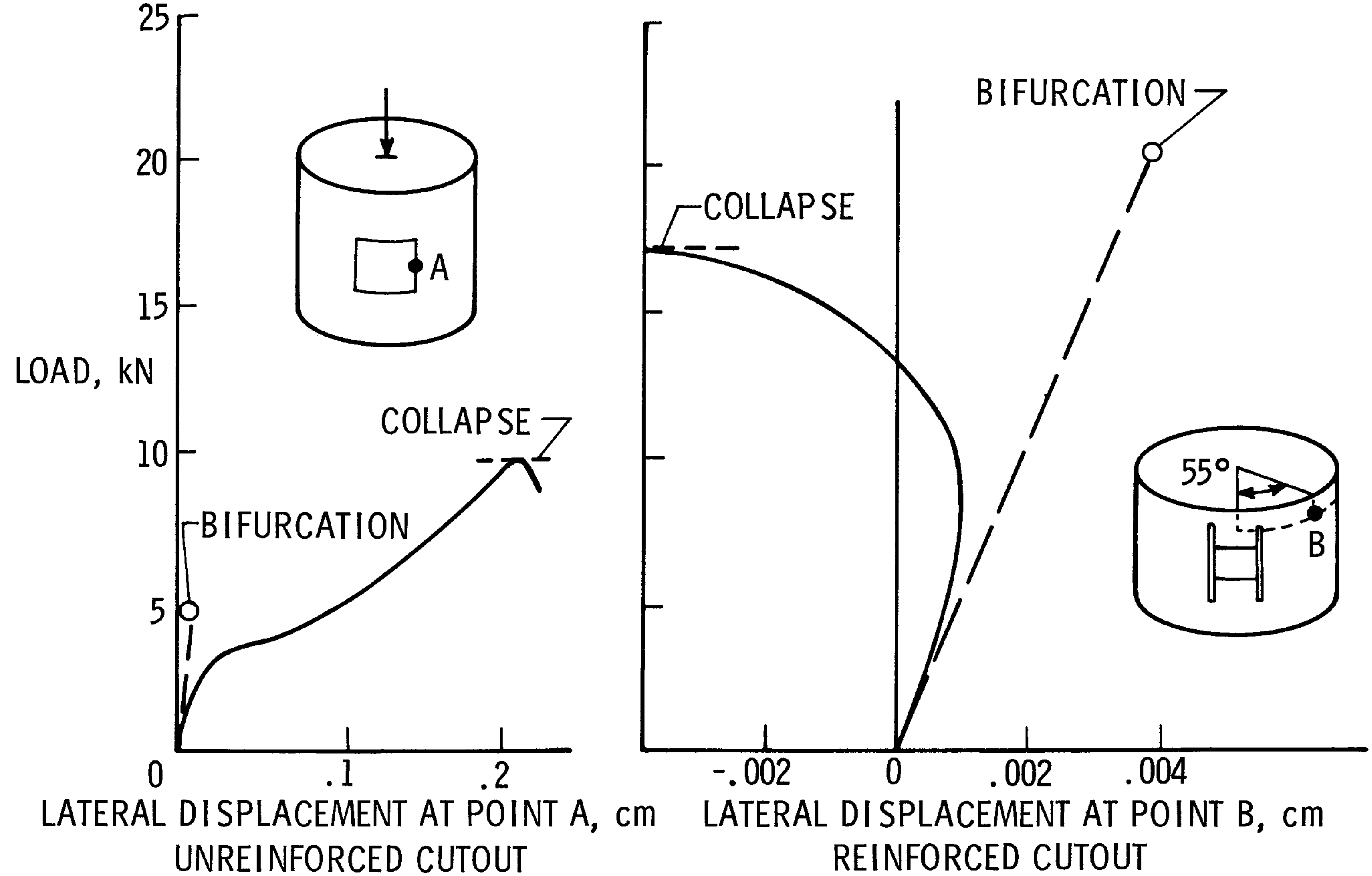

The design of the shuttle will require detailed stability analyses of large, complex, asymmetric structures. That STAGS is suitable for such analyses is readily illustrated by recent application to the analysis of the Skylab shrouds (ref. 20). As shown in the figure, the launch configuration of the forward structure of the Skylab consists of a series of circular cylindrical shells: the payload shroud (PS), the fixed airlock shroud (FAS), the instrument unit (IU), and the orbital workshop shroud (OWS). The strength and stability capabilities of the existing structure, that is, the IU and OWS, are well known from analyses and tests performed in connection with their previous applications. The purpose of the analysis of the Skylab shrouds was to determine the capabilities of the newly designed shells (PS and FAS).

The assemblage of the various cylindrical shells, each of which is of a different wall construction, is huge, some 660 cm in diameter by 1590 cm in length. The loads experienced by the launch configuration structure include combinations of air loads and inertia loads. A large portion of the inertia loads is transmitted from the heavy payloads to the cylinder at a number of locally reinforced points on rings and stringers. Since structural testing of such a large structure would be very costly, the design ground rules state that the PS and FAS should be designed to safety factors large enough to render testing unnecessary, with the safety factors determined by analysis. Since neither the structure nor the loads are rotationally symmetric, a rather sophisticated two-dimensional analysis was necessary. The analysis was required to include the possibility of long-wave instability modes extending over more than one of the cylindrical segments, and also the effects of severe discontinuities and eccentricities in load and geometry. Thus, analyses of individual sections of the structure were precluded, and the analytical model was required to represent the entire series of shells.

The requirements for an instability analysis as outlined above necessitated the solution of bifurcation buckling problems of immense size, as indicated in the figure. For one loading condition and structural arrangement, nearly 21 000 equations were solved. This is believed to be the largest bifurcation buckling problem ever solved. Thirty iterations each roughly equivalent to a static stress analysis were used; however, the total run time on a CDC 6600 computer was 40 minutes with a total residence time of 3 hours, 35 minutes. The run and total residence times are very reasonable considering the immense size of the problem (8.5×10^6 words of disk storage required and 3.33×10^8 words transferred between core and disk).

STAGS ANALYSIS OF LARGE COMPLEX STRUCTURE

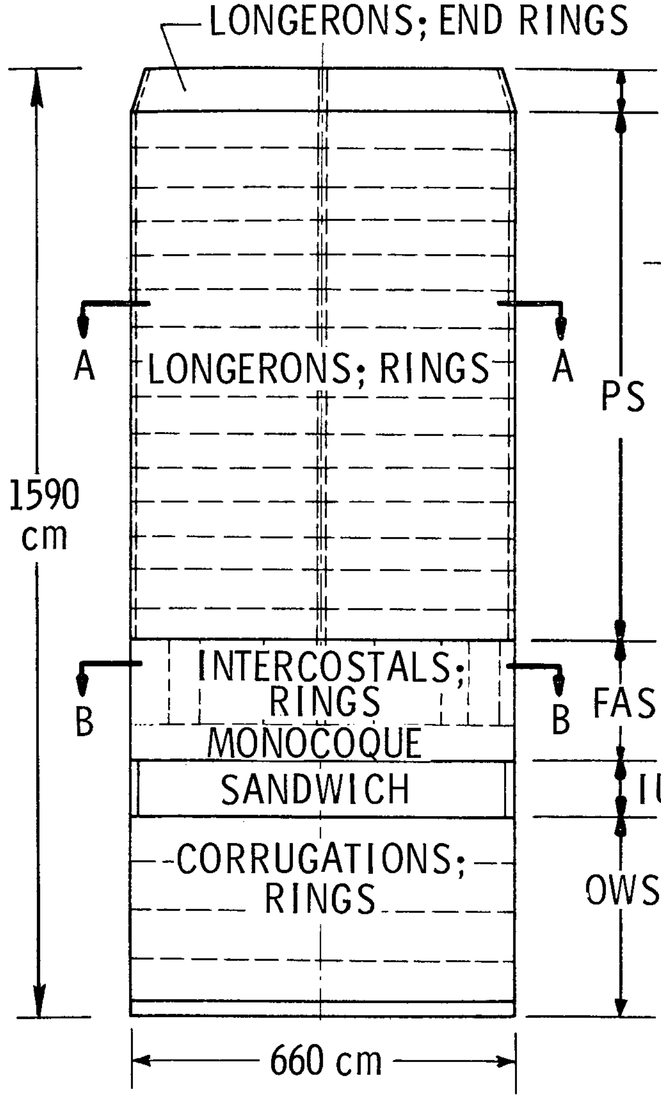

SKYLAB SHROUD STRUCTURE

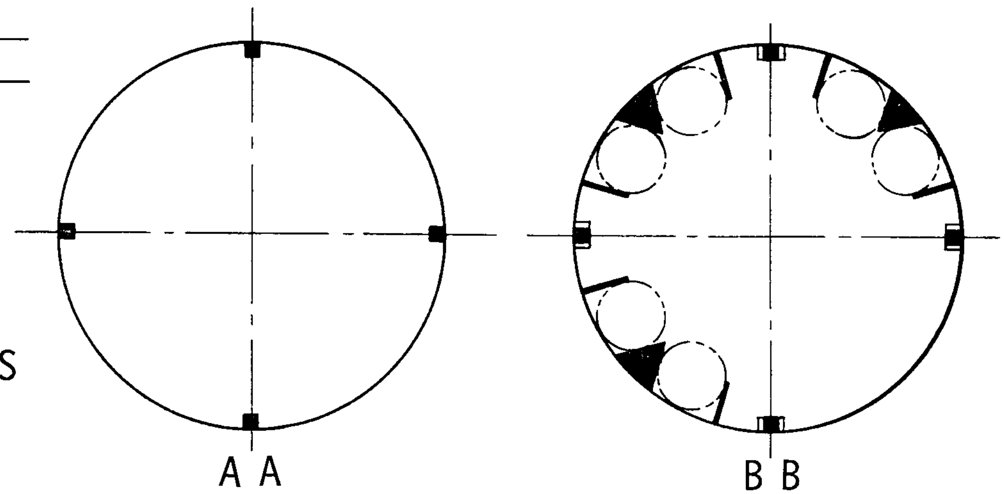

LINEAR BIFURCATION BUCKLING

NO. OF EQUATIONS = 20 910
SEMIBANDWIDTH = 252
TOTAL RUN TIME = 40 min

For analysis of a completely general structural arrangement, recourse is usually made to discretized formulations using finite elements. In this method, an idealized model of a complex structure is conceived by using simple structural elements such as beams and plates, as shown in the figure. The computer can be programed to assemble these elements, satisfy equilibrium and continuity conditions, and calculate the stresses or internal loads and deflections under prescribed loading conditions. The properties of a wide variety of structural elements have been cataloged in the literature for use in constructing appropriate idealizations.

An example of a large finite-element computer program is the NASTRAN system (refs. 13 and 14). There are many other finite-element programs in existence. Aerospace companies have their own which may have some of the same features as NASTRAN, but are tailored to the company's individual requirements. A representative list of finite-element programs, together with the company or agency responsible for their development, is given in reference 16. Discussion of finite-element programs herein will be limited to the NASTRAN system.

ANALYSIS OF GENERAL STRUCTURES

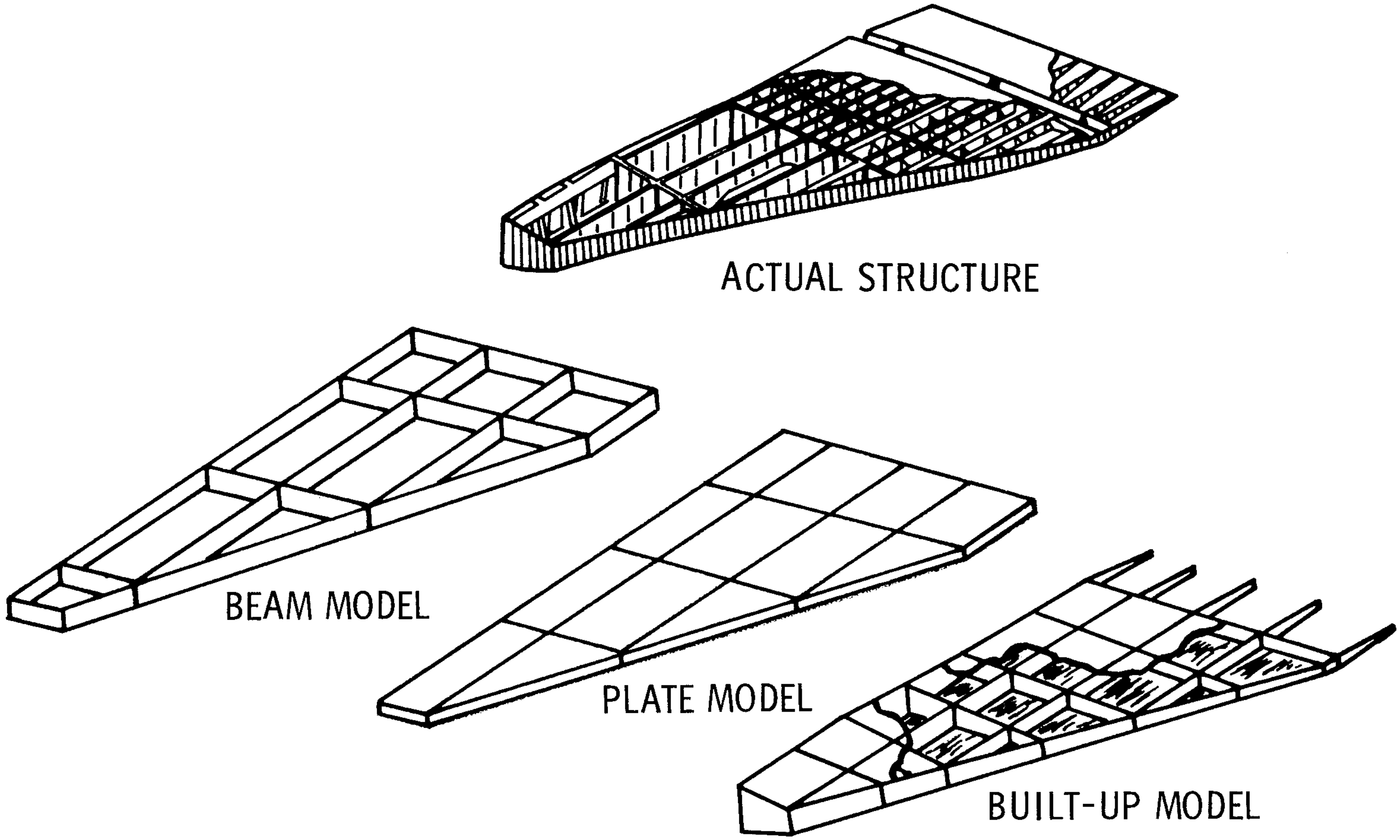

FINITE-ELEMENT MODELS

NASTRAN STRUCTURAL ANALYSIS PROGRAM

NASTRAN is a large (151 000 FORTRAN instructions) general-purpose finite-element structural analysis program developed by NASA during the period 1965 to 1970 at a cost of about $3,000,000. NASTRAN is well documented and is maintained by NASA through the NASTRAN System Management Office (NSMO) at the Langley Research Center.

The basic capabilities of NASTRAN for stress, vibration, buckling, and dynamic response analyses were outlined at the 1971 NASA Space Shuttle Technology Conference (ref. 15). Current and planned extensions and improvements to the current version of NASTRAN (Level 12) are discussed herein. These improvements include substructuring, computational efficiency, new elements, and heat-transfer analysis capability. Level 15, which is targeted for public release in June 1972, will have substructuring capability. Improvements in the other three areas will be included to some extent in Level 15, but much more comprehensively in Level 16, which is targeted for release in May 1973. These improvements are illustrated in more detail in the next few figures.

NASTRAN STRUCTURAL ANALYSIS PROGRAM

- CAPABILITIES: GENERAL-PURPOSE FINITE-ELEMENT PROGRAM, WELL DOCUMENTED
- MAINTAINED BY NASA

- IMPROVEMENTS TO CURRENT VERSION (LEVEL 12)
  - SUBSTRUCTURING - LEVEL 15
  - COMPUTATIONAL EFFICIENCY - LEVEL 15, LEVEL 16
  - NEW ELEMENTS - LEVEL 15, LEVEL 16
  - HEAT TRANSFER - LEVEL 15, LEVEL 16

- LEVEL 15 TO BE RELEASED JUNE 1972
- LEVEL 16 RELEASE PLANNED FOR MAY 1973

MODEL USED IN NASTRAN EFFICIENCY STUDIES

The figure shows the finite-element model used in computational efficiency studies for NASTRAN. The model, which represents one concept of a shuttle orbiter developed during the Phase B studies, is symmetrical about the center line of the vehicle. The half model contains 1261 nodes and over 3000 degrees of freedom. Rods, bars, and shear panels are the finite elements used to represent the structural members. A total of 2663 rods, 25 bars, and 1355 shear panels are included in the half model.

MODEL USED IN NASTRAN EFFICIENCY STUDIES

NODES	1261
BARS	25
RODS	2663
PANELS	1355
DEG. OF FREEDOM	3223

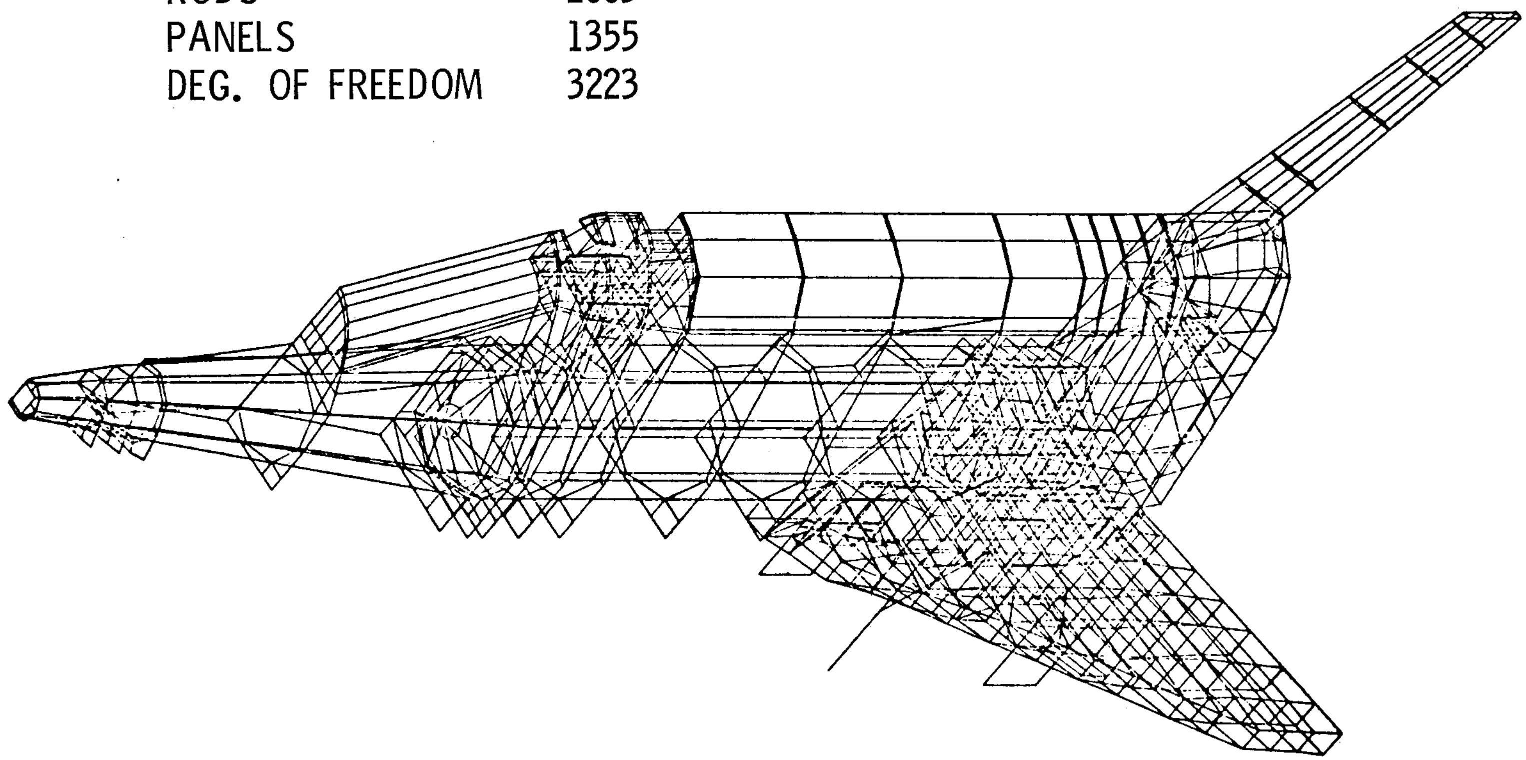

IMPROVEMENTS IN EFFICIENCY OF NASTRAN

The figure shows the central processing (CP) time required for a single static analysis of the half model of the shuttle orbiter shown in the previous figure. Results are shown for the current version of NASTRAN (Level 12), a prerelease version of NASTRAN Level 15, and an estimate for Level 16.

The results shown in the figure reveal that NASTRAN Level 15 is about a factor of two faster than the current Level 12 when operating on a CDC 6600 computer. Planned improvements to be incorporated into Level 16 are estimated to reduce run times by at least a factor of three compared with Level 15. With these improvements, NASTRAN with its broad and varied capability will approach the computational efficiency of other programs that have been developed specifically for rapid stress analysis.

IMPROVEMENTS IN EFFICIENCY OF NASTRAN

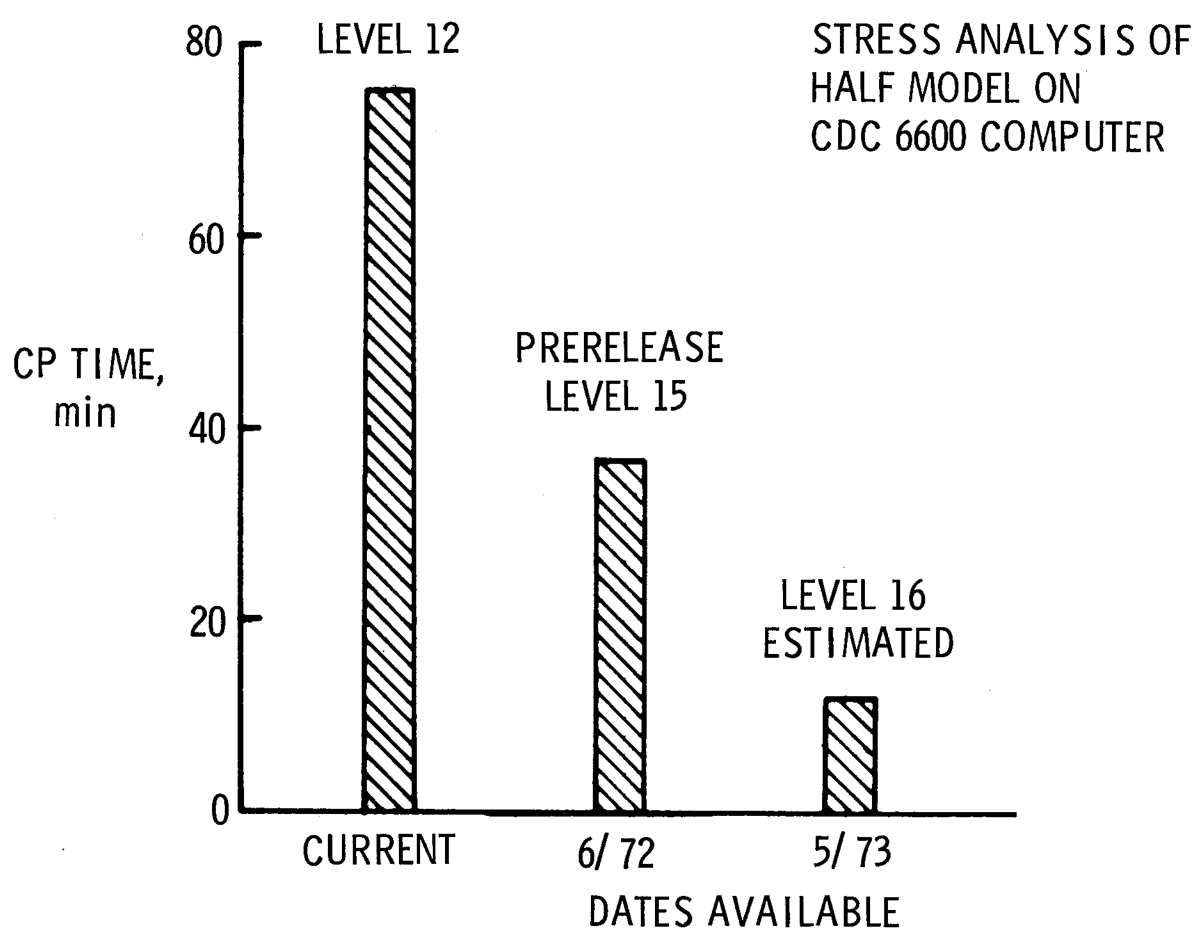

NEW ELEMENTS FOR NASTRAN

The types of new or improved elements under development for incorporation into NASTRAN are shown in the figure. Level 15 will have thermal bending bar and plate elements, hydroelastic capability, and tetrahedron and hexahedron solid elements. Level 16 will have a significant number of new elements. If the stiffness characteristics of a portion of a structure are known from tests or other analyses, they can be incorporated into a NASTRAN model by use of a general element defined by stiffness matrix. Level 16 will also have a rigid-body element which is essentially an automatic multipoint constraint (MPC) generator. In addition, Level 16 will make available to the analyst nonprismatic beam elements, improved solid-ring elements, triangular and quadrilateral shell elements, isoparametric solid and quadrilateral-membrane elements, improved shell-of-revolution elements, and multilayered composite plate elements.

NEW ELEMENTS FOR NASTRAN

LEVEL 15

- THERMAL BENDING ELEMENTS - BAR, PLATE
- HYDROELASTIC CAPABILITY
- SOLID ELEMENTS - TETRAHEDRON, HEXAHEDRON

LEVEL 16

- GENERAL ELEMENT DEFINED BY STIFFNESS MATRIX
- RIGID-BODY ELEMENT: AUTOMATIC MPC GENERATOR
- NONPRISMATIC BEAM
- IMPROVED SOLID RINGS
- TRIANGULAR AND QUADRILATERAL SHELL ELEMENTS
- ISOPARAMETRIC SOLID ELEMENTS
- ISOPARAMETRIC QUADRILATERAL MEMBRANE
- IMPROVED SHELL-OF-REVOLUTION ELEMENT
- MULTILAYERED COMPOSITE PLATE ELEMENT

NASTRAN THERMAL ANALYZER

A significant addition to NASTRAN analysis capability is the NASTRAN thermal analyzer. Level 15 will have the capability for calculating steady-state conduction only, but Level 16 will have the complete thermal analyzer capability which includes calculation of transient and steady-state temperature distributions due to radiation, convection through the boundary layer, and internally generated heat loads. The thermal analyzer can utilize the same finite-element model that is used in the stress analysis and thus avoid two separate modelings of the structure. With this capability, the analyst can specify thermal loads and perform thermal analyses to generate not only temperature distributions but also the thermal forces and moments which can then be used in a NASTRAN structural analysis to determine stresses, displacements, and so forth, due to the thermal loads and prescribed mechanical loads.

Inclusion of the thermal analyzer will broaden NASTRAN into an integrated multidisciplinary analysis program. Other additions of this type, such as aeroelasticity, are in the planning stages, but will not be included in Level 16.

NASTRAN THERMAL ANALYZER

LEVEL 15: STEADY-STATE CONDUCTION
LEVEL 16: TRANSIENT HEAT TRANSFER - CONDUCTION, CONVECTION, RADIATION

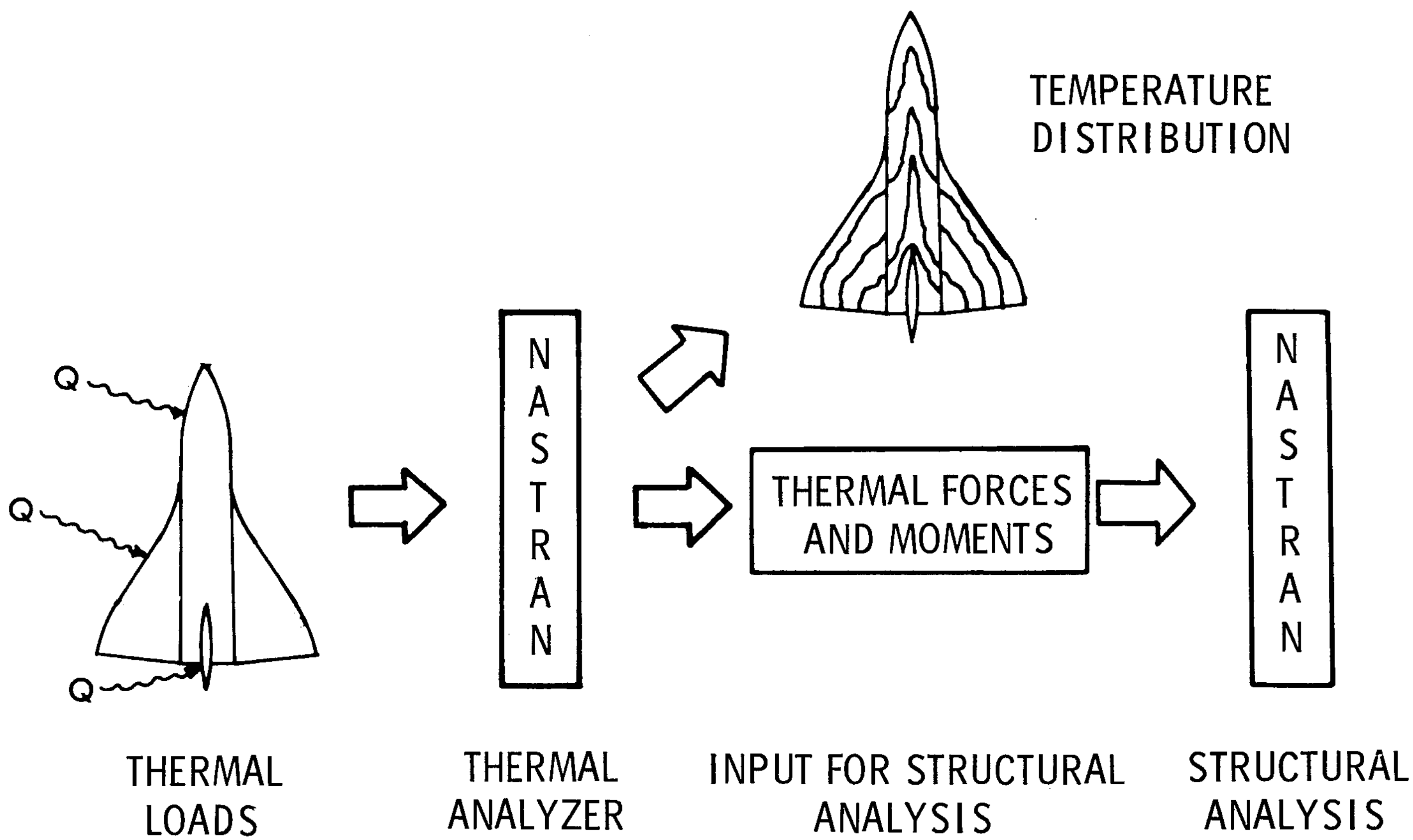

AUTOMATED ANALYSIS AND DESIGN

The structural design of the space shuttle can be enhanced not only by the recent significant advancements in structural analysis but also by developments in integrated analysis and automated design. Efforts to integrate several disciplines into unified systems of computer programs for analysis and design are summarized in references 15 to 17.

One such unified system is ATLAS (ref. 21), which integrates several disciplines, such as geometry, aerodynamics, loads, structures, and weights, and includes an executive routine which controls the sequence of analysis. ATLAS, which was developed by The Boeing Company, has been exercised on a model of the U.S. SST prototype. This model had earlier been analyzed by conventional methods which included many stages performed by hand. The manpower and project flow time required to do the same analysis task to the same depth and accuracy on the SST model with the integrated program and by conventional means are shown in the figure. The various markings on each bar are keyed to different parts of the analysis. On the flow-time chart, the bars are overlapped because some of these tasks can be carried out simultaneously. Both the manpower and the flow time were cut in half by use of the integrated program. These results, and the results of other aerospace companies (see, for example, ref. 22), have led to considerable interest in automated design.

There has been a continuing effort at the Langley Research Center to develop efficient automated methods for preliminary structural design. An exploratory study of the preliminary design process led to the DAWNS program (ref. 23), which completely automates the strength design of aircraft wing structures. This program was discussed in some detail at the 1971 NASA Space Shuttle Technology Conference (ref. 15). Developments since that time will be summarized in the remaining figures.

AUTOMATED ANALYSIS AND DESIGN

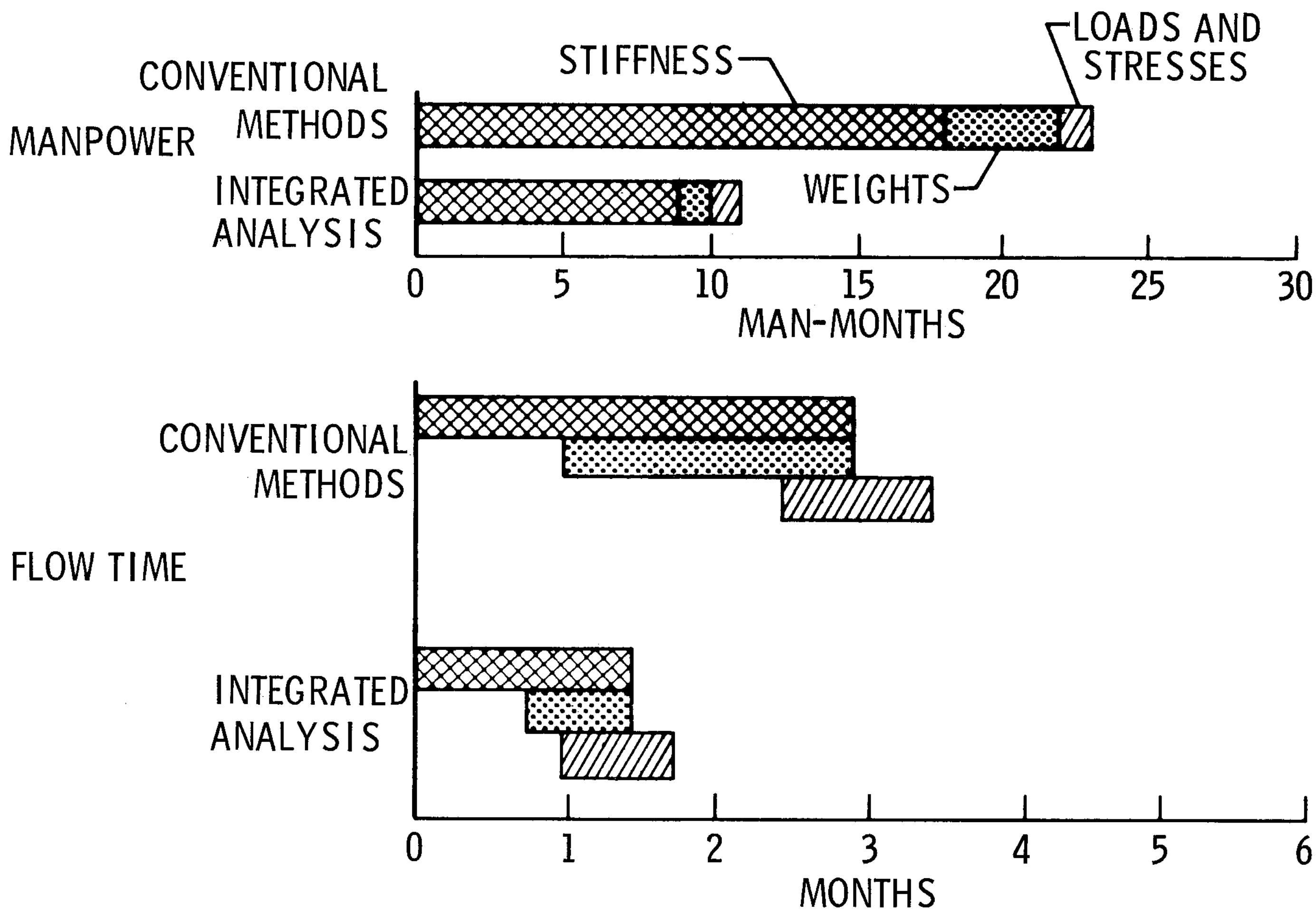

STRUCTURAL DESIGN PROCESS IN SAVES

Procedures intended to automate the preliminary structural design of a complete vehicle on the basis of both strength and stiffness requirements are currently under development at the Langley Research Center. The cyclic structural design process in the system of programs called Sizing of Aerospace Vehicle Structures, or SAVES (ref. 24), is illustrated in the figure. The boxes on the left show the portion of the process based on structural strength wherein the mass of the structure is minimized subject to the requirement of having sufficient strength to carry the external design loads. The boxes on the right illustrate the additional consideration of flutter, which depends on the stiffness of the structure.

Presently, the various modules indicated by the boxes in the figure are not integrated into a single automated program, but are operated as a system of separate programs with data transferred between modules by punched cards or magnetic tapes. Analytical models are used to represent the actual vehicle during this design process: panels arranged on the external surface of the vehicle are used for aerodynamic calculations and the structure is represented by an assemblage of finite elements. Simple yet versatile input is necessary in order that excessive time for input preparation does not negate the effectiveness of efficient design and analysis procedures. Thus, initial emphasis in the development of SAVES was placed on the development of automated input data generation routines.

Existing analysis and design programs of sufficient capability to handle refined models of a complete vehicle have been assembled into the SAVES system and are operational. Certain modules shown in the figure, such as EXTERNAL CONFIGURATION and GENERATE STRUCTURAL ARRANGEMENT, are well defined, whereas others (indicated by dashed lines), such as MASS PROPERTIES, have not yet been incorporated into SAVES. Future effort on SAVES will be directed at increasing the efficiency of existing modules, providing better integration of and data transfer between the various modules, and incorporating modules which currently are not included.

STRUCTURAL DESIGN PROCESS IN SAVES

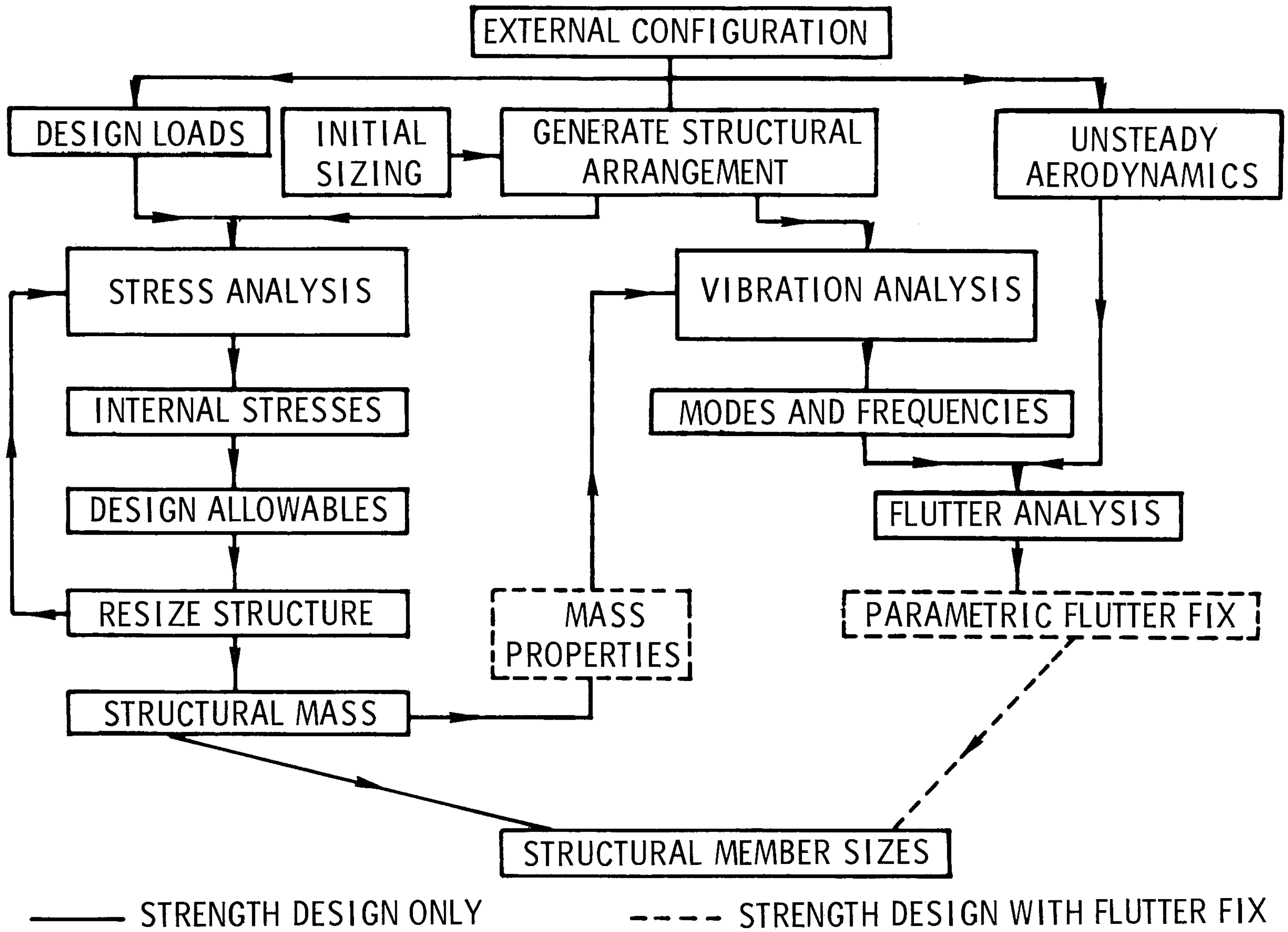

NUMERICAL DEFINITION OF ORBITER EXTERNAL SHAPE

Data generation routines substantially reduce the man-hours required for model preparation since they require a minimum of input data which can be readily obtained from preliminary drawings. The routines also greatly reduce errors due to such factors as mispunched data cards and incorrectly transcribed data, problems that are frequently experienced by the analyst when generating models by hand. An external shape is defined by using a computer program based on the methods described in reference 25. This shape is used in aerodynamic calculations and, in addition, the finite-element model of the structure is generated within this shape.

The numerically defined external shape for one concept of a shuttle orbiter (040A) is shown in the figure. User-required input to define this shape was 24 data cards. Some of the longitudinal lines defining the fuselage shape have kinks in the transition region from the circular forward section of the fuselage to the ⌂ shaped aft fuselage. These kinks are due to an inadequacy in the existing version of the program. Efforts are currently underway at the Langley Research Center to remove this inadequacy so that proper numerical definition of transition regions from one cross-sectional shape to another can be obtained.

NUMERICAL DEFINITION OF ORBITER EXTERNAL SHAPE

USER-REQUIRED INPUT: 24 DATA CARDS

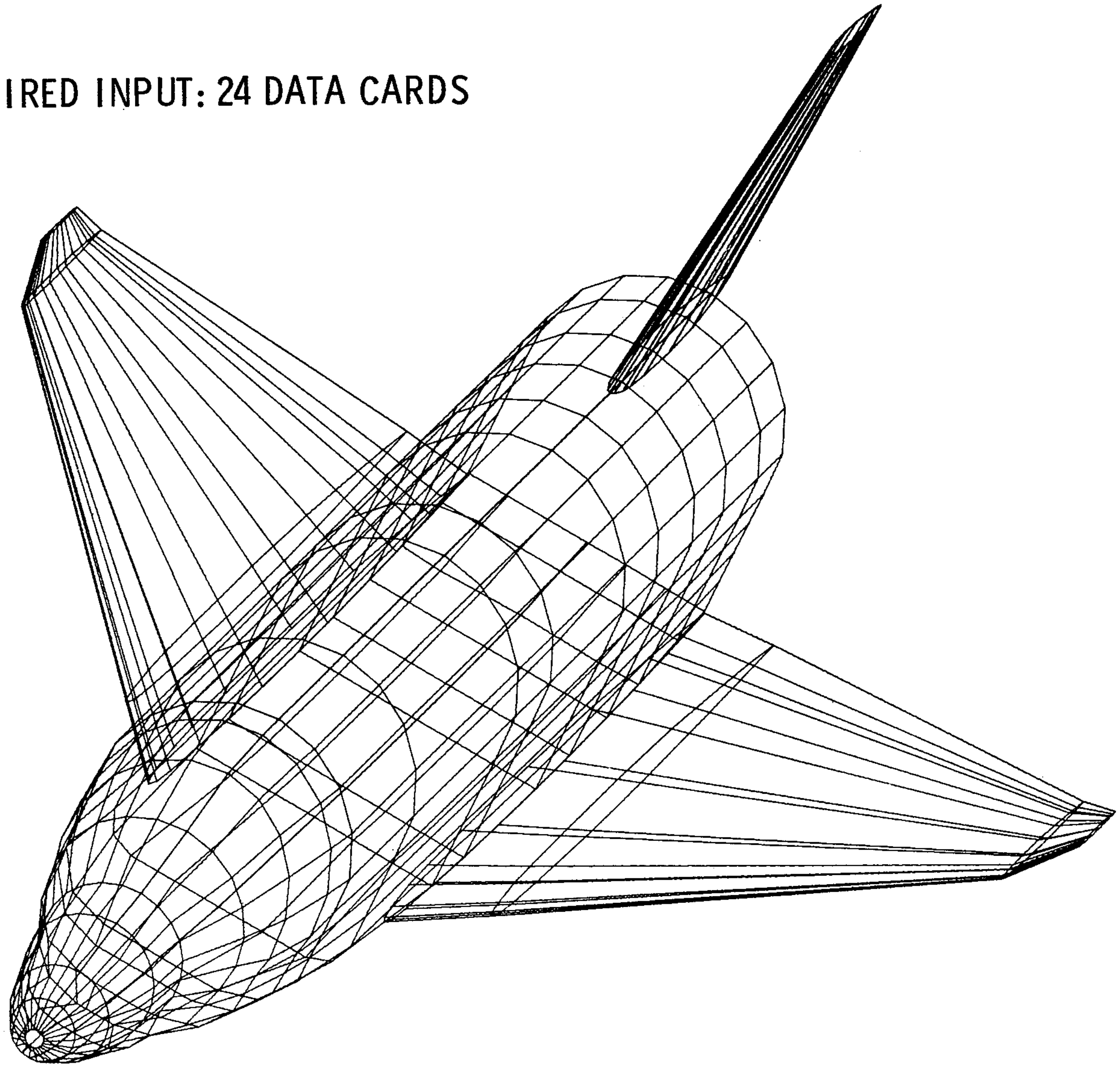

AUTOMATICALLY GENERATED STRUCTURAL MODEL

The figure shows the finite-element model that was automatically generated within the external shape shown in the previous figure. The model was generated by using computer routines developed for the SAVES program. Preliminary versions of these routines are described in reference 26. The generation of the finite-element model is not completely automated in that the major components of the structure (wing, fuselage, and empennage) are generated separately and alterations needed to connect these components are made by hand. The cutout appearing in the aft fuselage segment represents the area containing the non-load-carrying cargo bay doors. The finite-element model for the complete fuselage shell was automatically generated and then those elements representing the cargo doors were removed by hand.

The forward fuselage segment is of conventional aircraft construction, and the frames have been modeled as deep beams. The structure in the cargo bay area is more like a truss structure, and the frames have been modeled with beam elements. For both segments of the fuselage, the longerons were represented by rod elements. The wing ribs and spars are of truss construction; rod elements were used to represent the truss structure. The vertical tail was of conventional aircraft construction and shear elements were used to represent the ribs and spars. User-required input to define the model was 168 cards. The NASTRAN input deck that was automatically generated and punched consisted of approximately 6000 cards. About 7 man-hours were required to define the input data used to generate the finite-element model.

AUTOMATICALLY GENERATED STRUCTURAL MODEL

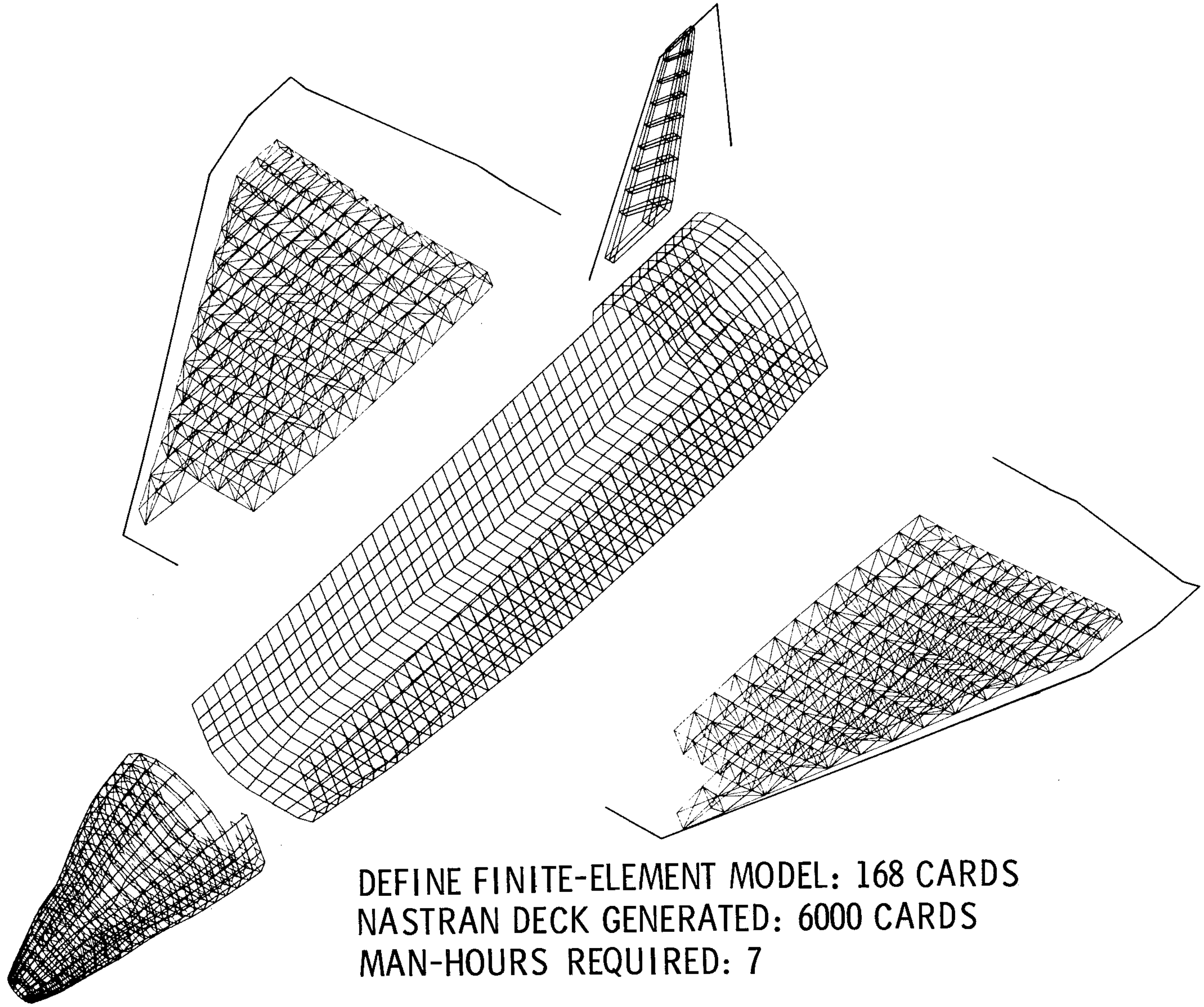

DEFINE FINITE-ELEMENT MODEL: 168 CARDS
NASTRAN DECK GENERATED: 6000 CARDS
MAN-HOURS REQUIRED: 7

DESIGN-DATA DISPLAY TECHNIQUES

Structural design programs provide the detailed information needed by the structural designer. Since the design data are so voluminous, an important part of a design system is the graphical output of these data.

Two techniques for graphical display of design data are shown in the figure. The automated wing design program DAWNS is implemented on an interactive cathode ray tube (CRT) console which gives immediate graphical displays of design data. The designer can assess visual displays of design information at various stages in the design process, make changes in design variables by using the alphanumeric keyboard, and control the sequence of program execution by using the function keyboard. Because of the larger computational times and computer storage required by the SAVES system of programs, the entire system has not been implemented on an interactive console. However, the ability to retrieve detailed information from storage in a data base and examine it in graphical format on a CRT would greatly facilitate the assessment of the data generated by SAVES.

Contour plots also provide a convenient means of displaying various types of design data. Contour plotting capability has been developed for the SAVES program, and a preliminary version of this procedure is discussed in reference 26. A contour plot of the Von Mises effective stress in the upper-surface cover panels of a shuttle orbiter wing is shown in the figure. The magnitudes of the contour labels have been scaled for ease of presentation and hence show only relative magnitudes. In addition to stress distributions, other quantities such as static displacements, vibration mode shapes, and panel thickness distributions can also be presented in this form.

DESIGN-DATA DISPLAY TECHNIQUES

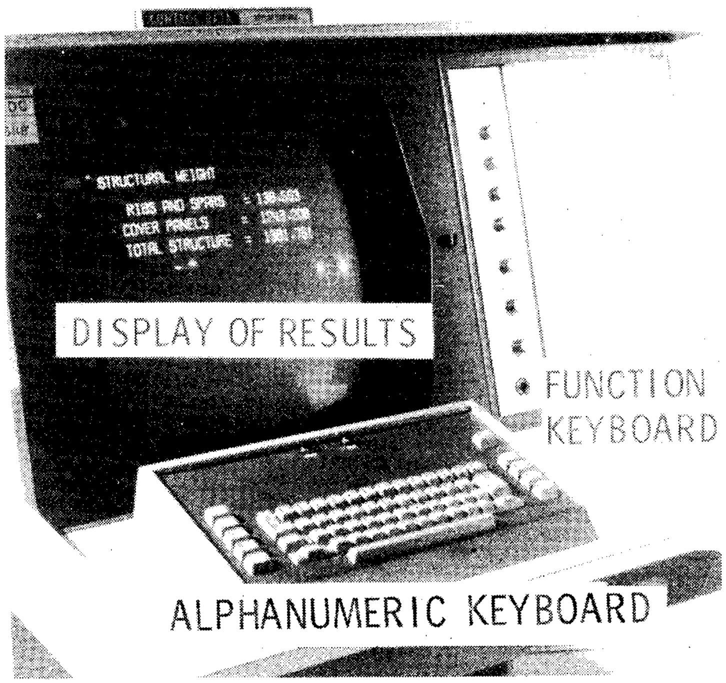

INTERACTIVE CRT CONSOLE

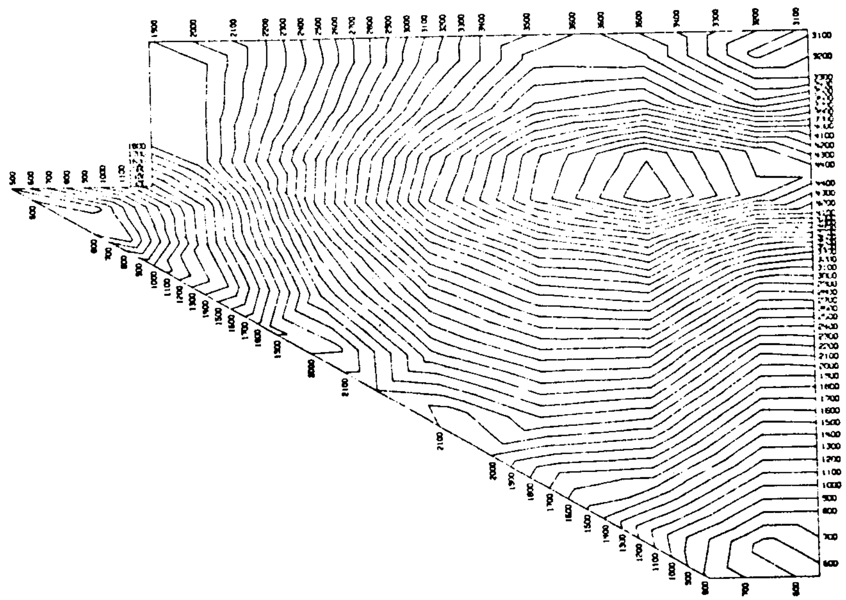

STRESS CONTOUR PLOT

SUMMARY OF CAPABILITIES AND BENEFITS

The status of the current capabilities for structural analysis is briefly summarized in the figure. The computer programs discussed in this paper provide accurate and efficient analysis capability for the design of the space shuttle primary structure. These programs are versatile and permit a high degree of detailed structural modeling, as evidenced by calculations presented for an HO tank structure and the Skylab shrouds. Finally, the programs are in the public domain and are well documented.

The benefits accruing to the space shuttle program from use of these programs are listed in the figure. These benefits include lighter and more reliable designs and reduced structural testing required for design verification. In addition, extensive use of the current technology should reveal potential structural problems sufficiently early in the design process to prevent costly downstream structural changes or redesign.

SUMMARY OF CAPABILITIES AND BENEFITS

ANALYSIS CAPABILITIES

- ACCURATE AND EFFICIENT
- VERSATILE - DETAILED STRUCTURAL MODELING
- GENERALLY AVAILABLE AND WELL DOCUMENTED

SHUTTLE BENEFITS

- LIGHTER AND MORE RELIABLE DESIGN
- REDUCED STRUCTURAL TESTING
- PREVENT COSTLY DOWNSTREAM CHANGES

REFERENCES

1. Cohen, Gerald A.: Computer Analysis of Asymmetrical Deformation of Orthotropic Shells of Revolution. AIAA J., vol. 2, no. 5, May 1964, pp. 932-934.
2. Cohen, Gerald A.: Computer Analysis of Asymmetric Free Vibrations of Ring-Stiffened Orthotropic Shells of Revolution. AIAA J., vol. 3, no. 12, Dec. 1965, pp. 2305-2312.
3. Cohen, Gerald A.: Computer Analysis of Asymmetric Buckling of Ring-Stiffened Orthotropic Shells of Revolution. AIAA J., vol. 6, no. 1, Jan. 1968, pp. 141-149.
4. Cohen, Gerald A.: Effect of a Nonlinear Prebuckling State on the Postbuckling Behavior and Imperfection Sensitivity of Elastic Structures. AIAA J., vol. 6, no. 8, Aug. 1968, pp. 1616-1619.
5. Almroth, B. O.; Bushnell, D.; and Sobel, L. H.: Buckling of Shells of Revolution With Various Wall Constructions. Vol. 1 - Numerical Results, NASA CR-1049; Vol. 2 - Basic Equations and Method of Solution, NASA CR-1050; Vol. 3 - User's Manual for BØSØR, NASA CR-1051, 1968.
6. Bushnell, David: Buckling and Vibration of Segmented, Ring-Stiffened Shells of Revolution - User's Manual for BOSOR 2. LMSC 6-78-68-40 (Contract N00014-67-C-0256), Lockheed Missiles & Space Co., Sept. 1968.
7. Bushnell, David: Stress, Stability, and Vibration of Complex Shells of Revolution: Analysis and User's Manual for BOSOR 3. SAMSO TR-69-375, U.S. Air Force, Sept. 6, 1969.
8. Bushnell, David: Stress, Stability, and Vibration of Complex Branched Shells of Revolution: Analysis and User's Manual for BØSØR4. LMSC-D243605 (Contract No. N00014-71-C-0002), Lockheed Aircraft Corp., Sept. 1971.
9. Anderson, M. S.; Fulton, R. E.; Heard, W. L., Jr.; and Walz, J. E.: Stress, Buckling, and Vibration Analysis of Shells of Revolution. Computers & Structures, vol. 1, nos. 1/2, Aug. 1971, pp. 157-192.
10. Brogan, Frank; and Almroth, Bo: Buckling of Cylinders With Cutouts. AIAA J., vol. 8, no. 2, Feb. 1970, pp. 236-240.
11. Almroth, B. O.; Brogan, F. A.; and Marlowe, M. B.: Collapse Analysis for Elliptic Cones. AIAA J., vol. 9, no. 1, Jan. 1971, pp. 32-37.
12. Almroth, B. O.; and Brogan, F. A.: Bifurcation Buckling as an Approximation of the Collapse Load for General Shells. AIAA J., vol. 10, no. 4, Apr. 1972, pp. 463-467.
13. Butler, Thomas G.; and Michel, Douglas: NASTRAN - A Summary of the Functions and Capabilities of the NASA Structural Analysis Computer System. NASA SP-260, 1971.
14. MacNeal, Richard H., ed.: The NASTRAN Theoretical Manual. NASA SP-221, 1970.

15. McComb, Harvey G., Jr.: Structural Analysis and Automated Design. NASA Space Shuttle Technology Conference, Vol. II, NASA TM X-2273, 1971, pp. 355-390.

16. Fulton, Robert E.; and McComb, Harvey G., Jr.: Automated Design of Aerospace Structures. Paper presented at the ASME International Conference on Design Automation (Toronto, Canada), Sept. 1971.

17. McComb, Harvey, G., Jr.: Automated Design Methods in Structural Technology. Vehicle Technology for Civil Aviation - The Seventies and Beyond, NASA SP-292, 1971, pp. 225-243.

18. Block, David L.; Card, Michael F.; and Mikulas, Martin M., Jr.: Buckling of Eccentrically Stiffened Orthotropic Cylinders. NASA TN D-2960, 1965.

19. Bushnell, David: Stress, Buckling, and Vibration of Prismatic Shells. AIAA J., vol. 9, no. 10, Oct. 1971, pp. 2004-2013.

20. Skogh, J.; Stern, P.; and Brogan, F.: Instability Analysis of Skylab Shrouds. LMSC-D246555, Lockheed Aircraft Corp., Jan. 20, 1972.

21. Miller, Ralph E., Jr.; and Hansen, Stanley D.: Large-Scale Structural Analysis of Current Aircraft. Paper presented to Symposium on Large Computations, Amer. Soc. Mech. Eng. (New York, N.Y.), Dec. 1970.

22. Wennagel, Glen A.; Mason, Philip W.; and Rosenbaum, Jacob D.: IDEAS, Integrated Design and Analysis System. [Preprint] 680728, Soc. Automot. Eng., Oct. 1968.

23. Giles, Gary L.: Procedure for Automating Aircraft Wing Structural Design. J. Struct. Div., Amer. Soc. Civil Eng., vol. 97, no. ST1, Jan. 1971, pp. 99-113.

24. Giles, Gary L.; Blackburn, Charles L.; and Dixon, Sidney C.: Automated Procedures for Sizing Aerospace Vehicle Structures (SAVES). AIAA Paper No. 72-332, Apr. 1972.

25. Craidon, Charlotte B.: Description of a Digital Computer Program for Airplane Configuration Plots. NASA TM X-2074, 1970.

26. Giles, Gary L.; and Blackburn, Charles L.: Procedure for Efficiently Generating, Checking, and Displaying NASTRAN Input and Output Data for Analysis of Aerospace Vehicle Structures. NASTRAN: Users' Experiences, NASA TM X-2378, 1971, pp. 679-696.

DEVELOPMENT OF METHODS FOR FRACTURE CONTROL OF SPACE SHUTTLE STRUCTURES

Gordon T. Smith
NASA Lewis Research Center
Cleveland, Ohio

and

Robert E. Johnson
NASA Manned Spacecraft Center
Houston, Texas

23

DEFINITION OF FRACTURE CONTROL

It seems appropriate to begin a discussion of the Shuttle vehicle fracture control with a statement of just what we mean by the term. The first figure provides a suitable definition--many others, equally correct, can be formulated. The point is that we are intending to apply the disciplines (the current state-of-the-art knowledge) of fracture mechanics and of nondestructive evaluation in a coordinated, integrated manner with all the development activities so that design practices, materials and process controls and prescribed operational conditions will provide a reliable and operationally effective vehicle system. These fracture control considerations are to be applied to certain vital components. Items A and B are suggested criteria for this determination.

The fracture control approach will not assume the fabrication of flaw-free structure but will consider the possibility of the initial presence of a crack-like defect in the most unfavorable location and orientation.

The implementation of the program will require all the disciplines listed on the figure and will involve all the organization elements with responsibility for development and operation of the Shuttle. To make the fracture control program work most effectively, it must be a continuous, start-to-finish activity.

DEFINITION OF FRACTURE CONTROL

PURPOSE

THE APPLICATION OF FRACTURE MECHANICS, DESIGN PRACTICES, MATERIALS & PROCESS CONTROL, NONDESTRUCTIVE EVALUATION, & OPERATIONAL CONTROLS TO REDUCE THE HAZARD OF UNCONTROLLED CRACK PROPAGATION IN CRITICAL STRUCTURE

CHARACTERISTICS

APPLICABLE TO COMPONENTS DETERMINED BY ANALYSIS & TEST TO BE:

A. SUSCEPTIBLE TO CRACKING OR FRACTURE ON THE BASIS OF ANTICIPATED LOADS & ENVIRONMENTS

B. CRITICAL TO EITHER CREW SAFETY OR SYSTEM PERFORMANCE

ASSUMPTIONS INCLUDE THE INITIAL PRESENCE OF CRACK-LIKE DEFECTS IN THE MOST UNFAVORABLE LOCATION & ORIENTATION

REQUIRES MULTIDISCIPLINARY TREATMENT OF SYSTEM INCLUDING DISCIPLINES OF MANAGEMENT, DESIGN, LOADS, MATERIALS, QUALITY CONTROL, TESTS, OPERATIONS, & MAINTENANCE

NASA-AIR FORCE FRACTURE CONTROL DOCUMENTS

Fracture control has become an issue of major concern for both NASA and the Air Force. The next figure indicates some of the key documents (references 1 through 8) which reflect the experiences encountered by each organization in the development and operation of advanced aerospace systems. The Air Force experience is concerned principally with airframe component problems while the NASA experience tends toward pressure vessel components. As a result of recent experience, the Air Force is imposing specific fracture control requirements on all new system development programs. The documents listed represent general technology papers which express the fracture control concepts and methods but which do not provide specific contractual requirements. The NASA pressure vessel experience is summarized in the SP series of documents 8040, 8025, and 8088. Reference 9 describes the application of these NASA guidelines to the design of the pressure vessels on the Viking vehicle.

The recent fracture experiences of the Air Force, Aerospace Industry, and NASA were pooled by a NASA-Industry Working Group which was convened last June at LRC for the purposes of formulating appropriate fracture control guidelines for the Shuttle vehicle. The resulting document has recently been designated SP 8095 and contains the statement of Shuttle fracture control guidelines as they were visualized last June. All of these NASA documents represent suggested guidelines only and are not intended as statements of contractual requirements. The Preliminary Criteria for Fracture Control of Space Shuttle Structures document provides a relatively complete identification of the fracture control organizational requirements and specific tasks which are required. Necessary analysis and test tasks are specified but the methods for implementing these tasks are not specified. Detailed development of these analysis methods and testing techniques must be accomplished as a part of the Shuttle development program.

The balance of this discussion will be directed toward the evaluation of the technology required to accomplish an effective fracture control program, and a description of the NASA fracture control technology programs which support this effort. Some representative program results will be shown to illustrate the program objectives and some final remarks will be made on remaining technology requirements for the Shuttle program.

NASA-AIR FORCE FRACTURE CONTROL DOCUMENTS

AIR FORCE	AFFDL-TR-71-89	"FRACTURE CONTROL PROCEDURE FOR AIRCRAFT STRUCTURAL INTEGRITY"
	AFFDL-TR-69-111	"FRACTURE MECHS GUIDELINES FOR AIRCRAFT STRUCTURAL APPLICATIONS"
NASA - GENERAL -	SP-8040	"FRACTURE CONTROL OF METALLIC PRESSURE VESSELS," MAY 1970
	SP-8082	"STRESS-CORROSION CRACKING IN METALS," AUG 1971
	SP-8025	"SOLID ROCKET MOTOR METAL CASES," APRIL 1970
	SP-8088	"LIQUID ROCKET TANKS & COMPONENTS," 1972
SPACE SHUTTLE -	SP-8057	"STRUCTURAL DESIGN CRITERIA APPLICABLE TO A SPACE SHUTTLE," JAN 1971
	SP-8095	"PRELIMINARY CRITERIA FOR THE FRACTURE CONTROL OF SPACE SHUTTLE STRUCTURES," JUNE 1971

FACTORS AFFECTING SERVICE PERFORMANCE

In order to discuss the fracture control technology requirements, it is necessary to identify the factors which determine structural performance and to identify the parameters which are used to correlate them. The service performance of a structural element depends on the flaw size initially present in the element, the growth characteristics of the flaw in service, and the size of flaw necessary to cause a structural failure (e.g., leakage or fracture).

The initial flaw size can be screened by proof test or NDT procedures and most often by a combination of both.

The critical flaw size is dependent on the fracture toughness of the material, the applied stress level, and the configuration of the flaw and the structural element.

The flaw growth characteristics which can be used to describe the flaw enlargement processes between initial and critical size are indicated on the figure. The cyclic growth rate, da/dN, the stress intensity threshold for sustained-load flaw growth, K_{TH}, or K_{Iscc} (if an aggressive environment is present) and the sustained-load growth rate, da/dt.

The residual strength of the element at any time will depend on the applied stress level and the ratio of the stress intensity factor at the crack to the critical value of stress intensity. The concept of crack tip stress intensity is illustrated on the next figure.

FACTORS AFFECTING SERVICE PERFORMANCE

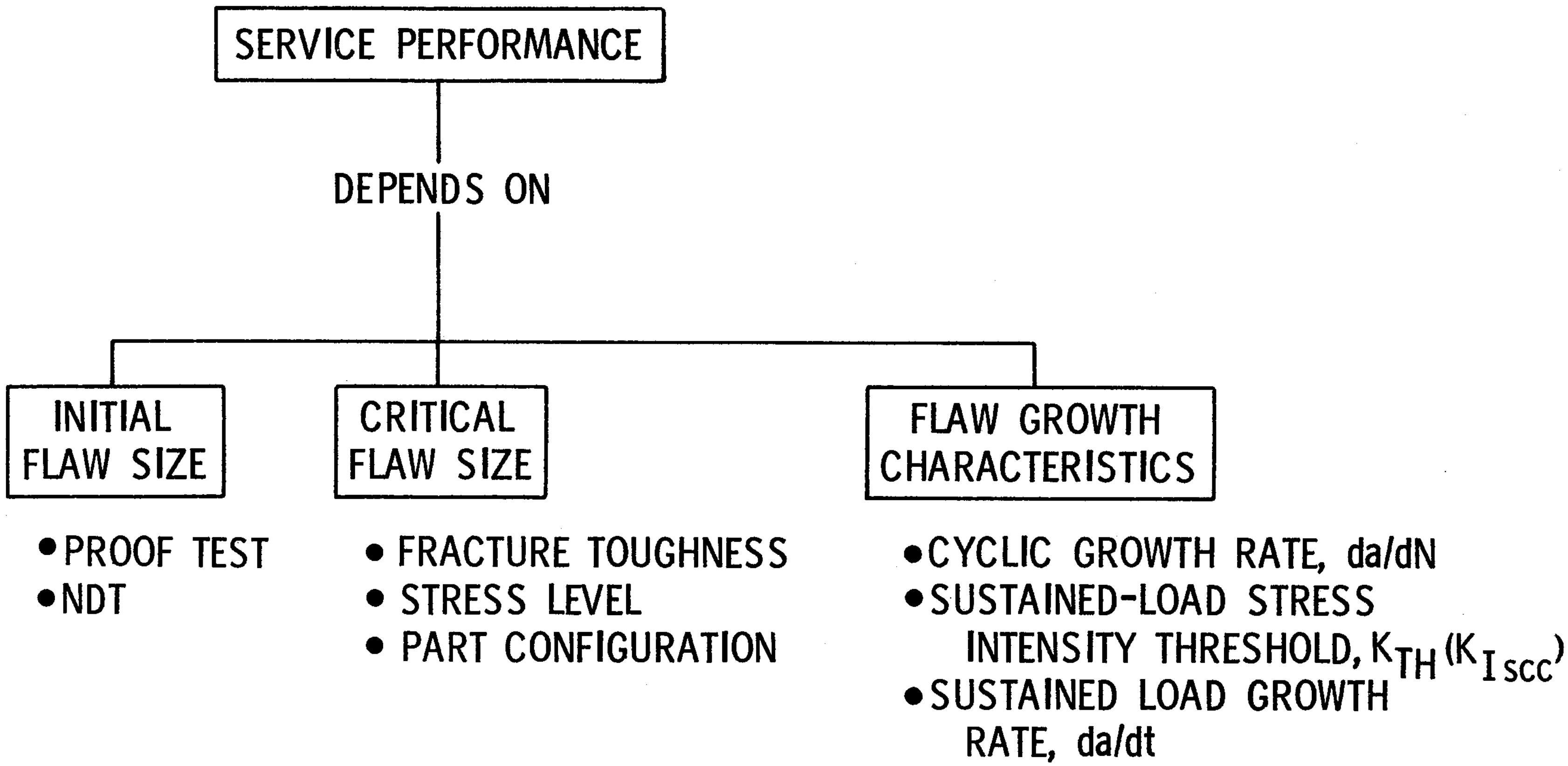

MODE I CRACK TIP STRESS FIELD

The stress intensity factor is a parameter obtained from linear elastic fracture mechanics. The basic assumption of linear elastic fracture mechanics is that the conditions which control the behavior of a defect can be completely characterized by the elastic stress field surrounding the defect. For elastic conditions and tension loading (mode I loading) the near-tip stress field is described by the equations on the lower part of the figure. These equations are written in terms of the normal coordinate system centered at the crack tip as shown in the sketch. Other terms which are nonsingular in r are contained in the complete stress field expansion and are the additional discarded terms indicated by the dots. These terms become relatively insignificant compared to the $1/\sqrt{r}$ terms as $r \rightarrow 0$ and accordingly are dropped for the near tip stress field equations (at distances from the crack tip which are large compared to r/a, where a is the crack depth, a valid representation of the elastic stress field must include these additional terms). The distribution of x, y and z stress is schematically illustrated for plane strain conditions for the crack propagation plane $\theta = 0$. The stress field has a singular characteristic at the crack tip and is completely determined by the single parameter K_I. Once K_I is established a unique descriptor of the crack tip stress field is determined. Values of K_I must be established by an accurate elastic analysis of the cracked body. Unfortunately this is not a simple task. Only a limited number of solutions of useful accuracy are available and these are generally confined to relatively simple crack-part shapes. Development of stress intensity solutions for cracked bodies of practical shape is an involved task and is the object of continuous effort.

MODE I CRACK TIP STRESS FIELD

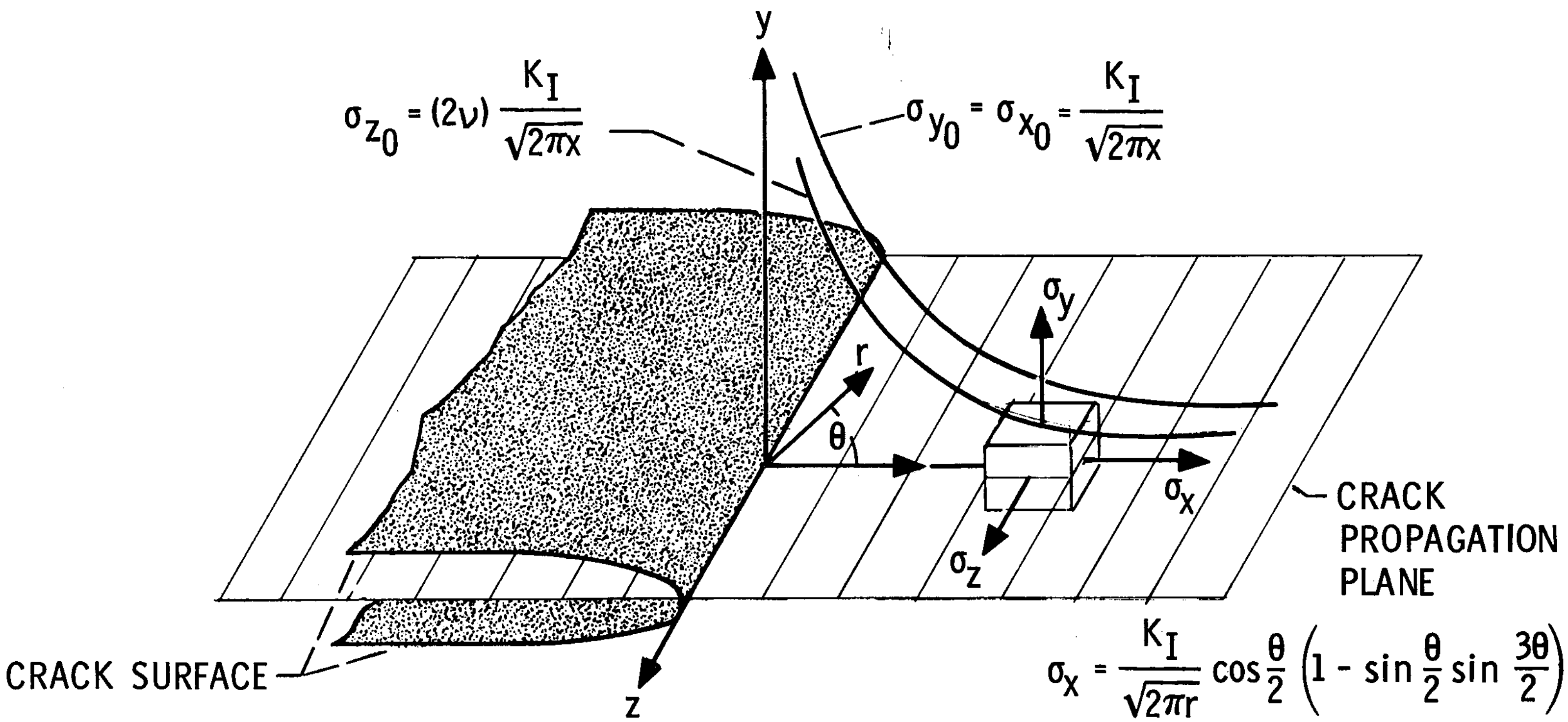

$$\sigma_x = \frac{K_I}{\sqrt{2\pi r}} \cos\frac{\theta}{2}\left(1 - \sin\frac{\theta}{2}\sin\frac{3\theta}{2}\right) + \ldots$$

$$\sigma_y = \frac{K_I}{\sqrt{2\pi r}} \cos\frac{\theta}{2}\left(1 + \sin\frac{\theta}{2}\sin\frac{3\theta}{2}\right) + \ldots$$

$\sigma_z = \nu(\sigma_x + \sigma_y)$ PLANE STRAIN

$= 0$ PLANE STRESS

$$\tau_{xy} = \frac{K_I}{\sqrt{2\pi r}} \cos\frac{\theta}{2}\left(\sin\frac{\theta}{2}\cos\frac{3\theta}{2}\right) + \ldots$$

CRACK PART GEOMETRY WITH AVAILABLE MODE I STRESS INTENSITY SOLUTIONS

The next figure indicates several crack-part geometry situations for which linear-elastic stress intensity solutions of useful accuracy are available. The solutions for the center-cracked finite sheet, the edge crack in a finite plate, the external notched round and the surface flawed configurations are the basis for many of the test specimens used to measure fracture toughness. References 10 and 11 provide a detailed account of available stress intensity solutions. These available stress intensity solutions do not provide a complete coverage of the crack-part geometry situations encountered in actual hardware components. Approximations which result in corrections to the available solutions can be devised by experienced elasticians for some of the more practical flaw geometry problems likely to be encountered in the fracture control analysis of an actual structural component. Loading conditions as well as geometry are involved. It is important to recognize the need for these "educated guesses" and also important that the "guesses" should be made by qualified people with prudent allowances for the uncertainties involved.

CRACK PART GEOMETRY WITH AVAILABLE MODE I STRESS INTENSITY SOLUTIONS

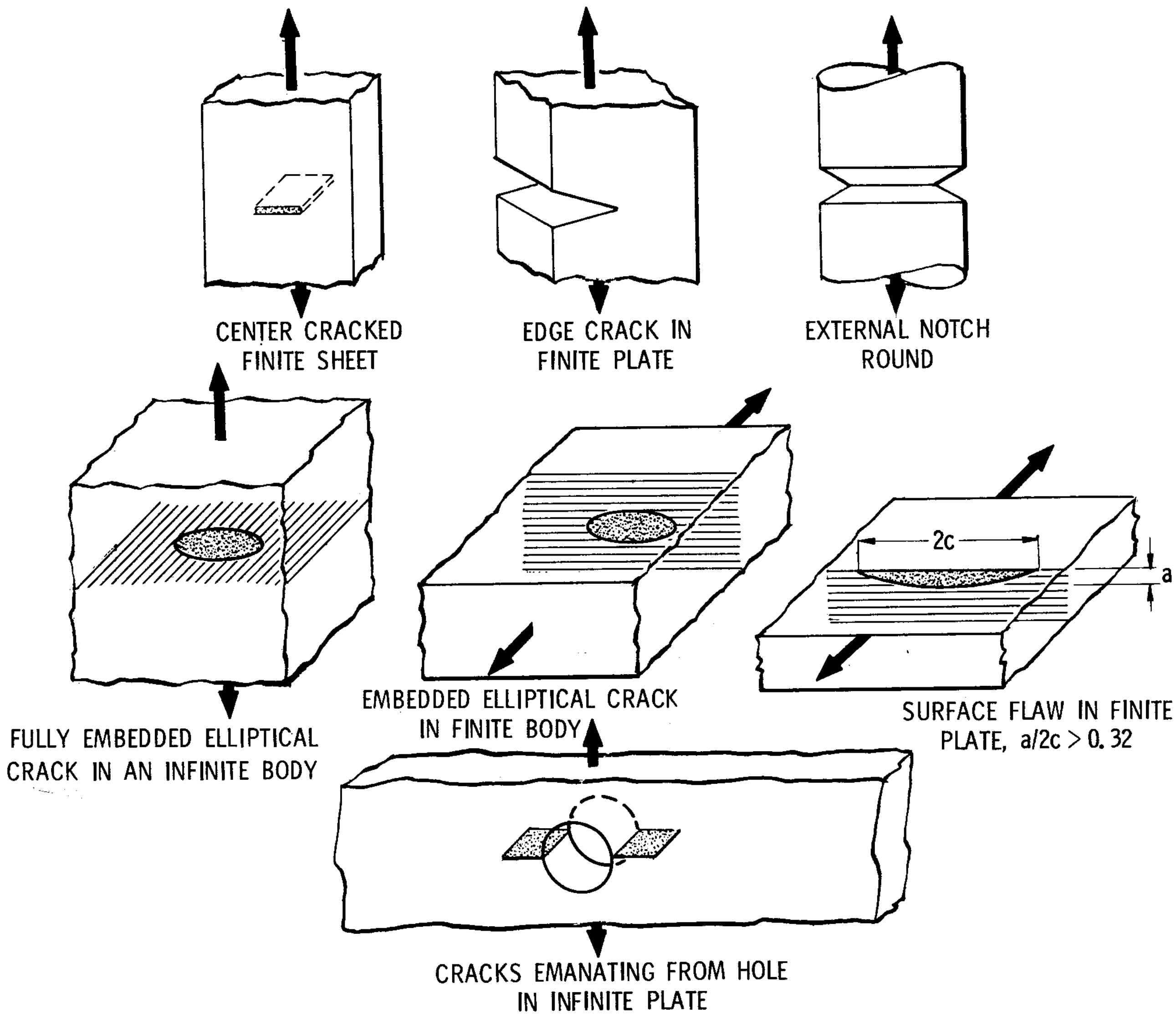

DESIRED STRESS INTENSITY SOLUTIONS

The next figure illustrates several of the practical crack configurations which are of practical interest and for which no fully satisfactory stress intensity solutions are available. Solutions for the case of the deep surface flaw with depth-to-length ratios less than 0.32 are needed. Cracks emanating from circular holes or similar penetrations are frequently encountered. The extensive amount of material removal and complex part configuration encountered on integrally stiffened membrane tanks or wing skins result in a relatively high probability of encountering defects in regions where inspection is difficult. Finally, cylindrical and tubular structural members are frequent in aircraft structures and improved knowledge of the stress intensity for flaws in these configurations is needed. The fracture control analysis of the Shuttle will require evaluation of the consequences of flaws under a variety of such situations. This evaluation will require that crack tip stress intensity estimates be established. Such estimates should be obtained from qualified people with an understanding for the uncertainties involved in the elastic analysis.

DESIRED STRESS INTENSITY SOLUTIONS

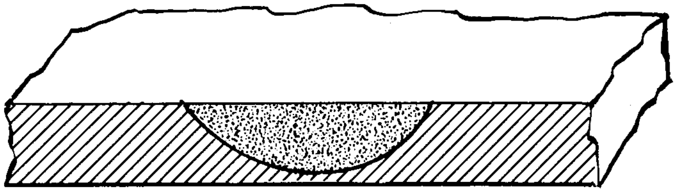

DEEP FLAW - FINITE PLATE
$a/2c < 0.3$

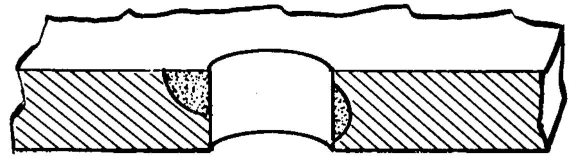

PART THROUGH CRACKS
EMANATING FROM HOLES

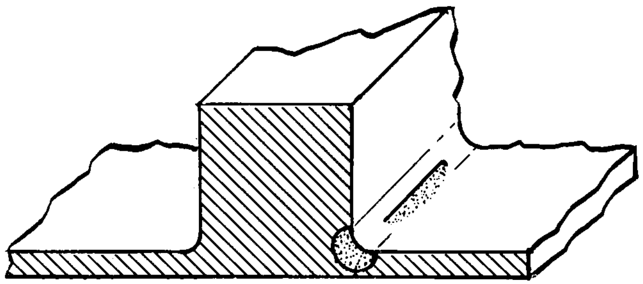

CRACKS AT STIFFENER
MEMBRANE JUNCTURE

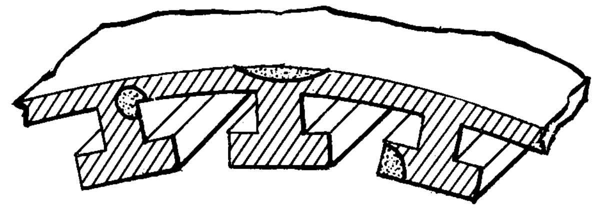

CRACKS ON INTEGRALLY
STIFFENED SKIN

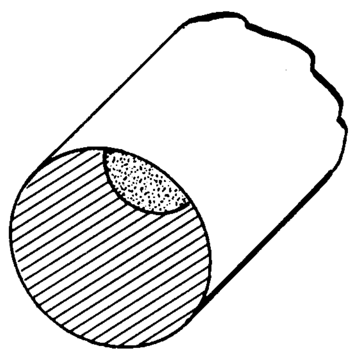

SURFACE FLAWED
CYLINDRICAL ELEMENT

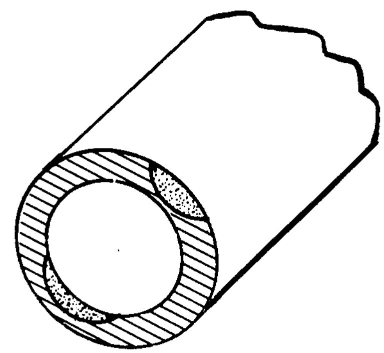

INTERNALLY &/OR EXTERNALLY
SURFACE FLAWED TUBLAR ELEMENT

PLASTICITY EFFECTS

The next figure illustrates a condition in which the plastically deformed region in front of the actual crack tip causes additional uncertainties in the use of linear-elastic theory.

The assumption that the elastic stress field conditions completely dominate the behavior of the flaw and can be used as an unambiguous descriptor of the flaw propagation becomes increasingly invalid as the plastically deformed region becomes significant relative to the dimensions of the flaw and the section thickness.

Although the work necessary to advance the crack front may be principally supplied from the surrounding elastic material, the characterization of the elastic field in terms of the physical flaw dimensions of length and depth (obtained from the linear elastic analysis) becomes lost. The maximum stress intensity for the elastic field is obviously not at the end of the minor axis of the flaw but is displaced laterally and probably vertically.

Additionally, the maximum value of local elastic stress intensity may not represent the critical toughness condition due to the complex dependence of toughness on thickness caused by varying of transverse constraint.

For conditions involving yet more extensive plasticity, the analytical characterization of the elastic stress field by the stress intensity parameters (which involve only terms of inverse square root variation of the stress with distance) is obviously inaccurate. Such terms require an inverse square root singularity at the border of the elastic field but considerations of continuity at the plastic zone border would call for very different conditions. The accurate characterization of the elastic field and of the extent of the plastically deformed region are contingent on development of effective methods of elastic-plastic analysis.

In addition to the development of suitable methods of elastic-plastic analysis, measurements of the fracture and crack growth characteristics of candidate structural alloys containing deep surface flaws are needed to establish the limits of applicability for the correlations based on linear elastic theory. Beyond that point, a suitable empirical description of the fracture condition is needed to guide the development of the elastic-plastic analysis and to provide direct empirical data for fracture control use. Several NASA technology programs are addressed to these objectives.

PLASTICITY EFFECTS

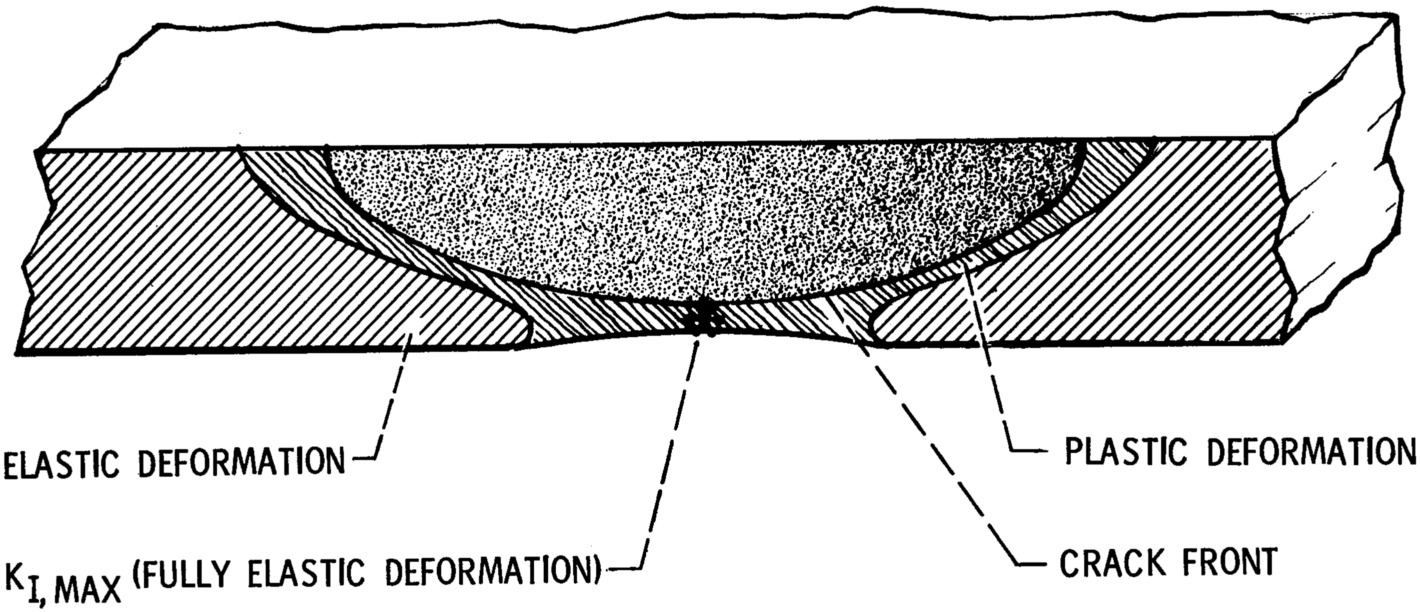

PRIMARY LOADING CONDITIONS

The next figure illustrates the nomenclature by which the loading conditions on a cracked body are described. Mode I represents loading normal to the crack plane. This is the most commonly considered case and is generally thought to represent the worst loading condition. Mode II loading is an inplane shear loading with the applied shear loads normal to the crack front. Mode III loading is shear loading with the applied shear parallel to the crack front. This condition is frequently called the tearing or torsion mode. Any loading can be represented by suitable combinations of these three basic loading conditions. The crack tip stress intensity factors for each case are designated K_I, K_{II}, and K_{III} as shown. Like the Mode I stress intensity, K_I, K_{II} and K_{III} must be obtained from an elastic analysis of the cracked body. The same problems of limited availability of accurate solutions for practical hardware shapes exist. In addition to the problems imposed by lack of stress intensity solutions and the effects of local plastic deformation, there exists an insufficient characterization of the effects of various loading conditions on crack growth behavior. Combined tension and bending, tension-shear, and tension-torsion conditions are frequently encountered in practice. Effects of loading sequence and the load-time profile on cyclic flaw growth are not sufficiently well understood to permit effective generalization of the usual constant amplitude uniaxial laboratory test data. Environmental effects, which in practice may vary within a given loading cycle, provide additional factors which must be evaluated. The NASA technology program attempts to address such problems.

PRIMARY LOADING CONDITIONS

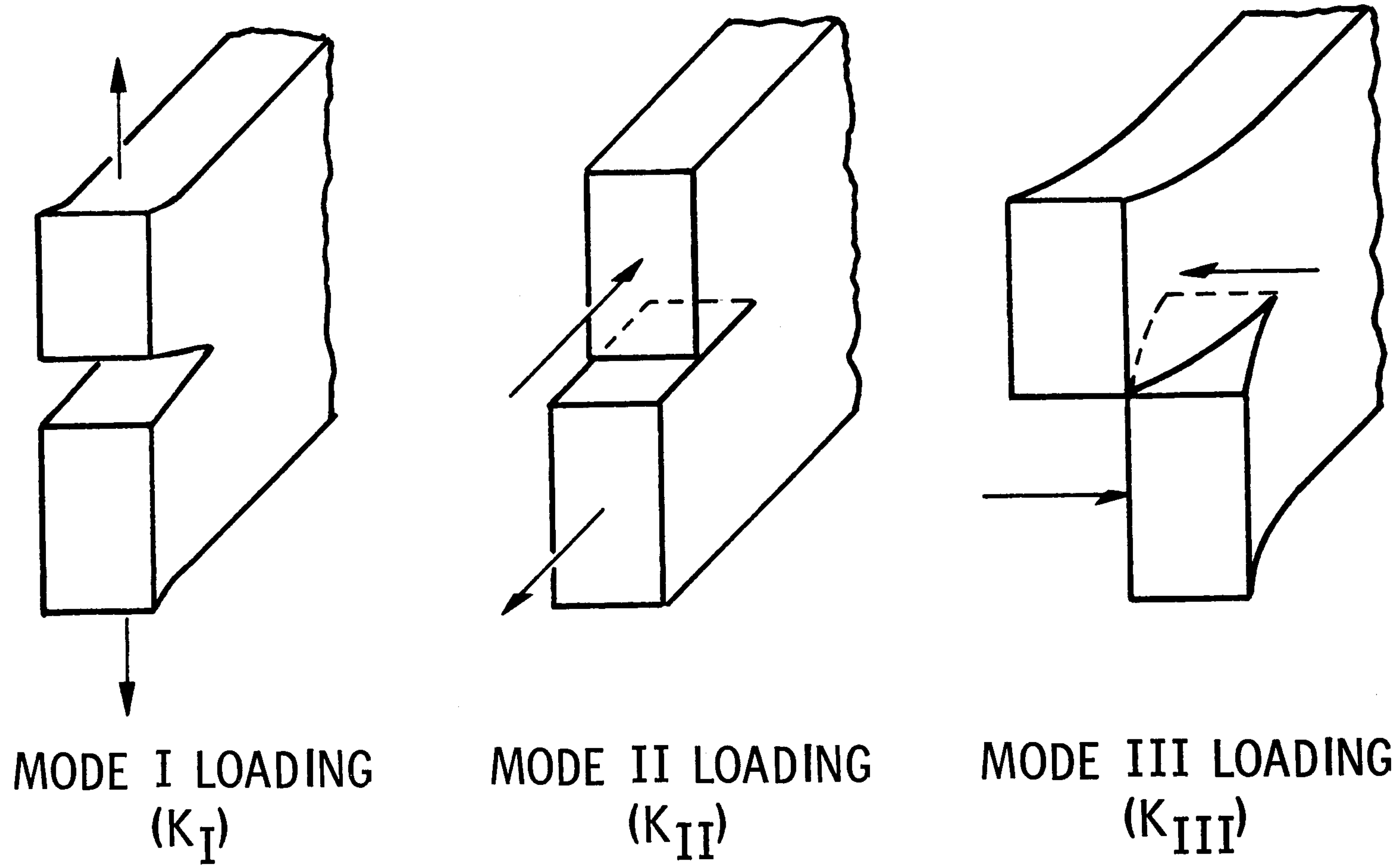

NASA FRACTURE CONTROL PROGRAM

FRACTURE MECHANICS PROGRAMS

NASA fracture mechanics programs have been divided into three groups. The first group of programs is concerned with crack tip stress field analysis. A total of five programs are involved, two are directed to obtaining improved elastic stress intensity solutions and three to development of techniques for elastic-plastic analysis.

The second group of programs is concerned with the application of fracture mechanics parameters to the problem of developing fracture control criteria for the Shuttle vehicle. Of the total of eight programs, four can be described as development of design methods, two with the definition of design philosophy--that is, definition of the criteria for fail safe and safe life elements consistent with fracture control requirements. The remaining two programs involve definition of proof test factors for Shuttle pressure vessels.

The third group involves a total of 25 programs. These programs have been further subdivided to indicate the distribution of effort. The first group is developing information on various loading conditions. Combined mode loading effects and loading pattern effects are the subject of these four programs. Some representative results from these programs will be shown later.

The second subgroup of three programs is directed at deep flaw problems. One of these programs is complete and a final report draft is being reviewed for a second program.

Environmental effects are being studied on four programs. Measurements of the stress intensity threshold for sustained-load growth and of the cyclic crack growth rates are being obtained for a variety of materials and alloys of significance to the Space Shuttle. 2219 aluminum has been examined for a variety of propellant and environmental conditions. GH_2 effects are being determined on candidate engine alloys with emphasis on Inconel 718.

The final subgroup of programs involves material fracture characterization testing. Here the principal objective is providing fracture toughness data on parent and weld material. The materials are listed. The aluminum, titanium, and Inconel 718 materials are principally candidates for the orbiter and engine structures while the high strength steels are candidates for the solid rocket motor case materials.

NASA FRACTURE CONTROL PROGRAM

FRACTURE MECH PROGRAMS

FRACTURE MECHANICS ANALYSIS (5 PROGRAMS)

- STRESS INTENSITY SOLUTIONS
- ELASTIC PLASTIC ANALYSIS

DESIGN METHODS & DESIGN CRITERIA STUDIES (8 PROGRAMS)

- FRACTURE CONTROL DESIGN METHODS
- DEFINE SAFE LIFE/FAIL SAFE CRITERIA
- ESTABLISH PROOF TEST REQUIREMENTS

EXPERIMENTAL FRACTURE MECHANICS (25 PROGRAMS)

1. LOADING EFFECTS (4 PROGRAMS)
    - EFFECTS OF LOADING MODE
    - EFFECTS OF LOADING PATTERN
2. CONFIGURATION & PLASTICITY EFFECTS (3 PROGRAMS)
3. ENVIRONMENTAL EFFECTS (4 PROGRAMS)
    - EFFECTS OF SHUTTLE ENVIRONMENT ON Al
    - EFFECTS OF GH_2
4. MATERIAL CHARACTERIZATION (14 PROGRAMS)
    - 2219 ALUMINUM
    - 7075 ALUMINUM
    - 6Al-4V TITANIUM
    - 5Al-2.5 Sn TITANIUM
    - INCONEL 718
    - HY 150 STEEL
    - MARAGING STEEL
        - 12Ni
        - 18Ni
    - DUAL HARDENING 10Ni STEEL

DEEP FLAW MAGNIFICATION OF STRESS INTENSITY

As a growing flaw becomes deep relative to the wall thickness, a condition of considerable practical interest to pressure vessel designers develops. It is highly desirable to operate a pressure vessel at stress level such that a flaw, growing subcritically by cyclic loading, will penetrate the wall and cause failure by leakage rather than a catastrophic burst. To insure leakage, one must have a stress intensity solution which is valid as the flaw front approaches the rear face.

Some recent analytical results for deep flaws, along with some supporting data from brittle epoxy specimens, is shown on the next figure. Plotted are the results of a three-dimensional numerical elastic solution for a flaw in a finite plate. The flaw front is a circular arc rather than an elliptical shape. The equation shown in the figure gives the stress intensity factor at the base of a surface flaw. The solution has been obtained from a solution for a flaw in an infinite body and the effects of the stress-free front and rear faces, labeled as 1 and 2, are provided by the magnification factors M_1 and M_2 in the equation. The results for a semi-circular flaw show very little magnification effect. As the crack shape factor $a/2c$ decreases to .32, a strong influence of the crack front approach to the back face can be seen. Thus far, the program has not been able to overcome computational difficulties which arise as the crack shape is reduced below .32. A numerical boundary collocation solution by Gross is indicated as a possible limiting case for $a/2c = 0$.

The analytical estimates for the magnification of stress intensity are compared with experimentally determined values from very brittle epoxy specimens. These specimens were sufficiently brittle that the elasticity assumptions should be quite valid. Although there is considerable scatter in the data, the analysis appears to accurately predict the trends and does not do a bad job of predicting the results for an $a/2c$ ratio of 0.32.

COMPARISON OF BACK SURFACE MAGNIFICATION FACTOR, M_2, WITH BRITTLE SPECIMEN DATA

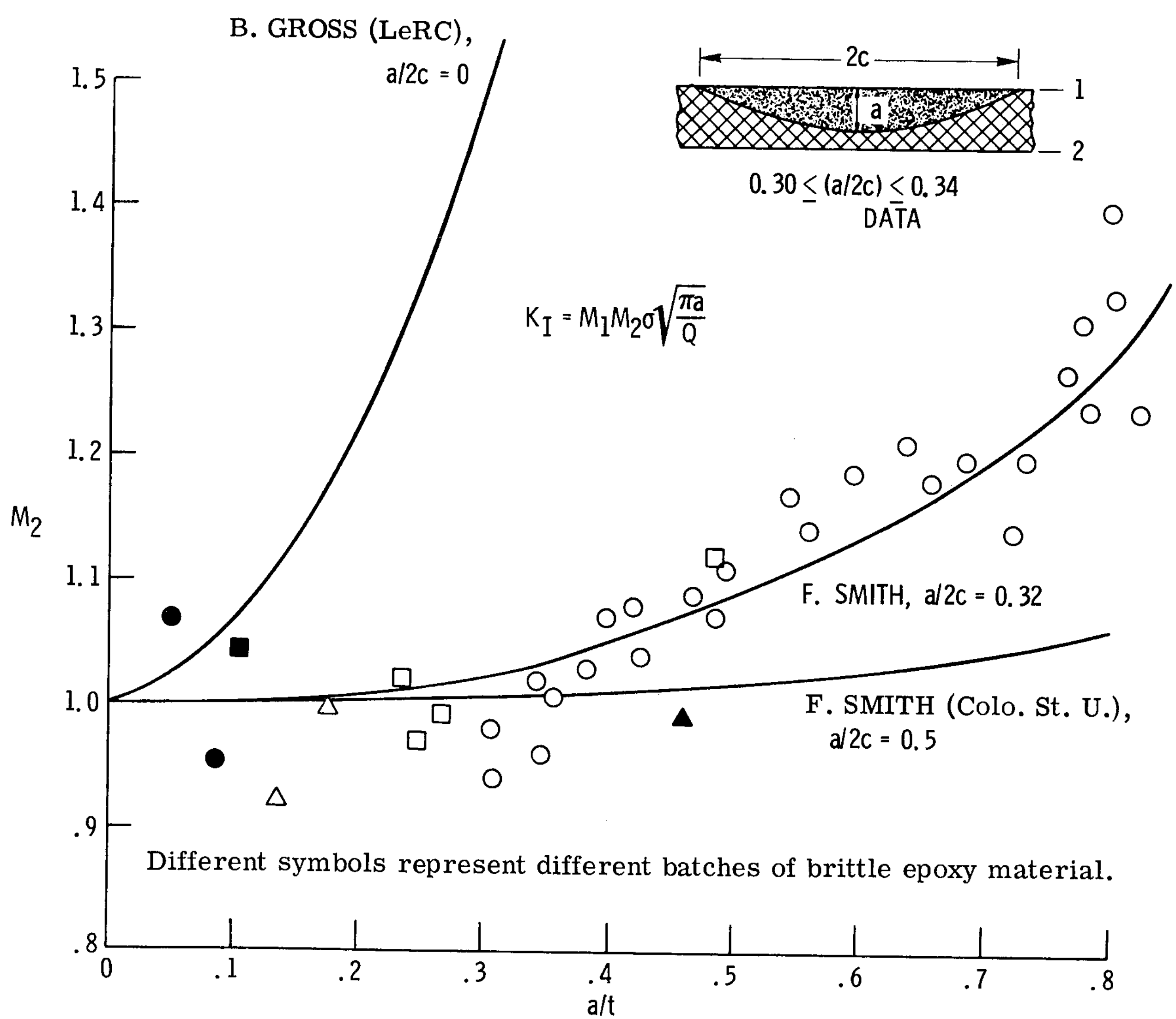

EFFECT OF MODE III LOADING ON TENSILE LOAD CARRYING ABILITY OF A CYLINDRICAL ELEMENT

This figure shows data which has been developed to assess the effects of combined loading on fracture conditions. The data and solid line shown are for 4340 steel at $144^{o}K$ (that's $-200^{o}F$). The dashed curve is for 7075 aluminum tested at room temperature obtained from reference 12. The ordinate represents the fraction of critical Mode I stress intensity and the abscissa the fraction of critical Mode III. The test specimens were externally notched round bars with fatigue sharpened notches. Simultaneous tension and torsion were applied in various ratios to get the fracture data shown. These data suggest there is very little loss in tensile load carrying ability of these specimens due to the torsional load. Additional data is being developed for 2219 aluminum and 6Al-4V (STA) titanium. Surface flaws as well as full circumferential external flaws are being tested. In addition, cyclic growth data under these combined loading conditions will be obtained and compared with corresponding Mode I data.

EFFECT OF MODE III LOADING ON TENSILE LOAD CARRYING ABILITY OF A CYLINDRICAL ELEMENT

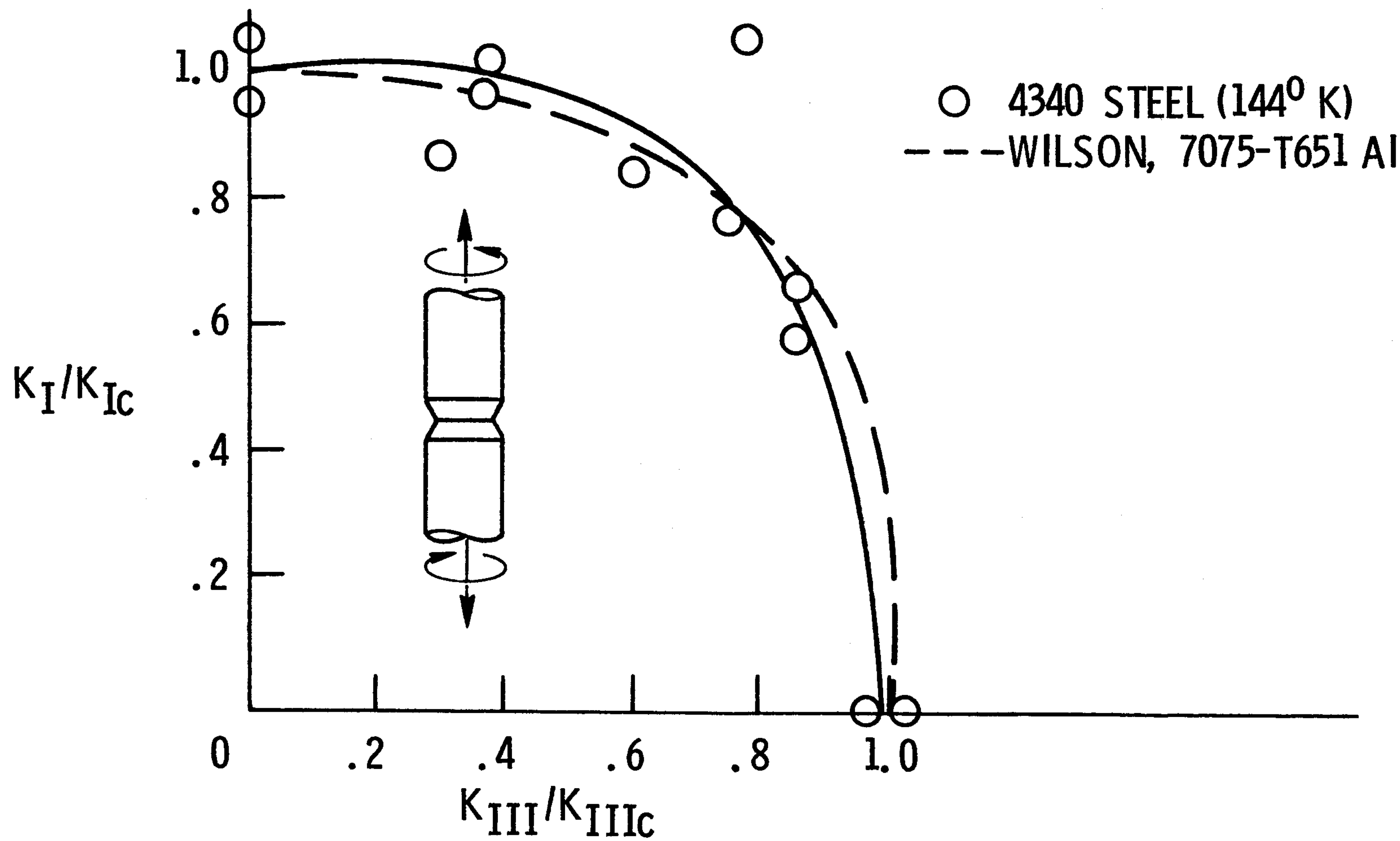

EFFECT OF MODE II LOADING ON TENSILE LOAD CARRYING ABILITY OF PLATE ELEMENTS

The next figure also shows the effects of combined mode loading on fracture. This time, the results are not so encouraging. The test specimens used for the data were for through cracked plates with the cracks inclined at various angles to the loading direction. As indicated by the detail sketch, this produces a combination of tension and Mode II shear loading at the crack tip. This time the 4340 steel data is in obvious disagreement with the reference 16 aluminum data and shows a strong effect of the shear component on the tensile load carrying ability of the specimens. Again, additional data with surface flaw specimens and aluminum and titanium are being tested. Since many Shuttle components may experience such loading conditions, the degradation experienced by the 4340 steel specimens must be carefully checked for specific Shuttle material-thickness-loading conditions.

EFFECT OF MODE II LOADING ON TENSILE LOAD CARRYING ABILITY OF PLATE ELEMENTS

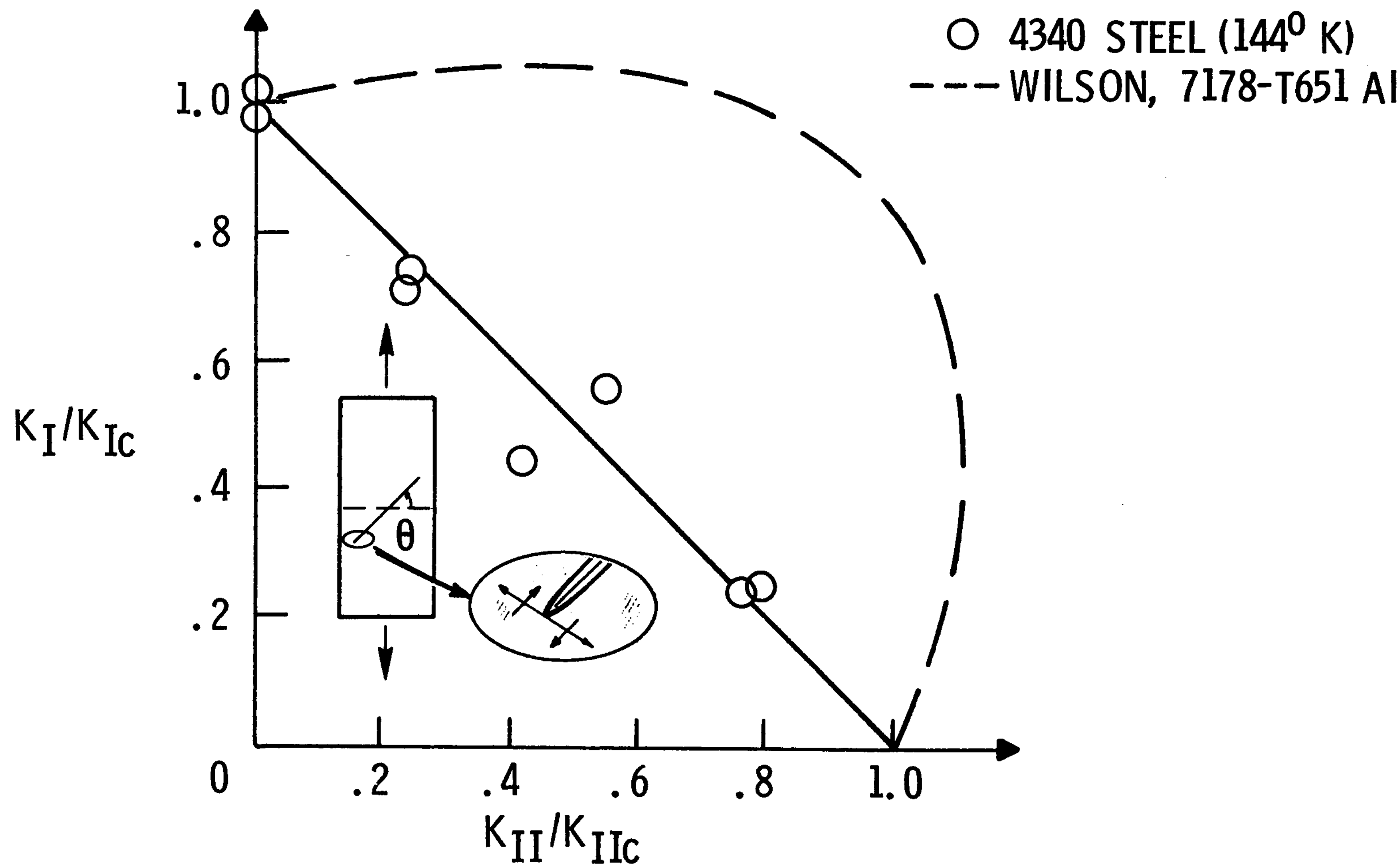

EFFECT OF PROOF TEST TEMPERATURE ON SUBSEQUENT CYCLIC LIFE OF 2219-T87 ALUMINUM

The next figure shows data obtained to investigate possible damaging effects, on subsequent cyclic life, produced by a proof test. Surface flawed specimens of 2219-T87 aluminum were proof loaded as indicated by the symbols at the top of the figure. Several combinations of proof test temperatures and subsequent cyclic test temperatures were investigated. The data are compared with results of previous programs which involved no preload conditions. These previous results are shown as the cross hatched band in each of the three figures. Each figure presents the cyclic life of the specimen as a function of the ratio of initial stress intensity to critical stress intensity. For the specimens cycled to failure at room temperature, there appears to be an increase in cyclic life. For the liquid nitrogen and the liquid hydrogen specimens, no significant effect of proof testing is apparent. In general, no degradation appears to be associated with any of these preload conditions. The preload levels produced proof stress intensity levels between about 75 and 95 percent of critical.

EFFECT OF PROOF TEST TEMPERATURE ON SUBSEQUENT CYCLIC LIFE OF 2219-T87 ALUMINUM

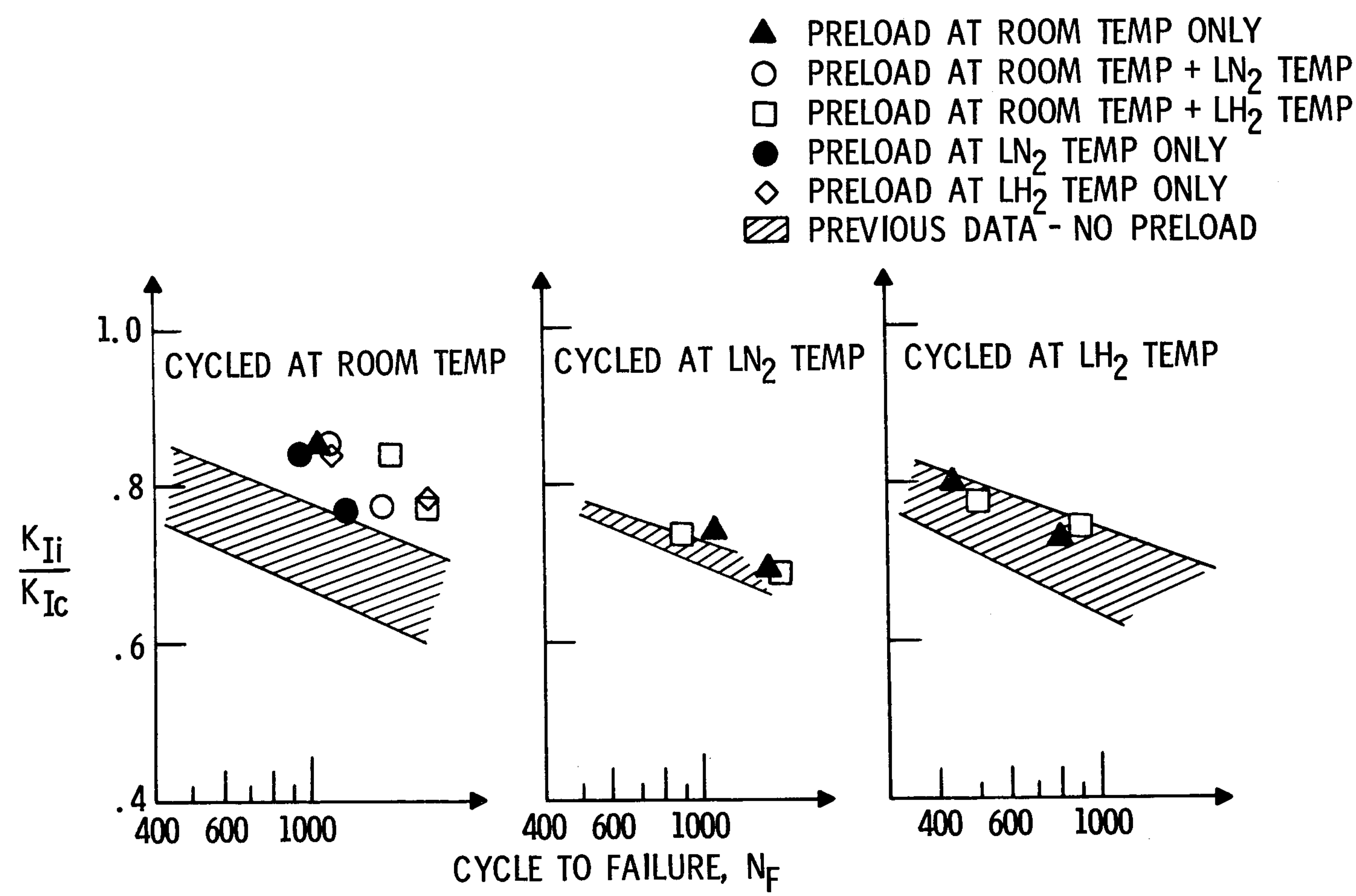

SHUTTLE MATERIAL NDT REQUIREMENTS AND CAPABILITIES

Fracture mechanics parameters can be applied to provide a reasonable set of NDT requirements for fracture control purposes. The depth of a long surface flaw which would produce a stress intensity factor equal to the plane strain fracture toughness if loaded to the material yield strength can be used as an indicator of the flaw size which should be screened out for proof tests conducted near yield. The left-hand curve in this illustration shows such a flaw depth for several candidate structural materials. The materials corresponding to each data point are identified on the abscissa of the right-hand bar chart. Actually, due to departure of the fracture from plane strain linear-elastic conditions, a slightly smaller flaw size could cause failure at proof tests conducted near yield strength. As a result, an NDT inspection objective of one-half the value given by the curve has been selected and is shown as the height of the shaded bars on the right-hand bar chart. The critical flaw size for each alloy when used at 2/3 σ_{ys} is indicated by the tops of the open bar as shown by the legend at the upper right corner.

These NDT objectives are compared with estimates of NDT capabilities for three inspection conditions. The lower horizontal line is an estimate of the inspection capability for an ultrasonic system for finding an open flaw in an easily inspectable, simple shaped specimen. A series of specimens with internal flaws with a face separation of 0.254-mm were used to establish this limit. The band labeled "typical" flaw limit is an estimate for the reliable detection limit for typical fatigue cracks. The "tight" flaw limit region applies for lack of fusion type defects having significant residual compressive stresses causing crack face closure. No upper limit is indicated as very large flaws of this type have too frequently been missed. Special NDT methods are believed necessary for such defects.

Note that even under ideal flaw geometry and inspection conditions, many materials are marginal for effective preproof test screening. Only 2219-T87, Inconel 718, the maraging steels, and HY-150 steel are safely inspectable by the selected standard. In-service inspection requirements represented by the open bars would suggest inspection problems with 7075 aluminum and with 6Al-4V (STA) titanium and the D6 steels. Unless near ideal inspection conditions can be produced, use of 2024-T851 aluminum and Inconel 718 also may impair operational reliability. 2219 aluminum and the HY 150 and maraging steel SRM case materials do not appear to be seriously restricted by inspection capabilities. A more detailed look at in-service inspection is shown by the next figure.

SHUTTLE MATERIAL NDT REQUIREMENTS AND CAPABILITIES

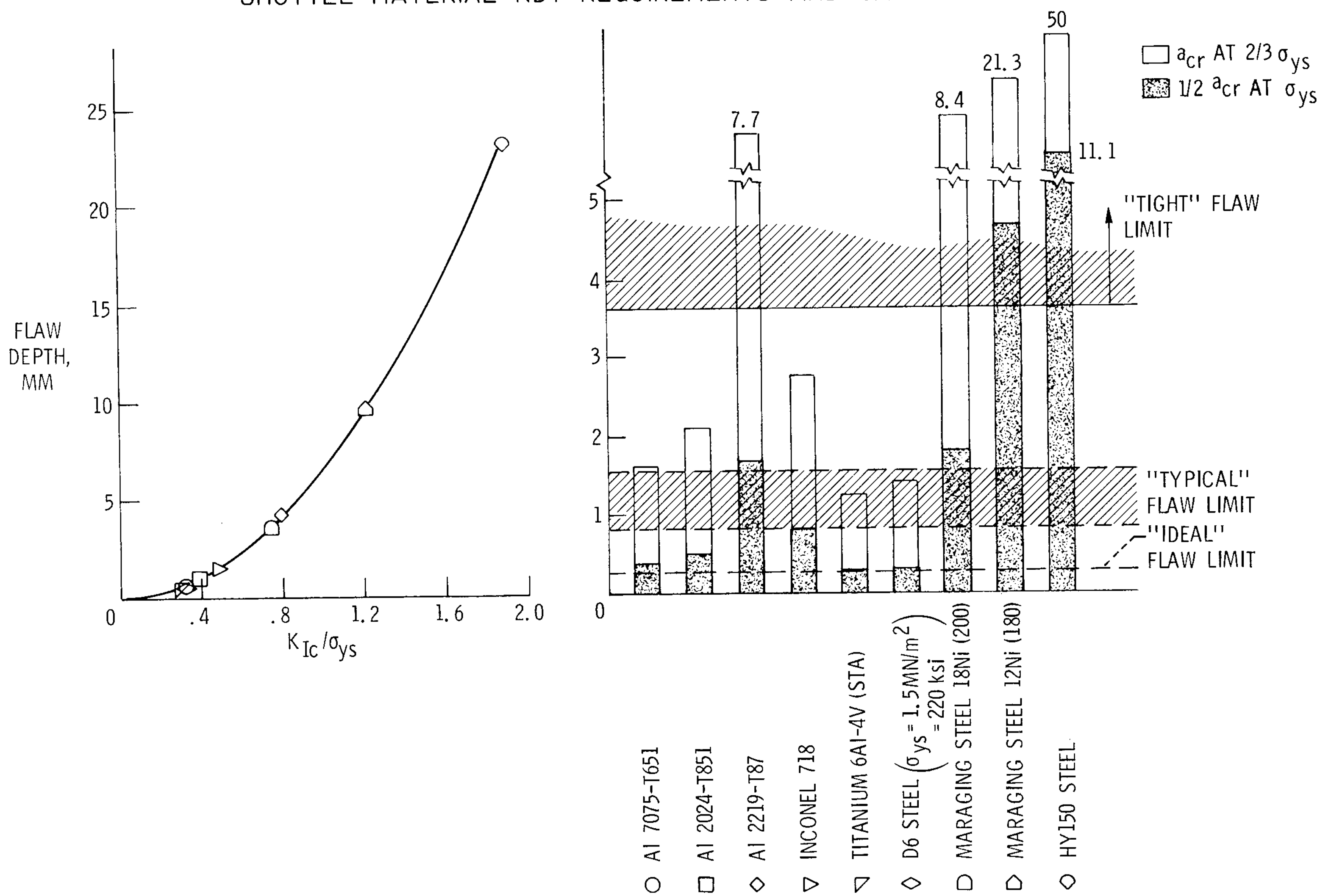

EFFECT OF STRESS LEVEL AND INSPECTION OPPORTUNITIES ON NDT INSPECTION REQUIREMENTS FOR 100 CYCLE LIFE

An idea of the potential usefulness of NDT systems for detection of growing flaws during service life can be obtained from the next figure. The surface flaw depth, (a/Q), which must be detected in a structural element designed for a 100-cycle service life is plotted as a function of the working stress-to-yield stress ratio. Flaw growth data for 2219-T87 aluminum and 6Al-4V(STA) forged titanium were used to construct the flaw growth curves which correspond to failure in 100 cycles. Such plots were constructed for a series of stress levels between 0.3 σ_{ys} and σ_{ys}. Cross plotting the results provided the curves shown. The (a/Q) values represent the crack sizes which correspond to selected inspection points. Only the 0 and 100-cycles curves are shown. All other curves are enveloped by these flaw size curves for 0 and 100 cycles. The 100-cycle curve corresponds to the proof test critical sizes and the 0-cycle curve to the flaw sizes critical at the working stress. No inspection opportunities are possible for this latter condition. For inspections conducted prior to reaching this critical size, the NDT detection requirement lies between this upper curve and the proof test critical curve. The more inspection opportunities provided, the smaller is the flaw at the first inspection point, and the closer the curve lies to the lower boundary.

Comparison between the two materials clearly shows the 2219 aluminum to have the most detectable flaw conditions. If the Air Force B-1 limit is taken as a representative detection condition, the use of 6Al-4V titanium would preclude effective service inspection unless the stress level was about 0.3 σ_{ys}.

The effect of the operating stress on the NDT detection requirements is very pronounced. A relatively small change in operating stress causes a significant change in the NDT detection requirement. For tough materials like the 2219 aluminum, the NDT detection capability might be used to establish the working stress without suffering a severe weight increase. Such a design practice is contingent upon demonstration of the assumed detection capability on typical hardware components to an acceptable level of reliability.

EFFECT OF STRESS LEVEL AND INSPECTION OPPORTUNITIES ON NDT INSPECTION REQUIREMENTS FOR 100 CYCLE LIFE

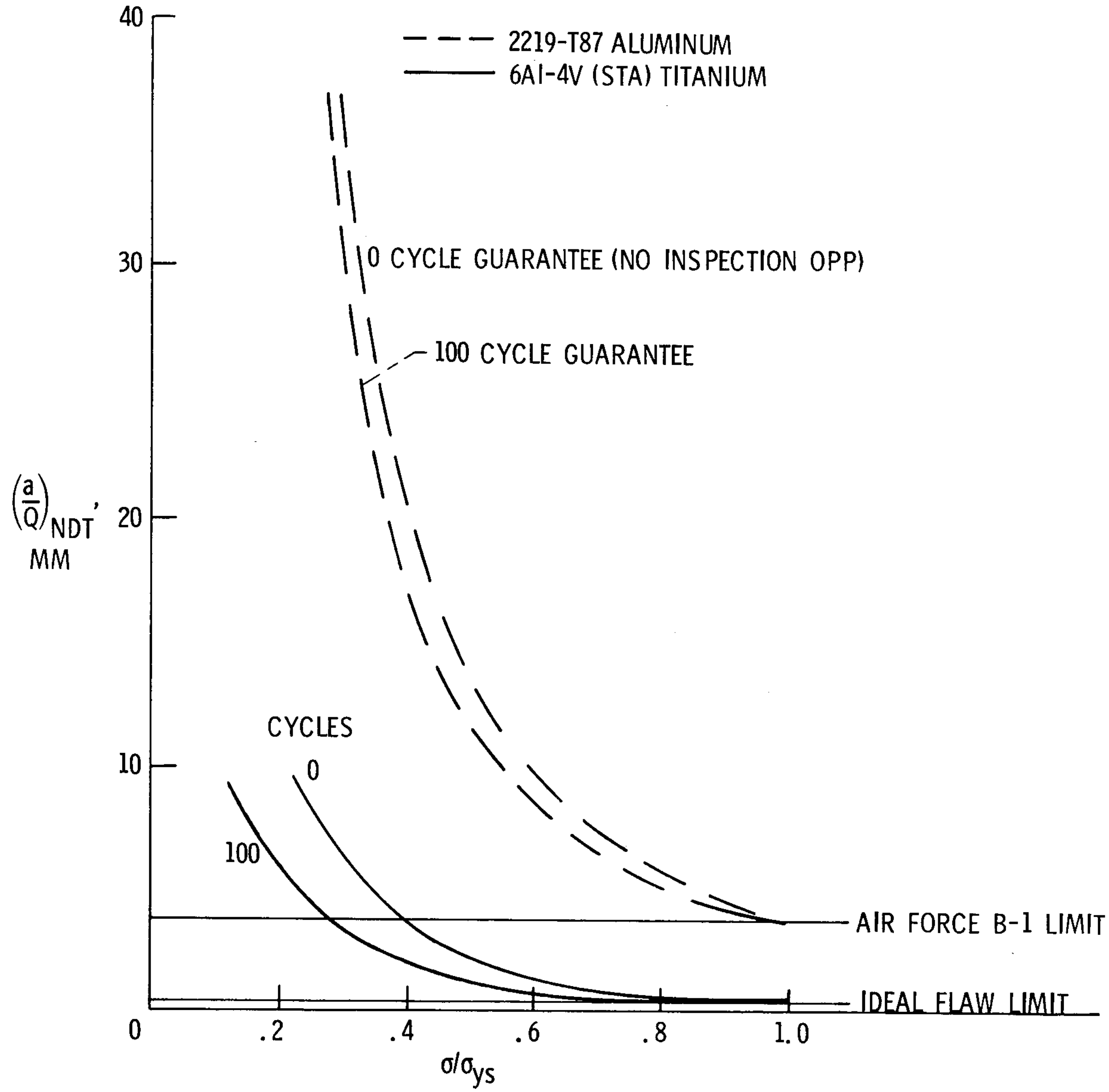

NDT FRACTURE CONTROL CONSIDERATIONS

The effective use of NDT in a fracture control plan is contingent upon early consideration of the NDT operations. After the NDT system capabilities have been established for the materials and components, it is still necessary to have part accessibility, an inspectable part configuration, and flaw detectability requirements within the demonstrated capability of the inspection system. These factors are controlled by early design decisions. For certain materials, the inspectability limit of the NDT system may be used for selecting a design stress, particularly if the service life of the component cannot be established by proof testing.

Fabrication procedures can have a strong effect on the detectability of defects. Surface finish, transition radii, and residual stress due to welding and forming operations can produce the tight crack conditions which provide major NDT uncertainty.

Residual stress fields which depend on the loading conditions may affect the in-service detectability of fatigue cracks. Evaluation of flaw detection limits on fatigue cracks produced under simulated design loading conditions is advisable.

Finally, for components fabricated from tough materials, the NDT detection capabilities may be used to aid selection of the material, material heat treatment, and the design stress level. The crack detectability which is insured by this procedure is of particular importance to the reliability of elements which cannot be proof tested for assurance of the design life. For safe-life elements which cannot be proof tested, such procedures are essential.

NDT FRACTURE CONTROL CONSIDERATIONS

1. COMPARISON OF a_{cr}, a_i WITH NDT CAPABILITY ON FAB PART
2. DESIGN FOR IMPROVED INSPECTABILITY
   - ACCESSIBILITY
   - CONFIGURATION
3. INSPECTION INTERVALS FOR CRITICAL STRUCTURE
   - BASED ON FLAW GROWTH DATA
   - MULTIPLE DETECTION OPPORTUNITIES
4. DESIGN LOAD & RESIDUAL FAB STRESS AFFECT DETECTABILITY

NASA FRACTURE CONTROL PROGRAMS

NONDESTRUCTIVE TESTING PROGRAMS

The nondestructive test programs are divided between equipment improvement type activities and development of improved techniques for utilizing existing equipment. Both are important and necessary. The most immediate payoff is probably going to be obtained from the second group.

The equipment development programs include automation of both radiographic and ultrasonic techniques. The radiography efforts include computerized enhancement of radiographs and development of pattern recognition routines. The ultrasonic programs are directed to automatic monitoring control of inspection variables, real time display of flaw data, permanent recording of all test variables and automated comparison of subsequent tests for flaw growth evaluation. Onboard monitoring systems include both acoustic emission and ultrasonic approaches. Residual stress conditions affect the NDT system crack detectability and, conversely, UT evaluation of residual stress conditions should be possible. This approach is also being pursued.

The development of improved inspection techniques and evaluation of the capability of current systems on fatigue cracks is essential to the quantitative use of NDT in a fracture control plan. Detection of tight weld defects is being approached by inspection under load and by the application of opaque films to the faying surfaces prior to welding. Various stable films or thin copper foil appear visible to radiography and ultrasonic inspection if the surfaces are not completely fused together. The systematic evaluation of detectability of fatigue cracks to reduce (or perhaps to better position) the uncertainty bands that were shown on an earlier figure is of primary importance.

The application of acoustic emission systems to flaw detection during proof test and during flight operations is being evaluated. Special inspection techniques directed at the RSI are included here for completeness.

NASA FRACTURE CONTROL PROGRAMS

NONDESTRUCTIVE TESTING PROGRAMS

EQUIPMENT DEVELOPMENT (10 PROGRAMS)

- AUTOMATION OF NDT SYSTEM
- IMAGE ENHANCEMENT
- NEUTRON RADIOGRAPH
- ON BOARD CHECKOUT
- RESIDUAL STRESS DETECTION

INSPECTION TECHNIQUES & CAPABILITY EVALUATION (9 PROGRAMS)

- TIGHT CRACK SYSTEM
- FATIGUE CRACK DETECTION
- ACOUSTIC EMISSION DETECTION
- RSI CRACK DETECTION

EFFECT OF APPLIED LOAD ON UT SYSTEM SIGNAL STRENGTH

The effect of applied load on the output signal strength of an ultrasonic shear wave test setup is illustrated on this figure (personal communication from G. W. Yee, General Dynamics Corporation, Fort Worth Division, Fort Worth, Texas). An EDM reference slot with the dimensions shown on the figure was used to establish the reference screen amplitude height of about 40-mm. Two fatigue cracked 6Al-4V titanium specimens were examined with this reference setting. At zero applied load the output signal strength of both fatigue cracks was below that of the reference output. For the specimen containing the 3.2-mm flaw, the signal strength output more than tripled before the maximum signal strength was achieved. For the specimen containing the shorter, 2.67-mm flaw, the output signal strength more than doubled. These significant increases in output were obtained at load levels between 10 and 20 percent of the yield strength. It is apparent that inspection techniques which permit UT inspection of critical regions to be performed with low tensile loading applied to the part can provide increased detectability for fatigue cracks.

EFFECT OF APPLIED LOAD ON UT SYSTEM SIGNAL STRENGTH

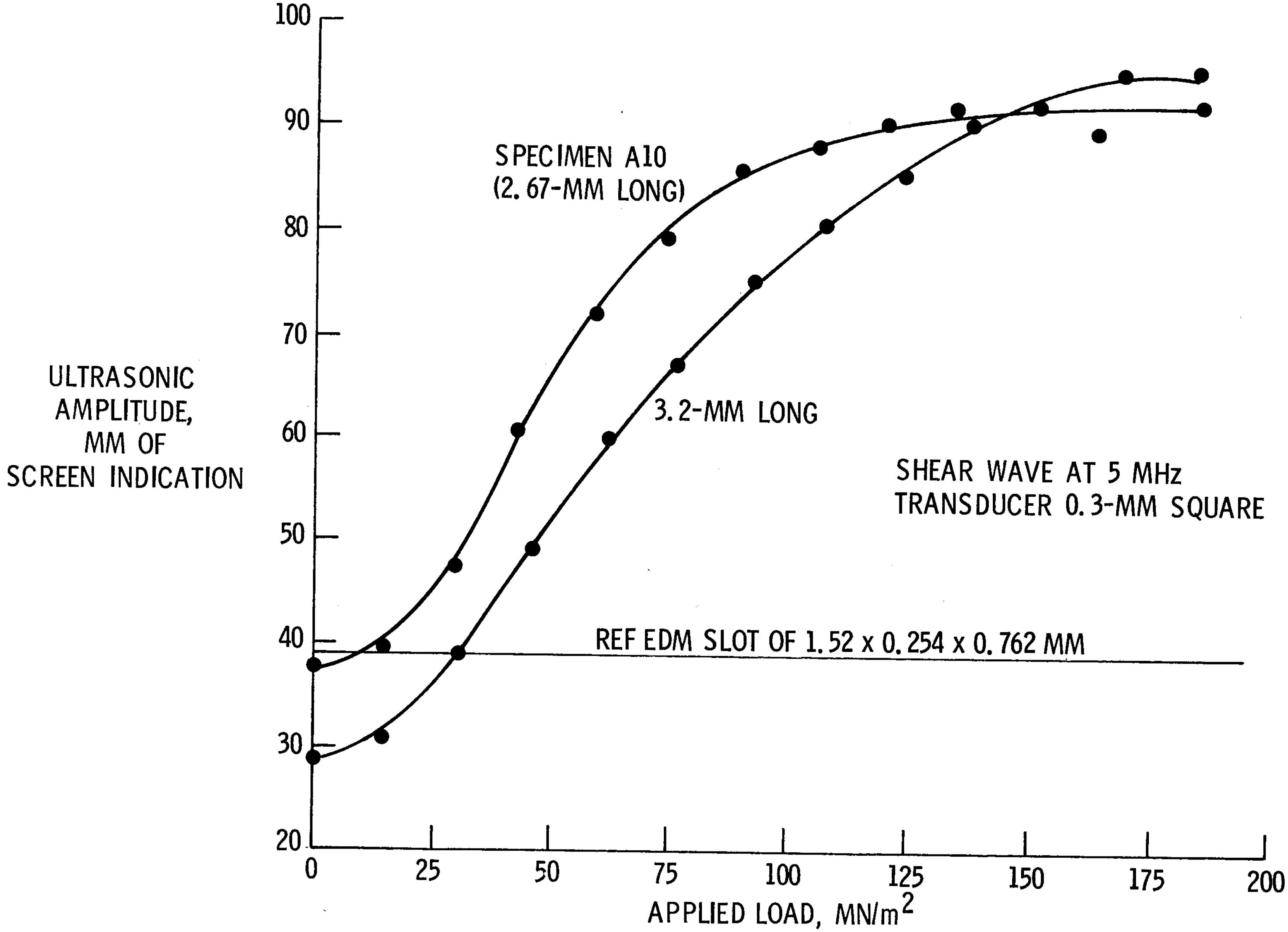

BACK SURFACE DIMPLING FOR DETECTION OF SURFACE OR EMBEDDED FLAWS

The next figure indicates an interesting series of NDT experiments which were reported at a fracture control symposium held at the Lewis Research Center in January 1972. The presence of an embedded flaw or of a deep surface flaw originating on the opposite face can frequently be identified by the presence of a dimple on an inspectable surface. The practicality of using this dimple for a detection technique depends on the visibility of the dimple and the dependence of that visibility on applied load. The back surface dimple is shown under inclined lighting for a 2.54 mm (0.1-in) thick titanium specimen in the photograph. The actual surface displacements are shown for the loaded and unloaded specimen by the plots. (The span of the curves on the abscissa corresponds to about 1/4-inch.) Data in the table are for 3.17 mm thick (1/8-in) 2219-T87 aluminum specimens. Notice that for a crack depth of about 1/2 the thickness, there was eyeball detection of dimpling at very low load levels. Safe inspection of components can be conducted at these loading conditions. The maximum load level required was less than 25 percent of the yield strength and most flaws became detectable at stress levels between 8 and 14 percent of the yield strength. Although these detectability limits would undoubtedly change for fabricated components, it appears that the concept is promising and should be pursued further.

BACK SURFACE DIMPLING FOR DETECTION OF SURFACE OR EMBEDDED FLAWS

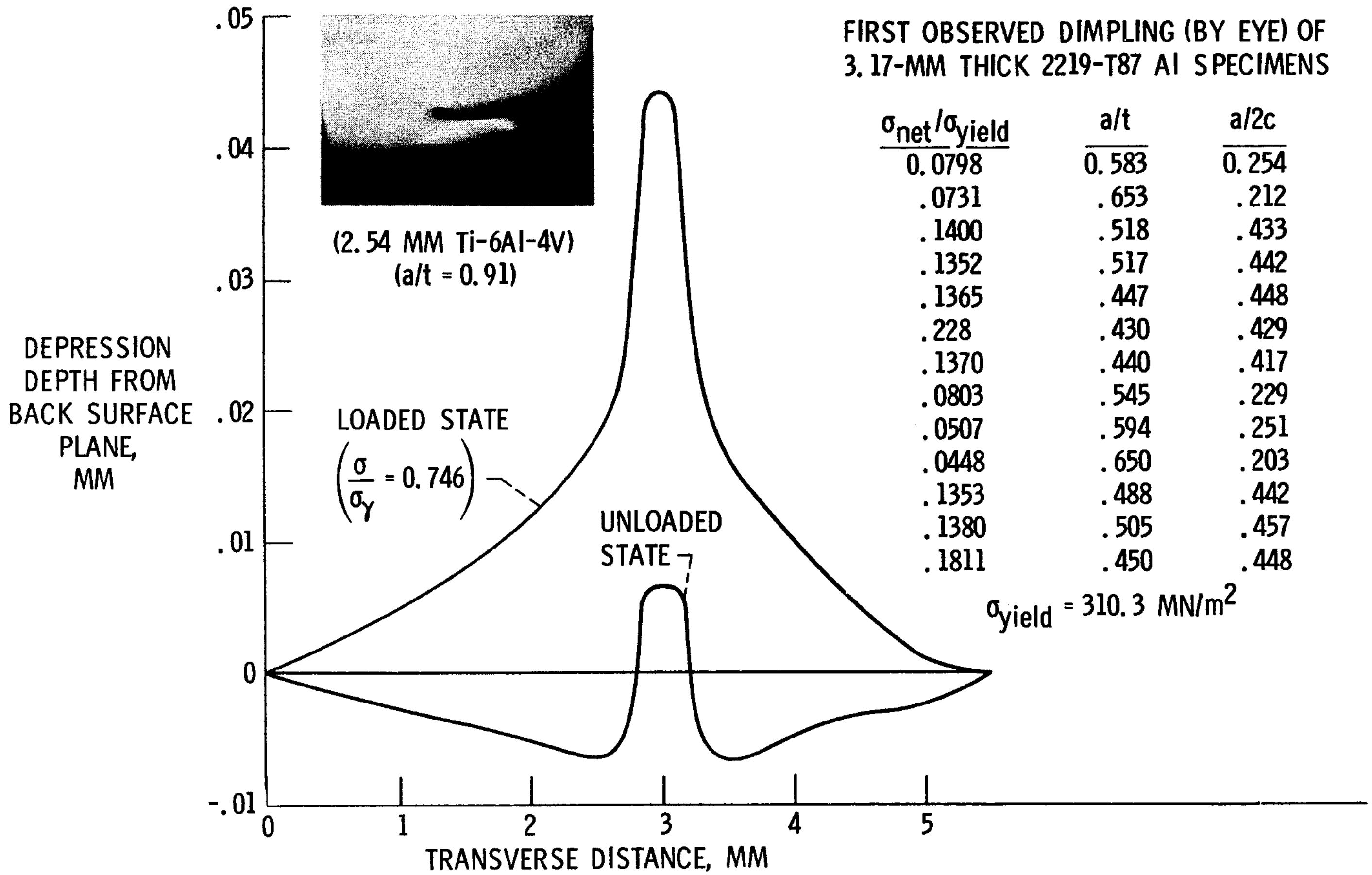

FIRST OBSERVED DIMPLING (BY EYE) OF
3.17-MM THICK 2219-T87 Al SPECIMENS

$\sigma_{net}/\sigma_{yield}$	a/t	a/2c
0.0798	0.583	0.254
.0731	.653	.212
.1400	.518	.433
.1352	.517	.442
.1365	.447	.448
.228	.430	.429
.1370	.440	.417
.0803	.545	.229
.0507	.594	.251
.0448	.650	.203
.1353	.488	.442
.1380	.505	.457
.1811	.450	.448

$\sigma_{yield} = 310.3\ MN/m^2$

NDT ASSESSMENT

The current NDT state-of-the-art for Shuttle is indicated by the items of the next figure. Based on open flaw detection limits established with a UT system on a simple laboratory test specimen, the detection capability appears adequate for primary candidate alloys. This assumes that NDT inspection can be performed under approximately the same ideal conditions used for the laboratory tests. Real hardware components such as the integrally stiffened skin do not provide such conditions. The detection capability of NDT devices, tailored to Shuttle inspection conditions, must be evaluated to establish flaw detection threshold and reliability characteristics. The capability for detection of fatigue flaws and tight lack-of-fusion type defects is not well established but is being evaluated on several of the current NASA technology programs. Further NDT development for Shuttle specific conditions will be needed as the critical components become identified and the fabrication procedures established.

For tight flaws, reliable detection will be very difficult and special detection enhancement techniques, such as inspection under load and after proof test loading, may be required. Novel approaches such as surface dimple detection during loading may be useful.

Automation of various NDT systems is highly desirable. Inspection of large components provides an obvious advantage for automation to speed the process and reduce operator fatigue. Variability of results between laboratory and production inspection experience using the same type system and among different individuals on a specific setup are concerns to which some development programs are directed. Systems to monitor in-flight conditions of critical elements and the conditions during proof testing are being developed.

NDT ASSESSMENT

1. CURRENT DETECTION CAPABILITY ADEQUATE FOR OPEN FLAWS IN INSPECTABLE PARTS
2. NDT CAPABILITY IS NOT ADEQUATELY EVALUATED FOR
   - REALISTIC COMPONENT SHAPES
   - FATIGUE CRACKS & TIGHT (LACK OF FUSION) DEFECTS
3. IMPROVED DETECTABILITY THRESHOLDS & IMPROVED INSPECTION TECHNIQUES DESIRABLE
4. INSPECTION UNDER LOAD APPEARS PROMISING
5. AUTOMATED NDT SYSTEMS
   - LARGE AREA INSPECTION
   - ELIMINATION OF OPERATOR VARIABILITY
   - MONITOR CRITICAL ELEMENTS DURING OPERATION
   - REMOTE OPERATION DURING PROOF TEST

SUMMARY COMMENTS

This final figure summarizes the technology situation with respect to fracture control requirements of the Shuttle. The current state-of-the-art does permit an approach based on linear elastic fracture mechanics concepts. This means that initial design definition must recognize and provide for the presence of a sharp, crack-like defect in the as-fabricated structural components. The current RFP is specific with respect to this point.

The current technology developments are evolving at a rapid pace through many programs underway in Government, industry, and academic laboratories; however, certain basic deficiencies should be acknowledged. These include the items listed on the figure. Development and implementation of a fracture control plan should recognize these deficiencies and provide adequate resources for the extensive empirical test data which will be required. With respect to the cost impact of such tests, recent experiences involving advanced aircraft systems have seen unit cost increases of from 200 to 500 percent. Recent estimates for a comprehensive program on the B-1 bomber indicate the fracture control program will represent substantially less than one percent of the total RTD & E costs. It is clear that the costs of not providing an effective fracture control plan are far in excess of the costs of a properly executed program.

SUMMARY COMMENTS

1. FRACTURE CONTROL APPROACH
   - CRACK INITIALLY PRESENT
   - FRACT MECH & NDT PROVIDE CONTROL CRITERIA & TECHS
2. DEFICIENCIES EXIST FOR BOTH FRACT MECH & NDT
   - LIMITATIONS OF ELASTIC ASSUMPTIONS & ANALYSIS
   - INCOMPLETE DEFINITION OF LOADING & ENVIRON EFFECTS
3. CURRENT NASA PROGRAMS WILL PROVIDE PARTIAL ANSWERS. SOME GAPS EXIST.
   - ARREST OF CRACKS
   - FRACT MECH DATA UNDER DESIGN LOAD & ENVIRON CONDS
   - NDT DEMONSTRATION OF SHUTTLE COMPONENTS
4. EFFECTIVE FRACT CONTROL PROGRAM CAN BE DEVELOPED BASED ON CURRENT TECH STATUS
   - RECOGNIZE UNCERTAINTIES
   - DESIGN AROUND UNCERTAINTIES
   - CONDUCT MODEL TESTS
5. COST & OPERATIONAL FACTORS OF SHUTTLE MAKE COST OF FRACT CONTROL PROGRAM MINOR COMPARED TO COST OF STRUCTURAL FAILURES

REFERENCES

1. Wood, Howard A.: Fracture Control Procedures for Aircraft Structural Integrity. AFFDL-TR-71-89, U.S. Air Force, July 1971. (Available from DDC as AD 731565.)
2. Wilhem, D. P.: Fracture Mechanics Guidelines for Aircraft Structural Applications. AFFDL-TR-69-111, U.S. Air Force, Feb. 1970.
3. Anon.: Fracture Control of Metallic Pressure Vessels. NASA Space Vehicle Design Criteria (Structures). NASA SP-8040, 1970.
4. Anon.: Stress-Corrosion Cracking in Metals. NASA Space Vehicle Design Criteria (Structures). NASA SP-8082, 1971.
5. Anon.: Solid Rocket Motor Metal Cases. NASA Space Vehicle Design Criteria (Chemical Propulsion). NASA SP-8025, 1970.
6. Anon.: Liquid Rocket Tanks and Components. NASA Space Vehicle Design Criteria (Chemical Propulsion). NASA SP-8088, 1972.
7. Anon.: Structural Design Criteria Applicable to a Space Shuttle. NASA Space Vehicle Design Criteria (Structures). NASA SP-8057, 1971.
8. Anon.: Preliminary Criteria for the Fracture Control of Space Shuttle Structures. NASA Space Vehicle Design Criteria (Structures). NASA SP-8095, 1971.
9. Guy, L. D.; Mershon, F. E.; and Snyder, R. E.: The Use of Linear Elastic Fracture Mechanics in Viking Pressure Vessel Design. Technology Today and Tomorrow, Proceedings of Eighth Space Congress, vol. II, Canaveral Council of Technical Societies, c.1971, pp. 7-1 - 7-8.
10. Bhatt, S. J.: Fracture Mechanics Evaluation of Stress Intensity Factors for Various Crack Geometries and Loading Conditions. WAPD-TM-976 (Contract AT-11-1-GEN-14), Bettis Atomic Power Lab., Dec. 1970.
11. Paris, Paul C.; and Sih, George C.: Stress Analysis of Cracks. Fracture Toughness Testing and Its Applications, Spec. Tech. Publ. No. 381, Amer. Soc. Testing Mater., c.1965, pp. 30-83.
12. Wilson, William Kent: Combined Mode Fracture Mechanics. Ph. D. Thesis, Univ. of Pittsburgh, 1969.